Full length article

Natural two-dimensional pyrophyllite: Nanoscale lubricant, electrical insulator and easily-machinable material

Borislav Vasić [a],[*], Radoš Gajić [a], Ivana Milošević [a], Žarko Medić [a], Marina Blagojev [b], Marko Opačić [a], Aleksandar Kremenović [c], Dejan Lazić [d]

[a] *Institute of Physics Belgrade, University of Belgrade, Pregrevica 118, 11080 Belgrade, Serbia*
[b] *Faculty of Mining and Geology, University of Belgrade, Đušina 7, 11000 Belgrade, Serbia*
[c] *Laboratory of Crystallography, Faculty of Mining and Geology, University of Belgrade, Đušina 7, 11000 Belgrade, Serbia*
[d] *Biotech Engineering D.O.O, Golsvordijeva 32, 11000 Belgrade, Serbia*

A R T I C L E   I N F O

A B S T R A C T

Pyrophyllite, with the chemical formula $Al_2Si_4O_{10}(OH)_2$, is a naturally occurring and abundant van der Waals mineral belonging to the group of phyllosilicates. It is very soft, layered crystal used for sculpting and an excellent electrical and thermal insulator aimed for the operation at high pressure and temperature. Here, for the first time, two-dimensional (2D) pyrophyllite obtained by both mechanical and liquid phase exfoliation is presented and investigated at the nanoscale. The layered structure provides low friction coefficient of around 0.1 as measured by friction force microscopy. The wear properties, studied by atomic force microscope (AFM) based scratching, are distinctly different from graphene. Since the wear is initiated at low normal forces, 2D pyrophyllite can be routinely carved by the AFM tip and it is suitable for scratching based nanolithography. According to our optical measurements, 2D pyrophillite is an insulator with a band gap of ∼ 5.2 eV. Local current measurements by conductive AFM reveal that 2D pyrophyllite flakes behave as efficient electrical insulators with a breakdown voltage of around 6 MV/cm. Therefore, the obtained results indicate possible applications of 2D pyrophyllite as a low-cost electric insulator and lubricant, as well as an easily-machinable material at the nanoscale.

1. Introduction

Layered materials are usually defined as a special crystal class existing in the form of weakly stacked atomic layers, like graphene in graphite. General property of these materials are the strong in-plane bonds and very weak interactions perpendicular to the planes, typically of the van der Waals type. Therefore, layered materials that can be exfoliated into atomically thin layers are often called van der Waals materials. Two dimensional (2D) materials concerns crystalline solids consisting of a single or few atomic layers. Huge interest for them started when large graphene flakes were isolated for the first time in 2004 by Novoselov et al. using mechanical exfoliation [1]. Extraordinary properties of graphene [2] triggered the search for new 2D materials. Nowadays hundreds of different 2D materials beyond graphene have been devised and thoroughly investigated because of their extraordinary properties that are not present in corresponding counterpart bulk materials. As a result, 2D materials find numerous applications in nanoelectronics, nanophotonics and optoelectronics, spintronics, sensing and many other fields [3–5].

After the discovery of graphene, the second generation of 2D materials, which includes hexagonal boron nitride, 2D transition metal dichalcogenides (such as MoS_2, WS_2, $MoSe_2$, WSe_2, $MoTe_2$) and functionalized graphene, quickly appeared [6–11]. The third-generation of 2D materials includes elemental analogues of graphene such as silicene, germanene, stanene, phosphorene [12], as well as with 2D transition metal carbides and carbonitrides (MXenes) [13], 2D silicon dioxide [14], and minerals [15]. Interestingly, many of them were firstly discovered by numerical calculations, and afterwards, experimentally obtained [16].

The most of 2D materials are synthetic, for instance large-scale 2D materials are commonly prepared by chemical vapour deposition. On the other hand, natural van der Waals minerals exist in most classes of 2D materials like semi-metallic graphite and semiconducting molybdenite MoS_2 and tungstenite WS_2. In recent years, a new family of 2D materials has appeared. It is based on layered natural minerals as a source of 2D materials [15]. This family includes 2D insulating materials based on phyllosilicates such as talc [18–24], muscovite (mica) [25],
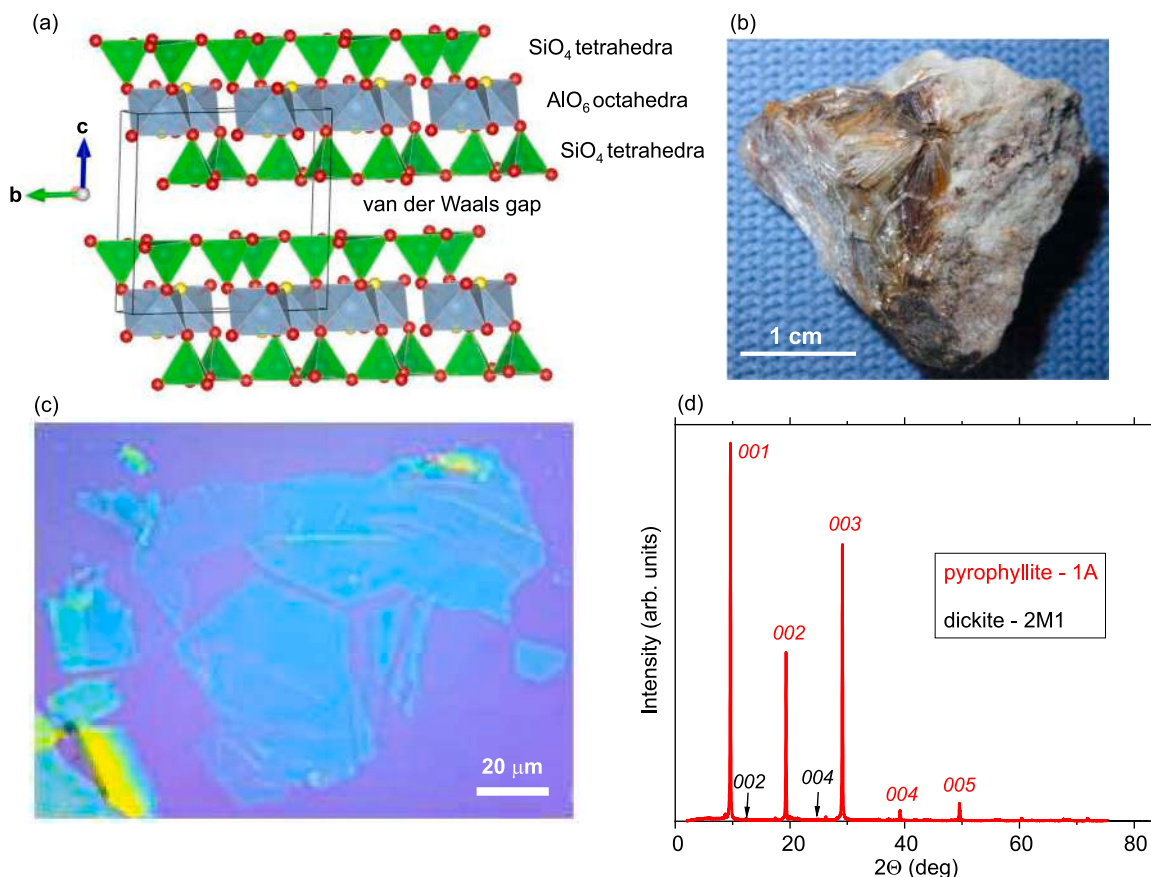

Fig. 1. (a) Polyhedral representation of pyrophyllite-1A structure: SiO$_4$ tetrahedra in green, AlO$_6$ octahedra in blue, oxygen atoms in red, OH group in yellow. The unit cell is outlined in black. VESTA program [17] was used for three-dimensional visualization of the crystal structure. (b) Optical image of the crystalline pyrophyllite used in this study. (c) Optical micrograph of mechanically exfoliated 2D pyrophillite flakes. (d) XRPD pattern of bulk pyrophyllite crystal which contains pyrophyllite-1A (PDF card # 01-075-0856) and small amount (near detection limit) of dickite-2M1 (PDF card # 00-058-2002). Most intense *hkl* reflections are marked.

biotite [26], vermiculite [27], clinochlore [28], and phlogopite [29], as well as 2D magnetic materials such as cylindrite [30] and iron-rich talc [31]. Furthermore, semiconducting van der Waals mineral franckeite has been used for the exfoliation of 2D van der Waals heterostructures [32–34]. Therefore, 2D materials can be obtained directly from natural minerals by just simple exfoliation and without complex synthetic procedures. As a result, search of 2D materials among natural minerals can be particularly interesting. Furthermore, clay minerals are abundant in Earth crust and therefore they serve as cost-effective sources of 2D materials. This mainly concerns phyllosilicates or layered silicates such as talc, pyrophyllte, kaolinite, gibbsite, etc., which are the most common and abundant clays.

Pyrophyllite (from Greek pyro—fire and phyllos—a leaf) is natural van der Waals mineral which belongs to the talc–pyrophyllite family of phyllosilicates. It is a hydrous aluminum silicate with the chemical formula Al$_2$Si$_4$O$_{10}$(OH)$_2$. Single layer of pyrophyllite consists of the AlO$_6$ octahedral sheet sandwiched between two SiO$_4$ tetrahedral layers (Fig. 1(a)). Pyrophyllite is a chemically inert material, good electrical and thermal insulator with a high melting point [35] and with a fairly high dielectric constant [36,37]. As a clay mineral, it is abundant and inexpensive. Therefore, it is widely used in refractories, high-grade ceramics, electric insulators, and as a filler in order to improve properties of paper, plastic, rubber, paint and other mixtures [35]. As a van der Waals material, pyrophyllite has a lamellar structure which indicates good frictional properties and its applications as a lubricant [38]. It is very soft mineral [35] which provides easy machining and making of various profiles, while at the same time, it can withstand large pressures. Therefore, bulk pyrophyllite mineral exhibits interesting properties with a broad range of potential applications. Still,

its 2D form has not been studied so far, although small flakes of few layer pyrophyllite have been obtained by liquid phase exfoliation [39], whereas thermal exfoliation was investigated as well [40], but not in the context of 2D layers.

Here we present our report on 2D pyrophyllite with the focus on its properties related to potential applications as 2D electric insulator, lubricant and material suitable for nanolithography. Using mechanical and liquid phase exfoliation (LPE), we routinely fabricated few-layer pyrophyllite which can be exfoliated down to single-layer thickness. The initial characterization was done by X-ray powder diffraction (XRPD), Raman spectroscopy, UV–VIS spectroscopy, and optical microscopy. Afterwards, we focused on nanoscale mechanical and electrical properties of 2D pyrophyllite such as friction, wear, nanoscale machining, as well as insulating properties and dielectric breakdown, which were investigated by atomic force microscopy (AFM) based methods.

2. Experimental methods

2.1. Sample preparation

Here we used the crystalline pyrophyllite from Hillsborough, Orange County, North Carolina, USA (Fig. 1(b)). 2D pyrophyllite flakes were obtained by the mechanical exfoliation [41] onto SiO$_2$/Si substrate (with 300 nm thick SiO$_2$). Briefly, thick pyrophyllite flakes were separated from the bulk crystal by an adhesive tape. These flakes were further thinned by multiple peeling against two pieces of the tape, and finally transferred onto the substrate. The flakes of interest were selected by optical microscopy (typical optical micrograph depicted in Fig. 1(c)).

The starting material for LPE of pyrophyllite was ground pyrophyllite crystal (Hillsborough mine, Orange County, North Carolina, USA). Its dispersion was obtained in N-N-Dimethylformamide (DMF, Sigma Aldrich, product no. D4551), while the initial concentration of pyrophillite was 10 mg/mL (in 10 mL cylindrical vial). The solution was then sonicated in a low-power ultrasonic bath for 12 h. The resulting yellowish dispersion was centrifuged for 15 min at 1000 rpm. In order to fabricate pyrophyllite films from the obtained dispersion, Langmuir–Blodgett Assembly (LBA) technique at a water–air interface was used. This technique was previously employed for the preparation of graphene films as well [42,43]. In the first step, a small amount of pyrophyllite dispersion in DMF was added at the water–air interface. Then, after the pyrophyllite film was formed at the interface, it was slowly picked up by desired substrate. Three different substrates were used: SiO_2/Si for AFM measurements (morphological characterization), Au-coated SiO_2/Si for C-AFM measurements (current maps and breakdown voltage), and quartz for UV–VIS spectroscopy.

2.2. XRPD measurements, Raman and UV–VIS spectroscopy

The structural characterization was done by XRPD which was conducted at room temperature on Rigaku Smartlab X-ray Diffractometer in $\theta-\theta$ geometry (the sample in the horizontal position) in parafocusing Bragg–Brentano geometry using D/teX Ultra 250 strip detector in 1D standard mode with $CuK\alpha_{1,2}$ radiation source (U = 40 kV and I = 30 mA). The XRPD pattern was collected in $2-90°$ 2θ range, with the step of $0.01°$, and data collection speed of $6°/min$. The pyrophyllite sample was spinning in the horizontal plane with the speed of 60 rounds per minute. The low background single crystal silicon sample holder was used to minimize the background. The PDXL2 integrated XRPD software (Version 2.8.30; Rigaku Corporation) was employed for XRPD data treatment.

Raman scattering measurements were performed on Tri Vista 557 Raman system, in backscattering micro-Raman configuration. The 514.5 nm line of an Ar^+/Kr^+ gas laser was used as an excitation source. Laser power was less than 1 mW on a sample in order to minimize its local heating. A microscope objective with the 50x magnification was used for focusing the laser beam. All measurements were performed at ambient conditions.

Optical transmittance of the pyrophyllite film (obtained by liquid phase exfoliation) was measured by ultraviolet–visible (UV–VIS) spectrophotometer Beckman Coulter DU 720 in the range from 200 to 900 nm.

2.3. AFM measurements

The morphological characterization of 2D pyrophillite was done by imaging in the tapping AFM mode. Friction was measured using friction force microscopy, by recording the lateral force which corresponds to the lateral torsion of the AFM cantilever during scanning in the contact AFM mode. The friction signal was calculated as a half difference between lateral forces measured in forward and backward scan direction. The measurements were done using NSG01 probes (nominal stiffness 5 N/m) from NT-MDT, while the applied normal load was up to ~300 nN, well below the threshold force needed to initiate wear. The wedge calibration of frictional forces was used in order to transform measured lateral signal into frictional forces [44].

Wear properties were studied by scratching the pyrophyllite flakes in the AFM contact mode. Square domains were scratched with an increased normal force (applied by the AFM tip) from the bottom to the top of the scan regions. The maximal normal load needed to initiate wear was around 1 μN. When a wear was initiated, the normal force was held constant. Mechanically robust and stiff, diamond coated probes DCP11 (nominal stiffness 11.5 N/m) from NT-MDT were used since they allowed high normal forces needed for scratching as well as subsequent imaging of scratched areas in the tapping AFM mode.

The AFM based nano-lithography was done using diamond coated probes HA_HR_DCP (nominal stiffness 35 N/m) from NT-MDT in three modes: nanoindentation and two lithographic modes, vector and raster. The nanoindentation mode is very similar to the measurement of force–displacement curves. The AFM scanner holding a sample was moved only vertically (without scanning in the horizontal plane) toward the AFM tip in order to induce a point-like deformation in pyrophyllite. For this purpose, the applied normal load was around 6 μN. In the lithographic modes, pyrophillite surface was scratched in the AFM contact mode according to predefined templates. In the case of the vector lithography, the templates were defined by discrete lines only, whereas in the case of the raster lithography, the square domains were taken for simplicity. During the nano-lithography, two force levels were applied. The low force level was applied along trajectories of the AFM tip which should stay intact (the movements between discrete line segments to be scratched, from the initial position to the first line segment, and from the last line segment back to the initial position). On the other hand, a high force level in the range ~2–6 μN was applied on segments which are to be scratched. The scratching velocity was around 0.2 μm/s. It was significantly decreased compared to the scanning speed in order to provide an efficient lithography.

The study of insulating properties and dielectric breakdown requires 2D pyrophyllite flakes placed between two metallic electrodes. In order to make possible study at the nanoscale, conductive AFM (C-AFM) was employed. For this purpose, the pyrophyllite flakes obtained by LPE method were deposited on a gold substrate. Then, a metallic AFM tip on the top of a pyrophyllite flake served as a top electrode, while the underlying gold was a bottom electrode. The bias voltage was applied on the gold, while the AFM tip in contact with the pyrophyllite flakes was (virtually) grounded. The current imaging was done by scanning in C-AFM mode, using highly doped and conductive, diamond coated probes DCP11, and simultaneously recording topography and local current. Dielectric breakdown was examined by measuring local I/V curves at single point, while the bias voltage was swept in a range ±10 V.

3. Results and discussion

3.1. Structural and vibrational properties

The results of XRPD measurements presented in Fig. 1(d) show that the specimen predominantly contains crystalline pyrophyllite-1A (PDF (Powder Diffraction File) card # 01-075-0856), whereas a small amount (near detection limit) of dickite-2M1 (PDF card # 00-058-2002) was also identified. The most intense reflections in the XRPD pattern of the dominant phase are 00l ($l = 1-5$) which is in accordance with the layered structure of pyrophyllite-1A. The XRPD results indicate that a crystalline pyrophyllite sample (Fig. 1(b)) has a triclinic lattice and 2:1 structure (two tetrahedral sheets and one octahedral sheet) depicted in Fig. 1(a). The refined unit cell parameters for pyrophyllite-1A are the following (estimated standard deviations in parenthesis): $a = 5.14(2)$ Å, $b = 8.99(4)$ Å, $c = 9.28(4)$ Å, $\alpha = 91.88(8)°$, $\beta = 99.36(15)°$, $\gamma = 89.16(15)°$, $V = 423(3)$ Å^3. The refined values, within an experimental error, are in a very good agreement with the values obtained for pyrophyllite-1A (OH group in the structure) in both single crystal XRD experiment [45] and powder XRD experiment [46].

Raman spectra of the bulk crystalline pyrophyllite are presented in Fig. 2 in the spectral ranges from 50 to 1100 cm^{-1} and 3600 to 3750 cm^{-1}. The first range describes the fundamental vibrations of all phyllosilicates, whereas the second one displays the vibrations of the H_2O/OH group [47–49]. Our spectra are fully consistent with the previous published Raman spectra of crystalline pyrophyllite [47]. They contain all fundamental modes up to 1100 cm^{-1} as well as H_2O/OH peak at 3670 cm^{-1}. Details and the full assignment of all modes could be found elsewhere [47].
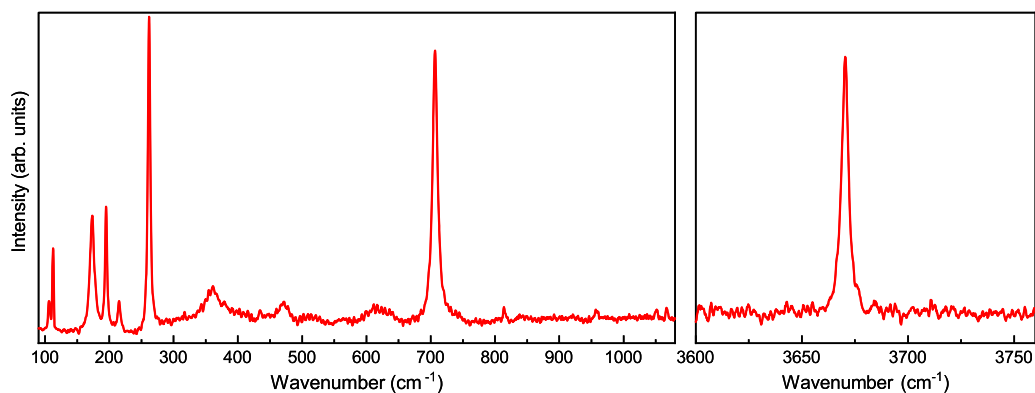
Fig. 2. Raman spectrum of a bulk pyrophyllite for two spectral ranges: the fundamental vibrations of phyllosilicates (left) and the H_2O/OH range (right).
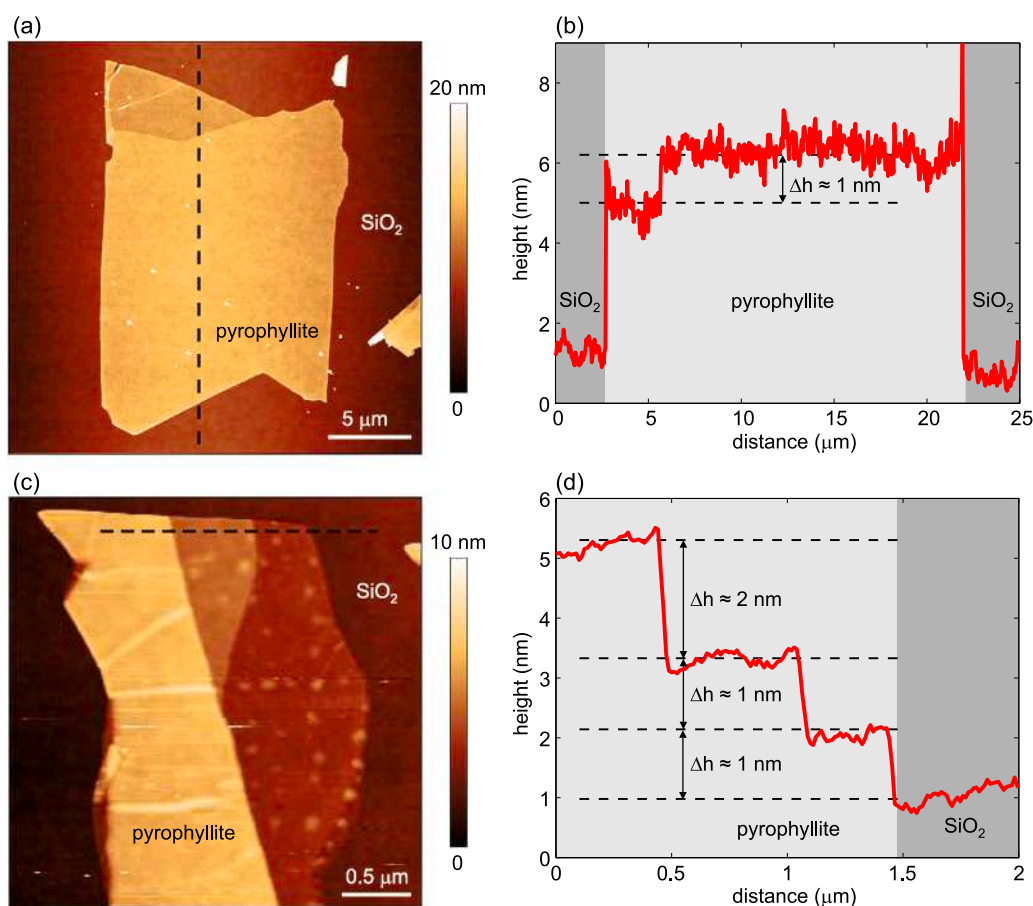

Fig. 3. (a), (c) Topographic images of pyrophillite flakes mechanically exfoliated on Si/SiO_2 with (b), (d) corresponding height profiles along dashed lines with indicated characteristic step heights.

3.2. Morphology

Fig. 3(a) depicts the topography of a typical flake obtained by mechanical exfoliation, with the height profile given in Fig. 3(b). It is a few-layer pyrophyllite with a thickness of ∼5 nm and an area of ∼15 × 20 μm^2. The root-mean-square roughness calculated on 5 × 5 μm^2 areas is only 0.6 nm indicating atomically flat surface free of residues. The height profile (Fig. 3(b)) reveals that a step height between two domains is only ∼1 nm.

The trilayer structure of the pyrophyllite unit cell displayed in Fig. 1(a) consists of AlO_6 octahedral sheet sandwiched between two SiO_4 tetrahedral layers. According to XRPD results, the thickness of the neutral trilayer is 6.39 Å, whereas the thickness of van der Waals

gap is 2.76 Å [45], measuring from the center of oxygen ions ($O^{2−}$). Accordingly, the effective thickness of the trilayer is around 9.2 Å, measuring from the top to bottom oxygen surfaces since we have to add two oxygen ion radii of 2.8 Å. Therefore, the thickness of single layer pyrophyllite measured by AFM should be around more or the same. The smallest thickness measured in our AFM experiments was always around 1 nm. The same minimal thickness was observed in AFM scratching based experiments as discussed below. Therefore, this value corresponds to the single layer of pyrophyllite. The small discrepancy between expected (around 9.2 Å) and measured thickness (around 1 nm) probably appears due to adsorbed water layer which is inevitable at ambient conditions and/or due to measurements done in
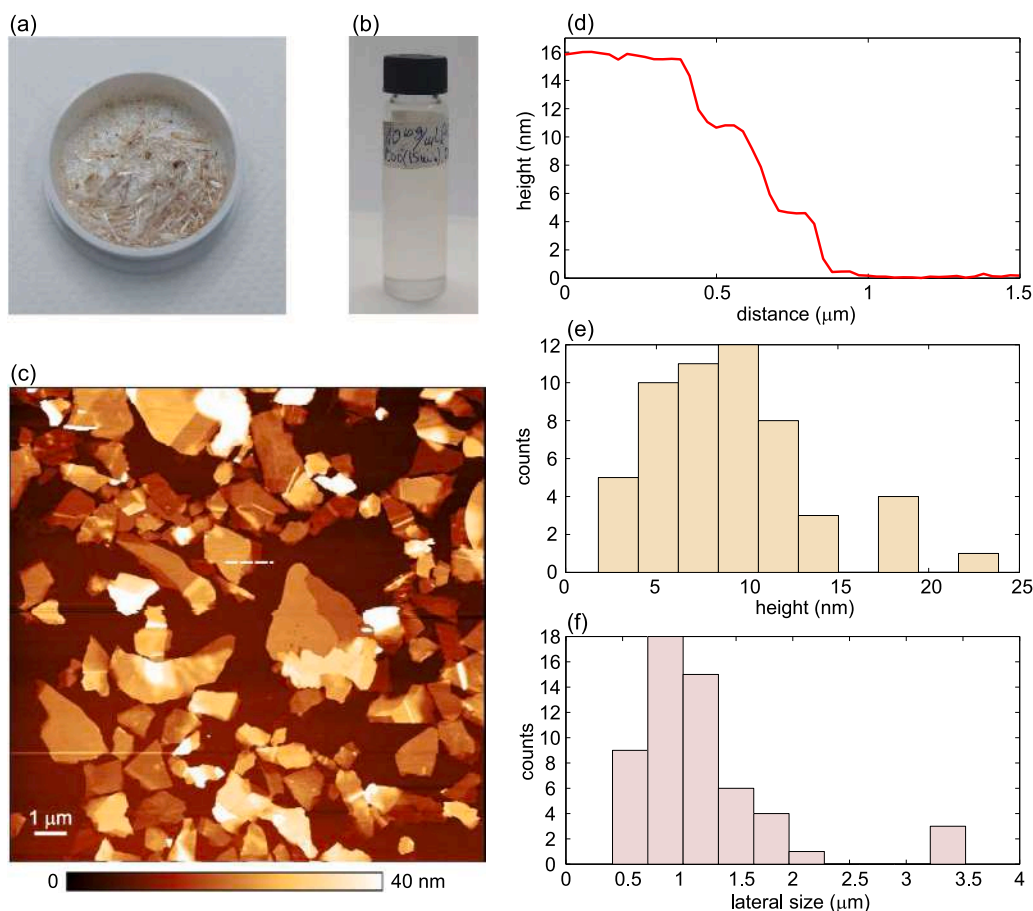
Fig. 4. (a) Ground pyrophyllite mineral used as a starting material for LPE and (b) the resulting dispersion employed for LBA. (c) Topographic image of pyrophillite flakes obtained by LPE and subsequent LBA on Si/SiO$_2$. (d) Height profile along the dashed line in (c). Histograms of (e) height and (f) lateral size of the flakes shown in (c).

tapping AFM mode, which commonly gives an increased step height on atomically thin layers [50].

Generally, we routinely exfoliated few layer pyrophillite flakes with the lateral size larger than 10 μm. On the other hand, yield of single layers was low, while their size was significantly smaller. One example is illustrated in Fig. 3(c). The corresponding height profile in Fig. 3(d) displays two single-layer step heights of ~1 nm, and the third step height of ~2 nm which corresponds to double-layer flake. As can be seen, the area of the single layer pyrophyllite is only several square micrometers.

The ground pyrophyllite crystal and its yellowish dispersion used in LPE are depicted in Fig. 4(a) and (b), respectively. Topography of 2D pyrophyllite obtained by the LPE method is depicted in Fig. 4(c). The height profile in Fig. 4(d) displays three step heights of ~5 nm. Samples produced by the LPE method consist of a network of flakes with a typical height of 5−15 nm (Fig. 4(e)) and lateral dimensions of ~1 μm (Fig. 4(f)). The flakes have well defined shapes, flat surface and regular edges. Although they are thicker and smaller compared to those fabricated by the mechanical exfoliation, LPE method provides large scale production of 2D pyrophyllite. At the same time, the LPE method can be easily adapted to various substrates. This was employed below in the study of insulating properties and dielectric breakdown of 2D pyrophyllite, where the flakes were deposited on a gold substrate.

3.3. Friction

Friction properties are analyzed on a small segment of the pyrophyllite layer surrounded by SiO$_2$ as depicted in Fig. 5(a). In the friction force map displayed in Fig. 5(b), the pyrophyllite is represented by

a dark contrast, thus indicating decreased friction compared to SiO$_2$. The height and friction force profiles from Fig. 5(c) reveal three times lower friction on the pyrophyllite. The same measurements were done for the normal force in the range ~30−330 nN. Average friction forces on both pyrophyllite and SiO$_2$ were calculated from the histograms of friction maps and the corresponding results are presented in Fig. 5(d). As can be seen, the friction force approximately linearly increases with the normal force in accordance with Amonton's law. The friction coefficients were calculated from the slopes of the linear fits (dashed lines in Fig. 5(d)). The obtained friction coefficient of the pyrophyllite flake $\mu_{pyr} = 0.12$ is more than four times lower than the friction coefficient of surrounding silicon-dioxide substrate ($\mu_{SiO_2} = 0.5$). At the same time, μ_{pyr} is very similar to the friction coefficient of graphene grown by chemical vapour deposition [51] and 2D talc [21]. Therefore, the presented results indicate good lubricating properties of few-layer thick pyrophyllite.

Generally, mechanical and liquid phase exfoliation give 2D layers with the same physical properties. The main difference between two methods is morphology of produced layers, the lateral size of the flakes before all. Therefore, we expect the same friction properties of pyrophyllite obtained by both methods. Additional friction measurements on LPE pyrophyllite prove this predictions. The results presented in figure S1 of Supplementary material show that pyrophyllite flakes obtained by LPE has a low friction coefficient of around 0.14, that is, very similar to pyrophyllite obtained by the mechanical exfoliation (0.12). Compared to the surrounding silicon-dioxide substrate, the friction is again decreased by around four times.

In our previous manuscript [21] we investigated friction as a function of talc thickness in detail. Talc friction reduces with number of layers (talc thickness), which is similar to other 2D materials, since so
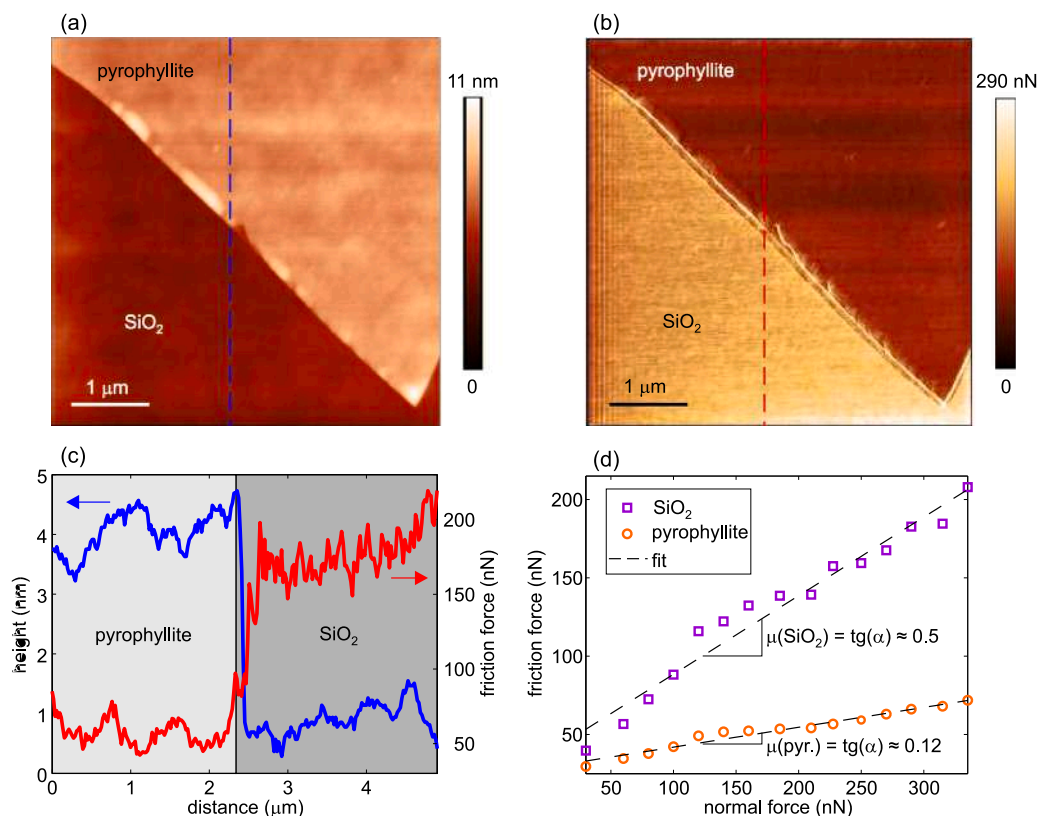
Fig. 5. (a) Topography and (b) friction force map of pyrophyllite flake on Si/SiO_2. (c) Height and force profiles along dashed lines in (a) and (b), respectively. (d) Average friction force (calculated from histograms of friction maps such as the one presented in (b)) as a function of the normal force applied by the AFM tip. Friction coefficients were calculated as slopes of the linear fits represented by dashed lines.

called puckering effect, responsible for the friction of 2D materials, is less pronounced for thicker layers due to larger bending rigidity. In the case of talc, this dependence is rather weak, since single layer is 1 nm thick and already consists of three atomic planes. Pyrophyllite and talc belong to the family of 2:1 phyllosilicates. Their chemical formulas are almost identical (pyrophyllite - $Al_2Si_4O_{10}(OH)_2$, talc - $Mg_3Si_4O_{10}(OH)_2$) and they have practically the same structure (octahedral plane with metallic (Al or Mg) ion sandwiched between two tetrahedral SiO layers). The thickness of the single layer (around 1 nm) is similar in both materials. Therefore, dependence of the friction as a function of pyrophyllite thickness should be the same as for talc. This conclusion is further confirmed in figure S1(b) of Supplementary material depicting friction map of pyrophyllite flakes produced by LPE. Although their thicknesses vary in a broad range from only several nanometers to several tens of nanometers, the friction force on the pyrophyllite is associated with a single peak in the corresponding histogram given in figure S1(c) (the observed dispersion (width of the histogram peak) is very similar to the dispersion of the friction force measured on SiO_2 substrate).

3.4. Wear

The next step was to analyze wear properties and behavior of 2D pyrophyllite for high normal load applied by the AFM tip during scanning in contact mode. Fig. 6(a) displays the topography recorded after the AFM scratching of the central square domain. From the right, left, and top side, the scratched domain is surrounded by walls (represented by a bright contrast) formed from the material deposited by the AFM tip. Enlarged topographic image of the scratched area is presented in Fig. 6(b) together with the characteristic height profile in Fig. 6(c). At the bottom of the figure, the pyrophyllite surface is flat and without visible wear scars due to low normal load. At the same

time, the lateral force recorded during the AFM scratching is low and approximately constant as depicted in Fig. 6(d) and (e). Since there is no wear, the lateral force corresponds to the friction between the AFM tip and pyrophyllite.

In the experiment, the normal load was increasing as the AFM tip was moving from the bottom to the top. For high enough normal load of around 1.1 μN, the wear was initiated and afterwards, the normal load was held constant. As a result of the wear, pyrophyllite surface became crumpled with many local holes and bumps. The holes present local depressions made by peeling pyrophyllite layers, while bumps are local hills formed out of the material previously peeled off (Fig. 6(c)). The height profile in Fig. 6(c) reveals several step heights of ~1 nm. They correspond to single layer of pyrophyllite which therefore indicates that the AFM scratching leads to layer-by-layer peeling. The lateral force during the scratching (Fig. 6(d) and (e)) is increased compared to the bottom area without wear scars. Although this is expected due to higher normal load applied by the AFM tip, the lateral force profile is not flat anymore, but strongly oscillating. Obviously, bright puddles in the force map (Fig. 6(d)) and peaks in the force profile (Fig. 6(e)) correspond to strongly increased lateral force required for tearing and peeling of pyrophyllite layers.

According to the presented results, during the AFM scratching, pyrophyllite behaves in a different manner compared to well known 2D materials such as graphene and transition metal dichalcogenides (MoS_2, and WS_2) [52,53]. The scratching of these materials is associated with wrinkling at the initial stage, while at higher normal loads, it is followed by a sudden tearing along the direction of the AFM tip movement, and finally by a peeling of large segments and their folding. On the other hand, in the case of pyrophillite, exfoliated segments made by the AFM scratching are small, not folded, and they form local bumps of irregular shapes. Recently, similar results have been obtained for muscovite (mica), another phyllosilicate van der Waals mineral, and
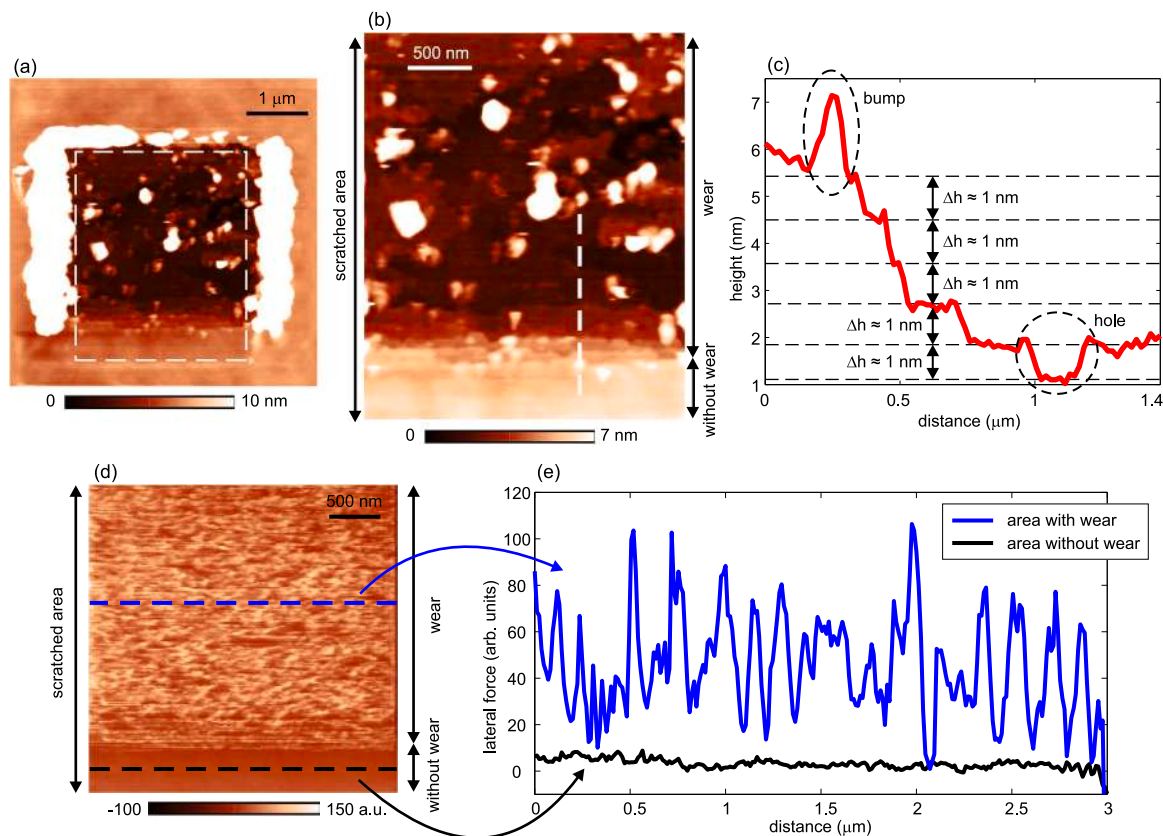
Fig. 6. (a) Topographic image of a pyrophyllite flake after the AFM scratching. (b) The topographic image of the domain encircled by the dashed line in (a) focusing on the scratched area only. (c) The height profile along the dashed line in (b) with indicated step heights of ∼1 nm and local hole/bump (encircled by dashed lines). (d) The lateral force map recorded during the AFM scratching. (e) The lateral force profiles along two dashed lines in (d), standing for the area with and without wear.

the observed difference in wear properties were explained by different mechanical properties [53]. Accordingly, significant thickness of single layer of pyrophyllite (∼1 nm) and large bending rigidity of ∼70 eV [54] limit its flexibility and folding. At the same time, Young's modulus (modulus of elasticity) of ∼100 GPa [55,56] and tensile strength less than 10 GPa [56,57] are much lower than in the case of graphene and transition metal dichalcogenides, which indicates much brittle structure of pyrophyllite. This can be indirectly confirmed by comparing threshold normal loads needed to initiate wear. In the case of graphene and transition metal dichalcogenides, the threshold load is at least several μN [52,53], while in the case of pyrophyllite, it is much lower, around 1 μN. As a result, pyrophillite layers are easily torn into small pieces during AFM scratching.

Wear of 2D materials is always started from their edges (these are weak points for wear), and not on homogeneous (flat) 2D flakes [58]. Since LPE 2D materials are associated with small flakes and huge number of exposed edges, their wear resistance is determined by their edges [59], and it is always lower that the wear resistivity of 2D material itself. For this reason, wear of LPE pyrophyllite was not studied here.

3.5. Nanoscale machining and nanolithography

As mentioned in the previous section, the AFM scratching of graphene and transition metal dichalcogenides generally leads to their peeling, but not to local cutting along directions defined by the movement of the AFM tip. On the other hand, lower elasticity and tensile strength of 2D pyrophyllite indicate that it could be suitable material for AFM scratching based nanolithography. The results of the nanolithography of 2D pyrophyllite are presented in Fig. 7. Three basic shapes and characteristic height profiles are presented for the following

cases: the hole made by nanoindentation (Fig. 7(a–b)), the trench carved out by line scratching (Fig. 7(c–d)), and the square crater made by raster scratching (Fig. 7(e–f)). As can be seen, the AFM tip induces local carving of a pyrophyllite flake. This process is associated with the tearing of the pyrophyllite into small pieces, which are then deposited around the tip during its motion. The deposited material was then removed by several additional scans in contact AFM mode (not shown here). They were done at lower normal load, which was insufficient to cause pyrophyllite cutting and wear, but high enough to provide pushing of the deposited material by the AFM tip.

As can be seen, 2D pyrophyllite is efficiently carved by applying a local pressure at single point (Fig. 7(a)) as well as during AFM tip motion (Fig. 7(c)). Making of holes on wider areas is successfully achieved by AFM scratching along array of parallel lines (Fig. 7(e)). Depth of created objects was controlled by applied normal load as illustrated in Fig. 7(e–f) showing that a deeper crater was formed by a higher normal force. The width of the line trench in Fig. 7(c) is 150−300 nm. It is strongly influenced by the width of the diamond coated probes employed here, and it is reasonable to expect that a better resolution and more narrow features could be created with sharper AFM tips.

3.6. Electronic bandgap

Electronic bandgap was estimated from UV–VIS spectroscopic measurements. For that purpose, a large-area pyrophyllite film was obtained by LPE. The film thickness was around 20 nm as determined by AFM measurement. Transmittance through the pyrophyllite film for wavelengths in the range 200−900 nm is displayed in the inset of Fig. 8. As can be seen, the film is transparent with the transmittance in the visible region above 97%. The obtained transmittance spectrum allows the calculation of an intrinsic optical absorption coefficient
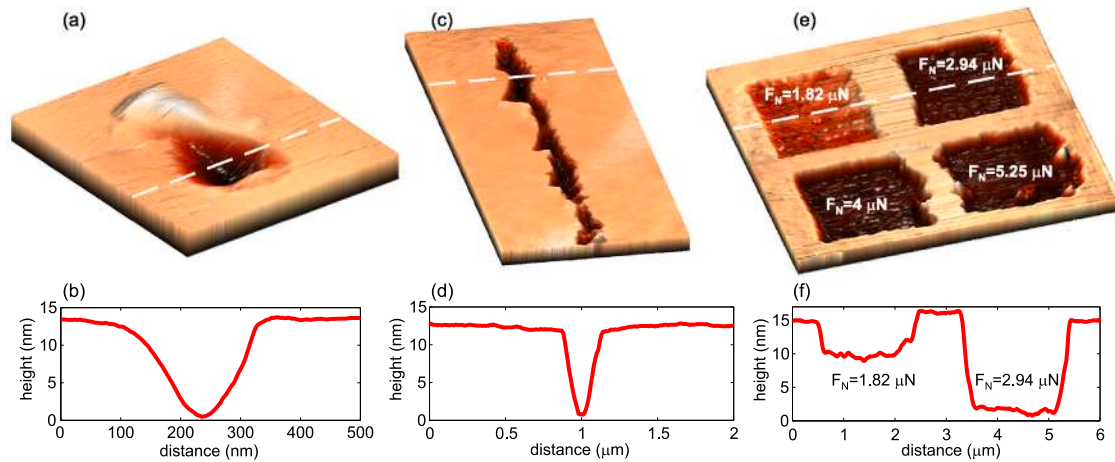
Fig. 7. The topographic images and the height profiles for three characteristic structures made by nanolithography of pyrophyllite: (a–b) single hole obtained by nanoindentation, (c–d) trench made by the AFM scratching along single line, (e–f) four square domains made by raster scratching.
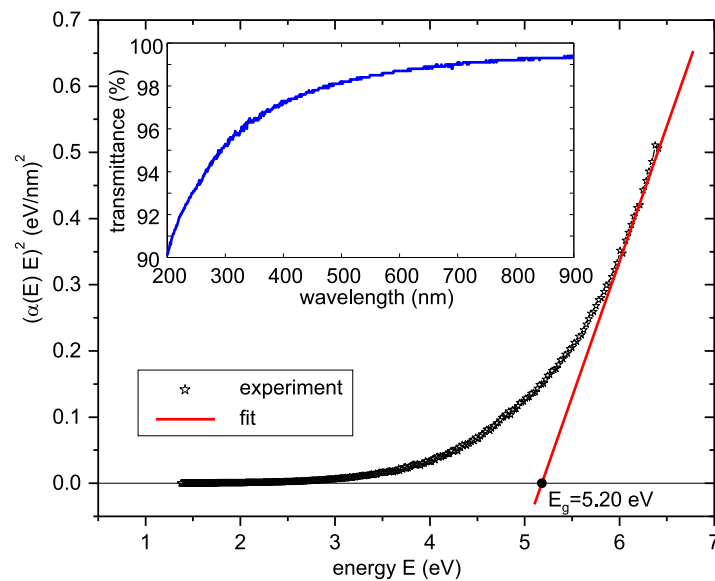

Fig. 8. The Tauc plot with estimated bandgap energy of ~5.20 eV obtained from the transmittance (plot in the inset) through ~20 nm thick pyrophyllite film obtained by LPE on a quartz substrate.

$\alpha(E)$. Namely, the well known Bourguer–Lambert–Beer (BLB) law gives the absorption coefficient as $\alpha_{\text{BLB}}(E) = (1/d)\ln(1/T)$, where d is the film thickness and T the measured transmittance [60]. This is the simplest law representing the optical absorption in semiconductors, and in practice the BLB law turned out to be more than a good enough approximation.

For the estimation of a direct optical bandgap E_g, we used the Tauc method [61] and the standard fitting procedure of the linear part of $(\alpha(E)E)^2$ (Tauc plot), i.e. $(\alpha(E)E)^2 = \text{const} \cdot (E - E_g)$. The Tauc plot displaying $(\alpha(E)E)^2$ as a function of the energy of incident light $E = h\nu$ (h is the Planck constant, ν is the frequency of incident photon) is given in Fig. 8. The plot indicates that the pyrophyllite film has a direct band gap of around 5.20 eV (the value obtained as the intersection point of the linear fit of the Tauc plot and x-axis). The obtained value is consistent with the theoretical value of 5.42 eV [55], whereas to best of our knowledge, this is the first experimentally obtained value of the pyrophyllite bandgap. The measured value is also close to the band gap of 2D hexagonal boron nitride (~6 eV) [62], which implies that pyrophyllite can be considered as efficient 2D insulator as well.

3.7. Insulating properties and dielectric breakdown

Hexagonal boron nitride has been a standard choice as insulator in 2D electronics [63–67]. Insulating properties and dielectric breakdown are usually explored by placing materials between two metallic electrodes in order to form a capacitor. Furthermore, C-AFM [68, 69] provides characterization at the nanoscale [63–65,70–72]. Recent studies have extended the family of 2D insulators to materials with improved properties, such as high-k van der Waals dielectrics [70].

In order to study dielectric properties, 2D pyrophyllite flakes obtained by LPE were deposited on a conductive substrate—thin gold film, which acted as a bottom electrode, while the AFM tip had a role of the top electrode. The topography image (Fig. 9(a)), corresponding current map (Fig. 9(b)), and characteristic profiles (Fig. 9(c)) reveal that pyrophyllite flakes with a thickness ranging from 3 nm to 22 nm are associated with a dark (black) contrast in the current map and zero current. The black color of pyrophyllite flakes in the current map in Fig. 9(b) is spatially homogeneous and therefore it does not contain current spikes which would indicate a possible dielectric breakdown. As a result, at the applied bias voltage $U = 2$ V, several nanometer thick pyrophyllite behaves as 2D insulator.
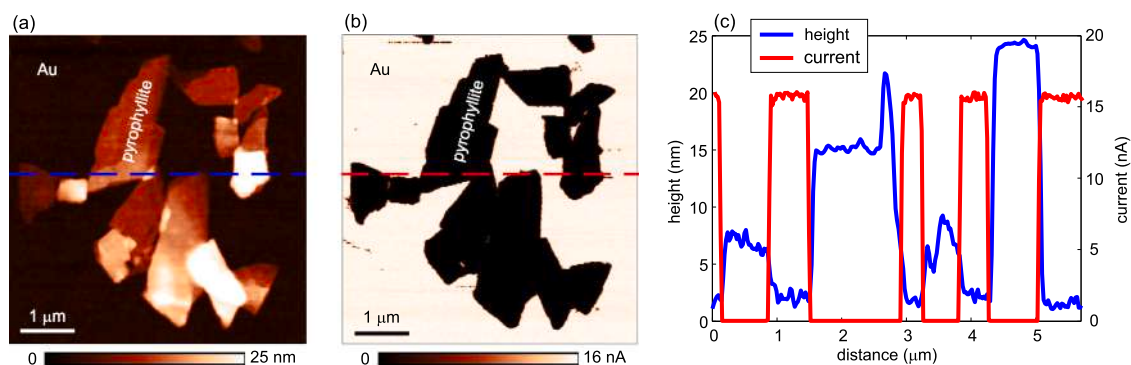
Fig. 9. (a) Topography and (b) the corresponding current maps of the pyrophillite flakes (obtained by LPE) deposited onto gold substrate. (c) The overlapped height and current profiles along the dashed lines in (a) and (b).
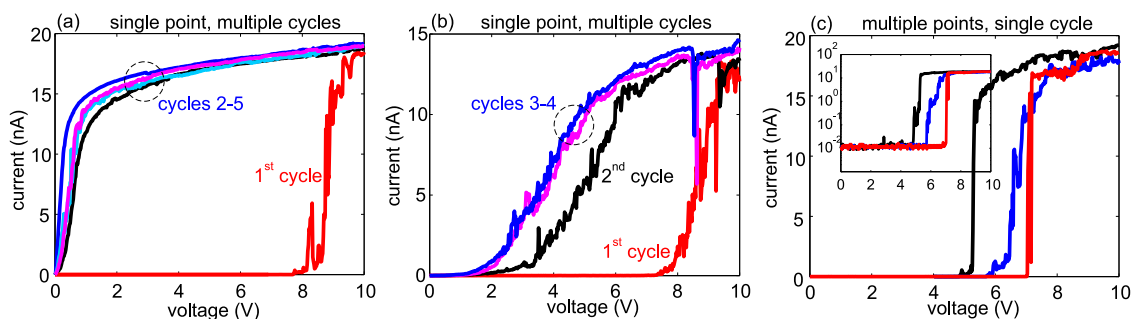

Fig. 10. (a) and (b) Successive cycles of the I/V curves measured at single point (but two different points). (c) The I/V curves (the first cycle only) measured at three different points of the same 10 nm thick pyrophyllite flake. The inset displays the I/V curves in semi-logarithmic scale.

In order to induce a dielectric breakdown, local I/V curves were measured in a wider voltage range. Typical results are given in Fig. 10(a) showing five successive cycles measured at the same point in the voltage range ±10 V. In the first cycle, the current is zero for voltages below ∼8 V. After reaching this threshold voltage, the current rapidly grows indicating dielectric breakdown. In the next cycles (2–5), for small voltages below ∼0.5 V, the current practically linearly increases with the applied bias voltage without any threshold (small nonlinearities around the zero voltage indicate possible Schottky barriers at the tip-sample contact, whereas the decreased slope of I/V curves for the voltages higher than ∼0.5 V is due to limitations of the current amplifier). Therefore, pyrophyllite does not behave as an insulator anymore and the metallic AFM tip is practically short circuited by the bottom gold electrode. In another case presented in Fig. 10(b), after the first cycle and dielectric breakdown, the region with zero (or near to zero) current becomes narrower indicating gradually decreasing the electronic bandgap of pyrophyllite.

Fig. 10(c) displays the I/V curves (only the first cycles shown) measured at three different points on the same flake. Rapid increase of the current is observed for threshold voltage in the range 5–7 V. The semilogarithmic scale displayed in the inset reveals that below the threshold voltage, the current is at almost constant level in the order of 10^{-2} nA. Taking into account that the thickness of examined pyrophyllite flake was ∼10 nm, the dielectric breakdown strength of 2D pyrophyllite is around 6 MV/cm. Although the obtained value is slightly below the strength of 2D hexagonal boron-nitride (∼8 MV/cm) [63], the presented results indicate that 2D pyrophyllite has good insulating properties and could be considered as an efficient 2D dielectric and gate oxide. One of the main issue with applications of hexagonal boron-nitride as 2D insulator is its low dielectric constant (∼3.9) responsible for high leakage currents. Although dielectric measurements of pyrophyllite are very rare [36,37], it is reasonable to expect lower leakage currents due to larger dielectric constant of pyrophyllite of around 10, which is also similar to the permittivity of the second

member of 2:1 family of phyllosilicates—talc [73]. Still, this has to be confirmed in future studies since leakage currents are influenced by other factors, such as layers' quality (absence of structural defects) and the conduction/valence band discontinuity with respect to the substrate.

Morphological changes after the dielectric breakdown of phyrophyllite are illustrated in Fig. 11. Two- and three-dimensional images of the pyrophyllite flake (Fig. 11(a) and (b), respectively) are recorded in tapping mode after 30 I/V curves measured in the range ±10 V at the point marked by the arrow. As can be seen, a small hole appeared at the point where the I/V curves were measured, while protrusions appeared around the hole. Height profile in Fig. 11(c) reveals that the hole depth is around 1 nm which corresponds to the thickness of single layer of pyrophyllite. The presented results demonstrate that high local electric fields causing dielectric breakdown lead to local fracture of 2D pyrophyllite. The hole depth equal to the thickness of single layer of pyrophyllite indicates that in the considered case, only the most top pyrophyllite layer was locally cut, while the pyrophyllite thickness is reduced at this point. Although additional measurements should be done in future studies, these results suggest layer-by-layer breakdown of pyrophyllite which was previously confirmed in the case of hexagonal boron nitride [65].

Friction measurements done after the induced dielectric breakdown demonstrate that the point where I/V curves were previously measured is associated with increased friction compared to the rest of pyrophyllite flake. The increased friction indicates some chemical and/or structural changes on the pyrophyllite surface which should be further explored in future studies.

4. Conclusions

In a summary, we have thoroughly characterized pyrophyllite crystal and then successfully fabricated 2D flakes by using both mechanical exfoliation and LPE. Pyrophyllite was exfoliated down to single layer.
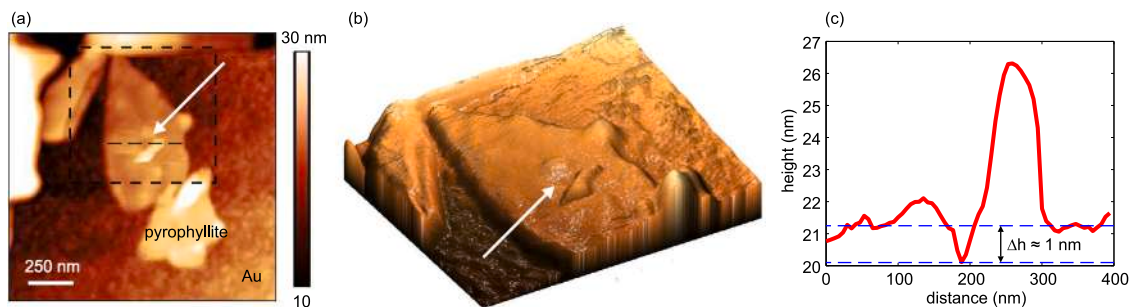
Fig. 11. (a) Two-dimensional topographic image of the pyrophyllite flake after 30 I/V curves measured in the range ±10 V at the point marked by the arrow. (b) Three-dimensional topographic image of the area marked by dashed square in (a). (c) Height profile along the dashed line marked in (a).

The lateral size of typical few-layer flakes was in the order of 10 μm in the case of the mechanical exfoliation, and 1 μm in the case of the LPE. 2D pyrophyllite has different wear properties compared to graphene and transition metal dichalcogenides. The wear is initiated at much lower normal loads while AFM based scratching leads to the tearing of pyrophyllite into small pieces, contrary to nano-exfoliation and folding, typically observed on graphene for example. Such wear properties provide easy machining at the nanoscale by the AFM tip which can be used as a tool for local carving and reshaping of pyrophyllite flakes. At the same time, 2D pyrophyllite has a low friction coefficient of ∼0.1 and therefore, it joins the family of other van der Waals layered materials as a potential candidate for ultra-thin coatings aimed for solid lubrication in micro- and nano-mechanical devices. The optical measurements on thin (∼20 nm) 2D pyrophyllite film obtained by the LPE reveal that it is transparent in the visible domain, with a large band gap of 5.2 eV. The local studies by C-AFM demonstrated that several nanometer thick pyrophyllite flakes behaves as 2D insulators with a high breakdown voltage of around 6 MV/cm, which is close to hexagonal boron-nitride. In addition, the larger dielectric permittivity of pyrophyllite compared to the boron nitride could provide lower leakage currents which needs to be confirmed in future studies.

CRediT authorship contribution statement

Borislav Vasić: Conceptualization, Investigation, Methodology, Formal analysis, Visualization, Writing – original draft. **Radoš Gajić:** Conceptualization, Investigation, Formal analysis, Resources, Supervision, Funding acquisition, Writing – review & editing. **Ivana Milošević:** Investigation, Visualization. **Žarko Medić:** Investigation, Visualization. **Marina Blagojev:** Investigation, Visualization. **Marko Opačić:** Investigation, Formal analysis, Visualization. **Aleksandar Kremenović:** Investigation, Formal analysis, Visualization, Writing – review & editing. **Dejan Lazić:** Investigation, Formal analysis.

Declaration of competing interest

The authors declare that they have no known competing financial interests or personal relationships that could have appeared to influence the work reported in this paper.

Data availability

Data will be made available on request.

Acknowledgments

Appendix A. Supplementary data

Supplementary material related to this article can be found online at https://doi.org/10.1016/j.apsusc.2022.155114.

References

[1] K.S. Novoselov, A.K. Geim, S.V. Morozov, D. Jiang, Y. Zhang, S.V. Dubonos, I.V. Grigorieva, A.A. Firsov, Electric field effect in atomically thin carbon films, Science 306 (2004) 666–669.

[2] A.K. Geim, K.S. Novoselov, The rise of graphene, Nature Mater. 6 (2007) 183–191.

[3] T.F. Avouris, P. nad Heinz, T. Low, 2D Materials, Cambridge University Press, 2017.

[4] Y.M. Jhon, J.H. Lee, 2D Materials for Nanophotonics, Elsevier, 2021.

[5] M. Houssa, A. Dimoulas, A. Molle, 2D Materials for Nanoelectronics, CRC Press, 2016.

[6] B. Radisavljevic, A. Radenovic, J. Brivio, V. Giacometti, A. Kis, Single-layer MoS₂ transistors, Nat. Nanotechnol. 6 (2011) 147–150.

[7] M. Xu, T. Liang, M. Shi, H. Chen, Graphene-like two-dimensional materials, Chem. Rev. 113 (2013) 3766–3798.

[8] S.Z. Butler, S.M. Hollen, L. Cao, Y. Cui, J.A. Gupta, H.R. Gutiérrez, T.F. Heinz, S.S. Hong, J. Huang, A.F. Ismach, E. Johnston-Halperin, M. Kuno, V.V. Plashnitsa, R.D. Robinson, R.S. Ruoff, S. Salahuddin, J. Shan, L. Shi, M.G. Spencer, M. Terrones, W. Windl, J.E. Goldberger, Progress, challenges, and opportunities in two-dimensional materials beyond graphene, ACS Nano 7 (2013) 2898–2926.

[9] R. Ganatra, Q. Zhang, Few-layer MoS₂: A promising layered semiconductor, ACS Nano 8 (2014) 4074–4099.

[10] S. Manzeli, D. Ovchinnikov, D. Pasquier, O.V. Yazyev, A. Kis, 2D transition metal dichalcogenides, Nat. Rev. Mater. 2 (2017) 17033.

[11] K. Zhang, Y. Feng, F. Wang, Z. Yang, J. Wang, Two dimensional hexagonal boron nitride (2D-hBN): synthesis, properties and applications, J. Mater. Chem. C 5 (2017) 11992–12022.

[12] S. Balendhran, S. Walia, H. Nili, S. Sriram, M. Bhaskaran, Elemental analogues of graphene: Silicene, germanene, stanene, and phosphorene, Small 11 (2015) 640–652.

[13] M. Naguib, V.N. Mochalin, M.W. Barsoum, Y. Gogotsi, 25Th anniversary article: MXenes: A new family of two-dimensional materials, Adv. Mater. 26 (7) (2014) 992–1005.

[14] S. Shaikhutdinov, H.-J. Freund, Ultrathin silica films on metals: The long and winding road to understanding the atomic structure, Adv. Mater. 25 (2013) 49–67.

[15] R. Frisenda, Y. Niu, P. Gant, M. Muñoz, A. Castellanos-Gomez, Naturally occurring van der waals materials, npj 2D Mater. Appl. 4 (2020) 38.

[16] T. Gould, S. Lebègue, T. Björkman, J.F. Dobson, 2D structures beyond graphene: The brave new world of layered materials and how computers can help discover them, in: F. Iacopi, J. Boeckl, C. Jagadish (Eds.), 2D Materials, Academic Press, 2016, pp. 1–33, Ch. 1.

[17] K. Momma, F. Izumi, *VESTA3* for three-dimensional visualization of crystal, volumetric and morphology data, J. Appl. Crystallogr. 44 (2011) 1272–1276.

[18] A.B. Alencar, A.P.M. Barboza, B.S. Archanjo, H. Chacham, B.R.A. Neves, Experimental and theoretical investigations of monolayer and few-layer talc, 2D Mater. 2 (2015) 015004.

[19] A. Harvey, J.B. Boland, I. Godwin, A.G. Kelly, B.M. Szydłowska, G. Murtaza, A. Thomas, D.J. Lewis, P. O'Brien, J.N. Coleman, Exploring the versatility of liquid phase exfoliation: producing 2D nanosheets from talcum powder, cat litter and beach sand, 2D Mater. 4 (2017) 025054.

[20] A.R. Cadore, E. Mania, A.B. Alencar, N.P. Rezende, S. de Oliveira, K. Watanabe, T. Taniguchi, H. Chacham, L.C. Campos, R.G. Lacerda, Enhancing the response of NH₃ graphene-sensors by using devices with different graphene-substrate distances, Sensors Actuators B 266 (2018) 438–446.

[21] B. Vasić, C. Czibula, M. Kratzer, B.R.A. Neves, A. Matković, C. Teichert, Two-dimensional talc as a van der Waals material for solid lubrication at the nanoscale, Nanotechnology 32 (2021) 265701.

[22] D. Nutting, G.A. Prando, M. Severijnen, I.D. Barcelos, S. Guo, P.C.M. Christiansen, U. Zeitler, Y. Galvão Gobato, F. Withers, Electrical and optical properties of transition metal dichalcogenides on talc dielectrics, Nanoscale 13 (2021) 15853–15858.

[23] G.A. Prando, M.E. Severijnen, I.D. Barcelos, U. Zeitler, P.C.M. Christiansen, F. Withers, Y. Galvão Gobato, Revealing excitonic complexes in monolayer WS$_2$ on talc dielectric, Phys. Rev. Appl. 16 (2021) 064055.

[24] A.C. Gadelha, T.L. Vasconcelos, L.G. Cançado, A. Jorio, Nano-optical imaging of in-plane homojunctions in graphene and MoS$_2$ van der Waals heterostructures on talc and SiO$_2$, J. Phys. Chem. Lett. 12 (2021) 7625–7631.

[25] A. Castellanos-Gomez, M. Wojtaszek, N. Tombros, N. Agraït, B.J. van Wees, G. Rubio-Bollinger, Atomically thin mica flakes and their application as ultrathin insulating substrates for graphene, Small 7 (2011) 2491–2497.

[26] X. Ji, Y. Kang, J. Ouyang, Y. Chen, D. Artzi, X. Zeng, Y. Xiao, C. Feng, B. Qi, N.Y. Kim, P.E. Saw, N. Kong, O.C. Farokhzad, W. Tao, 2D black mica nanosheets: Synthesis of ultrathin biotite nanosheets as an intelligent theranostic platform for combination cancer therapy, Adv. Sci. 6 (2019) 1970118.

[27] Z. Huang, T. Lan, L. Dai, X. Zhao, Z. Wang, Z. Zhang, B. Li, J. Li, J. Liu, B. Ding, A.K. Geim, H.-M. Cheng, B. Liu, 2D functional minerals as sustainable materials for magneto-optics, Adv. Mater. 34, 2110464.

[28] R. de Oliveira, L.A.G. Guallichico, E. Policarpo, A.R. Cadore, R.O. Freitas, F.M.C. da Silva, V. d. C. Teixeira, R.M. Paniago, H. Chacham, M.J.S. Matos, A. Malachias, K. Krambrock, I.D. Barcelos, High throughput investigation of an emergent and naturally abundant 2D material: Clinochlore, Appl. Surf. Sci. 559 (2022) 153959.

[29] A.R. Cadore, R. de Oliveira, R. Longuinhos, V. de C. Teixeira, D.A. Nagaoka, V.T. Alvarenga, J. Ribeiro-Soares, K. Watanabe, T. Taniguchi, R.M. Paniago, A. Malachias, K. Krambrock, I.D. Barcelos, C.J.S. de Matos, Exploring the structural and optoelectronic properties of natural insulating phlogopite in van der waals heterostructures, 2D Mater. 9 (2022) 035007.

[30] Y. Niu, J. Villalva, R. Frisenda, G. Sanchez-Santolino, L. Ruiz-González, E.M. Pérez, M. García-Hernández, E. Burzurí, A. Castellanos-Gomez, Mechanical and liquid phase exfoliation of cylindrite: a natural van der Waals superlattice with intrinsic magnetic interactions, 2D Mater. 6 (2019) 035023.

[31] A. Matković, L. Ludescher, O.E. Peil, A. Sharma, K.-P. Gradwohl, M. Kratzer, M. Zimmermann, J. Genser, D. Knez, E. Fisslthaler, C. Gammer, A. Lugstein, R.J. Bakker, L. Romaner, D.R.T. Zahn, F. Hofer, G. Salvan, J.G. Raith, C. Teichert, Iron-rich talc as air-stable platform for magnetic two-dimensional materials, npj 2D Mater. Appl. 5 (2021) 94.

[32] A.J. Molina-Mendoza, E. Giovanelli, W.S. Paz, M.A. Niño, J.O. Island, C. Evangeli, L. Aballe, M. Foerster, H.S.J. van der Zant, G. Rubio-Bollinger, N. Agraït, J.J. Palacios, E.M. Pérez, A. Castellanos-Gomez, Franckeite as a naturally occurring van der Waals heterostructure, Nature Commun. 8 (2017) 14409.

[33] M. Velický, P.S. Toth, A.M. Rakowski, A.P. Rooney, A. Kozikov, C.R. Woods, A. Mishchenko, L. Fumagalli, J. Yin, V. Zólyomi, T. Georgiou, S.J. Haigh, K.S. Novoselov, R.A.W. Dryfe, Exfoliation of natural van der Waals heterostructures to a single unit cell thickness, Nature Commun. 8 (2017) 14410.

[34] K. Ray, A.E. Yore, T. Mou, S. Jha, K.K.H. Smithe, B. Wang, E. Pop, A.K.M. Newaz, Photoresponse of natural van der Waals heterostructures, ACS Nano 11 (2017) 6024–6030.

[35] M.A. Ali, H.A.M. Ahmed, H.M. Ahmed, M. Hefni, Pyrophyllite: An economic mineral for different industrial applications, Appl. Sci. 11 (2021) 11357.

[36] G.W. Timco, Z. Dvorak, H.H. Schloessin, Dielectric properties of pyrophyllite as a function of water vapor pressure, J. Appl. Phys. 47 (1976) 2232–2233.

[37] E. Izci, The investigation of dielectric properties of pyrophyllite, Key Eng. Mater. 264–268 (2004) 1361–1364.

[38] E.W. Bucholz, X. Zhao, S.B. Sinnott, S.S. Perry, Friction and wear of pyrophyllite on the atomic scale, Tribol. Lett. 46 (2012) 159–165.

[39] E.L. Brightbill, Design Rules for Discovering 2D Materials from 3D Crystals, University of North Carolina at Chapel Hill, 2016.

[40] M. Shamim, T.K. Mukhopadhyay, K. Dana, Kinetic pathway for thermal exfoliation of pyrophyllite, Appl. Clay Sci. 114 (2015) 40–47.

[41] K.S. Novoselov, D. Jiang, F. Schedin, T.J. Booth, V.V. Khotkevich, S.V. Morozov, A.K. Geim, Two-dimensional atomic crystals, Proc. Natl. Acad. Sci. USA 102 (2005) 10451–10453.

[42] A. Matković, I. Milošević, M. Milićević, T. Tomašević-Ilić, J. Pešić, M. Musić, M. Spasenović, D. Jovanović, B. Vasić, C. Deeks, R. Panajotović, M.R. Belić, R. Gajić, Enhanced sheet conductivity of Langmuir–Blodgett assembled graphene thin films by chemical doping, 2D Mater. 3 (2016) 015002.

[43] I.R. Milošević, B. Vasić, A. Matković, J. Vujin, S. Aškrabić, M. Kratzer, T. Griesser, C. Teichert, R. Gajić, Single-step fabrication and work function engineering of Langmuir–Blodgett assembled few-layer graphene films with Li and Au salts, Sci. Rep. 10 (2020) 8476.

[44] M. Varenberg, I. Etsion, G. Halperin, An improved wedge calibration method for lateral force in atomic force microscopy, Rev. Sci. Instrum. 74 (2003) 3362–3367.

[45] J.H. Lee, S. Guggenheim, Single crystal X-ray refinement of pyrophyllite-1Tc, Am. Mineral. 66 (1981) 350–357.

[46] R. Wardle, G.W. Brindley, The crystal structures of pyrophyllite, 1Te, and of its dehydroxylate, Am. Mineral. 57 (1972) 732–750.

[47] A. Wang, J.J. Freeman, B.L. Jolliff, Understanding the Raman spectral features of phyllosilicates, J. Raman Spectrosc. 46 (2015) 829–845.

[48] J. Kloprogge, Chapter 6 - Raman spectroscopy of clay minerals, in: W.P. Gates, J.T. Kloprogge, J. Madejová, F. Bergaya (Eds.), Infrared and Raman Spectroscopies of Clay Minerals, in: Developments in Clay Science, vol. 8, 2017, pp. 150–199.

[49] B. Lafuente, R.T. Downs, H. Yang, N. Stone, 1. The power of databases: The RRUFF project, 2015, pp. 1–30.

[50] P. Nemes-Incze, Z. Osváth, K. Kamarás, L.P. Biró, Anomalies in thickness measurements of graphene and few layer graphite crystals by tapping mode atomic force microscopy, Carbon 46 (2008) 1435–1442.

[51] K.-S. Kim, H.-J. Lee, C. Lee, S.-K. Lee, H. Jang, J.-H. Ahn, et al., Chemical vapor deposition-grown graphene: The thinnest solid lubricant, ACS Nano 5 (2011) 5107–5114.

[52] B. Vasić, A. Matković, U. Ralević, M. Belić, R. Gajić, Nanoscale wear of graphene and wear protection by graphene, Carbon 120 (2017) 137–144.

[53] A. Özoğul, E. Gnecco, M.Z. Baykara, Nanolithography-induced exfoliation of layered materials, Appl. Surf. Sci. Adv. 6 (2021) 100146.

[54] Y.-T. Fu, G.D. Zartman, M. Yoonessi, L.F. Drummy, H. Heinz, Bending of layered silicates on the nanometer scale: Mechanism, stored energy, and curvature limits, J. Phys. Chem. C 115 (2011) 22292–22300.

[55] X. Qin, J. Zhao, J. Wang, M. He, Atomic structure, electronic and mechanical properties of pyrophyllite under pressure: A first-principles study, Minerals 10 (2020) 778.

[56] A. Castellanos-Gomez, M. Poot, A. Amor-Amorós, G.A. Steele, H.S.J. van der Zant, N. Agraït, G. Rubio-Bollinger, Mechanical properties of freely suspended atomically thin dielectric layers of mica, Nano Res. 5 (2012) 550–557.

[57] G.D. Zartman, H. Liu, B. Akdim, R. Pachter, H. Heinz, Nanoscale tensile, shear, and failure properties of layered silicates as a function of cation density and stress, J. Phys. Chem. C 114 (2010) 1763–1772.

[58] B. Vasić, A. Matković, R. Gajić, I. Stanković, Wear properties of graphene edges probed by atomic force microscopy based lateral manipulation, Carbon 107 (2016) 723–732.

[59] R. Buzio, A. Gerbi, S. Uttiya, C. Bernini, A.E. Del Rio Castillo, F. Palazon, A.S. Siri, V. Pellegrini, L. Pellegrino, F. Bonaccorso, Ultralow friction of ink-jet printed graphene flakes, Nanoscale 9 (2017) 7612–7624.

[60] M. Fox, Optical Properties of Solids, Oxford University Press, 2010.

[61] P. Makuła, M. Pacia, W. Macyk, How to correctly determine the band gap energy of modified semiconductor photocatalysts based on UV–Vis spectra, J. Phys. Chem. Lett. 9 (2018) 6814–6817.

[62] G. Cassabois, P. Valvin, B. Gil, Hexagonal boron nitride is an indirect bandgap semiconductor, Nat. Photonics 10 (2016) 262–266.

[63] G.-H. Lee, Y.-J. Yu, C. Lee, C. Dean, K.L. Shepard, P. Kim, J. Hone, Electron tunneling through atomically flat and ultrathin hexagonal boron nitride, Appl. Phys. Lett. 99 (2011) 243114.

[64] L. Britnell, R.V. Gorbachev, R. Jalil, B.D. Belle, F. Schedin, M.I. Katsnelson, L. Eaves, S.V. Morozov, A.S. Mayorov, N.M.R. Peres, A.H. Castro Neto, J. Leist, A.K. Geim, L.A. Ponomarenko, K.S. Novoselov, Electron tunneling through ultrathin boron nitride crystalline barriers, Nano Lett. 12 (2012) 1707–1710.

[65] Y. Hattori, T. Taniguchi, K. Watanabe, K. Nagashio, Layer-by-layer dielectric breakdown of hexagonal boron nitride, ACS Nano 9 (2015) 916–921.

[66] Y.Y. Illarionov, T. Knobloch, M. Jech, M. Lanza, D. Akinwande, M.I. Vexler, T. Mueller, M.C. Lemme, G. Fiori, F. Schwierz, T. Grasser, Insulators for 2D nanoelectronics: the gap to bridge, Nature Commun. 11 (2020) 3385.

[67] K.K. Kim, H.S. Lee, Y.H. Lee, Synthesis of hexagonal boron nitride heterostructures for 2D van der Waals electronics, Chem. Soc. Rev. 47 (2018) 6342–6369.

[68] F. Giannazzo, G. Fisichella, G. Greco, P. Fiorenza, F. Roccaforte, Conductive atomic force microscopy of two-dimensional electron systems: From AlGaN/GaN heterostructures to graphene and MoS$_2$, in: M. Lanza (Ed.), Conductive Atomic Force Microscopy: Applications in Nanomaterials, WILEY-VCH Verlag, Weinheim, Germany, 2017, pp. 163–186, Ch. 7.

[69] F. Giannazzo, G. Greco, F. Roccaforte, C. Mahata, M. Lanza, Conductive AFM of 2D materials and heterostructures for nanoelectronics, in: U. Celano (Ed.), Electrical Atomic Force Microscopy for Nanoelectronics, Springer, Berlin, Germany, 2019, pp. 303–350, Ch. 10.

[70] C.-Y. Zhu, J.-K. Qin, P.-Y. Huang, H.-L. Sun, N.-F. Sun, Y.-L. Shi, L. Zhen, C.-Y. Xu, 2D indium phosphide sulfide (In$_2$P$_3$S$_9$): An emerging van der Waals high-k dielectrics, Small 18 (2022) 2104401.

[71] Y. Ji, C. Pan, M. Zhang, S. Long, X. Lian, F. Miao, F. Hui, Y. Shi, L. Larcher, E. Wu, M. Lanza, Boron nitride as two dimensional dielectric: Reliability and dielectric breakdown, Appl. Phys. Lett. 108 (2016) 012905.

[72] A. Ranjan, N. Raghavan, M. Holwill, K. Watanabe, T. Taniguchi, K.S. Novoselov, K.L. Pey, S.J. O'Shea, Dielectric breakdown in single-crystal hexagonal boron nitride, ACS Appl. Electron. Mater. 3 (2021) 3547–3554.

[73] J.L. Rosenholtz, D.T. Smith, The dielectric constant of mineral powders, Am. Mineral. 21 (1936) 115–120.

Full Length Article

Low-friction, wear-resistant, and electrically homogeneous multilayer graphene grown by chemical vapor deposition on molybdenum

Borislav Vasić[a,*], Uroš Ralević[a], Katarina Cvetanović Zobenica[b], Milče M. Smiljanić[b], Radoš Gajić[a], Marko Spasenović[b], Sten Vollebregt[c]

[a] *Graphene Laboratory of Center for Solid State Physics and New Materials, Institute of Physics Belgrade, University of Belgrade, Pregrevica 118, 11080 Belgrade, Serbia*
[b] *Center of Microelectronic Technologies, Institute of Chemistry, Technology and Metallurgy, University of Belgrade, Njegoševa 12, 11000 Belgrade, Serbia*
[c] *Department of Microelectronics, Delft University of Technology, Feldmannweg 17, 2628CT Delft, the Netherlands*

ABSTRACT

Chemical vapour deposition (CVD) is a promising method for producing large-scale graphene (Gr). Nevertheless, microscopic inhomogeneity of Gr grown on traditional metal substrates such as copper or nickel results in a spatial variation of Gr properties due to long wrinkles formed when the metal substrate shrinks during the cooling part of the production cycle. Recently, molybdenum (Mo) has emerged as an alternative substrate for CVD growth of Gr, mainly due to a better matching of the thermal expansion coefficient of the substrate and Gr. We investigate the quality of multilayer Gr grown on Mo and the relation between Gr morphology and nanoscale mechanical and electrical properties, and spatial homogeneity of these parameters. With atomic force microscopy (AFM) based scratching, Kelvin probe force microscopy, and conductive AFM, we measure friction and wear, surface potential, and local conductivity, respectively. We find that Gr grown on Mo is free of large wrinkles that are common with growth on other metals, although it contains a dense network of small wrinkles. We demonstrate that as a result of this unique and favorable morphology, the Gr studied here has low friction, high wear resistance, and excellent homogeneity of electrical surface potential and conductivity.

1. Introduction

Chemical vapour deposition (CVD) is the most dominant method for fabrication of large-area single- and few-layer graphene (Gr) films on various metallic substrates (catalysts) [1–4]. After the growth, Gr films are transferred onto desired substrates that allow practical use [5,6]. The main advantages of CVD over other fabrication techniques are its relative simplicity, low cost, and industrial applicability [7–9]. Still, CVD growth and Gr transfer yield films with defects such as grain boundaries [10–16], wrinkles [17–23] and cracks. Formation of wrinkles, for example, occurs due to a large difference in thermal expansion coefficients of Gr and the catalytic substrate, which results in different shrinking rates during cooling at the end of the CVD growth process. Wrinkles in Gr have been shown to be highly detrimental to the mechanical robustness and electrical homogeneity of graphene [23]. CVD graphene is prone to formation of defects both on most commonly used catalytic metal substrates such as copper [1–3] and nickel [4], as well as on less traditional substrates such as ruthenium, iridium, and platinum [9].

Recently, Gr grown by CVD on thin molybdenum (Mo) films

sputtered on silicon wafers [24–26] has emerged as an alternative to Gr grown on traditional metal substrates. Growth on Mo offers several advantages. Namely, the thermal expansion coefficient of Mo is well matched to that of Gr, supporting wrinkle-free growth [25]. Also, Mo has a high melting point, resulting in less restructuring of the Mo substrate compared to copper during the CVD process. Finally, low solubility of carbon in bulk Mo facilitates easy growth of Gr layers [24], making the process attractive for high-volume applications. In addition to the advantages for growth, graphene on a thin sputtered layer of Mo has advantages for subsequent processing. The Mo layer can be patterned prior to growth, enabling patterning of CVD graphene without post-growth lithography, and the Mo can be easily removed once Gr is grown on it, which allows transfer-free fabrication of Gr devices that is compatible with CMOS processes [27,28]. Graphene grown with this novel process was shown to have applications in anti-corrosion coatings [29–31], gas [27,32] and pressure sensors [28]. Although Gr grown on Mo has high potential for practical use, the relation between microscopic morphology, distribution and geometry of wrinkles, and their influence on the mechanical and electrical properties of the material have not yet been studied.

* Corresponding author.
  E-mail address: bvasic@ipb.ac.rs (B. Vasić).

Using atomic force microscopy (AFM) based methods, here we present nanoscale analysis of the morphology, mechanical and electrical properties of few-layer Gr grown by CVD on Mo. We demonstrate that the material contains very few wrinkles and that those wrinkles have dimensions that are much smaller than those typically encountered in Gr grown on copper foils. Gr grown on Mo has low friction and high wear resistance as demonstrated by friction force microscopy and nanoscale wear tests. Using Kelvin probe force microscopy (KPFM) and conductive AFM (c-AFM) we show that this material has high uniformity of the Fermi level (work function) and electrical conductivity, respectively, over large areas. These results allude to strong potential uses of Gr grown on Mo for both mechanical and electrical applications such as ultrathin solid lubricants, electrodes and membranes for nano and microelectromechanical systems.

2. Experimental

2.1. Graphene fabrication and transfer

We studied both Gr on Mo as grown, as well as Gr transferred from Mo to Si/SiO$_2$. The 50 nm thick Mo catalyst was deposited using magnetron sputter coating on top of a Si/SiO$_2$ wafer (p-type, 10 cm, (1 0 0) orientation). SiO$_2$ was approximately 600 nm thick and it was grown using wet thermal oxidation. The Mo target purity was 99.95%. Gr was deposited using an AIXTRON Blackmagic Pro system at 915 °C using 960/40/25 sccm of Ar/H$_2$/CH$_4$ at 25 mbar for 30 min and cooled to room temperature under an Ar atmosphere. After this, the wafers were cut into smaller dies for sample preparation. Further details of the CVD growth of Gr on Mo can be found in our previous paper [25].

Graphene was transferred by first immersing dice of Gr on wafer in 30% hydrogen-peroxide for 25 min. Hydrogen peroxide etches away the Mo underneath the Gr layer and Gr is released, floating on the surface of the hydrogen peroxide solution. Gr was transfered into a Petri dish, 5 cm in diameter and 17 ml of volume, with H$_2$O$_2$. Hydrogen peroxide was exchanged with deionized (DI) water. The DI water was exchanged three times to ensure complete removal of peroxide. Gr was then carefully picked up onto a Si/SiO$_2$ wafer die. The sample was dried at room temperature for 25 min, and was put under a glass bell for the next 24 h to dry completely.

2.2. AFM and Raman characterization

All AFM measurements were performed with an NTEGRA Spectra system at ambient conditions. Morphology was measured in tapping AFM mode with NSG01 probes. The surface roughness was measured across ten 50 × 50 μm^2 areas, calculated as the root-mean square of the height distributions, and then averaged. Phase lag of the AFM probes was measured simultaneously with topography in order to achieve better contrast of small topographic features and to check for possible changes in material contrast on the sample surface.

Wear tests were done in contact AFM mode on 5–10 different 10 × 10 μm^2 areas with diamond coated probes DCP20. In order to initiate Gr wear, the normal load was kept constant during scanning within 1 μm wide parallel stripes and increasing in steps of around 1 μN from stripe to stripe, for a total range between 0.5 μN and 5 μN [23]. During the wear tests, we recorded the lateral forces in both forward and backward directions. These forces correspond to the lateral torsion of the AFM cantilever due to the AFM tip-Gr friction. The friction force was determined as the half-difference between the lateral force in the forward and backward direction. The normal force was calculated according to force–displacement curves, whereas the friction force was calibrated on a standard Si grating [33].

Kelvin probe force microscopy (KPFM) and Pt coated NSG01/Pt probes were employed in order to measure local electrical surface potential. KPFM is a two-pass AFM-based measurement technique which returns a local contact potential difference (CPD) between a metallic

AFM tip and the sample surface. The topographic profile of the sample was measured in the first pass. In the second pass, the AFM probe was lifted by 20 nm and scanned along the same topographic line as in the first pass, while a sum of DC and variable AC voltages was applied between the probe and the sample. The role of the AC voltage was to electrically excite probe oscillations, while the DC voltage was controlled by the AFM feedback loop in order to nullify these oscillations. The value of DC voltage which nullifies AFM probe oscillations is equal to the local CPD between the AFM tip and the sample.

Since CPD is equal to the difference between the work functions of the AFM tip (WF$_{tip}$) and the sample (WF$_{sample}$), in order to find the absolute value of WF$_{sample}$, the WF$_{tip}$ of the Pt coated AFM probes was calibrated on a HOPG sample with a well known work function of 4.6 eV [34]. Measurements on HOPG yielded WF$_{tip}$ = 5 eV. The work functions of the Gr samples were calculated as WF$_{Gr}$ = CPD − WF$_{tip}$. As in the case of the surface roughness and wear tests, the CPD was measured on 5–10 different areas (50 × 50 μm^2 in the case of Gr grown on Mo, and 30 × 30 μm^2 on Gr transferred on SiO$_2$) and then averaged.

Conductive AFM (C-AFM) with highly doped diamond coated probes DCP20 was used for characterization of local conductivity. In C-AFM, during standard topographic imaging in AFM contact mode, a DC voltage in a range between 1 V and 2 V was applied between the probe and the sample. The resulting DC current through the AFM probe, proportional to the local conductivity of Gr samples, was simultaneously measured with a built-in current amplifier. In order to avoid wear of AFM tips and achieve reliable current measurements, C-AFM was done using diamond coated DCP20 probes which were heavily doped by nitrogen. The diamond coating provides the robustness and wear resistance of AFM tips, while the high doping makes them highly conductive. As a result, these probes enabled reliable current mapping in contact AFM mode.

Raman imaging of CVD Gr transferred on Si/SiO$_2$ was performed on the same NTEGRA Spectra module equipped with a confocal Raman system (NA 0.7). Raman maps were measured with a step of 0.5 μm. The wavelength of the excitation laser was 532 nm.

3. Results and discussion

3.1. Morphology

3.1.1. CVD Gr on Mo

The topography of CVD Gr on Mo is depicted in Fig. 1 on two different length scales. One of the main motivations and potential benefits of CVD on Mo is the growth of wrinkle-free Gr since the thermal expansion coefficient of Mo is much better matched to that of Gr than the thermal expansion coefficients of copper or nickel. Indeed, in these topographic images there are no long wrinkles typically observed in traditional CVD Gr grown on copper.

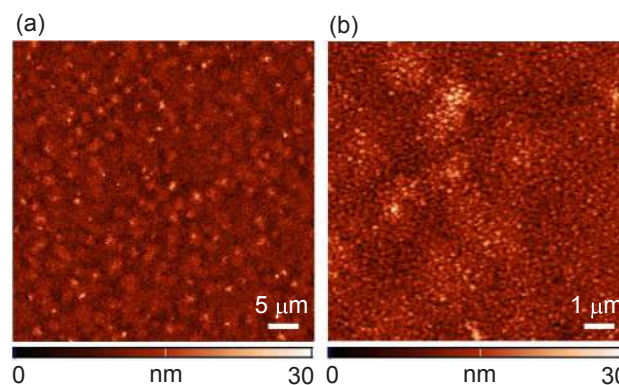Still, very short wrinkles can sometimes be observed on small-scale

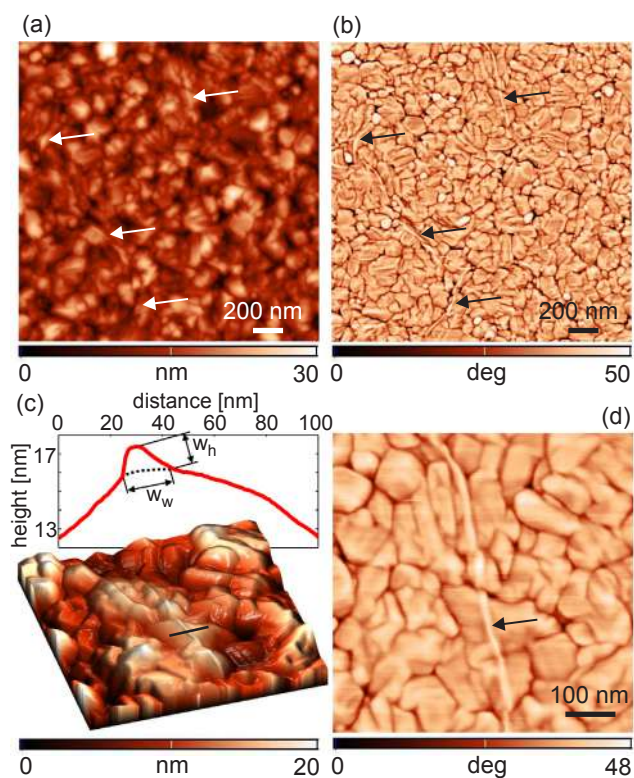**Fig. 1.** Morphology of CVD Gr on Mo: (a) 50 × 50 μm^2 and (b) 10 × 10 μm^2 area.

Fig. 2. Wrinkles in CVD Gr on Mo: (a) topography and (b) phase of $2 \times 2\,\mu m^2$ area. (c) Three-dimensional topography and (d) phase of $0.6 \times 0.6\,\mu m^2$ area. Wrinkles are marked by arrows. The inset in part (c) depicts the topographic cross-section across the wrinkle, along the solid line. The dotted line is a guide to the eye which follows the surface of the grain in order to emphasize the wrinkle geometry.

Fig. 3. Morphology of CVD Gr on SiO₂: (a) $50 \times 50\,\mu m^2$ and (b) $7 \times 7\,\mu m^2$ area.

images. A typical example is presented in the topographic and phase images in Figs. 2(a) and 2(b), respectively. Usually it is difficult to recognize wrinkles in topographic images since they are very small. On the other hand, wrinkles can be resolved in the phase image as elongated, curved lines, several hundreds of nanometers long (denoted by arrows). By using the position of wrinkles found from the phase image to carefully search the topographic map, one can identify bright and narrow lines indicating that here Gr is locally wrinkled. The local Gr wrinkling is best visualized if we further zoom into an area containing a single wrinkle, as illustrated in Figs. 2(c) and 2(d), with the three-dimensional topographic and phase image, respectively. The inset in part (c) depicts the height profile across the wrinkle. Its width w_w and height h_w are around 20 nm and 1.5 nm, respectively.

Surface roughness of Gr calculated from large-scale images such as from Fig. 1(a) was 2.9 ± 0.1 nm (averaged over ten $50 \times 50\,\mu m^2$ areas). Lower roughness could be achieved by using Mo foils as substrates [26], but foils are not compatible with semiconductor technologies. Therefore, we have considered Gr grown on thin films such as sputtered Mo, which is fully compatible with CMOS processing [27,28].

The roughness of Gr originates from patches with slightly increased height and from the grain structure of the underlying substrate. Gr patches in topographic images in Fig. 1 look like brighter domains, with a lateral size of several microns, and a height of several nanometers. A high-resolution image of an $2 \times 2\,\mu m^2$ area, depicted in Fig. 2(a), reveals that Gr follows the morphology of the underlying Mo substrate while the grain structure of Mo is imprinted and replicated onto Gr. As a result, the grain structure of Mo dominates the measured topography thus contributing to increased surface roughness. It should be emphasized that as deposited Mo is very flat with sub-nm roughness. However, the Mo turns into Mo₂C upon exposure to CH₄ before the Gr formation starts [26], and due to this recrystallization into Mo₂C, the roughness
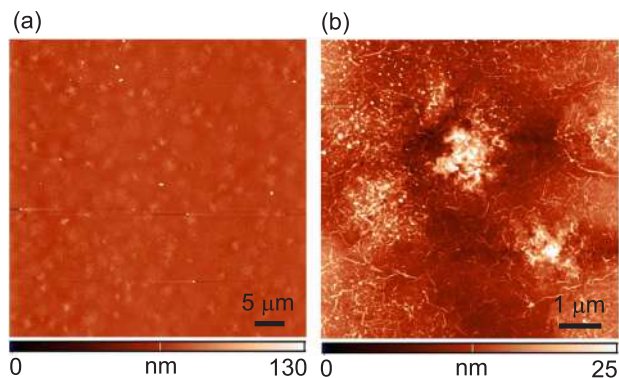
increases.

Grain structure and especially grain boundaries are even better visualized in the corresponding phase image in Fig. 2(b). Since the phase signal is generally very sensitive to sudden and sharp topographic features such as hills (grains) or narrow holes (grain boundaries), it can be used for their visualization with even better resolution than in pure topographic images. As can be seen, the shape of grains is rather irregular, with an average grain diameter of around 100 nm. The autocorrelation function of the height distribution (not-shown here) is isotropic, indicating that on average, there is no preferential in-plane anisotropy of the grain structure.

3.1.2. CVD Gr on SiO₂

The morphology of CVD Gr transferred on SiO₂ is presented in Fig. 3. The calculated surface roughness was 3.8 ± 1 nm (averaged over ten $50 \times 50\,\mu m^2$ areas). Therefore, the roughness slightly increased after the transfer mainly because micron-size patches with a slightly increased height were more evident than in the previous case of Gr on Mo. In addition, Gr on SiO₂ has a rather dense network of short wrinkles as depicted in Fig. 3 and it contains nano-particles, represented by bright, isolated point-like features in Fig. 3(a), which are most probably residues from the transfer process.

As mentioned above, Mo thin films as substrates allow transfer-free Gr fabrication, thus making the fabrication simpler and compatible with semiconductor technologies [27,28]. Here we consider Gr transferred on SiO₂ because it facilitates characterization and analysis, but it should be emphasized that the chemical treatment is the same in both cases (i.e. Gr is immersed in hydrogen-peroxide in both cases, the only difference is that in the transfer-free approach, the original growth substrate is reused, whereas during the transfer, another substrate is used for picking Gr up). Therefore, the results presented here hold for transfer-free Gr as well.

Short Gr wrinkles observed in Fig. 3(b) are better visualized in the small-scale images in Fig. 4(a) and 4(b). The typical height profile of a wrinkle is depicted in Fig. 3(c), whereas the distributions of wrinkle widths and heights are given in Fig. 4(d). The height can be fitted with a linear function of the width. According to Ref. [[20]], there are three classes of wrinkle geometry: ripples, standing collapsed wrinkles and folded wrinkles. Since the wrinkle width in our case is less than ~50 nm, they have the geometry of ripples, while higher wrinkles are most probably standing collapsed ones. This is a significant difference compared to CVD Gr grown on copper [23] where thermally induced wrinkles are much wider, up to several hundreds of nanometers, and belong to the class of folded wrinkles. On the Gr studied here, wrinkles are generally short, most of them with lengths in the range $100 - 200$ nm. They do not have any preferential direction, while shorter wrinkles are usually curved. These wrinkles appear during transfer onto SiO₂. According to wrinkle lengths, shapes, and their mutual distances, it seems that they correspond to grain boundaries of Gr on Mo - narrow, irregular and curved domains along which Gr on Mo
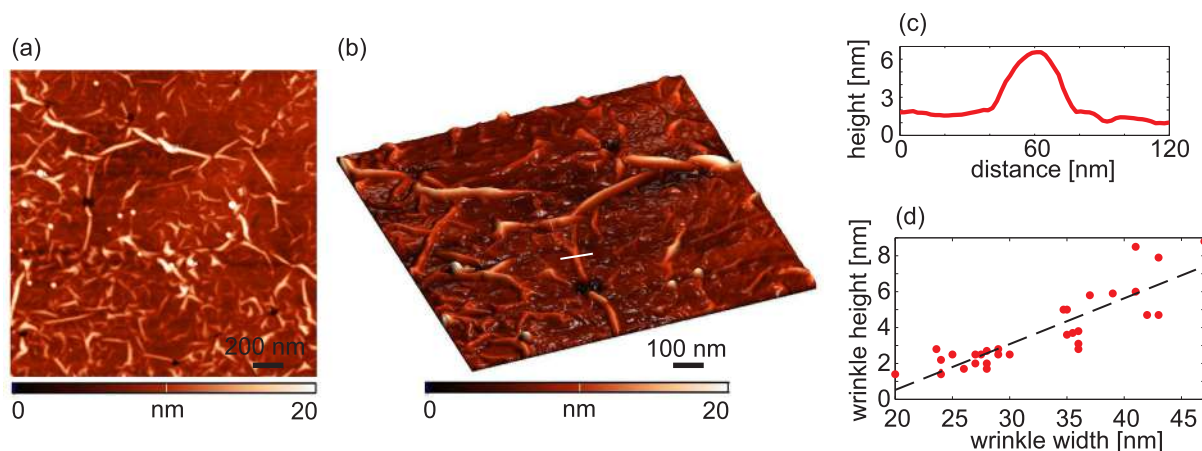
Fig. 4. Wrinkles in CVD Gr on SiO$_2$: (a) two-dimensional topographic image of $2 \times 2 \, \mu m^2$ area, and (b) three-dimensional $1 \times 1 \, \mu m^2$ area, (c) the height profile of the wrinkle along the solid line in part (b), and (d) the distribution of wrinkle widths and heights from part (c). The dashed line in the distribution plot is a linear fit.

was locally bent and corrugated. The different wrinkle type of Gr grown on Mo compared to that grown on copper is the most probable reason for improved mechanical and electrical properties, as will be discussed in the following sections.

3.2. Raman analysis

Further characterization of CVD Gr transferred on SiO$_2$ was done by combined AFM and Raman mapping. The results are presented in Fig. 5 with the topography (part (a)), integrated Raman intensity (part (b)), the ratio between the intensity of G and 2D Raman modes (part (c)), and Raman spectra taken at three representative points (part (d)). As can be seen, the characteristic Raman modes of Gr, G (around

1586 cm^{-1}) and 2D (around 2700 cm^{-1}) modes are clearly resolved. Still, the appearance of the defect mode D (around 1350 cm^{-1}) indicates non-negligible defects in CVD Gr. The 2D peak is slightly shifted to longer wavenumbers which indicates that the considered CVD Gr is multi-layered. The ratio G/2D is in the range between 0.5 and 0.7, which corresponds to a thickness of 4–6 layers [35]. The same thickness is confirmed by AFM measurements as shown in Fig. S1 of Supplementary material. By comparing encircled domains in all maps, most of the patches with increased height correspond to domains with decreased total Raman intensity and increased G/2D ratios. Therefore, the number of Gr layers is locally increased within those patches. Still, some patches where the G/2D ratio is not increased (or has even slightly decreased) likely contain just locally wrinkled and/or folded layers. Raman spectra
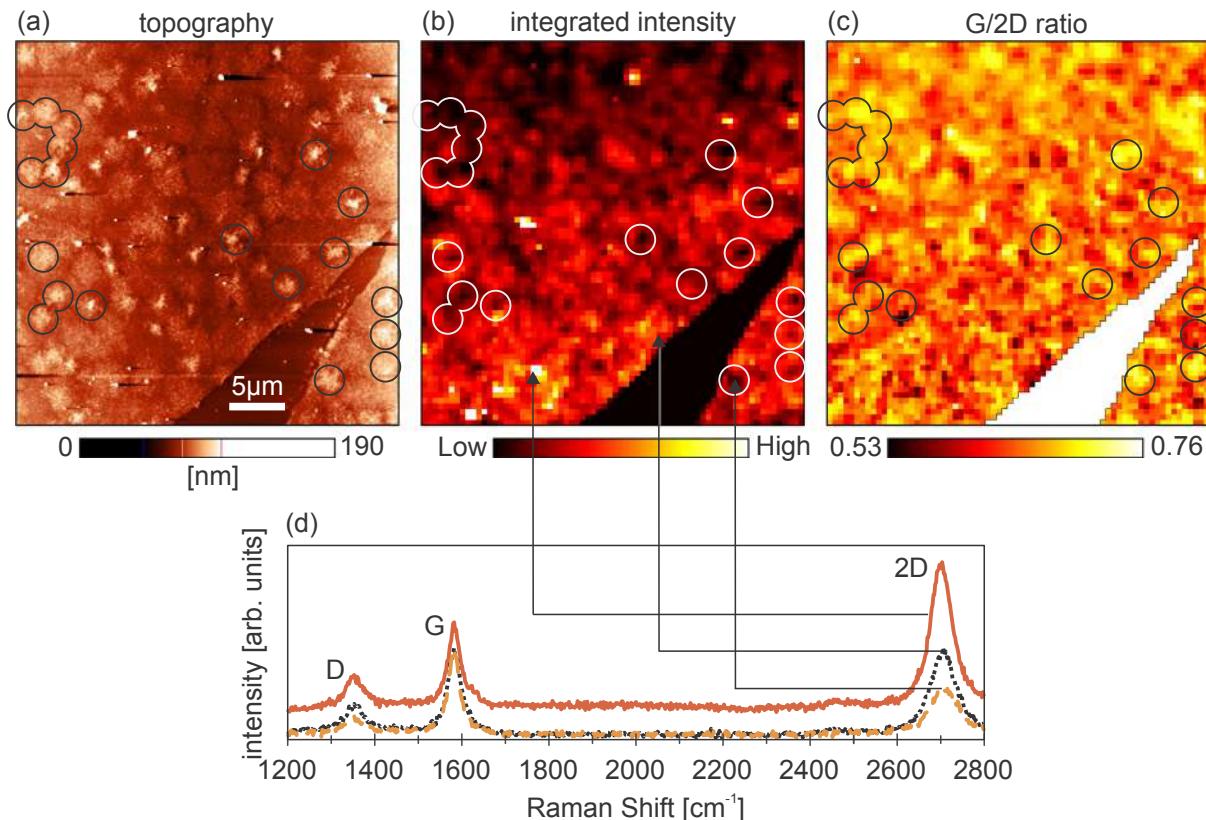

Fig. 5. (a) Topography, (b) total Raman intensity integrated between 1200 cm^{-1} and 2800 cm^{-1}, (c) the ratio between the intensity of G and 2D Raman modes, and (d) Raman spectra measured at three points marked in part (b).
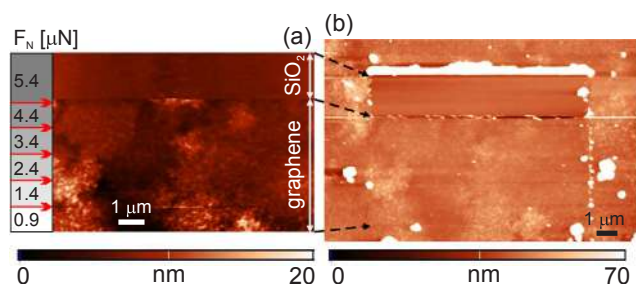
Fig. 6. Wear test: (a) topography during scratching in AFM contact mode, and (b) topography of enlarged area measured in tapping AFM mode after scratching. The value of the normal load is presented on the left side of part (a). The arrows in part (a) mark positions where the normal load was increased.

of samples stored in ambient conditions for over two years reveal no deterioration due to aging.

3.3. Friction and wear properties

Wear tests were done by scratching CVD Gr on SiO_2 in contact AFM mode. The results are presented in Figs. 6(a) and 6(b), that depict topography obtained during scratching and an enlarged topographic image recorded in tapping mode after scratching, respectively. The scratching was done from the bottom to the top. The normal load was increased in a range starting from $0.9\,\mu N$ applied to the bottom Gr stripe with $1\,\mu m$ width, to $5.4\,\mu N$ applied on the top of the image where tearing occured. The points where the normal load was increased are marked by arrows in Fig. 6(a). When the normal load reached a threshold value of $5.4\,\mu N$, Gr started to tear. The moment of tearing is clearly visible as a sudden change in the contrast of both topographic images in Fig. 6. The normal load was then kept at a high value, while Gr was peeled off by the AFM probe within the scan area. The area where Gr was peeled off is apparent in Fig. 6(b) as a rectangular stripe with bare SiO_2. Peeled Gr was rolled and deposited at the top of this domain, where scratching was stopped, and it is visible as a bright and narrow horizontal stripe.

The same wear experiment was repeated on five different areas of the Gr sample. The results were similar in all cases - sudden Gr tearing at a high enough normal load, while the threshold normal force needed for Gr tearing varied in the range $3.4 - 5.4\,\mu N$. The mechanism of Gr tearing can be explained in the following way. High normal forces applied by the AFM tip during wear test lead to plastic deformations of Gr beneath the tip [36]. The plastic deformations are characterized with various defects, mostly by vacancy defects, which degrade the mechanical properties of Gr and its breaking strength [37]. By increasing normal force, Gr becomes more defective while the breaking strength of Gr becomes very small, which results in Gr fracture and tearing. The average threshold force for the tearing of CVD Gr considered here is around $4\,\mu N$ and it is much higher, at least by an order of magnitude, than in CVD Gr grown on copper and transferred on SiO_2, where Gr tearing was always initiated from long and wide, thermally grown wrinkles, for normal loads less than $0.5\,\mu N$ [23] and sometimes already at around 100 nN [38]. Although in the former cases single-layer Gr samples were considered, the wear resistance of CVD Gr grown on Mo seems to be higher because of the different type of wrinkles in CVD Gr grown on Mo. Here they are small and narrow (simple ripples [20]) and can be easily pressed by the AFM tip without tearing, while the Gr sheet is simultaneously just locally flattened.

The lateral force recorded during the scratching test is displayed in Fig. 7(a). The force increases with the normal load in stepwise fashion before Gr tearing. The friction force was calculated according to the lateral force recorded in forward and backward directions. The friction map is depicted in Fig. 7(b), whereas the corresponding histogram is presented in Fig. 7(c). The friction map is characterized by two distinct
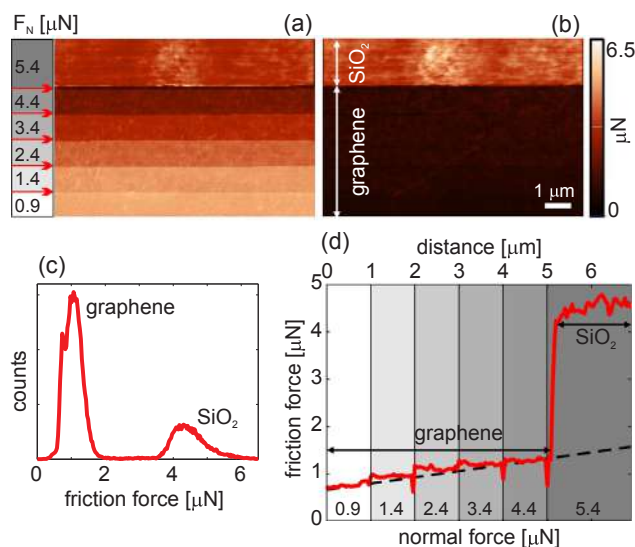

Fig. 7. Friction during the wear test: (a) lateral force map and (b) corresponding friction map during the scratching experiment from Fig. 6, (c) histogram of the friction map, and (d) the average vertical profile of the friction force map. The averaging was applied in order to filter out noise and better present stepwise increase of the friction force. The dashed line in part (d) is a liner fit to the stepwise increasing friction force during the scratching of Gr. The slope of this curve corresponds to the friction coefficient of Gr.

domains: the bottom part with low friction on Gr covered SiO_2 and the top part with high friction on bare SiO_2. According to the histogram, friction on Gr is more than 4 times smaller than on SiO_2, indicating good lubrication properties of Gr.

The average profile of the friction map along the vertical direction is given in Fig. 7(d). The friction force increases stepwise with the normal load. When the threshold force for Gr tearing is reached, the friction increases abruptly and stays at a constant level representing friction on bare SiO_2. The initial stepwise increase of the friction can be approximated by a linear function represented by the dashed line in Fig. 7(d). The slope of this linear curve is the ratio between the friction force and applied normal load and it yields a friction coefficient of Gr of only 0.13. This value is similar to that obtained earlier for Gr grown on copper and nickel [39]. Friction is also influenced by defects in Gr [40], mainly by exposed Gr edges and wrinkles, which lead to increased friction [38,41]. As mentioned above, the considered CVD graphene is almost free of cracks and exposed edges. At the same time, friction maps (the typical one shown in Fig. 7(b)) do not show increased friction due to Gr wrinkles, because they are small and narrow and could be easily pressed by the AFM tip. According to these results, CVD Gr grown on Mo could be an excellent choice for making large-scale and ultrathin solid lubricants with increased wear resistance for friction [39,42,43] and wear reduction [36,44–46] of underlying substrates.

3.4. Electrical surface potential

3.4.1. CVD Gr on Mo

Homogenity of electrical surface potential was investigated by KPFM. Topography of CVD Gr on Mo and the corresponding CPD map are given in Figs. 8(a1) and (a2), respectively, whereas the histogram of the CPD map is shown in Fig. 8(a3). The histogram contains a single, narrow peak indicating that the measured CPD is rather uniform over a wide $50 \times 50\,\mu m^2$ area. Averaged CPD (taking into account 10 different areas) was 352 ± 6 mV. The absolute value of the work function of the considered CVD Gr on Mo is thus 4.66 eV. The maximal half-width of all CPD maps measured on $50 \times 50\,\mu m^2$ areas was only around 5 mV, indicating a very uniform electrical surface potential distribution. Still, CPD maps clearly show irregularly shaped potential puddles. The
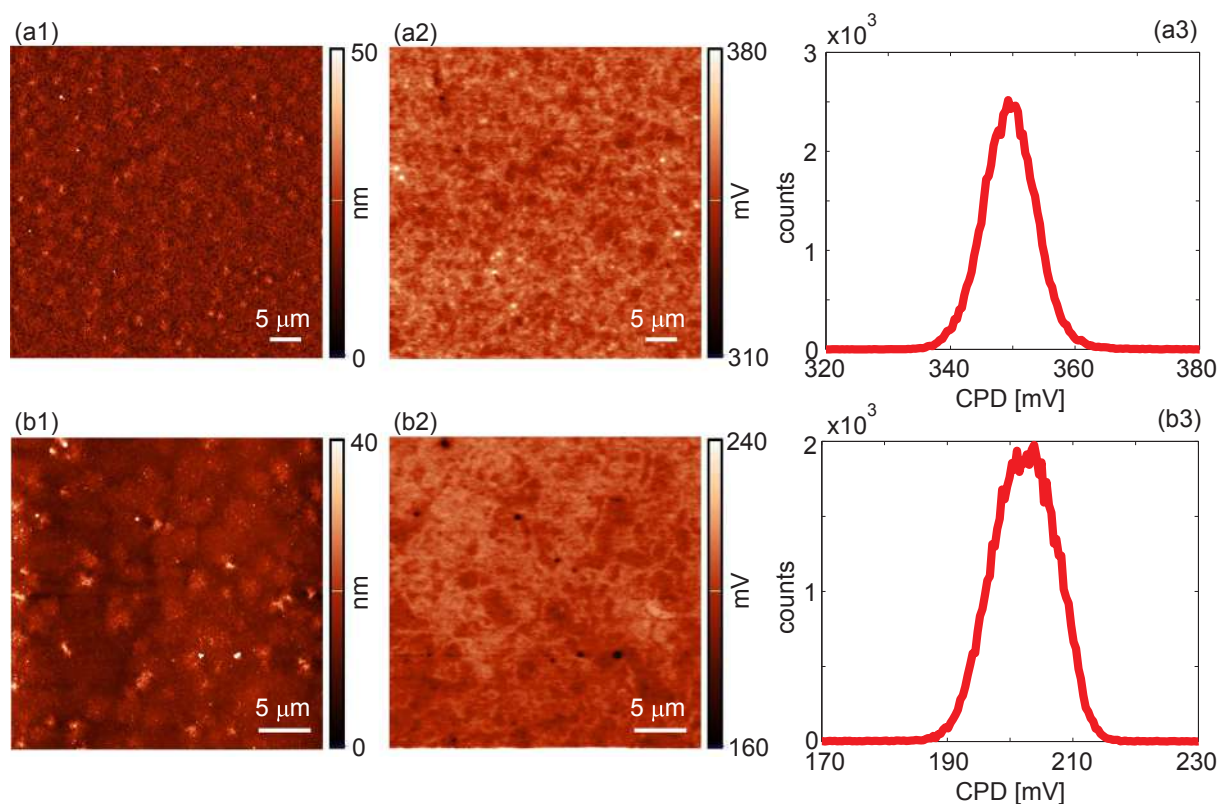
Fig. 8. (a1) Morphology of CVD Gr on Mo, (a2) the corresponding CPD map measured by KPFM, and (a3) the histogram of the CPD map. (b1) Morphology of CVD Gr transferred on SiO$_2$, (b2) the corresponding CPD map measured by KPFM, and (b3) the histogram of the CPD map.

potential between adjacent puddles varies by several mV, while their lateral shapes can not be related to any morphological features such as patches with increased height. Similar electron-hole puddles have been already observed in graphene [47–50] due to charge impurities in the substrate, intercalated between Gr and the substrate, or due to intrinsic ripples in Gr.

3.4.2. CVD Gr on SiO$_2$

Similar analysis of the distribution of electrical surface potential was done for CVD Gr transferred on SiO$_2$. The results are given in Fig. 8(b) representing $30 \times 30 \, \mu m^2$ topographic and KPFM images (parts (b1) and (b2), respectively), and the CPD histogram (part (b3)). CPD maps exhibit similar features as in the previous case, with a very flat surface potential, implying that CVD Gr on SiO$_2$ is electrically homogeneous. Since wrinkles are narrow and small, Gr is free of wrinkle-induced potential variations previously observed in other forms of CVD Gr [23,21,22]. However, small and irregular charge puddles are still present, as in the case on Mo. The average CPD was 205 ± 4 mV, thus giving the absolute value of the work function of Gr transferred on SiO$_2$ of 4.8 eV. Therefore, there was a small difference of around 0.14 eV between the work functions of Gr on Mo and SiO$_2$. In the former case, Gr was most probably not thick enough to completely screen an electric field originating from the underlying Mo with a lower work function than Gr. As a result, the work function of Gr on Mo was slightly decreased. A second possibility is that Mo dopes the Gr by charge transfer, again lowering its work function [51,52].

The work function of a material or surface is a key property that determines its behavior in an electronic circuit. Energy level differences between different constituent layers of a device dictate functionality ranging from Ohmic contacts to Schottky barriers. One of the primary strengths of silicon and other materials of choice in the semiconductor industry is their uniform work function, or surface potential. Bare silicon surfaces, typically used as references for KPFM measurements,

have RMS uniformity on the order of 3 mV [53]. Aside from their use in integrated electronics, surfaces with flat topography and surface potential are also of interest as substrates for self-assembly. The quality of molecular self-assembly is critically determined by the electronic structure of the substrate surface and by variations of its surface potential due to charge transfer between the substrate and adsorbed molecules. As a result, highly homogeneous metal surfaces are often the substrate of choice due to well-defined molecule-metal interactions [54–57].

Here we show that few-layer Gr grown by CVD on sputtered Mo films has an extremely uniform surface potential profile over large areas, as measured by KPFM. In addition, such Gr that has been transferred, keeps the excellent uniformity, with RMS variability in surface potential in the order of 4 mV for areas as large as $30 \times 30 \, \mu m^2$. This is an improvement compared to the epitaxial Gr grown on SiC which has surface potential with RMS uniformity on the order of ~10 mV, however domains of few-layer Gr and steps in the SiC spoil this homogeneity in the surface potential at scales larger than 1 μm [58]. Monolayer Gr grown by CVD on copper contains wrinkles that also introduce inhomogeneity in surface potential on the order of ~20 mV [23]. Even metal films, such as sputtered gold, display larger variability of surface potential over large areas [59], whereas films deposited with atomic layer deposition display variability on the order of ~10 mV [60].

3.5. Electrical conductivity

3.5.1. CVD Gr on Mo

Homogenity of electrical conductivity was studied by C-AFM. Topography and corresponding current maps are presented in Figs. 9(a) and 9(b), respectively. The current map exhibits rather homogeneous and high current. The corresponding histogram is displayed in Fig. 9(c). As can be seen, the current distribution is characterized with a single peak around 14.5 nA, with a half-width of around 1 nA. The broadening
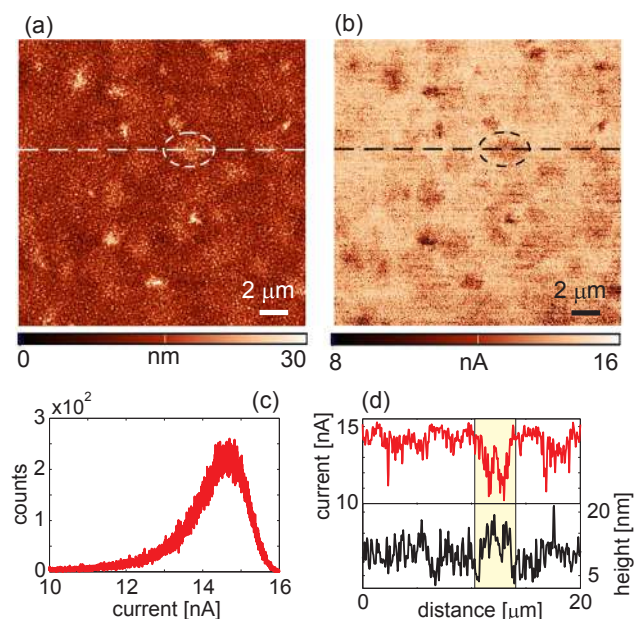
Fig. 9. (a) Morphology of CVD Gr on Mo and (b) corresponding current map measured by C-AFM. (c) Histogram of the current distributions in map (b). (d) Height and current profiles along the dashed lines in parts (a) and (b), respectively. Dashed circles in (a) and (b) correspond to the region with lower current which is highlighted by yellow in (d). (For interpretation of the references to colour in this figure legend, the reader is referred to the web version of this article.)

of the current peak appears due to decreased conductivity on the patches with increased thickness. The height and current profiles across one such patch (along the dashed lines indicated in Figs. 9(a) and 9(b)) are depicted in Fig. 9(d). As can be seen from these profiles, the current drops by several nA on the patch. In addition, small current drops (shown in Fig. S2 of Supplementary material) are visible along narrow Mo grain boundaries (imprinted in Gr as well) because of unstable contact with the AFM tip.

3.5.2. CVD Gr on SiO_2

As in the previous case for the electrical surface potential, a similar analysis of the current distribution was conducted for CVD Gr on SiO_2. The conductivity exhibits the same characteristics as previously observed for Gr on Mo: homogeneous and high current except on thicker patches (results presented in Fig. S3 of Supplementary material).

The small-scale images with topographic and current maps are presented for two cases: Figs. 10(a1) and 10(a2) for flat Gr (without patches) and Figs. 10(b1) and 10(b2) across a Gr patch. Both current images show homogeneous current despite of a dense network of Gr wrinkles. As we discussed above, wrinkles in the considered case have the geometry of simple, small and narrow ripples [20]. Then, during scanning in AFM contact mode, such wrinkles are pressed by the AFM tip leading to local Gr flattening, which finally gives a constant and high current. At the same time, Gr is wear resistant, so this local mechanical deformation does not result in Gr tearing. This is a significant improvement compared to CVD Gr grown on copper, where wrinkles are much wider and folded [20], leading to a more pronounced current drop. In the worst case, an AFM tip going across such wrinkles easily initiates local Gr tearing thus producing narrow and insulating trenches in a Gr sheet with zero current [23].

Still, the current map in Fig. 10(b2) contains local, point-like domains, represented by dark contrast, with a slightly decreased current. Reduced conductivity across patches indicates possible irregularities in the growth of these additional layers. However, the current drops only along patch edges or at pronounced topographic features such as point-
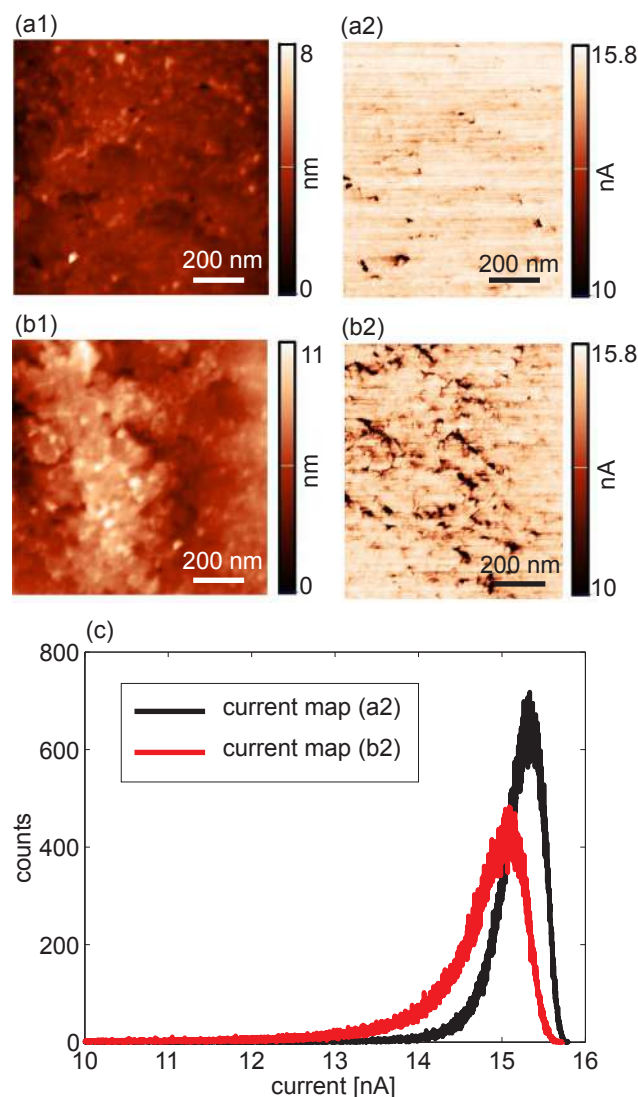

Fig. 10. (a1) Morphology and (a2) current map of CVD Gr transferred on SiO_2 without patches. (b1) Morphology and (b2) current map of Gr with a patch. (c) Histograms of the current distributions from parts (a2) and (b2).

like bumps. Therefore, one possible reason of decreased current on these parts is a less stable electrical contact between the AFM tip and Gr. Further improvement in the Gr growth process is needed in order to avoid these imperfections. Current histograms for both Gr with and without patches are given in Fig. 10(c). As can be seen, due to a slightly decreased conductivity of the domain with patches, the current peak is shifted by around 0.2 nA to a lower value.

4. Conclusion

In summary, we have demonstrated that although few-layer Gr grown on Mo does contain wrinkles with a height of several nanometers, the wrinkles are much narrower than in CVD Gr grown on copper, and they do not have a detrimental effect on uniformity of wear and electrical properties. It is shown that few-layer Gr grown by CVD on sputtered Mo films is characterized with a very low friction coefficient of around 0.13. Its wear resistance is improved compared to CVD Gr grown on copper, giving the threshold normal load for wear of around $4 \mu N$. The considered Gr has very uniform surface potential over large areas, with RMS variability on the order of 5 mV for areas as large as $50 \times 50 \mu m^2$. The uniformity of electrical properties is better than in other types of Gr and is on par with industrial-grade materials such as

silicon and metals deposited by atomic layer deposition. The local conductivity of the Gr films is also uniform, although with small variations at the edges of Gr patches with varying thickness. The patches are a result of the growth process which should be further optimized in order to overcome this issue.

We thus propose that few-layer Gr grown on Mo holds strong potential for use as an ultrathin solid lubricant for friction and wear reduction. It can also be used as an ultrathin electrode in integrated electronics, allowing wafer-scale device uniformity and reproducibility. Furthermore, the material holds potential as a substrate for self-assembly and for other uses that require uniform and well-defined electrical properties over large areas.

Declaration of Competing Interest

There are no conflict of interest in this work.

Acknowledgements

Appendix A. Supplementary material

Supplementary data associated with this article can be found, in the online version, at https://doi.org/10.1016/j.apsusc.2019.144792.

References

[1] X. Li, W. Cai, J. An, S. Kim, J. Nah, D. Yang, R. Piner, A. Velamakanni, I. Jung, E. Tutuc, S.K. Banerjee, L. Colombo, R.S. Ruoff, Large-area synthesis of high-quality and uniform graphene films on copper foils, Science 324 (2009) (2009) 1312–1314.

[2] A.N. Obraztsov, E.A. Obraztsova, A.V. Tyurnina, A.A. Zolotukhin, Chemical vapor deposition of thin graphite films of nanometer thickness, Carbon 45 (2007) (2007) 2017–2021.

[3] H. Zhou, W.J. Yu, L. Liu, R. Cheng, Y. Chen, X. Huang, Y. Liu, Y. Wang, Y. Huang, X. Duan, Chemical vapour deposition growth of large single crystals of monolayer and bilayer graphene, Nat. Comm. 4 (2013) (2013) 2096.

[4] K.S. Kim, Y. Zhao, H. Jang, S.Y. Lee, J.M. Kim, K.S. Kim, J.-H. Ahn, P. Kim, J.-Y. Choi, B.H. Hong, Large-scale pattern growth of graphene films for stretchable transparent electrodes, Nature 457 (2009) (2009) 706–710.

[5] X. Li, Y. Zhu, W. Cai, M. Borysiak, B. Han, D. Chen, R.D. Piner, L. Colombo, R.S. Ruoff, Transfer of large-area graphene films for high-performance transparent conductive electrodes, Nano Lett. 9 (2009) (2009) 4359–4363.

[6] J. Kang, D. Shin, S. Bae, B.H. Hong, Graphene transfer: key for applications, Nanoscale 4 (2012) (2012) 5527–5537.

[7] C. Mattevi, H. Kim, M. Chhowalla, A review of chemical vapour deposition of graphene on copper, J. Mater. Chem. 21 (2011) (2011) 3324–3334.

[8] Y. Zhang, L. Zhang, C. Zhou, Review of chemical vapor deposition of graphene and related applications, Acc. Chem. Res. 46 (2013) (2013) 2329–2339.

[9] C.-M. Seah, S.-P. Chai, A.R. Mohamed, Mechanisms of graphene growth by chemical vapour deposition on transition metals, Carbon 70 (2014) (2014) 1–21.

[10] C.S. Ruiz-Vargas, H.L. Zhuang, P.Y. Huang, A.M. van der Zande, S. Garg, P.L. McEuen, D.A. Muller, R.G. Hennig, J. Park, Softened elastic response and unzipping in chemical vapor deposition graphene membranes, Nano Lett. 11 (2011) (2011) 2259–2263.

[11] G.-H. Lee, R.C. Cooper, S.J. An, S. Lee, A. van der Zande, N. Petrone, A.G. Hammerberg, C. Lee, B. Crawford, W. Oliver, J.W. Kysar, J. Hone, High-strength chemical–vapor–deposited graphene and grain boundaries, Science 340 (2013) (2013) 1073–1076.

[12] H.I. Rasool, C. Ophus, W.S. Klug, A. Zettl, J.K. Gimzewski, Measurement of the intrinsic strength of crystalline and polycrystalline graphene, Nat. Commun. 4 (2013) (2013) 2811.

[13] J.C. Koepke, J.D. Wood, D. Estrada, Z.-Y. Ong, K.T. He, E. Pop, J.W. Lyding, Atomic-scale evidence for potential barriers and strong carrier scattering at graphene grain boundaries: a scanning tunneling microscopy study, Nano Lett. 7 (2013) (2013) 75–86.

[14] K.W. Clark, X.-G. Zhang, I.V. Vlassiouk, G. He, R.M. Feenstra, A.-P. Li, Spatially resolved mapping of electrical conductivity across individual domain (grain) boundaries in graphene, Nano Lett. 7 (2013) (2013) 2811.

[15] P. Nemes-Incze, P. Vancsó, Z. Osváth, G.I. Márk, X. Jin, Y.-S. Kim, C. Hwang, P. Lambin, C. Chapelier, L.B. Biró, Electronic states of disordered grain boundaries in graphene prepared by chemical vapor deposition, Carbon 64 (2013) (2013) 178–186.

[16] A.W. Cummings, D.L. Duong, V.L. Nguyen, D. Van Tuan, J. Kotakoski, J.E. Barrios Vargas, Y.H. Lee, S. Roche, Charge transport in polycrystalline graphene: challenges and opportunities, Adv. Mater. 26 (2014) 5079–5094.

[17] K. Xu, P. Cao, J.R. Heath, Scanning tunneling microscopy characterization of the electrical properties of wrinkles in exfoliated graphene monolayers, Nano Lett. 9 (2009) (2009) 4446–4451.

[18] N. Liu, Z. Pan, L. Fu, C. Zhang, B. Dai, Z. Liu, The origin of wrinkles on transferred graphene, Nano Res. 4 (2011) (2011) 996–1004.

[19] M. Ahmad, H. An, Y.S. Kim, J.H. Lee, J. Jung, S.-H. Chun, Y. Seo, Nanoscale investigation of charge transport at the grain boundaries and wrinkles in graphene film, Nanotechnology 23 (2012) (2012) 285705.

[20] W. Zhu, T. Low, V. Perebeinos, A.A. Bol, Y. Zhu, H. Yan, J. Tersoff, P. Avouris, Structure and electronic transport in graphene wrinkles, Nano Lett. 12 (2012) (2012) 3431–3436.

[21] S. Ladak, J.M. Ball, D. Moseley, G. Eda, W.R. Branford, M. Chhowalla, T.D. Anthopoulos, L.F. Cohen, Observation of wrinkle induced potential drops in biased chemically derived graphene thin film networks, Carbon 64 (2013) (2013) 35–44.

[22] P. Willke, C. Möhle, A. Sinterhauf, T. Kotzott, H.K. Yu, A. Wodtke, M. Wenderoth, Local transport measurements in graphene on SiO₂ using Kelvin probe force microscopy, Carbon 102 (2016) (2016) 470–476.

[23] B. Vasić, A. Zurutuza, R. Gajić, Spatial variation of wear and electrical properties across wrinkles in chemical vapour deposition graphene, Carbon 102 (2016) (2016) 304–310.

[24] Y. Wu, G. Yu, H. Wang, B. Wang, Z. Chen, Y. Zhang, B. Wang, X. Shi, X. Xie, Z. Jin, X. Liu, Synthesis of large-area graphene on molybdenum foils by chemical vapor deposition, Carbon 50 (2012) (2012) 5226–5231.

[25] Y. Grachova, S. Vollebregt, A.L. Lacaita, P.M. Sarro, High quality wafer-scale CVD graphene on molybdenum thin film for sensing application, Proc. Eng. 87 (2014) (2014) 1501–1504.

[26] Z. Zou, L. Fu, X. Song, Y. Zhang, Z. Liu, Carbide-forming groups IVB-VIB metals: a new territory in the periodic table for CVD growth of graphene, Nano Lett. 14 (2014) (2014) 3832–3839.

[27] C. Schiattarella, S. Vollebregt, T. Polichetti, B. Alfano, E. Massera, M.L. Miglietta, G. Di Francia, P.M. Sarro, CVD transfer-free graphene for sensing applications, Beilstein J. Nanotechnol. 8 (2017) (2017) 1015–1022.

[28] S. Vollebregt, R.J. Dolleman, H.S.J. van der Zant, P.G. Steeneken, P.M. Sarro, Suspended graphene beams with tunable gap for squeeze-film pressure sensing, 2017 19th International Conference on Solid-State Sensors, Actuators and Microsystems (TRANSDUCERS), 2017, pp. 770–773.

[29] S. Naghdi, I. Jevremović, V. Mišković-Stanković, K.Y. Rhee, Chemical vapour deposition at atmospheric pressure of graphene on molybdenum foil: effect of annealing time on characteristics and corrosion stability of graphene coatings, Corros. Sci. 113 (2016) (2016) 116–125.

[30] S. Naghdi, K. Nešović, V. Mišković-Stanković, K.Y. Rhee, Comprehensive electrochemical study on corrosion performance of graphene coatings deposited by chemical vapour deposition at atmospheric pressure on platinum-coated molybdenum foil, Corros. Sci. 130 (2018) (2018) 31–44.

[31] S. Naghdi, K.Y. Rhee, S.J. Park, Oxidation resistance of graphene-coated molybdenum: Effects of pre-washing and hydrogen flow rate, Int. J. Refract. Metals Hard Mater. 65 (2017) (2017) 29–33.

[32] F. Ricciardella, S. Vollebregt, T. Polichetti, M. Miscuglio, B. Alfano, M.L. Miglietta, E. Massera, G. Di Francia, P.M. Sarro, Effects of graphene defects on gas sensing properties towards NO₂ detection, Nanoscale 9 (2017) (2017) 6085–6093.

[33] D.K. Hong, S.A. Han, J.H. Park, S.H. Tan, N. Lee, Y. Seo, Frictional force detection from lateral force microscopic image using a Si grating, Colloids Surf. A 313–314 (2008) (2008) 567–570.

[34] Y.-J. Yu, Y. Zhao, S. Ryu, L.E. Brus, K.S. Kim, P. Kim, Tuning the graphene work function by electric field effect, Nano Lett. 9 (2009) (2009) 3430–3434.

[35] D. Graf, F. Molitor, K. Ensslin, C. Stampfer, A. Jungen, C. Hierold, L. Wirtz, Spatially resolved Raman spectroscopy of single- and few-layer graphene, Nano Lett. 7 (2007) (2007) 238–242.

[36] B. Vasić, A. Matković, U. Ralević, M. Belić, R. Gajić, Nanoscale wear of graphene and wear protection by graphene, Carbon 120 (2017) (2017) 137–144.

[37] A. Zandiatashbar, G.-H. Lee, S.J. An, S. Lee, N. Mathew, M. Terrones, T. Hayashi, C.R. Picu, J. Hone, N. Koratkar, Effect of defects on the intrinsic strength and stiffness of graphene, Nat. Commun. 5 (2014) (2014) 3186.

[38] M. Tripathi, F. Awaja, R.A. Bizao, S. Signetti, E. Iacob, G. Paolicelli, S. Valeri, A. Dalton, N.M. Pugno, Friction and adhesion of different structural defects of graphene, ACS Appl. Mater. Inter. 10 (2018) (2018) 44614–44623.

[39] K.-S. Kim, H.-J. Lee, C. Lee, S.-K. Lee, H. Jang, J.-H. Ahn, J.-H. Kim, H.-J. Lee, Chemical vapor deposition-grown graphene: the thinnest solid lubricant, ACS Nano 5 (2011) (2011) 5107–5114.

[40] S. Zhang, T. Ma, A. Erdemir, Q. Li, Tribology of two-dimensional materials: from mechanisms to modulating strategies, Mater. Today 26 (2019) (2019) 67–86.

[41] A. Vasić, B. Matković, R. Gajić, I. Stanković, Wear properties of graphene edges probed by atomic force microscopy based lateral manipulation, Carbon 107 (2016) (2016) 723–732.

[42] D. Berman, A. Erdemir, A.V. Sumant, Graphene: a new emerging lubricant, Mater. Today 17 (2014) (2014) 31–42.

[43] P. Egberts, G.H. Han, X.Z. Liu, A.T.C. Johnson, R.W. Carpick, Frictional behavior of atomically thin sheets: hexagonal-shaped graphene islands grown on copper by chemical vapor deposition, ACS Nano 8 (2014) (2014) 5010–5021.

[44] M.-S. Won, O.V. Penkov, D.-E. Kim, Durability and degradation mechanism of graphene coatings deposited on Cu substrates under dry contact sliding, Carbon 54 (2013) (2013) 472–481.

[45] D. Berman, S.A. Deshmukh, S.K.R.S. Sankaranarayanan, A. Erdemir, A.V. Sumant, Extraordinary macroscale wear resistance of one atom thick graphene layer, Adv. Funct. Mater. 24 (2014) (2014) 6640–6646.

[46] A. Klemenz, L. Pastewka, S.G. Balakrishna, A. Caron, R. Bennewitz, M. Moseler, Atomic scale mechanisms of friction reduction and wear protection by graphene, Nano Lett. 14 (2014) (2014) 7145–7152.

[47] J. Martin, N. Akerman, G. Ulbricht, T. Lohmann, J.H. Smet, K. von Klitzing, A. Yacoby, Observation of electron-hole puddles in graphene using a scanning single-electron transistor, Nat. Phys. 4 (2007) (2007) 144.

[48] Y. Zhang, V.W. Brar, C. Girit, A. Zettl, M.F. Crommie, Origin of spatial charge in-homogeneity in graphene, Nat. Phys. 5 (2009) (2009) 722.

[49] S.C. Martin, S. Samaddar, B. Sacépé, A. Kimouche, J. Coraux, F. Fuchs, B. Grévin, H. Courtois, C.B. Winkelmann, Disorder and screening in decoupled graphene on a metallic substrate, Phys. Rev. B 91 (2015) (2015) 041406.

[50] A. Deshpande, W. Bao, F. Miao, C.N. Lau, B.J. LeRoy, Spatially resolved spectro-scopy of monolayer graphene on SiO_2, Phys. Rev. B 79 (2009) (2009) 205411.

[51] G. Giovannetti, P.A. Khomyakov, G. Brocks, V.M. Karpan, J. van den Brink, P.J. Kelly, Doping graphene with metal contacts, Phys. Rev. Lett. 101 (2008) (2008) 026803.

[52] A. Matković, M. Chhikara, M. Milićević, U. Ralević, B. Vasić, D. Jovanović, M. Belić, G. Bratina, R. Gajić, Influence of a gold substrate on the optical properties of gra-phene, J. Appl. Phys. 117 (2015) (2015) 015305.

[53] C. Leung, H. Kinns, B.W. Hoogenboom, S. Howorka, P. Mesquida, Imaging surface charges of individual biomolecules, Nano Lett. 9 (2009) (2009) 2769–2773.

[54] L. Bartels, Tailoring molecular layers at metal surfaces, Nat. Chem. 2 (2010) (2010) 87–95.

[55] J. Wyrick, D.-H. Kim, D. Sun, Z. Cheng, W. Lu, Y. Zhu, K. Berland, Y.S. Kim, E. Rotenberg, M. Luo, P. Hyldgaard, T.L. Einstein, L. Bartels, Do two-dimensional noble gas atoms produce molecular honeycombs at a metal surface? Nano Lett. 11 (2011) (2011) 2944–2948.

[56] A.S. DeLoach, B.R. Conrad, T.L. Einstein, D.B. Dougherty, Coverage dependent molecular assembly of anthraquinone on Au(111), J. Chem. Phys. 147 (2017) (2017) 184701.

[57] C. Krull, M. Castelli, P. Hapala, D. Kumar, A. Tadich, M. Capsoni, M.T. Edmonds, J. Hellerstedt, S.A. Burke, P. Jelinek, A. Schiffrin, Iron-based trinuclear metal-or-ganic nanostructures on a surface with local charge accumulation, Nat. Commun. 9 (2018) (2018) 3211.

[58] O. Kazakova, V. Panchal, T.L. Burnett, Epitaxial graphene and graphene-based devices studied by electrical scanning probe microscopy, Crystals 3 (2013) (2013) 191–233.

[59] S. Hormeño, M. Penedo, C.V. Manzano, M. Luna, Gold nanoparticle coated silicon tips for Kelvin probe force microscopy in air, Nanotechnology 24 (2013) (2013) 395701.

[60] R. Huang, S. Ye, K. Sun, K.S. Kiang, C.H.K. de Groot, Fermi level tuning of ZnO films through supercycled atomic layer deposition, Nanoscale Res. Lett. 12 (2017) (2017) 541.

Full Length Article

Local electrical properties and charging/discharging of CdSe/CdS core-shell nanoplatelets

Borislav Vasić[a,*], Sonja Aškrabić[b], Milka M. Jakovljević[a], Mikhail Artemyev[c]

[a] *Graphene Laboratory of Center for Solid State Physics and New Materials, Institute of Physics Belgrade, University of Belgrade, Pregrevica 118, 11080 Belgrade, Serbia*
[b] *Nanostructured Matter Laboratory of Center for Solid State Physics and New Materials, Institute of Physics Belgrade, University of Belgrade, Pregrevica 118, 11080 Belgrade, Serbia*
[c] *Research Institute for Physical Chemical Problems of the Belarusian State University, Minsk 220006, Belarus*

A B S T R A C T

Quantum confinement in two-dimensional semiconductor nanoplateletes (NPLs) is determined by their thickness which can be precisely controlled during the synthesis. As a result, NPLs have a very narrow luminescence spectrum and they can provide light sources with very high color purity. Switchable light sources needed for a wide range of applications require the dynamic control of the luminescence. One efficient approach for this purpose is direct charge injection into NPLs. In order to study charging/discharging processes and local electrical properties of CdSe/CdS core-shell NPLs as the model system, here we employed electrical methods based on atomic force microscopy (AFM). Simple and efficient procedures for "write/read/erase" operations are presented: charges are written by a biased AFM tip in contact with the NPLs, their charge state is read by Kelvin probe force or electric force microscopy, whereas injected charges are erased by inversely biased AFM tip. The amount of injected charges is well controlled by a magnitude, polarity and duration of the applied bias voltage, whereas the rate of subsequent spontaneous charge relaxation is dominantly determined by ambient humidity.

1. Introduction

Optoelectronic applications of colloidal semiconductor nanocrystals (NCs) in light-emitting diodes (LEDs) [1] and solar cells [2] are based on their size-tunable electronic and optical properties [3,4]. Due to quantum confinement, discrete energy levels which determine the electronic band gap and optical transitions can be precisely controlled by modifying the size and shape of semiconductor NCs. As a result, they are characterized with a narrow and tunable emission spectrum covering a broad range from ultraviolet, through visible to near-infrared region [1,5–7]. At the same time, relatively simple, cost-effective, flexible and environment-friendly fabrication methods of colloidal chemistry, compatible with various assembling techniques, provide large-area structures needed for applications [8,9].

Although the optoelectronic properties of semiconductor NCs are most relevant for applications, electrostatic properties play a significant role as well, since the charge occupation of discrete electronic states determines the strength and rates of optical transitions [10,11]. Therefore, charging can be an efficient method for the switching of luminescence in semiconductor NCs. This property is very interesting from practical point of view and such dynamic control significantly

extends the scope of NCS' applicability. In this context, the most suitable control methods are the electrical ones, such as direct charge injection [12–14], doping [15,16], electric-field control [17–19], or incorporation into LED devices [1,5–7].

Electrical properties of semiconductor NCs are commonly investigated at macro-scale, on large ensembles of nanostructures [20,21]. On the other hand, atomic force microscopy (AFM) based methods enable local studies with a high spatial resolution reaching the single-nanoparticle level. As a result, these methods could provide additional information about local transport properties [22–24] and electronic band structure [25,26]. In addition, AFM based methods are very efficient for the local charging of semiconductor NCs and modulation of their photoluminescence [27] and electrical properties [28], or for the demonstration of inverse effects, where an external light induces local charges in semiconductor NCs leading to photoionization [10,11,29,30] or charge separation [31–33].

Recently, two-dimensional (2D) nanoplatelets (NPLs), a new class of colloidal semiconductor NCs, have attracted a lot of attention because the quantum confinement is determined by NPL thickness [34–37]. Since the thickness can be controlled more precisely than the geometry (size and shape) of standard three-dimensional NCs such as quantum

---

* Corresponding author.
  E-mail address: bvasic@ipb.ac.rs (B. Vasić).

dots, 2D NPLs provide more narrow emission and light sources with improved color purity. Although, the luminescence control of 2D NPLs by electrical methods has been demonstrated recently [38–40], their electrostatic properties at nanoscale and their control by direct charge injection have been still unexplored.

In this paper, we use AFM based electrical methods, Kelvin probe force microscopy (KPFM) and electric force microscopy (EFM), in order to study local electrical properties of 2D CdSe/CdS core-shell NPLs. They were selected as the model system due to enhanced spontaneous emission and lasing compared to the core-only NPLs [41,42]. We show that charging/discharging of NPLs can be well controlled by a magnitude, polarity and duration of the bias voltage applied by the AFM tip. The paper is organized in the following way. After the initial morphological analysis in Section 3.1, the results for the local electrical surface potential of the NPLs are presented in Section 3.2. Write operation or local charging of the NPLs by the AFM tip as a function of the tip bias voltage and hold time is demonstrated in Section 3.3. KPFM and EFM methods are employed for the read operation and characterization of charged NPLs. The time relaxation of injected charges is studied in Section 3.4 by successive KPFM measurements. Finally, in Section 3.5, a simple AFM based method for the erase operation and fast discharging is illustrated.

2. Material and methods

2.1. Sample preparation

Core-shell CdSe/CdS NPLs having 4.5 ML CdSe core and 3 ML CdS shell, with ca. 20 nm × 30 nm lateral size, were synthesized according to a published procedure [43–45]. These NPLs, being hydrophobic, were functionalized with mercaptoacetic acid (MAA) and thereby negatively charged. After the treatment with MAA, NPLs were rinsed with isopropanol and dispersed in water. Commercial highly n-doped Si wafer with 85 nm thick SiO_2 film on the top was treated in aminopropyl trietoxy silane (APTS) dissolved in toluene, in order to positively charge SiO_2. After being left in solution for 20 min, the substrate was rinsed with toluene. In the next step, the colloidal solution of negatively charged CdSe/CdS NPLs was dropcast onto the wafer covered with ATS and left for 20 min in order to allow for electrostatic self-assembly to occur. After 20 min the substrate was rinsed and 2D layer of close-packed core-shell NPLs on SiO_2 surface was obtained. According to the preparation procedure, the investigated sample can be considered as a film consisting of CdSe/CdS NPLs functionalized with MAA and thin layer of APTS polyelectrolyte underneath. Hereafter it will be called CdSe/CdS film.

2.2. AFM measurements

In order to investigate morphology and local electrical properties of CdSe NPLs, we employed NTEGRA Prima AFM system. Basic topographic imaging was performed in tapping AFM mode. AFM phase and magnitude signals were recorded simultaneously with the topography in order to resolve shape and edges of NPLs with a better resolution. The phase signal corresponds to the phase lag of the AFM cantilever, while the magnitude signal represents the oscillation amplitude of the AFM cantilever.

Local electrical properties were characterized by two-pass techniques, EFM and KPFM. AFM probes NSG01/Pt from NT-MDT with Pt coating were used. In both EFM and KPFM, topography was measured in the first pass by AFM tapping mode. Then, the AFM probe was lifted by 20 nm and the scanning was performed along the same topographic line measured in the first pass. During the second pass in EFM, DC voltage was applied between the AFM probe and the sample while the probe was excited mechanically. The measured EFM signal in the second pass corresponds to the phase lag of the AFM cantilever which is proportional to the gradient of the normal electric force. In order to

avoid any confusion with the AFM phase measured during basic topographic imaging, this signal will be hereafter called EFM phase.

On the other hand, during the second pass in KPFM, a sum of AC and variable DC voltage was applied between the AFM probe and sample. The AC voltage excited oscillations of the AFM probe, while the value of the variable DC voltage which canceled these oscillations was equal to the electrical surface potential or to the contact potential difference (CPD) between the probe and sample. The CPD is equal to the work function difference between the tip and sample, WF_{tip} and WF_s, respectively. The absolute value of the sample work function WF_s was calculated as $WF_s = WF_{tip} - CPD$, where the work function of Pt coated AFM tips were calibrated using HOPG as a reference [46].

In order to interpret EFM measurements and the interaction between biased AFM tip and the sample, i.e. whether this interaction is attractive or repulsive, and in order to determine the polarity of charges injected into the sample, the phase signal was adjusted prior to EFM measurements in the following way. By varying the phase of the piezo-driver, the initial AFM phase was set to 90° at the mechanical resonance of employed AFM cantilever, with a decreasing phase across the resonance (with a negative slope). Taking into account that the attractive (repulsive) AFM tip-sample interaction shifts the resonance to lower (higher) frequencies, the attractive (repulsive) interaction is characterized by a decrease (increase) of the phase shift in the considered case.

AFM methods for local charging and subsequent charge detection [47] have been well developed in recent years for semiconductor NCs [27,28], organic nanostructures [48,49], carbon nanotubes [50], 2D materials [51–53] and even biological nanostructures [54]. In this study, the local charging was performed according to the following procedure. After the initial electrical characterization carried out in either KPFM or EFM mode, the AFM system was switched into contact mode, the AFM tip approached to the sample surface, and DC voltage in the range ± 10 V was applied to the AFM tip. The hold time (defined as a time during the bias voltage was applied) was varied from several seconds up to several minutes. After that, the probe was lifted, the voltages were turned off, and the system was switched back into one of the targeted electrical modes in order to characterize changes in electrical properties induced by the injected charges.

3. Results and discussion

3.1. Morphology

Transmission electron microscopy (TEM) image of CdSe/CdS NPLs is given in Fig. 1(a). As can be seen, the NPLs are randomly oriented and typically more elongated in one direction having approximately a rectangular shape with the size of several tenths of nanometers. Although TEM provides the best spatial resolution, AFM enables simpler and faster morphological characterization. 2D and three-dimensional (3D) topographic images of CdSe/CdS film obtained by AFM are depicted in Fig. 1(b) and (c), respectively. Film thickness of 4.7 ± 1.5 nm was determined as an average value of the height distribution while the deviation was calculated as an average roughness. The autocorrelation image is given in Fig. 1(d). The dominant feature is the bright circular domain in the middle. Since the autocorrelation image is approximately isotropic, NPLs do not have any preferential orientation in the plane. Due to the convolution with the AFM tip, NPLs look like rounded grains in topographic images. Therefore, in the grain-size analysis, they were approximated with circular plates. The histogram of their size distribution is displayed in Fig. 1(d). As can be seen, the average NPL radius is around 15 nm, implying that a typical NPL can be represented by a thin disc with a diameter of around 30 nm.

The AFM phase and magnitude signals are displayed in Fig. 1(e) and (f), respectively. As can be seen, boundaries between adjacent NPLs are better resolved whereas the contrast between the NPLs and underlying substrate is more pronounced due to generally higher sensitivity of
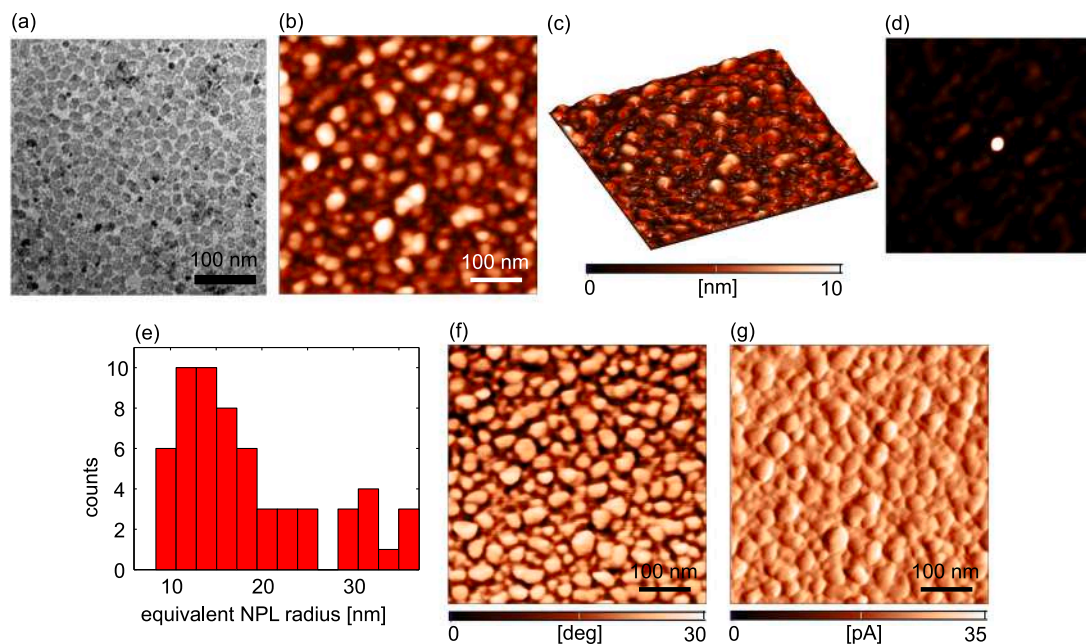
Fig. 1. Morphology of CdSe NPLs: (a) TEM image, (b) 2D and (c) 3D topographic image, (d) autocorrelation image, (e) histogram of the equivalent NPL radius, (f) AFM phase and (g) AFM magnitude image.

phase and magnitude signals to NPL edges. Therefore, these AFM modes provide a high spatial resolution for the imaging of 2D NPLs similar to TEM.

3.2. Electrical surface potential

Topography and CPD map of CdSe/CdS film measured by KPFM are presented in Fig. 2(a) and (b), respectively. The histogram of the CPD map is depicted in Fig. 2(c). It is characterized with a single and narrow peak with the average CPD of 817 ± 7 mV. Taking into account measurements on five different $2 \times 2 \, \mu m^2$ areas, the average CPD is 800 ± 25 mV, demonstrating that CdSe/CdS NPLs have uniform surface potential. The absolute value of the work function of CdSe/CdS film was found to be 4.13 ± 0.04 V (after the calibration of the Pt coated AFM tip) which is in good agreement with literature data [55].

Although KPFM is a convenient technique which directly gives CPD as a result, the spatial resolution limited to 20–30 nm does not allow resolving of individual NPLs. In order to overcome this limitation, EFM was employed instead. The EFM phase signal is proportional to gradient of the electric force in the normal direction. As a result, although EFM and KPFM share similar experimental setups, the EFM phase calculated as a spatial derivative is much more sensitive to spatial variations of surface electrical properties. Topography and EFM phase map of CdSe/CdS film are given in Fig. 3(a) and (b), respectively. As can be seen,

individual NPLs are clearly resolved in both topographic and EFM image. Most of NPLs have similar EFM contrast. Still, the EFM phase signal is correlated with the topography, which implies that bigger topographic features, which correspond to clusters of several NPLs (appeared during sample preparation), give more pronounced EFM phase contrast.

In order to obtain quantitative information from EFM measurements, the EFM imaging was performed as a function of the EFM bias voltage in the range ± 10 V. For every bias voltage, an average EFM phase shift of CdSe/CdS NPLs was determined. The results of these measurements are summarized in Fig. 3(c) showing a parabolic dependence of the EFM phase on the EFM tip voltage. The experimental data were fitted by the following function [48,53,54]

$$\Phi_{\text{EFM}} = C_1 (V_{\text{EFM}} - V_{\text{sp}})^2 + C_2 (V_{\text{EFM}} - V_{\text{sp}}) + \Phi_0, \tag{1}$$

where V_{EFM} is the EFM voltage applied on the AFM probe in the second pass of EFM imaging, V_{sp} is the electrical surface potential which corresponds to the CPD measured by KPFM, whereas C_1, C_2, and Φ_0 are additional fitting constants. The first term in Eq. (1) corresponds to the capacitive tip-sample interaction, whereas the second term represents the Coulombic interaction between biased AFM probe and localized charges at the sample surface [48,53,54].

The fitting curve is presented in Fig. 3(c) by the solid line, the dashed line shows the contribution of the parabolic function (the
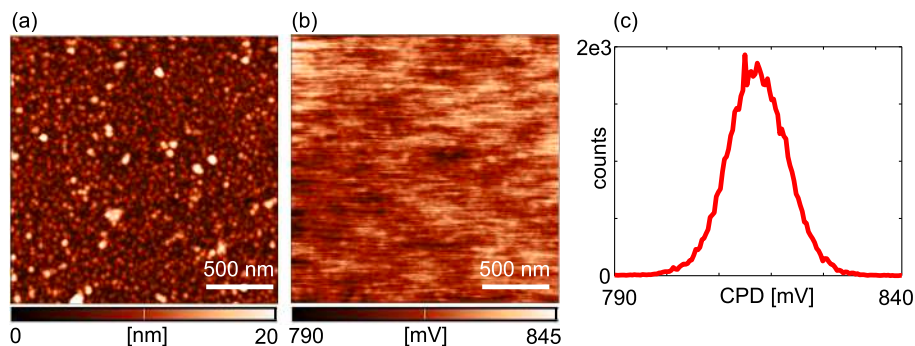

Fig. 2. (a) Topography and (b) CPD measured by KPFM. (c) Histogram of the CPD distribution.
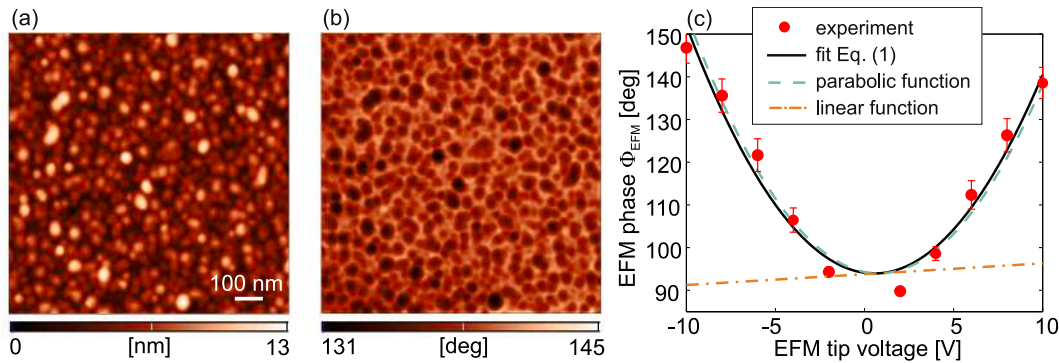
Fig. 3. (a) AFM topographic and (b) EFM phase image. The EFM voltage in the second pass was − 8 V. (c) An average EFM phase of CdSe/CdS NPLs as a function of EFM voltage in the second pass. Dots stand for experimentally measured values, the solid line is fit to Eq. (1), whereas the dashed and dashed-dotted lines stand for the contribution of the parabolic and linear term from Eq. (1), respectively. Every dot represents the EFM phase obtained by the averaging of all NPLs within one scan area of $1 \times 1 \, \mu m^2$ for a given EFM voltage.

capacitive interaction), whereas the dashed-dotted line represents the linear function (Coulombic interaction) from Eq. (1). The local electrical surface potential V_{sp} of CdSe/CdS film obtained from the fit is 0.795 ± 0.025 V. V_{sp} corresponds to the EFM voltage where the EFM phase curve reaches the minimum Φ_0. This is exactly the voltage by which the EFM phase curve is shifted along the voltage axis. The fitting procedure gives non-zero and positive coefficient C_2 meaning that Coulombic interaction has a certain contribution in the measured EFM phase shift. As can be seen in Fig. 3(c), for the positive (negative) voltage difference $V_{EFM} - V_{sp} > 0$ ($V_{EFM} - V_{sp} < 0$), Coulombic interaction leads to a higher (lower) EFM phase shift represented as a change between the solid and dashed line. According to the phase convention explained in Section 2.2, an attractive (repulsive) interaction is characterized by a decrease (increase) of the phase shift. Therefore, in the considered case, the electrical interaction is repulsive (attractive) for positive (negative) voltage difference $V_{EFM} - V_{sp}$ meaning that as-deposited NPLs are slightly positively charged. This is inconsistent with the preparation procedure where NPLs were negatively charged. However, after the deposition, the NPLs inevitably come into the contact with oxygen from air which is well known as p-type dopant for metal chalcogenide quantum dots [56]. Similar p-doping after the exposure to air and the reaction with oxygen was observed for other 2D system such as graphene [57] and thin organic films [48]. Therefore, positive charging of as-deposited NPLs most probably originates from the doping by ambient oxygen. According to the results presented in Fig. 3, EFM allows for a high-resolution electrical imaging of CdSe/CdS films at the single-nanoparticle level. At the same time, electrical surface potential and properties of the electrical interaction can be determined with the same spatial resolution, but an additional processing and fitting of experimentally measured data are necessary.

3.3. Local charging

Results for the electrical surface potential and EFM phase measured after the local charging of CdSe/CdS film at a single point are presented in Fig. 4. The KPFM map measured after the charging at the central point, for the bias voltage $V_{ch} = -8$ V and hold time $T_{ch} = 30$ s is depicted in Fig. 4(a). The cross section of the CPD map along the dashed line is given in Fig. 4(b) showing a significant drop in CPD around the charging point of around $\Delta CPD \approx 200$ mV (ΔCPD was calculated as a difference between CPD of uncharged (CPD_0) and charged areas (CPD_{ch})). The EFM phase maps after the local charging at a negative bias voltage are depicted in Fig. 4(c) for a positive (top) and negative (bottom) EFM voltage. EFM phase profiles along the dashed lines are given in Fig. 4(d). As can be seen, the EFM phase contrast is reversed upon changing the polarity of the EFM voltage which proves Coulombic tip-sample interaction.
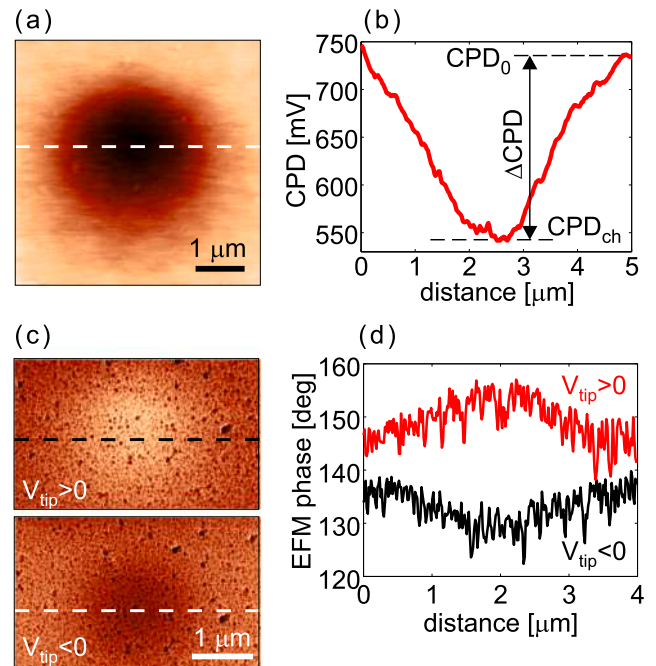

Fig. 4. Electrical characterization after the local charging at the bias voltage $V_{ch} = -8$ V and for the hold time $T_{ch} = 30$ s: (a) CPD map measured by KPFM, and (b) the cross section of the CPD along the dashed line in part (a), (c) EFM phase maps for positive (top) and negative EFM voltage (bottom), and (d) cross sections along the dashed lines in (c).

The EFM phase grows up for the positive EFM voltage when the electrical tip-sample interaction is repulsive. On the other hand, the EFM phase falls down for the negative EFM voltage when the interaction is attractive. Therefore, the sample is locally positively charged, although the charging was performed at a negative bias voltage. This is in accordance with KPFM measurements which indicate a local decrease of Fermi level. According to these results, the mechanism of local charging is not based on charge injection by a biased AFM tip, but on the polarization of the sample surface. This means that negatively biased AFM tip does not inject negative charges, but polarizes the surrounding medium and attracts positive charges.

While the CPD map measured after the charging in Fig. 4(b) consists of a rather smooth potential dip, EFM phase profiles consist of a smooth dip/rise (depending on the bias voltage during the charging) and of superimposed oscillating phase. The oscillating part corresponds to individual NPLs which become either brighter (top EFM image in Fig. 4(c)) or darker (bottom EFM image in Fig. 4(c)) than surrounding
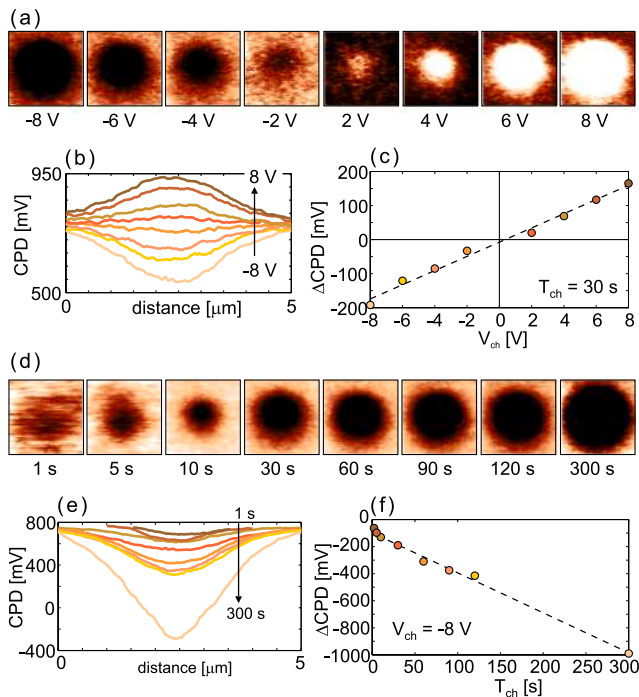
Fig. 5. Change of CPD as a function of bias voltage during the local charging: (a) CPD maps measured by KPFM after the charging for bias voltages in the range ± 8 V for the fixed hold time $T_{ch} = 30$ s (the scan size is 5×5 μm² whereas the CPD scale is $700 - 770$ mV ($760 - 810$ mV) for the negative (positive) bias voltages), (b) CPD profiles extracted from the maps in part (a), and (c) ΔCPD (calculated from the profiles in part (b) for the central points) as a function of the bias voltage with a linear fit represented by the dashed line. Change of CPD as a function of the hold time during the local charging: (d) CPD maps measured by KPFM after the charging for the hold time in the range $1 - 300$ s and at the fixed bias voltage $V_{ch} = -8$ V (the scan size is 5×5 μm² whereas the CPD scale is $630 - 760$ mV), (e) CPD profiles from the maps in part (d), and (f) ΔCPD (calculated from the profiles in part (e) for the central points) as a function of the hold time with a linear fit represented by the dashed line.

and uncharged NPLs. The modified EFM phase of NPLs after the charging indicates that charge storage can be detected in individual NPLs.

In order to test the influence of the voltage V_{ch} applied during the charge injection, electrical surface potential was measured by KPFM after the charging for V_{ch} in the range ± 8 V and for the fixed hold time $T_{ch} = 30$ s. Corresponding CPD maps and profiles are depicted in Fig. 5(a) and (b), respectively. As can be seen, the charged areas have a circular shape with a diameter increasing with $|V_{ch}|$ and reaching around 5 μm for the highest voltage. These areas behave like potential wells while their depth increases with $|V_{ch}|$. Change of the CPD between charged and uncharged areas, ΔCPD, as a function of V_{ch} is plotted in Fig. 5(c). ΔCPD can be fitted with a linear curve represented by the dashed line. For the chosen range of V_{ch}, ΔCPD changes almost linearly in the range ≈ ±200 mV.

Similar study was carried out in order to test the influence of the hold time in the range $1 - 300$ s, while keeping constant the voltage during charging ($V_{ch} = -8$ V). CPD maps measured after the charging are shown in Fig. 5(d). The central black circle becomes wider and darker with increasing T_{ch}, reaching around 5 μm in a diameter for the longest hold time. CPD profiles are given in Fig. 5(e) showing potential wells whose depth increases with T_{ch}. The change of the CPD between charged and uncharged areas, ΔCPD, as a function of $T_{ch} = 30$ s is depicted in Fig. 5(f). Dashed line stands for a fit to the experimentally measured points. By omitting two starting points and going from $T_{ch} = 10$ s, ΔCPD grows practically linearly with T_{ch} up to $- 1000$ mV.

Injected charges are trapped in CdSe/CdS film, in CdSe/CdS NPLs and/or in the underneath polyelectrolyte layer, whereas they can be

stored at the surface of underlying silicon-dioxide as well. The considered system can be approximated as a plane capacitor. The bottom electrode is silicon, the top electrode consists of CdSe/CdS film and top charged layer of silicon-dioxide, whereas the rest of the silicon-dioxide layer acts as a dielectric. Surface density of injected charges can be approximately calculated according to the following expression $\sigma = \varepsilon_0 \varepsilon_r / t_d \cdot$ΔCPD, where ΔCPD is change in CPD due to charging, ε_0 is the vacuum permittivity, whereas ε_r and t_d are the permittivity and thickness of a dielectric layer between the NPLs and silicon layer. According to results from Fig. 5, the following relations hold, ΔCPD = $\alpha_V V_{ch}$ and ΔCPD = $\alpha_T T_{ch}$, where α_V and α_T are the slopes of the linear fits in Fig. 5(b) and (d), respectively. Surface charge density can be then represented as , where $C_s = \varepsilon_0 \varepsilon_r / t_d$ is the capacitance per area. Therefore, although density of charges injected just into NPLs can not be determined, according to the last formula, density of injected charges can be simply controlled and adjusted by V_{ch} and T_{ch}.

3.4. Time relaxation of injected charges

Time relaxation of injected charges was studied by successive KPFM mapping after the initial charging. The KPFM mapping was maintained until the complete charge relaxation characterized by a nearly flat CPD map. The consecutive CPD maps measured by KPFM are presented in Fig. 6(a) and (d) for the charging by a positive and negative bias voltage, respectively. Corresponding CPD profiles are given in Fig. 6(b)
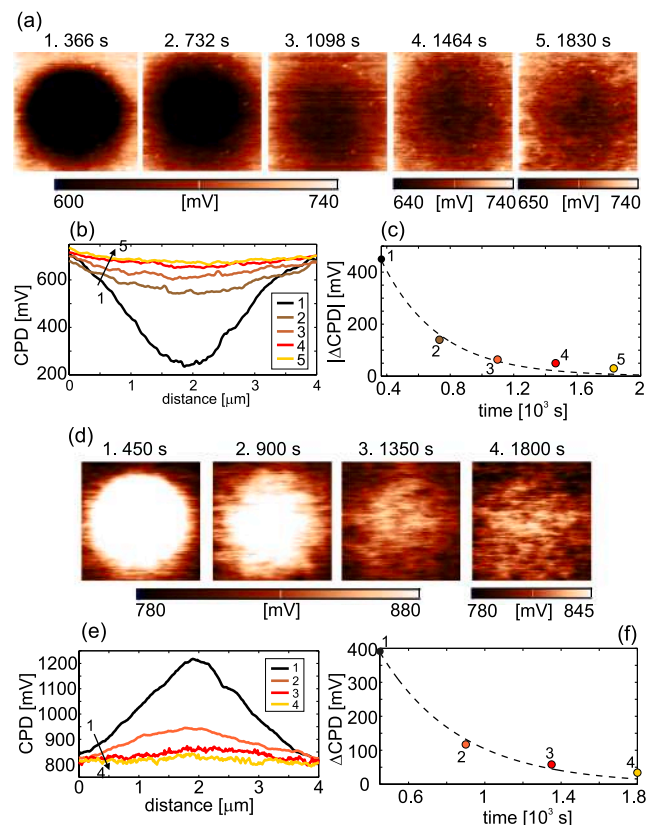

Fig. 6. Time relaxation of the charges injected by applying $- 8$ V for 60 s: (a) successive CPD maps measured by KPFM before almost complete relaxation (the scan size is 4×4 μm²), (b) CPD profiles, and (c) change of the —CPD— as a function of time. Time relaxation of the charges injected by applying 8 V for 120 s: (d) successive CPD maps measured by KPFM (the scan size is 4×4 μm²), (e) CPD profiles, and (f) change of the CPD as a function of time. Dashed lines in parts (c) and (f) stand for the exponential fits to the experimentally determined points. Time difference between adjacent points is equal to the time needed for one complete KPFM scan which is 366 s for the case in parts (a–c), and 450 s for the case in parts (d–f).
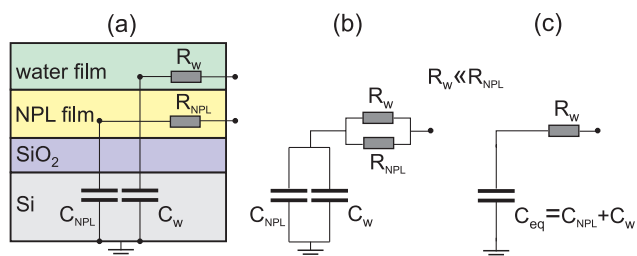
Fig. 7. Physical models for the time relaxation: (a), (b) the equivalent electrical scheme, and (c) a simplified scheme taking into account that the water-layer resistance R_w is much smaller than the in-plane resistance R_{NPL} of the CdSe/CdS film consisting of CdSe/CdS NPLs functionalized with MAA and a thin layer of APTS polyelectrolyte underneath.

and (e), whereas the change of CPD as a function of time is given in Fig. 6(c) and (f), respectively. The absolute value $|\Delta CPD|$ was fitted by an exponential function $\Delta CPD_0 \cdot \exp(-t/\tau)$, where t is time, τ stands for the time constant of the relaxation process, whereas ΔCPD_0 is the absolute value of ΔCPD at the initial moment (the moment when the first KPFM scan was finished). According to the fitting results, the time relaxation constants are 418 s and 358 s for positive and negative V_{ch}, respectively, therefore, around $6 - 7$ min.

The relaxation rates strongly depend on humidity. At ambient conditions, the sample surface is covered by a thin water layer acting as an additional conducting channel through which injected charges flow away [51]. Simple physical model of the considered system is depicted in Fig. 7(a). As can be seen, there are two films at the top of the silicon-dioxide: the first one is the CdSe/CdS film which consists of CdSe/CdS NPLs functionalized with MAA and a thin layer of APTS polyelectrolyte underneath, whereas the second film is a water layer. Both films have corresponding capacitances with respect to the grounded silicon substrate, C_{NPL} and C_w, respectively. Since the charge transport through the films is lateral, they are modeled by two resistors, R_{NPL} and R_w. Equivalent electrical scheme is given in Fig. 7(b). It is a series circuit between two parallel capacitances, C_{NPL} and C_w, and resistances, R_{NPL} and R_w.

The lateral current through CdSe/CdS film measured by conductive AFM (C-AFM) was zero which indicated a very high resistance R_{NPL}. In order to study charge relaxation in such high-resistance films, KPFM was employed instead [22]. At high humidities above 50%, discharge was very fast (much faster than several minutes needed for one KPFM scan) and it was not possible to observe any charging. Obviously, in this case the water film resistance R_w is very low. On the other hand, the charge relaxation measurements presented in Fig. 6 were done at a lower humidity of around 30%. As a result, the water film resistance R_w is increased, while discharge process is prolonged and can be followed by KPFM. According to the previous analysis, the water layer resistance R_w is much lower than the resistance of CdSe/CdS film, R_{NPL}. Therefore, R_{NPL} can be then omitted, whereas a simplified electrical scheme is given in Fig. 7(c). The time constant of the RC circuit is $\tau = R_w C_{eq}$, where $C_{eq} = C_{NPL} + C_w$. As a result, the relaxation time depends dominantly on the water film resistance R_w, which falls down at increased humidity thus making the relaxation and discharging very fast.

3.5. "Write/read/erase" operations

In addition to charge injection by a biased AFM tip or "writing" operation and KPFM/EFM measurements aimed for "reading" operation, a full control of the charge density requires an efficient mechanism for fast charge erasing in order to avoid long process of spontaneous relaxation discussed in the previous section. In order to erase or nullify charges, it is necessary to ground the sample or to inject charges of opposite polarity during a certain hold time. Such procedure is illustrated in Fig. 8(a). The first CPD map was recorded after charging at
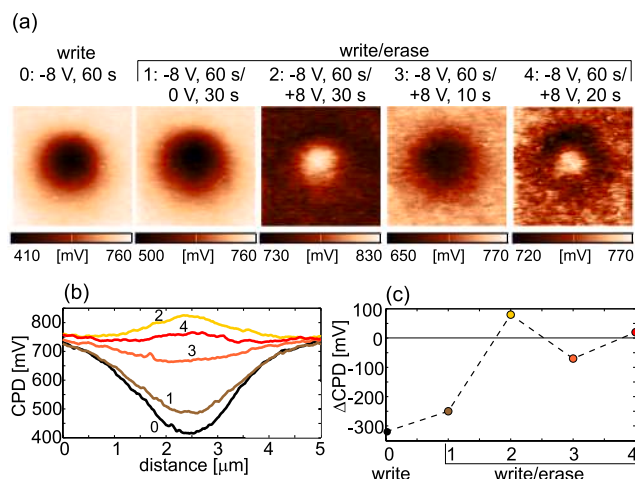

Fig. 8. Write/erase operation: (a) CPD maps measured by KPFM after (0) the writing operation only (charge injection at the negative bias voltage), and (1–4) several trials for the writing and subsequent erasing of injected charges with different combinations of the positive bias voltages and hold times, (b) CPD profiles extracted from the maps in part (a), and (c) change of the CPD for all five cases in part (a). The dashed line is a guide to eye. The scan size of CPD maps is $5 \times 5 \mu m^2$.

$- 8$ V for 60 s. The next four CPD maps represent trials aiming to nullify the injected charges in the following way: by subsequent grounding the film for 30 s and by charging the film at the positive voltage of 8 V for three different hold times 30 s, 10 s and 20 s. CPD profiles are presented in Fig. 8(b) whereas the evolution of ΔCPD is shown in Fig. 8(c). The writing operation at $- 8$ V for 60 s generates a potential well with a depth of around 300 mV. Erasing operation should flatten the potential as much as possible and give zero ΔCPD. In this respect, the erasing operation 4 gives the best performance.

4. Conclusion

In a summary, the initial work function of CdSe/CdS film of around 4 eV can be locally modified by the charging with a biased AFM probe. Such "write" operation generated 2D, circular potential wells, with a diameter of several microns and a depth of several hundreds of milivolts. Since the silicon-dioxide and the polyelectrolyte layer beneath NPL can also trap charges, it was not possible to determine the exact density of charges stored in NPLs only. Still, it was shown that the magnitude, polarity and duration of applied bias voltage very efficiently controlled the depth and diameter of the induced potential wells. Therefore, it is reasonable to expect that a proper combination of these control parameters would give a desired charge density in NPLs. "Read" operation was based on KPFM and EFM methods. While the first one gave CPD and work function of NPLs directly as an output, EFM had a better spatial resolution which allowed the electrical imaging of single NPLs. The rate of the spontaneous charge relaxation was dictated by environmental humidity. At the humidity of around 30%, the time relaxation constant was around 5 min, whereas at higher humidities injected charges could not be detected by KPFM/EFM due to very fast discharging through a water adlayer on NPLs. In order to avoid the spontaneous relaxation, trapped charges can be nullified and erased by inversely polarized AFM tip. Presented procedures for "write/read/erase" operations provide efficient means for dynamic control of a charge state of CdSe/CdS NPLs, while further experiments should explore capability of these procedures for the luminescence control.

Declaration of Competing Interest

There are no conflict of interest in this work.

Acknowledgements

References

[1] Y. Shirasaki, G.J. Supran, M.G. Bawendi, V. Bulović, Emergence of colloidal quantum-dot light-emitting technologies, Nat. Photon. 7 (2012) 13.

[2] P.V. Kamat, Quantum dot solar cells. Semiconductor nanocrystals as light harvesters, J. Phys. Chem. C 112 (2008) 18737–18753.

[3] A.P. Alivisatos, Perspectives on the physical chemistry of semiconductor nanocrystals, J. Phys. Chem. 100 (1996) 13226–13239.

[4] A.M. Smith, S. Nie, Semiconductor nanocrystals: structure, properties, and band gap engineering, Acc. Chem. Res. 43 (2010) 190–200.

[5] V.L. Colvin, M.C. Schlamp, A.P. Alivisatos, Light-emitting diodes made from cadmium selenide nanocrystals and a semiconducting polymer, Nature 370 (1994) 354–357.

[6] S. Coe, W.-K. Woo, M. Bawendi, V. Bulović, Electroluminescence from single monolayers of nanocrystals in molecular organic devices, Nature 420 (2002) 800–803.

[7] A.H. Mueller, M.A. Petruska, M. Achermann, D.J. Werder, E.A. Akhadov, D.D. Koleske, M.A. Hoffbauer, V.I. Klimov, Multicolor light-emitting diodes based on semiconductor nanocrystals encapsulated in GaN charge injection layers, Nano Lett. 5 (2005) 1039–1044.

[8] V. Lesnyak, N. Gaponik, A. Eychmüller, Colloidal semiconductor nanocrystals: the aqueous approach, Chem. Soc. Rev. 42 (2013) 2905–2929.

[9] J. Chang, E.R. Waclawik, Colloidal semiconductor nanocrystals: controlled synthesis and surface chemistry in organic media, RSC Adv. 4 (2014) 23505–23527.

[10] T.D. Krauss, L.E. Brus, Charge, polarizability, and photoionization of single semiconductor nanocrystals, Phys. Rev. Lett. 83 (1999) 4840–4843.

[11] T.D. Krauss, S. O'Brien, L.E. Brus, Charge and photoionization properties of single semiconductor nanocrystals, J. Phys. Chem. B 105 (2001) 1725–1733.

[12] C. Wang, M. Shim, P. Guyot-Sionnest, Electrochromic nanocrystal quantum dots, Science 291 (2001) 2390–2392.

[13] W.-K. Woo, K.T. Shimizu, M.V. Jarosz, R.G. Neuhauser, C.A. Leatherdale, M.A. Rubner, M.G. Bawendi, Reversible charging of CdSe nanocrystals in a simple solid-state device, Adv. Mater. 14 (2002) 1068–1071.

[14] P.P. Jha, P. Guyot-Sionnest, Photoluminescence switching of charged quantum dot films, J. Phys. Chem. C 111 (2007) 15440–15445.

[15] M. Shim, P. Guyot-Sionnest, n-type colloidal semiconductor nanocrystals, Nature 407 (2000) 981–983.

[16] D. Mocatta, G. Cohen, J. Schattner, O. Millo, E. Rabani, U. Banin, Heavily doped semiconductor nanocrystal quantum dots, Science 332 (2011) 77–81.

[17] E. Rothenberg, M. Kazes, E. Shaviv, U. Banin, Electric field induced switching of the fluorescence of single semiconductor quantum rods, Nano Lett. 5 (2005) 1581–1586.

[18] S.-J. Park, S. Link, W.L. Miller, A. Gesquiere, P.F. Barbara, Effect of electric field on the photoluminescence intensity of single CdSe nanocrystals, Chem. Phys. 341 (2007) 169–174.

[19] F. Vietmeyer, T. Tchelidze, V. Tsou, B. Janko, M. Kuno, Electric field-induced emission enhancement and modulation in individual CdSe nanowires, ACS Nano 6 (2012) 9133–9140.

[20] N.Y. Morgan, C.A. Leatherdale, M. Drndić, M.V. Jarosz, M.A. Kastner, M. Bawendi, Electronic transport in films of colloidal CdSe nanocrystals, Phys. Rev. B 66 (2002) 075339.

[21] D.S. Ginger, N.C. Greenham, Charge injection and transport in films of CdSe nanocrystals, J. Appl. Phys. 87 (2000) 1361–1368.

[22] M. Drndić, R. Markov, M.V. Jarosz, M.G. Bawendi, M.A. Kastner, N. Markovic, M. Tinkham, Imaging the charge transport in arrays of CdSe nanocrystals, Appl. Phys. Lett. 83 (2003) 4008–4010.

[23] D. Toker, I. Balberg, O. Zelaya-Angel, E. Savir, O. Millo, Size-dependent local conductance properties of CdSe nanocrystal ensembles, Phys. Rev. B 73 (2006) 045317.

[24] R.K. Singha, S. Manna, R. Bar, S. Das, S.K. Ray, Surface potential, charging and local current transport of individual Ge quantum dots grown by molecular beam epitaxy, Appl. Surf. Sci. 407 (2017) 418–426.

[25] B. Alperson, S. Cohen, I. Rubinstein, G. Hodes, Room-temperature conductance spectroscopy of CdSe quantum dots using a modified scanning force microscope, Phys. Rev. B 52 (1995) R17017–R17020.

[26] I. Tanaka, E. Kawasaki, O. Ohtsuki, K. Uno, M. Hara, H. Asami, I. Kamiya, Conductive-tip atomic force microscopy of CdSe colloidal nanodots, Surf. Sci. 532–535 (2003) 801–805.

[27] S. Schäfer, Z. Wang, T. Kipp, A. Mews, Fluorescence modulation of single CdSe nanowires by charge injection through the tip of an atomic-force microscope, Phys. Rev. Lett. 107 (2011) 137403.

[28] S.V. Kondratenko, V.S. Lysenko, Y.N. Kozyrev, M. Kratzer, D.P. Storozhuk, S.A. Iliash, C. Czibula, C. Teichert, Local charge trapping in Ge nanoclusters detected by Kelvin probe force microscopy, Appl. Surf. Sci. 389 (2016) 783–789.

[29] O. Cherniavskaya, L. Chen, L. Brus, Imaging the photoionization of individual CdSe/CdS core-shell nanocrystals on n- and p-type silicon substrates with thin oxides, J. Phys. Chem. B 108 (2004) 4946–4961.

[30] S. Li, M.L. Steigerwald, L.E. Brus, Surface states in the photoionization of high-quality CdSe core/shell nanocrystals, ACS Nano 3 (2009) 1267–1273.

[31] R. Costi, G. Cohen, A. Salant, E. Rabani, U. Banin, Electrostatic force microscopy study of single Au-CdSe hybrid nanodumbbells: evidence for light-induced charge separation, Nano Lett. 9 (2009) 2031–2039.

[32] S. Schäfer, Z. Wang, R. Zierold, T. Kipp, A. Mews, Laser-induced charge separation in CdSe nanowires, Nano Lett. 11 (2011) 2672–2677.

[33] S. Schäfer, A. Reich, Z. Wang, T. Kipp, A. Mews, Charge separation in CdSe/CdTe hetero-nanowires measured by electrostatic force microscopy, Appl. Phys. Lett. 100 (2012) 022110.

[34] S. Ithurria, M.D. Tessier, B. Mahler, R.P.S.M. Lobo, B. Dubertret, A.L. Efros, Colloidal nanoplatelets with two-dimensional electronic structure, Nat. Mater. 10 (2011) 936.

[35] B. Mahler, B. Nadal, C. Bouet, G. Patriarche, B. Dubertret, Core/shell colloidal semiconductor nanocrystals, J. Am. Chem. Soc. 134 (2012) 18591–18598.

[36] A.W. Achtstein, A. Schliwa, A. Prudnikau, M. Hardzei, M.V. Artemyev, C. Thomsen, U. Woggon, Electronic structure and exciton-phonon interaction in two-dimensional colloidal CdSe nanosheets, Nano Lett. 12 (2012) 3151–3157.

[37] A.V. Antanovich, A.V. Prudnikau, D. Melnikau, Y.P. Rakovich, A. Chuvilin, U. Woggon, A.W. Achtstein, M.V. Artemyev, Colloidal synthesis and optical properties of type-II CdSe-CdTe and inverted CdTe-CdSe core-wing heteronanoplatelets, Nanoscale 7 (2015) 8084–8092.

[38] Z. Chen, B. Nadal, B. Mahler, H. Aubin, B. Dubertret, Quasi-2D colloidal semiconductor nanoplatelets for narrow electroluminescence, Adv. Funct. Mater. 24 (2014) 295–302.

[39] F. Fan, P. Kanjanaboos, M. Saravanapavanantham, E. Beauregard, G. Ingram, E. Yassitepe, M.M. Adachi, O. Voznyy, A.K. Johnston, G. Walters, G.-H. Kim, Z.-H. Lu, E.H. Sargent, Colloidal CdSe$_{1-x}$S$_x$ nanoplatelets with narrow and continuously-tunable electroluminescence, Nano Lett. 15 (2015) 4611–4615.

[40] A.G. Vitukhnovsky, V.S. Lebedev, A.S. Selyukov, A.A. Vashchenko, R.B. Vasiliev, M.S. Sokolikova, Electroluminescence from colloidal semiconductor CdSe nanoplatelets in hybrid organic–inorganic light emitting diode, Chem. Phys. Lett. 619 (2015) 185–188.

[41] C. She, I. Fedin, D.S. Dolzhnikov, A. Demortière, R.D. Schaller, M. Pelton, D.V. Talapin, Low-threshold stimulated emission using colloidal quantum wells, Nano Lett. 14 (2014) 2772–2777.

[42] B. Guzelturk, Y. Kelestemur, M. Olutas, S. Delikanli, H.V. Demir, Amplified spontaneous emission and lasing in colloidal nanoplatelets, ACS Nano 8 (2014) 6599–6605.

[43] G.H.V. Bertrand, A. Polovitsyn, S. Christodoulou, A.H. Khan, I. Moreels, Shape control of zincblende CdSe nanoplatelets, Chem. Commun. 52 (2016) 11975–11978.

[44] S. Ithurria, D.V. Talapin, Colloidal atomic layer deposition (c-ALD) using self-limiting reactions at nanocrystal surface coupled to phase transfer between polar and nonpolar media, J. Am. Chem. Soc 134 (2012) 18585–18590.

[45] A. Antanovich, A. Prudnikau, M. Artemyev, Optical Properties of Semiconductor Colloidal Quantum Wells, in: A. Maffucci, S.A. Maksimenko (Eds.), Fundamental and Applied Nano-Electromagnetics, Springer, Netherlands, 2016, p. 220.

[46] Y.-J. Yu, Y. Zhao, S. Ryu, L.E. Brus, K.S. Kim, P. Kim, Tuning the graphene work function by electric field effect, Nano Lett. 9 (2009) 3430–3434.

[47] F. Marchi, R. Dianoux, H.J.H. Smilde, P. Mur, F. Comin, J. Chevrier, Characterisation of trapped electric charge carriers behaviour at nanometer scale by electrostatic force microscopy, J. Electrostat. 66 (2008) 538–547.

[48] T. Heim, K. Lmimouni, D. Vuillaume, Ambipolar charge injection and transport in a single pentacene monolayer island, Nano Lett. 4 (2004) 2145–2150.

[49] O.J. Dautel, M. Robitzer, J.-C. Flores, D. Tondelier, F. Serein-Spirau, J.-P. Lère-Porte, D. Guérin, S. Lenfant, M. Tillard, D. Vuillaume, J.J.E. Moreau, Electroactive Nanorods and Nanorings Designed by Supramolecular Association of π-conjugated, Oligomers, Chem.: Eur. J. 14 (2008) 4201–4213.

[50] M. Zdrojek, T. Mélin, H. Diesinger, D. Stiévenard, W. Gebicki, L. Adamowicz, Charging and discharging processes of carbon nanotubes probed by electrostatic force microscopy, J. Appl. Phys. 100 (2006) 114326.

[51] A. Verdaguer, M. Cardellach, J.J. Segura, G.M. Sacha, J. Moser, M. Zdrojek, A. Bachtold, J. Fraxedas, Charging and discharging of graphene in ambient conditions studied with scanning probe microscopy, Appl. Phys. Lett. 94 (2009) 233105.

[52] B. Vasić, M. Kratzer, A. Matković, A. Nevosad, U. Ralević, D. Jovanović, C. Ganser, C. Teichert, R. Gajić, Atomic force microscopy based manipulation of graphene using dynamic plowing lithography, Nanotechnology 24 (2012) 015303.

[53] S.E. Yalcin, C. Galande, R. Kappera, H. Yamaguchi, U. Martinez, K.A. Velizhanin, S.K. Doorn, A.M. Dattelbaum, M. Chhowalla, P.M. Ajayan, G. Gupta, A.D. Mohite, Direct imaging of charge transport in progressively reduced graphene oxide using electrostatic force microscopy, ACS Nano 9 (2015) 2981–2988.

[54] N.S. Malvankar, S.E. Yalcin, M.T. Tuominen, D.R. Lovley, Visualization of charge propagation along individual pili proteins using ambient electrostatic force microscopy, Nat. Nanotech. 9 (2014) 1012.

[55] B. Mahler, L. Guillemot, L. Bossard-Giannesini, S. Ithurria, D. Pierucci, A. Ouerghi, G. Patriarche, R. Benbalagh, E. Lacaze, F. Rochet, E. Lhuillier, Metallic functionalization of CdSe 2D nanoplatelets and its impact on electronic transport, J. Phys. Chem. C 120 (2016) 12351–12361.

[56] A. Stavrinadis, G. Konstantatos, Strategies for the controlled electronic doping of colloidal quantum dot solids, ChemPhysChem 17 (2016) 632–644.

[57] S. Ryu, L. Liu, S. Berciaud, Y.-J. Yu, H. Liu, P. Kim, G.W. Flynn, L.E. Brus, Atmospheric oxygen binding and hole doping in deformed graphene on a SiO$_2$ Substrate, Nano Lett. 10 (2010) 4944–4951.

PAPER

Check for updates

Molecules on rails: friction anisotropy and preferential sliding directions of organic nanocrystallites on two-dimensional materials†

Borislav Vasić, [ID] *[a] Igor Stanković, [ID] *[b] Aleksandar Matković,*[c] Markus Kratzer,[c] Christian Ganser, [ID] ‡[c] Radoš Gajić[a] and Christian Teichert [ID] [c]

Two-dimensional (2D) materials are envisaged as ultra-thin solid lubricants for nanomechanical systems. So far, their frictional properties at the nanoscale have been studied by standard friction force microscopy. However, lateral manipulation of nanoparticles is a more suitable method to study the dependence of friction on the crystallography of two contacting surfaces. Still, such experiments are lacking. In this study, we combine atomic force microscopy (AFM) based lateral manipulation and molecular dynamics simulations in order to investigate the movements of organic needle-like nanocrystallites grown by van der Waals epitaxy on graphene and hexagonal boron nitride. We observe that nanoneedle fragments – when pushed by an AFM tip – do not move along the original pushing directions. Instead, they slide on the 2D materials preferentially along the needles' growth directions, which act as invisible rails along commensurate directions. Further, when the nanocrystallites were rotated by applying a torque with the AFM tip across the preferential sliding directions, we find an increase of the torsional signal of the AFM cantilever. We demonstrate in conjunction with simulations that both, the significant friction anisotropy and preferential sliding directions are determined by the complex epitaxial relation and arise from the commensurate and incommensurate states between the organic nanocrystallites and the 2D materials.

1. Introduction

Bulk layered materials such as graphite, transition-metal dichalcogenides, and hexagonal boron-nitride exhibit low friction because of their lamelar structure and easy shearing of layers. For these reasons, they are widely used as solid lubri-

[a] Graphene Laboratory of Center for Solid State Physics and New Materials, Institute of Physics Belgrade, University of Belgrade, Pregrevica 118, 11080 Belgrade, Serbia. E-mail: bvasic@ipb.ac.rs
[b] Scientific Computing Laboratory, Center for the Study of Complex Systems, Institute of Physics Belgrade, University of Belgrade, 11080 Belgrade, Serbia.
E-mail: igor.stankovic@ipb.ac.rs
[c] Institute of Physics, Montanuniversität Leoben, Franz Josef Strasse 18, 8700 Leoben, Austria. E-mail: aleksandar.matkovic@unileoben.ac.at

†Electronic supplementary information (ESI) available: Epitaxial relations and lattice registries between 6P and Gr/hBN (Fig. S1 and S2, respectively), snapshots of top, side, and bottom view of a particular simulation run demonstrating the MD simulation setup (Fig. S3), topographic AFM images during the fabrication of a short needle (Fig. S4), topographic AFM images and lateral force profiles during the rotations across the registry state determined by direction D_2 on Gr (Fig. S5), ESI Movie 1 (2) which contains a sequence of all AFM tapping mode images recorded after all AFM manipulation steps on hBN (Gr) and ESI Movie 3 which presents a sequence of snapshots of the bottom layer of 6P needle fragment on Gr obtained by MD simulations during the needle rotation. See DOI: 10.1039/C8NR04865G

‡ Present address: Department of Physics, Nagoya University, Furo-cho, Chikusa-ku, Nagoya, Aichi, 464-8602, Japan.

cants.[1] Still, bulky lubricants are not appropriate for nano-devices where ultra-thin coatings with a maximal thickness of only several nanometers are required.[2] As a result, atomically thin, two-dimensional (2D) materials and especially graphene (Gr) have been recently envisaged as solid lubricants for friction and wear reduction in nanomechanical systems.[3–8]

Layered materials are single crystals with van der Waals bonding in only one direction, allowing exposure of atomically flat and dangling-bond free surfaces by simple mechanical cleavage. Therefore, besides the technological applications, they are also suitable for fundamental tribological studies mostly performed by atomic force microscopy (AFM).[9–19] These studies demonstrated that the substrates' crystal structure determines several fundamental properties, like the existence of friction anisotropy,[9–12] preferential sliding directions,[9,13] and structural lubricity, a state with a low friction between two surfaces sliding through incommensurate states.[14–25] Still, the influence of the epitaxial relation between two contacting surfaces on the resulting sliding directions and friction anisotropy has been explored much less. Until now, the underlying epitaxial relations were considered only for simple triangular and square lattices.[9,13,22]

Frictional properties of 2D materials were investigated so far only by AFM derived friction force microscopy (FFM).[2,4–8,26–29] However, the often ill-defined structure of the

AFM tip is an obstacle to study friction as a function of the relative orientation between the crystal lattices of two contacting surfaces.[9,30] For this purpose, AFM based lateral manipulation[9,11,13,15,16,19] of particles with well defined crystallographic structures and epitaxial relations to 2D materials is a more appropriate technique than standard FFM.

Van der Waals (vdW) heterostructures consisting of epitaxially grown organic crystallites on 2D materials can serve as an excellent paradigmatic system to explore the influence of the inherent epitaxial relation on the friction during AFM based lateral manipulation. 2D materials are superior substrates for the epitaxial growth[31] of organic molecules.[32–38] They are atomically smooth with no dangling bonds and trapped charges at the interface, thus providing a pure vdW interface between two contacting surfaces. While friction studies are usually constrained by contaminant molecules[15,19,39] and chemical interactions,[40] 2D materials may provide a clean interface between the contacting surfaces. At the same time, organic crystallites form complex epitaxial relations with 2D materials,[32–34] while their strong intrinsic anisotropy makes them suitable for AFM studies of friction anisotropy and related phenomena.[41–45]

In this work, we consider, as representative vdW heterostructures, organic, needle-like nanocrystallites (also called nanoneedles, nanowires, or nanorods) formed by *para*-hexaphenyl (6P) molecules grown by vdW epitaxy on Gr and hexagonal boron nitride (hBN). These organic nanocrystallites are large enough to be considered as bulk structures, they are strongly anisotropic and stable under ambient conditions. By combined AFM manipulations and molecular dynamics (MD) simulations, we investigate lateral movements of 6P needles on 2D materials. We identified preferential sliding directions, *i.e.*, registry states, which are different from the pushing directions defined by the AFM tip movement. During rotations of 6P needles, an increased friction force was observed when crossing the registry states on the 2D substrates, indicating a pronounced friction anisotropy.

2. Experimental

2.1. Sample preparation

Flakes of single- and multi-layer Gr and multi-layer hBN – prepared by mechanical exfoliation and transferred onto SiO$_2$/Si following known recipes[46] – have been used as substrates for the growth of parahexaphenyl (6P). The molecules were deposited by hot wall epitaxy (HWE).[47] As a source material, commercially available 6P from TCI Chemicals (S0220) was used. The base pressure of the HWE chamber was ~2 × 10^{-6} mbar, source and wall temperatures were kept fixed at 510 K and 520 K, respectively. Substrate temperature during the growth was varied between 380 K and 420 K. The amount of 6P deposited on the surface of the samples corresponds to an equivalent of 0.8–1.2 monolayers of 6P. Here, a monolayer is defined by the molecular density in the beta-phase 6P (001) plane (4.4 × 10^{14} molecules per cm^2).[48] On both, Gr and hBN,

6P molecules were found to form three-dimensional needle-like crystallites.[32–34,49,50] In the case of 6P needles, not always the molecules assume a "lying" orientation having their long molecular axes (LMA) parallel to the substrate plane.[32,51,52] These needle-like crystallites are large enough to be considered as β-phase bulk 6P, in which the molecules have a herringbone motif.[53] The chosen growth parameters result in tens of micrometer long and 5–10 nm tall 6P needles that follow six directions dictated by the epitaxial relation between 6P and the 2D material substrate.[32,34,52]

2.2. AFM measurements

AFM measurements were performed using an NTEGRA Prima AFM system from NT-MDT and an Asylum Research MFP 3D device. AFM imaging and manipulations were done with NSG01 (Gr substrate) and FMG01 (hBN substrate) probes from NT-MDT. Spring constant calibration of AFM cantilevers was performed *via* the thermal noise method,[54] employing the MFP 3D AFM. All measurements were performed under ambient conditions.

After initial sample imaging in tapping mode, the first step was to prepare a short 6P needle suitable for AFM manipulations. For this purpose, an appropriate long 6P needle was selected and then cut by AFM manipulation in contact mode.[55] The typical procedure is illustrated in Fig. S4 of ESI.† Cutting was repeated if needed for several times until a short needle of around 200 nm–400 nm was obtained.

AFM manipulations were done in a standard way following procedures in ref. 30, 56 and 57. A selected short needle was first imaged in tapping mode. Then we switched to contact mode. The AFM probe was moved in *x*-direction with the cantilever's long axis oriented in *y*-direction like conventionally done in friction force microscopy. The AFM tip was pushed towards one of the needle's endings for a certain distance. The reason we pushed needles from their endings was because we were not interested in the trivial case where needles, pushed in the center were just translated along the tip path direction. The path length was in the range of 500 nm–1500 nm, while the normal force (determined by the AFM cantilever bending) during the pushing was around 100 nN. After each manipulation step, the needle was imaged in tapping mode in order to visualize its movement. This procedure was repeated by around 100 times with the same probe, and it was performed for selected short needles on both, Gr and hBN. Compared to AFM manipulation experiments of nanorods,[58] here all movements were performed just once, along a single line, while the focus was on the influence of the crystal structure of substrates on the resulting motion.

In each manipulation step, simultaneously with movements of 6P needles, the lateral force – proportional to the AFM cantilever torsion – was recorded. The lateral force signal was calibrated according to the procedure introduced by Varenberg *et al.*[59] All AFM manipulations presented in the paper were done along the *x*-axis. In cases where needles were almost aligned with the *x*-axis, they were pushed along the *y*-axis to reorient them. However, these manipulation steps were not

taken into consideration since lateral forces could not be measured.

2.3. Molecular dynamics simulations

In our atomistic model, a 90 Å × 300 Å 6P needle was placed on a 380 Å × 380 Å Gr sheet. Periodic boundary conditions were set in x and y direction. The crystallographic data for the unit cell of β-phase 6P bulk was taken from the paper of Baker *et al.*[53] The lattice parameters of the monoclinic unit cell including two molecules were a = 26.241 Å, b = 5.568 Å, and c = 8.091 Å and the angle $β$ = 98.17°. The herringbone arrangement of the unit cell was defined by the intersection angles $ω$ = 26° and $ϕ$ = 71°, and setting angle $Θ$ = 55°. The herringbone angle, calculated from previous values, was $τ$ = 61°. The contact plane of 6P needle was (11$\bar{1}$).[33,49]

The interatomic forces within Gr were derived using the appropriate Tersoff potential.[60] Interactions between 6P molecules were modeled using empirical CHARMM force field parameters.[61] The adhesion forces between the carbon atoms in 6P molecules and Gr were modeled with a registry dependent Kolmogorov–Crespi potential.[62] For the interaction of C atoms in Gr with hydrogen atoms of the 6P molecules, CHARMM force field parameters were utilized.

The molecular dynamics (MD) simulations were performed using LAMMPS, a commonly used distributed classical MD code.[63] The 15 Å thick 6P needle was displaced on the Gr sheet with steps of 0.5 fs. The top-most layer of 6P molecules had relative position fixed, while the following three layers towards the interface with Gr and the Gr substrate itself were thermalized at 300 K. The top layer of the molecules was used to move the needle on the Gr surface. The initial configuration was equilibrated for 1 ns. The distance between Gr and the bottom 6P molecules was roughly 3.2 Å.

3.   Results and discussion

The results are presented in five sections. The epitaxial relations between 6P molecules and hBN/Gr are elaborated in the first part. Then, in the second section, we summarize all experimental results for AFM manipulations of 6P needles. After that, in the third section we analyze the rotation of the needles and the observed friction anisotropy, while the corresponding results of MD simulations are discussed in the fourth section. Finally, in the fifth part, translations of the needles and their preferential sliding directions are discussed.

3.1.   Epitaxial relations

Friction anisotropy and preferential sliding directions of 6P needles on 2D material substrates stem from their epitaxial relations. Both individual 6P molecules and 6P needles are intrinsically anisotropic structures and can be considered as quasi one-dimensional objects. As such, there are two main directions to be considered within 6P needles: 1. the long molecular axis (LMA) or the axis along the phenylene backbone of the individual molecules, and 2. the long needle axis

(LNA) that indicates the preferred growth direction of the needle on a given substrate.[52] Additional data on the orientations of LMA and LNA on Gr are given in Fig. S3 of ESI.† Furthermore, preferential growth directions are also influenced by the interactions with the substrate, since the individual molecules tend to adsorb only at specific sites on the substrate. The growth directions of the needles (LNA) are then finally defined by the relation between the LMA and the high-symmetry directions of the substrate (armchair and zigzag directions of Gr and hBN, respectively) and the particular contact plane of the molecular crystal that is best matching the arrangement of the molecules at the interface with the substrate to that of the bulk structure.

If assumed that the molecular crystal remains in the bulk to the very interface, then there is no distinctive registry between the substrate lattice and the deposited lattice, resulting in translational incommensurism.[64–69] However, molecular crystals can accommodate large strain, and molecules at the surface frequently rearrange to accommodate both inter-molecular interactions that drive the formation of the bulk molecular crystal and interaction with the substrate. As a consequence, the bulk structure of the molecular crystal is not kept at the very interface, and commonly only rotational commensurism is maintained, regardless of the lattice mismatch.[31] More detailson the epitaxial relation between 6P and Gr/hBN is given in the first section of ESI.†

In the case of hBN supported 6P, individual molecules tend to align their LMA exactly with an armchair direction, thus giving the molecular arrangement at the surface well matching the ($\bar{6}$29) plane of bulk 6P.[34] As a result, 6P needles on hBN follow six preferential growth directions as shown in Fig. 1(a). In this case, the orientation of the LNAs are split by ±4.5° from a zigzag direction of hBN. The preferential growth directions of 6P needles can be determined from AFM topographic images. A typical topographic image of 6P needles grown on hBN is given in Fig. 1(b), while the corresponding 2D fast Fourier transform (2D-FFT) is represented in Fig. 1(c). Please note that the 2D-FFT image is rotated by 90° in order to match the real space directions. The bright lines in Fig. 1(c) indicate the preferred growth directions of the needles (LNAs), determined from 2D-FFT with a precision of ±2°. The bright lines appear in pairs which are separated from each other by 60° due to the sixfold symmetry of hBN. Two bright lines within a single pair are separated from each other by around 9°, whereas the hBN zigzag directions run along the angle bisector between them. These orientations match quite well the previous observation that the LNA directions split by ±5° (with a tolerance of 2°) from a zigzag direction.[34]

For 6P on Gr, preferential growth directions (LNAs) and the orientation of the individual molecules (LMAs) with respect to Gr's high symmetry directions are shown in Fig. 1(d). In this case, it has been reported earlier that 6P molecules align with their LMA ±11° rotated from an armchair direction of Gr (graphite).[33,49] The packing motif at the surface then closely resembles the (11$\bar{1}$) plane of bulk 6P,[33] thus resulting in a total of six LNA directions split by ±5° also from an armchair direc-
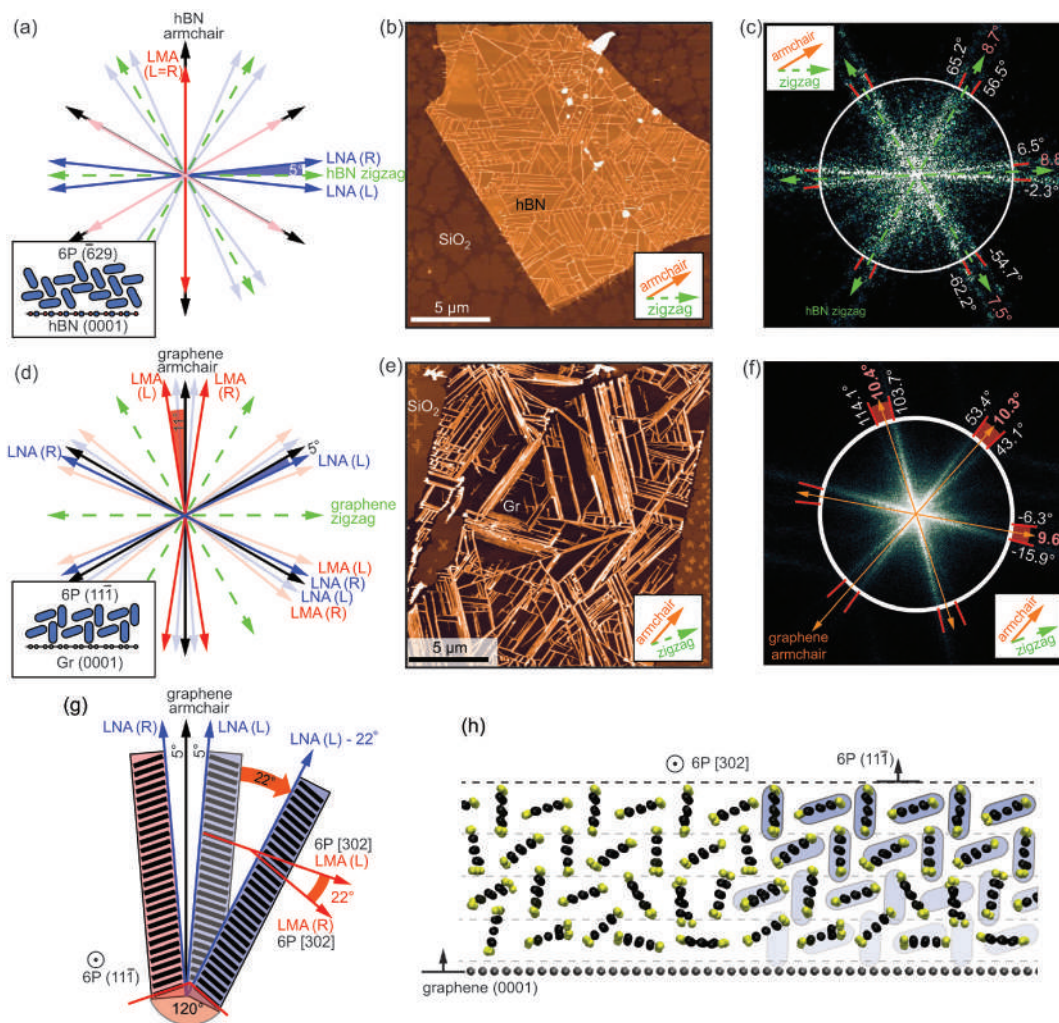
Fig. 1 Preferential growth directions of 6P on hBN and Gr: (a), (d) sketches of the preferential molecule orientation (LMA) and needle growth directions (LNA) with respect to high-symmetry directions (zigzag and armchair) of hBN and Gr, respectively. Insets of (a) and (d) illustrate side views of the molecular packing at the interface with hBN and Gr, respectively, considering only the epitaxial relation between 6P molecules and these two materials. (b), (e) Characteristic AFM images of needles grown on hBN (z-scale is 60 nm) and Gr (z-scale is 20 nm), respectively. Islands observed at the edges of the AFM images are located on SiO_2 support and are formed by up-right standing molecules, which is a characteristic growth mode on SiO_2. (c), (f) 2D-FFT images of the topographic images (given in (b) and (e)) for hBN and Gr, respectively. The 2D-FFT diagrams are rotated by 90° to match directly with the orientations of the preferential needle growth directions (LNA). 2D-FFT images are generated from binary masks of the topography images set to highlight only the needles. Dashed (green) and solid (orange) arrows, respectively, indicate zigzag and armchair directions of both, Gr and hBN with respect to the x-axis of the AFM scanner. White circles are guides to the eye and their radius is 10 μm^{-1}. (g) Schematic illustration, how the 6P needle – aligned along LNA(L) direction – falls into a rotationally commensurate registry state when rotated clockwise by 22°. The resulting state does not coincide with any of LNAs (is not a growth direction). In (a), (d), and (g) solid red arrows indicate LMA directions, solid blue arrows indicate LNA directions, dashed green and solid black arrows indicate zigzag and armchair directions of the 2D material substrate, while "L" and "R" stand for left- and right-handed chiral pairs of the crystallites. More details on epitaxial relations are given in Fig. S1 and S2 of ESI.† (h) A side view along LMA of a 300 K MD simulation snapshot for a 6P needle on Gr. The overlay in the right part with an ideal molecular packing from the inset in (d) illustrates the (11$\bar{1}$) contact plane of bulk 6P. Results for the top and bottom views of the needles are given in Fig. S3 of ESI.†

tion.[32,49] Fig. 1(e) depicts a characteristic AFM topography image of the 6P needles on Gr. The corresponding 2D-FFT is given in Fig. 1(f). As in the case with hBN substrate, the bright lines in Fig. 1(f) mark the preferred growth directions of the needles. They again appear in pairs which are separated from each other by 60° due to the sixfold symmetry of Gr. Now, two bright lines within a single pair are separated from each other by around 10°, whereas the Gr armchair directions run along

the angle bisector between them. These bright lines match very well the prediction that the LNA directions are split by ±5° from an armchair direction.[32,49]

Since the LMA of 6P on Gr do not coincide with high symmetry directions of the substrate, it is possible to access only rotationally commensurate states. In the true commensurate states (growth directions), the molecules in the contact with Gr have both, their positions and their LMA matching the pre-

ferred adsorption sites of the individual molecules. On the other hand, in a rotationally commensurate state, only the relative angle between 6P LMA and Gr is maintained, while the exact positions (translational symmetry) of the molecules do not match the preferred adsorption sites. Therefore, the crystallites will not grow in these directions. Fig. 1(g) illustrates such a case, and the impact of these states on the friction anisotropy of 6P on Gr will be discussed later.

MD simulations give a realistic picture of the orientation of 6P molecules within a needle and their contact with the substrate. The side view of the MD simulation setup for a 6P needle on Gr is depicted in Fig. 1(h) by a snapshot of the MD simulation. The 6P molecules in the top layer of a 4 layer thick needle are fixed to fit the 6P $(11\bar{1})$ plane, while the rest of the system is free to move. 6P molecules from the bottom layer at the interface tend to occupy commensurate states with the underlying Gr with their LMA rotated from an armchair direction by ±11°. As a result, the bottom layer consists of almost "flat-lying" 6P molecules which are nearly commensurate with Gr, and "edge-on" molecules, which tend to have the plane of their π-system normal or inclined to the Gr plane. The bulk herringbone structure (shown as the overlay in Fig. 1(h)) consists of molecules with alternate inclination of the short molecular axes of 21.3° and 90° relative to the substrate. As a result, 6P molecules inside the needle are relaxed as represented by the transition from the bottom layer in contact with Gr to bulk herringbone structure with $(11\bar{1})$ contact plane on the top. Additional data on the MD simulation setup with top and bottom views as well, are presented in Fig. S3 of ESI.†

3.2. AFM manipulations

After the growth of 6P needles, AFM in contact mode was employed under ambient conditions to cut them in order to fabricate short needle fragments appropriate for AFM manipulations. The typical procedure for the cutting is illustrated in Fig. S4 of ESI.† The AFM topography image in Fig. 2(a) displays

characteristic short needles cut from two long needles. The former edges of these as-grown needles are indicated by dashed lines. The cutting of long needles was a sudden process initiated by a high enough normal load, and we did not observe a significant needle bending prior to the cutting. This is in accordance with the results for manipulations of organic nanofibers,[55] but different to InAs nanorods, which were first bent during the AFM manipulation, and then cut.[70] The histogram of the needle length distribution is presented in Fig. 2(b) revealing that the typical length of a short needle is around 200 nm. Beyond this approximate length limit, the cutting was not possible anymore and intended AFM manipulations led only to needle movements which are investigated in detail in the following.

After cutting, the same short needle was pushed by the AFM tip in contact mode for about 100 times. Topographic images were recorded in tapping mode after each manipulation step. The short needles were always pushed from one of their endings and always along the x-axis. This procedure was performed on both, hBN and Gr substrates. Sequences of all AFM tapping mode images are presented in ESI (Movies 1 and 2†).

The evolution and the histogram of the needle angle (calculated with respect to the x-axis for all manipulation steps) are presented in Fig. 3(a1) and (a2) for hBN substrate, and in Fig. 3(b1) and (b2) for Gr substrate. In Fig. 3(a1) and (b1), the arrays of successive points with the same needle angle denote the needle translations. Therefore, the needle on hBN was translated along direction D_1 for steps 4–8, 42–45, and 80–88, and along D_3 for steps 18–24 and 59–66. Directions D_1–D_3 mark the preferential growth directions as depicted in the inset of Fig. 3(a) with the AFM topography image. They were found according to the growth directions of two long adjacent 6P needles and the six-fold symmetry of the hBN substrate (more details are provided in the description of Fig. S4 of ESI†). For the Gr substrate, the needle was translated along direction D_1 for steps 3–9, 17–20, 25–29, 36–40, 48–54, 71–73, 75–78, and 81–83, whereas translations along D_3 were rarely observed, only in the two steps 41–42. Similar to the previous case, three preferential growth directions were marked with D_1–D_3 in the inset of Fig. 3(b) with AFM topography image. They were determined according to the position of the adjacent long needle and the six-fold symmetry of Gr. In Fig. 3(a2) and (b2), the corresponding histograms of the needle angle are presented. The peaks in the histograms are clearly located around the preferential growth directions.

According to these results, we identified preferential directions for the sliding of 6P needles on hBN and Gr. These directions match quite well the preferential growth directions of the needles on both substrates, and they will be called registry states in the following. Although they are closely related to the commensurate contact planes between two crystal lattices, we believe that this is a more proper term, because only "flatlying" 6P molecules in the bottom needle layer are commensurate with Gr and hBN. The registry states can be imagined as rails which define needle trajectories. Needles just slide along
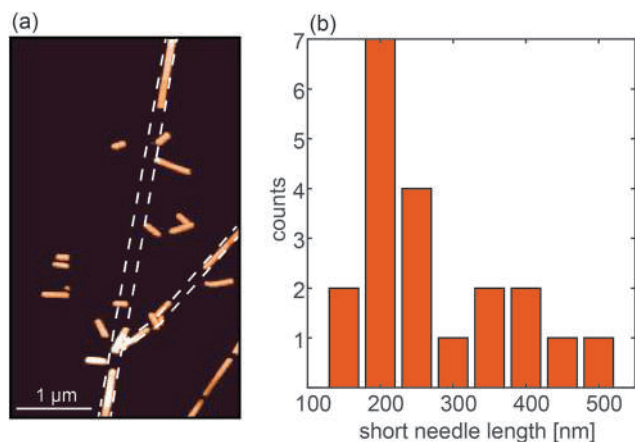

Fig. 2 (a) AFM topography image of short needles cut from two former long needles marked by dashed lines. z-scale is 10 nm. (b) Histogram of the length distribution of the short needles after the cutting.
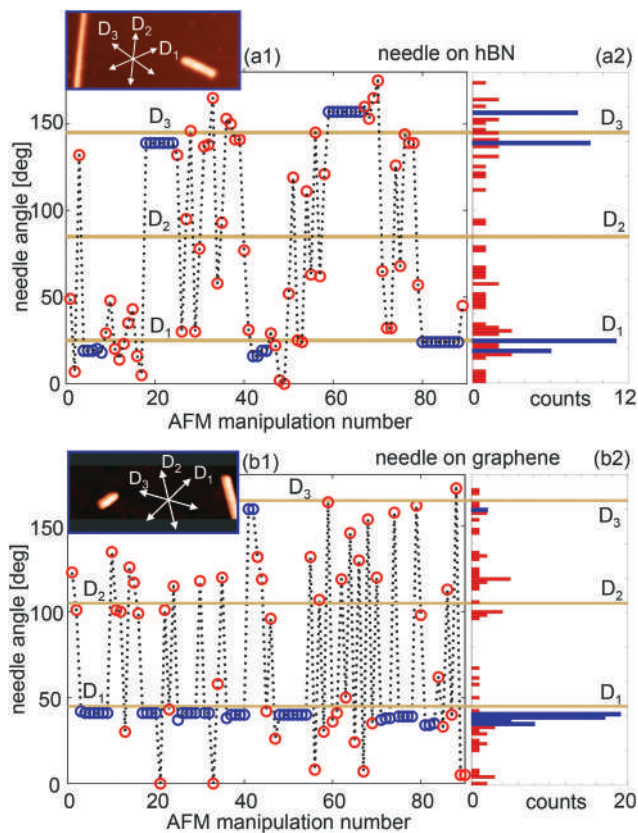
Fig. 3 Change of the needle angle during AFM manipulations on (a1) hBN and (b1) Gr. The needle angle is defined as the angle between x-axis of the AFM scanner and long needle axis (LNA or needle direction). Parts (a2) and (b2) give the corresponding histograms for hBN and Gr, respectively. Horizontal solid lines D_1–D_3 mark the preferential growth directions. D_1–D_3 are also denoted in the insets with topographic images in parts (a1) and (b1). For the particular samples shown in the insets, D1–D3 directions denote LNA(R) for hBN, and LNA(L) for Gr. Histogram peaks (blue bars around D_1 and D_3) mark sequences where the needle fragments were translated along the registry states. The needle fragments are translated if the angle stays the same between two successive manipulation steps corresponding to red circles, while they are rotated if the angle changes between two successive manipulation steps. The point pairs where one point is below and other one above direction D_2 correspond to the rotations across the registry state D_2.

these rails, *i.e.*, registry states, although pushed in a different direction.

During AFM manipulations, besides translations, we observed needle rotations across the registry states. They correspond to pairs of points in Fig. 3(a1) and (b1), with one point above and the second one below the line for D_2. The sliding along direction D_2 was not observed, neither for Gr nor for hBN because the angle between D_2 and the manipulation direction is close to 90°. As a result, the applied torque was always too large leading to needle rotations across the registry state defined by D_2. By measuring lateral forces during needle rotations, it was possible to map the existing friction anisotropy of the underlying substrates. This will be analyzed in detail in the next section.

3.3. Friction anisotropy

Typical images for the rotations on hBN and Gr substrates are presented in Fig. 4(a) and (b), respectively. Topographic images before and after the rotation are shown in the top and middle row, respectively, whereas the corresponding lateral force profile during AFM probe movement is given in the bottom row. As can be seen, first the AFM tip slides on the bare 2D material substrate, while the lateral force and thus the corresponding friction are low. Then, the AFM tip approaches the end of a needle fragment (purple dot) and starts to push the needle. This initial movement is described with an increase of the lateral force to the level F_{stat} (red square) which corresponds to the static friction.[15,16,19,30] The needle is out of the registry at the beginning of the rotation, so the resulting friction between the needle and underlying substrate is low. For this reason, the lateral force drops from F_{stat} to F_{dyn} (black circle) corresponding to dynamic friction.[15,16,19,30] With further rotation, the needle falls into the registry determined by direction D_2, accompanied by a significant increase of the lateral force to F_{reg} (yellow diamond). After crossing the registry, the lateral force drops down (orange circle).

Fig. 5 presents cases on Gr, where the needles are rotated across a registry state and simultaneously also translated, as can be seen by comparing to a reference point in the image, *i.e.*, the end of a long as-grown needle. Fig. 5(a) demonstrates a case where the needle fragment is out of the registry state during the translation. In the force profile, again there are three already mentioned levels, namely, static friction at the beginning, dynamic friction after the needle is moved, and then a significant increase of the force when the needle is crossing the registry state defined by direction D_2. After the needle passes across the registry state, the lateral force
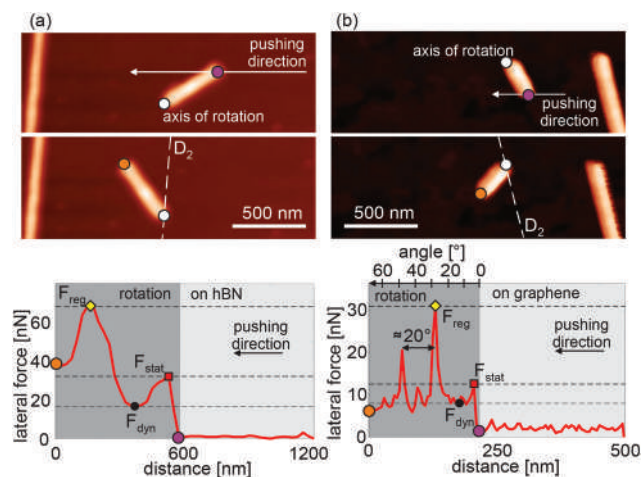

Fig. 4 Rotations of 6P needle fragments across the registry state determined by direction D_2: (a) on hBN (z-scale is 15 nm), (b) on Gr (z-scale is 10 nm). Top row: topographic images before AFM manipulation. Middle row: topographic images after the AFM manipulations. Bottom row: force profiles during the AFM manipulations. Arrows mark pushing directions and the path of pushing. Dashed lines denote the registry state D_2.
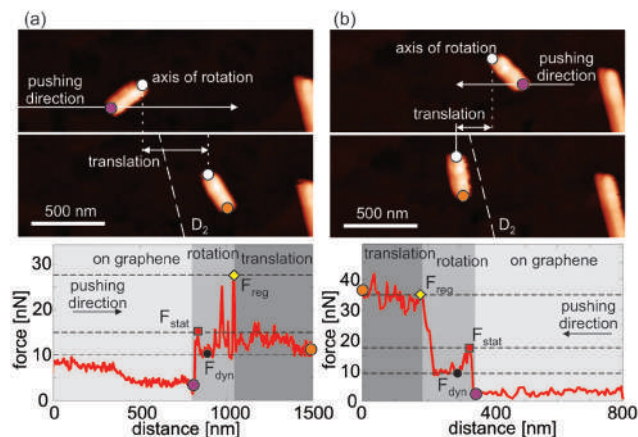
Fig. 5 Rotation on Gr together with translation: (a) the needle is out of the registry state (defined by direction D_2) during the translation, and (b) the needle remains in the registry state during the translation. Top row: topographic images before AFM manipulation. Middle row: topographic images after the AFM manipulations. Bottom row: lateral force profiles during the AFM manipulations. z-scale in the images is 10 nm. Arrows mark pushing directions and the path of pushing. Dashed lines denote the registry state D_2.

fluctuates between F_{stat} and F_{dyn}. In this region, the needle is sliding on the Gr substrate, but is not falling into a registry state. On the other hand, in the example presented in Fig. 5(b), after reaching of the high level F_{reg}, the force practically stays on the same level until the end of moving. In this case, the needle is aligned in direction D_2 at the end of the movement, meaning that after it felt into the registry, it remains in this state during the further translation.

Distributions of the characteristic force levels F_{stat}, F_{dyn}, and F_{reg} during all recorded needle rotations are presented in Fig. 6(a) and (b) for the manipulations on Gr and hBN, respectively. The characteristic force levels are very well distributed into three distinct ranges corresponding to static and dynamic friction, and as well as the friction in the registry state. As can be seen, F_{reg} is approximately 5 or 3 times higher than F_{dyn} on Gr and hBN, respectively, clearly indicating a significant friction anisotropy. Besides the described scenarios for needle rotations, we observed also cases where the needles were initially positioned in registry states. Then, the lateral force started from F_{reg} at the beginning of the rotation and then dropped. During some rotations, the registry state was not achieved at all due to a too small rotation angle. Since we could not measure all three force levels of interest in these cases, such cases were excluded from the analysis.

Now we return to a speciality only observed for the rotation of 6P needle fragments on Gr. In both Fig. 4(b) and 5(a), two peaks in the lateral force are observed during the rotation across the registry state. The case with a pure rotation (without translation) was given in Fig. 4(b). Here, it was possible to approximately transform a distance into an angle according to the initial and final angles between the needle and the x-axis (the angle axis is indicated in the top of the force profile in
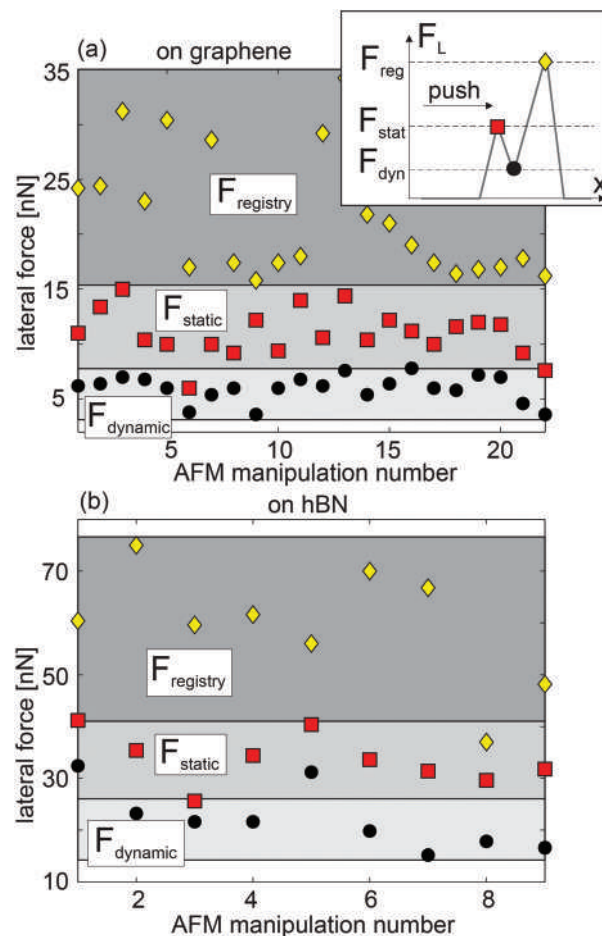

Fig. 6 Characteristic lateral force (F_L) levels F_{stat}, F_{dyn}, and F_{reg} during needle rotations on (a) Gr and (b) hBN.

Fig. 4(b)). As can be seen, two peaks are separated by around 20° from each other. Other images for the rotations on Gr together with lateral force profiles are provided in ESI in Fig. S3.† Fig. S3(c), S3(l), and S3(p)† present cases of pure rotations where the angle between two peaks was always observed to be around 20°. All other cases in Fig. S3† contain combined manipulations, consisting of both rotations and translations. For this reason, it was not possible to transform a distance into an angle. Still, all lateral force profiles in Fig. S3† as well as in Fig. 5(a) exhibit such double peaks during needle manipulations. On the other hand, in the case of hBN, always only single peaks in the lateral force were observed as can be seen in Fig. 4(a).

3.4. MD simulations of needle movement

The results of MD simulations for the determination of the lateral force during 6P needle rotations (both clockwise and anticlockwise) on Gr are shown in Fig. 7 as a function of rotation angle ϕ. The orientations of the needle and 6P molecules with respect to Gr at four characteristic points (a)–(d) (indicated in Fig. 7) are depicted in Fig. 8. The animation of the needle rotation is given in ESI (Movie 3†). As can be seen
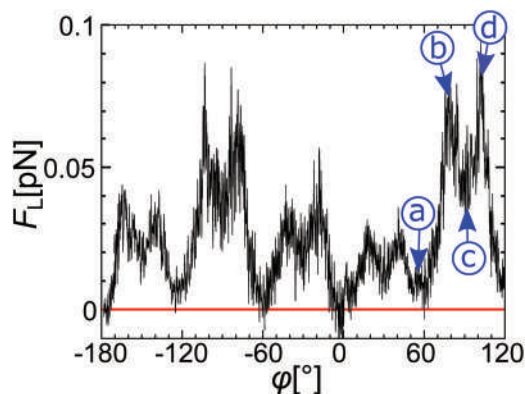
Fig. 7 MD simulation results for the change of the lateral force with rotation of a needle fragment composed of 64 × 4 × 4 6P molecules. F_L is the mean lateral force of the bare Gr substrate acting on the needle. The results are presented for both clockwise (negative angles ϕ) and anticlockwise rotation (positive angles ϕ). Configurations for typical points (a), (b), (c), and (d) are indicated in Fig. 8.

Fig. 8 Snapshots of the bottom layer of a 6P needle on Gr obtained by MD simulations during needle rotations, shown at 4 typical stages during the rotation: (a) global minimum of the lateral force when 6P molecules are 30° away from the Gr armchair direction, *i.e.* aligned with the Gr zigzag direction, (b) first maximum of the lateral force when 6P molecules are 11° away from the Gr armchair direction in the clockwise direction, (c) local minimum of the lateral force when 6P molecules are aligned with the Gr armchair direction, (d) second maximum of the lateral force when 6P molecules are 11° away from the Gr armchair direction in anticlockwise direction. The corresponding zooms of domains within the blue squares and a schematic representation of relative orientation between Gr and 6P molecule are presented. The Gr lattice is indicated in red and two phenyl rings of the 6P molecules are shown in black. The Gr armchair direction is oriented along the *y*-axis. The red arrow denotes the rotation direction (counterclockwise).

from Fig. 7, the friction force is approximately a periodic function of the rotation angle, with a period of about 60°, because of the six fold symmetry of Gr. Every period contains two peaks at characteristic points (b) and (d) with increased lateral force. The angular separation between these two peaks is in all periods around 20°.

As can be seen from the configurations in Fig. 8(b) and (d), at points (b) and (d), the long axis of 6P molecules is 11° away from the Gr armchair direction (aligned along *y*-axis). Thus, at points (b) and (d), the LMA directions are rotationally commensurate with the substrate.[33] Therefore, MD simulations indicate two close registry states, tilted by ±11° from an armchair direction of Gr either in clockwise or anticlockwise direction. When 6P molecules are aligned with the Gr armchair direction, there is a local minimum in the lateral force at point (c). The global minimum in the lateral force is reached at point (a), when 6P molecules are aligned with the Gr zigzag direction.

As explained in Fig. 1, there are not only three, but three pairs of preferential growth directions. They are denoted with LNA, while two directions within a single LNA pair are marked with L and R (chiral pairs), and they are separated for Gr by around 10° as schematically displayed in Fig. 1(g). Still, only one direction, either L or R, in each pair can be a true registry state for the same short needle. In this state, both rotational and translational epitaxial relations between a "flat-lying" 6P molecule and the Gr lattice are conserved.

As mentioned earlier, 6P molecules that are in contact with the Gr have their preferential adsorption site with the LMA tilted by ~11° from an armchair direction.[33,49] Two chiral pairs, L and R, are then separated by ~22°. During a needle rotation, it is possible that the needle (LNA direction) falls in a state where the molecules in contact with Gr are only rotationally commensurate with the substrate, but do not match the exact positions as would be the case for the true commensu-
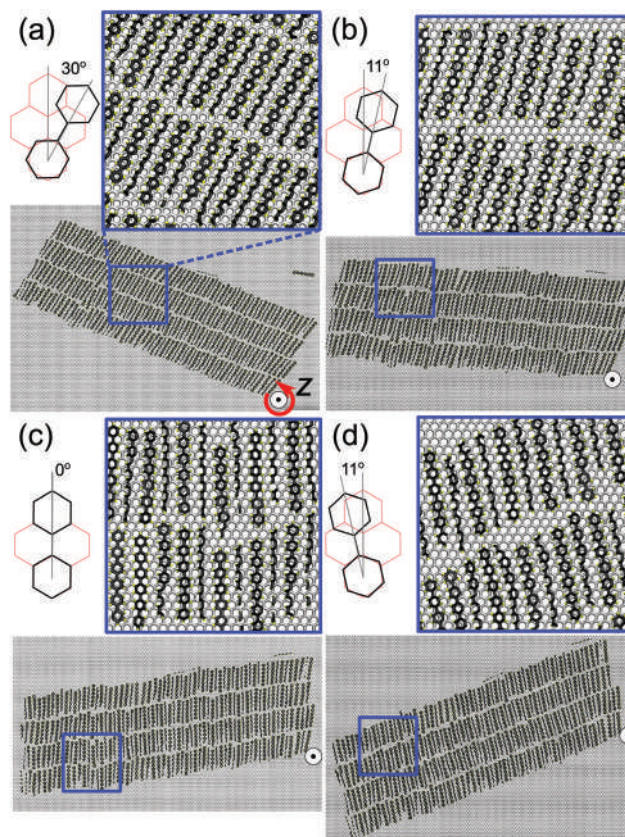
rate state and for as-grown needles. This situation is depicted in Fig. 1(g) for the needle with a true commensurate state denoted with LNA(L), and when it is rotated by 22° in the clockwise direction (then it is aligned with the direction marked with LNA(L)-22°). Such states should still present sufficiently deep potential energy minima for the "flat-lying" molecules at the interface with Gr. This fact really explains the existence of the two friction maxima (commensurate states) during the rotation of the 6P needle on Gr which are separated by around 20° as confirmed by both experiments and MD simulations.

In the case of hBN, 6P molecules in face-on position have their LMA oriented exactly parallel to the armchair direction of hBN.[34] Therefore, only one friction maximum appears when

the LMA of 6P molecule is rotated across the armchair direction of hBN, which is in accordance with the experimental results in Fig. 4(a).

3.5. Preferential sliding directions

The observed friction anisotropy also explains the existence of preferential sliding directions where short needles are just translated along the registry states. The results for the translation of a short needle on hBN are shown in Fig. 9. It represents two sequences of 9 needle positions during pushing. The part of the long needle LN_1 on the left side of the images was taken as a reference object. As can be seen, the short needle was pushed along the x-axis from its left and right ending, while it was translated along the directions D_3 (Fig. 9(a)) and D_1 (Fig. 9(b)), respectively. The resulting shifts along these directions were below 100 nm, and have been determined by the distance along which the AFM tip was in contact with the needle.

A characteristic example for the preferential sliding on Gr is presented in Fig. 10. Here, the end of a long needle LN on the

Fig. 10 Sequence of AFM images for 6P needle sliding on Gr. The end of the long needle (LN) is taken as a reference point. Arrows mark pushing directions and the path of pushing. Oblique dashed lines denote the initial needle direction making visible a small needle shift in x-direction as well, not only along the preferential direction D_1. z-scale in the images is 10 nm.
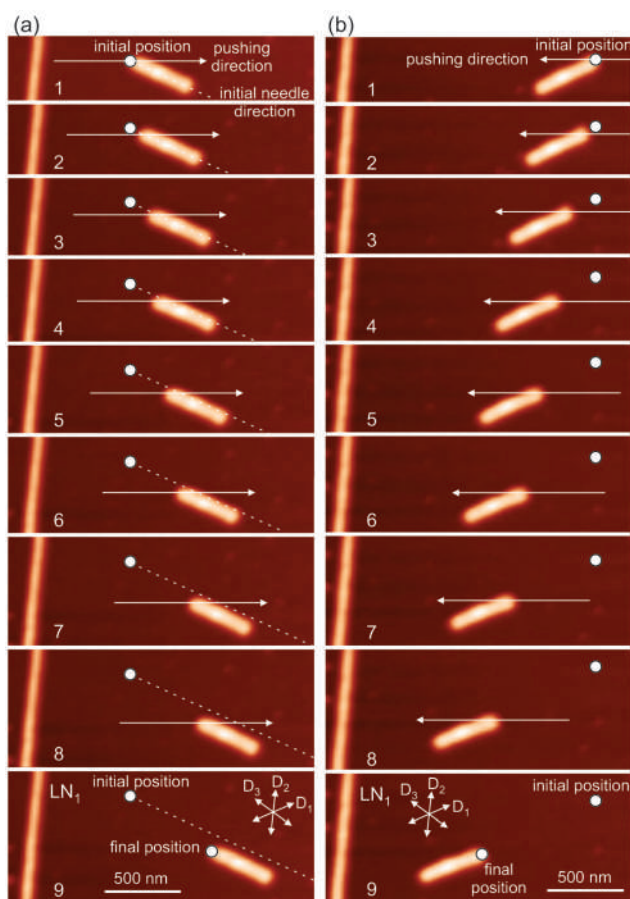
right side serves as a reference object. The short needle was pushed both in positive (steps 1–4, left hand side of Fig. 10) and negative x direction (steps 4–7, right hand side of Fig. 10). Still, as a result of this pushing, the needle was just translated along the preferential direction D_1.

As can be seen in Fig. 3, experimentally measured preferential sliding directions slightly differ from the marked preferential growth directions D_1–D_3. There are several possible reasons for these deviations. Preferential directions D_1–D_3 were determined from directions of adjacent long needles (two of them in the case of hBN and one needle in the case of Gr) and the six-fold symmetry of both substrates. This could lead to a small error of a few degrees. 6P needles could also be slightly rotated from the preferential growth directions during AFM manipulations. For example, on the hBN substrate, 6P molecules prefer to be oriented exactly along armchair directions. Small rotations of the molecules with respect to armchair directions by a few degrees lead only to a slight increase of the adsorption energy as shown in ref. 34. Still, even such states can be regarded as commensurate for 6P molecules, and can define preferential sliding directions.

Oblique dashed lines in Fig. 9(a) and 10 denote the initial needle direction. As can be seen, during the sliding, needles are not just moved along the preferential directions, but they could be slightly shifted to an adjacent registry state. Inspite of this shift, they still stay aligned with the preferential sliding directions. Therefore, Gr and hBN substrates can be imagined as arrays of parallel rails. When pushed by the AFM probe, 6P needles slide along a single rail, but at some points, they can jump to the next parallel rail due to the pushing force. After this jumping, the sliding continues along the same preferential direction. Slight shifts to adjacent registry states can be explained in the following way. Direction of the registry state is the principal direction of friction. If the needle slides along

Fig. 9 Sequences of AFM images for 6P needle sliding on hBN: (a) sliding along preferred direction D_3 and (b) D_1. The long needle LN_1 is taken as a reference. Arrows mark pushing directions and the path of pushing. Dotted lines in column (a) denote the initial needle direction making visible a small needle shift in x-direction as well, not only along the preferential direction D_3. z-scale in all images is 15 nm.

the principal direction, the friction force is parallel, but with the opposite direction. However, if the needle is not completely in the registry state (for example, misaligned by several degrees), or if the pushing force slightly moves it from the registry state, then an additional force component appears along the direction normal to the registry state,[12,71,72] and this additional force can be responsible for the observed needle movement in the lateral direction (with respect to the direction of the registry state).

4. Conclusions

To summarize, using combined AFM based manipulation and MD simulations, we investigated the influence of the epitaxial relations between organic 6P needles and Gr/hBN substrates on the resulting needle movement and the underlying friction. It was demonstrated that the preferential growth directions, split by ±5° from high symmetry directions of Gr and hBN, determine registry states for short 6P needle fragments that have been cut by AFM manipulations out of long needles. During the AFM manipulations of short 6P needles, we observed both, their translations and rotations. In the case of the translations, we revealed that the preferential sliding directions coincide with the preferential growth directions of a crystallite with a particular chirality, and that these directions are in accordance with the underlying epitaxial relations. In the case of rotations across registry states, the friction was increased by around 5 and 3 times on Gr and hBN respectively, compared to the dynamic friction out of the registry. Therefore, our results reveal that the organic nanocrystallites behave on 2D materials as if they would follow invisible rails of commensurate directions, and tend to slide along or switch between these "rails". These results provide new insights into frictional properties of 2D materials and also prove that AFM manipulation of nanoparticles is an efficient technique to study friction in vdW heterostructures.

Conflicts of interest

There are no conflicts to declare.

Acknowledgements

References

1 C. Donnet and A. Erdemir, *Surf. Coat. Technol.*, 2004, **180**, 76–84.
2 C. Lee, Q. Li, W. Kalb, X.-Z. Liu, H. Berger, R. W. Carpick and J. Hone, *Science*, 2010, **328**, 76–80.
3 D. Berman, A. Erdemir and A. V. Sumant, *Mater. Today*, 2014, **17**, 31–42.
4 T. Filleter, J. L. McChesney, A. Bostwick, E. Rotenberg, K. V. Emtsev, T. Seyller, K. Horn and R. Bennewitz, *Phys. Rev. Lett.*, 2009, **102**, 086102.
5 K.-S. Kim, H.-J. Lee, C. Lee, S.-K. Lee, H. Jang, J.-H. Ahn, J.-H. Kim and H.-J. Lee, *ACS Nano*, 2011, **5**, 5107–5114.
6 A. Klemenz, L. Pastewka, S. G. Balakrishna, A. Caron, R. Bennewitz and M. Moseler, *Nano Lett.*, 2014, **14**, 7145–7152.
7 D. Berman, S. A. Deshmukh, S. K. R. S. Sankaranarayanan, A. Erdemir and A. V. Sumant, *Adv. Funct. Mater.*, 2014, **24**, 6640–6646.
8 B. Vasić, A. Matković, U. Ralević, M. Belić and R. Gajić, *Carbon*, 2017, **120**, 137–144.
9 P. E. Sheehan and C. M. Lieber, *Science*, 1996, **272**, 1158–1161.
10 M. R. Falvo, J. Steele, R. M. Taylor and R. Superfine, *Phys. Rev. B: Condens. Matter Mater. Phys.*, 2000, **62**, R10665–R10667.
11 E. Tranvouez, A. Orieux, E. Boer-Duchemin, C. H. Devillers, V. Huc, G. Comtet and G. Dujardin, *Nanotechnology*, 2009, **20**, 165304.
12 S. G. Balakrishna, A. S. de Wijn and R. Bennewitz, *Phys. Rev. B: Condens. Matter Mater. Phys.*, 2014, **89**, 245440.
13 P. E. Sheehan and C. M. Lieber, *Nano Lett.*, 2017, **17**, 4116–4121.
14 M. Dienwiebel, G. S. Verhoeven, N. Pradeep, J. W. M. Frenken, J. A. Heimberg and H. W. Zandbergen, *Phys. Rev. Lett.*, 2004, **92**, 126101.
15 D. Dirk, R. Claudia, T. Mönninghoff, H. Fuchs, A. Schirmeisen and U. D. Schwarz, *Phys. Rev. Lett.*, 2008, **101**, 125505.
16 D. Dietzel, M. Feldmann, U. D. Schwarz, H. Fuchs and A. Schirmeisen, *Phys. Rev. Lett.*, 2013, **111**, 235502.
17 E. Koren, E. Lörtscher, C. Rawlings, A. W. Knoll and U. Duerig, *Science*, 2015, **348**, 679–683.
18 S. Kawai, A. Benassi, E. Gnecco, H. Söde, R. Pawlak, X. Feng, K. Müllen, D. Passerone, C. A. Pignedoli, P. Ruffieux, R. Fasel and E. Meyer, *Science*, 2016, **351**, 957.
19 E. Cihan, S. İpek, E. Durgun and M. Z. Baykara, *Nat. Commun.*, 2016, **7**, 12055.
20 M. Hirano, K. Shinjo, R. Kaneko and Y. Murata, *Phys. Rev. Lett.*, 1991, **67**, 2642–2645.
21 Z. Liu, J. Yang, F. Grey, J. Z. Liu, Y. Liu, Y. Wang, Y. Yang, Y. Cheng and Q. Zheng, *Phys. Rev. Lett.*, 2012, **108**, 205503.
22 A. S. de Wijn, *Phys. Rev. B: Condens. Matter Mater. Phys.*, 2012, **86**, 085429.
23 X. Feng, S. Kwon, J. Y. Park and M. Salmeron, *ACS Nano*, 2013, **7**, 1718–1724.
24 Y. Liu, F. Grey and Q. Zheng, *Sci. Rep.*, 2014, **4**, 4875.

25 D. Berman, S. A. Deshmukh, S. K. R. S. Sankaranarayanan, A. Erdemir and A. V. Sumant, *Science*, 2015, **348**, 1118–1122.

26 H. Lee, N. Lee, Y. Seo, J. Eom and S. Lee, *Nanotechnology*, 2009, **20**, 325701.

27 S. Kwon, J.-H. Ko, K.-J. Jeon, Y.-H. Kim and J. Y. Park, *Nano Lett.*, 2012, **12**, 6043–6048.

28 G. Fessler, B. Eren, U. Gysin, T. Glatzel and E. Meyer, *Appl. Phys. Lett.*, 2014, **104**, 041910.

29 H. Chen and T. Filleter, *Nanotechnology*, 2015, **26**, 135702.

30 D. Dietzel, T. Mönninghoff, L. Jansen, H. Fuchs, C. Ritter, U. D. Schwarz and A. Schirmeisen, *J. Appl. Phys.*, 2007, **102**, 084306.

31 A. Koma, *J. Cryst. Growth*, 1999, **201**, 236–241.

32 M. Kratzer and C. Teichert, *Nanotechnology*, 2016, **27**, 292001.

33 G. Hlawacek, F. S. Khokhar, R. van Gastel, B. Poelsema and C. Teichert, *Nano Lett.*, 2011, **11**, 333–337.

34 A. Matković, J. Genser, D. Lüftner, M. Kratzer, R. Gajić, P. Puschnig and C. Teichert, *Sci. Rep.*, 2016, **6**, 38519.

35 G.-H. Lee, C.-H. Lee, A. M. van der Zande, M. Han, X. Cui, G. Arefe, C. Nuckolls, T. F. Heinz, J. Hone and P. Kim, *APL Mater.*, 2014, **2**, 092511.

36 C.-H. Lee, T. Schiros, E. J. G. Santos, B. Kim, K. G. Yager, S. J. Kang, S. Lee, J. Yu, K. Watanabe, T. Taniguchi, J. Hone, E. Kaxiras, C. Nuckolls and P. Kim, *Adv. Mater.*, 2014, **26**, 2812–2817.

37 Y. Zhang, J. Qiao, S. Gao, F. Hu, D. He, B. Wu, Z. Yang, B. Xu, Y. Li, Y. Shi, W. Ji, P. Wang, X. Wang, M. Xiao, H. Xu, J.-B. Xu and X. Wang, *Phys. Rev. Lett.*, 2016, **116**, 016602.

38 D. Jariwala, S. L. Howell, K.-S. Chen, J. Kang, V. K. Sangwan, S. A. Filippone, R. Turrisi, T. J. Marks, L. J. Lauhon and M. C. Hersam, *Nano Lett.*, 2016, **16**, 497–503.

39 G. He, M. H. Müser and M. O. Robbins, *Science*, 1999, **284**, 1650–1652.

40 D. Dietzel, J. Brndiar, I. Štich and A. Schirmeisen, *ACS Nano*, 2017, **11**, 7642–7647.

41 R. M. Overney, H. Takano, M. Fujihira, W. Paulus and H. Ringsdorf, *Phys. Rev. Lett.*, 1994, **72**, 3546–3549.

42 R. W. Carpick, D. Y. Sasaki and A. R. Burns, *Tribol. Lett.*, 1999, **7**, 79–85.

43 V. Kalihari, G. Haugstad and C. D. Frisbie, *Phys. Rev. Lett.*, 2010, **104**, 086102.

44 M. Campione and E. Fumagalli, *Phys. Rev. Lett.*, 2010, **105**, 166103.

45 A. Perez-Rodriguez, E. Barrena, A. Fernandez, E. Gnecco and C. Ocal, *Nanoscale*, 2017, **9**, 5589–5596.

46 K. S. Novoselov, A. K. Geim, S. V. Morozov, D. Jiang, Y. Zhang, S. V. Dubonos, I. V. Grigorieva and A. A. Firsov, *Science*, 2004, **306**, 666–669.

47 A. Lopez-Otero, *Thin Solid Films*, 1978, **49**, 3–57.

48 T. Potocar, S. Lorbek, D. Nabok, Q. Shen, L. Tumbek, G. Hlawacek, P. Puschnig, C. Ambrosch-Draxl, C. Teichert and A. Winkler, *Phys. Rev. B: Condens. Matter Mater. Phys.*, 2011, **83**, 075423.

49 F. Balzer, H. H. Henrichsen, M. B. Klarskov, T. J. Booth, R. Sun, J. Parisi, M. Schiek and P. Bøggild, *Nanotechnology*, 2013, **25**, 035602.

50 M. Kratzer, S. Klima, C. Teichert, B. Vasić, A. Matković, U. Ralević and R. Gajić, *J. Vac. Sci. Technol., B: Nanotechnol. Microelectron.: Mater., Process., Meas., Phenom.*, 2013, **31**, 04D114.

51 G. Hlawacek and C. Teichert, *J. Phys.: Condens. Matter*, 2013, **25**, 143202.

52 C. Simbrunner, *Semicond. Sci. Technol.*, 2013, **28**, 053001.

53 K. N. Baker, A. V. Fratini, T. Resch, H. C. Knachel, W. W. Adams, E. P. Socci and B. L. Farmer, *Polymer*, 1993, **34**, 1571–1587.

54 J. L. Hutter and J. Bechhoefer, *Rev. Sci. Instrum.*, 1993, **64**, 1868.

55 J. Kjelstrup-Hansen, O. Hansen, H.-G. Rubahn and P. Bøggild, *Small*, 2006, **2**, 660–666.

56 T. Junno, K. Deppert, L. Montelius and L. Samuelson, *Appl. Phys. Lett.*, 1995, **66**, 3627–3629.

57 L. Theil Hansen, A. Kühle, A. H. Sørensen, J. Bohr and P. E. Lindelof, *Nanotechnology*, 1998, **9**, 337.

58 E. Gnecco, A. Rao, K. Mougin, G. Chandrasekar and E. Meyer, *Nanotechnology*, 2010, **21**, 215702.

59 M. Varenberg, I. Etsion and G. Halperin, *Rev. Sci. Instrum.*, 2003, **74**, 3362.

60 J. Tersoff, *Phys. Rev. B: Condens. Matter Mater. Phys.*, 1989, **39**, 5566–5568.

61 B. R. Brooks, C. L. Brooks, A. D. Mackerell, L. Nilsson, R. J. Petrella, B. Roux, Y. Won, G. Archontis, C. Bartels, S. Boresch, A. Caflisch, L. Caves, Q. Cui, A. R. Dinner, M. Feig, S. Fischer, J. Gao, M. Hodoscek, W. Im, K. Kuczera, T. Lazaridis, J. Ma, V. Ovchinnikov, E. Paci, R. W. Pastor, C. B. Post, J. Z. Pu, M. Schaefer, B. Tidor, R. M. Venable, H. L. Woodcock, X. Wu, W. Yang, D. M. York and M. Karplus, *J. Comput. Chem.*, 2009, **30**, 1545–1614.

62 A. N. Kolmogorov and V. H. Crespi, *Phys. Rev. B: Condens. Matter Mater. Phys.*, 2005, **71**, 235415.

63 S. Plimpton, *J. Comput. Phys.*, 1995, **117**, 1–19.

64 D. E. Hooks, T. Fritz and M. D. Ward, *Adv. Mater.*, 2001, **13**, 227–241.

65 S. C. B. Mannsfeld, K. Leo and T. Fritz, *Phys. Rev. Lett.*, 2005, **94**, 056104.

66 T. Haber, R. Resel, A. Thierry, M. Campione, A. Sassella and M. Moret, *Phys. E*, 2008, **41**, 133–137.

67 L. Raimondo, M. Moret, M. Campione, A. Borghesi and A. Sassella, *J. Phys. Chem. C*, 2011, **115**, 5880–5885.

68 L. Raimondo, E. Fumagalli, M. Moret, M. Campione, A. Borghesi and A. Sassella, *J. Phys. Chem. C*, 2013, **117**, 13981–13988.

69 M. Campione, A. Sassella, M. Moret, A. Papagni, S. Trabattoni, R. Resel, O. Lengyel, V. Marcon and G. Raos, *J. Am. Chem. Soc.*, 2006, **128**, 13378–13387.

70 G. Conache, S. M. Gray, A. Ribayrol, L. E. Fröberg, L. Samuelson, H. Pettersson and L. Montelius, *Small*, 2009, **5**, 203–207.

71 M. Campione, S. Trabattoni and M. Moret, *Tribol. Lett.*, 2012, **45**, 219–224.

72 M. Campione and G. C. Capitani, *Nat. Geosci.*, 2013, **6**, 847.

PAPER

Correlation between morphology and local mechanical and electrical properties of van der Waals heterostructures

View the article online for updates and enhancements.

Correlation between morphology and local mechanical and electrical properties of van der Waals heterostructures

Borislav Vasić[1] , **Uroš Ralević**[1], **Sonja Aškrabić**[1], **Davor Čapeta**[2] **and Marko Kralj**[2]

[1] Institute of Physics Belgrade, University of Belgrade, Pregrevica 118, 11080 Belgrade, Serbia
[2] Center of Excellence for Advanced Materials and Sensing Devices, Institute of Physics, Bijenička 46, 10000, Zagreb, Croatia

E-mail: bvasic@ipb.ac.rs

Abstract
Properties of van der Waals (vdW) heterostructures strongly depend on the quality of the interface between two dimensional (2D) layers. Instead of having atomically flat, clean, and chemically inert interfaces without dangling bonds, top-down vdW heterostructures are associated with bubbles and intercalated layers (ILs) which trap contaminations appeared during fabrication process. We investigate their influence on local electrical and mechanical properties of MoS_2/WS_2 heterostructures using atomic force microscopy (AFM) based methods. It is demonstrated that domains containing bubbles and ILs are locally softer, with increased friction and energy dissipation. Since they prevent sharp interfaces and efficient charge transfer between 2D layers, electrical current and contact potential difference are strongly decreased. In order to reestablish a close contact between MoS_2 and WS_2 layers, vdW heterostructures were locally flattened by scanning with AFM tip in contact mode or just locally pressed with an increased normal load. Subsequent electrical measurements reveal that the contact potential difference between two layers strongly increases due to enabled charge transfer, while local I/V curves exhibit increased conductivity without undesired potential barriers.

Keywords: van der Waals heterostructures, two-dimensional materials, atomic force microscopy, Kelvin probe force microscopy, conductive atomic force microscopy, nanofriction, energy dissipation

(Some figures may appear in colour only in the online journal)

1. Introduction

Van der Waals (vdW) heterostructures are vertical stacks of different two dimensional (2D) materials [1–3]. Since individual 2D layers hold together by weak vdW forces without chemical bonding, their stacking is not constrained by the crystal lattice matching. As a result, arbitrary combinations of 2D materials can be fabricated by transferring them on top of each other [4].

Since 2D materials are associated with electronic band-gaps in a broad range, they provide metallic (such as graphene), semiconducting (such as transition metal dichalcogenides (TMDs)) and insulating layers (such as hexagonal

boron nitride). Heterostructures obtained by their combinations bring novel and unique functionalities and devices with properties exceeding those of constituent materials. Characteristic examples are barrier-free electrical contacts [5], efficient substrates for 2D electronic devices with reduced charge scattering [6], and tunneling and field-effect transistors [7–9].

TMDs are 2D semiconductors with the band-gap in the visible and near-infrared domain, with a direct band-gap in the case of the monolayer limit, and correspondingly with a strong photoluminescence [10]. Heterostructures comprising of 2D semiconductors with different band gap are of special importance since they act as atomically sharp vertical

p–n-junctions [11] with obvious applications for rectifying junctions [12, 13]. They are also very interesting for optoelectronics and photovoltaic applications [14] such as atomically-thin photodetectors and solar cells [15–19] and light emitting devices [20, 21].

While recent studies were mainly focused on possible applications in electronics and optoelectronics, vdW heterostructures have interesting mechanical properties as well. They provide robust sliding of adjacent layers through incommensurate states which results in a superlubric state associated with an ultra low dissipation and friction [22–28].

Properties of vdW heterostructures strongly depend on the quality of the interface between 2D layers. In an ideal case, the interface is atomically flat, clean, and chemically inert without dangling bonds. Still, in reality 2D materials are associated with contaminations due to airborne hydrocarbon molecules [29] or intercalated water layers (inevitable under ambient humidity conditions) [30, 31], and due to various residues from polymers employed during fabrication [32] (mechanical exfoliation and transfer). After the transfer process, vdW interaction tends to bring adjacent 2D layers into contact, while the contaminations trapped at the interface are simultaneously squeezed into localized pockets called bubbles [33–39]. Bubbles and layers intercalated between 2D materials (hereafter intercalated layers—ILs) are kind of imperfections and understanding of their formation, chemical composition and physico-chemical properties is essential in order to assess properties of realistic vdW heterostructures.

So far the chemical composition of the contaminations has been investigated using electron microscopy [33, 40], spectroscopic techniques [29, 41, 42] or indirectly, by heating and following morphological changes [34, 43]. Since the thickness of ILs is in the order of nanometer and since bubbles are localized to lateral domains with the size in the order of 100nm, true nanoscale resolution in the chemical identification of these imperfections was achieved by using atomic force microscopy (AFM) based techniques coupled with infrared spectroscopy [44] or by using scanning near-field optical microscopy [45]. AFM was also demonstrated as an efficient tool to manipulate morphology of vdW heterostructures in order to locally flatten and clean them [44, 46–48]. Still, the influence of bubbles and ILs on local mechanical and electrical properties of vdW heterostructures has remained unexplored so far.

Here we investigate the vdW heterostructures consisting of MoS_2 flakes stacked onto WS_2 layers. Using AFM methods, we demonstrate that bubbles and ILs make the heterostructures softer and increase the friction and dissipation of the mechanical energy in dynamic mode (tapping AFM mode). AFM based electrical measurements reveal that bubbles and ILs are obstacles for uniform charge transfer between MoS_2 and WS_2 layers, resulting in a decreased contact potential difference. In a similar way, local electrical current strongly decreases on domains with bubbles which prevent vertical transport of charge carriers between layers. At the end, we provide methods to overcome observed issues. Clean contact between MoS_2 and WS_2 layers is reestablished by AFM based flattening of vdW heterostructures using scanning

in contact mode or by applying an increased normal load from AFM probe at single point. Subsequent measurements of electrical properties prove that both contact potential difference and conductivity are increased.

2. Experimental methods

2.1. Sample preparation

Starting MoS_2 and WS_2 layers were synthesized by chemical vapor deposition (CVD). MoS_2 was grown in homemade CVD system from MoO_3 and S [49]. Sulfur vapor was produced by heating 50–100 mg of S to 150 °C by separate heater, and carried to substrate by 100 SCCM of Ar. Growth substrate, 300 nm SiO_2 on highly doped Si, was placed in center of furnace and heated to 800 °C during growth. For the growth of WS2, substrates were drop coated with 10 ppm by weight solution of sodium tungstate dihydrate [50]. After drying, they were sulfurized in a similar setup also under 100 SCCM Ar, with substrate temperature 850 °C and S heated at 180 °C. After the growth, the substrate was cooled in furnace to 250 °C in Ar before removal.

vdW heterostructures of MoS_2 and WS_2 layers were then fabricated using a variant of the wet transfer method [51]. The SiO_2/Si substrate carrying the MoS_2 monolayers was covered by Polidimethylsiloxane (PDMS) film and subsequently immersed into aqueous solution of ammonium hydroxide. This solution separates the MoS_2 monolayers and the substrate, leaving the monolayers attached to the PDMS. The PDMS film is then fished out of the ammonium hydroxide, laminated on top of the other SiO_2/Si substrate which carries WS_2 monolayers and finally peeled off slowly using tweezers. The optical image of fabricated vdW heterostructures is depicted in figure 1(a) indicating small MoS_2 triangles deposited onto larger triangular WS_2. We did not apply any post-fabrication technique, such as common post annealing [34], in order to minimize bubbles and ILs, since the aim of the study was to investigate their influence on mechanical and electrical properties of vdW heterostructures.

2.2. Raman characterization

Raman measurements were performed using TriVista 557 spectrometer equipped with a triple monochromator coupled to a microscope and a CCD detector with liquid nitrogen cooling. Raman spectra were excited with 488 nm and 514.5 nm lines of Ar_+/Kr_+ laser. Triple monochromator configuration was 900/900/1800 grooves per mm. Low laser power of 0.3 mW was used in order to minimize sample degradation.

2.3. AFM measurements

All AFM measurements were done using NTEGRA Prima system from NT-MDT. Initial morphological measurements of MoS_2/WS_2 heterostructures were always done in tapping mode. Simultaneous phase measurements were used to assess dissipation of the mechanical energy. Namely, the energy dissipation E_{diss} is proportional to the phase lag φ
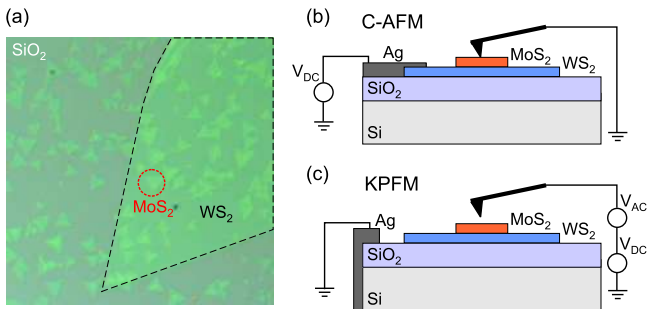
Figure 1. (a) The optical image of fabricated vdW heterostructures. The part of bigger WS_2 triangle is marked by dashed line, while one MoS_2 triangle is encircled by dotted line. The average lateral size of MoS_2 triangles is around 5 μm. Experimental setups for (b) C-AFM and (c) KPFM measurements.

$(E_{diss} \sim \sin(\phi))$ of the AFM cantilever oscillations during the scanning in tapping mode [52].

The local flattening was performed by AFM operating in contact mode [44, 46, 47]. FMG01 probes from NT-MDT (with a typical force constant of $3\,N\,m^{-1}$) were employed. After the selection of an appropriate square domain, it was raster scanned for several times (5–10), while the normal load was increased at the beginning of every scan (in the range from ∼20 nN to ∼130 nN). After the flattening and scanning in contact mode, we switched back into tapping AFM mode, selected a larger scan area (than the previously chosen squared domain aimed for flattening), and made topographic imaging in order to detect morphological changes.

Distribution of the local stifness was qualitatively assessed by force modulation microscopy (FMM). In this mode, measurements were performed in contact mode, while an AC voltage was applied to the AFM scanner causing its oscillations in the vertical direction, together with the sample placed on the top of the scanner. The scanner (sample) movement (described with the vertical coordinate z_s) results in the oscillations of AFM tip and cantilever (represented with the vertical coordinate z_c) with the same frequency. Generally, the scanner movement is equal to the sum of the movement of the AFM cantilever and sample indentation δ: $z_s = z_c + \delta$. On hard samples, the indentation is practically zero, therefore, $z_c = z_s$. On the other hand, on locally softer regions, the indentation depth is not negligible and the cantilever oscillations are decreased: $z_c = z_s - \delta$. Therefore, the amplitude of the AFM cantilever oscillations follows the variations of the sample stifness, implying that larger (smaller) oscillation amplitude is measured on stiffer (softer) regions. FMM measurements were done using CSG10 probes (with a nominal stiffness of $0.11\,N\,m^{-1}$) from NT-MDT, while the frequency of the applied oscillations on AFM scanner was around 10 kHz.

Local friction during the sliding of AFM tip on MoS_2/WS_2 heterostructure was measured by friction force microscopy (FFM) using CSG01 probes (with a nominal stiffness of $0.03\,N\,m^{-1}$) from NT-MDT. The measurements were done in contact mode by the recording of the lateral

torsion of the AFM cantilever due to local friction between the tip and sample surface. The friction signal was obtained as a half of the difference of the lateral force signal measured in forward and backward scan directions. During the measurements, the fast-scan axis was normal to the AFM cantilever.

Current mapping was performed in contact mode using conductive AFM (C-AFM). During the scanning, DC bias voltage was applied to the sample while the AFM tip was virtually grounded (figure 1(b)). Since the aim of the study was to detect the influence of bubbles and intercalated water layers on properties of vdW heterostructures, the C-AFM imaging was done with very soft probes CSG01/TiN (with a nominal stiffness of 0.03 N/m and TiN conductive coating) and at low normal loads in the order of 1 nN. These probes were selected in order to avoid flattening of vdW heterostructures by the applied normal load from AFM tip [44, 46, 48]. I/V curves were measured at single point, at constant normal load, by sweeping the bias voltage in the range ±10 V.

Kelvin probe force microscopy (KPFM) was employed in order to map local electrical surface potential of vdW heterostructures. Diamond coated probes DCP11 and NSG01 probes coated with Pt coating NSG01/PT from NT-MDT were employed. The measurements were done using a standard two-pass technique, where the sample morphology was recorded in the first pass, while the contact potential difference (CPD) between the AFM tip and sample surface was measured in the second pass. In the later case, the AFM cantilever was raised by 20 nm in order to measure only electrostatic interaction and avoid the influence of vdW forces. During the second pass, the sum of AC voltage and variable DC voltage (figure 1(c)) was applied on the AFM cantilever (with grounded sample). The applied AC voltage resulted in AFM cantilever oscillations while the electrical feedback loop automatically adjusted the value of variable DC voltage in order to cancel the oscillations. The value of the DC voltage which nullified the AFM cantilever oscillations is equal to the local CPD.

3. Results and discussion

MoS_2/WS_2 vdW heterostructures considered in this study belong to type II of semiconductor heterojunctions which are associated with a staggered band-gap. Excellent rectifying properties, high photo-responsivity [53] and large surface photovoltage [54] make them good candidates for photo-detection [55–58]. Besides interesting optoelectronic properties, MoS_2 and WS_2 are TMDs with excellent elastic [59] and frictional properties [60, 61] as well. Optical properties and absorption of these heterostructures strongly depend on the interlayer coupling and charger transfer between constituent layers [62–64]. At the same time, mechanical properties (elasticity and friction, sliding and deformation) are also strongly influenced by interlayer interactions and stacking [27, 65, 66]. Therefore, MoS_2/WS_2 vdW heterostructure is a
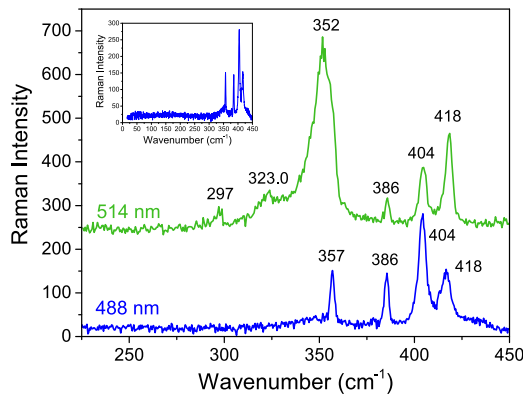
Figure 2. Raman spectra of as-obtained MoS_2/WS_2 heterostructure, excited with 514 nm (green line) and 488 nm (blue line). The inset depicts the Raman spectrum in the low-frequency region (starting from 15 cm^{-1}), excited with 488 nm line.

convenient platform to explore how inhomogeneities, such as bubbles and ILs, influence interlayer interactions and local mechanical and electrical properties.

3.1. Identification of layers

In order to detect the presence of MoS_2 and WS_2 in investigated samples and related interlayer coupling effects, Raman spectroscopy was used. MoS_2 has two Raman active vibrations, E'/E_{2g}^1 (in-plane), positioned at ~ 386 cm^{-1}, and A_1'/A_{1g} (out-of-plane), positioned at ~ 404 cm^{-1} [67]. WS_2 has two first order Raman active modes, E_{2g}^1 and A_{1g}, positioned at ~ 357 cm^{-1} and ~ 418 cm^{-1} [67, 68]. When a resonant excitation of 514.5 nm is used, second order peaks, mainly acoustic phonons such as 2LA(M) positioned at 297 cm^{-1}, 323 cm^{-1} and 350 cm^{-1}, become prominent due to phonon–exciton coupling [67, 68]. The 2LA mode of highest intensity is positioned very closely to the E_{2g}^1 mode and the two are superposed into one wide peak at 352 cm^{-1}. When a non-resonant excitation line such as 488 nm is used, only first-order Raman modes appear in spectra of WS_2 [68].

Raman spectra of MoS_2/WS_2 heterostructures, depicted in figure 2, contain both MoS_2 and WS_2 Raman modes which confirms presence of these layers in the heterostructure. The spectrum excited with 488 nm line contains only first-order WS_2 modes, E_{2g}^1 and A_{1g}, whereas the spectrum excited with 514 nm line contains also resonantly enhanced second-order modes. In the low frequency Raman spectrum, which is excited with 488 nm line and displayed in the inset of figure 2, no interlayer modes were observed which suggests scarce coupling between the MoS_2 and WS_2 monolayers [64].

3.2. Bubbles and intercalated layers

AFM topographic image of the characteristic heterostructure (figure 3(a)) consists of the triangular MoS_2 flake on the top of the WS_2 flake. Such geometry with a smaller MoS_2 triangle on a larger WS_2 layer was common for all heterostructures considered in this study. Bright localized domains on the surface of MoS_2 represent bubbles formed at the interface

between MoS_2 and WS_2. The bright lines represent wrinkled MoS_2 domains. Bubbles do not appear below WS_2 since it was directly grown on SiO_2/Si substrate without additional transfer. Small bright dots on WS_2 stand for residues appeared during the transfer process of MoS_2 or adsorbates originating from environment. Previous works already demonstrated that bubbles contain hydrocarbon molecules [33] and/or residues originating from polymers used for the transfer [44]. Taking this information into account, the aim of our work was to study to what extent bubbles and intercalated layers degrade mechanical and electrical properties of vdW heterostructures.

Local flattening based on contact AFM mode was done within the square domain denoted by the dotted line in figure 3(a). Topography recorded in tapping mode after the flattening shown in figure 3(b) reveals that bright domains representing bubbles and wrinkles practically disappeared. During the flattening, surface adsorbates were pushed by AFM tip in a scanning direction and deposited at the rims of the square domain. Height profiles across the MoS_2 flake before and after the flattening in figure 3(c) prove that MoS_2 thickness is decreased from approximately 3 nm to only 1 nm due to squeezing out contaminants trapped between MoS_2 and WS_2. The height of bubbles before the flattening was up to 15 nm. On the other hand, after the flattening, density of all surface corrugations was very low, while their height was less than 2 nm.

Still, after the flattening, the MoS_2 surface contains local depressions which are emphasized in figure 3(d). Characteristic profiles in figure 3(e) taken across local depressions reveal that their depth is around 0.5 nm which corresponds to the thickness of MoS_2. Therefore, the observed depressions represent holes in MoS_2 which appear due to its local tearing at the position of bubbles and wrinkles [47]. The maximal normal loads applied during AFM based flattening were up to around 150 nN. In order to induce wear of mechanically exfoliated 2D materials by AFM tip scratching, the applied normal load should be at least several μN [69, 70]. Therefore, the threshold force is much higher than the load applied in the current study. However, in the case of layers grown by chemical vapor deposition, wear could start already at normal loads of only several hundreds of nN [71]. In this case, the wear is initiated by AFM tip going across wrinkles which present out-of-plane local deformations and obviously decrease the wear resistance. Since wrinkles and bubbles are similar imperfections (the main difference is that the wrinkles are line deformations), we can expect that wear of vdW heterostructures during AFM based flattening could be also initiated for forces in the order of 100 nN. Therefore, larger normal loads applied during the AFM based flattening give more flat layers and heterostructures, but on the other hand, they could lead to local tearing of bubbles which present local out-of plane deformations and therefore reduce wear resistance of 2D layers.

In order to further analyze the morphology of bubbles, we used a segment of the heterostructure depicted in figure 4(a) (only the surface of top MoS_2 displayed). We note that smaller bubbles have circular bases, larger ones appear in triangular and trapezoidal bases, while several biggest

bubbles have more complex shapes with polygonal bases. For the sake of simplicity, in our analysis, all bases were approximated with discs described with an effective radius R_{eq}. Relations between bubbles' geometrical parameters are depicted in figure 4(b). Bubbles' maximal height H_{max} approximately linearly increases with effective radius R_{eq} (bottom part of figure 4(b)), while the slope of the linear dependence is around 0.1 (the ratio of H_{max}/R_{eq} as a function of R_{eq} presented in top part of figure 4(b)). The value of the slope agrees well with H_{max}/R_{eq} ratios for bubbles formed in other vdW heterostructures, which are in the range 0.1–0.2 [35, 39]. Since the formation of bubbles is generally governed by the competition between vdW attractive forces (which tend to bring adjacent 2D layers into contact, while the contaminations are simultaneously squeezed into bubbles) and the in-plane stiffness and bending rigidity of the top 2D layer (which try to prevent local bending of the layer and formation of bubbles), H_{max}/R_{eq} depends on the ratio between adhesion energy and Young's modulus of elasticity, and is therefore universal for all bubbles [35].

Although here we considered vdW heterostructures consisting of 2D layers grown by chemical vapor deposition, we expect similar results for the heterostructures made from mechanically exfoliated layers. Possible differences could appear due to applied transfer method. In the wet transfer method, in order to separate MoS_2 from SiO_2/Si substrate, samples were first covered by PDMS and subsequently immersed into aqueous solution of ammonium hydroxide. Nanometric thin fluid layers could then stick to MoS_2 and then become trapped after the transfer onto WS_2. As a result, it is reasonable to expect more pronounced ILs in the heterostructures produced by the wet transfer method, compared to the dry transfer method.

3.3. Stiffness

The imaging in FMM mode reveals that bubbles, represented by brighter contrast in the topographic image (figure 5(a)), correspond to domains with lower magnitude of AFM cantilever oscillations (darker domains in figure 5(b)). The profiles in figure 5(c) display that the bubble represented by a large bump (located at a distance of around 0.4 μm) exactly corresponds to a huge dip in the magnitude signal. Since lower magnitude of the AFM cantilever oscillations in FMM implies softer regions, bubbles present locally softer domains compared to surrounding flat parts.

The mechanical response of layered systems is dominantly determined by the softest layers. In the considered case, the softest layer is the one with trapped contaminations. During the scanning of 2D materials in FMM mode, the local pressure exerted by AFM tip is transferred to the medium below them. Therefore, by scanning across MoS_2 bubbles, the AFM tip locally probes the stiffness of the material trapped within the bubbles. Since they are filled with soft materials such as gases, liquids and polymers (due to trapped air, water, hydrocarbon and/or polymer residues), the AFM tip indents the bubbles and therefore oscillates with decreased magnitude.

The oscillation magnitude image (figure 5(b)) reveals that even flat regions of MoS_2 (which are free of large bubbles) are slightly darker than WS_2. A slight decrease of the oscillation magnitude is indicated by Δmag in the profile in figure 5(c). This implies that MoS_2 and WS_2 are lying on substrates with different stiffness. Since WS_2 was directly grown on SiO_2 and possesses intrinsic growth strain, it is lying on a hard substrate which practically prevents any indentation. As a result, the AFM tip here oscillates with the maximal magnitude determined by the oscillations of AFM scanner. On the other hand, lower oscillation magnitude observed on flat regions of MoS_2 indicates that it is lying on a softer IL. Therefore, both ILs and especially bubbles define local domains in vdW heterostructures with lower stiffness.

3.4. Friction

Friction measurements were done on the MoS_2/WS_2 heterostructure depicted in figure 6(a). Top MoS_2 flake consists of three parts: bright domain 1 in the right-bottom corner, dark domain 2 in the middle, and small bright domain 3 in the left-top corner. The friction map in figure 6(b) reveals brighter contrast on domains 1 and 3, and therefore larger friction than on domain 2. Practically there is no friction contrast between MoS_2 domain 2 and surrounding WS_2 due to similar friction coefficients of two materials [72].

The characteristic height profiles depicted in figure 6(c) illustrate that MoS_2 thickness is $\Delta h_1 \approx 2$ nm for domain 1 and $\Delta h_2 < 1$ nm for domain 2. Domain 1 (and domain 3 as well) is thicker since it is decoupled from the underlying WS_2 by an IL. The friction profile in figure 6(c) displays two force levels while the histogram of the friction map in figure 6(d) exhibits two peaks. The lower peak and lower force level F_2 correspond to domain 2 without IL. On the other hand, the upper peak and higher force level F_1 correspond to domains 1 and 3 which contain ILs. As can be seen, the friction on domains with ILs (1 and 3) is increased by even 50% compared to the friction on domains without them (domain 2).

Increased friction observed on domains with ILs and trapped contaminations is in agreement with previous results obtained on single 2D materials [73–75]. Namely, various contaminations, such as hydrocarbon molecules which are inevitable on surfaces exposed to air, act as 'third bodies' at the interface between two sliding surfaces. They could lock two surfaces into contact or initiate their pristine chemical bonding. Generally, they disturb easy sliding of two contacting surfaces through incommensurate states which results in increased friction. More recently, it has been demonstrated that a water layer intercalated below 2D materials forms hydrogen-bonded clusters which impede easy sliding [76, 77] and increases density of phonon states which provides additional channels for the dissipation of frictional energy [78].

3.5. Energy dissipation in dynamic AFM mode

Friction generally leads to an undesired energy dissipation and losses. In the previous section we considered the case
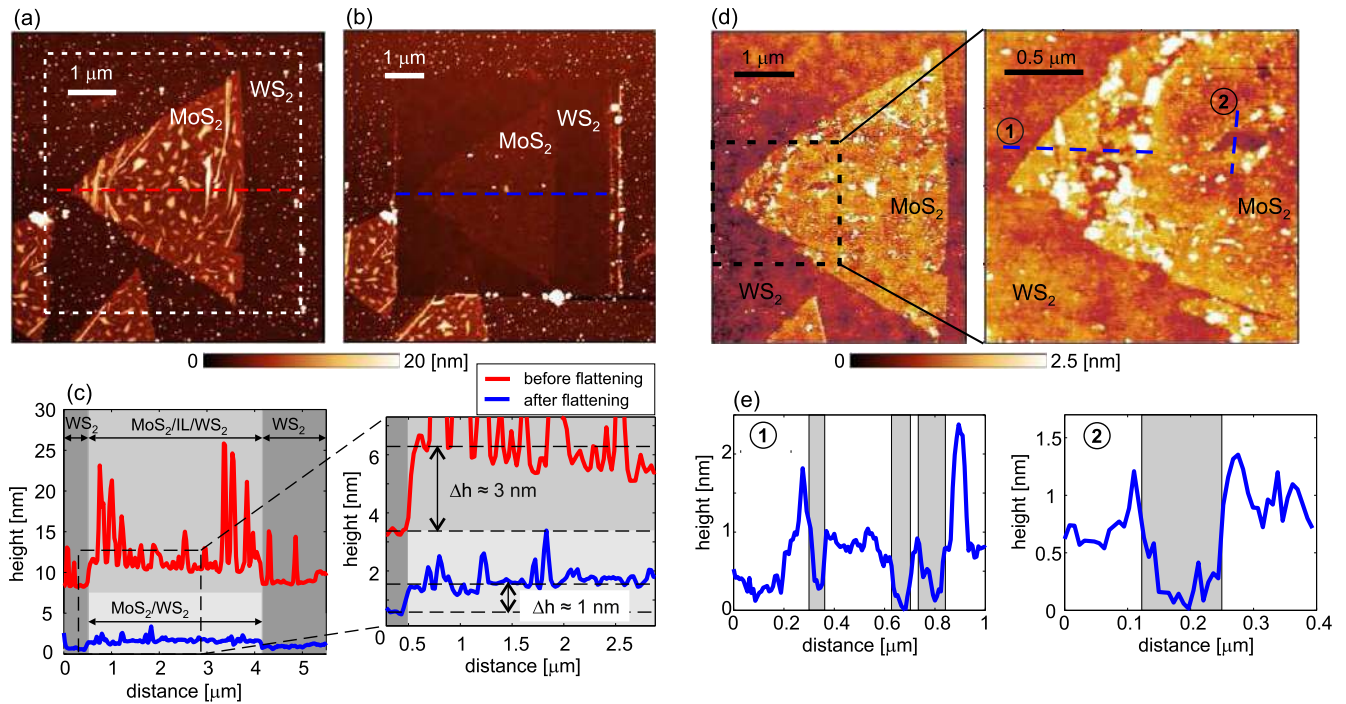
Figure 3. Morphology of the considered MoS$_2$/WS$_2$ vdW heterostructure (a) before and (b) after the AFM based flattening. The flattening was performed within the square domain marked in (a). (c) Height profiles along dashed lines in (a) and (b). (d) Morphology of the heterostructure after the flattening with the focus on the area with MoS$_2$. (e) Height profiles (along dashed lines 1 and 2 in (d)) taken across holes in MoS$_2$ layer.
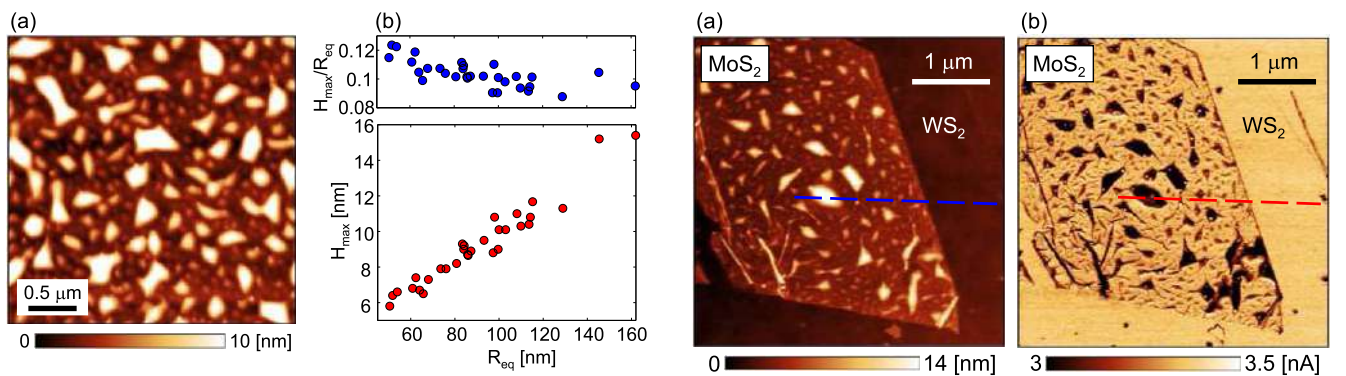

Figure 4. (a) Morphology of bubbles emphasizing variations of their basis, ranging from circular to triangular and polygonal bases. (b) Bubbles' maximal height as a function of their effective radius (bottom) and the slope of H_{max}/R_{eq} as a function of R_{eq} (top).

when the AFM tip is in the mechanical contact with sample surface. Still, the energy can be dissipated by a vibrating tip in dynamic AFM modes as well [52]. In order to check dissipation during the interaction between oscillating AFM tip and vdW heterostructures, we employed tapping AFM mode. Here the dissipation of the mechanical energy E_{diss} is proportional to $\sin(\Phi)$, where Φ is the phase lag of the AFM cantilever oscillations during the tapping mode imaging [52].

Phase maps for the heterostructure in figure 7(a) are presented in figures 7(b) and 7(c), for both the in-phase and out-of-phase oscillations, respectively (the in-phase/out-of-
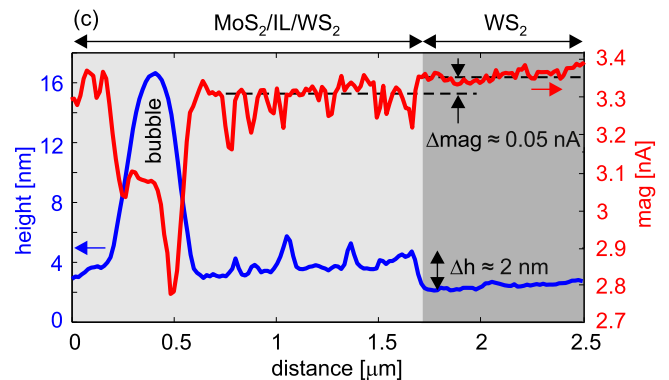

Figure 5. (a) Morphology of MoS$_2$/WS$_2$ heterostructure, (b) corresponding magnitude of the AFM cantilever oscillations recorded in FMM mode. (c) Height and magnitude profiles along dashed lines in (a) and (b), respectively.
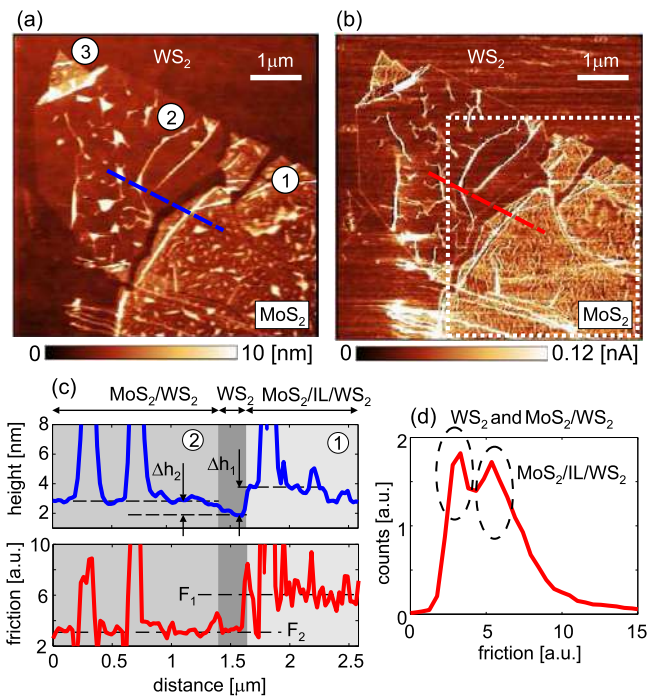
Figure 6. (a) Morphology of MoS$_2$/WS$_2$ heterostructure and (b) corresponding friction map. (c) Height and friction profiles along dashed lines in (a) and (b), respectively. (d) Histogram of the friction map calculated for the square domain marked by dotted line in (b).
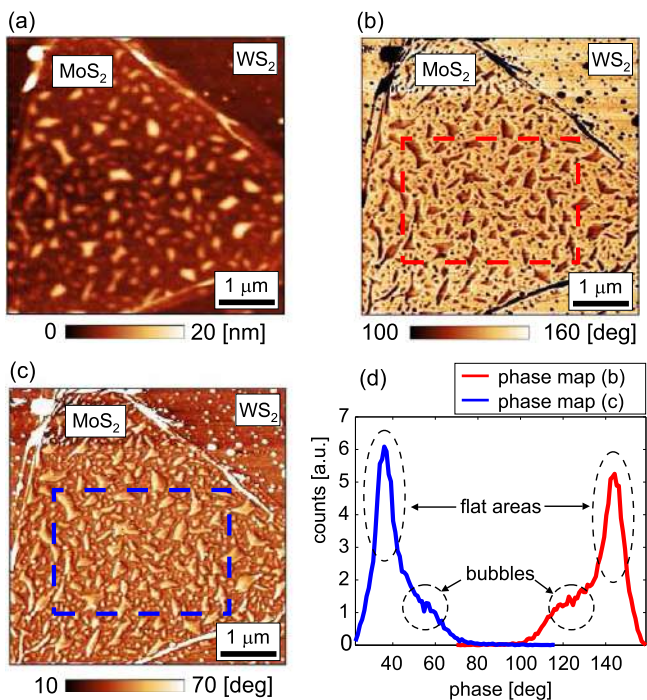

Figure 7. (a) Morphology of MoS$_2$/WS$_2$ heterostructure, (b) phase map for the in-phase AFM cantilever oscillations (z-scale from 100° to 160°), (c) phase map for the out-of-phase AFM cantilever oscillations (z-scale from 10° to 70°), (d) histograms of both phase maps.

phase oscillations are associated with increasing/decreasing phase as a function of frequency [79]). In the former (latter) case, the measured phase signal is above (below) 90°, while bubbles are represented by darker (brighter) contrast.
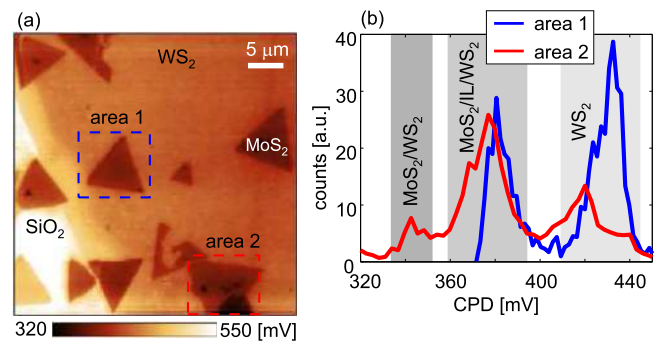

Figure 8. (a) CPD map of MoS$_2$/WS$_2$ heterostructures measured by KPFM and (b) corresponding histogram for the indicated areas.
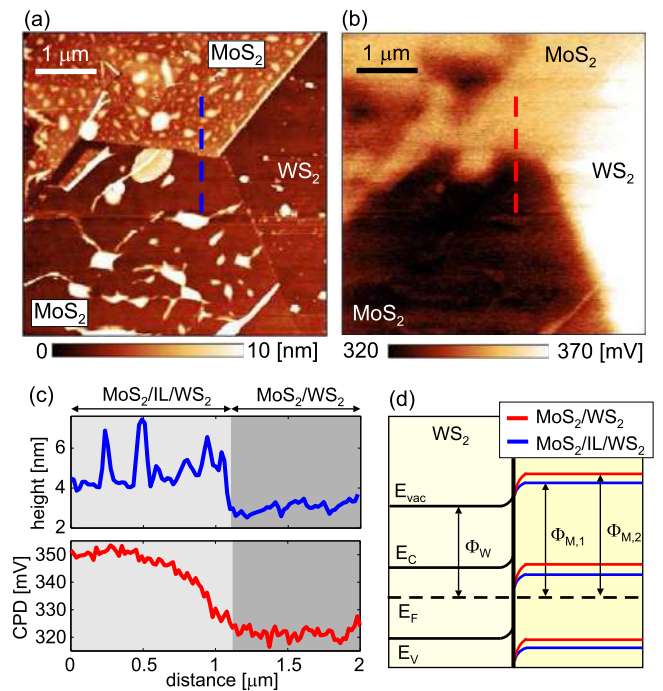

Figure 9. (a) Topography of domain 2 from figure 8(a) and (b) corresponding CPD map. (c) Height and CPD profiles along dashed lines marked in (a) and (b), respectively. (d) Schematic representation of the band structure for domain 2 according to KPFM measurements.

Therefore, lower (higher) phase lag was measured on the bubbles than on their surrounding. The phase contrast was the same in both forward and backward directions, and therefore, it indicates true variations of the local mechanical properties of the vdW heterostructure.

Recently, the phase imaging has been employed in order to study and map local inhomogeneities and bubbles of transferred graphene, while the observed contrast has been explained by variations in local stiffness [80]. Here we relate the observed contrast to variations in energy dissipation. The phase histograms in figure 7(d) reveal two peaks for both cases: around 122° (bubbles) and 144° (surrounding area) for the phase map from figure 7(b), and around 56° (bubbles) and 36° (surrounding area) for the phase map from figure 7(c).
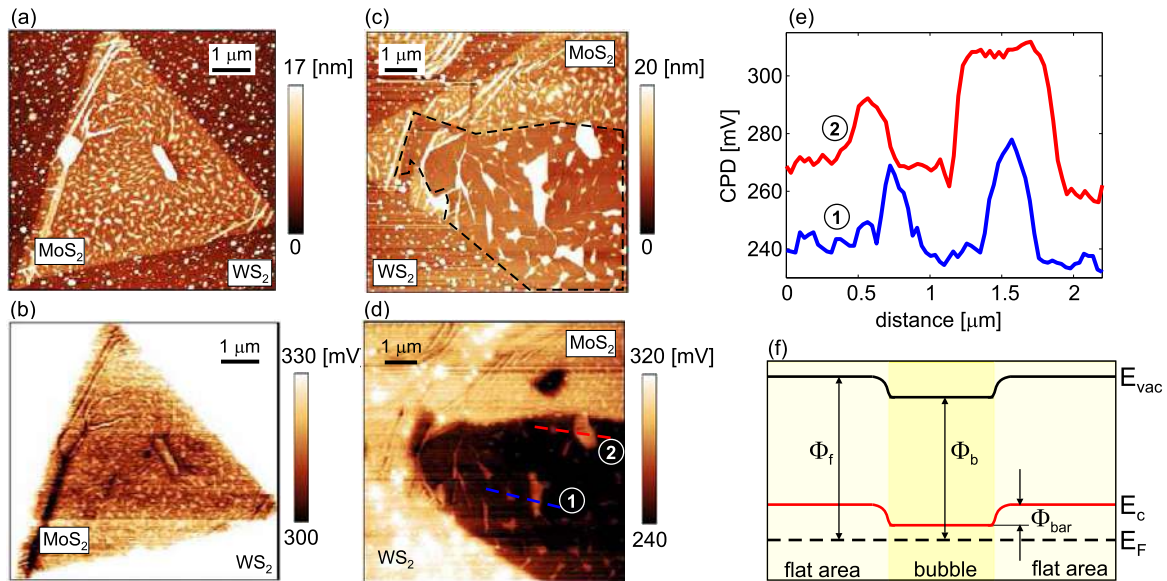
Figure 10. (a) Topography and (b) CPD map of MoS_2/WS_2 heterostructure revealing increased CPD on bubbles. (c) Topography and (d) CPD map of the heterostructure where the bottom part (encircled by the dashed line) is free of ILs and with larger bubbles. (e) CPD profiles along several bubbles from the bottom part of the heterostructure in part (d) (the second profile lifted up by 30 mV for better visibility). (f) Schematic representation of the band diagram indicating local band bending around bubbles.

Since $E_{diss} \sim \sin(\Phi)$, E_{diss} is larger on the bubbles by around 30% compared to their flat surroundings. The same conclusion holds for both in-phase and out-of-phase oscillations, confirming that the dissipation is independent on the initial scanning conditions [79].

During tapping mode imaging with a vibrating AFM tip, the mechanical energy is usually dissipated due to long- and short-range surface adhesion hysteresis [52]. Still, in the case of vdW heterostructure, the dominant phase contrast is observed across the bubbles which contain trapped fluids and/or polymer residues. Such viscoelastic materials generally introduce an additional dissipation channel due to hysteresis of the viscoelastic force during the tip approach and retract [52]. This seems the main cause of the increased dissipation observed on bubbles.

3.6. Electrical surface potential

The influence of the morphology of MoS_2/WS_2 heterostructures on their local electrical properties was first studied by KPFM. In the CPD map in figure 8(a), top triangular MoS_2 flakes are well resolved. They are represented by darker contrast and lower CPD compared to WS_2. While the potential of MoS_2/WS_2 heterostructure in domain 1 is spatially homogeneous, the heterostructure in domain 2 exhibits an inhomogeneous CPD with two different levels. Histograms for two characteristic domains are given in figure 8(b). Taking into account that $CPD = \Phi_t - \Phi_s$ (CPD is equal to the difference between the work functions of AFM tip (Φ_t) and sample (Φ_s)), the following relations can be derived. Higher CPD of WS_2 indicates lower work function than on MoS_2/WS_2 heterostructures. Therefore, when MoS_2 is deposited onto WS_2, in order to equilibrate their Fermi levels, electrons are transferred from WS_2 to MoS_2.

The histogram of domain 2 displays two peaks for MoS_2 on WS_2: at around 380 mV (marked by $MoS_2/IL/WS_2$) and 340 mV (marked by MoS_2/WS_2). In order to clarify the observed inhomogeneity, additional small-scale imaging of this domain was done. Topography in figure 9(a) and characteristic height profiles in figure 9(c) show that the heterostructure consists of two areas with different heights. The upper area ($MoS_2/IL/WS_2$) is thicker by ~ 2 nm due to an IL between MoS_2 and WS_2. At the same time, these areas are associated with two different CPD levels which are separated by ~ 30 mV as displayed in figures 9(b) and (c).

Previous works demonstrated that water layers intercalated between a substrate and 2D materials prevented commonly observed charge doping from the substrate [81, 82]. Therefore, ILs can be regarded as obstacles for charge transfer. KPFM results can be then interpreted using the schematic representation of the band diagram in figure 9(d) in the following way. The heterostructure without IL (MoS_2/WS_2) has lower CPD. Therefore, it has higher work function $\Phi_{M,2}$ compared to $MoS_2/IL/WS_2$ with work function $\Phi_{M,1}$. Increased work function $\Phi_{M,2}$ implies larger potential difference compared to WS_2 work function Φ_W. As a result, the charge transfer of electrons from WS_2 to MoS_2 is more efficient. Therefore, areas of MoS_2/WS_2 without IL are associated with more pronounced charge transfer leading to larger CPD contrast between MoS_2/WS_2 and bare WS_2.

Bubbles induce inhomogeneous strain in two-dimensional materials and consequently local band bending [83–85]. Possible variations of electrical surface potential across bubbles were explored by KPFM. The comparison of topographic image (Figure 10(a)) and corresponding CPD map (figure 10(b)) reveals that bubbles are represented by brighter domains in the CPD map. This is even more pronounced in the case of heterostructures without ILs and with
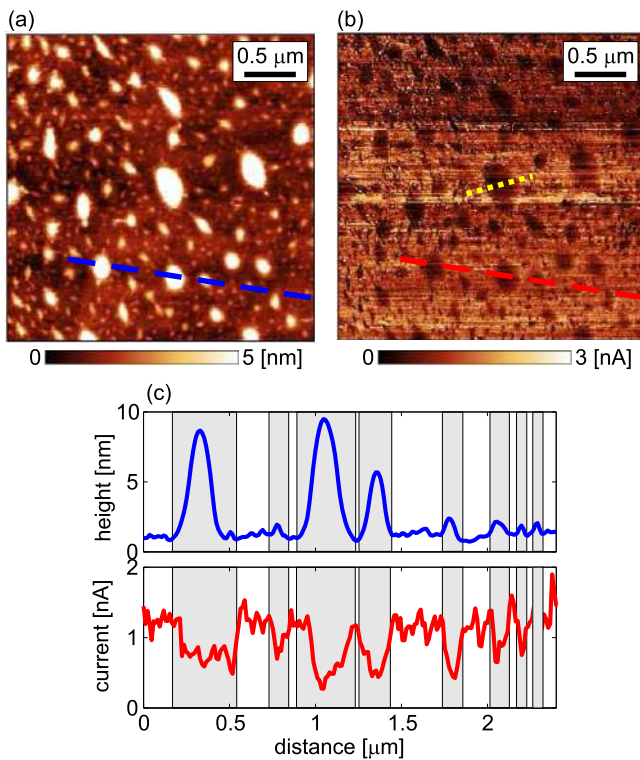
Figure 11. (a) Topography and (b) current map of MoS$_2$/WS$_2$ heterostructure. Since the selected scan size was smaller than the size of top MoS$_2$ flake, surrounding WS$_2$ flake is not displayed. (c) Corresponding height (top) and current (bottom) profiles taken along dashed lines indicated in (a) and (b), respectively. Shaded domains emphasize overlapping between bubbles and regions with decreased current.

Figure 12. I/V curves measured on MoS$_2$/WS$_2$ heterostructure across a bubble (the dotted line indicated in figure 11(b)). The inset depicts the current map measured on the area with the bubble. The line schematically presents the points where the I/V curves were measured. The I/V curves at high normal load were measured on a flat region without bubbles.

larger bubbles. Such case is presented in the bottom part of the heterostructure presented in figures 10(c) (topography) and 10(d) (CPD map). CPD profiles in figure 10(e) taken across large bubbles with a diameter of several hundreds of nm reveals that the surface potential is increased by several tens of mV. As a result, the band diagram and local band bending around bubbles can be represented by a scheme in figure 10(f). Brighter contrast in CPD maps indicates that bubbles can be considered as local domains with a lower work function Φ_b. They are surrounded by flat areas with a larger work function Φ_f. Therefore, electrons in MoS$_2$ layer placed on bubbles are sitting in potential wells.

3.7. Electrical conductivity

Local conductivity was investigated on the heterostructure displayed in figure 11(a) presenting only a segment of the top MoS$_2$ layer. DC bias voltage was applied to the bottom WS$_2$ layer, while the electrical current was simultaneously measured through the metallic AFM tip in contact with top MoS$_2$ layer. In the topographic image, bubbles are represented by bright, circular and elliptical domains. As already mentioned, in order to avoid any tip-induced flattening of the heterostructure and to preserve all topographic features such as bubbles, the measurements were done with a soft probe and at a low normal load in the order of 1 nN. The resulting current
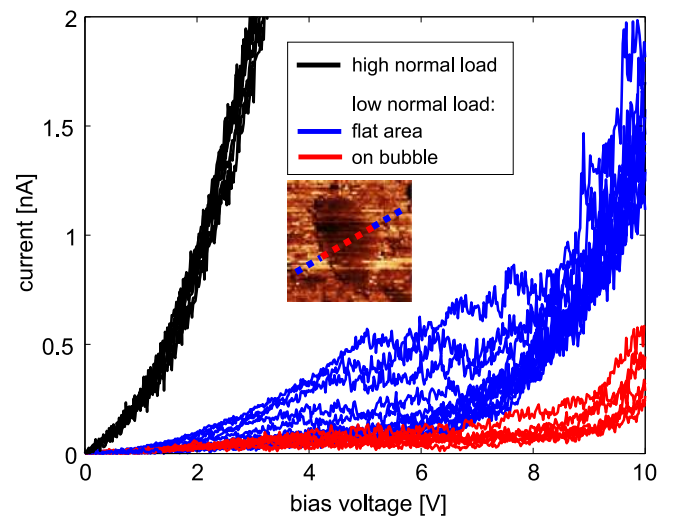
map in figure 11(b) displays darker circular and elliptical domains with locally decreased current. Practically the same current maps were measured in both forward and backward directions, thus excluding any tip-shape effects on the obtained results. The observed darker domains correspond exactly to bubbles. This is further proved in figure 11(c) which presents a topographic and corresponding current profile. As can be seen, the electrical current drops exactly on bubbles (shaded regions), and compared to the current measured on flat areas, it decreases by up to $\sim 50\%$.

In order to further explore the origin of a low current measured on bubbles, local I/V curves were measured across them. Characteristic results presented in figure 12 display nonlinear I/V curves with large turn-on voltages. At the same time, the I/V curves are well grouped into two sets. The curves measured exactly on the area with a bubble display much lower currents with increased turn-on voltage of around 9 V. On the other hand, the I/V curves measured on flat areas around the bubble present much larger conductivity and lower turn-on voltage in a wide range of 1–7 V. Therefore, besides lower conductivity, local I/V measurements indicate appearance of an additional potential barrier on bubbles compared to flat areas.

Electrical current measured in C-AFM is dominantly determined by the contact resistance (the resistance between the AFM tip and sample surface) which is proportional to the local resistivity of the sample surface below the AFM tip [86]. Considered MoS$_2$/WS$_2$ heterostructures practically consist of two parallel current sheets which can be therefore represented as two parallel resistors with similar resistances. When bubbles are present between two current sheets, the system can be represented with only one resistor corresponding to the top MoS$_2$ layer. As a result, the total resistance in the latter case is approximately two times larger than in the former case
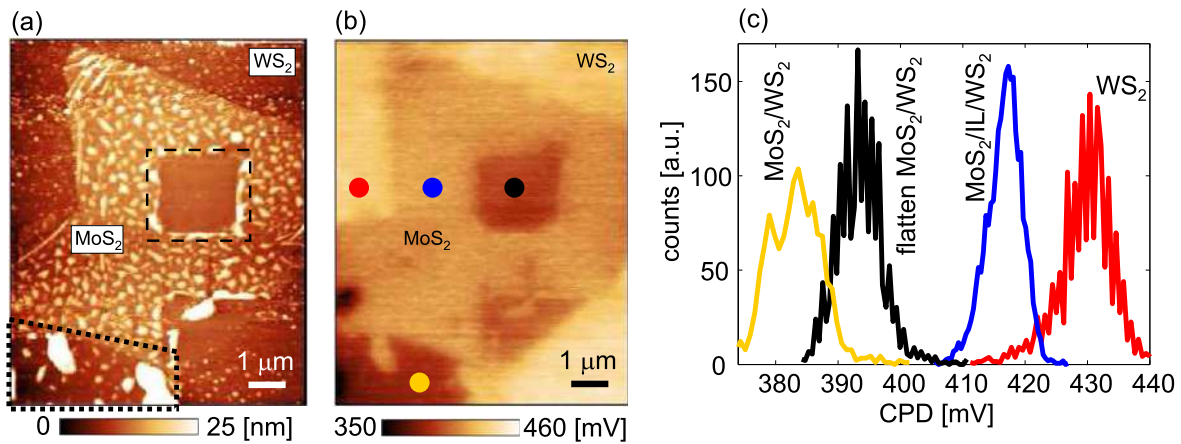
Figure 13. (a) Topography and (b) CPD map of the heterostructure after the AFM based flattening of the square domain marked by dashed line in (a). (c) Histogram of CPD for four areas indicated by dots in part (b): bare WS$_2$ (domain marked by red dot in (b)), the heterostructure with IL (domain marked by blue dot in (b)), the flatten part of the heterostructure (domain marked by black dot in (b) and by dashed rectangle in (a)), and the heterostructure without IL (domain marked by yellow dot in (b) encircled by dotted line in (a)).

which explains the observed decrease of current in C-AFM by ~50%.

C-AFM and I/V curves were measured for the bias voltage applied on bottom WS$_2$ (figure 1(b)). Therefore, for a high enough positive bias voltage, electrons are transferred from MoS$_2$ to WS$_2$ and then into external electrical contact. Still, bubbles prevent direct tunneling of the electrons from MoS$_2$ to underlying WS$_2$. Electrons in these regions first have to reach flat MoS$_2$ areas. For that purpose, they have to overcome a potential barrier $\Phi_{bar} = \Phi_f - \Phi_b$ observed in KPFM measurements. After that, they can be transferred from MoS$_2$ to WS$_2$. The potential barriers associated with bubbles could be an additional reason for the observed lower conductivity and larger turn-on voltages (measured in I/V curves) observed on the bubbles.

Figure 12 shows that I/V curves measured on flat regions surrounding bubbles exhibit also rather high turn-on voltages. Still, they practically disappear for high normal load applied on AFM probe during I/V curve measurements as will be discussed in the next section. This indicates that practically whole MoS$_2$ flake is separated from WS$_2$ by a thin IL, with a thickness of around 1 nm. Then high enough turn-on voltage is needed to overcome a potential barrier induced by such insulating layer and to initiate electron flow.

3.8. Electrical properties improved by local AFM based flattening

The previous analysis indicates that in order to provide an efficient charge transfer, it is necessary to remove all contaminations between heterostructure's layers. Previous works [44, 46–48] and our results presented in figure 3 demonstrate that AFM based flattening could be an efficient technique for this purpose. The final goal of our study was to explore if the AFM based flattening could improve the efficiency of charge transfer and overall electrical properties of vdW heterostructures.

First we consider the influence of local flattening on electrical surface potential. Topography and CPD map

measured after the flattening of a small square domain within MoS$_2$/WS$_2$ heterostructure are presented in figures 13(a) and (b), respectively. We distinguish four levels in CPD which are associated with the following areas: MoS$_2$/IL/WS$_2$ (thicker part of the heterostructure with IL), MoS$_2$/WS$_2$ (thiner part without IL), flattened MoS$_2$/WS$_2$ (the central square domain flatten by AFM), and bare WS$_2$. The CPD histogram in figure 13(c) shows that CPD of domains with and without IL differs by around 40 mV. The CPD of the area flattened by AFM is decreased compared to non-flattened heterostructure MoS$_2$/IL/WS$_2$ by ~30 mV. Therefore, the CPD of the flattened area approaches the CPD of the heterostructure without IL. In the considered case their difference was decreased to only ~10 mV which indicates that AFM based flattening can be really employed as an efficient method for removing contaminations and facilitating charge transfer between layers in vdW heterostructures.

In a similar way, we have tested the influence of the normal force applied during I/V curve measurements on resulting currents. Figure 12 depicts also I/V curves measured at the normal load increased above ~ 100 nN. As can be seen, resulting curves are still nonlinear, but the turn-on voltage practically disappeared. Therefore, for a high enough normal load, contaminations were expelled from the interface between MoS$_2$ and WS$_2$. As a result, potential barriers for charge carriers were removed and high conductivity was reestablished.

4. Conclusions

In a summary, using AFM methods, we have demonstrated that bubbles and ILs deteriorate both mechanical and electrical properties of vdW heterostructures. These imperfections with trapped contaminations prevent direct contact between constituent 2D layers and interlayer interactions. As a result, from a mechanical point of view, they behave as a third body which prevents easy sliding of 2D layers one over each other thus leading to increased friction. In addition, bubbles and ILs

present locally softer domains which open additional dissipation channels, probably due to viscoelastic damping. In an analogous way, from an electrical point of view, bubbles and ILs behave as insulating layers and potential barriers which block charge transfer between constituent 2D layers. As a result, local electrical conductivity on domains with bubbles and ILs decreases, while the difference of the surface potential between constituent layers is lowered.

In order to improve properties of vdW heterostructures after the transfer process, we have demonstrated that it is necessary to apply high enough normal load by AFM probe in order to locally remove contaminations trapped in bubbles and ILs. We illustrated two approaches. The first one is based on AFM flattening of square areas where constituent 2D layers are returned back into a close contact by a scanning in contact AFM mode. As a result, due to reestablished charge transfer between constituent layers, the flattened areas exhibit increased difference of surface potential approaching the levels measured on areas without bubbles and ILs. In the second approach, local I/V curves measured at increased normal load exhibit significantly improved electrical conductivity of vdW heterostructures.

Acknowledgments

Data availability statement

All data that support the findings of this study are included within the article (and any supplementary files).

ORCID iDs

Borislav Vasić ● https://orcid.org/0000-0002-1575-8004
Marko Kralj ● https://orcid.org/0000-0002-9786-3130

References

[1] Geim A K and Grigorieva I V 2013 Van der Waals heterostructures *Nature* **499** 419–25
[2] Liu Y, Weiss N O, Duan X, Cheng H-C, Huang Y and Duan X 2016 Van der Waals Heterostructures and Devices *Nat. Rev. Mater.* **1** 16042
[3] Li M-Y, Chen C-H, Shi Y and Li L-J 2016 Heterostructures based on two-dimensional layered materials and their potential applications *Mater. Today* **19** 322–35
[4] Frisenda R, Navarro-Moratalla E, Gant P, Pérez De Lara D, Jarillo-Herrero P, Gorbachev R V and Castellanos-Gomez A 2018 Recent progress in the assembly of nanodevices and van der Waals heterostructures by deterministic placement of 2D materials *Chem. Soc. Rev.* **47** 53–68
[5] Liu Y *et al* 2015 Toward barrier free contact to molybdenum disulfide using graphene electrodes *Nano Lett.* **15** 3030–4
[6] Dean C R *et al* 2010 Boron nitride substrates for high-quality graphene electronics *Nat. Nanotechnol.* **5** 722–6
[7] Britnell L *et al* 2012 Field-effect tunneling transistor based on vertical graphene heterostructures *Science* **335** 947–50
[8] Yu W J, Li Z, Zhou H, Chen Y, Wang Y, Huang Y and Duan X 2013 Vertically stacked multi-heterostructures of layered materials for logic transistors and complementary inverters *Nat. Mater.* **12** 246–52
[9] Roy T, Tosun M, Kang J S, Sachid A B, Desai S B, Hettick M, Hu C C and Javey A 2014 Field-effect transistors built from all two-dimensional material components *ACS Nano* **8** 6259–64
[10] Jariwala D, Sangwan V K, Lauhon L J, Marks T J and Hersam M C 2014 Emerging device applications for semiconducting two-dimensional transition metal dichalcogenides *ACS Nano* **8** 1102–20
[11] Frisenda R, Molina-Mendoza A J, Mueller T, Castellanos-Gomez A and van der Zant H S J 2018 Atomically thin p-n junctions based on two-dimensional materials *Chem. Soc. Rev.* **47** 3339–58
[12] Chuang S, Kapadia R, Fang T, Chia Chang H, Yen W-C, Chueh Y-L and Javey A 2013 Near-ideal electrical properties of InAs/WSe$_2$ van der Waals heterojunction diodes *Appl. Phys. Lett.* **102** 242101
[13] Deng Y, Luo Z, Conrad N J, Liu H, Gong Y, Najmaei S, Ajayan P M, Lou J, Xu X and Ye P D 2014 Black phosphorus-monolayer MoS$_2$ van der waals heterojunction p-n diode *ACS Nano* **8** 8292–9
[14] Jariwala D, Davoyan A R, Wong J and Atwater H A 2017 Van der Waals materials for atomically-thin photovoltaics: Promise and outlook *ACS Photonics* **4** 2962–70
[15] Britnell L *et al* 2013 Strong light-matter interactions in heterostructures of atomically thin films *Science* **340** 1311–4
[16] Furchi M M, Pospischil A, Libisch F, Burgdöfer J and Mueller T 2014 Photovoltaic effect in an electrically tunable van der waals heterojunction *Nano Lett.* **14** 4785–91
[17] Lee C-H *et al* 2014 Atomically thin p-n junctions with van der Waals heterointerfaces *Nat. Nanotechnol.* **9** 676–81
[18] Ahn J, Jeon P J, Raza S R A, Pezeshki A, Min S-W, Hwang D K and Im S 2016 Transition metal dichalcogenide heterojunction PN diode toward ultimate photovoltaic benefits *2D Mater.* **3** 045011
[19] Wong J, Jariwala D, Tagliabue G, Tat K, Davoyan A R, Sherrott M C and Atwater H A 2017 High photovoltaic quantum efficiency in ultrathin van der waals heterostructures *ACS Nano* **11** 7230–40
[20] Cheng R, Li D, Zhou H, Wang C, Yin A, Jiang S, Liu Y, Chen Y, Huang Y and Duan X 2014 Electroluminescence and photocurrent generation from atomically sharp WSe$_2$/MoS$_2$ heterojunction p–n diodes *Nano Lett.* **14** 5590–7
[21] Lopez-Sanchez O, Alarcon Llado E, Koman V, Fontcuberta i Morral A, Radenovic A and Kis A 2014 Light generation and harvesting in a van der waals heterostructure *ACS Nano* **8** 3042–8
[22] Feng X, Kwon S, Park J Y and Salmeron M 2013 Superlubric sliding of graphene nanoflakes on graphene *ACS Nano* **7** 1718–24
[23] Leven I, Krepel D, Shemesh O and Hod O 2013 Robust superlubricity in graphene/h-BN heterojunctions *J. Phys. Chem. Lett.* **4** 115–20
[24] Sheehan P E and Lieber C M 2017 Friction between van der Waals solids during lattice directed sliding *Nano Lett.* **17** 4116–21

[25] Song Y, Mandelli D, Hod O, Urbakh M, Ma M and Zheng Q 2018 Robust microscale superlubricity in graphite/hexagonal boron nitride layered heterojunctions *Nat. Mater.* **17** 894–9

[26] Vasić B, Stanković I, Matković A, Kratzer M, Ganser C, Gajić R and Teichert C 2018 Molecules on rails: Friction anisotropy and preferential sliding directions of organic nanocrystallites on two-dimensional materials *Nanoscale* **10** 18835–45

[27] Ru G, Qi W, Tang K, Wei Y and Xue T 2020 Interlayer friction and superlubricity in bilayer graphene and MoS$_2$/MoSe$_2$ van der Waals heterostructures *Tribol. Int.* **151** 106483

[28] Gao E, Wu B, Wang Y, Jia X, Ouyang W and Liu Z 2021 Computational prediction of superlubric layered heterojunctions *ACS Appl. Mater. Interfaces* **13** 33600–8

[29] Li Z *et al* 2013 Effect of airborne contaminants on the wettability of supported graphene and graphite *Nat. Mater.* **12** 925–31

[30] Xu K, Cao P and Heath J R 2010 Graphene visualizes the first water adlayers on mica at ambient conditions *Science* **329** 1188–91

[31] He K T, Wood J D, Doidge G P, Pop E and Lyding J W 2012 Scanning tunneling microscopy study and nanomanipulation of graphene-coated water on mica *Nano Lett.* **12** 2665–72

[32] Rezania B, Dorn M, Severin N and Rabe J P 2013 Influence of graphene exfoliation on the properties of water-containing adlayers visualized by graphenes and scanning force microscopy *J. Colloid Interface Sci.* **407** 500–4

[33] Haigh S J, Gholinia A, Jalil R, Romani S, Britnell L, Elias D C, Novoselov K S, Ponomarenko L A, Geim A K and Gorbachev R 2012 Cross-sectional imaging of individual layers and buried interfaces of graphene-based heterostructures and superlattices *Nat. Mater.* **11** 764–7

[34] Uwanno T, Hattori Y, Taniguchi T, Watanabe K and Nagashio K 2015 Fully dry PMMA transfer of graphene on h-BN using a heating/cooling system *2D Mater.* **2** 041002

[35] Khestanova E, Guinea F, Fumagalli L, Geim A K and Grigorieva I V 2016 Universal shape and pressure inside bubbles appearing in van der Waals heterostructures *Nat. Commun.* **7** 12587

[36] Ghorbanfekr-Kalashami H, Vasu K S, Nair R R, Peeters F M and Neek-Amal M 2017 Dependence of the shape of graphene nanobubbles on trapped substance *Nat. Commun.* **8** 15844

[37] Sanchez D A, Dai Z, Wang P, Cantu-Chavez A, Brennan C J, Huang R and Lu N 2018 Mechanics of spontaneously formed nanoblisters trapped by transferred 2D crystals *Proc. Natl. Acad. Sci.* **115** 7884–9

[38] Sanchez D A, Dai Z and Lu N 2021 2D Material Bubbles: Fabrication, characterization, and applications *Trends Chem.* **3** 204–17

[39] Blundo E, Yildirim T, Pettinari G and Polimeni A 2021 Experimental adhesion energy in van der waals crystals and heterostructures from atomically thin bubbles *Phys. Rev. Lett.* **127** 046101

[40] Algara-Siller G, Lehtinen O, Wang F C, Nair R R, Kaiser U, Wu H A, Geim A K and Grigorieva I V 2015 Square ice in graphene nanocapillaries *Nature* **519** 443–5

[41] Vasu K S *et al* 2016 Van der Waals pressure and its effect on trapped interlayer molecules *Nat. Commun.* **7** 12168

[42] Gasparutti I, Song S H, Neumann M, Wei X, Watanabe K, Taniguchi T and Lee Y H 2020 How clean is clean? recipes for van der waals heterostructure cleanliness assessment *ACS Appl. Mater. Interfaces* **12** 7701–9

[43] Pizzocchero F, Gammelgaard L, Jessen B S, Caridad J M, Wang L, Hone J, Bøggild P and Booth T J 2016 The hot pick-up technique for batch assembly of van der Waals heterostructures *Nat. Commun.* **7** 11894

[44] Schwartz J J, Chuang H-J, Rosenberger M R, Sivaram S V, McCreary K M, Jonker B T and Centrone A 2019 Chemical identification of interlayer contaminants within van der waals heterostructures *ACS Appl. Mater. Interfaces* **11** 25578–85

[45] Vincent T, Hamer M, Grigorieva I, Antonov V, Tzalenchuk A and Kazakova O 2020 Strongly absorbing nanoscale infrared domains within strained bubbles at hbn-graphene interfaces *ACS Appl. Mater. Interfaces* **12** 57638–48

[46] Rosenberger M R, Chuang H-J, McCreary K M, Hanbicki A T, Sivaram S V and Jonker B T 2018 Nano-'Squeegee' for the creation of clean 2D Material interfaces *ACS Appl. Mater. Interfaces* **10** 10379–87

[47] Tan B H, Zhang J, Jin J, Ooi C H, He Y, Zhou R, Ostrikov K, Nguyen N-T and An H 2020 Direct measurement of the contents, thickness, and internal pressure of molybdenum disulfide nanoblisters *Nano Lett.* **20** 3478–84

[48] Kim Y, Herlinger P, Taniguchi T, Watanabe K and Smet J H 2019 Reliable postprocessing improvement of van der waals heterostructures *ACS Nano* **13** 14182–90

[49] Delač Marion I, Čapeta D, Pielić B, Faraguna F, Gallardo A, Pou P, Biel B, Vujičić N and Kralj M 2018 Atomic-scale defects and electronic properties of a transferred synthesized MoS$_2$ monolayer *Nanotechnology* **29** 305703

[50] Lau C S *et al* 2021 Gate-defined quantum confinement in CVD 2D WS$_2$ *Adv. Mater.* **33** 2103907

[51] Niehues I, Blob A, Stiehm T, Schmidt R, Jadriško V, Radatović B, Čapeta D, Kralj M, de Vasconcellos S M and Bratschitsch R 2018 Strain transfer across grain boundaries in MoS$_2$ monolayers grown by chemical vapor deposition *2D Mater.* **5** 031003

[52] Garcia R, Gómez C J, Martinez N F, Patil S, Dietz C and Magerle R 2006 Identification of nanoscale dissipation processes by dynamic atomic force microscopy *Phys. Rev. Lett.* **97** 016103

[53] Huo N, Kang J, Wei Z, Li S-S, Li J and Wei S-H 2014 Novel and enhanced optoelectronic performances of multilayer MoS$_2$-WS$_2$ heterostructure transistors *Adv. Funct. Mater.* **24** 7025–31

[54] Kim B, Kim J, Tsai P-C, Choi H, Yoon S, Lin S-Y and Kim D-W 2021 Large Surface Photovoltage of WS$_2$/MoS$_2$ and MoS$_2$/WS$_2$ Vertical Hetero-bilayers *ACS Appl. Electron. Mater.* **3** 2601–6

[55] Xue Y *et al* 2016 Scalable production of a few-layer MoS$_2$/WS$_2$ vertical heterojunction array and its application for photodetectors *ACS Nano* **10** 573–80

[56] Wang G, Li L, Fan W, Wang R, Zhou S, Lü J-T, Gan L and Zhai T 2018 Interlayer coupling induced infrared response in WS$_2$/MoS$_2$ heterostructures enhanced by surface plasmon resonance *Adv. Funct. Mater.* **28** 1800339

[57] Ye K *et al* 2019 Lateral bilayer MoS$_2$-WS$_2$ heterostructure photodetectors with high responsivity and detectivity *Adv. Opt. Mater.* **7** 1900815

[58] Kanade C K, Seok H, Kanade V K, Aydin K, Kim H-U, Mitta S B, Yoo W J and Kim T 2021 Low-temperature and large-scale production of a transition metal sulfide vertical heterostructure and its application for photodetectors *ACS Appl. Mater. Inter.* **13** 8710–7

[59] Bertolazzi S, Brivio J and Kis A 2011 Stretching and breaking of ultrathin MoS$_2$ *ACS Nano* **5** 9703–9

[60] Vaziriseseshk M R, Hasz K, Zhao M-Q, Johnson A T C, Carpick R W and Martini A 2020 Nanoscale friction behavior of transition-metal dichalcogenides: Role of the chalcogenide *ACS Nano* **14** 16013–21

[61] Rapuc A, Wang H and Polcar T 2021 Nanotribology of transition metal dichalcogenide flakes deposited by chemical vapour deposition: The influence of chemical composition and sliding speed on nanoscale friction of monolayers *Appl. Surf. Sci.* **556** 149762

[62] Hong X, Kim J, Shi S-F, Zhang Y, Jin C, Sun Y, Tongay S, Wu J, Zhang Y and Wang F 2014 Ultrafast charge transfer in atomically thin MoS$_2$/WS$_2$ heterostructures *Nat. Nanotechnol.* **9** 682–6

[63] Tongay S *et al* 2014 Tuning interlayer coupling in large-area heterostructures with CVD-Grown MoS$_2$ and WS$_2$ monolayers *Nano Lett.* **14** 3185–90

[64] Zhang J *et al* 2016 Observation of strong interlayer coupling in MoS$_2$/WS$_2$ heterostructures *Adv. Mater.* **28** 1950–6

[65] Liu K *et al* 2014 Elastic properties of chemical-vapor-deposited monolayer MoS$_2$, WS$_2$, and their bilayer heterostructures *Nano Lett.* **14** 5097–103

[66] Susarla S, Manimunda P, Morais Jaques Y, Hachtel J A, Idrobo J C, Syed Amnulla S A, Galvão D S, Tiwary C S and Ajayan P M 2018 Deformation mechanisms of vertically stacked WS$_2$/MoS$_2$ heterostructures: The role of interfaces *ACS Nano* **12** 4036–44

[67] Cong X, Liu X-L, Lin M-L and Tan P-H 2020 Application of Raman spectroscopy to probe fundamental properties of two-dimensional materials *Npj 2D Mater. Appl.* **4** 13

[68] Berkdemir A *et al* 2013 Identification of individual and few layers of WS$_2$ using Raman Spectroscopy *Sci. Rep.* **3** 1755

[69] Vasić B, Matković A, Ralević U, Belić M and Gajić R 2017 Nanoscale wear of graphene and wear protection by graphene *Carbon* **120** 137–44

[70] Özoğul A, Gnecco E and Baykara M Z 2021 Nanolithography-induced exfoliation of layered materials *Appl. Surf. Sci. Adv.* **6** 100146

[71] Vasić B, Zurutuza A and Gajić R 2016 Spatial variation of wear and electrical properties across wrinkles in chemical vapour deposition graphene *Carbon* **102** 304–10

[72] Fang L, Liu D-M, Guo Y, Liao Z-M, Luo J-B and Wen S-Z 2017 Thickness dependent friction on few-layer MoS$_2$, WS$_2$, and WSe$_2$ *Nanotechnology* **28** 245703

[73] He G, Müser M H and Robbins M O 1999 Adsorbed layers and the origin of static friction *Science* **284** 1650–2

[74] Dietzel D, Ritter C, Mönninghoff T, Fuchs H, Schirmeisen A and Schwarz U D 2008 Frictional duality observed during nanoparticle sliding *Phys. Rev. Lett.* **101** 125505

[75] Dietzel D, Brndiar J, Štich I and Schirmeisen A 2017 Limitations of structural superlubricity: chemical bonds versus contact size *ACS Nano* **11** 7642–7

[76] Khare H S and Burris D L 2013 The effects of environmental water and oxygen on the temperature-dependent friction of sputtered molybdenum disulfide *Tribol. Lett.* **52** 485–93

[77] Stella M, Lorenz C D and Righi M C 2021 Effects of intercalated water on the lubricity of sliding layers under load: a theoretical investigation on MoS$_2$ *2D Mater.* **8** 035052

[78] Lee H, Jeong H, Suh J, Doh W H, Baik J, Shin H-J, Ko J-H, Wu J, Kim Y-H and Park J Y 2019 Nanoscale friction on confined water layers intercalated between MoS$_2$ flakes and silica *J. Phys. Chem.* C **123** 8827–35

[79] Vasić B, Matković A and Gajić R 2017 Phase imaging and nanoscale energy dissipation of supported graphene using amplitude modulation atomic force microscopy *Nanotechnology* **28** 465708

[80] Xu C, Yao Q, Du H, Hong C, Xue T, Kang Y and Li Q 2021 Abnormal raman characteristics of graphene originating from contact interface inhomogeneity *ACS Appl. Mater. Interfaces* **13** 22040–6

[81] Shim J, Lui C H, Ko T Y, Yu Y-J, Kim P, Heinz T F and Ryu S 2012 Water-gated charge doping of graphene induced by mica substrates *Nano Lett.* **12** 648–54

[82] Lee H, Ko J-H, Song H C, Salmeron M, Kim Y-H and Park J Y 2018 Isotope- and thickness-dependent friction of water layers intercalated between graphene and mica *Tribol. Lett.* **66** 36

[83] Feng J, Qian X and Huang C-W 2012 Strain-engineered artificial atom as a broad-spectrum solar energy funnel *Nat. Photon.* **6** 866–72

[84] Li H *et al* 2015 Optoelectronic crystal of artificial atoms in strain-textured molybdenum disulphide *Nat. Commun.* **6** 7381

[85] Tyurnina A, Bandurin D A, Khestanova E, Kravets V G, Koperski M, Guinea F, Grigorenko A N, Geim A K and Grigorieva I V 2019 Strained bubbles in van der waals heterostructures as local emitters of photoluminescence with adjustable wavelength *ACS Photonics* **6** 516–24

[86] Moerman D, Sebaihi N, Kaviyil S E, Leclère P, Lazzaroni R and Douhéret O 2014 Towards a unified description of the charge transport mechanisms in conductive atomic force microscopy studies of semiconducting polymers *Nanoscale* **6** 10596–603

Electrochemical reduction of thin graphene-oxide films in aqueous solutions – Restoration of conductivity

Dalibor Karačić [a], Sanjin J. Gutić [b], Borislav Vasić [c], Vladimir M. Mirsky [d],
Natalia V. Skorodumova [e], Slavko V. Mentus [a,f], Igor A. Pašti [a,e,*]

[a] *University of Belgrade – Faculty of Physical Chemistry, Studentski trg 12-16, 11000 Belgrade, Serbia*
[b] *University of Sarajevo, Faculty of Science, Department of Chemistry, Zmaja od Bosne 33-35, Sarajevo, Bosnia and Herzegovina*
[c] *Institute of Physics Belgrade, University of Belgrade, Pregrevica 118, 11080 Belgrade, Serbia*
[d] *Institute of Biotechnology, Department of Nanobiotechnology, Brandenburgische Technische Universität Cottbus-Senftenberg, 01968 Senftenberg, Germany*
[e] *Department of Materials Science and Engineering, School of Industrial Engineering and Management, KTH – Royal Institute of Technology, Brinellvägen 23, 100 44 Stockholm, Sweden*
[f] *Serbian Academy of Sciences and Arts, Knez Mihajlova 35, 11000 Belgrade, Serbia*

ARTICLE INFO

ABSTRACT

Graphene oxide finds applications in different fields of science, including energy conversion. Electrochemical reduction of graphene oxide (GO) significantly improves its conductivity. However, the kinetics of this process depends on the solvent, supporting electrolyte, pH, and numerous other factors. Most studies report the macroscopic views and *ex-situ* properties of reduced GO. To expand the knowledge about GO reduction, in this study, we used cyclic voltammetry (CV), simultaneous 2 points and 4 points resistance measurement (s24), conductive atomic force microscopy (AFM), and theoretical calculations. Using CV, we demonstrated that the choice of supporting electrolyte (KCl or LiCl) influences the potential range in which electrochemical GO reduction occurs. The activation energy of this process was estimated to be below 30 kJ mol^{-1} in both electrolytes, being significantly lower than that required for thermal reduction of GO. Simultaneous *in situ* s24 resistance measurements suggest that GO films reach a highly conductive state at deep negative potentials, with an abrupt, irreversible switch from non-conductive to the conductive state. However, conductive AFM presents a more exact picture of this process: the reduction of GO films starts locally while the formed conductive islands grow during the reduction. This mechanism was confirmed by theoretical calculations indicating that the reduction starts on isolated oxygen-functional groups over the GO basal plane, while clustered OH groups are more difficult to reduce. The presented results can help in tailoring reduced GO for a particular electrochemical application by precisely controlling the reduction degree and percentage of the conductive area of the reduced GO films.

1. Introduction

Since its discovery, graphene has found numerous applications in various fields of science and technology, including, but not limited to, energy conversion and storage, biomedical engineering, electronics, sensors, aerospace applications, and others [1]. A vast number of existing reports list some of the well-known properties of the idealized graphene sheet (pristine infinite 2D sheet of hexagonal carbon), such as large specific surface area, high carrier mobility, and good mechanical properties as a determinant for graphene applications [1]. However, this can be considered as an exaggeration as pristine graphene is practically non-existing. Moreover, even experimentally realized, ideal graphene would be practically useless in some technologies, like electrochemical energy conversion and storage [2]. This observation is clearly demonstrated by the fact that, in comparison to the basal plane, the graphene edges provide four orders of magnitude higher specific capacitance associated with double layer charging, much faster electron transfer rate, and fair electrocatalytic activity [3]. Thus, for most electrochemical devices, a material with some features of the perfect graphene (such as high surface area and high electrical conductivity) but with a significant number of structural imperfections and chemical moieties [4–6] is required.

---

* Corresponding author.
E-mail address: igor@ffh.bg.ac.rs (I.A. Pašti).

Desired chemical moieties and defects in graphene can be introduced by using, for example, selective oxidation [7]. However, a more viable route is the production of reduced graphene oxide (rGO) from graphene oxide (GO) obtained by chemical exfoliation of oxidized graphite by chemical, thermal, or electrochemical reduction [8,9]. Upon GO reduction, irrespective of the particular reduction technique, enhanced capacitance and charge transfer properties of rGO are evidenced, along with the decreased O/C ratio connected to enhanced conductivity [8, 10]. However, one has to find a proper balance between the amount of oxygen functional groups and the conductivity of rGO to reach optimal capacitance [11,12]. Such precise tuning and controllable modifications of structural and chemical properties of graphene oxide are of general importance for applying graphene-based materials in different electrochemical systems [7]. They can be easily achieved using electrochemical reduction, employing electrode potential to control the reduction degree of final rGO.

For electrochemical reduction, GO can be either suspended in an electrolyte solution or deposited directly on the electrode surface as a thin film [9]. The reduction was previously performed in aqueous and non-aqueous electrolytes [13], while characterization is typically performed using *ex-situ* techniques (X-ray photoelectron spectroscopy, XPS, Fourier Transform Infrared Spectroscopy, FTIR, Raman spectroscopy). It was shown [13–16] that different O-functional groups are reduced at different potentials, while the effects of solvent and pH on the behavior of resulting rGO were evidenced. The process is rather complex, being dependent on the nature of supporting electrolytes [12]. The effects of the GO reduction on its electrochemical properties are clear. However, electrochemically produced rGO films are typically characterized using various techniques that provide a macroscopic average of the final rGO. For example, XPS, FTIR, and Temperature Programmed Desorption (TPD) revealed the presence of different functional groups on the rGO surface, while Raman spectroscopy was routinely employed to investigate a structural disorder in rGO. In addition, macroscopically averaged properties are obtained using electrochemical tests with the ferro/-ferricyanide system to assess charge transfer properties of rGO. Thus, we are still not fully aware of how electrochemical reduction of GO proceeds at the submicron scale in terms of local distribution of reduced domains and their impact on the conductivity of electrochemically reduced GO films. At the same time, the conductivity of the electrode material affects its overall electrochemical performance. Adjusting conductivity of rGO is crucially related to the optimization of capacitive response [12], but also the understanding of the GO reduction process is necessary for the efficient formation of rGO-based composites with high catalytic activity [17]. The lack of atomic-level information is clear, and during the writing of this paper, a study combining scanning transmission X-ray microscopy and Kelvin probe force microscopy [18] was published. However, in this particular work, Rodriguez *et al.* focused on the local work function variations, showing that they arise due to the presence of oxygen functional groups, being of crucial importance for photovoltaic behavior [18].

In this contribution, we address the electrochemical reduction of thin films of GO in aqueous solutions of LiCl and KCl using, for experimental considerations, cyclic voltammetry, *in situ* simultaneous 2-point and 4-point resistance measurements, and *ex-situ* conductive atomic force microscopy. The results show that the electrochemical reduction of GO has low apparent activation energies while the reduction process commences locally. The conductive islands start to coalesce at deep negative potentials making the film completely conductive. Furthermore, the differences in the GO film reduction process in LiCl and KCl solutions are explained using semiempirical quantum chemical and Density Functional Theory calculations.

2. Experimental

2.1. Electrochemical reduction of GO thin films

The reduction of GO thin films at different temperatures and in different electrolytes was done as follows. First, aqueous GO suspension (standard solution, 4 mg ml^{-1}, confirmed by gravimetric measurements; Graphenea, Spain [19]) was diluted to obtain 1 mg ml^{-1} in a 6:4 water/ethanol (v/v) mixture. After sonication (2 times for 5 min, with 1 min resting period, 35 W), 10 μl of the obtained GO suspension was drop-casted onto the copper foil and dried under vacuum at room temperature, giving a circular GO film of (3.2 ± 0.1) mm in diameter. Using 3D SEM surface reconstruction, the film thickness is estimated to (250 ± 30) nm. Before the drop-casting process, copper foils (99.99% Cu) were mechanically cleaned (polished with alumina with 0.05 μm particles) and washed in 0.1 mol dm^{-3} HNO$_3$ and deionized water. Pt foil served as the counter and Ag/AgCl (saturated KCl) as the reference electrode. Before the measurements, Pt counter electrode was cleaned using flame annealing, while the potential of the reference electrode was regularly checked versus Reversible Hydrogen Electrode (0.1 mol dm^{-3} HClO$_4$), and another saturated Ag/AgCl electrode. Tolerance for the potential difference was 10 mV. When not used, the reference electrode was immersed into saturated KCl solution. All potentials are indicated *versus* this reference electrode. Ivium Vertex.One potentiostat was used for the measurements. Electrochemical measurements were performed in 0.1 mol dm^{-3} aqueous LiCl and KCl solution at pH adjusted to ∼ 6.6 ± 0.1 (using KOH, LiOH or HCl). GO reduction was done by a single potentiodynamic scan at 10 mV s^{-1} between −0.5 (starting potential) and −1.6 V (KCl solution) or −1.8 V (LiCl solution). The measurements were done at four temperatures: 7.5, 20, 30, and 40 °C. For this purpose, the cell containing the working and counter electrodes was thermostated while the compartment with the reference electrode was held at 25 °C and connected to the cell using a salt bridge with a Lugin capillary. The *iR* drop was compensated using the positive feedback scheme. The values of the electrolyte resistance used to compensate the *iR* drop were measured using impedance measurement at 100 kHz at −0.5 V *vs.* Ag/AgCl. Typical values ranged from 10 to 15 Ω for KCl solutions and 13–20 Ω for LiCl solutions. All electrochemical measurements were performed in N$_2$-purged solutions (N$_2$ 99.995%) to remove dissolved O$_2$. We also note that variations in measured electrochemical response were under 5% upon repeated measurements with drop-casted layers.

2.2. In situ resistance measurements during the GO thin film reduction

The electrical resistance of (r)GO films was measured as described elsewhere [20,21] using simultaneous two- and four-point techniques (s24-technique). Shortly, 10 mV pulses of alternating polarity were applied, and the total resistance was calculated. This resistance includes both the bulk resistance of the sensing composite and the contact resistance (R_c). It corresponds to the resistance that would be measured using the conventional two-point technique, and it is denoted here as $R2$. Simultaneously, the potential drop between the inner electrodes of the four-strip electrode structure (see further) was measured with the electrometric voltmeter (Keithley-617) and used to calculate the bulk material resistance. This resistance corresponds to that measured by the four-point technique, and we denote it here as $R4$. Then the contact resistance (R_c) can be determined as $R_c = R2 – \alpha \bullet R4$ (see **Scheme S1** for more details, Supporting information). For the electrode structures used in this work, the parameter α, which primarily depends on the geometry, is determined to be around 3 [22]. Alternatively, one can use the $R2/R4$ ratio to estimate the contribution of the contact resistance R_c into $R2$. For the geometry of our sensors, the $R2/R4$ ratio should be around 3 if no contribution of the contact resistance into $R2$ occurs [20,22]. The electrodes were prepared by drop-casting 2.5 μL of diluted GO dispersion (0.04 wt.% or 0.004 wt.%, Graphenea, Spain [19]. The spot size of dried GO film was (1.5 ± 0.1) mm. Higher concentration dispersion

(0.04 wt.%) gives ∼2.5 smaller geometric surface compared to the films in Section 2.1. Thus, as the concentration is 2.5 smaller, the film thickness is approximately the same. For lower concentration dispersion, the film thickness can be assumed to be around 25 nm. Before the drop-casting step, gold electrodes used for the s24-measurements were washed in acetone to remove the protective polymer layer and in Piranha solution to remove any organic residues. Upon drying the GO film, the electrodes were transferred into the electrochemical cell (one compartment all-glass cell), and the measurements were done as described below.

The measurement system has a sampling interval of around three seconds which imposes the lower limit for the measurements under potentiodynamic conditions. For this reason, the reduction of the thin film of GO was made in steps using a program consisting of cyclic voltammetry steps (one cycle to the given cathodic vertex potential; potential sweep rate of 10 mV s^{-1}) and potentiostatic steps for the resistance measurements. Each scan started from −0.5 V vs. Ag/AgCl (common anodic to vertex) and was performed to the cathodic vertex starting from −0.8 V down to −1.3 V vs. Ag/AgCl (KCl solution) or −1.4 V vs. Ag/AgCl (LiCl solution). The cathodic vertex was reduced by 0.1 V every cycle, from −0.8 V to −1.3 V (KCl solution) or −1.4 V (LiCl solution). After each cycle to a given cathodic vertex potential, s24 measurements were performed under potentiostatic conditions (−0.5 V vs. Ag/AgCl), and the resistance values were collected for 1 min. The measured values were averages over this sampling period (20 measurements points) and for three separate samples. The reduction steps were performed by connecting all the contacts of the four-strip electrode structure to the AutoLab potentiostat PGSTAT12. After each reduction step, the contacts were re-connected to the s24 measurement system, and the resistances were recorded (see **Scheme S2**, Supplementary Information).

2.3. SEM, Raman spectroscopy and AFM characterization of reduced GO films

The GO thin films reduced during the *in-situ* resistance measurements were characterized using Raman spectroscopy. Raman spectra (excitation wavelength 532 nm) were collected on a DXR Raman microscope (Thermo Scientific, USA) equipped with an Olympus optical microscope and a CCD detector. The laser beam was focused on the sample using objective magnification 50×. The scattered light was analyzed by the spectrograph with a 900 lines mm^{-1} grating. Laser power on the sample was kept at 2.0 mW. Given Raman spectra present the average of 3 spectra collected from the surface spots of 1 × 1 μm in lateral dimensions.

SEM with EDX was done using Phenom ProX (Phenom, The Netherlands). Chemical analysis was done using an acceleration voltage of 15 kV. SEM images and 3D surface reconstruction was done using an acceleration voltage of 10 kV. Presented chemical compositions are averaged over five sampling points, with a sampling time of 1 min each. The samples were investigated as-prepared, without deposition of the conductive layer on top of them.

An analogous series of the reduced GO thin films were produced for the analysis by atomic force microscopy (AFM). The reduced GO films were prepared on copper foils and reduced in KCl or LiCl solutions (0.1 mol dm^{-3}) at potentials between −0.8 and −1.5 V using potentiostatic steps of 10 s duration. The reduction was made with a 0.1 V resolution. After electrochemical reduction, the electrode with GO film was dried in ambient conditions. AFM-based analysis of GO films was done using Ntegra Prima. Local current maps were measured by conductive AFM (C-AFM), and diamond coated probes DCP20 from NT-MDT. During C-AFM measurements, the bias voltage of 10 V was applied on the backside of GO films, while the grounded probe scanned the top surface in contact AFM mode. Therefore, opposite to the previous s24-technique, where the measurements correspond to the lateral transport of charge carriers along the film surface, in C-AFM, the measured current corresponds to

the vertical charge transport. Thus, the current path goes from top AFM tip, through GO film and ends up at the bottom Cu foil. In order to provide a stable AFM tip-sample contact during imaging, a high enough normal load was applied by the AFM probe. For each reduction potential (from −0.8 to −1.5 V vs. satd. Ag/AgCl, with 0.1 V resolution), five 10 × 10 μm^2 current maps were measured on different sample locations. In order to characterize the sample conductivity, two characteristic values were calculated for each current map: the average current and the ratio between the conductive and scanned 10 × 10 μm^2 area (in percents). The resolution of AFM images was 256 × 256 data points *per* image, so the average current was calculated as a mean value of the corresponding two-dimensional matrix. In order to calculate the ratio between the conductive and scanned area, $I_{thr} = 0.1$ nA was selected as a current threshold, meaning that points on a sample surface were counted as conductive ones only if the measured current was higher than I_{thr}. I_{thr} was determined empirically, from histograms of current maps, as a maximal current which corresponds to the unreduced areas of GO films. Finally, the average current and conductive area for each reduction potential were obtained by averaging results obtained on five different sample locations.

2.4. Theoretical calculation

Theoretical calculations were performed to understand better the interactions of metal atoms/cations with GO surface and functional groups. The GO model was set as a finite sheet with H-saturated edges containing several oxygen functional groups. We have investigated the interactions of metal atoms with clustered and isolated OH groups on this GO sheet model. The details on the calculation setup are provided below.

The first-principle DFT calculations were performed using the Vienna *ab initio* simulation code (VASP) [23–25]. The Generalized Gradient Approximation (GGA) in the parametrization by Perdew, Burk, and Ernzerhof [26] combined with the projector augmented wave (PAW) method was used [27]. Cut-off energy of 450 eV and Gaussian smearing with a width of $\sigma = 0.025$ eV for the occupation of the electronic levels were used. Brillouin zone was sampled using Γ-point only. During structural optimization, the relaxation of all atoms in the simulation cell was allowed. The relaxation proceeded until the Hellmann–Feynman forces acting on all the atoms became smaller than 10^{-2} eV Å^{-1}. Spin polarization was included in all calculations.

Semiempirical calculations were done using MOPAC2016 code [28] with PM7 method [29]. Full structural relaxation was done. The analysis was performed in the presence of water as a solvent. The solvent was included in the analysis implicitly, using the Conductor-like Screening Model (COSMO) method [30]. Additionally, 1–3 explicit water molecules were introduced into the solvation spheres of Li or K.

Visualization was done using VESTA [31] and Jmol [32].

3. Results and discussion

3.1. Electrochemical reduction of GO films – overview and activation energies

First, electrochemical reduction of thin GO films was investigated in 0.1 mol dm^{-3} LiCl and KCl solutions using cyclic voltammetry. As previously demonstrated [12] the reduction process is fast and irreversible (**Fig. 1**, see also **Figure S1**, Supporting Information), where one major reduction peak is observed (**Fig. 1**). The reduction commences at lower potentials in LiCl solution (roughly around −0.8 V vs. reference), and with decreasing the temperature from 40 to 7.5 °C, the reduction peak shifts to lower potentials (from −1.32 to −1.55 V vs. reference). The same situation is observed for KCl, but the separation of reduction peaks increases upon decreasing the temperature, while the reduction peaks get broader and lower in the current (absolute values).

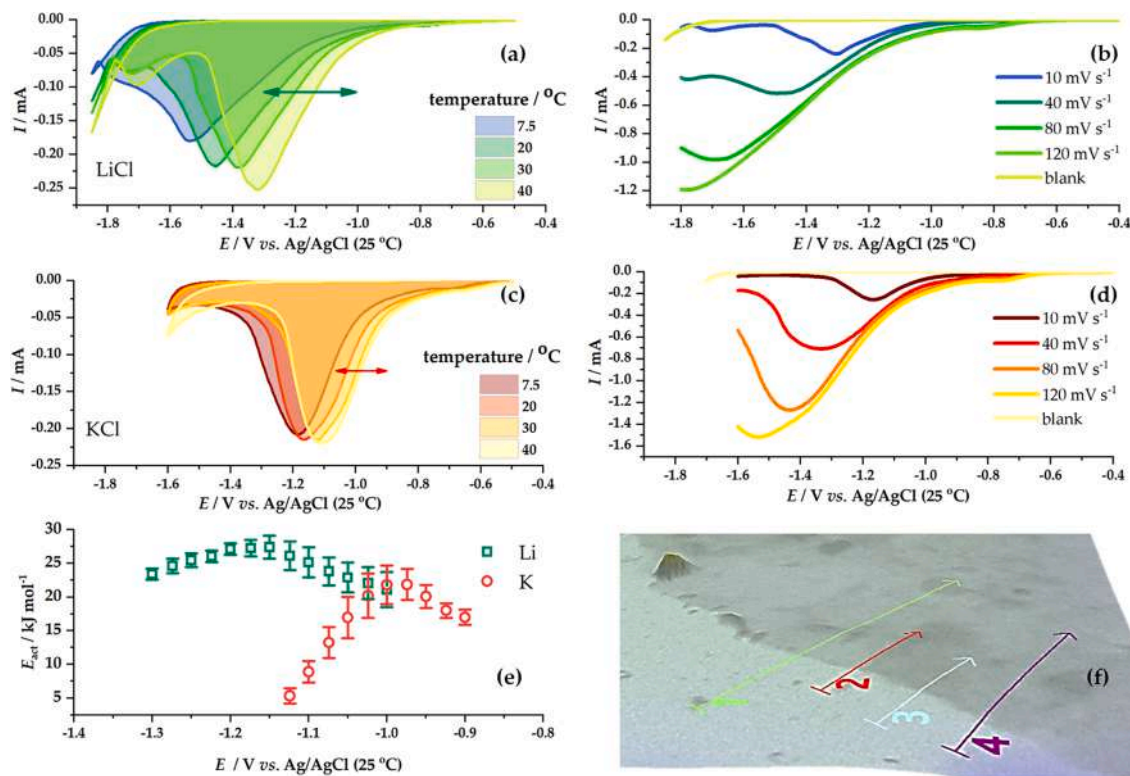The temperature dependence of measured current can be expressed

Fig. 1. Reduction of GO thin films as seen using cyclic voltammetry: GO thin film reduction in 0.1 mol dm^{-3} LiCl (a) and linear voltammetry for four different scan rates (b). The corresponding cyclic voltammograms for KCl (c) at four different temperatures, potential sweep rate: 10 mV s^{-1}., and linear voltammetry for four different scan rates (d). The horizontal arrows indicate the potential ranges in which the apparent activation energies for GO reduction were calculated. Plot (e) gives the evaluated activation energies, while the (f) gives the 3D SEM reconstruction of the substrate/GO layer interface. Upon averaging heights along the indicated paths, the GO film thickness was evaluated to (250 ± 30) nm.

in a general form as:

$$i(E) = C(E) \times \exp\left(-\frac{E_{act}(E)}{RT}\right) \quad (1)$$

where $C(E)$ (given in Amps) assembles all the constants (including electrode potential dependent term), and R and T are universal gas constant (8.134 J mol^{-1} K^{-1}) and absolute temperature (in [K]) while ($E_{act}(E)$) is the apparent activation energy for this process (with dimension [J mol^{-1}]). Therefore, for a given electrode potential E,

$$\ln i(E) = \ln C(E) - \frac{E_{act}(E)}{RT} \quad (2)$$

assuming that $C(E)$ does not depend on temperature. Upon processing recorded I-E curves, E_{act} was found to increase as the cathodic polarization increases up to the potentials corresponding to approx. 70% of the cathodic peak recorded at 40 °C, upon which it starts to decrease. The values are slightly lower in KCl (22 kJ mol^{-1}) than in LiCl (27 kJ mol^{-1}).

The values of E_{act} obtained near room temperature are expected to be significantly lower than those at elevated temperatures. Experimental data confirmed it. For example, the resistivity measurements on individual single-layer GO platelets at temperatures above 140 °C give the activation energy of (155 ± 4) kcal mol^{-1}. On the other hand, the TPD measurements of multilayer films of GO platelets give the activation energy of (134 ± 17) kJ mol^{-1} [33]. During the low-temperature annealing, the resistivity measurements gave the activation energy of 1.65 eV (i.e., 159 kJ mol^{-1}) [34] it was ascribed to the processes of desorption of epoxy and alkoxy oxygen atoms together with carbon [35] and to the restoration of non-oxidized graphene domains. Obviously, the electrochemical reduction of GO being completed within minutes is a much faster process than the low-temperature annealing taking 2–4 h

[33]. Finally, we must comment that the values of activation energies derived here and in other papers should be interpreted carefully. This unit should be understood as the energy *per* Avogadro number of chemical bonds. Namely, due to a scatter in the content of surface oxygen, one mole of GO is poorly defined, and molar values cannot be undoubtedly associated with converting one mole of GO to rGO. These results are better to be interpreted at one mole of chemical bonds present in GO which get broken during the reduction process and averaged over the ensemble of groups present in a particular GO sample. However, we note that the change of the nature of dominant oxygen functional groups in a given GO sample cannot compensate for the difference between E_{act} for electrochemical reduction against low-temperature annealing, since, in the latter case, the process is much slower.

3.2. Lateral conductivity and reduction of films of GO

The resistance of GO films during annealing is decreasing for seven orders of magnitudes [34], as a consequence of thermally induced oxygen release. We have investigated the changes of resistance using simultaneous 2-point and 4-point measurements, which provide information on the lateral and contact resistances of GO films during the electrochemical reduction (**Fig. 2**). The results were found to depend on the film thickness. For thinner films, $R2$ was found to decrease slowly from very high values (10^7 Ω) with increasing cathodic potential, until −1.1 V is reached. Then, $R2$ decreases by two orders of magnitude for the film reduced in KCl and continues to decrease for the film reduced in LiCl (**Fig. 2**, c). The $R4$ values show a similar trend but with a characteristic increase (**Fig. 2**, c) at potentials close to the reduction peak potential (**Fig. 1**). Looking at the $R2/R4$ ratios (**Fig. 2**, c, inset), for the non-reduced GO films, the ratio is much higher than the theoretical value for zero contact resistance (i.e., ∼ 3), amounting to ∼20. These
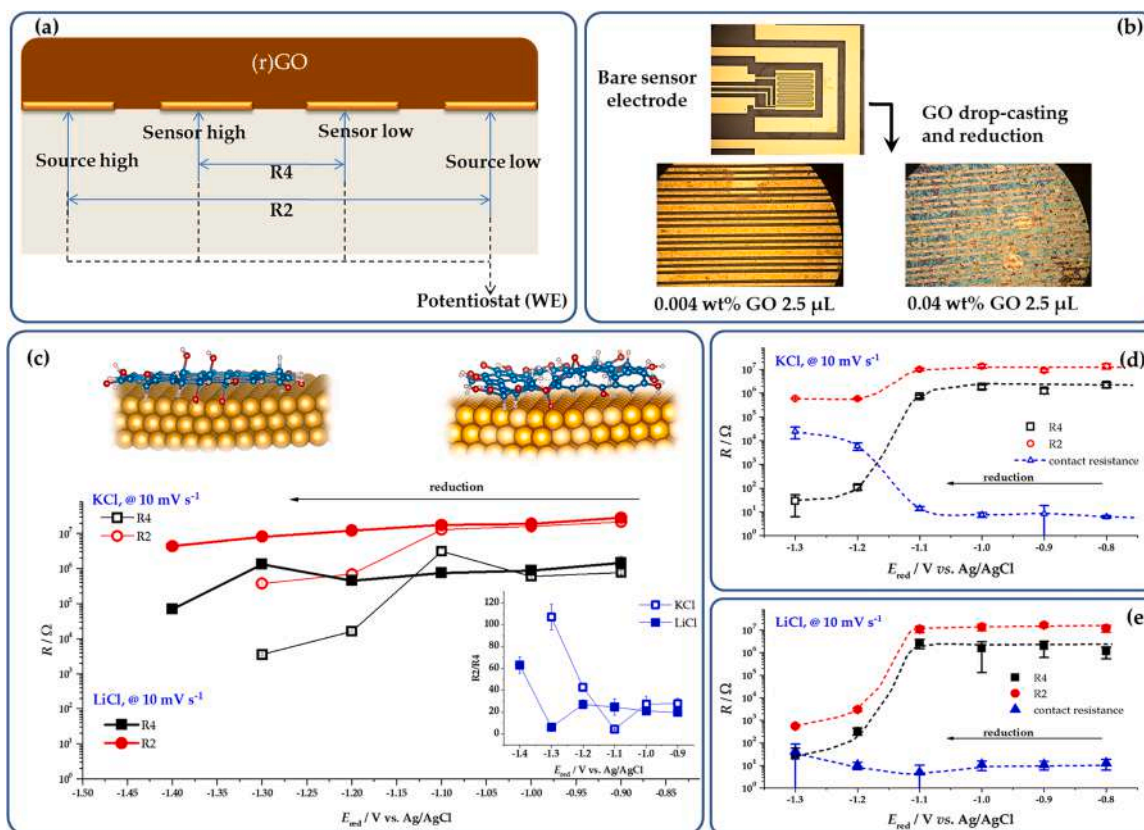
Fig. 2. Reduction of GO deposited on the four-strip gold electrode as seen using s24 measurements. (a) Schematic representation of the connection of the four-strip gold electrode to the resistance measurement system (full lines) or the potentiostat (dashed lines), components for s24 measurements are not shown (for more details see **Schemes S1** and **S2**, Supporting Information, and Refs. [20–22]), (b) optical micrographs of the four-folded-strip electrode and magnified parts of the electrode upon reduction of the GO film of different thickness, (c) s24 measurements for GO film obtained upon drop-casting of 2.5 μL of 0.004 wt.% GO dispersion in KCl and LiCl at different reduction potential corresponding to non-reduced GO and reduced GO film (schematically shown for two vertex potentials), inset gives the $R2/R4$ ratios for two electrolytes, (d) s24 measurements for GO film obtained upon drop-casting of 2.5 μL of 0.04 wt.% GO dispersion in KCl, with evaluated contact resistance, (e) the same as for (d) but for the reduction in LiCl solution.

values suggest a poor electric contact between the GO film and the gold electrode due to the non-conductive nature of GO film. When the reduction process starts, the value of the $R2/R4$ ratio drops down to the value of ~3, after which they increase significantly, with the increment being more pronounced for KCl. The behavior of thicker films is similar (**Fig. 2**, d and e), but the resistance changes are much more pronounced, and $R4$ values change for six orders of magnitude for the films reduced in both LiCl and KCl. However, in the KCl solution, the $R2$ drops by only one order of magnitude, and the contact resistance reaches the values of 10^4 Ω. For the films reduced in LiCl, $R4$ changes for four orders of magnitude, and the contact resistance reaches the values of 60 Ω.

The large differences in the behavior of the contact resistance between two electrolytes can be explained by faster reduction of GO in KCl, resulting in pronounced evolution of CO, CO_2, and H_2O from the GO sheets [36]. However, one should also consider the H_2 evolution on the gold electrode, weakening the contact between the GO film and the electrode. Namely, the H_2 evolution on the gold electrode is more pronounced in K^+-containing electrolyte than in Li^+-containing one [37]. Thus, more intense H_2 evolution in KCl can also contribute to the weaker contact between the gold electrode and the reduced GO film. It is also interesting to observe a certain improvement in the contact before reduction. The initially evolved CO, CO_2, and H_2O probably improve the compactness of the film and the contact with the Au electrode, as out-of-plane surface groups start to be removed and the stacking of the layers is improved. Such compactization could also be associated with previously observed changes (using *in situ* surface-enhanced infrared spectroscopy) in the double layer at the GO film–electrolyte interface

and hydrogen bonding of intercalated water between the GO sheets at moderate reduction potentials (−1.1 V for KCl to −1.3 V for LiCl solution) before reducing O-functional groups commences [38]. However, as the evolution of gasses continues, the formed microbubbles weaken the contact between the reduced GO sheet and the Au electrode. Finally, the non-conductive to conductive state transitions are clear for thinner films, seen by measured $R2$ and $R4$ in LiCl and KCl solutions (**Fig. 2**, c). However, for thicker films, the change of resistance appears at the same potential (just below −1.1 V, **Fig. 2**, d and e). Such behavior can be understood assuming that for thicker films, a sufficient amount of reduced GO sheets is formed in both electrolytes so that the conductive network is built and the lateral conductivity of the films increases. Another possibility is that upon repeated cycling of a GO film to progressively higher cathodic vertex potentials, the degree of reduction increases over the value corresponding to the degree reached during a single scan to a given cathodic vertex. This scenario is feasible as we found that electrochemical GO reduction is also sensitive to the scan rate and shows typical irreversible character so that higher degrees of reduction can be achieved at lower potentials with very slow potential scans.

To confirm the differences between the GO films reduced in LiCl and KCl solutions (supporting electrolyte effect), the reduced GO films on Au electrodes used in the resistance measurements were subjected to Raman and EDX analysis (**Fig. 3**). We note that the recorded Raman spectra of fully reduced rGO films showed very good repeatability, as shown in **Figure S2** (Supplementary Information). Thus, further reported bands intensity ratios have relative uncertainties below 5%,
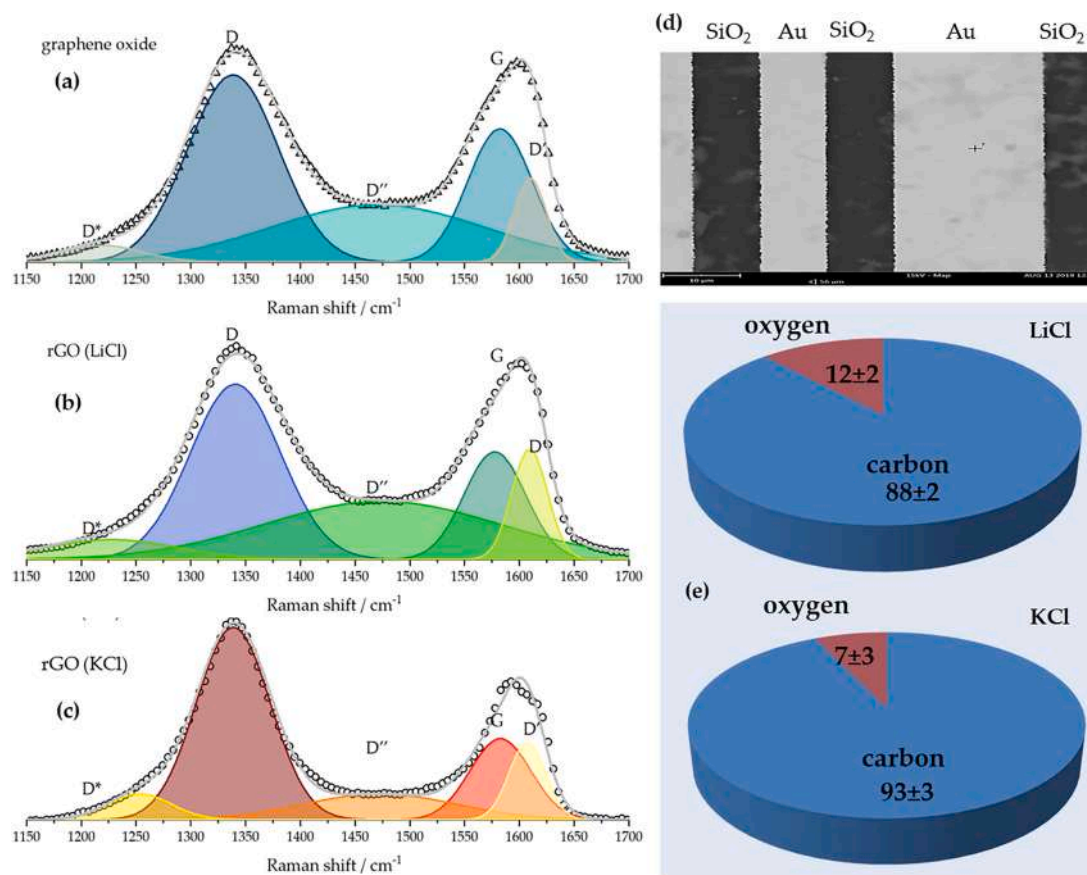
Fig. 3. *Ex-situ* **characterization of reduced GO films on the four-strip folded gold electrode.** Raman spectra of GO thin film deposited on four-strip gold electrode (2.5 µL of 0.004 wt.% GO) before reduction (a) and after electrochemical reduction in LiCl solution (b) and KCl solution (c). Both films are reduced using a single cyclic voltammetry scan from -0.5 to -1.3 V vs. Ag/AgCl with a sweep rate of 10 mV s^{-1}. On the right SEM image of the four-stip gold electrode with rGO film is given (d), and the results of EDX chemical analysis of the GO film in LiCl (C:O ratio 7.6 $\pm$ 1.2) and KCl (C:O ratio 13.9 $\pm$ 3.4).

dominantly caused by the repeatability of the drop-casting procedure and the errors of the fitting procedure. The Raman spectra in the 1150–1700 cm^{-1} region were deconvoluted into five components using Gaussian profiles. For this reason, the reported band intensity ratios are obtained using the peaks areas [39]. For non-reduced GO film, the G band is located at 1582 cm^{-1}, while the I_D/I_G ratio is 2.0. For the film reduced in LiCl solution, the G band is at 1577 cm^{-1}, and for the GO film reduced in KCl, it is found at 1583 cm^{-1}. The corresponding I_D/I_G ratios are 2.4 and 2.9, respectively. Considering a high oxygen content and practically no sp^2 bonded carbon in the used GO sample [19], the as-received GO sample can be located in stage 3 of the amorphization trajectory [39]. However, there is a clear D band compared to the tetrahedral amorphous carbon where the D band intensity is null. However, for fluorinated graphene with a high degree of sp^3-type defects, the D band intensity was also found not to be zero [40]. The C:O ratios found in reduced GO films (**Fig. 3**, e) suggest that the GO films are reduced to a lower degree in LiCl compared to that reduced in KCl. As the G band is located at a slightly lower wavenumber and the I_D/I_G ratio is smaller for the GO film reduced in LiCl, it can be placed in stage 2 of amorphization trajectory (positioned between nanocrystalline graphite and amorphous carbon-based on Raman spectrum) [39,41]. Formally, the film reduced in KCl can also be placed in the same stage but closer to stage 1, as indicated by a higher position of the G band and a higher I_D/I_G ratio. This conclusion is also in line with the $I_{D'}/I_G$ ratios for reduced GO films, amounting to 0.60 and 0.57 for films reduced in LiCl and KCl solution, respectively [41].

The question is, which types of defects are present in the reduced films? Using the $I_D/I_{D'}$ ratios, it is, in principle, possible to resolve the type of defects present in graphene [41]. The non-reduced GO film has

the $I_D/I_{D'}$ ratio of 6.3, close to the typical value for vacancy-like defects ($I_D/I_{D'} = 7$, [41]). However, the same ratios for reduced GO films are smaller than for non-reduced GO, 4.0 and 5.1 for films reduced in LiCl and KCl, respectively. At least for the film reduced in LiCl, this might indicate the dominant presence of boundary-like defects. However, there is also a possibility that a hysteresis appears during the reduction of GO [39], as, in fact, reduction of GO goes along the ordering trajectory.

For this reason, it is rather difficult to derive a precise conclusion of the type of defects in reduced GO films. However, as CO and CO$_2$ evolve and the process is rather fast (tenths of seconds *vs.* hundreds of minutes in thermal reduction procedure), it can be expected that reduced GO is rich in vacancies. This conclusion is aligned with the fact that the starting GO is also exceptionally rich in very large vacancies [19]. This is in line with previous conclusions that electrochemical reduction of GO cannot heal the vacancies initially present in GO [9]. In contrast, it was recently suggested [42] that electrochemical reduction favors the formation of sp^3-like defects over vacancies. However, we suspect that the reduction of GO films was incomplete in these experiments as performed only down to -1 V *vs.* Ag/AgCl electrode in NaCl solutions. This potential actually corresponds to very low reduction degrees of GO (**Fig. 1**, and Ref. [12]).

Considering the above discussion, we do not make any definite comparison of our data to the existing literature. Moreover, we note that the structure of the resulting rGO, formed by electrochemical reduction, is highly dependent on the structure of the initial GO (for example, the presence of vacancies or other types of defects), as well as the experimental conditions, which might be the source of frequently opposing findings reported in the literature. These include, but are not limited to,

the conditions of the electrochemical experiments, supporting electrolyte, pH, temperature. On the other hand, controlled experiments where Raman spectroscopy is used to follow the structural evolution of electrochemically reduced GO would certainly provide useful insights, considering the mentioned factors that affect the reduction process. Such a series of Raman spectra recorded for rGO reduced at different potentials (potentiostatic, 10 s of reduction, see Section 2.3) are given in **Figure S3** (Supplementary Information). As can be seen, fully reduced films show quite good agreement between Raman spectra taken at different spots on the film. The situation gets worse for lower degrees of GO reduction, particularly at the wavenumbers where D' band is located (associated with the level of disorder and types of defects present in rGO samples, as discussed above). This indicates that local inhomogeneities exist in rGO films that are not fully reduced compared to fully reduced films (**Figure S2**, Supplementary Information). The complete analysis of structural evolution of electrochemically formed rGO films is beyond the scope of the present work, focusing on conductivity restoration. Thus, we turn to C-AFM analysis of reduced GO films, which can resolve the local variations in conductivity with a high resolution.

3.3. Reduction and transversal conductivity of electrochemically reduced GO films

The reduced GO films were also analyzed using C-AFM. In contrast to s24 measurements, this method measured transversal conductivity through GO film. A simplified scheme of C-AFM measurement setup is given in **Scheme S3**, Supplementary Information, along with the discussion of different contributions to the measured current maps. Typical current maps for several reduction potentials and the LiCl electrolyte are depicted in **Fig. 4**(a). For the low reduction potential (−0.8 V), GO films behave as insulators with a current below 120 pA (represented by a dark contrast) across the whole sample surface. An increase of the reduction potential till −0.9 V and −1.1 V leads to the appearance of small bright patches in the current maps indicating a formation of conductive and spatially separated islands. At higher reduction potentials (−1.3 V), the current maps become inverted, consisting of a bright (conductive) surface with small and isolated dark (insulating) domains. At the highest reduction potential (−1.5 V), the dark domains practically disappear. Therefore, GO films become highly conductive, containing only small

insulating patches.

The changes in the current maps as a function of the reduction potential were quantified by calculation of the average current and relative area of conductive domains in the scanned areas. They are presented in **Fig. 4**, (b) and (c), respectively, for both LiCl and KCl electrolytes. As can be seen, the reduction of GO films has the same trend in both electrolytes, but the reduction in KCl starts earlier. At a reduction potential of −1 V, the average current is so high as ∼9 nA, and the relative area of conductive domains is ∼85%. In LiCl, a pronounced reduction happens later. Only at the reduction potential of −1.3 V almost the entire GO films become conductive while the average current jumps to 15 nA. As explained in Supplementary Information, Section S4, we note that the measured current maps also include a contact resistance between the rGO layer and the underlying Cu foil. The performed C-AFM is an *ex-situ* technique thus, the formation of the surface oxide layer and its reduction at low potentials could affect this contact. However, the s24 measurements suggest an increased contact resistance at deep anodic potentials (**Fig. 2**), which shows an opposite trend to the one observed in the C-AFM measurements. Thus, it can be unambiguously concluded that the decrease of rGO resistivity dominates the C-AFM measurements (see also Section S4, Supplementary Information).

Using the results of the C-AFM measurements, one can conclude that the sharp decrease in the film resistance ($R4$) obtained using s24 measurements corresponds to the point when the conduction islands of reduced GO coalesce, forming a conductive network that bridges the gap between the electrodes in the 4-electrode sensor. We note that in the s24 measurements, the reduction of the GO film starts locally at the points where the film is in contact with the Au layer and spreads into the gap between two Au stripes (**Fig. 3**, d). The distance between the Au stripes is under 10 μm, which matches the maximum lateral size of GO sheets used in this work. Hence, the measured resistance is also affected by the migration rate of reduced GO front in the gap region between two Au stripes. For this reason, the measured activation energy would be affected by the rate of the reduced GO front migration into the inter-Au region. However, we note that this setup can also be used to estimate the rate of this migration. When a cyclic voltammetry sweep is performed at a higher rate (25 mV s^{-1}), we did not observe any resistance change, although the color change from yellow to black was visible. This observation indicates that the GO film was reduced at the places where it
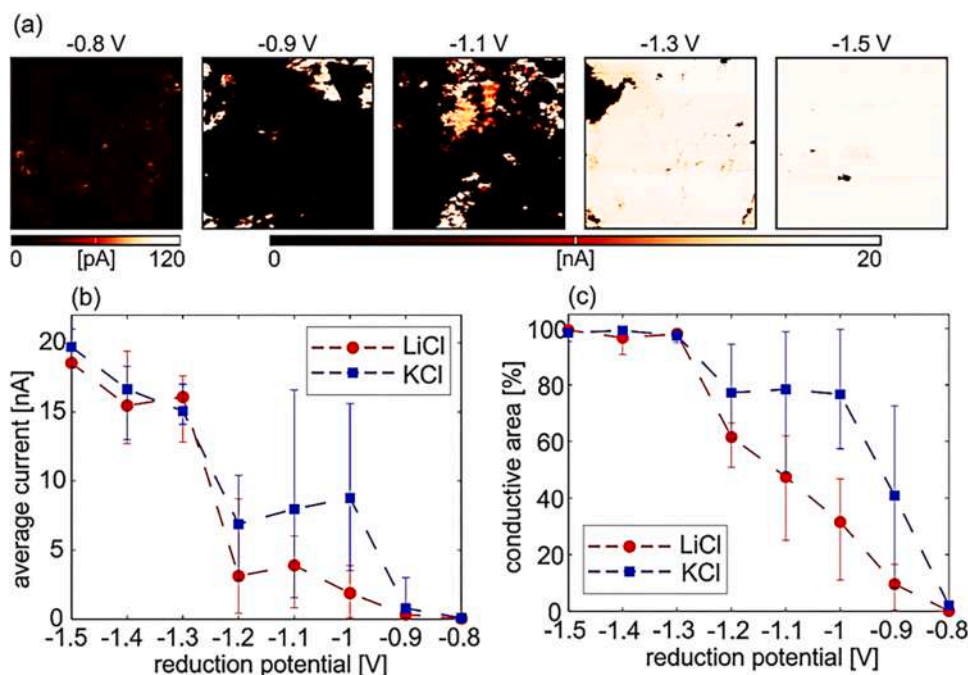

Fig. 4. The reduction of GO film as seen by C-AFM. (a) Characteristic current maps for five selected reduction potentials measured in LiCl electrolyte. The scan size is 10×10 μm^2. The current scale is 20 nA except for the left map (−0.8 V), where the scale is so low as 120 pA because of the very low conductivity of unreduced samples. (b) Average current and (c) relative conductive area (calculated as a ratio between conductive and scanned, 10×10 μm^2 area, in percent) averaged on five different sample locations for each reduction potential.

is in direct contact with the Au electrodes but not in-between them. As a cyclic voltammetry scan between -0.5 and -1.3 V at 25 mV s^{-1} requires 32 s to complete, and the reduced GO film should cross 5 μm to connect into a conductive layer, it can be concluded that the reduced GO film progresses laterally at a rate below 1.6×10^{-7} m s^{-1} when not in direct contact with the current collector. However, this value is just a rough estimate as the reduction process does not occur during the entire potentiodynamic scan, while the reduced fragments of the GO film could act as current collectors for the reduction of adjacent GO parts.

3.4. Theoretical modeling of GO reduction

To model the process of GO reduction, we have performed a series of semiempirical and DFT calculations on a model of GO sheet (**Fig. 5** and **Fig. 6**). According to the Lerf–Klinowski model [43], epoxide and hydroxyl groups dominate the GO basal plane [44,45]. As we have previously discussed the differences in alkali and alkali earth metals with epoxide [12], here we focus on hydroxyl groups. This is also important considering that OH groups were recently found to be the first to reduce electrochemically [18]. The model contained several OH groups clustered together, knowing that such type of sp^3 defects appears in dimers or clusters [46,47]. The formal stoichiometry of the considered mode was $C_{58}H_{33}O_6$. An additional model was constructed so that it also contained one isolated OH group over the GO basal plane beside a cluster of OH groups (stoichiometry $C_{58}H_{34}O_7$).

In semiempirical calculations, water was added implicitly as a solvent, but we also considered explicit solvation of Li$^+$ and K$^+$ ions in our models. For Li$^+$, we have considered up to three explicit H$_2$O molecules in the hydration sphere, while for K$^+$ we considered systems with one or no H$_2$O molecules. When considered metal ions were brought in contact with the OH groups cluster, no detachment of OH groups and formation of MOH unit was observed. The same was when considered the interaction of metal ions with an isolated OH group. However, the oxygen atom in the OH groups is susceptible to electrophile attack. Thus, we added the H atom close to the O in the OH group interacting with the metal cation in the next step. The addition of the H atom is analogous to the addition of H$^+$ through the electrolyte and one electron through the external electric circuit during the electrochemical reduction of GO, as we considered the whole systems as singlets and bearing one positive charge. A spontaneous detachment of the metal-H$_2$O complex is observed upon the relaxation in all the cases (**Fig. 5**). The main results that should be emphasized here are the following: (i) the total energy balance is always more negative for K$^+$ compared to the analogous scenario with Li$^+$ ions, and (ii) it is always energetically more favorable to remove an isolated OH group than the one from the cluster (**Fig. 5**, see energy balances). The first result can be understood by extensive solvation of Li$^+$ ion, which screens the Li$^+$ ion and weakens the interaction with the detached H$_2$O molecule. The second result can be understood by stabilizing OH clusters due to the extended sp^3 hybridization and the non-covalent interactions that stabilize an OH cluster (**Fig. 5**, isosurfaces).

Even more striking differences in the behavior of isolated *versus* clustered OH groups can be seen in the results of DFT calculations (**Fig. 6**). In this case, we performed calculations on charge-neutral systems and without implicit solvent. Hence, by adding one metal atom to the system, we simulate the addition of M$^+$ from the solution and electron through the external circuit. If Li or K atom is interacting with the OH groups cluster (**Fig. 6**, a and b), no chemical change is observed.
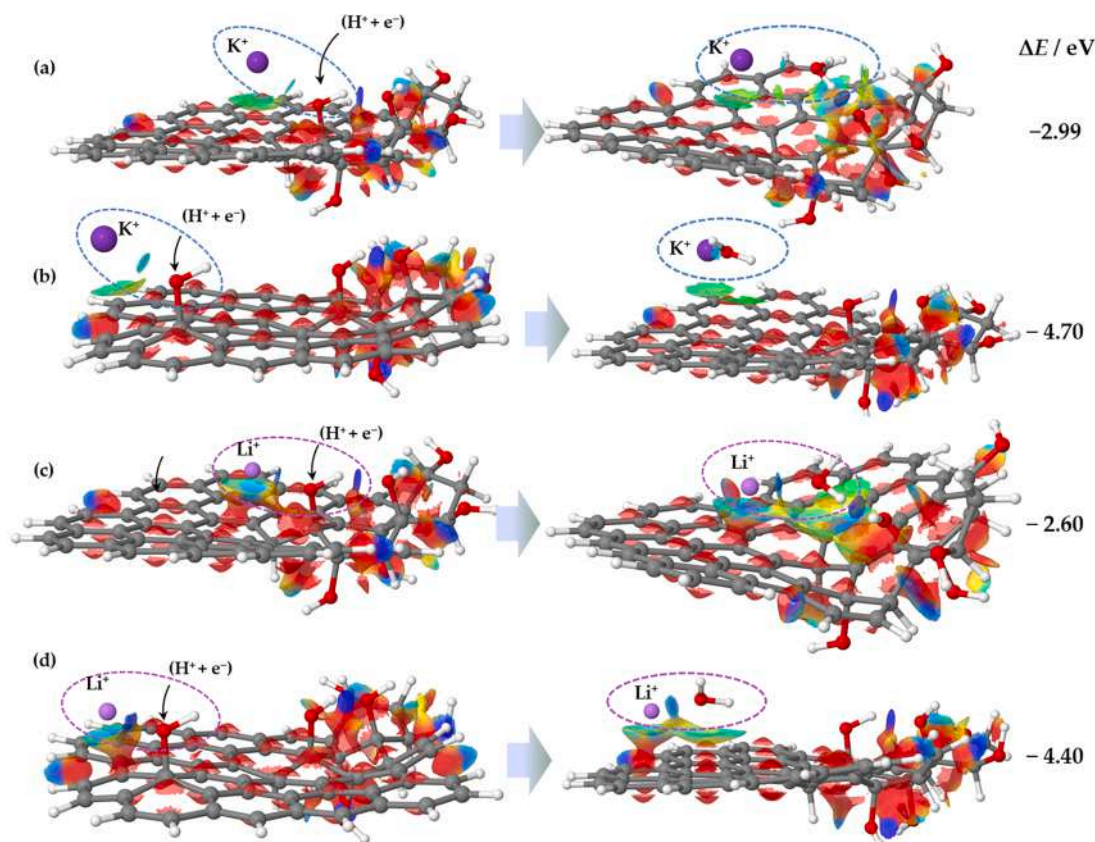

Fig. 5. GO reduction as seen by semiempirical quantum chemical calculations. (a) Optimized structure of (K$^+$ + GO) before and after the addition of one hydrogen (H$^+$ + e$^-$) to the system when K$^+$ interacts with agglomerated OH groups, (b) optimized structure of (K$^+$ + GO) before and after the addition of one hydrogen (H$^+$ + e$^-$) to the system when K+ interacts with an isolated OH group at the GO sheet, (c) the same as for (a) but for the interaction with Li$^+$, (d) the same as for (b) but for the case of Li$^+$. At the right, energy balances are provided. All the systems are calculated as singlets having one positive charge. Isosurfaces show the regions of non-covalent interactions present in the studied systems.
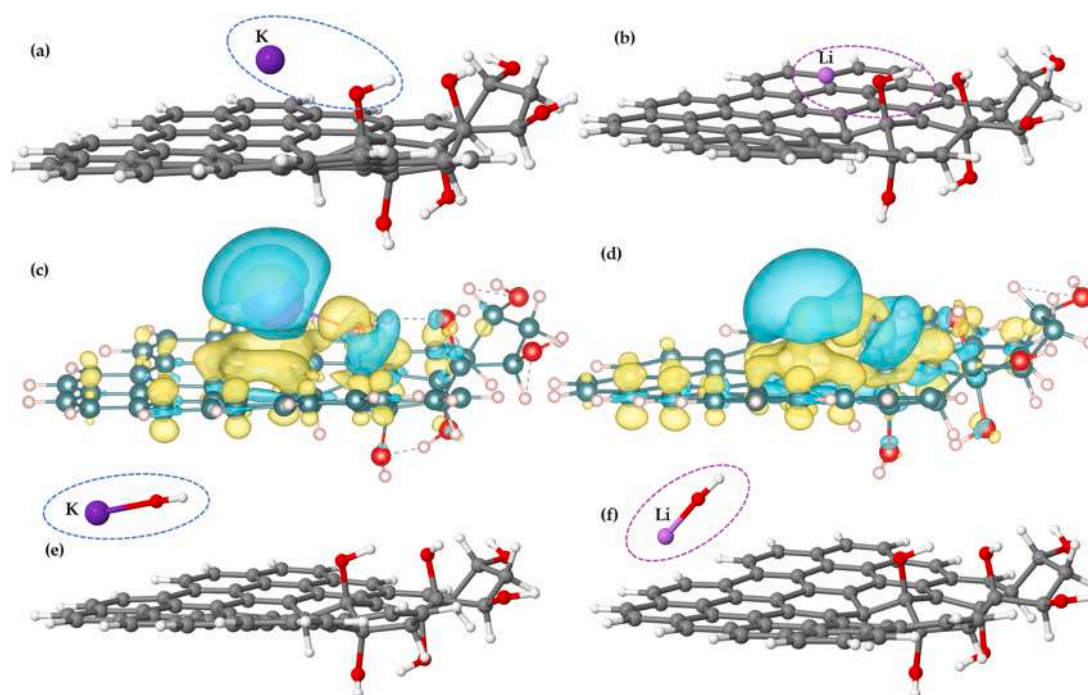
Fig. 6. GO reduction as seen by DFT. Optimized structures for the interaction between K atom (a) and Li atom (b) with agglomerated OH groups, and the corresponding charge different plots (K – (c), Li – (d); isosurface values 1.2×10^{-3} e Å^{-3}, blue surface indicate charge loss and yellow surfaces indicate charge accumulation), (e) optimized structures of the systems upon the interaction of K atom with an isolated OH group on GO basal planes, (f) the same as (e) but for the case of Li atom. The starting structures for (e) and (f) were as in Fig. 5(b) and (d) (left). All the systems were calculated as charge neutral. (For interpretation of the references to color in this figure legend, the reader is referred to the web version of this article.)

In other words, one ns electron from a metal atom is efficiently transferred to the GO sheet and stored in the basal plane. Although there is some charge depletion in the HO—C bond (Fig. 6, c and d), the MOH unit is not detached. The situation is the opposite when M is brought in contact with an isolated OH group on the GO basal plane (Fig. 6, d and e). In this case, the result is a spontaneous formation of MOH. These findings confirm that isolated OH groups over GO basal are more susceptible to reduction than clustered ones, agreeing with previous theoretical calculations [47]. Moreover, previous calculations have also shown that the interactions of K with clustered OH groups are energetically more favorable compared to the analogous interactions of Li with the same moieties.

Based on theoretical results, one could also understand why the apparent activation energy for electrochemical GO reduction increases with reduction potential to a certain point (Fig. 1). This part of the E_{act}-electrode potential dependency could be correlated with the removal of easily reducible oxygen functional groups and the formation of reduced conductive domains with regenerated sp^2 hybridization, in line with experimental observations [18]. This hypothesis is also in line with the C-AFM measurements (Fig. 4). Upon the progression of electrochemical GO reduction, hardly reducible oxygen groups are being removed, and breaking the structure of the O-moieties clusters makes their removal easier. For this reason, once the integrity of O-moieties clusters is compromitted, the activation energy for reduction begins to decay (Fig. 1).

4. Conclusions

Contrary to a thermally induced oxygen release, electrochemical reduction of GO in LiCl and KCl is a fast process with relatively low activation energy (below 30 kJ mol^{-1}), depending on the supporting electrolyte. The GO reduction occurs at lower potentials in KCl solution than in the LiCl solutions, which is observed not only by using cyclic voltammetry but also by simultaneous 2-point 4-point resistance

measurements on thin GO films. While these measurements suggest that the reduced GO films become conductive when reduction reaches high degrees, C-AFM measurements show that reduction takes place locally but continuously and that conductive islands grow during the reduction of GO films. Once these islands coalesce, the lateral conductivity of the reduced GO films reaches its maximum, observed as a sharp decrease of the film resistance in s24 measurements. Our results also suggest that the evolution of gasses during the GO film reduction (H$_2$, CO, CO$_2$) influences the contact between the reduced GO film and the substrate (in our case, Au electrode). This result is of high practical importance as a large contact resistance can cause significant energy losses in electrochemical energy conversion and storage applications of reduced GO films. Theoretical calculations show that the reduction of GO is more difficult if the oxygen functional groups are clustered over the GO basal plane. Hence, we propose that the GO reduction starts on isolated or low coordinated oxygen functional groups, which are easier to reduce. Then it progresses, causing a growth of the conductive islands. Presented results can help tailor reduced GO for capacitive and electrocatalytic applications. Such precise performance tuning can be enabled by exact control of the conductivity of the reduced GO films and of the amount of oxygen functional groups. This approach can be a way to maximize the performance of reduced GO in particular electrochemical applications.

Credit authors statement

Dalibor Karačić: Methodology, Formal analysis, Investigation, Writing - original draft. **Sanjin J. Gutić**: Conceptualization, Writing - original draft, Supervision, Funding acquisition. **Borislav Vasić**: Methodology, Formal analysis, Writing - original draft. **Vladimir M. Mirsky**: Conceptualization, Methodology, Resources, Writing - review & editing, Funding acquisition. **Natalia V. Skorodumova**: Validation, Resources, Writing - review & editing, Funding acquisition. **Slavko V. Mentus**: Validation, Writing - review & editing, Funding acquisition. **Igor A. Pašti**: Conceptualization, Methodology, Resources, Investigation,

Writing - original draft, Writing - review & editing, Supervision, Funding acquisition.

Declaration of Competing Interest

The authors declare that they have no known competing financial interests or personal relationships that could have appeared to influence the work reported in this paper.

Acknowledgement

Supplementary materials

Supplementary material associated with this article can be found, in the online version, at doi:10.1016/j.electacta.2022.140046.

References

[1] V. Dhinakaran, M. Lavanya, K. Vigneswari, M. Ravichandran, M.D. Vijayakumar, Review on exploration of graphene in diverse applications and its future horizon, in: Materials Today: Proceedings, Elsevier Ltd, 2020, pp. 824–828, https://doi.org/10.1016/j.matpr.2019.12.369.

[2] L. Wang, Z. Sofer, M. Pumera, Will any crap we put into graphene increase its electrocatalytic effect? ACS Nano 14 (2020) 21–25, https://doi.org/10.1021/acsnano.9b00184.

[3] W. Yuan, Y. Zhou, Y. Li, C. Li, H. Peng, J. Zhang, Z. Liu, L. Dai, G. Shi, The edge- and basal-plane-specific electrochemistry of a single-layer graphene sheet, Sci. Rep. 3 (2013), https://doi.org/10.1038/srep02248.

[4] A.S. Dobrota, I.A. Pašti, S.v. Mentus, N.v. Skorodumova, A general view on the reactivity of the oxygen-functionalized graphene basal plane, Phys. Chem. Chem. Phys. 18 (2016) 6580–6586, https://doi.org/10.1039/c5cp07612a.

[5] S. Georgitsopoulou, N.D. Stola, A. Bakandritsos, V. Georgakilas, Advancing the boundaries of the covalent functionalization of graphene oxide, Surf. Interfaces 26 (2021), https://doi.org/10.1016/j.surfin.2021.101320.

[6] B.L. Dasari, J.M. Nouri, D. Brabazon, S. Naher, Graphene and derivatives – Synthesis techniques, properties and their energy applications, Energy 140 (2017) 766–778, https://doi.org/10.1016/j.energy.2017.08.048.

[7] M.P. Araújo, O.S.G.P. Soares, A.J.S. Fernandes, M.F.R. Pereira, C. Freire, Tuning the surface chemistry of graphene flakes: new strategies for selective oxidation, RSC Adv. 7 (2017) 14290–14301, https://doi.org/10.1039/c6ra28868e.

[8] Y. Shao, J. Wang, M. Engelhard, C. Wang, Y. Lin, Facile and controllable electrochemical reduction of graphene oxide and its applications, J. Mater. Chem. 20 (2010) 743–748, https://doi.org/10.1039/b917975e.

[9] S.Y. Toh, K.S. Loh, S.K. Kamarudin, W.R.W. Daud, Graphene production via electrochemical reduction of graphene oxide: synthesis and characterisation, Chem. Eng. J. 251 (2014) 422–434, https://doi.org/10.1016/j.cej.2014.04.004.

[10] X. Zhang, D.C. Zhang, Y. Chen, X.Z. Sun, Y.W. Ma, Electrochemical reduction of graphene oxide films: preparation, characterization and their electrochemical properties, Chin. Sci. Bull. 57 (2012) 3045–3050, https://doi.org/10.1007/s11434-012-5256-2.

[11] S.J. Gutić, D.K. Kozlica, F. Korać, D. Bajuk-Bogdanović, M. Mitrić, V.M. Mirsky, S. v. Mentus, I.A. Pašti, Electrochemical tuning of capacitive response of graphene oxide, Phys. Chem. Chem. Phys. 20 (2018) 22698–22709, https://doi.org/10.1039/c8cp03631d.

[12] D. Karačić, S. Korać, A.S. Dobrota, I.A. Pašti, N.v. Skorodumova, S.J. Gutić, When supporting electrolyte matters – Tuning capacitive response of graphene oxide via electrochemical reduction in alkali and alkaline earth metal chlorides, Electrochim. Acta 297 (2019) 112–117, https://doi.org/10.1016/j.electacta.2018.11.173.

[13] J. Kauppila, P. Kunnas, P. Damlin, A. Viinikanoja, C. Kvarnström, Electrochemical reduction of graphene oxide films in aqueous and organic solutions, Electrochim. Acta 89 (2013) 84–89, https://doi.org/10.1016/j.electacta.2012.10.153.

[14] O.C. Compton, S.T. Nguyen, Graphene oxide, highly reduced graphene oxide, and graphene: versatile building blocks for carbon-based materials, Small 6 (2010) 711–723, https://doi.org/10.1002/smll.200901934.

[15] W.J. Basirun, M. Sookhakian, S. Baradaran, M.R. Mahmoudian, M. Ebadi, Solid-phase electrochemical reduction of graphene oxide films in alkaline solution, Nanoscale Res. Lett. 8 (2013) 397, https://doi.org/10.1186/1556-276X-8-397.

[16] J. Ping, Y. Wang, K. Fan, J. Wu, Y. Ying, Direct electrochemical reduction of graphene oxide on ionic liquid doped screen-printed electrode and its electrochemical biosensing application, Biosens. Bioelectron. 28 (2011) 204–209, https://doi.org/10.1016/j.bios.2011.07.018.

[17] S.J. Gutić, A.S. Dobrota, M. Leetmaa, N.v. Skorodumova, S.v. Mentus, I.A. Pašti, Improved catalysts for hydrogen evolution reaction in alkaline solutions through the electrochemical formation of nickel-reduced graphene oxide interface, Phys. Chem. Chem. Phys. 19 (2017) 13281–13293, https://doi.org/10.1039/c7cp01237c.

[18] J.S.D. Rodriguez, T. Ohigashi, C.-.C. Lee, M.-.H. Tsai, C.-.C. Yang, C.-.H. Wang, C. Chen, W.-.F. Pong, H.-.C. Chiu, C.-.H. Chuang, Modulating chemical composition and work function of suspended reduced graphene oxide membranes through electrochemical reduction, Carbon 185 (2021) 410–418, https://doi.org/10.1016/j.carbon.2021.09.015.

[19] Graphenea, Graphene oxide water dispersion, (2020). http://www.graphenea.com/collections/graphene-oxide/products/graphene-oxide-4-mg-ml-water-dispersion-1000-ml (accessed November 4, 2021).

[20] U. Lange, V.M. Mirsky, Separated analysis of bulk and contact resistance of conducting polymers: comparison of simultaneous two- and four-point measurements with impedance measurements, J. Electroanal. Chem. 622 (2008) 246–251, https://doi.org/10.1016/j.jelechem.2008.06.013.

[21] V. Kulikov, V.M. Mirsky, T.L. Delaney, D. Donoval, A.W. Koch, O.S. Wolfbeis, High-throughput analysis of bulk and contact conductance of polymer layers on electrodes, Meas. Sci. Technol. 16 (2005) 95–99, https://doi.org/10.1088/0957-0233/16/1/013.

[22] Q. Hao, V. Kulikov, V.M. Mirsky, Investigation of contact and bulk resistance of conducting polymers by simultaneous two- and four-point technique, Sens. Actuators B 94 (2003) 352–357, https://doi.org/10.1016/S0925-4005(03)00456-8.

[23] G. Kresse, J. Hafner, *Ab initio* molecular dynamics for liquid metals, Phys. Rev. B 47 (1993) 558–561, https://doi.org/10.1103/PhysRevB.47.558.

[24] G. Kresse, J. Furthmüller, Efficiency of ab-initio total energy calculations for metals and semiconductors using a plane-wave basis set, Comput. Mater. Sci. 6 (1996) 15–50, https://doi.org/10.1016/0927-0256(96)00008-0.

[25] G. Kresse, J. Furthmüller, Efficient iterative schemes for *ab initio* total-energy calculations using a plane-wave basis set, Phys. Rev. B 54 (1996) 11169–11186, https://doi.org/10.1103/PhysRevB.54.11169.

[26] J.P. Perdew, K. Burke, M. Ernzerhof, Generalized gradient approximation made simple, Phys. Rev. Lett. 77 (1996) 3865–3868, https://doi.org/10.1103/PhysRevLett.77.3865.

[27] P.E. Blöchl, Projector augmented-wave method, Phys. Rev. B 50 (1994) 17953–17979, https://doi.org/10.1103/PhysRevB.50.17953.

[28] J.J.P. Stewart, Stewart computational chemistry - MOPAC, (2016). http://openmopac.net/ (accessed November 4, 2021).

[29] J.J.P. Stewart, Optimization of parameters for semiempirical methods VI: more modifications to the NDDO approximations and re-optimization of parameters, J. Mol. Model. 19 (2013) 1–32, https://doi.org/10.1007/s00894-012-1667-x.

[30] A. Klamt, G. Schüürmann, COSMO: a new approach to dielectric screening in solvents with explicit expressions for the screening energy and its gradient, J. Chem. Soc., Perkin Trans. 2 (1993) 799–805, https://doi.org/10.1039/P29930000799.

[31] K. Momma, F. Izumi, VESTA 3 for three-dimensional visualization of crystal, volumetric and morphology data, J. Appl. Crystallogr. 44 (2011) 1272–1276, https://doi.org/10.1107/S0021889811038970.

[32] Jmol, Jmol: an open-source Java viewer for chemical structures in 3D., (2010). http://www.jmol.org/ (accessed November 4, 2021).

[33] I. Jung, D.A. Field, N.J. Clark, Y. Zhu, D. Yang, R.D. Piner, S. Stankovich, D.A. Dikin, H. Geisler, C.A. Ventrice, R.S. Ruoff, Reduction kinetics of graphene oxide determined by electrical transport measurements and temperature programmed desorption, J. Phys. Chem. C 113 (2009) 18480–18486, https://doi.org/10.1021/jp904396j.

[34] O.M. Slobodian, P.M. Lytvyn, A.S. Nikolenko, V.M. Naseka, O.Yu. Khyzhun, A. v. Vasin, S. v. Sevostianov, A.N. Nazarov, Low-temperature reduction of graphene oxide: electrical conductance and scanning kelvin probe force microscopy, Nanoscale Res. Lett. 13 (2018) 139, https://doi.org/10.1186/s11671-018-2536-z.

[35] K. Yin, H. Li, Y. Xia, H. Bi, J. Sun, Z. Liu, L. Sun, Thermodynamic and kinetic analysis of lowtemperature thermal reduction of graphene oxide, Nano-Micro Lett. 3 (2011) 51–55, https://doi.org/10.1007/BF03353652.

[36] Y. Qiu, F. Collin, R.H. Hurt, I. Külaots, Thermochemistry and kinetics of graphite oxide exothermic decomposition for safety in large-scale storage and processing, Carbon 96 (2016) 20–28, https://doi.org/10.1016/j.carbon.2015.09.040.

[37] S. Xue, B. Garlyyev, S. Watzele, Y. Liang, J. Fichtner, M.D. Pohl, A.S. Bandarenka, Influence of alkali metal cations on the hydrogen evolution reaction activity of Pt,

Ir, Au, and Ag Electrodes in Alkaline Electrolytes, ChemElectroChem 5 (2018) 2326–2329, https://doi.org/10.1002/celc.201800690.

[38] A. Viinikanoja, Z. Wang, J. Kauppila, C. Kvarnström, Electrochemical reduction of graphene oxide and its in situ spectroelectrochemical characterization, Phys. Chem. Chem. Phys. 14 (2012) 14003–14009, https://doi.org/10.1039/c2cp42253k.

[39] A.C. Ferrari, J. Robertson, Interpretation of Raman spectra of disordered and amorphous carbon, Phys. Rev. B 61 (2000) 14095–14107, https://doi.org/10.1103/PhysRevB.61.14095.

[40] R.R. Nair, W. Ren, R. Jalil, I. Riaz, V.G. Kravets, L. Britnell, P. Blake, F. Schedin, A. S. Mayorov, S. Yuan, M.I. Katsnelson, H.M. Cheng, W. Strupinski, L.G. Bulusheva, A.v. Okotrub, I.v. Grigorieva, A.N. Grigorenko, K.S. Novoselov, A.K. Geim, Fluorographene: a two-dimensional counterpart of Teflon, Small 6 (2010) 2877–2884, https://doi.org/10.1002/smll.201001555.

[41] A. Eckmann, A. Felten, A. Mishchenko, L. Britnell, R. Krupke, K.S. Novoselov, C. Casiraghi, Probing the nature of defects in graphene by Raman spectroscopy, Nano Lett. 12 (2012) 3925–3930, https://doi.org/10.1021/nl300901a.

[42] J.A. Quezada Renteria, C. Ruiz-Garcia, T. Sauvage, L.F. Chazaro-Ruiz, J.R. Rangel-Mendez, C.O. Ania, Photochemical and electrochemical reduction of graphene

oxide thin films: tuning the nature of surface defects, Phys. Chem. Chem. Phys. 22 (2020) 20732–20743, https://doi.org/10.1039/d0cp02053b.

[43] A. Lerf, H. He, M. Forster, J. Klinowski, Structure of graphite oxide revisited, J. Phys. Chem. B 102 (1998) 4477–4482, https://doi.org/10.1021/jp9731821.

[44] X. Gao, J. Jang, S. Nagase, Hydrazine and thermal reduction of graphene oxide: reaction mechanisms, product structures, and reaction design, J. Phys. Chem. C 114 (2010) 832–842, https://doi.org/10.1021/jp909284g.

[45] S. Stankovich, D.A. Dikin, R.D. Piner, K.A. Kohlhaas, A. Kleinhammes, Y. Jia, Y. Wu, S.B.T. Nguyen, R.S. Ruoff, Synthesis of graphene-based nanosheets via chemical reduction of exfoliated graphite oxide, Carbon 45 (2007) 1558–1565, https://doi.org/10.1016/j.carbon.2007.02.034.

[46] D.W. Boukhvalov, M.I. Katsnelson, A.I. Lichtenstein, Hydrogen on graphene: electronic structure, total energy, structural distortions and magnetism from first-principles calculations, Phys. Rev. B 77 (2008), 035427, https://doi.org/10.1103/PhysRevB.77.035427.

[47] A.S. Dobrota, S. Gutić, A. Kalijadis, M. Baljozović, S.v. Mentus, N.v. Skorodumova, I.A. Pašti, Stabilization of alkali metal ions interaction with OH-functionalized graphene: via clustering of OH groups-implications in charge storage applications, RSC Adv. 6 (2016) 57910–57919, https://doi.org/10.1039/c6ra13509a.

The effects of deposition manner and rate on structure and morphology of porous ZnSe nanolayers: Modification of Phonon Confinement Model for resonant Raman conditions

D. Nesheva[a], M. Grujić-Brojčin[b,*], M.J. Šćepanović[b], Z. Levi[a], V. Dzhurkov[a], T. Hristova-Vasileva[a], B. Vasić[b]

[a] *Georgi Nadjakov Institute of Solid State Physics, Bulgarian Academy of Sciences, Tzarigradsko Chaussee 72, 1784 Sofia, Bulgaria*
[b] *Center for Solid State Physics and New Materials, Institute of Physics, University of Belgrade, Pregrevica 118, Belgrade 11080, Serbia*

ARTICLE INFO

ABSTRACT

Nanolayers of porous ZnSe with thickness of ~50 nm were prepared by thermal vacuum evaporation, applying continuous and periodically interrupted deposition at different deposition rates. The surface morphology and film composition are studied by SEM and EDS methods. The XRD and Raman scattering measurements are used to confirm zinc blende ZnSe crystal structure. The Phonon confinement model is modified to analyze the Raman spectra excited by different laser lines both in non-resonant and near-resonant conditions. This analysis provides more profound insight in the ZnSe layers composition, nano-crystallite size and crystal lattice strain. The Raman results are also supported by the spectroscopic ellipsometry regarding the energy gap and porous properties of ZnSe layers. This study shows that both manner and rate of deposition significantly affect the nanolayers structure, morphology and optical properties and provide preparation of films with properties suitable for application which requires specific porous parameters important for the films chemical sensitivity.

1. Introduction

Zinc selenide, ZnSe, is a semiconductor compound which has a variety of interesting properties that make it suitable for many applications. The large direct band gap and good transparency of ZnSe in the visible and infrared regions make it promising material for application in solar cells as window layer [1,2]. It can also be applied in light emitting devices and laser diodes [3–5], photodetectors [6,7], sensors, photocatalysts [8], etc. A variety of thin film deposition techniques, such as molecular beam epitaxy [9,10], RF sputtering [11], thermal vacuum evaporation [12–15], organometallic chemical vapor deposition [16,17], electrodeposition [18], solution growth [19], etc. has been employed for the growth of high-quality ZnSe thin films. Thermal vacuum evaporation of ZnSe is among the techniques frequently used for the film preparations, since it is relatively simple, low cost and allows high deposition rates and direct transfer of the stoichiometry of the source powder of an II-VI binary compound to the film on the substrate. Using this method one can also achieve

excellent film homogeneity, constant layer thickness and very good surface smoothness [20,21].

It is well known that the surface morphology, crystallinity, microstructure, optical and electrical properties of films depend on the deposition conditions and a careful selection of these conditions plays an important role in attaining the desired properties of thin films. Numerous articles have been published in the recent years regarding the structural, optical and electrical characterization of ZnSe thin films prepared by thermal vacuum evaporation on different types of substrates and under different vacuum pressures [22]. It has been demonstrated that the films properties depend significantly on the substrate and vacuum pressure, as well as on the substrate temperature and post-deposition thermal treatment. Significant attention has also been addressed to the effect of the ZnSe film thickness on the optical properties, microstructure and surface morphology of the films [20–24]. It has been also found that deposition rate is an important parameter that significantly affects the properties of films of various compositions prepared by physical vapor deposition [25–27]. However, in the case of ZnSe films prepared by thermal vacuum evaporation the effect of the deposition rate has not obtained proper attention. It has been shown recently that the change of the deposition rate causes changes in the

---

* Corresponding author.
E-mail address: myramyra@ipb.ac.rs (M. Grujić-Brojčin).

refractive index, optical band gap, dislocation density and surface morphology of the films [28].

Normally, when applying thermal vacuum evaporation/sublimation, a continuous vapor deposition on the substrate takes place. Although significantly less frequent, periodic interruption of the steam flow is made and the so-called step-by-step film deposition has been applied for thin film preparation [13,29,30]. A study on ZnSe thin films, prepared by closed space sublimation process and step-by-step deposition on substrates at room temperature, has shown that the films demonstrate a good quality, high stability, fine adhesion, and closely packed structure and they are suitable for optoelectronic applications [30]. We have shown that the preparation of ~ 50 nm thick CdSe films by applying of step-by-step deposition resulted in considerably smaller grain size when compared to continuous film deposition and this resulted in higher room temperature chemical sensitivity to a set of vapors (water, ethanol, ammonia, iodine and acetone in air) [31]. Moreover, our room temperature experiments on the sensitivity to ethanol vapors of step-by-step ZnSe layers have revealed an increase of the layers sensitivity with decreasing film thickness and deposition rate [32,33]. However, the effect of the manner of deposition on the properties of ZnSe films prepared by thermal vacuum evaporation has not been studied in detail. New information regarding this effect will allow preparation of films with properties suitable for certain application.

In this work, the influence of the deposition rate and manner of deposition (continuous, periodically interrupted) on the crystallinity, nanostructure, surface morphology and optical properties of ~50 nm thick ZnSe films prepared by thermal vacuum evaporation is explored. The films properties were studied by using the X-ray diffraction method, scanning electron microscopy, atomic force microscopy, spectroscopic ellipsometry, and micro-Raman scattering measurements under resonant and non-resonant conditions. A correlation between the results has been established. A modification of the Phonon Confinement Model (PCM) has been proposed, which for the first time, as far as we know, very well simulates the near-resonant Raman spectra of nanocrystalline materials.

2. Experimental details

Nanolayers of ZnSe were deposited on Corning 7059 glass substrates at room temperature with deposition rates V_d = 0.5, 1.5 and 3.0 nm/s. The layers were produced by thermal evaporation of powdered ZnSe (Merck, Suprapure) at a residual pressure of 3×10^{-4} Pa. A tantalum crucible located at the bottom of a cylindrical screen (not intentionally heated) was used for the evaporation of ZnSe. The top of the screen was close to the substrates; thus, evaporation in a quasi-closed volume was carried out. The deposition rate and layer thickness were controlled by a preliminary calibrated quartz microbalance system. The layers were prepared by applying two approaches: (*i*) continuous deposition (CD), in which the substrates were fixed over the crucible and (*ii*) periodically interrupted deposition (PD) - during the deposition the substrates were rotated at a rate of 8 turns min^{-1} and spend only 1/12 part of the turn time (~0.6 s) over the crucible. At each turn a portion of ZnSe vapors condenses on the substrates and the time interval between the consecutive portions reaching the substrates is around 7 s; the amount of material in each portion depends on the deposition rate. The film thickness determined from the spectroscopic ellipsometry data is given in Table 1 together with the film deposition rate. Relative high deviation (of ~20%) from the intentional thickness of ~ 50 nm is observed only at the highest deposition rate.

The films crystal structure was investigated by X-ray diffraction (XRD) measurements performed in the 2θ range by PANalytical Empyrean diffractometer using the CuKα line.

The surface morphology was investigated by scanning electron microscopy (SEM) using a JEOL JSM 6390 microscope, operated at 20 kV (magnification 2000×, 5000×, 10000×, 15000× and 20000× in conjunction with energy dispersive X-ray spectroscopy (EDS, Oxford INCA Energy 350) equipped with ultrahigh resolution scanning system (ASID-3D) in regimes of secondary electron image (SEI) and back scattered electron image (BEC). Also, the atomic force microscopy (AFM) based imaging of film surface was done at ambient conditions, using Ntegra Prima AFM system and NSG01 probes.

The optical refraction, absorption and porosity of the films were explored by multiple-angle spectroscopic ellipsometry (SE) measurements performed on a Woollam's automatic spectroscopic ellipsometer M2000D working in the reflection mode. SE data were taken in the wavelength range from 193 to 1000 nm at angles of incidence of 50°, 55° and 60°. Complete EASE 5.10 J. A. Woollam Co., Inc. software was used for data acquisition and analysis. A model based on the Bruggeman effective medium approximation was applied in the spectral range of 400–1000 nm. A modeled structure that consists of glass substrate and a porous ZnSe layer was used for sample description. During the fitting procedure reference data for bulk ZnSe were used, which are included in the Complete EASE program.

Raman scattering measurements were performed by using the TriVista TR557 triple spectrometer system equipped with a nitrogen-cooled CCD detector. The samples were excited in backscattering micro-Raman configuration by deep blue, blue, green or red line of a mixed Ar⁺/Kr⁺ laser with wavelengths of 457.9, 488, 514.5 and 647 nm, respectively. The Raman scattering measurements have been performed in the air, at room temperature, using objective lens with 50× or 100× magnification to focus the laser to a spot size of around 1 μm (depending on the numerical aperture of objectives and laser wavelength). The laser power under the objective was less than 0.5 mW, unless otherwise noted. To record the high resolution spectra 900/900/1800 grooves/mm diffraction grating combination was used in TriVista system.

3. Results and discussion

3.1. Surface morphology and film composition

The SEM and AFM imaging of the film surface allowed us to get general information about surface morphology. Two representative SEM images of the same magnification, taken on a step-by-step ZnSe thin film prepared at deposition rate of 0.5 nm/s and continuously prepared film at deposition rate of 3.0 nm/s are shown in the Fig. 1(a) and (b), respectively. It is seen that the surface is grainy with single outgrowths (hillocks) protruding out, more pronounced on the surface shown in Fig. 1(a). Two dimensional (2D) and three-dimensional (3D) AFM surface images of the sample prepared by step-by-step method at deposition rate of 0.5 nm/s are shown in Fig. 1(c) and 1(d), respectively. These images reveal porous structure of the film surface which is associated with big grains surrounded by large holes. The SEM and AFM results are in general agreement with the SE results on the film porosity shown later in the text. However, larger structures seen in AFM images, recorded few months after the SEM measurements, are probably induced by gradual merging/coalescence of the pores and the formation of larger islands and holes during this time period.

The vaporization of cadmium and zinc sulfides, selenides, and tellurides has been thoroughly examined in many studies [34] and references therein]. It has been reported that the vaporization coefficients of these compounds are in the range 0.1–0.3, which suggests that, not only the most stable diatomic molecules, but also free S, Se, and Te atoms can be detached from the surface in the course of vaporization. The EDS results obtained for a PD film deposited at a rate of 0.5 nm/s have shown that the film bulk is Se-rich

Table 1
Deposition manner and rate of ZnSe films together with film thickness estimated from SE measurements, and corresponding XRD results: the diffraction angle and FWHM of (111) diffraction peak (Lorentzian fit), used to calculate lattice parameter, nanocrystallite size, microstrain and dislocation density by the Eqs. (2), (1), (3) and (4), respectively.

Deposition manner/ Sample name	Deposition rate (nm/s)/ Film thickness (nm)	Diffraction angle 2θ (°)	FWHM (°)	Lattice parameter a (nm)	Nanocryst. size D (nm)	Microstrain ε (%)	Dislocation density δ (10^{11} cm^{-2})
Periodic PD12	0.5/56	27.49(6)	1.2(2)	0.5614(9)	7.0 ± 0.9	0.52(7)	20(5)
Continuous CD22	0.5/52	27.32(5)	0.9(1)	0.5649(5)	8.9 ± 0.7	0.41(3)	12(2)
Periodic PD32	1.5/51	27.26(4)	0.8(1)	0.5661(4)	9.9 ± 0.7	0.37(3)	10(1)
Continuous CD42	1.5/52	27.19(3)	0.67(8)	0.5675(2)	12.1 ± 0.7	0.30(2)	6.5(7)
Periodic PD62	3.0/43	27.27(6)	0.8(2)	0.5657(6)	10.1 ± 1.0	0.36(4)	9(2)
Continuous CD52	3.0/64	27.20(1)	0.44(3)	0.5673(1)	18.3 ± 0.6	0.198(7)	2.9(2)

(the ratio R = (at% of Zn)/(at% of Se) is around 0.8), while in the hillocks a Zn excess has been detected (R ~ 1.25). The existence of over stoichiometric Se in the sample bulk may be due to the low deposition rate which corresponds to relatively low temperature of the Ta crucible. No appreciable amount of carbon was detected and because of the usage of Corning 7059 glass substrate, no information was obtained for presence of oxygen atoms in the film and its amount.

3.2. Crystal structure and crystallite size estimated from XRD data

The X-ray diffraction patterns of ZnSe films, prepared with deposition rate of 0.5 nm/s, 1.5 nm/s and 3.0 nm/s by applying continuous or periodically interrupted deposition, together with the pattern of the Corning 7059 glass substrate, are shown in Fig. 2. The broad hump in the background of all ZnSe patterns originates mostly from the amorphous glass substrate, but also could point to the presence of some amorphous phase in the ZnSe thin films [35,36].

The most prominent diffraction peak at about $2\theta = 27.31°$, followed by two low intensity peaks at around 45.61° and 53.81°, are observed in all ZnSe XRD patterns. These features are in a very good agreement with the characteristic diffraction peaks corresponding to (111), (220), and (311) planes of a cubic zinc blende ZnSe structure (JCPDS card no. 37–1463 of ZnSe with lattice parameter a = 5.668 Å). The intensity of XRD peaks observed in ZnSe patterns varies with changing deposition rate and manner of deposition; it increases with increase of deposition rate and with application of continuous deposition. Also, these peaks were considerably broadened in comparison to bulk material due to small size of the ZnSe nanocrystallites in investigated films.

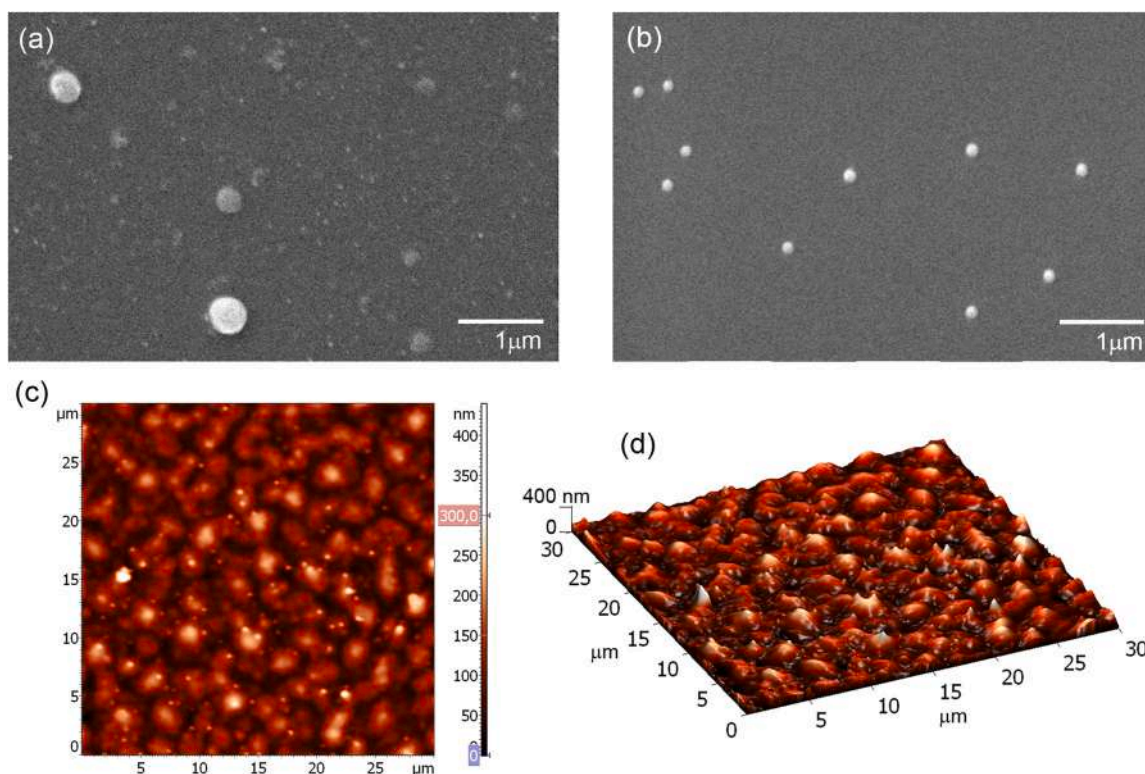The average nanocrystallite size (D) was estimated using the Scherrer formula [37]:

Fig. 1. SEM images of ZnSe thin films samples prepared by (a) step-by-step method at deposition rate of 0.5 nm/s and (b) continuous method at 3.0 nm/s rate; AFM images of the sample prepared by step-by-step method at deposition rate of 0.5 nm/s: (c) 2D topography and (d) 3D topography.
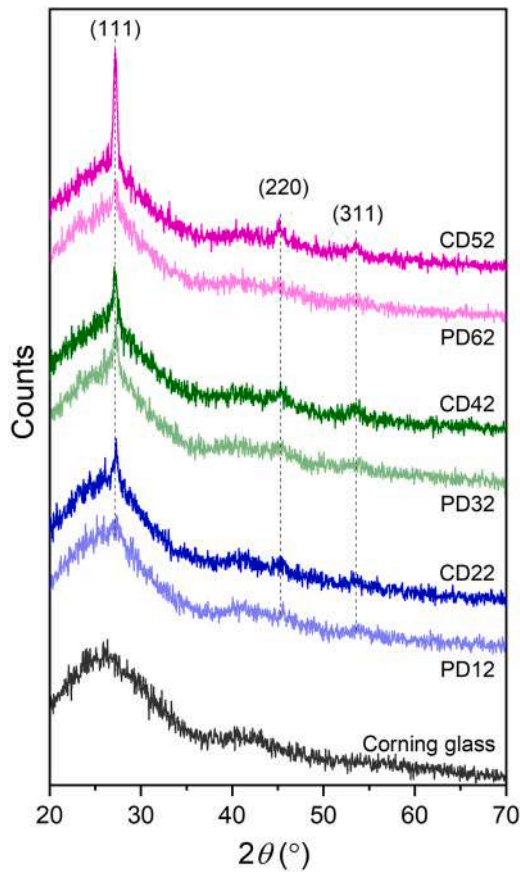
Fig. 2. X-ray diffraction patterns of pairs of ZnSe films prepared with deposition rate of 0.5 nm/s (PD12, CD22), 1.5 nm/s (PD32, CD42) and 3.0 nm/s (PD62, CD52) by applying continuous (CD) or periodically interrupted (PD) deposition, with characteristic Miller indices of zinc blende ZnSe crystal structure given in the parentheses. The patterns of ZnSe films are upshifted for clarity.

$$D = \frac{K\lambda}{\beta cos\theta} \tag{1}$$

where $\lambda = 1.5418$ Å is the wavelength of X-ray radiation and K is a Scherrer's constant with the most common value of 0.94 for spherical crystals with cubic symmetry [37]. Diffraction angle (θ) and full-widths-at-half-maximum (FWHM, β) estimated by fitting of (111) diffraction peak by Lorentzian shape, are shown in Table 1 for all investigated ZnSe samples. Based on these values, in addition to nanocrystallite size, the values of lattice parameter, microstrain, and dislocation density were also calculated (Table 1). The lattice parameter a in cubic structure is determined according to the equation:

$$d = \frac{a}{\sqrt{(h^2 + k^2 + l^2)}} \tag{2}$$

where the lattice spacing d is calculated using Bragg's formula ($d = \lambda/2sin\theta$), whereas h, k and l represent the lattice planes. The microstrain ε was calculated as [38].

$$\varepsilon = \beta cos\theta/4 \tag{3}$$

For cubic ZnSe thin films the dislocation density δ has been calculated on the basis of Williamson and Smallman method, using the formula [15].

$$\delta = 15\varepsilon/aD \tag{4}$$

From the interdependences of obtained values, as well as their dependences on deposition conditions several important conclusions may be drawn. It has been shown in Fig. 3 that the values of lattice parameter are around the ZnSe bulk value for the
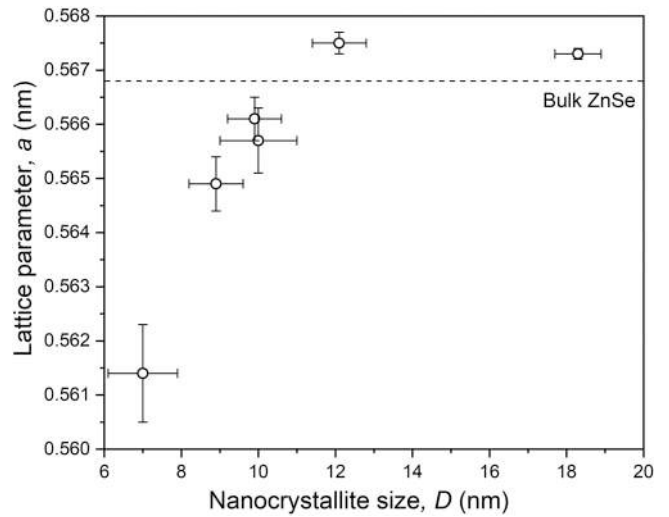

Fig. 3. The dependence of ZnSe lattice parameter on nanocrystallite size estimated from XRD data.
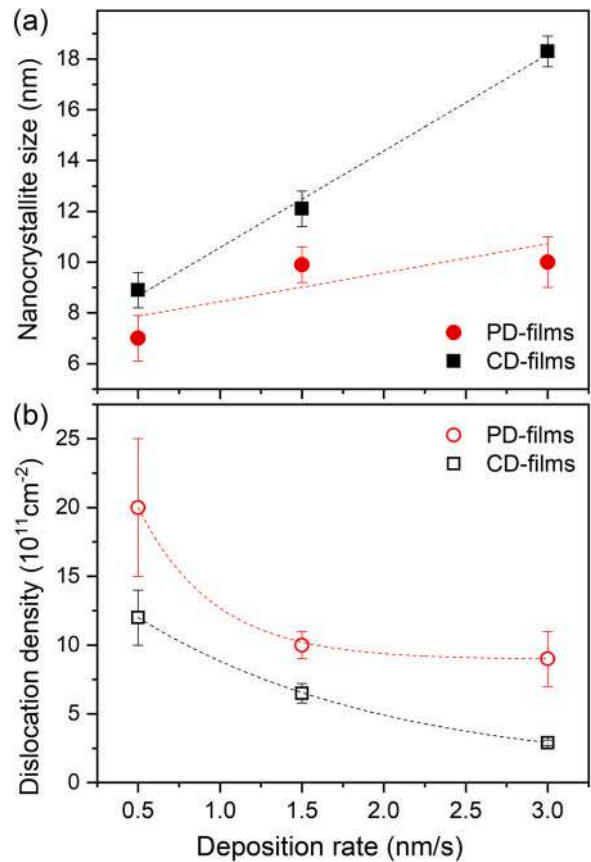

Fig. 4. The dependence of nanocrystallite size (a) and dislocation density (b) on film deposition rate. The dashed lines in (a) represent linear fits of the corresponding data points, whereas the lines in (b) are used as the guide for the eye only.

nanocrystallite size greater than 9 nm, whereas the reduction of nanocrystallite size is followed by drastic decrease in lattice parameter, indicating the existence of significant compressive strain in the films with small ZnSe nanocrystals. On the other hand, Fig. 4(a) shows that at each deposition rate the nanocrystallite size in CD-films is larger than that in the PD-films. Moreover, a considerable linear increase of the nanocrystallite size with increasing deposition rate is seen in continuously deposited CD-films (from 8.9 nm to
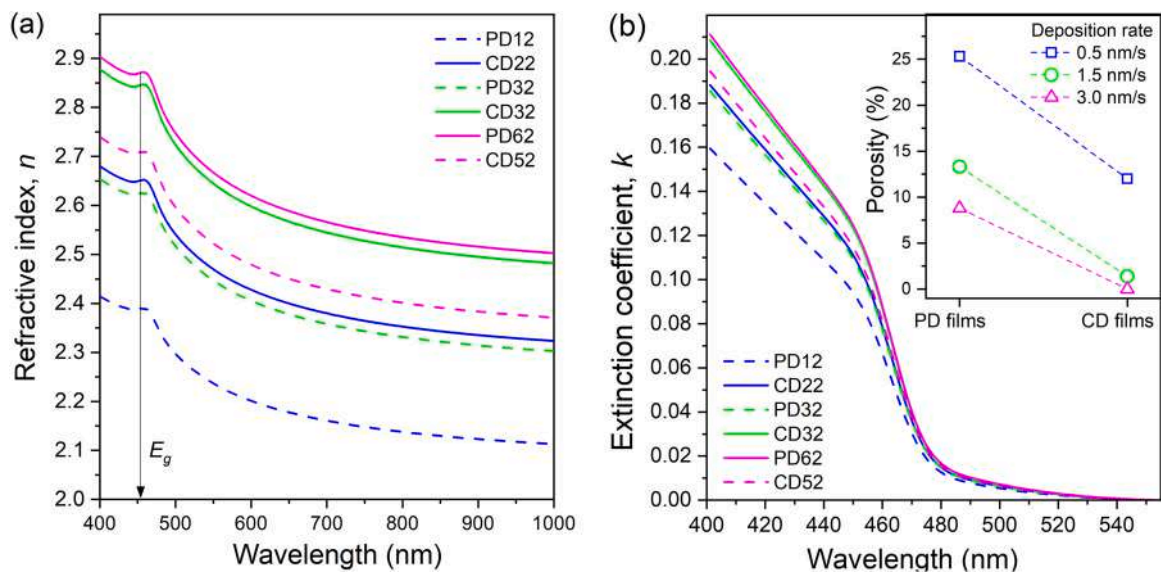
Fig. 5. Refractive index spectra (a), spectral dependences of the extinction coefficient (b) of 50 nm thick ZnSe thin films prepared at various deposition conditions denoted in the Figs. Porosity data are shown in the inset of (b).

~18 nm). A weaker size increase with the deposition rate is also observed in the PD-films, prepared by periodically interrupted deposition (from ~7 nm to ~10 nm). The crystallite size increase with the deposition rate has been reported for thin films from various materials prepared by thermal vacuum evaporation [25–27]. A linear increase of the crystallite size (in the range of 21.6–42.9 nm) has also been reported in Ref. [28] for 250 nm thick ZnSe films, prepared by continuous deposition on glass substrates at room substrate temperature, when the deposition rate increases from 0.2 to 0.8 nm/s. The grater crystallite sizes in these films are probably due to the five times larger film thickness [39,40]. Moreover, the Fig. 4(b) shows that the increase of deposition rate triggers off the decrease of dislocation density both in CD- and PD-films, indicating an improvement in ZnSe crystal quality with increasing deposition rate.

3.3. Optical properties determined by spectroscopic ellipsometry

From spectroscopic ellipsometry data refractive index n, extinction coefficient k and optical absorption coefficient α of the films in the spectral range of 400–1000 nm were calculated by applying the Bruggeman's effective medium approximation. Refractive index spectra of all types of ZnSe thin films are shown in Fig. 5(a). It can be seen that at each deposition rate n of the continuously deposited film has higher value than that of the corresponding periodically deposited film. Similar dependence is observed for the extinction coefficient in the wavelength region 400–450 nm (Fig. 5(b)). The optical band gap energy, estimated from the extinction coefficient k according to standard procedure [41] has almost the same value of $E_g \approx 2.73$ eV in all investigated films (as denoted in Fig. 5(a)).

The refractive index and extinction coefficient describe the light propagation in the films and, in general, the refractive index of a material increases with its density [42] but there is no an overall relationship between the refractive index and the density of all materials [43].

We supposed that the observed lower n (and k) values of the PD-films are related to lower films density. By applying the Bruggeman's effective medium approximation the film's porosity (i.e. the volume fraction of pores in the film in %) was determined. Below, porosity is used to follow the changes in the film's density caused by the changes in the preparation conditions. The porosity variations are shown in the inset of Fig. 5(b) It is clearly seen that for each

deposition rate the porosity value of the periodically deposited PD-film is significantly higher than that of the CD-film i.e. the application of periodic deposition results in lower film density than the application of continuous deposition. Moreover, one can see from the inset that the increase of the deposition rate results in a film density increase.

At the first stage of thin film deposition, an embryo (nanocluster) formation occurs which depends on the temperature, chemical nature, structure and cleanness of the substrate surface [39]. Further material deposition results in coalescence of nanoclusters and grain formation and therefore grainy microstructure has been observed for many evaporated and sputtered films [44]. As long as the deposition process involves a phase transformation from the vapor to the solid state, voids (pores) are generally formed in the films irrespective of the preparation method (evaporation, sputtering or electrodeposition) [45]. The observed variations in the films microstructure have been explained by the so-called structure zone model [46]. According to this model, at low substrate temperatures ($T_s < 0.3T_m$, T_m – melting temperature of the film material) the diffusion of atoms reaching the surface (adatoms) is too weak to ensure the filling of the shadowed surface regions (self-shadowing effect) and this leads to formation of columnar structure and pores. At higher temperatures ($T_s > 0.5T_m$) the surface diffusion of adatoms becomes intense and this leads to growth of dense films with big grains. In the present work, the ZnSe films were deposited at substrate temperature $T_s \approx 300$ K. Even if a slight heating of the substrates by radiation from the tantalum crucible occurs, the substrate temperature is rather low ($T_s < < 0.3T_m$) and according to the zone model the observed variations in the film microstructure should be caused by the changes of both the deposition rate and the manner of deposition.

The observed increase of the crystallite size with the increase of the deposition rate (Fig. 4(a)) can be understood by considering the processes of surface diffusion of adatoms, nucleation and coalescence of nuclei during deposition. In the case of thermal evaporation in vacuum the kinetic energy of atoms is only a few tenths of 1 eV [46]. Therefore, at substrate temperatures $T_s \approx 300$ K, the surface diffusion of Zn and Se atoms should be rather slow and the density of nuclei which can potentially coalesce to form grains is small, resulting in a small grain size. During continuous film deposition, when deposition rate increases, the number of atoms reaching the

surface per unit time is higher, the number of nuclei formed on the surface can be larger and their coalescence can result in greater crystallite size (Fig. 4(a)) and lower film porosity (the inset in Fig. 5(b)).

Residual gases under vacuum chamber can also influence the growth of the individual grains [47]. Adsorbed impurity atoms and/ or precipitates accumulated on the surface of growing crystallites can suppress their growth. It has been found that the ratio of the number of residual gas atoms adsorbed on the substrate (or on the surface of the growing film) to the number of film atoms arriving to the substrate surface per time and area is inversely proportional to the deposition rate [47] though the effect is not very strong. An increase of the deposition rate will reduce the influence of the residual gas atoms on the grain growth and will allow the formation of larger grains. Probably, in the case of continuous deposition of ZnSe films the observed linear nanocrystallite size increase with the deposition rate (Fig. 4(a)) is related to both the increase of the number of atoms reaching the surface per unit time and reduction of adsorbed residual atoms.

As seen in inset in Fig. 5(b) and Fig. 4(a) at a given deposition rate the nanocrystallite size in the ZnSe CD-film is larger than the size in the corresponding PD film and, also, the porosity of the PD-film is higher than that of the corresponding CD-film. It is mentioned in Experimental details that during periodically interrupted deposition the substrates were rotated at a rate of 8 turns min^{-1} and spend only 1/12 part of the turn time (~0.6 s) over the crucible as the time interval between two consecutive portions is ~7 s. Hence, one can assume that during the PD-deposition the amount of the adsorbed residual gas atoms is significantly greater than that adsorbed during the CD-deposition which can result in smaller nanocrystallite size and higher porosity of the PD-films.

3.4. Analysis of Raman scattering measurements results

In order to additionally analyze the nanostructure and phase composition of ZnSe films in dependence on deposition parameters, the Raman scattering measurements were performed using several laser lines of a mixed ArKr laser. Experimental Raman spectra of ZnSe films and Corning glass substrate taken by 514.5 nm laser line are shown in Fig. 6. The spectra of investigated ZnSe films are dominated by relatively broad feature, which is centered at about 254 cm^{-1} and has a similar maximum intensity in almost all films. Pronounced shoulders on both lower and higher frequency side of this feature indicate that it does not originate only from the longitudinal optical (LO) mode, positioned at ~252 cm^{-1} in bulk ZnSe crystal [48]. Mentioned feature is a bit narrower and centered at about 252 cm^{-1} without shoulder at higher frequency side only in the spectrum of the CD22 film. A feature which appears in all spectra of investigated films at about 210 cm^{-1} could be also attributed to ZnSe structure and it is assigned to transversal optical (TO) Raman mode. This mode is more pronounced in the spectra of CD films, whereas it is the least pronounced in the spectrum of the PD12 film. Beside the Raman feature in the frequency region of the first order TO and LO ZnSe modes, additional low intensity features could be noticed at the frequencies between 100 and 150 cm^{-1}, 350 and 400 cm^{-1}, as well as in the region of second order 2LO ZnSe mode, around 500 cm^{-1}.

When analyzing Raman spectra presented in Fig. 6, it should be kept in mind that the formation of Se phases during the deposition of porous ZnSe films is quite probable, as indicated by the results of EDS measurements, where the excess of Se in those films has been revealed. However, a detailed analysis of observed Raman features is not an easy task, primarily because selenium-related modes are often positioned at similar frequencies as modes originated from the ZnSe structure. Namely, the Se-related modes corresponding to trigonal t-Se chains at ~234 cm^{-1}, Se$_n$ chains in disordered
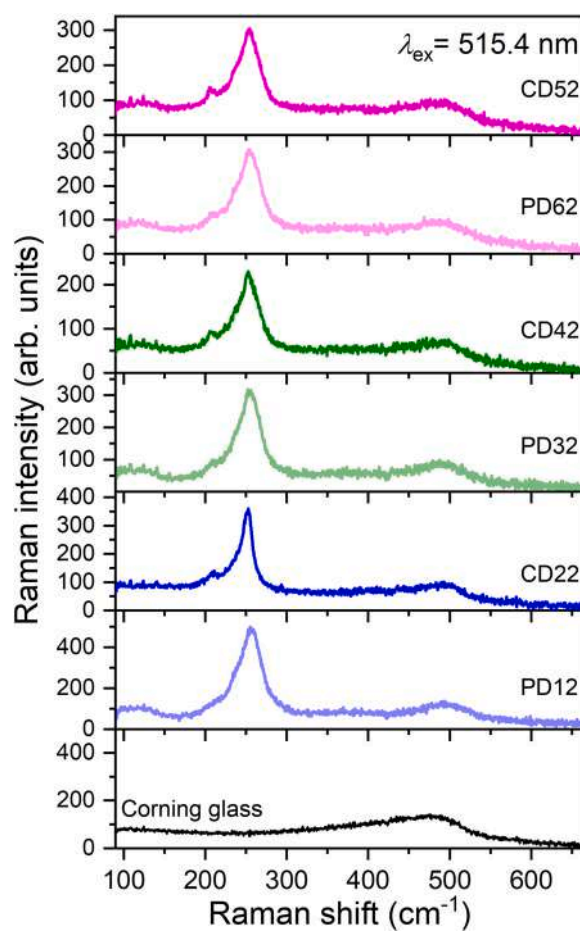

Fig. 6. Experimental Raman spectra of ZnSe films and Corning glass substrate taken by 514.5 nm laser line (all spectra are corrected with Bose-Einstein thermal correction factor). The irradiance $I_{ex} \approx 10^4$ Wcm^{-2}.

configurations at ~250 cm^{-1}, and Se$_8$ rings at ~260 cm^{-1} [49] are very close not only to the 1LO attributed to vibrations of only Se anions in ZnSe crystal lattice [50], but also to the surface optical mode and some second order ZnSe modes (which will be discussed below). An additional problem in Raman analysis is high sensitivity of selenium to laser irradiation. It is known that the increase of laser power density above 10^4 Wcm^{-2} during the Raman measurement leads to the appearance of modes related to t-Se [51], due to laser induced crystallization of amorphous selenium [52].

To reveal the selenium phase in as-deposited films the Raman measurements have been performed using red, green and blue laser lines, with the power density at the sample surface, so called irradiance $I_{ex} \approx 5 \times 10^3$ Wcm^{-2}. The spectra of the CD52 film are shown in Fig. 7(a) for the same irradiance of all three laser excitation wavelength. Note the absence of resonant enhancement of the t-Se phase related mode at about 235 cm^{-1} [51] in the case of excitation by the 647 nm laser line with photon energy close to the bandgap of Se (~1.9 eV at 300 K). On the other side, the slightly greater prominence of Se-related modes in the spectrum obtained by green line may be the consequence of their resonant enhancement at wavelength of 514.5 nm, also reported by Ohta et al. for selenium thin films with the structure resembling to the amorphous selenium [53]. In order to avoid possible resonant enhancement of the Se-related modes, the influence of laser power increase on Raman spectra of ZnSe films excited by 488 nm laser line is investigated. The spectra of CD52 presented in Fig. 7(b) have shown that increase of laser power causes the appearance and intensifying of Raman feature in the range of 105–140 cm^{-1}, which most likely originates (at least partially) from
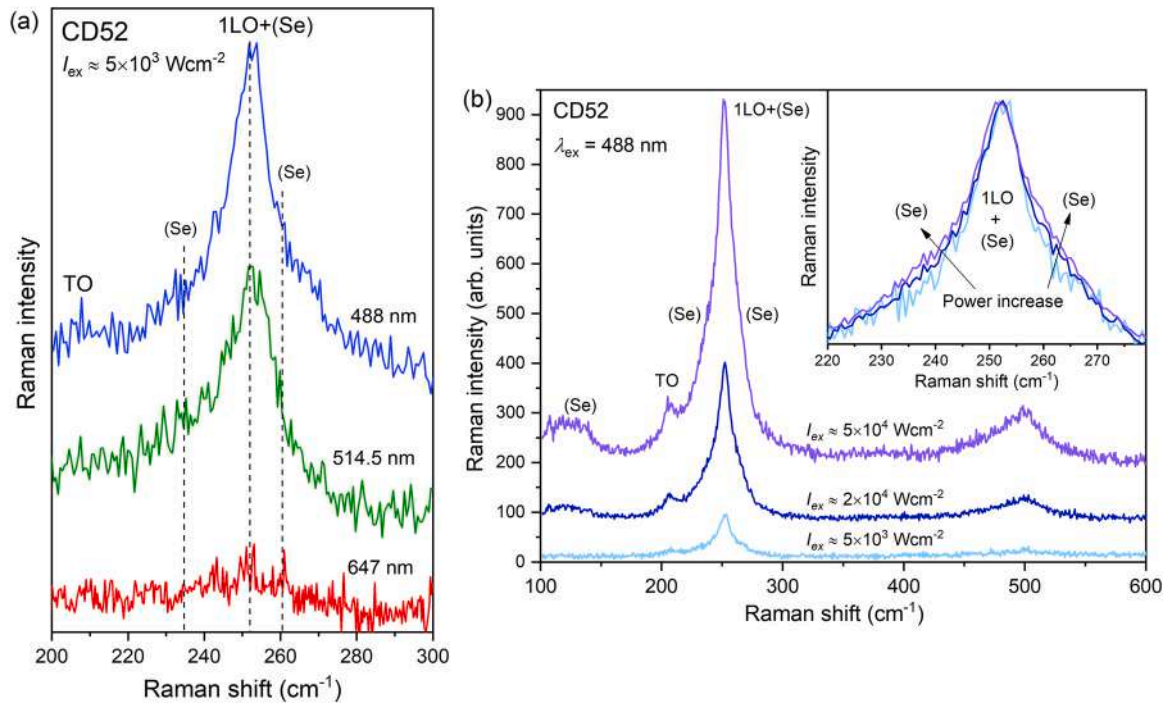
Fig. 7. Experimental Raman spectra of ZnSe film CD52 taken at (a) laser wavelengths of 488, 514.5 and 647 nm and (b) output laser power of 10, 40 and 100 mW at laser wavelength of 488 nm (the inset: normalized Raman spectra in the range of 1LO mode).

Se-related mode at about 115 cm^{-1} [53], as well as a slight increase in the intensity of the Se-related modes at around 235 and 265 cm^{-1} relative to the maximum intensity of central Raman feature at ~253 cm^{-1} (inset in Fig. 7(b)). These effects are accompanied by slight redshift of central position of the feature due to laser induced local heating at maximal applied power. All observations based on the results presented in Fig. 7 indicate that selenium exists mainly in amorphous phase in as-deposited films, but irradiation with higher laser power can lead to partial crystallization of the selenium phase.

In order to analyze numerous overlapping Raman modes in the range of 200–300 cm^{-1}, the Raman scattering measurements had to be performed under the conditions that provided the contribution of 1LO ZnSe mode to be emphasized, the impact of Se-related modes minimized, and the influence of Raman signal from glass substrate eliminated. Therefore, the Raman spectra of all ZnSe films were recorded using 457.9 nm laser line with photon energy of ~2.71 eV, which is very close to the band-gap energy (~2.73 eV) of investigated films, as estimated by SE measurements. It can be seen that Raman feature located at about 251 cm^{-1} in the spectra obtained by 457.9 nm line is centered at lower frequency, narrower and with less complex shape (Fig. 8) in comparison to the same feature in corresponding spectra recorded by 514.5 nm (Fig. 6) in all ZnSe films. The position, shape and intensity of this feature, together with the appearance of multiphonon modes at ~500 and 750 cm^{-1}, clearly indicate resonant enhancement of LO ZnSe Raman modes in all experimental spectra recorded by 457.9 nm laser line. This enhancement is the most pronounced in the spectrum of CD52 film, and it is the weakest in the spectra of PD12 and CD22 films. Thereby, the position of 1LO ZnSe mode slightly varies from about 250.6 (CD22) to 251.4 cm^{-1} (CD52), whereas the variation of mode linewidth is somewhat more pronounced, up to ~2 cm^{-1}.

The comparison of corresponding experimental spectra from Figs. 6 and 8, as well as the spectra shown in Fig. 7(a), point to variation of the 1LO Raman mode position and width with excitation laser energy. Note that similar behavior of 1LO mode has already
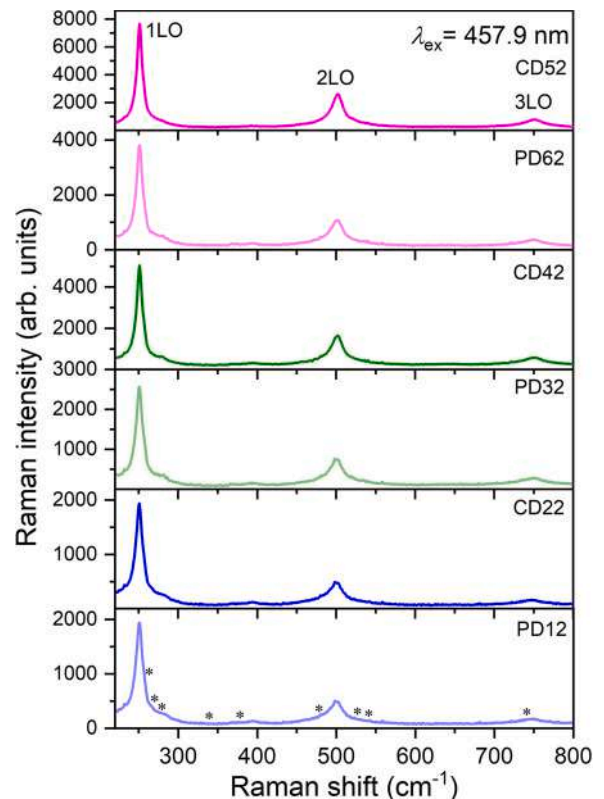

Fig. 8. Near-resonant Raman spectra of ZnSe films taken by 457.9 nm laser line with first (1LO), second (2LO), and third (3LO) order longitudinal optical Raman modes denoted. The asterisks denote the frequencies of plasma laser lines, where corresponding spectral points are obtained by extrapolation (all spectra are corrected with Bose-Einstein thermal correction factor). The irradiance $I_{ex} \approx 10^4$ Wcm^{-2}.

been observed in other II–VI semiconductor nanostructures, such as CdSe, CdS [54], but a complete explanation of this effect has not been given. So, Valakh et al. [55] have noticed a decrease of LO mode frequencies in the Raman spectra of CdSe nanoparticles with change of laser excitation wavelength λ_{ex} from 528.7 to 457.9 nm. These authors related this effect to the selection of smaller nanoparticles by shorter λ_{ex}, because smaller CdSe nanoparticles have a larger bandgap and LO mode redshift, due to stronger confinement of charge carriers and phonons, respectively. However, they have also noted that proposed explanation has a restriction: the shortening of wavelength excitation from 457.9 down to 441.7 nm is not followed by further redshift of LO frequency observed previously for longer λ_{ex} and predicted by the PCM. Probably best explanation for LO frequency variation with λ_{ex} has been offered for CdS quantum dots by Schreder et al. [56], assuming the nanocrystallite size distribution as a reason for the phonon shift, because different excitation wavelengths selectively enhance Raman contributions of quantum dots with certain diameters.

Because of all mentioned above, we have proposed in this paper a modification of the PCM that explains the changes of the 1LO mode shape and position with the change of excitation wavelengths, describing quantitatively its behavior in resonant conditions. To analyze the shift and broadening of 1LO Raman mode due to the effects of ZnSe nanocrystallite size and change in ZnSe lattice parameter, obtained both under non-resonant and near-resonant conditions, the PCM and modified PCM are used, respectively. Although phenomenological, the PCM successfully simulates important features such as phonon confinement and microstrain in relation to nanocrystallite size distribution. It also should be noted that PCM is not designed to consider some effects which also might have an impact on the Raman spectra, such as nonstoichiometry, electron-phonon interaction, plasmon modes phenomena, etc.

3.5. The modified phonon confinement model

The PCM is phenomenological method used to simulate experimental Raman spectra in order to take into account different nanosize induced effects. Several independent factors, like phonon confinement, strain, non-homogeneity of the size distribution and variations in phonon relaxation with crystallite size decreasing contribute to the position and linewidth of calculated Raman mode [48,57–60]. Due to crystallite size decrease, the phonons are confined and optical phonons over the entire Brillouin zone are contributing to the first-order Raman spectra. For effective crystallite size (or coherence length) L and Gaussian confinement function the Raman intensity $I(\omega,L)$ is calculated as a superposition of weighted Lorentzian contributions over the whole Brillouin zone [57,58]:

$$I(\omega, L) \propto \sum_{i=1}^{n} \int_{BZ} \frac{exp\left(\frac{-q^2L^2}{8\beta}\right)d^3q}{(\omega - (\omega_i(q) + \Delta\omega(q)))^2 + \left(\frac{\Gamma}{2}\right)^2} \tag{5}$$

with q as a wave vector, β - confinement strength and Γ - the intrinsic mode linewidth. The Brillouin zone is assumed to be homogeneous and isotropic sphere, and the sum is carried over n dispersion curves $\omega_i(q)$, with mode degeneracy and symmetry of directions in the Brillouin zone taken into account. Phonon dispersions are taken from corresponding bulk counterparts [59–61]. The additional shift $\Delta\omega(q)$ of Raman mode in Equation (r1), caused by relative variation of lattice parameter a, is introduced into the PCM as [48,60].

$$\Delta\omega(q) = -3\gamma\omega(q)\Delta a/a_0 \tag{6}$$

where γ represents Grüneisen parameter, $\Delta a/a_0$ - relative variation of unit cell parameter, and a_0 – unstrained unit cell parameter. According to this, the increase of unit cell parameter (tensile strain)

induces redshift of the Raman modes, whereas the decrease of unit cell parameter (compressive strain) leads to the blueshift.

For the nanocrystals with nanocrystallite size distribution the Raman scattering intensity $I(\omega)$ is given by [62,63],

$$I(\omega) \propto \int I(\omega, L)\rho(L)dL \tag{7}$$

The crystallite size distribution $\rho(L)$ here is defined as asymmetric Gaussian

$$\rho(L) = \frac{1}{\sqrt{2\pi}\sigma}\left\{[1 - h(L - L_0)]\exp\left(\frac{-(L - L_0)^2}{2\sigma_L}\right) + h(L - L_0)\right.$$
$$\left.\exp\left(\frac{-(L - L_0)^2}{2\sigma_R}\right)\right\} \tag{8}$$

with step-function

$$h(L - L_0) = \begin{cases} 0, & L < L_0 \\ 1, & L > L_0 \end{cases} \tag{9}$$

where L_0 is an effective crystallite size (correlation length), used as a central value of asymmetric Gaussian function, and σ is a mean halfwidth defined as $\sigma = (\sigma_L + \sigma_R)/2$. The σ_L and σ_R are standard deviations corresponding to left and right side of asymmetrical Gaussian curve.

Under resonant conditions, in nanomaterial with pronounced dependence of the energy gap on crystallite size and relatively wide nanocrystallite size distribution, the greatest contribution to the resonant Raman spectrum comes from Raman scattering on the crystallites whose energy gap is closest to the laser excitation energy. In order to simulate the resonant Raman spectrum, we have modified the PCM by introducing an additional weight function, in a manner which favors contributions of the particles with energy gap close to the excitation energy. For this purpose the Gaussian function is introduced into the integral over the nanocrystallite size (Eq. 7):

$$I(\omega) \propto \int I(\omega, L)\rho_{RES}(L)\rho(L)dL \tag{10}$$

where ρ_{RES} is narrow asymmetric Gaussian function (Eq. 8), centered around the size of the nanocrystallites whose gap corresponds exactly to the excitation energy, regardless the nanocrystallite size distribution in the sample.

The 1LO ZnSe Raman mode is simulated by using the following room temperature parameter set: the phonon strength $\beta = 4\pi^2$, intrinsic linewidth $\Gamma = 8$ cm^{-1} [64], Grüneisen parameter $\gamma = 0.82$ [65]. According phonon dispersions of zinc blende ZnSe by Kunc et al. [66], the dispersion functions along the high symmetry directions in Brillouin zone are expressed in approximate cosine form [60,67]:

$$\omega_i(q) = \omega_0 + B_i(1 - \cos(q\pi)) \tag{11}$$

where $\omega_0 = 252$ cm^{-1} [48] is the frequency of 1LO mode in the center of Brillouin zone, and the values of B_i constants (8, 18 and 26 cm^{-1}) are chosen do describe the phonon behavior outside the zone centre [66], along phonon dispersion curves Γ−X, Γ−K, and Γ−L, respectively. According to the XRD results (Fig. 2) lattice parameter a for nanocrystallites with size greater than 9 nm is assumed to be equal to bulk value (a_0 =0.5668 nm), whereas for smaller nanocrystallites parameter a is linearly decreased with the nanocrystallite size decreases. The crystallite size distribution $\rho(L)$ has been adjusted to obtain best fitting results. Through this procedure relatively wide nanocrystallite size distributions are estimated for each sample, similar to previous ZnSe film research [33,48,68]. In case of PCM modified to simulate the resonant spectra, the same weight function $\rho_{RES}(L)$ is used for all samples, as a very narrow profile centered around L_{RES}= 9.5 nm, because the bandgap corresponding this nanocrystallite size is equal to used laser excitation energy of 2.7077 eV
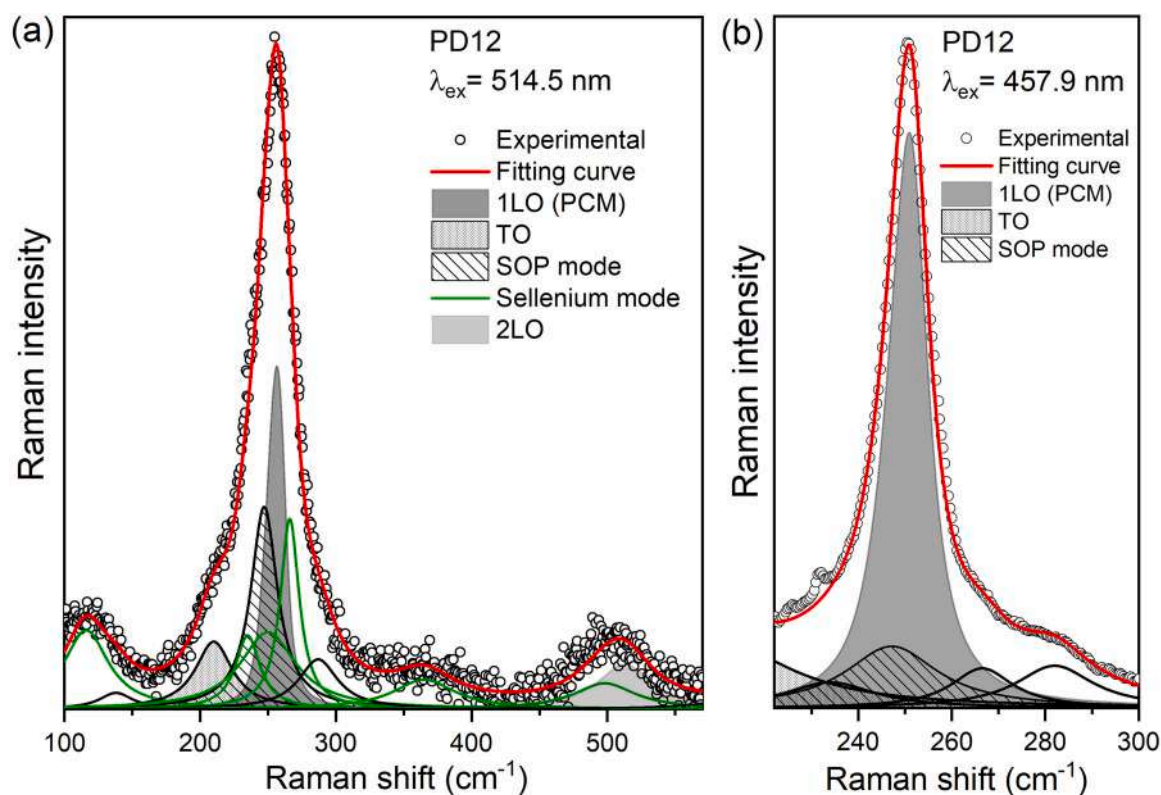
Fig. 9. An example of fitting procedure of experimental Raman spectra of ZnSe film (PD12) taken by 514.5 nm (a) and 457.9 nm (b) laser lines, together with the corresponding calculated results, given as the sum of 1LO ZnSe Raman mode obtained by the PCM, and other modes fitted by the Lorentzians (including surface optical phonon (SOP) mode). All experimental spectra are normalized to maximal intensity, corrected with Bose-Einstein thermal correction factor, and the spectra taken by 514.5 nm are additionally corrected by subtraction of appropriately scaled substrate spectrum.

Table 2
The results of PCM calculation of 1LO ZnSe Raman mode performed on experimental spectra taken by 457.9 and 515.4 nm.

Deposition manner/ Sample name	Phonon confinement model results				Nanocrystallite size, L_0 (nm)
	λ_{ex}= 457.9 nm		λ_{ex}= 514.5 nm		
	1LO Raman shift (cm^{-1})	1LO FWHM (cm^{-1})	1LO Raman shift (cm^{-1})	1LO FWHM (cm^{-1})	
Periodic PD12	250.9	10.2	256.4	16.5	7.0
Continuous CD22	250.6	9.8	252.2	13.2	9
Periodic PD32	250.6	9.7	252.7	15.3	9.6
Continuous CD42	250.9	9.1	251.7	13.3	11.5
Periodic PD62	250.7	9.5	252.3	15.2	10.5
Continuous CD52	251.4	8.2	251.6	12.0	17.0

(457.9 nm), according to correlation between the size of ZnSe nanocrystallites and their band gap [69].

In Fig. 9 experimental Raman spectra of CD52 ZnSe films taken by 514.5 nm and 457.9 nm laser lines are fitted by the sum of the 1LO ZnSe Raman profiles simulated by the PCM, and other modes fitted by Lorentzians. The Raman shift and FWHM of 1LO mode are estimated by PCM (Equation r3) in non-resonant (514.5 nm) conditions, whereas for estimation of these values in resonant (457.9 nm) conditions a modified PCM through the Equation r6 is used. The obtained results are summarized in Table 2 for all films. The ZnSe nanocrystallite size (L_0) estimated by PCM as fitting parameter are in the range from 7 nm (PD12) to 17 nm (CD52) (Table 2), which is in very good agreement with nanocrystallite size (D) obtained from XRD data (see Table 1).

The dependence of Raman shift and FWHM of ZnSe 1LO mode on L_0 in resonant and non-resonant conditions is illustrated in Fig. 10. In non-resonant conditions the frequency of calculated 1LO mode is decreased with the increase of nanocrystallite size (Fig. 10(a)). The 1LO frequencies are higher than bulk value for nanocrystallites from 7 to ~10 nm, and lower than bulk value for greater nanocrystallites. We remind that the XRD results have shown the reduction of nanocrystallite size followed by strong decrease of the lattice parameter, indicating the existence of significant compressive strain in the films with small ZnSe nanocrystals. Hence the 1LO frequency decrease with increasing nanocrystallite size is the consequence of dominant influence of compressive strain in small nanocrystallites, followed by the blueshift of Raman mode. On the other side, for nanocrystallites bigger than 10 nm the influence of phonon
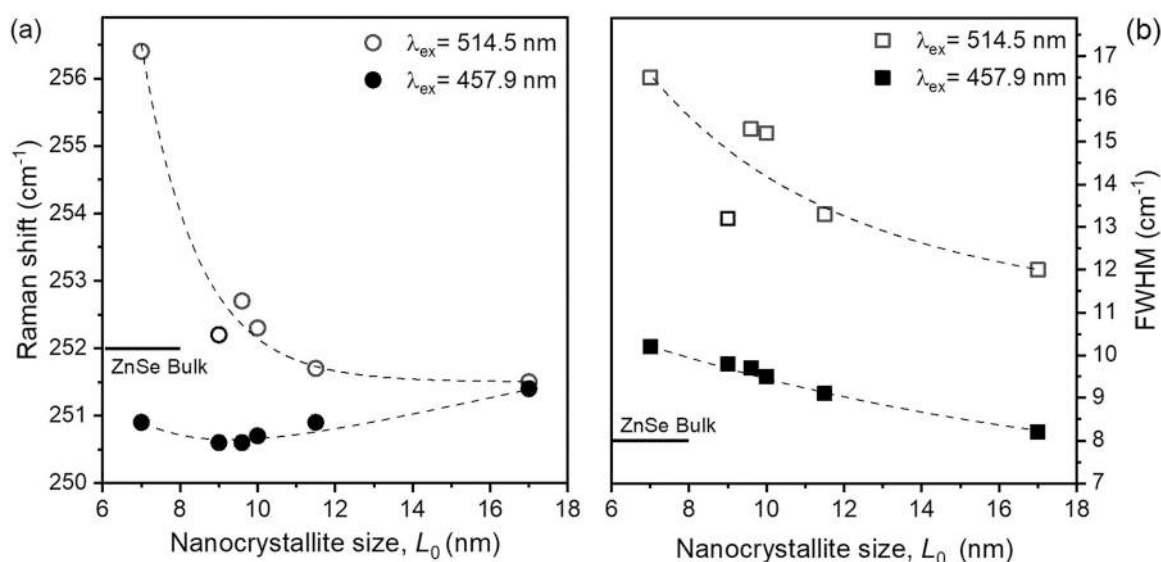
Fig. 10. The dependence of Raman shift (a) and FWHM (b) of 1LO ZnSe Raman mode on nanocrystallite size, all estimated by PCM for 514.5 and 457.9 nm laser lines. Dashed-lines should be used only as the guides for the eye.

confinement is dominant, leading to the redshift of 1LO mode in comparison to bulk value. Under resonant conditions simulated 1LO frequencies for all films are below bulk value and their variations with nanocrystallite size are significantly smaller in comparison to non-resonant conditions. The Raman shift is increased with the nanocrystallite size, approaching to the bulk value, with the exception of the $L_0 = 7$ nm (film PD12), where the influence of phonon confinement goes beyond the strain influence. The FWHM is above the bulk value in all samples, decreasing with the increase of nanocrystallite size in both non-resonant and resonant conditions (Fig. 10(b)), with significantly smaller values and variations in resonant conditions.

Note that the intensity of simulated 1LO Raman mode follows the variations of maximal intensity of the spectra taken by 514.5 nm (Fig. 6). This intensity is higher in the films with smaller nanoparticles, but the differences between intensities are not so significant. On the other side, in the near-resonant spectra taken by 457.9 nm (Fig. 8) the intensity of simulated 1LO modes in the spectrum of film with the biggest nanoparticles (CD52) is more than four times higher than in the spectra of film with the smallest nanoparticles (PD12). This confirms the essential assumption of modified PCM that nanoparticles of different size have different contribution to Raman spectra under the near-resonant conditions. Namely, enhanced Raman scattering from the nanoparticles with bandgap values close to excitation energy, leads to significantly higher intensity of 1LO Raman mode registered in films with bigger nanoparticles.

In the Raman spectra of porous II-VI semiconductor nanocrystals a broad Raman feature between TO and LO modes usually is assigned to the surface optical phonon (SOP) [54]. Specifically, Irmer et al. [51] have studied such porosity-induced vibrational modes as Fröhlich vibrational modes in nanoporous ZnSe layers. They concluded that Fröhlich mode is located between the TO and LO phonon modes, appearing at 239 cm^{-1} in the spectrum of ZnSe sample with the porosity of 50%. The SOP mode frequencies predicted by theoretical simulation, based on the effective medium theory [51 and references therein] for porosity values estimated from SE (Table 3), were used in fitting procedure of the non-resonant spectra of porous ZnSe films investigated here. Integrated intensity of so positioned SOP mode, estimated as a result of fitting process, is shown in Table 3 for all films. These results have shown that SOP integrated intensity has lower values in the films prepared by continuous deposition than in

their counterparts produced by periodically interrupted deposition, similar to the reduction of porosity in continuously deposited films. However, it should be noted that presented values for SOP integrated intensity are only indicative having in mind the large overlap of ZnSe- and Se-related modes in its vicinity.

Beside the first order Raman modes, several higher order ZnSe related modes can appear in the spectra of ZnSe nanostructures. So, second order LO Raman mode has been noticed at about 500 cm^{-1} in both near-resonant and non-resonant spectra, whereas third order LO mode at ~759 cm^{-1} is registered only in the near-resonant spectra of all investigated ZnSe films. Since overtone to fundamental intensity ratio in II-VI nanocrystals could give information about electron−phonon coupling strength in those materials, the integrated intensity ratio of the second to first order LO mode in near-resonant Raman spectra (2LO/1LO) is also listed in Table 2. These results have shown that the 2LO/1LO ratio has the highest value in the CD52, followed by CD42, and the lowest in the PD12 film. All other films have almost the same 2LO/1LO value. Since the 2LO/1LO ratio in resonant Raman spectra could be used as a quantitative parameter for crystalline perfection of the ZnSe bulk crystals, the value of 0.55 in the sample CD52, equal to bulk value [70], confirms good crystalline quality of this sample.

As for the other overtone ZnSe modes in non-resonant spectra, weak feature at about 140 cm^{-1} could be attributed to second order transversal acoustical 2TA mode, whereas the feature at around 290 cm^{-1} is ascribed to (LO+TA) [70], but also to defect related mode [71]. The Raman features at ~240, ~265, and around 280 cm^{-1} observed in resonant spectra of all ZnSe films may partially originate from some ZnSe second order modes related to the sum of longitudinal acoustical (LA) and TA phonons, (TO+TA) and (LO+TA) phonons, respectively [70 and references therein].

In line with the discussion referred to Fig. 7, contributions of several Se-related modes are included in the fitting of experimental Raman spectra recorded by 514.5 nm laser line. Their positions are in very good agreement with the frequencies of Raman modes usually assigned to selenium [53,72]. So, modes at about 116, 235, 250, 365, 500, and 614 cm^{-1} registered in thin selenium films with amorphous like structure [53], whereas mode at ~265 cm^{-1} is usually related to Se$_8$ rings vibration [49]. In as-deposited films selenium is most probably in amorphous phase and could be a part of amorphous ZnSe, but also could be in a form of excess Se inside or outside the ZnSe structure. The irradiation by 514.5 nm laser line with irradiance

Table 3
Deposition conditions, ZnSe films porosity estimated by spectroscopic ellipsometry (SE), integrated intensity of the SOP Raman mode and second to first LO Raman mode integrated intensity ratio (2LO/1LO). The λ_{ex} is laser excitation wavelength.

	SE results		Raman results	
			λ_{ex}= 514.5 nm	λ_{ex}= 457.9 nm
Deposition manner/ Sample name	Deposition rate (nm/s)	Porosity (%)	SOP mode integrated intensity	2LO/1LO integrated intensity ratio
Periodic PD12	0.5	25.3 ± 0.08	15	0.41
Continuous CD22	0.5	12.0 ± 0.04	10	0.43
Periodic PD32	1.5	13.3 ± 0.04	11	0.43
Continuous CD42	1.5	1.4 ± 0.04	6	0.46
Periodic PD62	3.0	8.8 ± 0.04	8.5	0.43
Continuous CD52	3.0	0.0 ± 0.04	5	0.55

of the order of 10^4 Wcm^{-2} (Fig. 6) may cause partial change in selenium phase. As previously mentioned, possible resonant enhancement of selenium modes could have led to great Raman intensity ratio of resonant selenium to non-resonant ZnSe modes in the spectra taken by 514.5 nm, giving unrealistic overestimation of selenium content. The only exception is the spectrum of CD22 (Fig. 6) which indicates a very low content of selenium outside the ZnSe structure, since the modes at about 116 and 265 cm^{-1} are not observed and the others that could be related to selenium are of very low intensity. Also, the increased laser power did not lead to a significant change in the spectrum of CD22 film.

When summarizing the results of Raman scattering measurements, first it should be noted that they confirm zinc blende structure of crystalline ZnSe in all investigated films. Unlike the XRD analysis which cannot for sure confirm the ZnSe phase from the patterns due to poor signal-to-noise ratio, making it difficult to distinguish overlapping zinc blende and wurtzite diffraction peaks, the Raman spectra clearly indicate the zinc blende ZnSe structure. Namely, the features at about 210 and 252 cm^{-1} are detected and ascribed to TO and LO ZnSe modes, respectively, whereas the mode E_1(TO) ~176 cm^{-1} characteristic for wurtzite ZnSe [73] is not observed in any spectra of investigated films.

Detailed analysis of Raman spectra obtained using different laser lines and laser powers have revealed the origin of the most observed Raman features. So, it is shown that the Raman feature at about 252 cm^{-1} is dominated by 1LO mode of zinc blend ZnSe in the spectra excited by λ_{ex} = 457.9 nm line (due to near-resonant conditions), whereas this feature appears as much more complex in non-resonant conditions (λ_{ex} = 514.5 nm), containing significant contribution of several Se-related modes which most likely originate from amorphous ZnSe and excess selenium. It has also been shown that there is probably a resonant enhancement of Se-related modes in the spectra taken by 514.5 nm, so that the excess selenium content may be overestimated. It can only be said with certainty that Se content was found to be significantly lower in the CD22 than the in all other films.

Besides the phase and composition, the Raman scattering measurements have also given the information about crystalline quality, based on 2LO/1LO integrated intensity ratio, as well as the intensity and linewidth of TO mode. These results point to better crystallinity of the CD films in comparison to their PD counterparts, and the best crystalline quality in CD52 film.

The PCM has been used in order to reveal of nanocrystalline structure from Raman data. To explain the differences in the position and shape of the 1LO mode in the spectra excited by different laser lines a PCM has been modified. It has been shown that modified PCM model simulate well both resonant and non-resonant Raman spectra with unique set of material parameters. Good agreement of numerically simulated and experimental Raman spectra on the one side, as well as agreement between XRD and Raman scattering results regarding nanostructure parameters (nanocrystallite size, lattice parameter) on the other, confirm the validity of this model.

The analysis of the SOP Raman mode, as a characteristic feature of small-size nanostructures, may give information on film morphology: lower SOP intensity in the CD films corresponds to reduction of porosity in CD films, in comparison to their PD counterparts.

4. Conclusion

The effect of deposition manner (continuous, CD, or periodically interrupted, PD) and deposition rate (V_d = 0.5, 1.5, 3.0 nm/s) on the structural and optical properties of 50 nm thick ZnSe films prepared by thermal vacuum evaporation is thoroughly studied. The obtained results can be summarized as follows:

1. EDS data show some excess of selenium in the films and Raman scattering analysis reveals presence of small amount of amorphous Se phase.
2. The films are nanocrystalline with cubic zinc blend crystal structure, confirmed by XRD and Raman scattering results, as the latter disclose better crystallinity of the CD films in comparison to their PD counterparts. The V_d increase causes decrease of dislocation density both in CD- and PD-films, indicating an improvement in ZnSe crystal quality.
3. At each V_d the size of the nanocrystals in the CD-layers is greater than that in the PD-layers and it increases linearly with the increase of the deposition rate - the increase is stronger for continuously deposited CDs (from 8.9 nm to ~18 nm) and weaker for PD films (from ~7 nm to ~10 nm).
4. The lattice parameter depends on the nanocystallite size – it is around the ZnSe bulk value for the size greater than 9 nm, whereas the reduction of size results in strong decrease in lattice parameter, indicating the existence of significant compressive strain in the films with small ZnSe nanocrystals.
5. Spectroscopic ellipsometry and Raman scattering results indicate that for each V_d the porosity of the periodically deposited PD-film is significantly higher than that of the corresponding CD-film and for each manner of deposition it increases with decreasing deposition rate. Mesopores are observed on the SEM images of films surface.

The variations of the crystallite size and porosity with changing V_d and manner of deposition are related to the processes of surface diffusion of adatoms, nucleation and coalescence of nuclei during deposition as well as adsorption of residual gases under vacuum chamber which can also influence the growth of the individual grains. It is suggested that during CD-deposition, the V_d increase results in an increase of the number of atoms reaching surface per unit time, the number of nuclei formed on the surface is larger and their coalescence results in greater crystallite size and lower film porosity. During PD-deposition the amount of the adsorbed residual gas atoms is significantly greater than that adsorbed during the CD-

deposition which can explain the observed smaller nanocrystallite size and higher porosity of the PD-films.

The phonon confinement model, PCM, is modified in order to explain the differences in the position and shape of the ZnSe 1LO mode in the spectra excited by different laser lines. It is shown that by applying modified PCM model one can simulate well both resonant and non-resonant Raman spectra with unique set of material parameters. The good agreement of numerically simulated and experimental Raman spectra, as well as the agreement between XRD and Raman scattering results regarding ZnSe nanocrystallite size and lattice parameter confirm the validity of this model. It is also demonstrated that the analysis of the surface optical phonon Raman mode, as a characteristic feature of small-size nanostructures, may give information on film morphology.

The presented results show that both manner of deposition and deposition rate significantly affect the films properties (structure, morphology and optical properties) and their combinations can be used for preparation of films with properties suitable for certain application. Our ethanol sensing experiments at room temperature have indicated that the films porosity plays an important role for the films sensitivity and the obtained results will be used for optimization of the chemical sensing of ZnSe films at room temperature.

CRediT authorship contribution statement

D. Nesheva: Conceptualization, Validation, Formal analysis, Writing – original draft, Writing – review & editing, Supervision, **M. Grujić-Brojčin:** Methodology, Software, Formal analysis, Investigation, Writing – original draft, Writing – review & editing, Visualization, **M.J. Šćepanović:** Conceptualization, Methodology, Validation, Formal analysis, Investigation, Writing – original draft, Writing – review & editing, **Z. Levi:** Resources, Investigation, **V. Dzhurkov:** Resources, Investigation, **T. Hristova-Vasileva:** Formal analysis, Investigation, **B. Vasić:** Formal analysis, Investigation.

Data availability

Data will be made available on request.

Declaration of Competing Interest

The authors declare that they have no known competing financial interests or personal relationships that could have appeared to influence the work reported in this paper.

Acknowledgements

References

[1] Z. Peng, Y. Liu, Y. Zhao, K. Chen, Y. Cheng, V. Kovalev, W. Chen, ZnSe passivation layer for the efficiency enhancement of CuInS2 quantum dots sensitized solar cells, J. Alloy. Compd. 587 (2014) 613–617.

[2] R. Kondrotas, M. Colina, M. Guc, M. Neuschitzer, S. Giraldo, X. Alcobé, F. Oliva, Y. Sánchez, P. Pistor, V. Izquierdo-Roca, A. Pérez-Rodriguez, E. Saucedo, Towards In reduced photovoltaic absorbers: evaluation of zinc-blende CuInSe2–ZnSe solid solution, Sol. Energy Mater. Sol. Cells 160 (2017) 26–33.

[3] K. Katayama, H. Matsubara, F. Nakanishi, T. Nakamura, H. Doi, A. Saegusa, T. Mitsui, T. Matsuoka, M. Irikura, T. Takebe, S. Nishine, T. Shirakawa, ZnSe-based white LEDs, J. Cryst. Growth 214–215 (2000) 1064–1070, https://doi.org/10.1016/S0022-0248(00)00275-X)

[4] U.K. Sahbudin, M.H.A. Wahid, P. Poopalan, N.A.M.A. Hambali, M.M. Shahimin, S.N. Ariffin, N.N.A. Saidi, M.M. Ramli, ZnSe Light Emitting Diode Quantum Efficiency and Emission Characterization MATEC Web of Conferences 78(16) (2016) 01114. https://doi.org/10.1051/matec(conf/20167801114).

[5] A. Gust, C. Kruse, M. Klude, E. Roventa, R. Kroeger, K. Sebald, H. Lohmeyer, B. Brendemuhl, J. Gutowski, D. Hommel, ZnSe-based laser diodes: New approaches, Phys. Stat. Sol. (C.) 2 (3) (2005) 1098–1110, https://doi.org/10.1002/pssc.200460673

[6] T.K. Lin, S.J. Changa, Y.K. Su, Y.Z. Chiou, C.K. Wang, S.P. Chang, C.M. Chang, J.J. Tang, B.R. Huang, ZnSe MSM photodetectors prepared on GaAs and ZnSe substrates, Mater. Sci. Eng. B 119 (2) (2005) 202–205, https://doi.org/10.1016/j.mseb.2005.03.002

[7] X. Fang, S. Xiong, T. Zhai, Y. Bando, M. Liao, U. Gautam, Y. Koide, X. Zhang, Y. Qian, D. Golberg, High-performance blue/ultraviolet-light-sensitive ZnSe-nanobelt photodetectors, Adv. Mater. 21 (48) (2009) 5016–5021.

[8] Q. Zhang, H. Li, Y. Ma, T. Zhai, ZnSe nanostructures: synthesis, properties and applications, Prog. Mater. Sci. 83 (2016) 472–535, https://doi.org/10.1016/j.pmatsci.2016.07.005

[9] T. Yao, M. Ogura, S. Matsuoka, T. Morishita, High-quality ZnSe thin films grown by molecular beam epitaxy, Appl. Phys. Lett. 43 (1983) 499, https://doi.org/10.1063/1.94366

[10] R.M. Park, ZnSe growth by conventional molecular beam epitaxy: a review of recent progress, in: H.E. Ruda (Ed.), Widegap II–VI Compounds for Opto-electronic Applications. Electronic Materials Series, vol 1, Springer, Boston, MA, 1992, , https://doi.org/10.1007/978-1-4615-3486-0_4

[11] O. Toma, L. Ion, S. Iftimie, V.A. Antohe, A. Radu, A.M. Raduta, D. Manica, S. Antohe, Physical properties of rf-sputtered ZnS and ZnSe thin films used for double-heterojunction ZnS/ZnSe/CdTe photovoltaic structures, Appl. Surf. Sci. 478 (2019) 831–839, https://doi.org/10.1016/j.apsusc.2019.02.032

[12] P. Kr. Kalita, B.K. Sarma, H.L. Das, Structural characterization of vacuum evaporated ZnSe thin films, Bull. Mater. Sci. 23 (2000) 313–317.

[13] M. Šćepanovic, M. Grujic-Brojcin, D. Nesheva, Z. Levi, I. Bineva, Z.V. Popovic, Characterization of ZnSe nanolayers by spectroscopic ellipsometry, Acta Phys. Pol. A 116 (4) (2009) 708–711.

[14] T.M. Khan, M.F. Mehmood, A. Mahmood, A. Shah, Q. Raza, A. Iqbal, U. Aziz, Synthesis of thermally evaporated ZnSe thin film at room temperature, Thin Solid Films 519 (18) (2011) 5971–5977, https://doi.org/10.1016/j.tsf.2011.03.045

[15] M.A. Sayeed, H.K. Rouf, K.M.A. Hussain, Effect of thickness on characteristics of ZnSe thin film synthesized by vacuum thermal evaporation, J. Theor. Appl., Phys. 14 (2020) 251–259, https://doi.org/10.1007/s40094-020-00378-1

[16] J.-C. Chen, B. Yang, A.F. Semendy, W.W. Clark III, P.R. Boyd, N. Bambha, High-quality ZnSe on GaAs grown by metal-organic chemical vapor deposition (MOCVD) using diethylzinc (DEZn) and diethyselenide (DESe), Proc. SPIE 2228, Prod. II-VI Mater. Devices (13 1994) 153, https://doi.org/10.1117/12.179654

[17] Y. Noda, T. Ishikawa, M. Yamabe, Y. Hara, Growth of ZnSe thin films by metalorganic chemical vapor deposition using nitrogen trifluoride, 1997, Appl. Surf. Sci., 113– 114 (1997) 28–32, https://doi.org/10.1016/S0169-4332(96)00811-2

[18] R.K. Pathak, S. Bais, Znse thin films - a brief review, Int. J. Adv. Eng. Technol. 7 (4) (2014) 1300–1305.

[19] H.K. Sadekar, A.V. Ghule, R. Sharma, Nanocrystalline ZnSe thin films prepared by solution growth technique for photosensor application, Compos. Part B: Eng. 44 (1) (2013) 553–557, https://doi.org/10.1016/j.compositesb.2012.03.003

[20] S. Antohe, L. Ion, M. Girtan, O. Toma, Optical and morphological studies of thermally vacuum evaporated ZnSe thin films, Rom. Rep. Phys. 65 (3) (2013) 805–811.

[21] G. Georgescu, A. Petris, Analysis of thickness influence on refractive index and absorption coefficient of zinc selenide thin films, Opt. Express 27 (24) (2019) 34803–34823, https://doi.org/10.1364/OE.27.034803

[22] M.T. Chowdhury, Md.A. Zubair, H. Takeda, K.Md.A. Hussain, Md.F. Islam, Optical and structural characterization of ZnSe thin film fabricated by thermal vapour deposition technique, AIMS Mater. Sci. 4 (5) (2017) 1095–1121, https://doi.org/10.3934/matersci.2017.5.1095 (and references therein).

[23] G.I. Rusu, V. Ciupina, M.E. Popa, G. Prodan, G.G. Rusu, C. Baban, Microstructural characterization and optical properties of ZnSe thin films, J. Non-Cryst. Solids 352 (2006) 1525–1528, https://doi.org/10.1016/j.jnoncrysol.2006.01.029

[24] M.F. Hasaneen, Z.A. Alrowaili, W.S. Mohamed, Structure and optical properties of polycrystalline ZnSe thin films: validity of Swanepol's approach for calculating the optical parameters, Mater. Res. Express 7 (2020) 016422.

[25] P.S. Raghupathi, J. George, C.S. Menon, The Effect of Deposition Rate on Electrical, Optical and Structural Properties of ITO Thin Films, E-J. Chem. 2 (3) (2005) 171–177.

[26] H.R. Fallah, M. Ghasemi, A. Hassanzadeh, H. Steki, The effect of deposition rate on electrical, optical and structural properties of tin-doped indium oxide (ITO) films on glass at low substrate temperature, Phys. B: Cond. Matter 373 (2) (2006) 274–279, https://doi.org/10.1016/j.physb.2005.11.159

[27] K. Bordo, H.-G. Rubahn, Effect of Deposition Rate on Structure and Surface Morphology of Thin Evaporated Al Films on Dielectrics and Semiconductors, Mater. Sci. 18 (4) (2012) 313–317, https://doi.org/10.5755/j01.ms.18.4.3088

[28] S. Momeni, M. Ghasemi, A. Taherian, The influence of deposition rate on optical and microstructural characteristics of nanostructured ZnSe films prepared by thermal evaporation technique, J. Interfaces Thin Films Low. Dim. Syst. 4 (2020) 347–356, https://doi.org/10.22051/jitl.2021.36255.1054

[29] D. Nesheva, M.J. Šćepanović, Z. Levi, S. Aškrabić, Z. Aneva, A. Petrova, Z.V. Popovic, Structural characterization and photoluminescence of ZnSe nanolayers, J. Optoel. Adv. Mater. 11 (9) (2009) 1351–1354.

[30] T.M. Khan, B. Tayyaba, Compatibility and optoelectronic of ZnSe nanocrystalline thin film, Chin. Phys. B 21 (9) (2012) 097303.

[31] D. Nesheva, Nanocrystalline and amorphous thin film systems including low-dimensional chalcogenide materials, in: H.S. Nalwa (Ed.), Handbook of Surfaces and Interfaces of Materials, Volume 3 Academic Press, 2001, pp. 239–279.

[32] V. Dzhurkov, Z. Levi, D. Nesheva, T. Hristova-Vasileva, Room temperature sensitivity of ZnSe nanolayers to ethanol vapours, 012023, J. Phys.: Conf. Ser. 1186 (1) (2009) 1–6, https://doi.org/10.1088/1742-6596/1186/1/012023

[33] V. Dzhurkov, Z. Levi, D. Nesheva, T. Hristova-Vasileva, Effect of layer thickness and preparation conditions on the properties and ethanol sensitivity of ZnSe thin films, Newest Updates Phys. Sci. Res. 3 (2021) 125–134, https://doi.org/10.9734/bpi/nupsr/v3/8080D

[34] B. L'vov, Sublimation and Decomposition Reactions, In: Thermal Decomposition of Solids and Melts, pp 163–228, 2007. Hot Topics in Thermal Analysis and Calorimetry, Volume 7. Springer, Dordrecht. https://doi.org/10.1007/978-1-4020-5672-7_16.

[35] J. Sharma, S.K. Tripathi, Effect of deposition pressure on structural, optical and electrical properties of zinc selenide thin films, Phys. B: Condens. Matter 406 (9) (2011) 1757–1762.

[36] D. Nesheva, D. Arsova, R. Ionov, Thin and superthin photoconductive CdSe films, deposited at room substrate temperature, J. Mater. Sci. 28 (1993) 2183–2186.

[37] B.E. Warren, X-Ray Diffraction, Dover Publications, New York, 1990.

[38] T.M. Khan, M. Zakria, R.I. Shakoor, M. Raf, M. Ahmad, Mechanisms of composite-hydroxide-mediated approach for the synthesis of functional ZnO nanostructures and morphological dependent optical emissions, Adv. Mater. Lett. 6 (2015) 592–599.

[39] K.L. Chopra, T.D. Shermergor (Ed.), Electrical Phenomena In Thin Films, Mir, Moskva, 1972, p. 11.

[40] L. Ion, S. Iftimie, A. Radu, V.A. Antohe, O. Toma, S. Antohe, Physical properties of RF-sputtered ZnSe thin films for photovoltaic applications: influence of film thickness, Proc. Rom. Acad., Ser. A 22 (1) (2021) 25–34.

[41] M. Grujić-Brojčin, S. Armaković, N. Tomić, B. Abramović, A. Golubović, B. Stojadinović, A. Kremenović, B. Babić, Z. Dohčević-Mitrović, M. Šćepanović, Surface modification of sol–gel synthesized TiO₂ nanoparticles induced by La-doping, Mater. Charact. 88 (2014) 30–41.

[42] D. Burnett, The Relation between refractive index and density, Math. Proc. Camb. Philos. Soc. 23 (8) (1927) 907–911, https://doi.org/10.1017/S0305004100013773

[43] K. Sangwal, W. Kucharczyk, Relationship between density and refractive index of inorganic solids, 1987 J. Phys. D: Appl. Phys. 20 (1987) 522, https://doi.org/10.1088/0022-3727/20/4/019 ⟨http://glassproperties.com/refractive_index/⟩.

[44] K.L. Westra, D.J. Thomson, The microstructure of thin films observed using atomic force microscopy, Thin Solid Films 257 (1995) 15–21, https://doi.org/10.1016/0040-6090(94)06351-6

[45] J.W. Dini, Electrodeposition, The Materials Science of Coatings and Substrates, Noyes Publications, New Jersey, USA, 1993.

[46] S. Pellicori, Fundamentals of Thin-film Growth and Influences on Mechanical and Environmental Durability Properties, Materion Coating Materials News, ⟨https://materion.com/resource-center/newsletters/coating-materials-news/fundamentals-of-thin-film-growth⟩.

[47] H. Qui, F. Wang, P. Wu, L. Pan, L. Li, L. Xiong, Y. Tian, Effect of deposition rate on structural and electrical properties of Al films deposited on glass by electron Z. Beam Evaporation, Thin Solid Films 414 (2002) 150–153, https://doi.org/10.1016/S0040-6090(02)00454-6

[48] B. Pejova, Optical phonons in nanostructured thin films composed by zincblende zinc selenide quantum dots in strong size-quantization regime: Competition between phonon confinement and strain-related effects, J. Solid State Chem. 213 (2014) 22–31.

[49] S.N. Yannopoulos Andrikopoulos, Raman scattering study on structural and dynamical features of noncrystalline selenium, J. Chem. Phys. 121 (2004) 4747–4758, https://doi.org/10.1063/1.1780151

[50] M. Dimitrievska, H. Xie, A.J. Jackson, X. Fontané, M. Espíndola-Rodríguez, E. Saucedo, A. Perez-Rodriguez, A. Walsh, V. Izquierdo-Roca, Resonant Raman scattering of ZnS_xSe_{1-x} solid solutions: the role of S and Se electronic states, Phys. Chem. Chem. Phys. 18 (2016) 7632–7640.

[51] G. Irmer, E. Monaico, I.M. Tiginyanu, G. Gartner, V.V. Ursaki, G.V. Kolibaba, D.D. Nedeoglo, Fröhlich vibrational modes in porous ZnSe studied by Raman scattering and Fourier transform infrared reflectance, J. Phys. D: Appl. Phys. 42 (2009) 045405.

[52] D. Nesheva, I.P. Kotsalas, C. Raptis, E. Vateva, On the structural stablity of amorphous Se/CdSe multilayers: a Raman study, J. Non-Cryst. Solids 224 (1998) 283–289.

[53] N. Ohta, W. Scheuermann, K. Nakamoto, Resonance Raman spectrum of selenium thin film, Solid State Commun. 27 (1978) 1325–1327.

[54] V.M. Dzhagan, M.Ya Valakh, A.E. Raevskaya, A.L. Stroyuk, S.Ya Kuchmiy, D.R.T. Zahn, Size effects on Raman spectra of small CdSe nanoparticles in polymer films, Nanotechnol 19 (2008) 1–6 305707.

[55] M.Ya Valakh, V.M. Dzhagan, A.E. Raevskaya, S.Ya Kuchmiy, Optical investigations of ultra-small colloidal nanoparticles and heteronanoparticles based on II-VI semiconductors, Ukr. J. Phys. 56 (10) (2011) 1080–1090.

[56] B. Schreder, C. Dem, M. Schmitt, A. Materny, W. Kiefer, U. Winkler, E. Umbach, Raman spectroscopy of II–VI semiconductor nanostructures: CdS quantum dots, J. Raman Spectrosc. 34 (2003) (2003) 100–103.

[57] H. Richter, Z.P. Wang, L. Ley, The one phonon Raman spectrum in microcrystalline silicon, Solid State Commun. 39 (1981) 625–629.

[58] I.H. Campbell, P.M. Fauchet, The effects of microcrystal size and shape on the one phonon Raman spectra of crystalline semiconductors, Solid State Commun. 58 (1986) 739–441.

[59] M.J. Šćepanović, M. Grujić-Brojčin, Z.D. Dohčević-Mitrović, Z.V. Popović, Temperature dependence of the lowest frequency Eg Raman mode in laser-synthesized anatase TiO₂ nanopowder, Appl. Phys. A86 (2007) 365–371.

[60] M. Grujić-Brojčin, M.J. Šćepanović, Z.D. Dohčević-Mitrović, Z.V. Popović, Use of phonon confinement model in simulation of Raman spectra of nanostructured materials, Acta Phys. Pol. A116 (1) (2009) 51–54.

[61] M.J. Šćepanović, M. Grujić-Brojčin, I. Bineva, D. Nesheva, Z. Aneva, Z. Levi, Z.V. Popović, Raman study of ZnSe/SiOₓ multilayers, J. Optoelectron. Adv. Mater. 9 (1) (2007) 178–181.

[62] S.K. Gupta, P.K. Jha, Modified phonon confinement model for size dependent Raman shift and linewidth of silicon nanocrystals, Solid State Commun. 149 (2009) 1989–1992.

[63] W. Ke, Xue Feng, Y. Huang, The effect of Si-nanocrystal size distribution on Raman spectrum, J. Appl. Phys. 109 (2011) 083526.

[64] B. Feng, J. Cao, D. Han, S. Yang, J. Yang, Study on growth mechanism and optical properties of ZnSe nanoparticles, J. Mater. Sci.: Mater. Electron. 26 (2015) 3206–3214.

[65] Y.C. Lin, C.H. Chiu, W.C. Fan, S.L. Yang, D.S. Chuu, W.C. Chou, Pressure-dependent Raman scattering and photoluminescence of $Z_{n1-x}C_{dx}Se$ epilayers, J. Appl. Phys. 101 (2007) 073507.

[66] K. Kunc, M. Balkanski, M.A. Nusimovic, Lattice dynamics of several A-vBs-N compounds having the zincblende structure, Phys. Stat. Sol. (b) 72 (1975) 229–248.

[67] M. Mikami, S. Nakamura, O. Kitao, H. Arakawa, Lattice dynamics and dielectric properties of TiO₂ anatase: a first-principles study, Phys. Rev. B66 (2002) 1–6 155213.

[68] M. Popa, Structural characteristics and optical properties of zinc selenide thin films, Optoelectron. Adv. Mater. - Rapid Commun. 5 (8) (2011) 842–845.

[69] P. Reiss, ZnSe based colloidal nanocrystals: synthesis, shape control, core/shell, alloy and doped systems, New J. Chem. 31 (2007) 1843–1852.

[70] Iu Nasieka, M. Boyko, V. Strelchuk, N. Kovalenko, A. Gerasimenko, N. Starzhinskiy, A. Zhukov, I. Zenya, D. Sofronov, Optical characterization of Er-doped ZnSe for scintillation applications, Opt. Mater. 38 (2014) 272–277.

[71] J.X. Aijiang, Lu, C. Wang, R. Zou, X. Liu, X. Wu, Y. Wang, S. Li, L. Sun, X. Chen, H. Oh, H. Baek, G.-C. Yi, J. Chu, ZnSe-based longitudinal twinning nanowires, Adv. Eng. Mater. 16 (4) (2014) 459–465.

[72] Q. Chen, C. Zhang, J. Liu, Y. Ye, P. Li, C. Liang, Solvent molecules dominated phase transition of amorphous Se colloids probed by in-situ raman spectroscopy, Appl. Surf. Sci. 466 (1) (2019) 1000–1006, https://doi.org/10.1016/j.apsusc.2018.10.080

[73] C.X. Shan, Z. Liu, X.T. Zhang, C.C. Wong, S.K. Hark, Wurtzite ZnSe nanowires: growth, photoluminescence, and single-wire Raman properties, Nanotechnology 22 (17) (2006) 5561.

PAPER • OPEN ACCESS

Two-dimensional talc as a van der Waals material for solid lubrication at the nanoscale

View the article online for updates and enhancements.

Two-dimensional talc as a van der Waals material for solid lubrication at the nanoscale

Borislav Vasić[1,*] , **Caterina Czibula**[2,3] , **Markus Kratzer**[2] ,
Bernardo R A Neves[4] , **Aleksandar Matković**[2,*] and **Christian Teichert**[2]

[1] Institute of Physics Belgrade, University of Belgrade, Pregrevica 118, 11080 Belgrade, Serbia
[2] Institute of Physics, Montanuniversität Leoben, Franz Josef Strasse 18, A-8700 Leoben, Austria
[3] Institute of Bioproducts and Paper Technology, Graz University of Technology, Inffeldgasse 23, A-8010 Graz, Austria
[4] Departamento de Física, ICEx, Universidade Federal de Minas Gerais, 30123-970 Belo Horizonte, MG, Brazil

E-mail: bvasic@ipb.ac.rs and aleksandar.matkovic@unileoben.ac.at

CrossMark

Abstract

Talc is a van der Waals and naturally abundant mineral with the chemical formula $Mg_3Si_4O_{10}(OH)_2$. Two-dimensional (2D) talc could be an alternative to hBN as van der Waals dielectric in 2D heterostructures. Furthermore, due to its good mechanical and frictional properties, 2D talc could be integrated into various hybrid microelectromechanical systems, or used as a functional filler in polymers. However, properties of talcas one of the main representatives of the phyllosilicate (sheet silicates) group are almost completely unexplored when ultrathin crystalline films and monolayers are considered. We investigate 2D talc flakes down to single layer thickness and reveal their efficiency for solid lubrication at the nanoscale. We demonstrate by atomic force microscopy based methods and contact angle measurements that several nanometer thick talc flakes have all properties necessary for efficient lubrication: a low adhesion, hydrophobic nature, and a low friction coefficient of 0.10 ± 0.02. Compared to the silicon-dioxide substrate, 2D talc flakes reduce friction by more than a factor of five, adhesion by around 20%, and energy dissipation by around 7%. Considering our findings, together with the natural abundance of talc, we put forward that 2D talc can be a cost-effective solid lubricant in micro- and nano-mechanical devices.

Supplementary material for this article is available online

Keywords: van der Waals materials, layered minerals, 2D talc, phyllosilicates (sheet silicates), nanofriction, atomic force microscopy

(Some figures may appear in colour only in the online journal)

1. Introduction

Tribological issues such as stiction, friction, and wear are responsible for a poor reliability of micro- and nano-mechanical devices [1]. Due to their continuous miniaturization, they need integral components with reduced dimensions. Therefore, very thin solid lubricants are required in order to reduce friction and wear of moveable mechanical
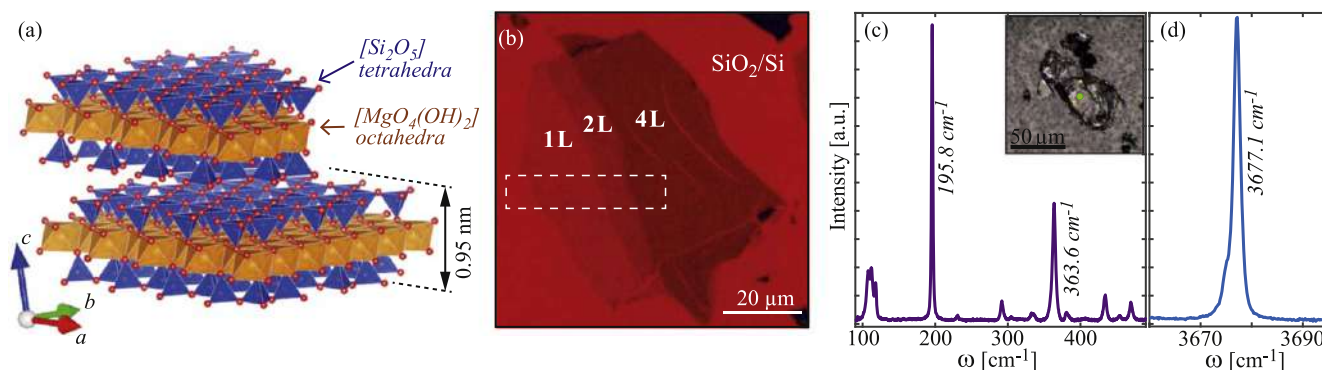
Figure 1. (a) Polyhedral structural model of talc, indicating a monolayer thickness of 0.95 nm. (b) Optical micrograph of a talc flake containing single-, bi-, and four-layer regions. Optical contrast is enhanced in order to highlight the mono-layer part of the flakes (see also figure S2 of supplementary material). Dashed white rectangle highlights the area where AFM topography measurements (presented in figure S2 of supplementary material) were used to confirm the flake thickness. (c) and (d) Raman spectra of a bulk talc flake: (c) modes that correspond to vibrations of Mg, (d) the Raman active mode of the -OH group. The inset in (c) provides an optical micrograph of the flake and its support. All Raman modes belong to the talc crystal, while exact frequencies are provided only for the most prominent ones for clarity.

parts in such devices. For that purpose, two-dimensional (2D) materials such as graphene, molybdenum disulfide, and hexagonal boron nitride are excellent candidates. Their Lamellar structure with weak van der Waals (vdW) forces between the layers enables easy shearing which results in low friction [2–4], while their crystal structure leads to preferential sliding directions [5–7] and superlubric sliding through incommensurate states [8–11]. Frictional properties and lubrication by 2D materials were extensively investigated in the last years [12–17], while most studies were focused on graphene demonstrating reduced friction [18, 19], wear [19–21], adhesion [18] and energy dissipation [22–24].

Recently, minerals such as franckeite [25–28], talc [29, 30], cylindrite [31] and serpentine [32] have attracted attention for the preparation of ultra-thin crystalline films and mono-layers. They extend the set of available vdW materials bringing novel and improved properties. For example, franckeite provides natural vdW heterostructures [25, 26] with possible applications in optoelectronic devices [27], whereas 2D cylindrite is an environmentally stable magnetic material [31].

Talc is a layered and naturally abundant mineral with the chemical formula $Mg_3Si_4O_{10}(OH)_2$. It belongs to the group of phyllosilicates. Talc is traditionally widely used as a filler, i.e. as a functional additive for various polymers in order to improve their mechanical properties [33–36]. Similar to graphite, molybdenum disulfide, and boron nitride, it has been also used as a lubricant in its bulk form for decades [37] and as an oil additive for friction reduction [38]. Geophysical studies revealed that the presence of talc decreases frictional strength of minerals [39, 40] and reduces the friction during sliding of crustal faults (planar fractures of rocks) with a strong influence on their seismic potential [41, 42]. Recently, mechanical [29] and liquid-phase [43] exfoliation have been used to obtain 2D talc flakes down to single layer thickness which is 0.95 nm. It was demonstrated that 2D talc is atomically flat [44] with good mechanical properties, a high breaking strength and elasticity [29]. The single layer of talc consists of the central $[MgO_4(OH)_2]$ octahedra 'sandwiched'

between $[Si_2O_5]$ tetrahedra, see figure 1(a). Such Lamellar structure facilitates easy shearing between the layers, the feature responsible for a good lubrication of the bulk form. However, frictional properties of 2D talc at the nanoscale have not been investigated so far.

In this paper, we study adhesion, friction, and energy dissipation of 2D talc crystals using atomic force microscopy (AFM) based methods. Force–displacement curves [45] have been recorded to obtain values for the adhesion. The frictional behavior has been characterized by friction force microscopy [46], whereas phase imaging in tapping AFM mode [47–49] has been applied to investigate energy dissipation. We demonstrate that 2D talc has a low friction coefficient of only 0.10 ± 0.02. Compared to the surrounding silicon-dioxide substrate, the 2D talc reduces friction by 5-6 times, whereas the adhesion and energy dissipation are decreased by around 20% and 7%, respectively. These results demonstrate that 2D talc can be a cost-effective solid lubricant at the nanoscale.

2. Experimental methods

2.1. Sample preparation

Monolayer and multilayer talc flakes were prepared by micromechanical exfoliation using Nitto Denko ELP BT150ECM sticky tape. The shematics of the preparation process is presented in figure S1 of supplementary material (available online at stacks.iop.org/NANO/32/265701/mmedia). As the starting material, two different sources of natural talc mineral were used: 'soap-stone' crystals from Styria in Austria and pure steatite single crystals from Minas Gerais state in Brazil. Bulk talc flakes were deposited onto Si wafers with 300 nm thick SiO_2 layer. Figure 1(b) shows an example of the prepared flakes. Labeled thicknesses were determined by AFM. Areas with potential mono- and multilayers (up to $\approx$30 layers) were selected by optical microscopy. Optical contrast of ultra-thin talc flakes on such

support is similar to those of hexagonal boron nitride on SiO_2 [50, 51].

2.2. Raman characterization

Raman spectroscopy was employed to confirm that the deposited material is talc with high crystallinity. A Horiba LabRam HR Evolution co-local Raman spectrometer was used with EMCCD detector, 532 nm laser (100 mW power on the sample surface), $100\times$ magnification lens, and 1800 lines mm^{-1} grating. Since talc has low Raman response —especially if compared to graphene—rather high acquisition times were used, from 20 s in the case of bulk up to 1200s for the flakes thinner than 10 nm. No sample damage was observed after prolonged exposure to the laser beam, which was confirmed by repeated Raman measurements and by AFM. Raman spectra were corrected for the background signal (obtained from the measurements of the nearby substrate) and cosmic rays were removed.

Figures 1(c), (d) presents Raman spectra of a bulk talc flake (shown in the inset of (c)) in the ranges of 100–500 cm^{-1} and 3660–3695 cm^{-1}, respectively. Vibrational modes of Mg were observed at lower frequencies (up to 900 cm^{-1}) [52]. Sharp vibrational mode of –OH group was observed at 3677 cm^{-1} [52]. Characteristic modes of water (3400–3600 cm^{-1} range) intercalating phyllosilicate structure were not observed. Bulk crystals were fixed on the tape which was used for the subsequent exfoliation of the same crystals. In such case, very low background signal was observed and modes of the supporting tape did not overlap with any characteristic modes of talc. All the modes presented in figures 1(c), (d) belong to talc vibrations and are in accordance with the data in the literature [52].

In the case of thin flakes on SiO_2/Si support (as shown in figure 1(b)), due to higher background signal and Si and SiO_2 modes which partly overlap with the modes of talc, only the most prominent modes at 195.8 cm^{-1}, 363.6 cm^{-1}, and 3677 cm^{-1} were clearly observed. For the flakes thinner than ≈ 10 layers only the characteristic mode of the OH vibrations was clearly observed, mainly since very low background signal at high frequencies allows for a much higher acquisition time. Results from Raman spectroscopy together with AFM and optical microscopy indicate that investigated talc samples are high-quality single crystals.

2.3. Water contact angle measurements of talc single crystals

Contact angle (CA) measurements have been performed with a Kruess DSA100 (Hamburg, Germany) at ambient conditions (23 °C and 55% relative humidity). For the investigation, water as a polar liquid ($\sigma_P = 50$ mN m^{-1}, $\sigma_D = 21.8$ mN m^{-1}) has been chosen. Water droplets with a volume of 1 μl have been deposited on the surface of SiO_2 and talc. Immediately afterwards, the CA has been evaluated via circle fitting in the Kruess Drop Shape Analysis software. For each substrate, four measurements have been performed. The values are given as mean, including standard deviation.

To provide a more realistic comparison with respect to exfoliated ultra-thin flakes, both samples for CA measurements were prepared in the manner which mimics the exfoliated flakes. For the SiO_2/Si, the chips were treated identically as for the exfoliation process, with the exception that only a bare tape was used instead of the tape containing talc flakes. For the talc samples, large-area, flat single crystals were chosen, with sample size of $\approx 8 \times 8$ mm^2. The surface was cleaved approximately 15 min prior to CA experiments, and the water droplets were deposited on areas where no features were observed on the surface by optical microscopy. During measurements, we have been careful in selecting only optically smooth and single-crystal talc surfaces which are significantly larger than water droplets. In this way we avoided any significant influence of local surface roughness variations on the obtained contact angle.

2.4. AFM measurements

AFM characterization of talc flakes was done by NTEGRA Prima AFM system from NT-MDT at ambient conditions. Nanoscale friction was measured by friction (lateral) force microscopy. Lateral force signals were measured during the imaging in contact AFM mode. These signals correspond to the lateral torsion of the AFM cantilever due to the friction between the AFM tip and sample surface during scanning. The friction signal was calculated as a half-difference between the lateral force signals measured in the forward and backward scan-directions. Calibration of the AFM cantilevers and the transformation of the measured friction signals into friction forces was done according to the well-established procedure described in [53]. Two different kinds of probes were used for friction measurements, moderately soft CSG10 and moderately stiff NSG01 probes from NT-MDT, with typical force constants of around 0.11 N m^{-1} and 5.1 N m^{-1}, respectively, and nominal tip curvature radius <10 nm.

Adhesion was determined from AFM based force–displacement curves obtained by the measurement of the AFM cantilever's normal deflection as a function of the vertical extension of the AFM scanner. The adhesion was calculated as the pull-off force needed to separate the AFM tip from the sample surface during tip retraction. Soft CSG01 probes from NT-MDT, with a typical force constant of around 0.03 N m^{-1} were used for that purpose. For each talc flake thickness, a 5×5 matrix of force–displacement curves was recorded on the flake as well as on the surrounding SiO_2 substrate. A value for the adhesion force was calculated by averaging each data set consisting of 25 measurement points.

Dissipation of the mechanical energy was determined in repulsive tapping AFM mode by measuring the phase lag of the AFM cantilever with respect to the phase of the piezo-excitation during the imaging. The phase lag originates from the tip-sample interaction which is controlled by a predefined set-point. A lower (higher) set-point means stronger (weaker) tip-sample interaction and reduced (enlarged) the AFM tip oscillation amplitude. The corresponding energy dissipation was calculated from the phase signal Φ according to the
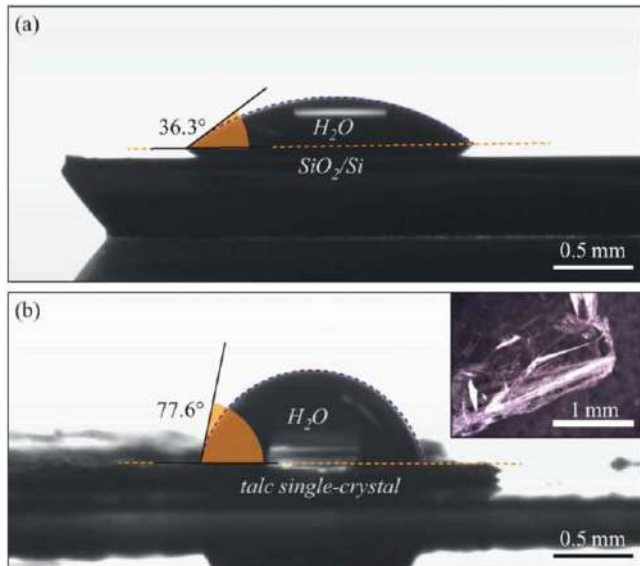
Figure 2. An example of the water CA measurements on (a) SiO_2/Si wafer and (b) talc single-crystal. Inset of (b) shows a low-magnification optical microscope image of one corner of the talc crystal which was used in the CA experiment presented in (b).

following formula [48, 49]

$$E_{dis} = \frac{\pi k A A_0}{Q}\left(\sin\Phi - \frac{A}{A_0}\right), \tag{1}$$

where A and A_0 are amplitude and free-oscillation amplitude of AFM cantilever oscillations, respectively, k is force constant of the AFM cantilever, whereas Q is its quality factor which is around 200. The amplitude ratio A/A_0 is proportional to the amplitude set-point in tapping AFM mode, thus lower (larger) A/A_0 means stronger (weaker) tip-sample interaction.

3. Results and discussion

Good lubrication requires surfaces with a low adhesion. Despite of intriguing wetting properties of talc, at ambient conditions it is hydrophobic [54–57] with a water CA of around 80° [54, 58, 59]. Hydrophobicity of talc should facilitate easier sliding between two contacting surfaces and contribute to better lubrication. Wetting properties of talc were first tested by water CA measurements on both SiO_2/Si wafers and talc crystals. On the silicon oxide surface, a contact angle of $(39 \pm 7)°$ has been obtained (figure 2(a)). This result is similar to literature values [60]. Compared to that, on the talc surface, a contact angle of $(80 \pm 24)°$ has been measured, again in a good agreement with literature [54, 58, 59]. It should be noted that the surface of the talc sample under investigation has a higher roughness than that of the SiO_2/Si wafer (which can be also seen in figure 2(b)), therefore, the deviation in the results is higher. However, the results for the contact angles clearly reveal that the talc surface is less wettable with water, and therefore, more hydrophobic than the SiO_2 surface.
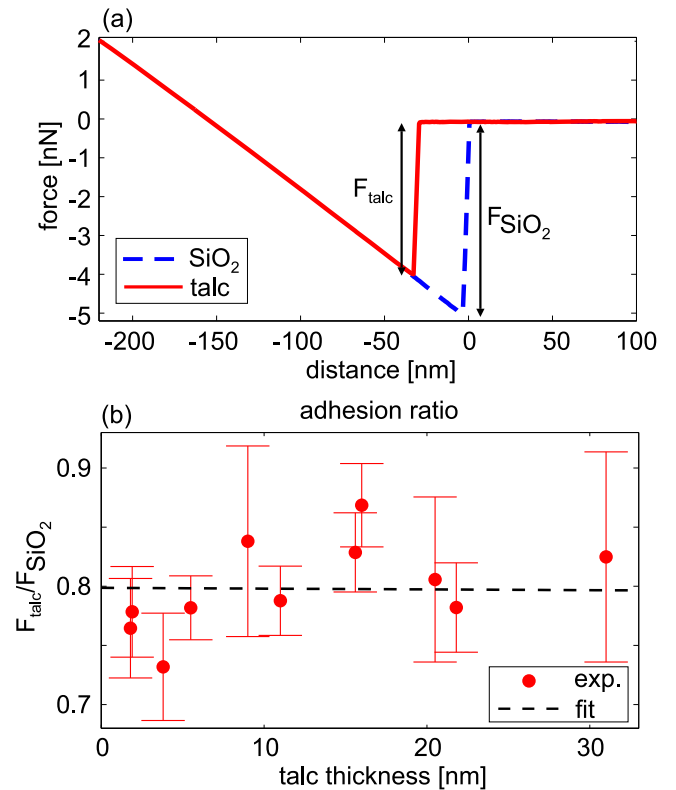

Figure 3. (a) Typical force–displacement curves measured by AFM. The adhesion force is calculated from the force–displacement curves as a pull-off force. (b) The ratio of adhesion forces measured on talc and the silicon-dioxide substrate as a function of the thickness of the talc flakes.

In order to test the adhesive properties of 2D talc flakes at the nanoscale, force–displacement curves were measured by AFM. Typical results are presented in figure 3(a). The adhesion force is marked as a pull-off force needed to separate the AFM tip from a surface and to overcome capillary forces due to an adsorbed water layer. As can be seen, the pull-off force is smaller on the talc covered SiO_2 substrate.

The ratio between adhesion force measured on 2D talc flakes and bare substrate is presented in figure 3(b) as a function of the thickness of talc flakes in the range of around 2–30 nm. Each point on the graph was obtained by averaging adhesion forces calculated from 25 force–displacement curves measured on the same flake. The average adhesion ratio of around 0.80 ± 0.12 means that the talc flakes reduce adhesion by around 20%. Such efficiency in adhesion reduction is similar to the one achieved by CVD graphene [18]. Adhesion measurements demonstrate that 2D talc is more hydrophobic than the surrounding silicon-dioxide substrate. This is in full accordance to the results obtained by CA measurements which reveal that talc is more hydrophobic than the SiO_2 surface. Therefore, the capillary adhesion is less pronounced which should facilitate lubrication. The experimentally measured points were fitted by a linear function represented by the dashed line. As can be seen, the fit is practically a horizontal line (slope of 10^{-4}) indicating that the adhesion force does not depend on the thickness of the talc flakes.
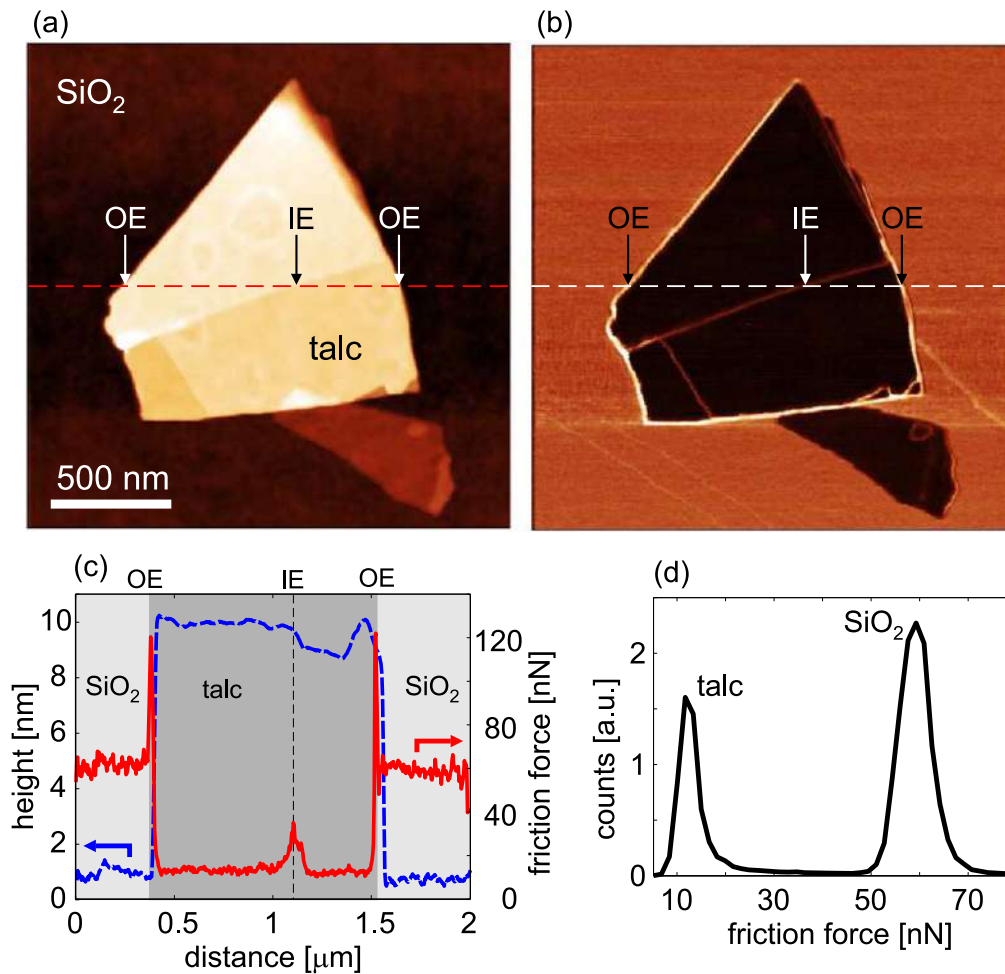
Figure 4. (a) Topography and (b) friction map of the talc flake which is characterized with four height levels (z-scales are 0–11 nm and 7.5–136.5 nN, respectively). Scanning was performed at a normal load $F_N = 138.4$ nN. (c) Cross-section of the topography and friction map along the dashed lines in (a) and (b). OE and IE stand for outer and inner talc edges, respectively. (d) Histogram of the friction map with two peaks corresponding to the friction of talc and bare silicon-dioxide substrate.

Topography and friction map of a typical multilayer talc flake recorded at a constant normal force $F_N = 138.4$ nN are presented in figures 4(a) and (b), respectively. Dark contrast of the talc flake in the friction map indicates decreased friction. Cross-section and histogram of the friction map, depicted in figures 4(c) and (d), respectively, provide more quantitative information. The friction force on the talc flake is around five times lower than on the bare SiO_2 substrate demonstrating very good lubricating properties. Although the talc flake consists of domains with different thickness, the friction on talc is rather homogeneous, characterized by an almost flat line in the friction force cross section and a narrow peak in the histogram, which indicates a weak dependence of the friction on the thickness of 2D talc.

Figure 4(c), with topography and friction profiles, displays that the friction peaks correspond to outer (transitions talc/substrate at a distance of around 0.4 and 1.5 μm) and inner talc edges (the inner step-height transition at a distance of around 1.1 μm between two parts with different thickness of around 1 nm). They are denoted with OE (outer edge) and IE (inner edge), respectively. It is well known that atomic step edges in both bulk [61, 62] and 2D layered materials [63–67]

are associated with enhanced friction which leads to decreased wear resistivity [68, 69]. In the case of non-exposed graphene edges (buried edges covered by graphene layer(s) on top), the friction originates from topographic effects, whereas in the case of exposed edges (bare and uncovered edges exposed to environment), the friction is much more pronounced due to chemically reactive dangling bonds [63, 65–67]. Similar reasoning should be applicable in order to explain the increased friction along talc edges, but a detailed study of the effect is beyond the scope of this manuscript.

The friction maps were measured on the same talc flake as a function of the normal load. For each normal load, the average friction forces for both talc flake and the substrate were calculated from corresponding histograms. The final results are presented in figure 5. The friction forces increase approximately linearly with the normal load whereas their slopes correspond to the friction coefficients. Accordingly, the friction coefficient on talc is 0.11, and it is almost six times lower than on silicon-dioxide (around 0.59) which confirms excellent lubricating properties of 2D talc.

In order to test the dependence of friction on the thickness of talc flakes, the same measurements and analyses were
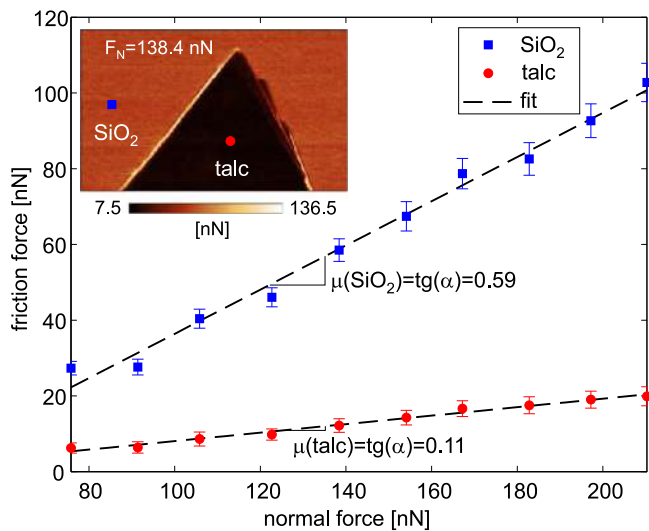
Figure 5. Friction force on talc and silicon-dioxide substrate as a function of the normal load applied by the AFM tip. Data were calculated for the talc flake (with a thickness of 9 nm) from the friction map (recorded at a normal load $F_N = 138.4$ nN) in the inset. Friction coefficients were determined from the slope of linear fits.

performed on different flakes (most of them with multiple height levels). As a result, the friction coefficient for the talc thickness in the range 1–18 nm is depicted in figure 6(a). For each talc flake with a given thickness, the friction coefficient of surrounding SiO_2 was measured as well with the results presented in the top panel of figure 6(a) in order to illustrate clear friction reduction by talc flakes (a bit larger data dispersion for SiO_2 originates probably from non-uniformly distributed contamination during exfoliation). Figure 6(b) illustrates the pair of points T and S corresponding to talc and SiO_2, respectively, for the talc thickness of 9 nm. The experimental points for the talc were fitted by two linear segments. The friction coefficient of talc significantly decreases from 0.16 to 0.1 for the thickness from 1 to 3 nm (1–3 talc layers). In this region with a pronounced dependence (darker region in figure 6(a)), the slope (absolute value) of the friction coefficient versus flake thickness is 0.9. On the other hand, for thicker flakes, from 3 to 18 nm, the friction coefficient is only weakly dependent on the thickness (brighter region in figure 6(a)), with the linear slope of 0.06 (absolute value), which is more than one order of magnitude lower than in the previous segment. The talc friction coefficient practically saturates for thicknesses >3 layers with a low value of only 0.10 ± 0.02. This value is similar to the case of chemical vapor deposited graphene on copper [18], while talc is a dielectric and therefore applicable in the cases where insulating layers are required. The value obtained for the friction coefficient of 2D talc is in accordance with the measurements of a bulk talc with the friction coefficient in a range 0.1–0.4 [70–72].

According to the presented results, friction of talc reduces with increasing material thickness in a similar way as other 2D materials [12], although slower compared to graphene and especially to molybdenum-disulfide and hexagonal boron-nitride. Generally, the friction of 2D materials
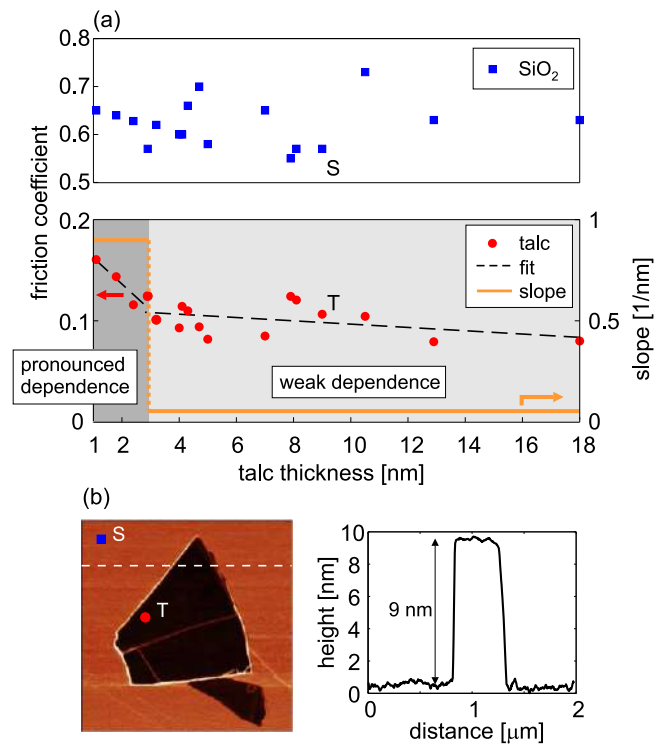

Figure 6. (a) Friction coefficient of talc flakes as a function of their thickness. Dashed line is linear fit, whereas the slope of the friction coefficient versus flake thickness (absolute value) is presented by the solid line. The experimental points are fitted by two linear parts with pronounced (darker region) and weak dependence (brighter) on the thickness. For each talc flake with a given thickness, the measured friction coefficient of surrounding SiO_2 is presented in the top panel. (b) As an illustration, the friction map (left) with the height profile (right) along the dashed line used to calculate points T and S from part (a), obtained for the talc thickness of 9 nm.

decreases with increasing thickness because of the puckering effect [12] and local out-of-plane deformations [73], which are explained as follows. During the sliding of the AFM tip, 2D material becomes locally wrinkled below the tip which effectively increases the contact area and friction [12]. Thicker flakes have larger bending rigidity, and they are less prone to local puckering and out-of-plane deformations which results in a lower friction. A single talc layer is already around 1nm thick, which is almost three times thicker than graphene with the nominal thickness of 0.34 nm. A talc layer consists of three planes: one plane comprises $[MgO_4(OH)_2]$ octahedra, which are 'sandwiched' between two planes containing $[Si_2O_5]$ tetrahedra. Numerical calculations have demonstrated that the bending rigidity of a talc layer is more than thirty times larger than that of graphene [29]. Therefore, the puckering effect and deformation of talc flakes should be less pronounced which is likely the reason behind the observed weaker dependency of the friction coefficient on talc thickness compared to graphene, molybdenum-disulfide, and hexagonal boron-nitride.

During the sliding of the AFM tip in continuous contact with the underlying surface, the dominant dissipation mechanism of the mechanical energy is related to friction. Energy dissipation also takes place when the AFM tip oscillates
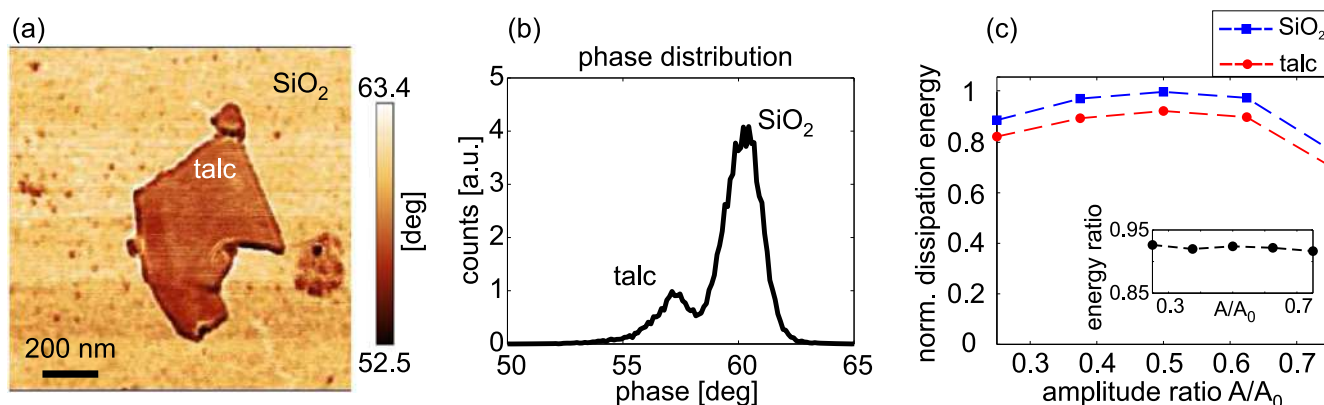
Figure 7. (a) Phase map of a talc flake (with a thickness 2.2 nm) acquired during tapping AFM mode imaging. (b) Histogram of the phase map. (c) Normalized dissipation energy as a function of the AFM amplitude ratio. The inset depicts the ratio between the energy dissipated on talc and bare silicon-dioxide substrate.

against the substrate as is the case in semi-contact (tapping) mode AFM. In order to measure the dissipation in such a case, the imaging in semi-contact (tapping) AFM mode was used. In tapping mode, the AFM tip is moving horizontally and simultaneously oscillating above the sample surface in the normal direction, while touching the surface once per each oscillation period. The dissipation energy is obtained from the simultaneously acquired phase signal according to equation (1).

A typical phase map of a 2D talc flake is displayed in figure 7(a), whereas the corresponding histogram is given in figure 7(b). As can be seen, the flake is darker, with a phase lag Φ lower by around $3°$ (calculated as a phase difference between two peaks in the histogram) than the phase measured on the bare silicon-dioxide substrate. Since the energy dissipation is proportional to $\sin(\Phi)$ (according to equation (1)), it exhibits a lower value on the talc flake. The same measurements and calculations were done for several amplitude ratios A/A_0. Corresponding results for the normalized energy dissipation calculated by equation (1) for both talc flake and bare SiO_2 substrate are shown in figure 7(c). The energy is represented as a function of the amplitude ratio A/A_0 which is inversely proportional to the strength of the AFM tip-substrate interaction. As can be seen, the dissipation is lower for a talc covered substrate. The ratio between the energy dissipated on the talc and the bare SiO_2 substrate, depicted in the inset of figure 7(c), is rather constant, around 0.92–0.93, meaning that the talc decreases dissipation by around 7%–8%. Similar levels of efficiency in reducing energy dissipation was demonstrated in the cases of graphene covered platinum and silicon-dioxide substrates as well [23, 24].

According to the concave, but also rather flat shape of the energy dissipation curve in figure 7(c), dominant dissipation mechanisms during tapping mode imaging are related to a combination of long-range vdW forces [48] and short-range surface hysteresis and capillary forces [48, 74]. It was demonstrated both experimentally [75] and theoretically [76, 77] that graphene and other 2D materials partially screen vdW interactions. Although this screening is less efficient for insulating graphene-like materials [77], it is reasonable to

expect that talc as a 2D insulator is also partially opaque for vdW interactions, the property which is then responsible for lower dissipation due to long-range interactions in dynamic AFM modes. At the same time, reduced adhesion on talc-covered areas, as we have shown, contributes to lower surface energy hysteresis and capillary forces.

4. Conclusions

In summary, we have demonstrated that 2D talc flakes thicker than 3 nm (3 monolayers) have a low friction coefficient of only 0.10 ± 0.02, which weakly depends on the flake thickness. With reduced thickness (<3 nm), the friction coefficient increases reaching a maximum of 0.16 for a monolayer flake ~ 1 nm. Compared to silicon-dioxide substrate, talc flakes reduce friction by more than a factor of five, CA is increased by more than a factor of two, while adhesion and energy dissipation are reduced by around 20% and 7%, respectively. Therefore, 2D talc has all properties necessary for efficient lubrication. The obtained results indicate that the efficiency of talc flakes for nanoscale lubrication is very similar to chemical vapor deposited graphene, while being dielectrics, they are applicable in the cases where insulating layers are required. The natural abundance of talc mineral makes it a cost-effective source of 2D flakes which can be easily exfoliated due to the vdW nature of the mineral. Therefore, 2D talc is a promising and also cost-effective candidate for lubrication at the nanoscale.

Data availability statement

All data that support the findings of this study are included within the article (and any supplementary files).

ORCID iDs

Borislav Vasić ● https://orcid.org/0000-0002-1575-8004
Caterina Czibula ● https://orcid.org/0000-0002-7962-5796
Markus Kratzer ● https://orcid.org/0000-0001-5181-6796
Bernardo R A Neves ● https://orcid.org/0000-0003-0464-4754
Aleksandar Matković ● https://orcid.org/0000-0001-8072-6220
Christian Teichert ● https://orcid.org/0000-0002-0796-2355

References

[1] Achanta S and Celis J-P 2015 *Fundamentals of Friction and Wear on the Nanoscale, chapter Nanotribology of MEMS/NEMS* (Switzerland: Springer International Publishing)

[2] Berman D, Erdemir A and Sumant A V 2018 Approaches for achieving superlubricity in two-dimensional materials *ACS Nano* **12** 2122–37

[3] Zhang S, Ma T, Erdemir A and Li Q 2019 Tribology of two-dimensional materials: from mechanisms to modulating strategies *Mater. Today* **26** 67–86

[4] Liu L, Zhou M, Jin L, Li L, Mo Y, Su G, Li X, Zhu H and Tian Y 2019 Recent advances in friction and lubrication of graphene and other 2D materials: Mechanisms and applications *Friction* **7** 199–216

[5] Feng X, Kwon S, Park J Y and Salmeron M 2013 Superlubric sliding of graphene nanoflakes on graphene *ACS Nano* **7** 1718–24

[6] Sheehan P E and Lieber C M 2017 Friction between van der Waals solids during lattice directed sliding *Nano Lett.* **17** 4116–21

[7] Vasić B, Stanković I, Matković A, Kratzer M, Ganser C, Gajić R and Teichert C 2018 Molecules on rails: friction anisotropy and preferential sliding directions of organic nanocrystallites on two-dimensional materials *Nanoscale* **10** 18835–45

[8] Dienwiebel M, Verhoeven G S, Pradeep N, Frenken J W M, Heimberg J A and Zandbergen H W 2004 Superlubricity of graphite *Phys. Rev. Lett.* **92** 126101

[9] Liu Z, Yang J, Grey F, Liu J Z, Liu Y, Wang Y, Yang Y, Cheng Y and Zheng Q 2012 Observation of microscale superlubricity in graphite *Phys. Rev. Lett.* **108** 205503

[10] Kawai S *et al* 2016 Superlubricity of graphene nanoribbons on gold surfaces *Science* **351** 957

[11] Song Y, Mandelli D, Hod O, Urbakh M, Ma M and Zheng Q 2018 Robust microscale superlubricity in graphite/hexagonal boron nitride layered heterojunctions *Nat. Mater.* **17** 894–9

[12] Lee C, Li Q, Kalb W, Liu X-Z, Berger H, Carpick R W and Hone J 2010 Frictional characteristics of atomically thin sheets *Science* **328** 76–80

[13] Li X, Yin J, Zhou J and Guo W 2014 Large area hexagonal boron nitride monolayer as efficient atomically thick insulating coating against friction and oxidation *Nanotechnology* **25** 105701

[14] Ky D L C, Tran Khac B-C, Le C T, Kim Y S and Chung K H 2018 Friction characteristics of mechanically exfoliated and CVD-grown single-layer MoS_2 *Friction* **6** 395–406

[15] Lavini F, Calò A, Gao Y, Albisetti E, Li T-D, Cao T, Li G, Cao L, Aruta C and Riedo E 2018 Friction and work function oscillatory behavior for an even and odd number of layers in polycrystalline MoS_2 *Nanoscale* **10** 8304–12

[16] Vaziriseteshk M R, Ye H, Ye Z, Otero-de-la Roza A, Zhao M-Q, Gao Z, Johnson A T C, Johnson E R, Carpick R W and Martini A 2019 Origin of nanoscale friction contrast between supported graphene, MoS_2, and a graphene/MoS_2 heterostructure *Nano Lett.* **19** 5496–505

[17] Tran-Khac B-C, Kim H-J, DelRio F W and Chung K-H 2019 Operational and environmental conditions regulate the frictional behavior of two-dimensional materials *Appl. Surf. Sci.* **483** 34–44

[18] Kim K-S *et al* 2011 Chemical vapor deposition-grown graphene: the thinnest solid lubricant *ACS Nano* **5** 5107–14

[19] Klemenz A, Pastewka L, Balakrishna S G, Caron A, Bennewitz R and Moseler M 2014 Atomic scale mechanisms of friction reduction and wear protection by graphene *Nano Lett.* **14** 7145–52

[20] Berman D, Deshmukh S A, Sankaranarayanan S K R S, Erdemir A and Sumant A V 2014 Extraordinary macroscale wear resistance of one atom thick graphene layer *Adv. Funct. Mater.* **24** 6640–6

[21] Vasić B, Matković A, Ralević U, Belić M and Gajić R 2017 Nanoscale wear of graphene and wear protection by graphene *Carbon* **120** 137–44

[22] Filleter T, McChesney J L, Bostwick A, Rotenberg E, Emtsev K V, Seyller T, Horn K and Bennewitz R 2009 Friction and dissipation in epitaxial graphene films *Phys. Rev. Lett.* **102** 086102

[23] Amadei C A, Lai C-Y, Esplandiu M J, Alzina F, Vecitis C D, Verdaguer A and Chiesa M 2015 Elucidation of the wettability of graphene through a multi-length-scale investigation approach *RSC Adv.* **5** 39532–8

[24] Vasić B, Matković A and Gajić R 2017 Phase imaging and nanoscale energy dissipation of supported graphene using amplitude modulation atomic force microscopy *Nanotechnology* **28** 465708

[25] Molina-Mendoza A J *et al* 2017 Franckeite as a naturally occurring van der Waals heterostructure *Nat. Commun.* **8** 14409

[26] Velický M *et al* 2017 Exfoliation of natural van der Waals heterostructures to a single unit cell thickness *Nat. Commun.* **8** 14410

[27] Ray K, Yore A E, Mou T, Jha S, Smithe K K H, Wang B, Pop E and Newaz A K M 2017 Photoresponse of Natural van der Waals Heterostructures *ACS Nano* **11** 6024–30

[28] Frisenda R *et al* 2020 Symmetry breakdown in franckeite: spontaneous strain, rippling and interlayer moiré *Nano Lett.* **20** 1147–1141

[29] Alencar A B, Barboza A P M, Archanjo B S, Chacham H and Neves B R A 2015 Experimental and theoretical investigations of monolayer and few-layer talc *2D Mater* **2** 015004

[30] Barcelos I D *et al* 2018 Infrared fingerprints of natural 2D talc and plasmon? Phonon coupling in graphene? Talc heterostructures *ACS Photonics* **5** 1912–8

[31] Niu Y, Villalva J, Frisenda R, Sanchez-Santolino G, Ruiz-González L, Pérez E M, García-Hernández M, Burzurí E and Castellanos-Gomez A 2019 Mechanical and liquid phase exfoliation of cylindrite: a natural van der Waals superlattice with intrinsic magnetic interactions *2D Mater.* **6** 035023

[32] Santos J C C, Barboza A P M, Matos M J S, Barcelos I D, Fernandes T F D, Soares E A, Moreira R L and Neves B R A 2019 Exfoliation and characterization of a two-dimensional serpentine-based material *Nanotechnology* **30** 445705

[33] Leong Y W, Abu Bakar M B, Mohd Ishak Z A, Ariffin A and Pukanszky B 2004 Comparison of the mechanical properties and interfacial interactions between talc, kaolin, and calcium carbonate filled polypropylene composites *J. Appl. Polym. Sci.* **91** 3315–26

[34] Lapcik L Jr+, Jindrova P, Lapcikova B, Tamblyn R, Greenwood R and Rowson N 2008 Effect of the talc filler content on the mechanical properties of polypropylene composites *J. Appl. Polym. Sci.* **110** 2742–7

[35] Arencón D and Velasco J I 2009 Fracture toughness of polypropylene-based particulate composites *Materials* **2** 2046–94

[36] Yu F, Liu T, Zhao X, Yu X, Lu A and Wang J 2012 Effects of talc on the mechanical and thermal properties of polylactide *J. Appl. Polym. Sci.* **125** E99–109

[37] Deacon R F, Goodman J F and Bowden F P 1958 Lubrication by lamellar solids *Proc. R. Soc.* A **243** 464–82

[38] Rudenko P and Bandyopadhyay A 2013 Talc as friction reducing additive to lubricating oil *Appl. Surf. Sci.* **276** 383–9

[39] Moore D E and Lockner D A 2011 Frictional strengths of talc-serpentine and talc-quartz mixtures *J. Geophys. Res. Solid Earth* **116** B01403

[40] Hirauchi K-I, den Hartog S A M and Spiers C J 2013 Weakening of the slab-mantle wedge interface induced by metasomatic growth of talc *Geology* **41** 75–8

[41] Moore D E and Rymer M J 2007 Talc-bearing serpentinite and the creeping section of the San Andreas fault *Nature* **448** 795–7

[42] Collettini C, Niemeijer A, Viti C and Marone C 2009 Fault zone fabric and fault weakness *Nature* **462** 907–10

[43] Harvey A, Boland J B, Godwin I, Kelly A G, Szydłowska B M, Murtaza G, Thomas A, Lewis D J, O'Brien P and Coleman J N 2017 Exploring the versatility of liquid phase exfoliation: producing 2D nanosheets from talcum powder, cat litter and beach sand *2D Mater.* **4** 025054

[44] Cadore A R, Mania E, Alencar A B, Rezende N P, de Oliveira S, Watanabe K, Taniguchi T, Chacham H, Campos L C and Lacerda R G 2018 Enhancing the response of NH_3 graphene-sensors by using devices with different graphene-substrate distances *Sensors Actuators* B **266** 438–46

[45] Cappella B and Dietler G 1999 Force–distance curves by atomic force microscopy *Surf. Sci. Rep.* **34** 1–104

[46] Bennewitz R 2015 *Fundamentals of Friction and Wear on the Nanoscale* (Switzerland: Springer International Publishing) chapter Friction Force Microscopy

[47] Magonov S N, Elings V and Whangbo M-H 1997 Phase imaging and stiffness in tapping-mode atomic force microscopy *Surf. Sci.* **375** L385–91

[48] Garcia R, Gómez C J, Martinez N F, Patil S, Dietz C and Magerle R 2006 Identification of Nanoscale Dissipation Processes by Dynamic Atomic Force Microscopy *Phys. Rev. Lett.* **97** 016103

[49] Anczykowski B, Gotsmann B, Fuchs H, Cleveland J P and Elings V B 1999 How to measure energy dissipation in dynamic mode atomic force microscopy *Appl. Surf. Sci.* **140** 376–82

[50] Gorbachev R V *et al* 2011 Hunting for monolayer boron nitride: optical and Raman signatures *Small* **7** 465–8

[51] Funke S, Wurstbauer U, Miller B, Matković A, Green A, Diebold A, Röling C and Thiesen P H 2017 Spectroscopic imaging ellipsometry for automated search of flakes of mono-and n-layers of 2D-materials *Appl. Surf. Sci.* **421** 435–9

[52] Wang A, Freeman J J and Jolliff B L 2015 Understanding the Raman spectral features of phyllosilicates *J. Raman Spectrosc.* **46** 829–45

[53] Varenberg M, Etsion I and Halperin G 2003 An improved wedge calibration method for lateral force in atomic force microscopy *Rev. Sci. Instrum* **74** 3362–7

[54] Michot L J, Villieras F, Francois M, Yvon J, Le Dred R and Cases J M 1994 The structural microscopic hydrophilicity of talc *Langmuir* **10** 3765–73

[55] van Oss C J and Giese R F 1995 The hydrophilicity and hydrophobicity of clay minerals *Clays Clay Miner.* **43** 474–7

[56] Rotenberg B, Patel A J and Chandler D 2011 Molecular explanation for why talc surfaces can be both hydrophilic and hydrophobic *J. Am. Chem. Soc.* **133** 20521–7

[57] Ou X, Lin Z and Li J 2018 Surface microstructure engenders unusual hydrophobicity in phyllosilicates *Chem. Commun.* **54** 5418–21

[58] Schrader M E and Yariv S 1990 Wettability of clay minerals *J. Colloid Interface Sci.* **136** 85–94

[59] Giese R F, Costanzo P M and van Oss C J 1991 The surface free energies of talc and pyrophyllite *Phys. Chem. Miner.* **17** 611–6

[60] Thomas R R, Kaufman F B, Kirleis J T and Belsky R A 1996 Wettability of polished silicon oxide surfaces *J. Electrochem. Soc.* **143** 643

[61] Hölscher H, Ebeling D and Schwarz U D 2008 Friction at atomic-scale surface steps: experiment and theory *Phys. Rev. Lett.* **101** 246105

[62] Steiner P, Gnecco E, Krok F, Budzioch J, Walczak L, Konior J, Szymonski M and Meyer E 2011 Atomic-scale friction on stepped surfaces of ionic crystals *Phys. Rev. Lett.* **106** 186104

[63] Lee H, Lee H-B-R, Kwon S, Salmeron M and Park J Y 2015 Internal and external atomic steps in graphite exhibit dramatically different physical and chemical properties *ACS Nano* **9** 3814–9

[64] Boland M J, Nasseri M, Hunley D P, Ansary A and Strachan D R 2015 Striped nanoscale friction and edge rigidity of MoS_2 layers *RSC Adv.* **5** 92165–73

[65] Lang H, Peng Y, Zeng X, Cao X, Liu L and Zou K 2018 Effect of relative humidity on the frictional properties of graphene at atomic-scale steps *Carbon* **137** 519–26

[66] Chen Z, Khajeh A, Martini A and Kim S H 2019 Chemical and physical origins of friction on surfaces with atomic steps *Sci. Adv.* **5** eaaw0513

[67] Chen L, Chen Z, Tang X, Yan W, Zhou Z, Qian L and Kim S H 2019 Friction at single-layer graphene step edges due to chemical and topographic interactions *Carbon* **154** 67–73

[68] Vasić B, Matković A, Gajić R and Stanković I 2016 Wear properties of graphene edges probed by atomic force microscopy based lateral manipulation *Carbon* **107** 723–32

[69] Qi Y, Liu J, Zhang J, Dong Y and Li Q 2017 Wear Resistance Limited by Step Edge Failure: The Rise and Fall of Graphene as an Atomically Thin Lubricating Material *ACS Appl. Mater. Interfaces* **9** 1099–106

[70] Moore D E and Lockner D A 2004 Crystallographic controls on the frictional behavior of dry and water-saturated sheet structure minerals *J. Geophys. Res. Solid Earth* **109** B03401

[71] Escartín J, Andreani M, Hirth G and Evans B 2008 Relationships between the microstructural evolution and the rheology of talc at elevated pressures and temperatures *Earth Planet. Sci. Lett.* **268** 463–75

[72] Chen X, Elwood Madden A S and Reches Z 2017 The frictional strength of talc gouge in high-velocity shear experiments *J. Geophys. Res. Solid Earth* **122** 3661–76

[73] Smolyanitsky A, Killgore J P and Tewary V K 2012 Effect of elastic deformation on frictional properties of few-layer graphene *Phys. Rev. B* **85** 035412

[74] Sahagún E, García-Mochales P, Sacha G M and Sáenz J J 2007 Energy dissipation due to capillary interactions: hydrophobicity maps in force microscopy *Phys. Rev. Lett.* **98** 176106

[75] Tsoi S, Dev P, Friedman A L, Stine R, Robinson J T, Reinecke T and Sheehan P E 2014 van der Waals screening by single-layer graphene and molybdenum disulfide *ACS Nano* **8** 12410–7

[76] Ambrosetti A and Silvestrelli P L 2018 Hidden by graphene? Towards effective screening of interface van der Waals interactions via monolayer coating *Carbon* **139** 486–91

[77] Liu X, Zhang Z and Guo W 2018 van der waals screening by graphenelike monolayers *Phys. Rev. B* **97** 241411

PAPER

Refractive index sensing with hollow metal–insulator–metal metasurfaces

View the article online for updates and enhancements.

You may also like

Refractive index sensing with hollow metal–insulator–metal metasurfaces

Borislav Vasić[1,*] and **Goran Isić**[1,2]

[1] Institute of Physics Belgrade, University of Belgrade, Pregrevica 118, 11080 Belgrade, Serbia
[2] Texas A&M University at Qatar, PO Box 23874, Education City, 23874 Doha, Qatar

E-mail: bvasic@ipb.ac.rs

CrossMark

Abstract

Refractive index sensing with metal–insulator–metal (MIM) metasurfaces featuring a continuous dielectric film between two metallic layers suffers from a low spatial overlap between high field enhancement regions and the analyte placed above. Recent studies have thus turned toward hollow MIM metasurfaces, particularly suited for fluid analytes which can infiltrate the hollow cavities. Here we describe a general procedure for reaching the optimal design in three most relevant configurations: mushroom-type structures with narrow dielectric pedestals carrying the top metallic ribbon array, hollow structures with the metallic ribbon array resting on a distant lateral support, and hollow structures in which the metallic ribbons are carried by an encapsulating layer from top. We contend that since a majority of the resonant eigenmode energy is contained within the analyte, very high refractive index sensitivities are possible for three different measurement methods: spectral, reflectance and phase interrogation. This is confirmed by numerical simulations demonstrating terahertz spectral sensitivities of above 700 GHz RIU^{-1} with a normalized sensitivity of around 0.6 RIU^{-1} (RIU stands for refractive index unit). Detection limits and dynamic ranges are estimated for both bulk refractive index sensing and thin film detection. Refractive index sensitivities and corresponding figure-of-merit factors are shown to reach maxima in the critical coupling regime characterized by equal radiative and non-radiative decay rates of the resonant mode which is controlled by cavity height. Since this regime is associated with a zero reflectance which prevents measurements of any signal, metasurfaces should operate close to the critical coupling point where reflected beam is still measurable. The final optimization is done by decay rate engineering in order to achieve narrower resonances and improve sensing performance.

Supplementary material for this article is available online

(Some figures may appear in colour only in the online journal)

1. Introduction

Metasurfaces comprising planar resonators with narrow spectral features and strong electric field enhancement are good candidates for efficient and label-free refractive index sensors. The flat outline is important because it simplifies fabrication and results in a compact structure while sharp spectral features can be accurately measured using well-established modern detection techniques. High sensitivity is ensured by designing the metasurface so that the analyte ends up at electric field hotspots, while the ensuing refractive-index dependent modification of the spectral response allows for label-free sensing and eliminates the need for a delicate labeling process. As the resonant frequency is swept across the entire electromagnetic spectrum simply by geometrical scaling, metasurfaces have

---

* Author to whom any correspondence should be addressed.

1

been found particularly interesting for applications at mid-infrared, terahertz and microwave frequencies where due to a long wavelength, a strong electric field enhancement is required for detecting refractive index changes of deeply sub-wavelength structures such as thin fluid and molecular films [1–4].

Initial work on metasurfaces for terahertz thin film sensing relied on standard split-ring resonators [5, 6]. Subsequently, it was established that increasing the Q-factor, e.g. by means of employing resonators with Fano lineshapes, improves the sensitivity [7–9]. Further progress was made upon realizing [1] that a large fraction of resonant eigenmode energy contained in the thick and typically high refractive index substrate harms sensitivity. Various approaches to increase the spatial overlap between the resonantly enhanced electric fields and analyte have been attempted, including the utilization of thin [10, 11] or low refractive index substrates [12], lifting of metasurfaces above substrates by dielectric pillars [13] or partially etching the substrates thus making pedestals which hold metasurfaces [14–17].

More recently, attention moved toward metasurfaces which, in addition to the layer of metallic elements on top, include a solid metal film underneath separated by an insulating layer [18], collectively referred to as metal–insulator–metal (MIM) metasurfaces. A distinct feature of such structures are leaky eigenmodes confined between the top metal patch and the underlying metal film [19], offering the possibility of highly enhanced field coupling with an analyte [20]. As a result, MIM metasurfaces have been recognized as promising platforms for sensing based on frequency shift measurements (spectral interrogation) [20–25]. The reflectance (intensity) interrogation based on the measurement of the reflected field intensity is also very efficient when MIM metasurfaces operate as electromagnetic absorbers. Then, a high electric field generated inside MIM cavities leads to a nearly complete absorption of an incident electromagnetic field and a near-zero reflection. Any change of the refractive index of a surrounding medium results in a huge relative change of the reflected field intensity [26, 27] which can be detected even by the naked eye [28]. Finally, the phase of reflected field is associated with a very steep slope in the case of a near-complete absorption. This feature provides a large phase variation upon refractive index changes and very efficient phase sensing [29, 30]. Generally, MIM metasurfaces operating as electromagnetic absorbers are very suitable for sensing since the wave injected into the MIM cavities remains trapped which results in an extreme sensitivity of reflected field to even small perturbations inside the MIM cavities [31]. However, in the original setting whereby the analyte layer is located on top of MIM cavities, the spatial overlap with resonant fields is still relatively low.

Further improvement is reached employing a structured dielectric layer [32–34], especially if parts of the dielectric under the metal patch are etched away forming narrow dielectric pedestals which carry the metal patches in so called mushroom-type MIM metasurfaces [35–37]. The highest analyte-resonant field overlap is achieved in hollow MIM metasurfaces [38–41] suitable especially for fluid analytes which can infiltrate the hollow cavities. In view of the

many diverse approaches and geometries considered for MIM metasurface sensing, a lack of well-defined design procedures and operating regimes which would yield optimal sensitivity is apparent. It should also be noted that so far only spectral interrogation has been considered, while questions on efficiency of sensing based on reflectance and phase measurements remain open.

Here, we present a general analysis of hollow MIM metasurfaces and describe a procedure by which the optimal design (an optimal metasurface is defined as the one with maximized refractive index sensitivity) can be attained for three most relevant configurations (two versions of hollow cavity arrays and the mushroom structure) operating with three different interrogation methods based on frequency, reflectance and phase measurements. The paper is organized in the following way. The modeling of metasurfaces and their operating regimes are described in section 2. The design procedure is discussed in section 3. The spatial overlap between an analyte and MIM cavity modes is analysed in section 4. Bulk refractive index sensitivities are evaluated and discussed in section 5. It is demonstrated that the refractive index sensitivity is maximized in the critically coupled regime where the radiative and non-radiative decay rates of the resonant mode are equal, while in practice, an optimal working point should be close to the critical coupling point. The dynamic range for the sensing and thin film sensitivities are considered in section 6. The final optimization is done by decay rate engineering in order to achieve narrower resonances, which is examined in section 7. At the end, in section 8, we discuss the operation at oblique incidence and issues relevant for practical realization.

2. Sensing structures, modeling and operating regimes

The schematics of four metasurfaces considered in this paper are shown in figure 1. For simplicity, we discuss metasurfaces which are periodic along x- and invariant along the y-direction, while the analysis of structures periodic along both directions would follow along the same lines. In each of cases depicted in figure 1, there is an array of parallel metallic ribbons on top. The dielectric-loaded MIM structure (metasurface 1) from figure 1(a) is transformed into a mushroom-type structure (metasurface 2) from figure 1(b) by etching away parts of the dielectric spacer in order to make isolated dielectric pedestals carrying the metallic ribbons. Two hollow geometries are investigated. The first one (metasurface 3) in figure 1(c) has a top metallic slit array which would, in practice, stand on very distant spacers such as dielectric beads. A fluid analyte, e.g. coming from environment above, can infiltrate the space between two metallic layers through slits. In the second hollow structure (metasurface 4), depicted in figure 1(d), the metallic ribbons are deposited on a transparent encapsulating layer which acts as their mechanical support. In this case, a fluid analyte can flow laterally through the hollow channel.

All configurations can be accounted for by varying the dielectric spacer width w_s in the following way: in dielectric-loaded metasurfaces it is equal to the unit cell width ($w_s = P$),
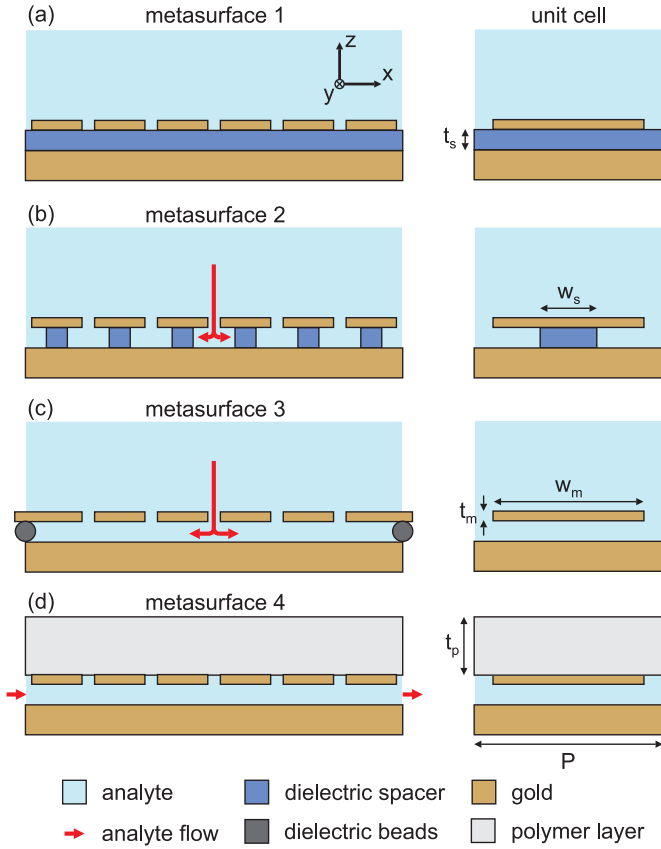
Figure 1. Cross sections (xz-plane) of MIM metasurfaces considered in this paper (left) and corresponding unit cells (right): (a) dielectric-loaded metasurface with a continuous dielectric spacer (metasurface 1), (b) mushroom-type metasurface with a dielectric pedestal in the center (metasurface 2), (c) hollow metasurface with the metallic ribbon array standing on a lateral support (metasurface 3), and (d) hollow metasurface encapsulated by a polymer layer (metasurface 4). All metasurfaces are periodic along x- and invariant along the y-direction.

Figure 2. (a) Reflectance and (b) phase spectra for two values of the analyte refractive index n_a and $n_a + \Delta n_a$. Corresponding changes of (c) reflectance (the absolute and relative changes, $\Delta R = R(n_a + \Delta n_a) - R(n_a)$ and $\rho R = \Delta R / R(n_a)$, respectively) and (d) phase ($\Delta \Phi = \Phi(n_a + \Delta n_a) - \Phi(n_a)$).

figure 1(a), in mushroom-type structures it is narrower than the metallic ribbon width ($w_s < w_m$), figure 1(b), while in hollow metasurfaces it is completely removed ($w_s = 0$), figures 1(c) and (d). Numerical calculations were done using rigorous coupled wave analysis implemented in the Reticolo code [42]. The unit cells of metasurfaces employed in simulations are presented on the right hand side of figure 1. The period P, metallic ribbon width w_m and spacer thickness (i.e. cavity height) t_s are selected according to the design procedure described below. The thickness of top metallic ribbons is $t_m = 300$ nm, whereas the metasurface from figure 1(d) is encapsulated by a polymer layer with the thickness $t_p = 40\,\mu$m.

The refractive index $n_a = 1.5$ of the reference analyte was chosen as representative for typical low-loss liquids at terahertz frequencies, such as hexane ($n_a = 1.37$), octane ($n_a = 1.391$), decane ($n_a = 1.405$), and ethanol ($n_a = 1.6$) [39, 43]. The refractive index sensitivity was calculated by increasing n_a to $n_a + \Delta n_a$, where $\Delta n_a = 0.1$ in the case of frequency interrogation, $\Delta n_a = 0.01$ in the case of reflectance interrogation, and $\Delta n_a = 0.001$ in the case of phase interrogation. Metallic parts were assumed to be
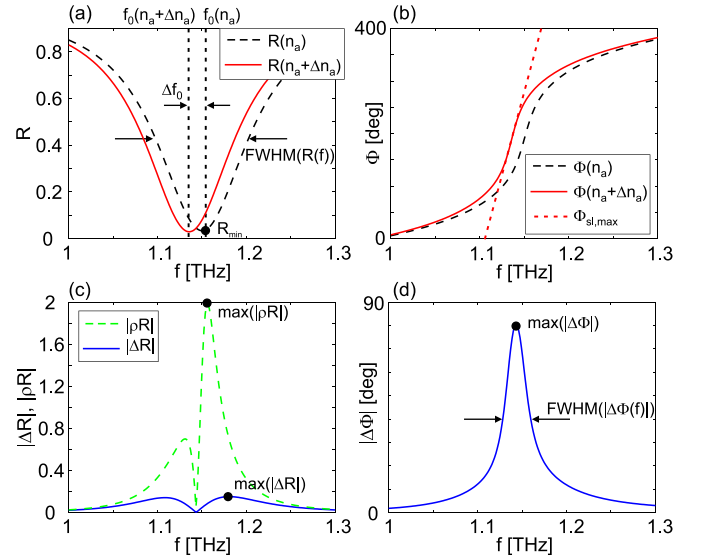
made of gold and modeled by Drude permittivity (plasma frequency $\omega_p = 1.37 \times 10^{16}$ rad s^{-1}, collision frequency $\gamma_c = 4.05 \times 10^{13}$ rad s^{-1}) [44] whereas polyimide with a refractive index of $n_s = 1.8 + j0.06$ [45, 46] was assumed for dielectric spacers in metasurfaces 1 and 2. The encapsulating layer for metasurface 4 in figure 1(d) was modeled by a low-loss polymer Zeonor with a refractive index of $n_p = 1.518 + j0.0009$ [47].

The sensing mechanism is based on shifting of a metasurface resonance due to small changes of n_a. As a result, the resonant frequency f_0 as well as the reflectance R and phase Φ at the operating frequency (not necessary equal to the resonant one) are changed as illustrated in figures 2(a) and (b). Three refractive index sensitivities (frequency, reflectance and phase), corresponding to three distinct interrogation methods, are calculated, as defined by the formula $S_I(f) = |\Delta I(f)| / \Delta n_a$, where f in parentheses denotes the operation frequency (relevant only for reflectance and phase interrogation). Depending on the chosen interrogation method, $I(f)$ stands for resonant frequency f_0, reflectance $R(f)$, or phase $\Phi(f)$. $\Delta I(f)$ denotes the change of $I(f)$ resulting from a given change Δn_a of n_a, as illustrated in figure 2. According to this definition, for reflectance and phase $S_I(f)$ is operation frequency dependent, while it is not the case for frequency interrogation.

Figure-of-merit (FOM) factors are introduced in order to evaluate the sensing efficiency from the viewpoint of listed interrogation methods. Each FOM factor is defined as the ratio between sensitivity $S_I(f)$ and a conveniently selected nonideality metric $N_I(f)$: $\text{FOM}_I(f) = S_I(f) / N_I(f)$. In spectral interrogation, narrower resonances are easier and more precisely detected. Therefore, N_f is usually taken as the resonance linewidth $\text{FWHM}\{R(f)\}$, defined as the full-width at half maximum (FWHM) of the reflectance spectra $R(f)$, figure 2(a). For intensity interrogation, $N_R(f)$ can be taken to
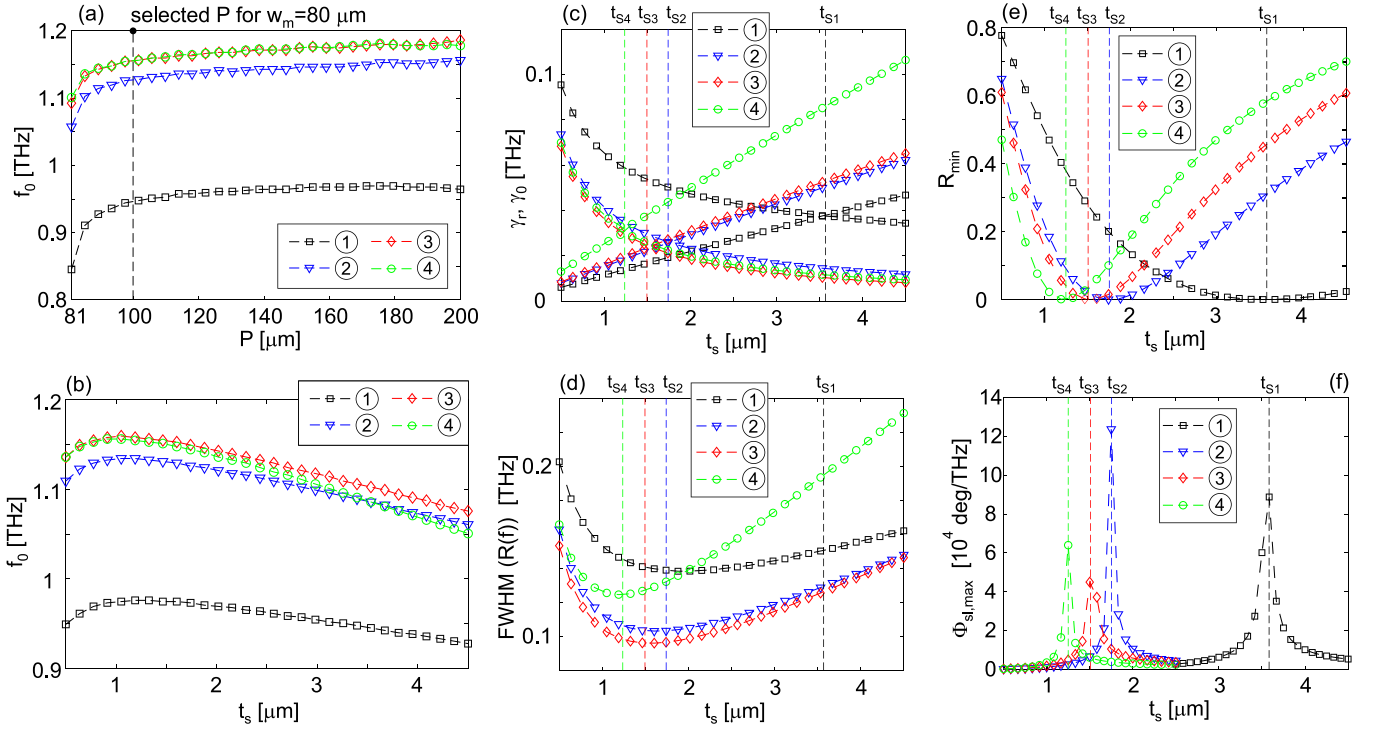
Figure 3. Resonant frequency as a function of (a) period P and (b) spacer thickness t_s. The vertical dashed line in (a) denotes the selected period of 100 μm. (c) Radiative and non-radiative decay rates, γ_r, γ_0, and (d) spectral width (FWHM) of resonant modes, (e) the minimal reflectance R_{min} and (f) the maximal phase slope $\Phi_{sl,max}$ (illustrated in figure 2(b)) for all considered metasurfaces as a function of t_s. The critical coupling for the considered metasurfaces 1–4 is approximately achieved for $t_{s1} = 3.5$ μm, $t_{s2} = 1.75$ μm, $t_{s3} = 1.5$ μm, and $t_{s4} = 1.25$ μm, respectively, which are denoted by the vertical dashed lines.

be equal to the reflectance [26] $R(f)$ at operation frequency. This is justified by the fact that the accuracy of measurements is maximized for structures operating near the point of darkness with a near zero reflection [26]. Then any variation of surrounding refractive index would result in a huge relative change of the reflectance (theoretically infinite for the zero reflectance in the working point) as shown in figure 2(c). In order to avoid extremely low and experimentally non-achievable values, the minimal reflectance in numerical calculations was set to 0.01. Finally, for phase interrogation, $N_\Phi(f)$ is set equal to the spectral width FWHM$\{\Delta\Phi(f)\}$, figure 2(d), because steeper phase change is easier to detect [48].

The spectral response of MIM metasurfaces is known to be determined through the interplay of radiative and non-radiative decay processes of the resonant mode [49], as quantified by their respective rates γ_r and γ_0. In this sense, there are three possible operating regimes [49, 50]: undercoupled ($\gamma_r < \gamma_0$), overcoupled ($\gamma_r > \gamma_0$), and critically coupled ($\gamma_r = \gamma_0$). Radiative and non-radiative decay rates are most directly obtained by fitting the actual reflection coefficient (measured or numerically simulated) to the so-called temporal coupled-mode theory model [51]. For the single channel case considered here, it amounts to fitting $R(f)$ to $R_{TCMT} = 1 - 4\gamma_0\gamma_r/((f-f_0)^2 + (\gamma_0 + \gamma_r)^2)$, with γ_r and γ_0 as fitting parameters [49, 52]. The calculations below were done for reflectance spectra with variable spacer thickness t_s (typical spectra for metasurface 4 are given in figure S1 of supplementary materials (available online at stacks.iop.org/JPD/54/285106/mmedia)). Since $R(f)$ has an inverted Lorentzian shape, its FWHM is qual to $2(\gamma_r + \gamma_0)$.

3. Design procedure

The geometry of MIM metasurfaces is determined by three parameters, metallic ribbon width w_m, period P, and spacer thickness t_s. The cavity mode is a standing wave with the wavelength determined by the metallic ribbon width. According to the cavity or standing-wave resonance model [49, 53], the resonant frequency of MIM cavities can be approximated with $f_0 = c/(2w_m n_c)$, where c is the velocity of light in vacuum and n_c is the cavity refractive index. The considered metasurfaces are designed for operation around 1 THz due to a straightforward fabrication of terahertz structures, whereas applications at higher frequencies are discussed below. For the chosen resonant frequency, the cavity model gives w_m around 83 and 100 μm for the spacer refractive index of 1.8 (polyimide spacer for metasurface 1) and 1.5 (spacer with completely infiltrated analyte for metasurfaces 3 and 4). Finally, we adopted $w_m = 80$ μm.

We start by considering a unit cell width that seems reasonable, $P = 100$ μm. In particular, it is chosen with the aim of achieving a large ratio w_m/P since it implies that the resonant eigenmode will span the majority of the unit cell (meaning that a high field enhancement over a large fraction of the unit cell is obtained). The resonant frequency is practically independent of P for periods larger than 100 μm as depicted in figure 3(a). On the other hand, for smaller periods the cavity modes are not localized anymore, and due to their hybridization [19], f_0 decreases. Later, in section 7, we will consider how changing P affects sensitivity, reaching a somewhat unexpected
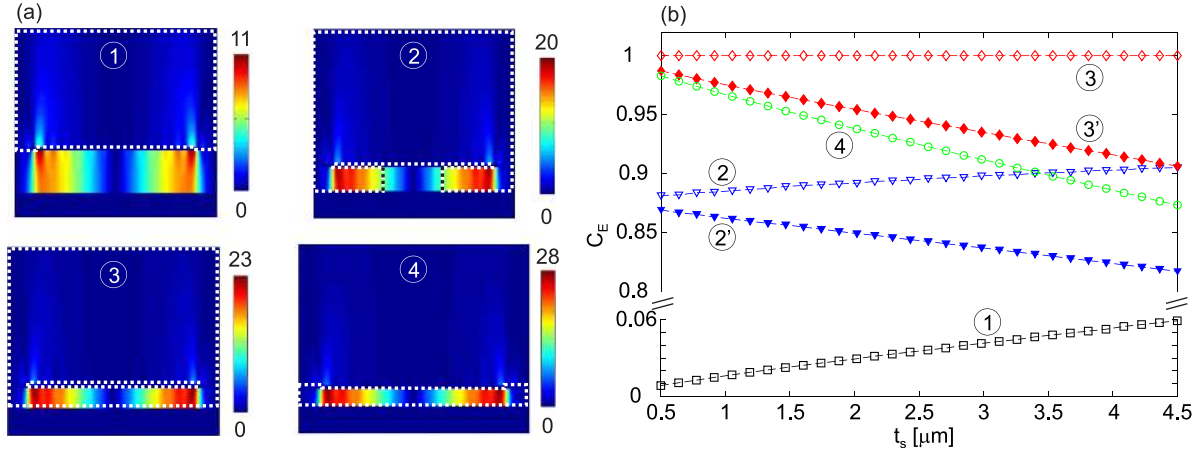
Figure 4. (a) Spatial distribution of the electric field enhancement $|E_z/E_0|$ of the resonant modes within unit cells for all four metasurfaces. The calculations were done for $t_{s1} = 3.5$ μm, $t_{s2} = 1.75$ μm, $t_{s3} = 1.5$ μm, and $t_{s4} = 1.25$ μm, respectively, and at resonant frequencies. The areas containing an analyte are encircled by dotted lines. (b) C_E factor as a function of spacer thickness. In structures 1–3, the height of the areas with the analyte was limited to 10 μm for the sake of numerical calculations. Metasurfaces marked with 2' and 3' are modified versions of metasurfaces 2 and 3, respectively, where the fraction of electric field energy in the analyte above the metasurfaces is omitted.

conclusion. In the dielectric pedestal case, metasurface 2 in figure 1(b), we fix $w_s = P/3$.

The resonant frequency weakly depends on the spacer thickness as shown in figure 3(b). On the other hand, t_s dominantly controls radiative and non-radiative decay rates, presented in figure 3(c), and thus determines the operating regime of MIM metasurfaces [49, 50]. Typically for MIM metasurfaces, γ_r grows approximately linearly with t_s while γ_0 decays as $1/t_s$ [49]). The critical coupling is determined by the point of intersection of these two curves when $\gamma_r = \gamma_0$. The intersection points from figure 3(c) approximately give the following spacer thicknesses (denoted by vertical lines in figure 3): $t_{s1} = 3.5$ μm for metasurface 1, $t_{s2} = 1.75$ μm for metasurface 2, $t_{s3} = 1.5$ μm for metasurface 3, and $t_{s4} = 1.25$ μm for metasurface 4. The resonance width is minimized for t_s values which are usually close to the critical coupling point, figure 3(d). A slight deviation is observed only for metasurface 1 due to higher non-radiative decay rates as a result of losses in the polyimide spacer. At the same time, the minimal reflectance $R_{\min}$, figure 3(e), and maximal phase slope $\Phi_{\text{sl,max}}$, figure 3(f), reach extrema exactly at the critical coupling point. These results indicate that the operation of metasurfaces around the critical coupling point could be beneficial for sensing since reduced resonance width and low reflectance provide enhanced FOMs with the spectral and reflectance interrogation, respectively, while a large phase slope facilitates sensing with phase interrogation.

4. Fraction of electric field energy in analyte

Regardless of interrogation method, the sensing is based on the spectral shift of a metasurface resonance due a small change of analyte refractive index. Therefore, a larger spectral shift is expected to give a larger refractive index sensitivity in all three interrogation methods. According to the perturbation theory, the relative frequency change $\Delta f_0/f$ of an electromagnetic

cavity with refractive index n and dielectric permittivity ε due to a small change of refractive index Δn is given by the following approximate equation [54, 55]

$$\frac{\Delta f_0}{f} = -\frac{\Delta n}{n} \frac{\int_{\text{analyte}} \varepsilon |E|^2 \mathrm{d}V}{\int_{\text{all space}} \varepsilon |E|^2 \mathrm{d}V} = -\frac{\Delta n}{n} C_E, \qquad (1)$$

where E is the electric field while C_E is the fraction of electric field energy confined within the volume of an analyte to be sensed. Therefore, the relative frequency shift for a given refractive index change $\Delta n/n$ depends only on factor C_E. The maximal relative frequency shift of $(\Delta f_0/f)_{\max} = \Delta n/n$ is then achieved for $C_E = 1$ when the entire electric field energy of an electromagnetic resonator is stored within the analyte.

Spatial distributions of the electric field enhancement $|E_z/E_0|$ (E_0 is the magnitude of the incident electric field) are displayed in figure 4(a) for all four metasurfaces. The cavity modes with a high field enhancement are excited between two metallic layers and their overlap with an analyte (encircled for a better visibility) is drastically increased in metasurfaces 2–4. Using such spatial distributions, factor C_E was calculated as a function of spacer thickness and depicted in figure 4(b). C_E is maximal and equal to 1 for metasurface 3 since the analyte is infiltrated both in MIM cavities as well as above them. For metasurfaces 2 and 4, a fraction of the electric energy is stored inside the dielectric pedestal (metasurface 2) and the encapsulating layer (metasurface 4) and therefore does not overlap with analyte. As a result, the nominator in equation (1) is decreased leading to a lower C_E. For t_s around 1.5 μm, C_E is reduced by only ~10% and ~5%, respectively. On the other hand, in the dielectric-loaded metasurface 1, the analyte is out of the region with a high field enhancement leading to a very low C_E less than 0.1.

In calculations of C_E factors for modified metasurfaces 2 and 3, marked with 2' and 3', only the electric field energy inside MIM cavities was taken into account, while
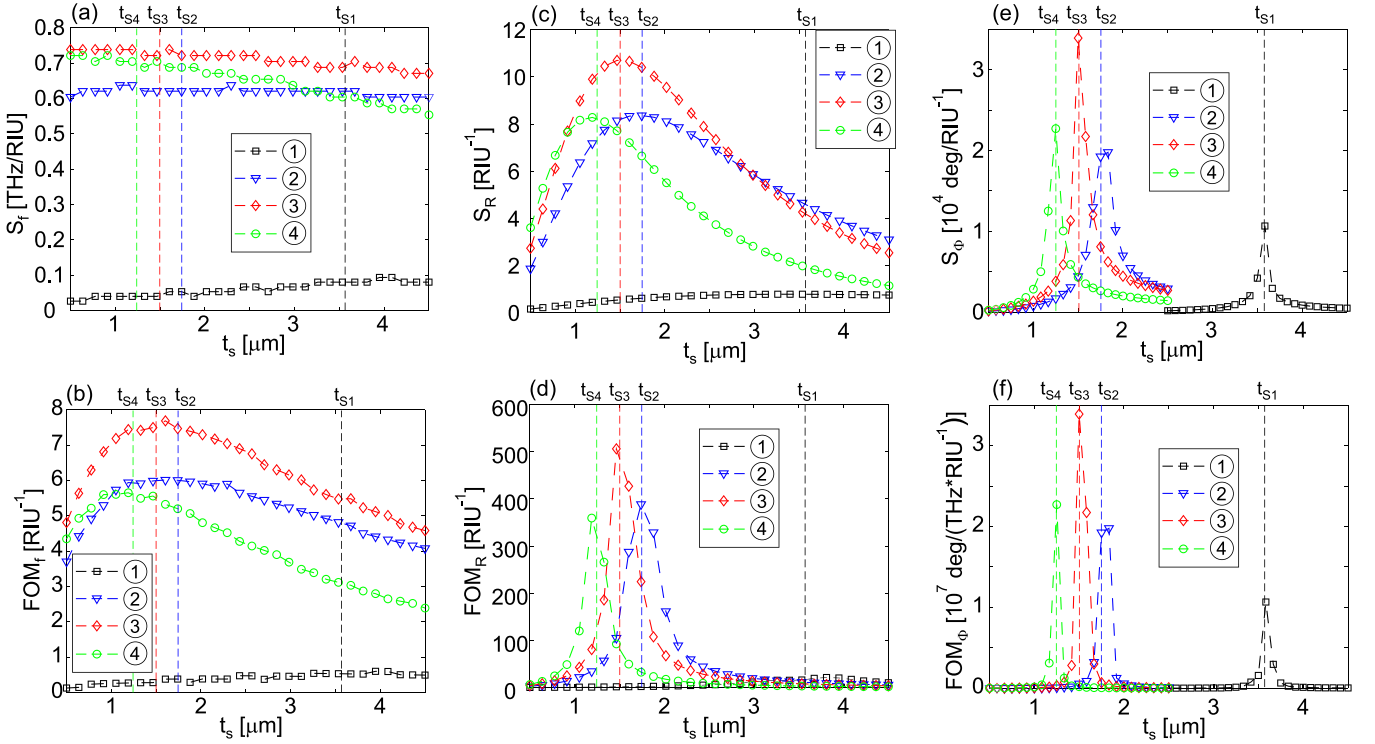
Figure 5. Bulk refractive index sensitivities and corresponding FOM factors: (a) S_f and (b) FOM$_f$, (c) S_R and (d) FOM$_R$, (e) S_Φ and (f) FOM$_\Phi$.

the fraction above the metasurfaces was omitted. An analogous case for metasurface 4 was not considered since the analyte is already confined between two metallic layers. Since the electric field enhancement is dominantly distributed inside the MIM cavities, C_E for the modified metasurfaces is only slightly decreased by around 5%. This indicates that metasurfaces 2 and 3 can operate with high refractive index sensitivities even for analytes confined just inside them as will be discussed later in section 6.

5. Bulk refractive index sensitivity

The numerically calculated refractive index sensitivities S_f, S_R, S_Φ, and corresponding FOM factors, FOM$_f$, FOM$_R$, FOM$_\Phi$ are given in figure 5. For reflectance and phase interrogation in which these quantities are operation frequency dependent, the operation frequency is set to the value at which sensitivity reaches its maximum over a conveniently chosen spectral interval enclosing the resonance (thus the operation frequency is slightly different at each t_s). Due to a large C_E factor of metasurfaces 2–4, the spectral and reflectance sensitivities are enhanced by around order of magnitude compared to the dielectric-loaded configuration of metasurface 1. The phase sensitivity of metasurfaces 2–4 is increased 2–3 times. The lower enhancement of the phase sensitivity is achieved because S_Φ dominantly depends on the phase slope which is very high in the case of the dielectric-loaded structure as well, figure 3(f). Except S_f which is independent on the operating regime, all sensitivities and FOM factors are maximized around the critical coupling point. In mushroom-type

metasurfaces, the pedestal width w_s of around 40% of the metallic ribbon width w_m is already sufficiently narrow to provide sensitivities comparable to hollow metasurfaces.

The spectral sensitivity S_f, figure 5(a), around the critical coupling point is above 0.6 THz RIU^{-1} for metasurface 2 and above 0.7 THz RIU^{-1} for metasurfaces 3 and 4 (RIU stands for refractive index unit). According to the perturbation theory and equation (1), $|S_f| = (f_0/n_a)C_E$ while the maximal sensitivity $|S_f|_{\max} = f_0/n_a$ is achieved for $C_E = 1$, when the fraction of the electric field energy in an analyte is maximized. As a result, the maximal theoretical sensitivities for the critically coupled metasurfaces are the following: 0.63 THz RIU^{-1} for metasurface 1 ($f_0 = 0.95$ THz), 0.75 THz RIU^{-1} for metasurfaces 2 ($f_0 = 1.12$ THz), and 0.77 THz RIU^{-1} for metasurfaces 3 and 4 ($f_0 = 1.15$ THz). The numerical results show that metasurfaces 2, 3, and 4 reach 83%, 95%, and 90% of the theoretically predicted spectral sensitivity, as a result of large C_E factors, $C_E \approx 0.89$, $C_E = 1$, and $C_E \approx 0.96$, respectively. On the other hand, metasurface 1 with a very low C_E factor less than 0.05 achieves only 13% of S_f predicted by the perturbation theory. While the spectral sensitivity does not depend on spacer thickness, FOM factor FOM$_f$, figure 5(b), is inversely proportional to resonance width FWHM($R(f)$) and reaches the maximum around the critical coupling point where FWHM is minimized, figure 3(d).

The reflectance sensitivity S_R, figure 5(c), has a maximum around the critical coupling point. Here the resonance width is minimized, figure 3(d), which provides maximal ΔR (illustrated in figure S2 of supplementary material). The maximal sensitivity is achieved with metasurface 3. Due to the largest

C_E factor, it is associated with largest spectral shifts reflectance changes for the same refractive index variation. FOM factor FOM_R, figure 5(d), inversely proportional to reflectance, has a sharp peak at the critical coupling point where the reflectance reaches the minimal value close to zero, figure 2(e).

The phase sensitivity S_Φ, figure 5(e), and corresponding FOM_Φ, figure 5(f), are also maximized at the critical coupling point. Phase difference due to refractive index change grows with the slope of the phase curve $\Phi(f)$ (illustrated in figure S3 of supplementary material), which is maximized at the critical coupling point as depicted in figure 3(f). FOM factor FOM_Φ is also maximized at the critical coupling point since it is inversely proportional to the spectral width of $\Phi(f)$ which is minimized at this point (given in figure S3 of supplementary material).

Although the refractive index sensitivities and FOM factors are maximized at the critical coupling point, this operating regime is associated with zero reflectance which prevents measurements of any signal. Therefore, practical devices should be designed to operate close to the critical coupling point where reflected beam is still measurable. Such small detuning from the critical coupling point can be also expected in realistic devices due to unintentional deviations of t_s introduced during fabrication. According to experimental data [56], it is safe to adopt that the minimal reflectance for reliable terahertz reflection and phase measurements is $R_{\text{th}} = 0.01$. According to figure 3(e), the minimal reflectance R_{min} is below the established threshold of 0.01 for $\Delta t_s \approx 150$ nm around t_{si} ($i = 1\text{--}4$). Therefore, realistic and experimentally measurable sensitivities are obtained for the spacer thicknesses $t_{\text{si}} \pm \Delta t_s$.

The spectral interrogation is independent on spacer thickness and obviously not influenced by fluctuations of t_s. The reflectance sensitivity is also robust, S_R for metasurface 3 decreases by only $\sim 3\%$ for $\Delta t_s = 150$ nm as can be seen from figure 5(c). On the other hand, the phase sensitivity, figure 5(e), is severely affected by deviations of t_s and it decreases by more than 50% for $\Delta t_s = 150$ nm. Therefore, realistic values for S_Φ are around 1×10^4 deg RIU^{-1}.

Bulk refractive index sensitivities S_f for metasurfaces 3 and 4 are above 700 GHz RIU^{-1}, while the normalized sensitivity S_f/f_0 is around 0.6 RIU^{-1} (for f_0 around 1.15 THz). These values are slightly larger than the best experimental results achieved so far with hollow metasurfaces and for similar n_a around 1.5 ($S_f \approx 500$ GHz RIU^{-1} [38], normalized sensitivity 0.31–0.55 RIU^{-1} [39]). The obtained sensitivities also exceeds the results previously obtained with other sensing platforms at terahertz frequencies, such as waveguides [57] ($S_f = 91.25$ GHz RIU^{-1}) and Fabry–Pérot cavities (normalized sensitivity of around 0.52 RIU^{-1}) [58]. At the same time, the cavity height of hollow metasurfaces (≈ 1.5 μm) is much smaller than the thickness of waveguide (≈ 1 mm) and Fabry–Pérot cavities $\approx 50\text{--}70$ μm which indicates that hollow metasurfaces are good candidates for more compact and lower limit of detection sensing.

The comparison of refractive index sensitivities with intensity (reflectance) interrogation is more difficult since it has been much less employed. The sensitivity of holey MIM metasurface operating in transmission mode [59] of around

0.67 RIU^{-1} is order of magnitude lower than the sensitivity of hollow metasurfaces. The main benefit of the reflectance interrogation is large FOM factor and relative reflectance change for structures operating with a near-zero reflection. The phase interrogation is still practically unexplored at terahertz frequencies. The obtained phase sensitivity of around 1×10^4 deg RIU^{-1} is comparable to maximal phase sensitivities of up to 10^5 deg RIU^{-1} obtained at optical frequencies [60]. Since metasurfaces 2–4 are associated with high spectral, reflectance, and phase sensitivities at the same time, the same MIM geometry can be employed for efficient sensing with multiple interrogation methods.

According to the calculated refractive index sensitivities for metasurface 3 of $S_f \approx 700$ GHz RIU^{-1}, $S_R \approx 10$ RIU^{-1}, and $S_\Phi \approx 10^4$ deg RIU^{-1} and the corresponding resolutions [61] for spectral, reflectance and phase measurements of $\delta f = 2\text{--}5$ GHz, $\delta R = 0.01$, and $\delta \Phi = 1°$, respectively, the limit of detection for refractive index sensing is estimated at 0.003–0.007 ($< 10^{-2}$) for the spectral interrogation, 10^{-3} for the reflectance interrogation, and finally, only 10^{-4} for the phase interrogation.

6. Dynamic range and thin film sensitivity

In previous sections, refractive index sensitivities have been calculated by increasing an analyte refractive index $n_a = 1.5$ for a fixed and small Δn_a. On the other hand, dynamic range defines the range of Δn_a for which the specified sensitivity can be reached. Figures 6(a)–(c) depict changes of a measured signal (Δf_0, ΔR, $\Delta \Phi$) for Δn_a varied up to 0.5 ($n_a + \Delta n_a$ in the range 1.5–2) for the spectral and reflectance interrogation, and up to 0.01 ($n_a + \Delta n_a$ in the range 1.5–1.51) for the phase interrogation. The insets of figures 6(a)–(c) display corresponding refractive index sensitivities. The sensing with spectral interrogation provides a wide dynamic range since $|\Delta f_0|$ almost linearly grows with Δn_a (figure 6(a)) in the whole range. At the same time, the resulting sensitivity S_f decreases by only 30% for $\Delta n_a = 0.5$. On the other hand, $|\Delta R|$ is approximately linear only for $n_a + \Delta n_a$ in the range from 1.5 to 1.6 (figure 6(b)). For $\Delta n_a \gtrsim 0.1$, the slope of $|\Delta R|$ curve progressively falls down while $|\Delta R|$ approaches the maximal value of 1. As a result, the reflectance sensitivity decreases by almost order of magnitude for $\Delta n_a = 0.5$. The phase interrogation is characterized with a very narrow dynamic range since $\Delta \Phi$ is linear up to only $\Delta n_a = 0.002$ while S_Φ falls down by four times for $\Delta n_a = 0.01$ (figure 6(c)). Therefore, from the point of view of the limit of detection, the phase interrogation provides the best sensing performance, but such high sensitivity is achievable in a very narrow range of Δn_a in the order of 10^{-3}.

So far we have considered bulk refractive index sensitivities, but they stay on the same level if an analyte is confined just within MIM cavity, in the channel between bottom metallic plate and top metallic resonators. This is illustrated in figure S4 of supplementary material for metasurfaces 2 and 3, while the analyte is already confined in metasurface 4. The reason for such behavior is high C_E factor even in the case when the fraction of electric field energy above metasurfaces is omitted,
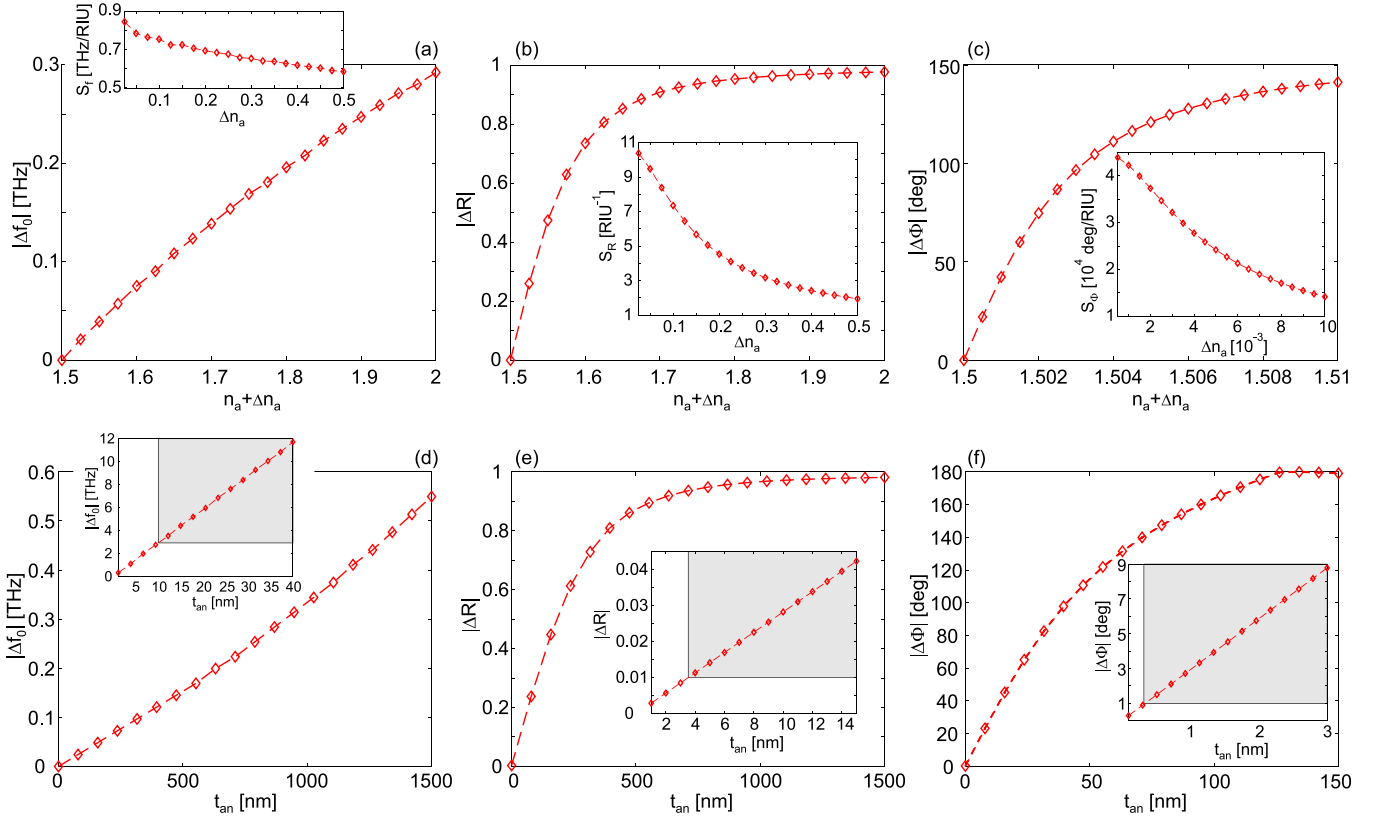
Figure 6. Dynamic range for metasurface 3: (a) $|\Delta f_0|$, (b) $|\Delta R|$, and (c) $\Delta\Phi$ for increasing Δn_a. The inset depicts changes of the corresponding sensitivities. Thin film refractive index sensitivities for metasurface 3: (d) $|\Delta f_0|$, (e) $|\Delta R|$, and (f) $\Delta\Phi|$ as a function of analyte thickness t_a. The inset depicts changes of the measured signal for ultra-thin films in order to determine limits of detection. Shaded areas denote measurable film thicknesses.

as illustrated for metasurfaces 2′ and 3′ in figure 4(b). Therefore, obtained bulk refractive index sensitivities can be easily transformed into thin film sensitivities by dividing them with spacer thickness (t_{s2}, t_{s3}, t_{s4}). For metasurfaces 3 and 4, thin film sensitivities in the spectral interrogation are around 4.7×10^5 GHz (RIU^{-1} mm^{-1}), and around 4×10^5 GHz (RIU^{-1} mm^{-1}) for metasurface 2. These values are very high considering the highest spectral sensitivities (in the range 10^3–2.1×10^5 GHz (RIU^{-1} mm^{-1})) reported so far with terahertz metasurfaces [4].

Metasurfaces 2–4 provide the sensing of analytes confined within MIM cavities and therefore with a deep subwavelength thickness, where the ratio of the free-space wavelength λ_0 and the analyte (spacer) thickness is around 150–200. As a result, such metasurfaces are suitable for sensing of thin films. Limits of detection were estimated for metasurface 3. In numerical calculations, a thin film with refractive index $n_a = 1.5$ and a variable thickness t_a up to the spacer thickness $t_s = 1.5 \mu$m was placed inside MIM cavities, on the top of the bottom metallic plate. The rest of the cavities remained hollow. The results for changes of resonant frequency, reflectance, and phase with increasing film thickness t_a are given in figures 6(d)–(f).

Similar to the previous analysis of dynamic range, $|\Delta f_0|$ approximately linearly grows with t_a up to the maximal thickness of 1.5 μm. On the other hand, the dynamic ranges for the reflectance and phase measurements are narrower, since

ΔR and $\Delta\Phi$ are linear up to $t_a \approx 250$ nm and $t_a \approx 40$ nm, respectively. At the same time, ΔR and $\Delta\Phi$ go into the saturation (characterized with maximal $\Delta R = 1$ and $\Delta\Phi = 180°$) for $t_a \approx 1\ \mu$m and $t_a \approx 130$ nm, respectively. Limits of detection of thin film thickness are determined from the insets of figures 6(d)–(f). If assumed resolution is $\delta f = 2$–5 GHz for the spectral interrogation and $\delta R = 0.01$ for the reflectance interrogation [61], the limits of detection are around 10 and 4 nm, respectively (the insets of figures 6(d) and (e)). Therefore, the spectral and reflectance interrogation allow detection of very thin films with a large λ_0/t_a ratio of around 5×10^4. The ultimate sensitivity for thin film detection is achieved with the phase interrogation since the accuracy of phase measurements of $\delta\Phi = 1°$ enables the detection of films with angstrom thickness as shown in the inset of figure 6(f). According to these results, hollow metasurfaces provide very high sensitivities for detection of thin film thickness as well, which are comparable to the best sensitivities achieved so far [62, 63].

7. Optimization by decay rate engineering

The main focus of the previous analysis was on the reaching of the maximal C_E factor by maximizing the overlap of an analyte and regions with a high electric field enhancement in order to minimize the influence of underlying substrate. Another direction to improve sensing performance is to design
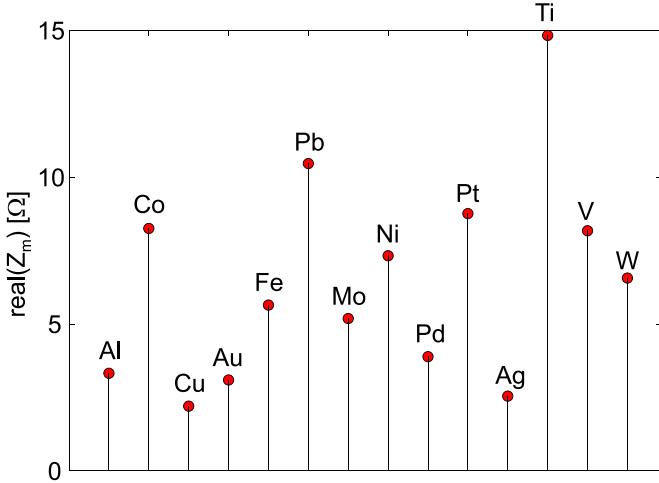
Figure 7. Real part of metal wave impedance Z_m for 14 metals [44] at 1 THz.
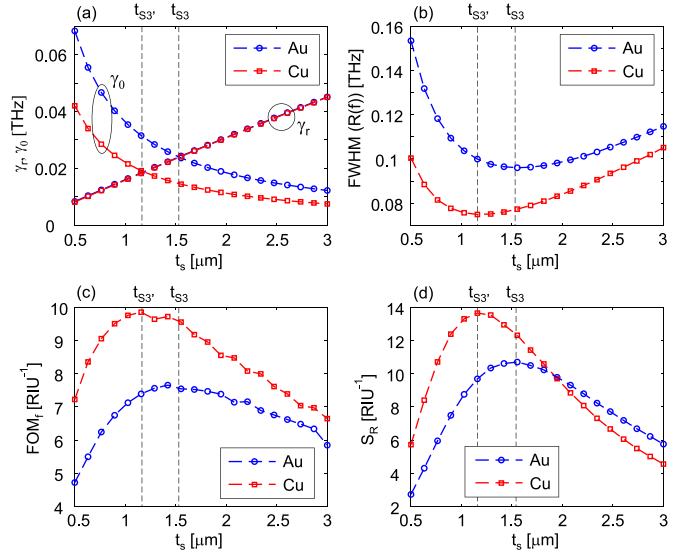

Figure 8. Metasurface 3 made with gold and copper: (a) decay rates, (b) resonance width, (c) FOM factor in the spectral interrogation, and (d) reflectance sensitivity.
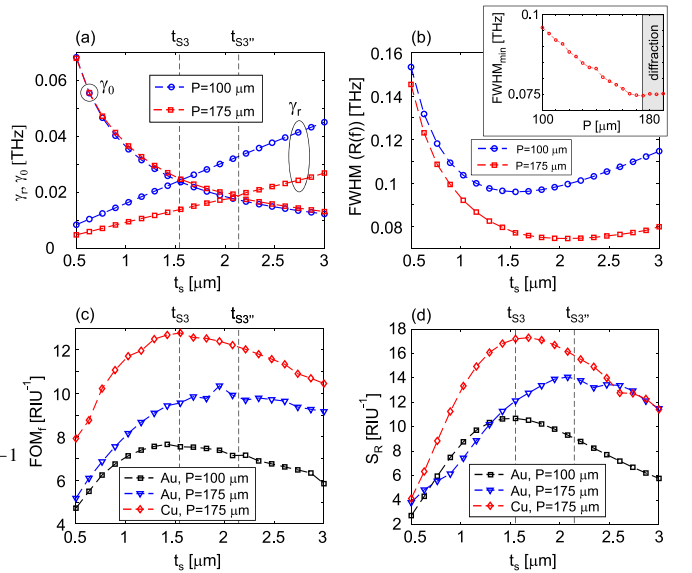

Figure 9. Metasurface 3 with larger period: (a) decay rates, (b) resonance width, (c) FOM factor in the spectral interrogation, and (d) reflectance sensitivity. The inset of (b) displays the resonance width as a function of a metasurface period.

metasurfaces with narrow resonances. Here we consider two possibilities: the utilization of a metal with lower losses and increasing of period P. Gold has been traditionally employed for making metallic parts of metasurfaces. Still, metal with lower losses would provide lower non-radiative decay rates, more narrow resonances and larger refractive index sensitivities. Metal losses are determined by the integral of Poynting vector flux through the surface enclosing metallic domains, and it can be shown that the metallic losses are proportional to the real part of the metal wave impedance ($Z_m = \sqrt{\mu_0/\varepsilon_0\varepsilon_m}$, where μ_0 is vacuum permeability, ε_0 is vacuum permittivity, and ε_m is metal permittivity) [52]. The real part of the metal wave impedance for 14 metals [44] at 1 THz (close to the operating frequency of considered metasurfaces) is presented in figure 7. As can be seen, copper has the lowest impedance and therefore, below it is considered as a candidate to replace gold.

In the numerical calculations, copper is modeled with Drude parameters, the plasma frequency $\omega_p = 1.12 \times 10^{16}$ rad s^{-1} and collision frequency $\gamma_c = 1.38 \times 10^{13}$ rad s^{-1} [44] which is four times lower than the collision frequency of gold. Decay rates for metasurface 3 made from gold and copper are depicted in figure 8(a). Radiative decay rates stay the same, but non-radiative decay rates are decreased in the case of copper resonators due to a lower absorption. As a result, the critical coupling is achieved for thinner spacer thickness $t_{s3'} \approx 1.2\ \mu$m (compared to $t_{s3} \approx 1.5\ \mu$m in the case of gold). The lower non-radiative decay rates result in narrower resonances with lower FWHM as shown in figure 8(b). Finally, copper based metasurface has a larger FOM$_f$ factor (by around 30%) and larger S_R (by around 25%) as displayed in figures 8(c) and (d), respectively. Influence of lower γ_0 on S_f and S_Φ is weak and they stay practically the same.

Increasing unit cell size and metasurface period P is another way to decrease resonance width. In this case, radiative decay rates are decreased since they scale as $\sim P^{-1}$ [64]. This is illustrated in figure 9(a) for metasurface 3 and periods $P = 100\ \mu$m (taken so far in the previous calculations) and $P = 175\ \mu$m. Non-radiative decay rates stay practically the same since they stem from losses in metallic parts which are fixed, whereas

the critical coupling is now shifted to thicker spacers with $t_{s3''} \approx 2.15\ \mu$m. The resonance width depicted in figure 9(b) is decreased for the larger period, while the minimal FWHM is reached for P around 175 μm as shown in the inset of figure 9(b). For larger periods, in addition to the zeroth order, the first diffraction order becomes propagative as well, which limits the minimal FWHM. As in the previous case, decreased resonance width leads to larger FOM$_f$ (by around 45%) and S_R (by around 30%) as presented in figures 9(c) and (d), respectively. Still, this improvement is achieved for the spacer thickness increased by around 40% which preserves thin film sensitivities at the same level. Finally, an optimal structure

J. Phys. D: Appl. Phys. **54** (2021) 285106

B Vasić and G Isić

would comprise of copper resonators with a larger period of $P = 175$ μm. Due to decreased both radiative and non-radiative decay rates in such structure, FOM_f and S_R are increased by around 85% and 60%, respectively (figures 9(c) and (d)), compared to the initial metasurface 3 made of gold and with the period $P = 100$ μm. The optimal structure is achieved for the same spacer thickness as the initial metasurface 3 ($t_{s3} \approx$ 1.5 μm) since the increase and decrease of t_s due to larger period and the utilization of copper, respectively, are compensated by each other. As a result, the observed improvement is reflected in thin film sensitivities as well.

8. Discussion

All presented results were obtained for the normal incidence. Still, the operation at oblique incidence could be more favorable for practical measurements in order to spatially separate the incoming and reflected beam. The cavity modes of MIM metasurfaces (field distributions plotted in figure 4(a)) are localized and their resonant frequencies weakly depend on angle of incidence (AOI) (depicted in figures S5(a) and (b) of supplementary material). The minimal reflectance increases (figure S5(c) of supplementary material) and the maximal phase slope decreases (figure S5(d) of supplementary material) with AOI which results in lower reflectance and phase sensitivity. For the operation at a larger AOI, metasurfaces can be always redesigned by tuning spacer thickness in order to reestablish the operation near to the critical coupling point. For example, the spacer thickness in metasurface 3 operating at AOI$= 30°$ should be just increased from $t_{s3} = 1.5$ to 2 μm as shown in figure S6 of supplementary material. On the other hand, tunable AOI can be used in order to adjust the optimal operating conditions when spacer thickness deviates from the optimal one mainly due to fabrication imperfections [29]. Taking metasurface 3 again as an example, deviation of the spacer thickness by $\Delta t_s = 250$ nm from the optimal value $t_s = 1.5$ μm is compensated by the operation at AOI around 20° when the structure is returned back near to the point of critical coupling as illustrated in figure S7 of supplementary material. At the same time, tunable AOI can be used in order to increase reflection and get sufficiently high signal (figure S5(c) of supplementary material).

Operation at oblique incidence provides an additional benefit since measurements can be performed by spectroscopic ellipsometry. This technique is very attractive for sensing devices [29] since it simultaneously gives both amplitude and phase signals while relative measurements provide an ultimate sensitivity for detection of thin films. Although the ellipsometry is dominantly employed at optical and infrared frequencies, recent developments make the technique applicable at terahertz frequencies as well [65, 66]. The operation of proposed sensing structures in transmission mode is possible with similar metasurfaces consisting of a double layer of spatially separated metallic patches and an analyte under investigation between them [67].

Hollow cavities of MIM metasurfaces can be easily infiltrated by a fluid analyte, bringing it into the region with a high

field enhancement. However, more sophisticated fabrication methods are required to produce such metasurfaces. In the case of mushroom-type structures [68], a partial etching of the dielectric spacer underneath top metallic stripes is needed to narrow the spacer and make a dielectric pedestal out of it. Such structures were successfully fabricated and employed for surface enhanced Raman spectroscopy [69, 70] as well as for refractive index sensing at mid-infrared [36] and even optical frequencies [35, 37].

Hollow structures were dominantly realized at microwaves [71] and terahertz frequencies [38–41, 72]. Similar planar MIM structures with a nanofluidic channel between two metallic layers were implemented at mid-infrared frequencies and applied for enhanced infrared spectroscopy of molecules and liquids [73–75], while vertical MIM cavities were used for gas sensing [76]. Finally, hollow MIM metasurfaces have been recently fabricated even at near-infrared frequencies [77]. In practical applications, hollow metasurfaces are convenient for the combination with a microfluidic channel placed between bottom metallic plate and array of top metallic resonators [39, 41].

The operation close to the critical coupling point can be adjusted by choosing an appropriate thickness of the dielectric pedestal in mushroom-type structures or lateral spacer height. In the static case when there is no possibility for a post-fabrication tuning of the spacer thickness, metasurfaces are designed with an analyte filled inside MIM cavities. On the other hand, the spacer thickness can be mechanically tunable in some hollow structures, by vertically moving the layer with top metallic resonators [71, 72]. With this option included, the critical coupling can be adjusted for a broader range of analyte refractive index. However, because of technological challenges, so far this option has been implemented only at microwaves [71] and terahertz frequencies [72]. In order to make metasurfaces more robust to fabrication inaccuracies and provide dynamically tunable critical coupling, an additional approach could be to employ the concept of disordered structures with just a few tunable unit cells [78].

An additional option to improve the sensitivity of the dielectric-loaded MIM metasurface from figure 1(a) is to use dielectric spacer as a label [79]. Although in this configuration an analyte is above the metasurface, due to its interaction with the label, the spacer properties (such as refractive index) are modified. In this way, changes in the analyte are transformed into changes of the spacer which is in a region with a high field enhancement. Still, such kind of sensing requires appropriate labeling for every analyte.

9. Conclusions

Hollow MIM metasurfaces enable an excellent spatial overlap between analyte and regions with high electric field enhancement, so that the fraction of resonant eigenmode energy stored in the analyte tends to unity. This is the dominant factor responsible for a large refractive index sensitivity (normalized sensitivity of above 0.6 RIU^{-1}). We have estimated the attainable detection limit for the refractive index sensing at

$< 10^{-2}$ RIU for spectral interrogation, 10^{-3} RIU for reflectance interrogation, and 10^{-4} RIU for phase interrogation. Such high resolutions are achievable in a dynamic range of around 0.5 and 0.1 RIU for the spectral and reflectance interrogation, respectively, whereas the price for the ultrahigh detection limit provided by the phase interrogation is a narrow dynamic range of only 10^{-3} RIU. Since the ratio of free-space wavelength and effective analyte thickness defined by cavity height is very large (around 150), hollow metasurfaces are promising for sensing low amounts of analyte with a deeply subwavelength thickness. The attainable detection limit for the film thickness sensing is in the order of nanometers for the spectral and reflectance interrogation, and in the order of angstroms in the case of the phase interrogation. At the critical coupling point with equal radiative and non-radiative decay rates of the resonant mode, the resonance width is minimized, reflectance tends to zero providing a huge relative change, while the phase slope is maximized. These properties enable maximal sensitivities and FOM factors simultaneously in all three interrogation methods (spectral, reflectance, and phase). Simple semi-analytical model of reflective metasurfaces based on temporal coupled-mode theory confirms that the critical coupling point is the optimal working regime for such sensing structures [80]. In order to provide high enough output reflectance, realistic structures should be slightly detuned from the critical coupling point by choosing a proper spacer thickness of MIM cavities prior to fabrication or by slightly adjusting AOI for a post-fabrication tuning. Improved FOM factor in the spectral interrogation and reflectance sensitivity were achieved by decreasing the resonant mode width, by using copper instead of gold due to lower losses, and by increasing metasurface period in order to decrease non-radiative losses. Following this approach, future study should focus on a design of MIM metasurfaces with asymmetric top metallic structures in order to achieve narrow resonances [81]. In order to employ hollow metasurfaces for the sensing of chiral analytes, future works should consider structures with chiral top metallic resonators [82]. In comparison with the standard dielectric-loaded MIM metasurfaces, the fabrication of hollow metasurfaces is more challenging. However, their implementation has already been demonstrated from microwave to near-infrared frequencies, where their full potential will be achieved by their integration with microfluidic structures.

Data availability statement

All data that support the findings of this study are included within the article (and any supplementary files).

Acknowledgments

ORCID iDs

Borislav Vasić ⓘ https://orcid.org/0000-0002-1575-8004
Goran Isić ⓘ https://orcid.org/0000-0002-6841-9356

References

[1] O'Hara J F, Singh R, Brener I, Smirnova E, Han J, Taylor A J and Zhang W 2008 Thin-film sensing with planar terahertz metamaterials: sensitivity and limitations *Opt. Express* **16** 1786–95

[2] Wu C, Khanikaev A B, Adato R, Arju N, Yanik A A, Altug H and Shvets G 2012 Fano-resonant asymmetric metamaterials for ultrasensitive spectroscopy and identification of molecular monolayers *Nat. Mater.* **11** 69–75

[3] O'Hara J F, Withayachumnankul W and Al-Naib I 2012 A review on thin-film sensing with terahertz waves *J. Infrared Millim. Terahertz Waves* **33** 245–91

[4] Beruete M and Jáuregui-López I 2020 Terahertz sensing based on metasurfaces *Adv. Opt. Mater.* **8** 1900721

[5] Driscoll T, Andreev G O, Basov D N, Palit S, Cho S Y, Jokerst N M and Smith D R 2007 Tuned permeability in terahertz split-ring resonators for devices and sensors *Appl. Phys. Lett.* **91** 062511

[6] Sun Y, Xia X, Feng H, Yang H, Gu C and Wang L 2008 Modulated terahertz responses of split ring resonators by nanometer thick liquid layers *Appl. Phys. Lett.* **92** 221101

[7] Debus C and Bolivar P H 2007 Frequency selective surfaces for high sensitivity terahertz sensing *Appl. Phys. Lett.* **91** 184102

[8] Reinhard B, Schmitt K M, Wollrab V, Neu J, Beigang R and Rahm M 2012 Metamaterial near-field sensor for deep-subwavelength thickness measurements and sensitive refractometry in the terahertz frequency range *Appl. Phys. Lett.* **100** 221101

[9] Singh R, Cao W, Al-Naib I, Cong L, Withayachumnankul W and Zhang W 2014 Ultrasensitive terahertz sensing with high-Q Fano resonances in metasurfaces *Appl. Phys. Lett.* **105** 171101

[10] Tao H *et al* 2010 Performance enhancement of terahertz metamaterials on ultrathin substrates for sensing applications *Appl. Phys. Lett.* **97** 261909

[11] Srivastava Y K, Cong L and Singh R 2017 Dual-surface flexible THz Fano metasensor *Appl. Phys. Lett.* **111** 201101

[12] Brian B, Sepúlveda B, Alaverdyan Y, Lechuga L M and Käll M 2009 Sensitivity enhancement of nanoplasmonic sensors in low refractive index substrates *Opt. Express* **17** 2015–23

[13] Dmitriev A, Hägglund C, Chen S, Fredriksson H, Pakizeh T, Käll M and Sutherland D S 2008 Enhanced nanoplasmonic optical sensors with reduced substrate effect *Nano Lett.* **8** 3893–8

[14] Otte M A, Estévez M-C, Carrascosa L G, González-Guerrero A B, Lechuga L M and Sepúlveda B 2011 Improved biosensing capability with novel suspended nanodisks *J. Phys. Chem. C* **115** 5344–51

[15] Aćimović S S, Šípová H, Emilsson G, Dahlin A B, Antosiewicz T J and Käll M 2017 Superior LSPR substrates based on electromagnetic decoupling for on-a-chip high-throughput label-free biosensing *Light Sci. Appl.* **6** 17042

[16] Moritake Y and Tanaka T 2018 Impact of substrate etching on plasmonic elements and metamaterials: preventing red shift and improving refractive index sensitivity *Opt. Express* **26** 3674–83

[17] Meng K *et al* 2019 Increasing the sensitivity of terahertz split ring resonator metamaterials for dielectric sensing by localized substrate etching *Opt. Express* **27** 23164–72

[18] Hibbins A P, Sambles J R, Lawrence C R and Brown J R 2004 Squeezing millimeter waves into microns *Phys. Rev. Lett.* **92** 143904

[19] Todorov Y, Tosetto L, Teissier J, Andrews A M, Klang P, Colombelli R, Sagnes I, Strasser G and Sirtori C 2010 Optical properties of metal-dielectric-metal microcavities in the THz frequency range *Opt. Express* **18** 13886–907

[20] Cong L, Tan S, Yahiaoui R, Yan F, Zhang W and Singh R 2015 Experimental demonstration of ultrasensitive sensing with terahertz metamaterial absorbers: a comparison with the metasurfaces *Appl. Phys. Lett.* **106** 031107

[21] Ye J and Van Dorpe P 2011 Improvement of figure of merit for gold nanobar array plasmonic sensors *Plasmonics* **6** 665

[22] Lu X, Zhang L and Zhang T 2015 Nanoslit-microcavity-based narrow band absorber for sensing applications *Opt. Express* **23** 20715–20

[23] Wang B-X, Zhai X, Wang G-Z, Huang W-Q and Wang L-L 2015 A novel dual-band terahertz metamaterial absorber for a sensor application *J. Appl. Phys.* **117** 014504

[24] Lu X, Wan R and Zhang T 2015 Metal-dielectric-metal based narrow band absorber for sensing applications *Opt. Express* **23** 29842–7

[25] Luo S, Zhao J, Zuo D and Wang X 2016 Perfect narrow band absorber for sensing applications *Opt. Express* **24** 9288–94

[26] Liu N, Mesch M, Weiss T, Hentschel M and Giessen H 2010 Infrared perfect absorber and its application as plasmonic sensor *Nano Lett.* **10** 2342–8

[27] Cheng F, Yang X and Gao J 2014 Enhancing intensity and refractive index sensing capability with infrared plasmonic perfect absorbers *Opt. Lett.* **39** 3185

[28] Wang X, Luo C, Hong G and Zhao X 2013 Metamaterial optical refractive index sensor detected by the naked eye *Appl. Phys. Lett.* **102** 091902

[29] Kravets V G *et al* 2013 Singular phase nano-optics in plasmonic metamaterials for label-free single-molecule detection *Nat. Mater.* **12** 304–9

[30] Vasić B and Gajić R 2014 Enhanced phase sensitivity of metamaterial absorbers near the point of darkness *J. Appl. Phys.* **116** 023102

[31] del Hougne P, Brahima Yeo K, Besnier P and Davy M 2019 On-demand coherent perfect absorption in complex scattering systems: time delay divergence and enhanced sensitivity to perturbations (arXiv: 2010.06438)

[32] Zhou H, Yang C, Hu D, Li D, Hui X, Zhang F, Chen M and Mu X 2019 Terahertz biosensing based on bi-layer metamaterial absorbers toward ultra-high sensitivity and simple fabrication *Appl. Phys. Lett.* **115** 143507

[33] Wang W *et al* 2020 Enhancing sensing capacity of terahertz metamaterial absorbers with a surface-relief design *Photon. Res.* **8** 519–27

[34] Li Y, McLamb M, Park S, Childers D, Boreman G D and Hofmann T 2020 Reciprocal plasmonic metasurfaces: theory and applications (arXiv: 2005.00685)

[35] Shen Y *et al* 2013 Plasmonic gold mushroom arrays with refractive index sensing figures of merit approaching the theoretical limit *Nat. Commun.* **4** 2381

[36] Bhattarai K, Ku Z, Silva S, Jeon J, Kim J O, Lee S J, Urbas A and Zhou J 2015 A large-area, mushroom-capped plasmonic perfect absorber: refractive index sensing and Fabry-Perot cavity mechanism *Adv. Optical Mater.* **3** 1779–86

[37] Zhu J, Lin G, Huang Y, Zhang K, Wu M, Wu W and Lu P 2020 Three-dimensional cavity-coupled metamaterials for plasmonic color and real-time colorimetric biosensors *Nanoscale* **12** 4418–25

[38] Soltani A, Neshasteh H, Mataji-Kojouri A, Born N, Castro-Camus E, Shahabadi M and Koch M 2016 Highly sensitive terahertz dielectric sensor for small-volume liquid samples *Appl. Phys. Lett.* **108** 191105

[39] Hu X, Xu G, Wen L, Wang H, Zhao Y, Zhang Y, Cumming D R S and Chen Q 2016 Metamaterial absorber integrated microfluidic terahertz sensors *Laser Photonics Rev.* **10** 962–9

[40] Duan G, Schalch J, Zhao X, Zhang J, Averitt R D and Zhang X 2018 An air-spaced terahertz metamaterial perfect absorber *Sens. Actuators* A **280** 303–8

[41] Lan F *et al* 2019 Dual-band refractometric terahertz biosensing with intense wave-matter-overlap microfluidic channel *Biomed. Opt. Express* **10** 3789–99

[42] Hugonin J P and Lalanne P 2005 *Reticolo Code for Grating Analysis* (Palaiseau: Institute d'Optique)

[43] Laib J P and Mittleman D M 2010 Temperature-dependent terahertz spectroscopy of liquid n-alkanes *J. Infrared Millim. Terahertz Waves* **31** 1015–21

[44] Ordal M A, Bell R J, Alexander J R W, Long L L and Querry M R 1985 Optical properties of fourteen metals in the infrared and far infrared: Al, Co, Cu, Au, Fe, Pb, Mo, Ni, Pd, Pt, Ag, Ti, V and W *Appl. Opt.* **24** 4493–9

[45] Tao H, Strikwerda A C, Fan K, Bingham C M, Padilla W J, Zhang X and Averitt R D 2008 Terahertz metamaterials on free-standing highly-flexible polyimide substrates *J. Phys. D: Appl. Phys.* **41** 232004

[46] Ma Y, Chen Q, Grant J, Saha S C, Khalid A and Cumming D R S 2011 A terahertz polarization insensitive dual band metamaterial absorber *Opt. Lett.* **36** 945–7

[47] George P A, Hui W, Rana F, Hawkins B G, Smith A E and Kirby B J 2008 Microfluidic devices for terahertz spectroscopy of biomolecules *Opt. Express* **16** 1577–82

[48] Lodewijks K, Van Roy W, Borghs G, Lagae L and Van Dorpe P 2012 Boosting the figure-of-merit of LSPR-based refractive index sensing by phase-sensitive measurements *Nano Lett.* **12** 1655–9

[49] Isić G, Vasić B, Zografopoulos D C, Beccherelli R and Gajić R 2015 Electrically tunable critically coupled terahertz metamaterial absorber based on nematic liquid crystals *Phys. Rev. Appl.* **3** 064007

[50] Qu C *et al* 2015 Tailor the functionalities of metasurfaces based on a complete phase diagram *Phys. Rev. Lett.* **115** 235503

[51] Fan S, Suh W and Joannopoulos J D 2003 Temporal coupled-mode theory for the Fano resonance in optical resonators *J. Opt. Soc. Am.* A **20** 569–72

[52] Isić G and Gajić R 2014 Geometrical scaling and modal decay rates in periodic arrays of deeply subwavelength terahertz resonators *J. Appl. Phys.* **116** 233103

[53] Balanis C A 2005 *Antenna Theory* (New York: Wiley)

[54] Joannopoulos J D, Johnson S G, Winn J N and Meade R D 2008 *Photonic Crystals: Molding the Flow of Light* (Princeton, NJ: Princeton University Press)

[55] Unger A and Kreiter M 2009 Analyzing the performance of plasmonic resonators for dielectric sensing *J. Phys. Chem.* C **113** 12243–51

[56] Miao Z, Wu Q, Li X, He Q, Ding K, An Z, Zhang Y and Zhou L 2015 Widely tunable terahertz phase modulation with gate-controlled graphene metasurfaces *Phys. Rev. X* **5** 041027

[57] Mendis R, Astley V, Liu J and Mittleman D M 2009 Terahertz microfluidic sensor based on a parallel-plate waveguide resonant cavity *Appl. Phys. Lett.* **95** 171113

[58] Liu Z *et al* 2020 High-Q metamaterials based on cavity mode resonance for THz sensing applications *AIP Adv.* **10** 075014

J. Phys. D: Appl. Phys. **54** (2021) 285106

B Vasić and G Isić

[59] Yahiaoui R, Strikwerda A C and Jepsen P U 2016 Terahertz plasmonic structure with enhanced sensing capabilities *IEEE Sens. J.* **16** 2484–8

[60] Huang Y H, Ho H P, Kong S K and Kabashin A V 2012 Phase-sensitive surface plasmon resonance biosensors: methodology, instrumentation and applications *Ann. Phys.* **524** 637–62

[61] Jepsen P U and Fischer B M 2005 Dynamic range in terahertz time-domain transmission and reflection spectroscopy *Opt. Lett.* **30** 29–31

[62] Park H-R, Chen X, Nguyen N-C, Peraire J and Oh S-H 2015 Nanogap-enhanced terahertz sensing of 1 nm thick ($\lambda/10^6$) dielectric films *ACS Photonics* **2** 417–24

[63] Srivastava Y K, Ako R T, Gupta M, Bhaskaran M, Sriram S and Singh R 2019 Terahertz sensing of 7 nm dielectric film with bound states in the continuum metasurfaces *Appl. Phys. Lett.* **115** 151105

[64] Isić G, Sinatkas G, Zografopoulos D C, Vasić B, Ferraro A, Beccherelli R, Kriezis E E and Belić M 2019 Electrically tunable metal semiconductor metal terahertz metasurface modulators *IEEE J. Sel. Top. Quantum Electron.* **25** 1–8

[65] Neshat M and Armitage N P 2013 Developments in THz range ellipsometry *J. Infrared Millim. Terahertz Waves* **34** 682–708

[66] Chen X, Parrott E P J, Huang Z, Chan H-P and Pickwell-MacPherson E 2018 Robust and accurate terahertz time-domain spectroscopic ellipsometry *Photon. Res.* **6** 768–75

[67] Karmakar S, Kumar D, Varshney R K and Chowdhury D R 2020 Strong terahertz matter interaction induced ultrasensitive sensing in Fano cavity based stacked metamaterials *J. Phys. D: Appl. Phys.* **53** 415101

[68] Ogawa S, Fujisawa D, Hata H, Uetsuki M, Misaki K and Kimata M 2015 Mushroom plasmonic metamaterial infrared absorbers *Appl. Phys. Lett.* **106** 041105

[69] Cetin A E, Yilmaz C, Galarreta B C, Yilmaz G, Altug H and Busnaina A 2020 Fabrication of sub-10-nm plasmonic gaps for ultra-sensitive Raman spectroscopy *Plasmonics* **15** 1165–71

[70] Dai F, Horrer A, Adam P-M and Fleischer M 2020 Accessing the hotspots of cavity plasmon modes in vertical metal-insulator-metal structures for surface enhanced Raman scattering *Adv. Optical Mater.* **8** 1901734

[71] Kim J, Jeong H and Lim S 2019 Mechanically actuated frequency reconfigurable metamaterial absorber *Sens. Actuators* A **299** 111619

[72] Schalch J, Duan G, Zhao X, Zhang X and Averitt R D 2018 Terahertz metamaterial perfect absorber with continuously tunable air spacer layer *Appl. Phys. Lett.* **113** 061113

[73] Le T H H and Tanaka T 2017 Plasmonics-nanofluidics hybrid metamaterial: an ultrasensitive platform for infrared absorption spectroscopy and quantitative measurement of molecules *ACS Nano* **11** 9780–8

[74] Le T H H, Morita A, Mawatari K, Kitamori T and Tanaka T 2018 Metamaterials-enhanced infrared spectroscopic study of nanoconfined molecules by plasmonics-nanofluidics hybrid device *ACS Photonics* **5** 3179–88

[75] Shih K, Ren Z, Wang C and Lee C 2019 MIR plasmonic liquid sensing in nano-metric space driven by capillary force *J. Phys. D Appl. Phys.* **52** 394001

[76] Su D-S, Tsai D P, Yen T-J and Tanaka T 2019 Ultrasensitive and selective gas sensor based on a channel plasmonic structure with an enormous hot spot region *ACS Sens.* **4** 2900–7

[77] Okatani T, Sekiguchi S, Hane K and Kanamori Y 2020 Surface-plasmon-coupled optical force sensors based on metal insulator metal metamaterials with movable air gap *Sci. Rep.* **10** 14807

[78] Imani M F, Smith D R and del Hougne P 2020 Perfect absorption in a disordered medium with programmable meta-atom inclusions *Adv. Funct. Mater.* **30** 2005310

[79] Lee M, Jeon H and Kim S 2015 A highly tunable and fully biocompatible silk nanoplasmonic optical sensor *Nano Lett.* **15** 3358–63

[80] Vasić B 2021 A semi-analytical approach for refractive index sensors based on reflective metasurfaces accepted for publication in *J. Opt. Soc. Am.* B **38** 1676–83

[81] Liu L, Li Z, Cai C, Zhu W, Zheng X, Zhang W, Xu J and Liu Z 2020 High-Q hybridized resonance in a plasmonic metasurface of asymmetric aligned magnetic dipoles *Appl. Phys. Lett.* **117** 081108

[82] Wang J, Li G, Ou K, Yu F, Chen J, Li Z, Chen X and Lu W 2021 Controllable chiral emissions from free-electron driven plasmonic metasurfaces *J. Phys. D: Appl. Phys.* **54** 105105

Beam Steering Efficiency in Resonant Reflective Metasurfaces

Goran Isić [ID], Dimitrios C. Zografopoulos [ID], Danka B. Stojanović [ID], Borislav Vasić [ID], and Milivoj R. Belić [ID]

Abstract—Beam steering is one of the prevailing functions performed by electromagnetic metasurfaces. Its efficiency depends on a large number of physical parameters associated with resonant elements comprising the metasurface and is thus notoriously difficult to optimize. Here we formulate a theoretical model for evaluating the diffraction efficiency of an array of lossy resonant elements whose spectral response is dominated by the coupling between a leaky eigenmode and a single incoming/outgoing channel. We use it to deduce a formula for the maximum attainable diffraction efficiency and the gradient parameter profile for which it is achieved. The optimization procedure is demonstrated on the example of an electrically tunable liquid-crystal terahertz beam steering metasurface. Finally, the proposed model is benchmarked against rigorous metasurface simulations.

Index Terms—Gradient metasurfaces, beam steering, temporal coupled-mode theory, tunable metamaterials.

I. INTRODUCTION

IN THE early days of optics, light has been directed using reflection and refraction exclusively. In contrast, radio waves have always been generated, guided and detected by components whose size is comparable to their free-space wavelength. Technological progress over the past decades, allowing the preparation of thin layers and fabrication of submicron structures, has gradually lead to the development of optical components that, similarly to their radio counterparts, have wavelength or subwavelength sized elements. These diffractive optical components have since been attracting a growing research attention for their potential to provide improved characteristics or entirely new functionality. Binary optics technology [1], involving surface relief gratings with step-like profiles for light guiding, is a prominent early example.

Electromagnetic metasurfaces [2] embody one of the more recent research topics in optics aimed at using subwavelength, often resonant, optically thin structures for purposes of controlling light. The subwavelength elements, organized into unit cells, can nowadays be fabricated with nanoscopic precision, a wide range of materials and physical parameters exhibiting a desired in-plane gradient, giving virtually an arbitrary number of degrees of freedom for designers of novel optical components [3], [4].

Beam steering, also called anomalous reflection in the literature [2], [5], [6], whereby the incoming beam is reflected into a desired direction, is amongst the simplest functions these structures can provide. Beam steering metasurfaces are graded structures [4], [7] in many ways analogous to reflectarray antenna used at microwave frequencies since the 1960s [8]. In fact, many resonant metasurface element designs have either been inspired by, or rediscovered independently from, the vast knowledge accumulated over the years on microwave reflectarrays [9]–[11]. The novel terminology is, however, usually warranted by specific traits associated with operation at terahertz or higher frequencies. A number of demonstrations has so far been reported, including operation at optical [5], [12] and terahertz [13], [14] frequencies. In terms of possible applications, tunable beam steering metasurfaces are particularly interesting, especially if tuning is performed by electrical means. Various ideas have been proposed, e.g. exploiting the electric field effect in conducting oxides [15], graphene [16], semiconductor heterojunctions [17] or by switching nematic liquid crystals [18], but only few have so far been actually demonstrated [19], [20].

A major problem in developing a novel beam steering metasurface implementation, especially if it involves tunable or reconfigurable operation, is making a realistic estimate of the attainable diffraction efficiency (DE). In all but the trivial case when resonant absorption is negligible and the available phase range equals 2π, increasing DE involves some kind of trade off between amplitude and phase characteristics achievable often only through blind fine-tuning a large number of parameters. In such circumstances it is virtually impossible to identify the
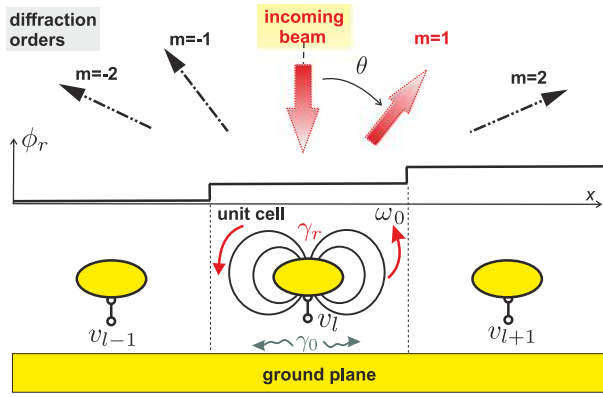
Fig. 1.   The generic beam steering metasurface considered in this article.

optimal gradient parameter profile, let alone understand the role of all resonant element physical parameters.

Here we formulate a theoretical model for beam steering efficiency, relying on scalar diffraction [21] and temporal coupled-mode theory [22]. We use it to derive analytical expressions for the optimal gradient profiles and the highest achievable DE for a wide class of reflective metasurfaces. As a proof of concept demonstration, our method is applied for the analysis of beam steering in electrically tunable liquid crystal (LC) terahertz metasurfaces [18], allowing the assessment of its accuracy and range of validity.

II. PROBLEM STATEMENT

A generic beam steering metasurface is depicted in Fig. 1. It comprises an array of resonant elements above an opaque, usually metallic, surface. While mutually similar, the resonant elements exhibit a gradual variation in one (or more) of their physical parameters, generating a step-like variation of phase shift ϕ_r the wave experiences upon reflection. This parameter will henceforth be referred to as the control parameter and denoted by v_l, as in Fig. 1. For clarity, we refer to v in singular number, but it makes no difference if it involves two or more actual physical parameters. For example, v may represent one (or more) of linear dimensions of the resonant element [5], [9], [12], [13], a voltage if the unit cell is electrically tunable [16]–[19] or anything else that can be used to modulate ϕ_r along the unit cell array.

We assume that the metasurface is a periodic array of supercells comprising N unit cells. Each unit cell is characterized by a set Π of parameters that are identical across the metasurface and the control parameter v which varies from cell to cell. Since the metasurface is periodic, the pattern of control parameters $\{v_n\}$ is also periodic, i.e. $v_{l+N} = v_l$ for any l. As N is arbitrarily selected, our analysis is applicable to a wide range of metasurfaces. Fig. 1 depicts a perpendicularly incident plane wave being diffracted into a number of diffraction orders $m = \pm 1, \pm 2, \ldots$, because the super cell width L is at least several times larger than the free-space wavelength λ. The device operates by ensuring that the phase shift ϕ_r provided by each unit cell is such that the diffraction efficiency η_m of all but one diffraction orders is close

to zero, so that the reflected field is dominated by one diffraction order whose propagation direction is $\theta_m = \mathrm{asin}(m\lambda/L)$.

The problem of designing an efficient metasurface can be broken down into two stages. The first has a character of local optimization. In it the optimal control profile $\{v_n\}$, defined as the one which maximizes η_m for a given supercell size N and with given unit cell parameters Π, needs to be determined. The brute-force search for $\{v_n\}$, whereby all possible profiles are evaluated, has exponential complexity $\mathcal{O}(c^N)$ and is thus unfeasible even with modern computational resources for any meaningful N, e.g. $N \geq 5$. Considering that one needs to solve Maxwell's equations rigorously for the entire supercell to evaluate η_m for any given $\{v_n\}$, which is often challenging to run once, let alone through a loop, the optimal $\{v_n\}$ can never be rigorously determined for all practical purposes. In the second stage, one needs to understand how Π affects the optimal η_m and possibly sweep the Π-space searching for the global optimum. It, of course, implies repeating the first stage as the optimal control profile changes with Π.

Under these circumstances, the best one can hope for is a simplified model providing guidelines on optimal control and selection of unit cell parameters that yield an acceptable efficiency. To this end, here we start by invoking the scalar diffraction theory and the Fraunhofer approximation [21], [23], according to which the diffraction efficiency into the m-th diffraction order can be written as

$$\eta_m = \mathrm{sinc}^2\left(\frac{m}{N}\right)|S_N|^2, \tag{1}$$

with the diffraction sum S_N given by

$$S_N = \frac{1}{N}\sum_{n=0}^{N-1} r_n e^{-imn\alpha}, \quad \alpha = \frac{2\pi}{N}. \tag{2}$$

In the above equation, r_n represents the reflection coefficient for an array of unit cells equal to the n-th cell in the considered metasurface, i.e. r_n corresponds to a metasurface in which the supercell comprises only one unit cell with control parameter equal to v_n. Equation (1) has been widely used in designing multilevel surface relief gratings [24] with many studies devoted to assessing its accuracy [25]. The extent to which Eq. (1) is applicable to resonant arrays is, on the other hand, currently unclear since it has so far not been investigated in context of metasurfaces. On general grounds, it may be expected to be exact in the limit of $\theta \to 0$, while for any finite deflection angle θ, the accuracy depends on the specific characteristics of the near fields at resonance. For purposes of illustration, in Section IV we demonstrate the validity of Eq. (1) by comparing its predictions with a rigorous numerical solution of Maxwell equations for the case of an array of metal-insulator-metal (MIM) resonators infiltrated by a nematic LC.

Our analysis is focused on the simplest type of resonant elements for which we demand that their spectral characteristic close to resonant frequencies is dominated by the interaction of a quasi-normal mode (i.e. leaky eigenmode) [26] with a single incoming/outgoing channel. More formally, we assume that the reflection coefficient $r(\omega)$ of a uniform array of such
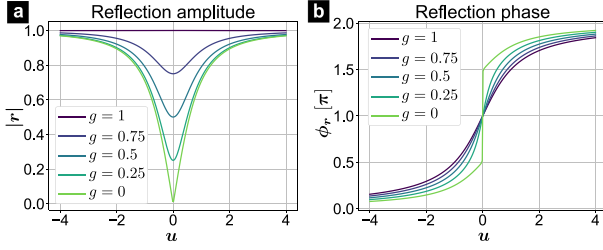
Fig. 2. Single-channel TCMT model: (a) Reflection amplitude and (b) phase drawn for various overcoupling parameter g values. The plots in this article have been prepared with the help of Matplotlib [30].

resonators can be accurately described by the temporal coupled-mode theory (TCMT) model for a single-channel resonant system [22], [27]

$$r(\omega) = \frac{u - \mathrm{i}g}{u + \mathrm{i}}, \quad u = \frac{\omega - \omega_0}{\gamma_\mathrm{r} + \gamma_0}, \quad g = \frac{\gamma_\mathrm{r} - \gamma_0}{\gamma_\mathrm{r} + \gamma_0}. \tag{3}$$

Here the resonant angular frequency ω_0, radiative decay rate γ_r and non-radiative decay rate γ_0 are the standard TCMT parameters, while ω denotes the operation frequency. For purposes of the analysis below, a representation of r in terms of two new parameters is more helpful. The parameter u, introduced as the normalized deviation from the resonant frequency in Eq. (3), can be seen as the resonators' state variable. Meanwhile, the overcoupling parameter g, defined as the normalized difference between the radiative and non-radiative decay rate and also related to the reflection coefficient at resonance frequency by $g = -r(\omega_0)$, quantifies the ability of the resonator array to generate phase shift without losing energy. Equation (3) provides an accurate description of resonator arrays with quality factors [28] high enough so that the direct (background) reflection defined as in Ref. [22] is spectrally flat in the resonance region. The formalism can readily be generalized [29] both in terms of multiple incoming/outgoing channels and quasi-normal modes. Fig. 2 shows $r(u)$ plotted according to Eq. (3).

III. OPTIMAL CONTROL

We will consider the optimization of $|S_N|$ only for the 1-st diffraction order, since for any $|m| > 1$ case there exists an equivalent $m = 1$ case (possibly with a smaller supercell). This is because the set of elements $\{e^{-\mathrm{i}mn\alpha}\}$ for $n = 0, 1, \ldots, N - 1$, which appear as summation terms in Eq. (2) for $|m| > 1$ is a subset of elements $\{e^{-\mathrm{i}n\alpha}\}$ for $n = 0, 1, \ldots, N - 1$ in the summation for $m = 1$.

Let $[u_{(1)}, u_{(2)}]$ denote the interval onto which v-space is mapped by $u(v)$ and let $v_{(i)}$, $i = 1, 2$, be defined by $u_{(i)} = u(v_{(i)})$. The procedure for identifying the optimal control profile $\{v_n\}$ may be classified based on how g depends on v. In order of how they are addressed below, we distinguish the (a) lossless case, (b) flat tuning, (c) general case and (d) skewed tuning.

The lossless case is characterized by $g(v) = 1$ and for it analytic expressions exist. We refer by flat tuning to the case $g(v) = g_0$ with g_0 being a constant and show that it can be reduced to the lossless case. For the general case, with $g(v)$

being arbitrary, we describe a simple numerical solution. Finally, by skewed tuning we denote the general case which fulfills the condition that $g(v) = g_0 + au(v)$ and we show that it can also be reduced to the lossless case in a similar manner as flat tuning. We show below that skewed tuning is an excellent approximation for realistic situations making it the model of choice in practice.

A. Lossless Resonators

In lossless (i.e. ideal) resonators $g_0 = 1$, so that, according to Fig. 2, changing u only affects ϕ_r, while $|r| = 1$. The optimal control then involves identifying the phase profile $\{\phi_n\}$ which maximizes $|S_N|$ as given by Eq. (2). If the tuning phase range $\Delta\phi$, defined as

$$\Delta\phi = \phi_{(2)} - \phi_{(1)}, \quad \phi_{(i)} = \phi_r(v_{(i)}), \quad i = 1, 2, \tag{4}$$

is greater or equal to $(N - 1)\alpha$, then it is obvious that there exists an equidistant phase profile $\{\phi_n\}$, with phase step equal to α, such that $|S_N| = 1$, which is the largest value $|S_N|$ can reach under any conditions.

For $\Delta\phi < (N - 1)\alpha$, which is likely to be the case almost always in practice, it is straightforward but a bit tedious (and hence omitted here) to show that the phase profiles $\{\phi_n^{\mathrm{id}}\}$ listed below maximize $|S_N|$ allowing it to reach the value denoted by S_N^{id} (the superscript 'id' here stands for ideal, i.e. lossless).

For odd $N = 2l + 1$ and s defined as $s = \Delta\phi/2\alpha$, $\{\phi_n^{\mathrm{id}}\}$ and S_N^{id} are given by

$$\phi_{l+1\pm k}^{\mathrm{id}} = \begin{cases} \phi_{\mathrm{mid}}, & k = 0, \\ \phi_{\mathrm{mid}} \pm k\alpha, & 0 < k \leq \lfloor s \rfloor, \\ \phi_{\mathrm{mid}} \pm \frac{\Delta\phi}{2}, & \lfloor s \rfloor < k \leq l \end{cases} \tag{5}$$

$$S_N^{\mathrm{id}} = 1 + 2\lfloor s \rfloor + 2\mathrm{Re}\left\{\frac{1 - e^{\mathrm{i}(l - \lfloor s \rfloor)\alpha}}{1 - e^{\mathrm{i}\alpha}}e^{\mathrm{i}(\lceil s \rceil - s)\alpha}\right\}. \tag{6}$$

Here $\lfloor x \rfloor$ denotes the largest integer less than or equal to x, $\lceil x \rceil$ is the smallest integer greater than or equal to x and $\phi_{\mathrm{mid}} = (\phi_{(1)} + \phi_{(2)})/2$ is the phase value at the middle of the available phase interval $[\phi_{(1)}, \phi_{(2)}]$.

For even $N = 2\tilde{l}$ and s defined as $s = \Delta\phi/2\alpha - 1/2$, we have

$$\phi_{l+1/2\pm(k+1/2)}^{\mathrm{id}} = \begin{cases} \phi_{\mathrm{mid}} \pm \left(k + \frac{1}{2}\right)\alpha, & 0 \leq k \leq \lfloor s \rfloor, \\ \phi_{\mathrm{mid}} \pm \frac{\Delta\phi}{2}, & \lfloor s \rfloor < k < l. \end{cases} \tag{7}$$

$$S_N^{\mathrm{id}} = 2 + 2\lfloor s \rfloor + 2\mathrm{Re}\left\{\frac{1 - e^{\mathrm{i}(l - 1 - \lfloor s \rfloor)\alpha}}{1 - e^{\mathrm{i}\alpha}}e^{\mathrm{i}(\lceil s \rceil - s)\alpha}\right\}. \tag{8}$$

To be accurate, we note that the expressions listed above provide the maximum attainable value of $|S_N|$ in all but some practically irrelevant cases that occur at $\Delta\phi < \pi/3$. The phase profiles as a function of $\Delta\phi$ given by Eqs. (5) and (7) might appear cumbersome, but their meaning is simple, as plotted in Fig. 3(a) and (b), by the $g_0 = 1$ curves. They merely show that the optimal profile in the lossless case involves equidistant spacing, with a step equal to α, distributed symmetrically around ϕ_{mid} until the phase range is exhausted, with setting all the remaining phase elements to $\phi_{(1)}$ and $\phi_{(2)}$.
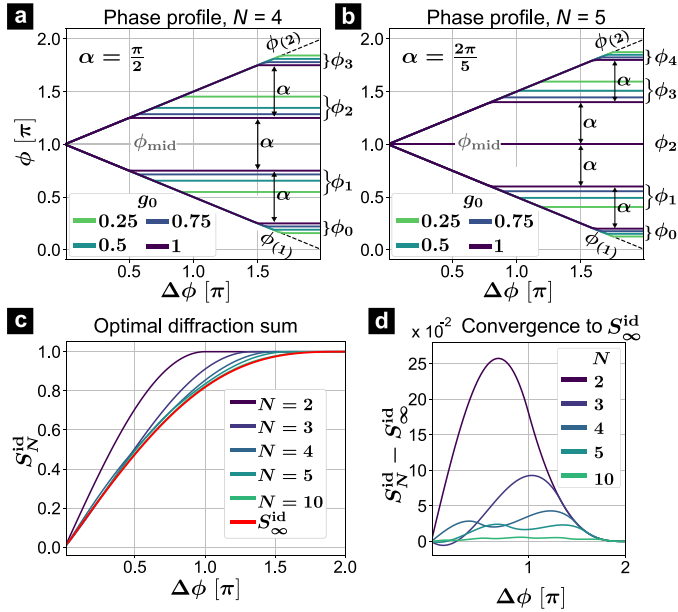
Fig. 3. Phase profiles under optimal control for the flat tuning problem, drawn assuming $\phi_{\mathrm{mid}} = \pi$ for (a) even $N = 4$ and (b) odd $N = 5$. The lossless case profiles ϕ_n^{id} correspond to ϕ_n for $g_0 = 1$. (c) Diffraction sum maxima as a function of available phase range for various N and (d) their convergence towards S_∞^{id}.

The resonator state profile $\{u_n^{\mathrm{oc}}\}$ under optimal control is found from $\{\phi_n^{\mathrm{id}}\}$ using

$$u_n^{\mathrm{oc}} = \tan \frac{\phi_n^{\mathrm{id}} - \pi}{2}, \qquad (9)$$

which follows from Eq. (3) when $g = 1$. Finally, one obtains the optimal control profile $\{v_n^{\mathrm{oc}}\}$ from $v_n^{\mathrm{oc}} = u^{-1}(u_n^{\mathrm{oc}})$, where $u^{-1}(u)$ is the inverse of $u(v)$.

The plots of S_N^{id}, evaluated as a function of $\Delta\phi$ according to Eqs. (6) and (8) are shown in Fig. 3(c) for several values of N. As expected, S_N^{id} reaches unity for any $\Delta\phi \geq (N-1)\alpha$ (note that α also changes with N). Although there is a variation of S_N^{id} with N, Fig. 3(c) shows that the S_N^{id} curves quickly converge towards their $N \to \infty$ asymptote S_∞^{id}. This is more evident in Fig. 3(d) where the differential $S_N^{\mathrm{id}} - S_\infty^{\mathrm{id}}$ is shown to be less than 0.03 for $N = 5$ and less than 0.01 for $N = 10$, for any $\Delta\phi$. Therefore, already for $N \geq 5$ one may safely use S_∞^{id} as an estimate for the maximum $|S_N|$ value achievable under optimal control.

B. Flat Tuning

Now, let us consider the more interesting case of $g_0 < 1$ and denote the maximum of $|S_N|$ (obtained under optimal control) by $S_N(g_0)$. As in the lossless case, tuning v leads to sweeping one of the constant-g curves in Fig. 2 within the $[u_{(1)}, u_{(2)}]$ interval, except that here $|r|$ also changes with v, so that ϕ_r values close to π (i.e. $u \approx 0$) are penalized by smaller values of $|r|$. The optimal control problem in this case can be reduced to the ideal $g_0 = 1$ case, by noting that for any profile $\{u_n\}$ the

following identity holds

$$\sum_{n=0}^{N-1} \frac{u_n - \mathrm{i}g_0}{u_n + \mathrm{i}} \mathrm{e}^{-\mathrm{i}n\alpha} = \frac{1 + g_0}{2} \sum_{n=0}^{N-1} \frac{u_n - \mathrm{i}}{u_n + \mathrm{i}} \mathrm{e}^{-\mathrm{i}n\alpha}, \qquad (10)$$

which can be seen by adding a factor proportional to $\sum_{n=0}^{N-1} \exp(-\mathrm{i}n\alpha) = 0$ to the left-hand side. This means that the S_N value of an array of g_0 resonators with state profile $\{u_n\}$ is equal $(1 + g_0)/2$ times the S_N value of lossless resonators ($g_0 = 1$) having the same state profile. It then implies that the considered array of g_0-resonators with the set of available states $[u_{(1)}, u_{(2)}]$ has the same state profile $\{u_n^{\mathrm{oc}}\}$ under optimal control as the array of lossless resonators with the same set of available states, while the maximal diffraction sum is

$$S_N(g_0) = \frac{1 + g_0}{2} S_N^{\mathrm{id}}. \qquad (11)$$

Now let us assume that we are given an array of g_0 resonators with specified values of $u_{(1)}$ and $u_{(2)}$ and asked to determine the corresponding optimal control profile $\{u_n^{\mathrm{oc}}\}$. The way we would do it is to first determine $\phi_{(1)}$ and $\phi_{(2)}$ which define the set of available phases corresponding to lossless resonators with the same $u_{(i)}$ values

$$\phi_{(i)} = 2 \arctan u_{(i)} + \pi, \quad i = 1, 2. \qquad (12)$$

Then, we proceed as in Section III-A to determine the corresponding $\{\phi_n^{\mathrm{id}}\}$ while $S_N(g_0)$ is obtained from Eq. (11) using the value S_N^{id} evaluated for $\Delta\phi = \phi_{(2)} - \phi_{(1)}$. Finaly, the desired $\{u_n^{\mathrm{oc}}\}$ is retrieved from $\{\phi_n^{\mathrm{id}}\}$ with the help of Eq. (9) and from it the control profile $\{v_n^{\mathrm{oc}}\}$ by inverting the corresponding $u(v)$ mapping. The phases $\{\phi_n\}$ under optimal control of the g_0-resonator array can be obtained as the arguments of the reflection coefficients $\{r_n\}$ evaluated by plugging $\{u_n^{\mathrm{oc}}\}$ into Eq. (3). These phase profiles are shown for several exemplary cases in Fig. 3(a) and (b) (the $g_0 < 1$ curves). As expected, the optimal phases are seen to be slightly deflected away from the $\phi \approx \pi$ region as it is associated with smaller $|r|$ values, with the deflection being larger for smaller g_0 values.

The outlined procedure for optimal control in case of flat tuning is straightforward, but non-trivial and thus understanding in which circumstances is it warranted would be helpful. Upon inspecting Fig. 3(a)–(d), one finds that for $g_0 > 0.75$, the optimal $\{\phi_n\}$ differs only very slightly from the $\{\phi_n^{\mathrm{id}}\}$ set, which means that the diffraction sum obtained by using simply $\{\phi_n^{\mathrm{id}}\}$ instead of the optimal $\{\phi_n\}$ will be only marginally smaller than the value given by Eq. (11). Meanwhile, from Fig. 3(c), one finds that $S_N^{\mathrm{id}} > 0.95$ if $\Delta\phi > 1.5\pi$, implying that not much is to be gained by fine optimization when the available phase range is above 1.5π. An analogous conclusion holds for the general and skewed tuning cases discussed below. Therefore, the analysis presented in this article makes most sense for lossy resonant metasurfaces - there is no point in applying it to systems with $g_0 \approx 1$ and $\Delta\phi \approx 2\pi$ as the accuracy of the underlying scalar diffraction theory is lower than the prescribed gain. In those cases one is likely to be well off using the lossless profile with phase steps equal to α, as given by Eqs. (5) and (7).
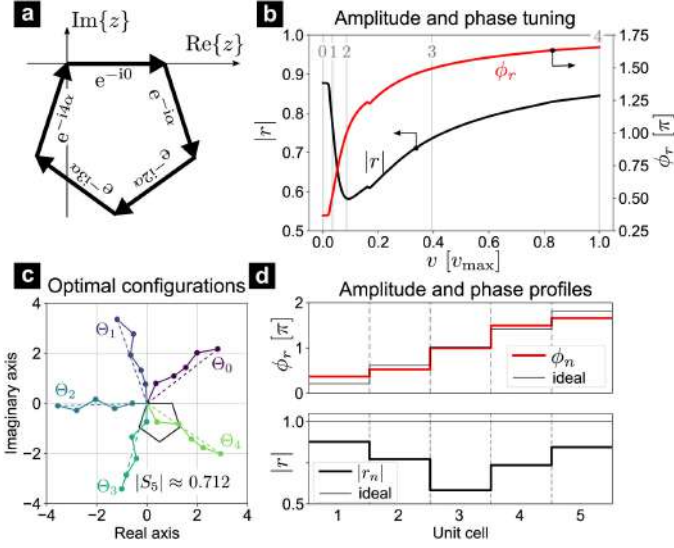
Fig. 4. (a) Graphical interpretation of the optimal control problem. (b) $r(v)$ example for the metasurface described in Section IV. (c) Maximal values of $|S_5|$ for $r(v)$ given under (b). (d) Optimal phase and amplitude profiles.

C. General Case

Let us, for the purposes of this section, leave aside all the previous considerations involving the TCMT model and the u and g parameters. Consider instead a more general problem of maximizing $|S_N|$ given by Eq. (2) by a control profile $\{v_n\}$ defining the r_n terms in Eq. (2) through $r_n = r(v_n)$, where $r(v)$ is an arbitrary complex-valued function such that $|r| \leq 1$.

This problem has a simple graphical interpretation if we look at how the different $\exp(-in\alpha)$ terms are added together in the complex plane. If $r_n = 1$ for all n, the $\exp(-in\alpha)$ terms form a regular convex N-sided poligon, as depicted in Fig. 4(a) for the $N = 5$ case. As pointed out before, any $m > 1$ case will involve the same terms but perhaps permuted, so that they form some other regular, convex or star, N'-sided polygon for N' being a divisor of N. Since the polygon is closed, the sum amounts to zero. The effect of multiplying by r_n amounts to rotating the corresponding $\exp(-in\alpha)$ term clockwise by ϕ_n and reducing its amplitude by a factor $|r_n|$. Therefore, maximizing $|S_N|$ is equivalent to maximizing the length of the broken line obtained by rectifying the mentioned polygons through multiplication by r_n.

This problem has a simple solution which we illustrate considering a particular example of $r(v)$, shown in Fig. 4(b). The shown curves represent the reflection coefficient on an array of MIM resonators infiltrated by a nematic LC, while v represents the gate voltage which tunes the nematic molecule orientation. Further details of this example will be given below and, in particular, in Section IV.

Finding the optimal $\{v_n\}$ can be broken down into two steps. In the first, we select an angle Θ and search for the $\{v_n\}$ that maximizes the projection of the broken line representing S_N onto that direction. Since the projection of S_N is equal to the sum of the projections of the $r_n \exp(-in\alpha)$ terms on Θ, this search involves N independent optimizations of each of the

$r_n \exp(-in\alpha)$ terms, which is easily done even by the brute-force sweep of the entire v space (i.e. available v values). The second step involves repeating the first step for all Θ between 0 and 2π, to find the direction $\Theta_{\max}$ onto which the S_N projection is maximal for $\{v_n^{\max}\}$. It is easy to see that the set $\{v_n^{\max}\}$ represents the optimal control profile for the initial problem.

Applying the above procedure onto the $N = 5$ example, with $r(v)$ given in Fig. 4(b), we obtain $N = 5$ values of $\Theta_{\max}$ which all yield the maximum of $|S_5| \approx 0.712$. These angles are denoted by Θ_i, $i = 0, 1, \ldots, 4$ and drawn in Fig. 4(c), together with the optimal broken lines. The multiplicity of equivalent optima is a consequence of the N-fold rotational symmetry of the geometrical problem, with each solution corresponding to one of the N cyclic permutations of $\{r_n\}$ in the supercell. This, of course, means that when searching for $\Theta_{\max}$, it is sufficient to sweep only the $[0, \alpha]$ range. The optimal $|r_n|$ and ϕ_n profiles corresponding to the Θ_0 case are shown in Fig. 4(d). The optimal voltage values $\{v_n^{\max}\}$ are indicated by the vertical gray lines in Fig. 4(b) and enumerated by the corresponding index $n = 0, 1, \ldots, 4$.

Although general and simple, easily reproducing the results from Sections III-A and III-B, the numerical procedure described in this section only provides the correct solution, with no insight on how it is conditioned by the unit cell characteristics.

D. Skewed Tuning

While capturing its nature, the flat tuning model of Section III-B does not give an accurate quantitative assessment in the tuning problem used as the example in Fig. 4 because the g value changes noticeably over the v space. To explain this, we will consider in more detail the characteristics of the LC cell whose reflection function was shown in Fig. 4(b). Again, for the purposes of this section, the LC cell is to be seen as a representative example of a terahertz metasurface while its specific details are given in Section IV. The reflection spectra for several typical v values are given in Fig. 5(a) and (b) (dots), together with best TCMT fits drawn by solid lines. In fact, the v_n, $n = 0, 1, \ldots, 4$ values for which these curves are drawn are equal to $\{v_n^{\max}\}$ from the previous section.

First, we notice that the TCMT fits reproduce the actual LC cell spectra rather well, thus justifying the use of the TCMT model. The $r(v)$ curves in Fig. 4(b) have, in fact, been drawn for the operation frequency $f = 1\,\text{THz}$, meaning that their values correspond to the intersection of the reflection spectra and the $f = 1\,\text{THz}$ vertical line in Fig. 5(a) and (b). The extracted TCMT parameters as a function of v are drawn in Fig. 5(c), while the functions $u(v)$ and $g(v)$ can be inferred from Eq. (3). In particular, with increasing v, u increases because $f_0 = \omega_0/2\pi$ decreases, as seen in Fig. 5(c). Meanwhile, g decreases from around 0.65 at v_0 to around 0.52 at v_4, which can be seen by observing that the $|r(\omega_0)|$ value (reflection amplitude at resonance) decreases for increasing v_n.

To account for the variation of g, let us assume that $u(v)$ and $g(v)$ are arbitrary but so that the linear relationship
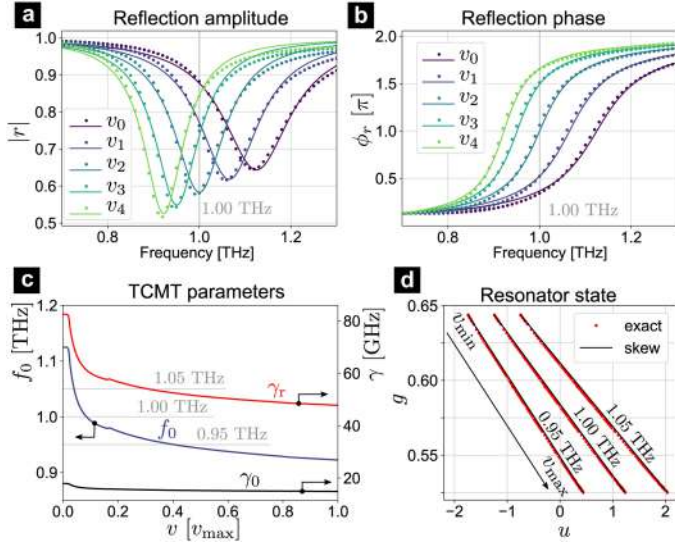
$$g(v) = g_0 + au(v), \tag{13}$$

Fig. 5.   (a) Reflection amplitude and (b) phase spectra for the metasurface described in Section IV, drawn for 5 values of v - the same ones that maximize $|S_5|$ in Fig. 4. Dots are the actual data points while solid lines represent the TCMT fit. (c) Extracted TCMT parameters as a function of v. (d) Plots of (u, g) pairs through which the resonator is swept by tuning v.

is fulfilled, which we refer to as skewed tuning because of the skewed appearance of successive reflection spectra with decreasing g as in Fig. 5(a). Introducing $g_{(i)} = g(v_{(i)})$, the coefficients g_0 and a can be expressed as

$$g_0 = \frac{u_{(2)}g_{(1)} - u_{(1)}g_{(2)}}{u_{(2)} - u_{(1)}}, \quad a = \frac{g_{(2)} - g_{(1)}}{u_{(2)} - u_{(1)}}. \qquad (14)$$

It turns out that Eq. (13) is an excellent approximation as long as the relative variation of g over the v space is small. To show this for the LC cell example, in Fig. 5(d) we plot the exact $(u(v), g(v))$ data points along with the lines generated by Eq. (13), for three different operation frequencies. The extent to which the skewed tuning model matches the exact u and g data, means that it is virtually exact in this case, which has been verified by comparing its prediction with the numerical model from the previous section. Taking this into account, it is reasonable to expect this to be an accurate model for other metasurface types.

As in the flat tuning case, one can easily show that the identity

$$\sum_{n=0}^{N-1} \frac{u_n - \mathrm{i}(g_0 + au_n)}{u_n + \mathrm{i}} e^{-\mathrm{i}n\alpha} =$$

$$\frac{1 + g_0 - \mathrm{i}a}{2} \sum_{n=0}^{N-1} \frac{u_n - \mathrm{i}}{u_n + \mathrm{i}} e^{-\mathrm{i}n\alpha}, \qquad (15)$$

holds for any profile $\{u_n\}$. This then implies that the maximal value of $|S_N|$ under optimal control in skewed tuning, denoted by $S_N(g_0, a)$, is given by

$$S_N(g_0, a) = \frac{|1 + g_0 - \mathrm{i}a|}{2} S_N^{\mathrm{id}} \approx \frac{1 + g_0}{2} S_N^{\mathrm{id}}, \qquad (16)$$
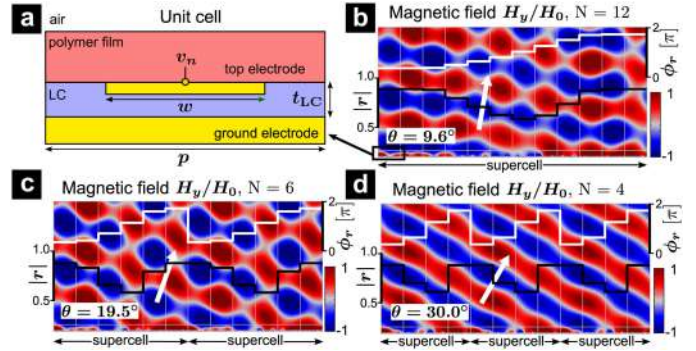

Fig. 6.   (a) The $x - z$ plane cross section of the LC MIM unit cell. (b)–(d) Scattered magnetic field colormaps with overlayed reflection amplitude and phase profiles, drawn over $x - z$ range $1800\,\mu m \times 900\,\mu m$ involving 12 unit cells. The supercell size is (b) $N = 12$, (c) $N = 6$ and (d) $N = 4$ while the unit cell parameters are given in Eq. (17).

and that the optimal control profile $\{v_n\}$ can be determined in a manner analogous to the flat tuning case.

Neglecting a in the right hand side of Eq. (16) is justified as follows: Firstly, a is at least several times smaller than $\Delta g = g_{(2)} - g_{(1)}$ in any practically relevant case because for reasonable tuning efficiency $\Delta u = u_{(2)} - u_{(1)}$ has to be at least 2, meaning that a is typically an order of magnitude smaller than $1 + g_0$. Secondly, because of the absolute value in the middle term in Eq. (16), a contributes to the factor that multiplies S_N^{id} via a term proportional to $a/(1 + g_0)$, meaning that the overall contribution of a is typically two orders of magnitude smaller than $1 + g_0$ and thus negligible. Therefore, the maximum attainable $|S_N|$ value under skewed tuning is given by an equation identical to the one for flat tuning, Eq. (11), the only difference being that now g_0 is determined by Eq. (14).

IV. Example: Terahertz Beam Steering With LC Metasurfaces

To validate our model and illustrate the design method on a realistic example, we consider a metasurface consisting of an array of MIM cavities infiltrated by a nematic LC depicted in Fig. 6(a). Here the control parameter v, exhibiting a gradual variation over the array of unit cells along the horizontal direction (x axis), is the voltage applied to the top electrode while the bottom metal layer serves as the ground. The structure is assumed invariant along the out-of-plane direction (y-axis), so that applying a distinct voltage to each cell is straightforward, similarly as in [19].

When $v = 0$, the nematic LC molecules are all oriented along the y-axis because of a thin polymer alignment layer covering the electrodes. Then the z-component of the LC permittivity tensor is equal to n_o^2, with n_o being the ordinary LC refractive index. Upon increasing v, the nematic molecules realign themselves along the vertical direction (z-axis). This process saturates at a voltage value $v_{\max}$ when virtually all LC molecules are vertically oriented with the z-component of the permittivity tensor becoming close to n_e^2 and n_e being the extraordinary

index. The physics of the devices considered herein is mod-elled by a rigorous multiphysics model involving Maxwell equations for electromagnetic waves and the $\mathbf{Q}$-tensor model for LC switching. The LC parameters of the nematic mixture 1825 [31] with $n_{\mathrm{o}} = 1.554 + 0.018\mathrm{i}$ ind $n_{\mathrm{e}} = 1.941 + 0.022\mathrm{i}$ have been assumed, while Zeonor is assumed for the encapsu-lating polymer layer carying the electrodes [32] with a refractive index of $n_{\mathrm{poly}} = 1.518 + 0.001\mathrm{i}$ [33] in the terahertz range. The electrodes are assumed to be made of copper, instead of the commonly used gold, because it is known to have a lower absorption rate at terahertz frequencies [34]. The copper per-mittivity $\varepsilon_{\mathrm{m}}(\omega)$ was assumed to have the Drude form with the copper plasma $\omega_{\mathrm{p}} = 1.12 \times 10^{16}$ rad/s and collision frequency $\gamma_{\mathrm{c,Cu}} = 1.38 \times 10^{13}$ rad/s taken from [35]. For further details on modelling LC MIM cavities in the terahertz, the reader is referred to our previous work [18], [36], [37].

The data shown in Figs. 4 and 5, and used as example in previous sections, corresponds to a unit cell having the following dimensions

$$w = 75\,\mu\mathrm{m}, \quad p = 150\,\mu\mathrm{m} \quad \text{and} \quad t_{\mathrm{LC}} = 5\,\mu\mathrm{m}. \quad (17)$$

The operation of an electrically tunable beam steering metasur-face utilizing such a unit cell is demonstrated in Fig. 6(b)–(d). The colormaps represent the $x - z$ plane cross section of the scattered field generated by a p-polarized ($\mathbf{H}$ field pointing out of plane) perpendicularly incident $f = 1\,\mathrm{THz}$ electromag-netic field with magnetic field amplitude H_0 illuminating the metasurface. Following the procedure described in previous sections, here the optimal control voltage profiles have been determined for three exemplary supercell sizes: $N = 12$, 6 and 4. Applying these voltages to LC MIM cells, results in the phase and amplitude profiles shown as overlays on Fig. 6(b)–(d) and leads to the scattered field being predominantly steered along the stated angle θ corresponding to the $m = 1$ diffraction order.

We now address the accuracy of the presented model. First we wish to assert the claim made earlier stating that the model becomes exact as the deflection angle $\theta \to 0$, which is a general feature of scalar diffraction theory. To this end, we again consider the metasurface with unit cell with parameters from Eq. (17) and determine the optimal control profiles for $N = 3, 4, \ldots, 40$. To obtain the exact η_1 values, we solve Maxwell's equations exactly for the supercell at $f = 1\,\mathrm{THz}$ and determine η_1 as the squared modulus of the 1-st term of the scattered field Fourier series. In Fig. 7(a) we plot this against the η_1 values obtained from our model

$$\eta_1 = \left| \mathrm{sinc}\left(\frac{1}{N}\right) \frac{1 + g_0}{2} S_N^{\mathrm{id}} \right|^2, \quad (18)$$

with g_0 given by Eq. (14). Values of η_1 obtained through nu-merical optimization following Section III-C overlap the plotted curve, demonstrating the accuracy of the skewed tuning model. For reference, the diffraction angles θ corresponding to the 1-st diffraction order are given in the inset of Fig. 7(a). Therefore, the model is rather accurate, especially for $N > 10$. A similar trend is to be expected for other unit cell parameters or different metasurface types, except that the particular N values may vary.
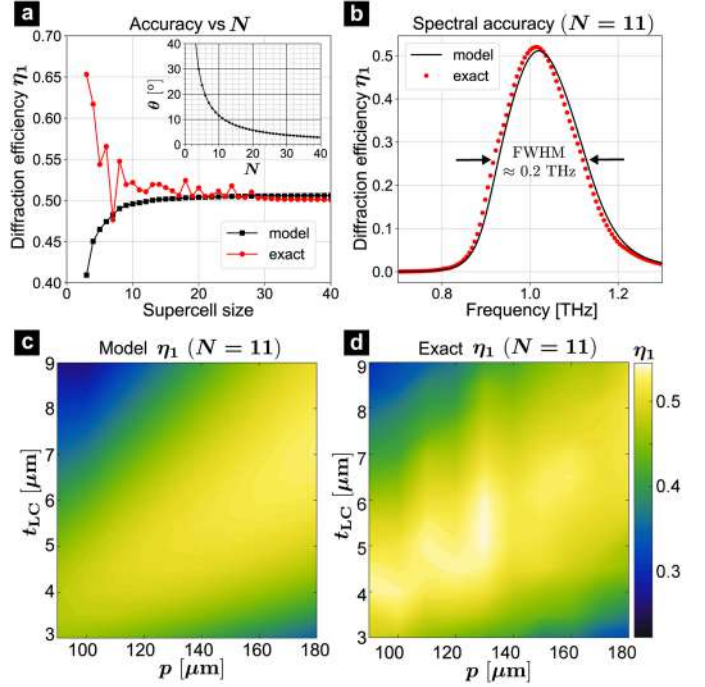

Fig. 7. Comparison of rigorously calculated η_1 with values obtained from the proposed model as a function of (a) supercell size, (b) operation frequency and (c), (d) unit cell width p and LC cell height t_{LC}. In each case, the applied voltage profile corresponds to optimal control at $f = 1.02\,\mathrm{THz}$. Colormaps have been prepared following [38].

Next, we test the spectral accuracy. For a particular supercell size ($N = 11$), we determine the spectral behavior of η_1 for the metasurface optimized at $f = 1\,\mathrm{THz}$ and compare it with values obtained by using Eqs. (1) and (3) but with changing f while keeping the TCMT parameter profiles optimized for $1\,\mathrm{THz}$. The results in Fig. 7(b) also show a remarkable accuracy, indicating that for $N > 10$ the presented model can be used for accurately determining the device operation bandwidth.

As pointed out before, the significance of the model pre-sented in this article is that it establishes a direct connection between η_1 and the unit cell parameters Π, helping the global optimization. For example, the physically intuitive relationship between TCMT parameters of terahertz MIM resonators and their various parameters has been addressed in our previous work, see [27], [36], [39]. To demonstrate how the presented model fares in terms of predicting the η_1 variation with unit cell geometrical parameters, we fix the supercell size to $N = 11$ and sweep both the unit cell width p and the LC cell height t_{LC}. For each geometry, we determine the optimal control voltage profile and assess η_1 both using Eq. (18) and the rigorous supercell simulations. The results are shown by the colormaps in Fig. 7(c) and (d). The model is again found to be rather accurate over the entire parameter plane, with deviations occuring for some p values, likely due to the onset of additional diffraction orders. Therefore, we conclude that the model described in this article can be used for understanding the variation of DE over the unit cell parameter space and thus provide help in designing novel beam steering metasurfaces.

V. Summary

We have formulated a theoretical model for assessing the diffraction efficiency of beam steering metasurfaces in terms of resonant eigenmode parameters. The model has been used to identify the control parameter profile yielding the highest diffraction efficiency and to express this efficiency by a simple formula. To illustrate the model and efficiency optimization procedure, a detailed example involving electrically tunable LC terahertz metasurfaces has been analyzed. The theoretical predictions of the model have been compared with rigorous numerical simulations involving large supercells and shown to exhibit remarkable accuracy for sufficiently small deflection angles. The results presented in this work will help the design of novel beam steering metasurfaces by providing optimization guidelines and a way to quickly assess the best possible performance achievable by a particular resonant element.

References

[1] G. Swanson, *Binary Optics Technology: The Theory and Design of Multilevel Diffractive Optical Elements*. MIT, Cambridge, MA, USA, Tech. Rep. 854, 1989.

[2] N. Yu *et al.*, "Light propagation with phase discontinuities: Generalized laws of reflection and refraction," *Science.*, vol. 334, pp. 333–337, 2011.

[3] P. Genevet, F. Capasso, F. Aieta, M. Khorasaninejad, and R. Devlin, "Recent advances in planar optics: From plasmonic to dielectric metasurfaces," *Optica.*, vol. 4, no. 1, pp. 139–152, Jan. 2017.

[4] F. Ding, A. Pors, and S. I. Bozhevolnyi, "Gradient metasurfaces: A review of fundamentals and applications," *Rep. Prog. Phys.*, vol. 81, 2018, Art. no. 026401.

[5] S. Sun *et al.*, "High-efficiency broadband anomalous reflection by gradient meta-surfaces," *Nano Lett.*, vol. 12, pp. 6223–6229, 2012.

[6] O. Tsilipakos *et al.*, "Pairing toroidal and magnetic dipole resonances in elliptic dielectric rod metasurfaces for reconfigurable wavefront manipulation in reflection," *Adv. Opt. Mater.*, vol. 6, no. 22, 2018, Art. no. 1800633.

[7] D. Headland, Y. Monnai, D. Abbott, C. Fumeaux, and W. Withayachumnankul, "Tutorial: Terahertz beamforming, from concepts to realizations," *APL Photon.*, vol. 3, no. 5, 2018, Art. no. 051101.

[8] D. Berry, R. Malech, and W. Kennedy, "The reflectarray antenna," *IEEE Trans. Antennas Propag.*, vol. AP-11, no. 6, pp. 645–651, Nov. 1963.

[9] D. Pozar and T. Metzler, "Analysis of a reflectarray antenna using microstrip patches of variable size," *Electron. Lett.*, vol. 29, pp. 657–658, Apr. 1993.

[10] J. Huang and J. Encinar, *Reflectarray Antenna*. Hoboken, NJ, USA: Wiley, 2008.

[11] F. Liu *et al.*, "Intelligent metasurfaces with continuously tunable local surface impedance for multiple reconfigurable functions," *Phys. Rev. Appl.*, vol. 11, 2019, Art. no. 044024.

[12] A. Pors, O. Albrektsen, I. Radko, and S. I. Bozhevolnyi, "Gap plasmon-based metasurfaces for total control of reflected light," *Sci. Rep.*, vol. 3, 2013, Art. no. 2155.

[13] T. Niu *et al.*, "Experimental demonstration of reflectarray antennas at terahertz frequencies," *Opt. Express*, vol. 21, no. 3, pp. 2875–2889, Feb. 2013.

[14] X. You *et al.*, "Terahertz reflectarray with enhanced bandwidth," *Adv. Opt. Mater.*, vol. 7, no. 20, 2019, Art. no. 1900791.

[15] A. Forouzmand and H. Mosallaei, "Tunable two dimensional optical beam steering with reconfigurable indium tin oxide plasmonic reflectarray metasurface," *J. Opt.*, vol. 18, 2016, Art. no. 125003.

[16] T. Yatooshi, A. Ishikawa, and K. Tsuruta, "Terahertz wavefront control by tunable metasurface made of graphene ribbons," *Appl. Phys. Lett.*, vol. 107, 2015, Art. no. 053105.

[17] P. P. Iyer, M. Pendharkar, and J. A. Schuller, "Electrically reconfigurable metasurfaces using heterojunction resonators," *Adv. Opt. Mater.*, vol. 4, pp. 1582–1588, 2016.

[18] B. Vasić, G. Isić, R. Beccherelli, and D. C. Zografopoulos, "Tunable beam steering at terahertz frequencies using reconfigurable metasurfaces coupled with liquid crystals," *IEEE J. Sel. Top. Quantum Electron.*, vol. 26, no. 5, Sep./Oct. 2020, Art. no. 7701609.

[19] Y.-W. Huang *et al.*, "Gate-tunable conducting oxide metasurfaces," *Nano Lett.*, vol. 16, pp. 5319–5325, 2016.

[20] J. Wu *et al.*, "Liquid crystal programmable metasurface for terahertz beam steering," *Appl. Phys. Lett.*, vol. 116, no. 13, 2020, Art. no. 131104.

[21] J. W. Goodman, *Introduction to Fourier Opt. Englewood*, CO, USA: Roberts & Company, 2005.

[22] S. Fan, W. Suh, and J. D. Joannopoulos, "Temporal coupled-mode theory for the fano resonance in optical resonators," *J. Opt. Soc. Am. A*, vol. 20, no. 3, pp. 569–572, Mar. 2003.

[23] M. Born and E. Wolf, *Principles of Optics*. Cambridge, U.K.: Cambridge Univ. Press, 2005.

[24] G. Swanson, *Binary Opt. Technol.: Theor. Limits on the Diffraction Efficiency of Multilevel Diffractive Opt. Elements*. Cambridge, MA, USA, MIT Tech. Rep. 914, 1991.

[25] D. A. Pommet, M. G. Moharam, and E. B. Grann, "Limits of scalar diffraction theory for diffractive phase elements," *J. Opt. Soc. Amer. A*, vol. 11, no. 6, pp. 1827–1834, Jun. 1994.

[26] P. Lalanne, W. Yan, K. Vynck, C. Sauvan, and J.-P. Hugonin, "Light interaction with photonic and plasmonic resonances," *Laser Photon. Rev.*, vol. 12, no. 5, Art. no. 1700113.

[27] G. Isić and R. Gajić, "Geometrical scaling and modal decay rates in periodic arrays of deeply subwavelength terahertz resonators," *J. Appl. Phys.*, vol. 116, no. 23, 2014, Art. no. 233103.

[28] T. Lepetit, E. Akmansoy, J.-P. Ganne, and J.-M. Lourtioz, "Resonance continuum coupling in high-permittivity dielectric metamaterials," *Phys. Rev. B*, vol. 82, 2010, Art. no. 195307.

[29] W. Suh, Z. Wang, and S. Fan, "Temporal coupled-mode theory and the presence of non-orthogonal modes in lossless multimode cavities," *IEEE J. Quantum Electron.*, vol. 40, no. 10, pp. 1511–1518, Oct. 2004.

[30] J. D. Hunter, "Matplotlib: A 2 d graphics environment," *Comput. Sci. Eng.*, vol. 9, no. 3, pp. 90–95, 2007.

[31] M. Reuter *et al.*, "Highly birefringent, low-loss liquid crystals for terahertz applications," *APL Mater.*, vol. 1, 2013, Art. no. 012107.

[32] A. Ferraro, D. C. Zografopoulos, R. Caputo, and R. Beccherelli, "Guided-mode resonant narrowband terahertz filtering by periodic metallic stripe and patch arrays on cyclo-olefin substrates," *Sci. Rep.*, vol. 8, 2018, Art. no. 17272.

[33] P. A. George *et al.*, "Microfluidic devices for terahertz spectroscopy of biomolecules," *Opt. Express*, vol. 16, pp. 1577–1582, 2008.

[34] M. A. Belkin *et al.*, "Terahertz quantum cascade lasers with copper metal-metal waveguides operating up to 178 k," *Opt. Express*, vol. 16, no. 5, pp. 3242–3248, Mar. 2008.

[35] M. A. Ordal, R. J. Bell, R. W. Alexander, L. L. Long, and M. R. Querry, "Optical properties of fourteen metals in the infrared and far infrared: Al, Co, Cu, Au, Fe, Pb, Mo, Ni, Pd, Pt, Ag, Ti, V, and W," *Appl. Opt.*, vol. 24, no. 24, pp. 4493–4499, Dec. 1985.

[36] G. Isić, B. Vasić, D. C. Zografopoulos, R. Beccherelli, and R. Gajić, "Electrically tunable critically coupled terahertz metamaterial absorber based on nematic liquid crystals," *Phys. Rev. Appl.*, vol. 3, Jun. 2015, Art. no. 064007.

[37] B. Vasić, D. C. Zografopoulos, G. Isić, R. Beccherelli, and R. Gajić, "Electrically tunable terahertz polarization converter based on overcoupled metal-isolator-metal metamaterials infiltrated with liquid crystals," *Nanotechnology.*, vol. 28, 2017, Art. no. 124002.

[38] P. Kovesi, "Good colour maps: How to design them," 2015, *arXiv/1509.03700*.

[39] G. Isić *et al.*, "Electrically tunable metal-semiconductor-metal terahertz metasurface modulators," *IEEE J. Sel. Top. Quantum Electron.*, vol. 25, no. 3, May/Jun. 2019, Art. no. 8500108.

Perspective

Polyaniline as a charge storage material in an aqueous aluminum-based electrolyte: Can aluminum ions play the role of protons?

Milica J. Vujković [a,*], Mihajlo Etinski [a], Borislav Vasić [b], Bojana Kuzmanović [c], Danica Bajuk-Bogdanović [a], Robert Dominko [d,e], Slavko Mentus [a,f]

[a] Faculty of Physical Chemistry, University of Belgrade, Studentski trg 12-16, 11158, Belgrade, Serbia
[b] Institute of Physics Belgrade, University of Belgrade, Pregrevica 118, 11080, Belgrade, Serbia
[c] Institute of Nuclear Sciences "Vinča", University of Belgrade, Mike Petrovića Alasa 12-14, 11001, Belgrade, Serbia
[d] National Institute of Chemistry, Hajdrihova 19, SI-1000, Ljubljana, Slovenia
[e] FKKT, University of Ljubljana, Večna pot 117, 1000, Ljubljana, Slovenia
[f] Serbian Academy of Sciences and Arts, Knez Mihajlova 35, 11000, Belgrade, Serbia

HIGHLIGHTS

- Redox activity of PANI-ES is verified in an aluminum nitrate solution.
- Better charge storage ability of PANI-ES in 1 M $Al(NO_3)_3$ than in 1 M HCl.
- PANI-ES supercapacitor using $Al(NO_3)_3$ delivers exceptional capacitance and stability.
- Secondary doping effect of Al salts into protonated PANI.
- Formation/breaking nitrate complexes during PANI's redox switching in $Al(NO_3)_3$.

GRAPHICAL ABSTRACT
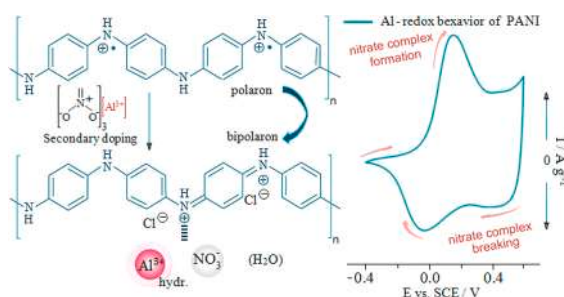
ARTICLE INFO

ABSTRACT

The high redox activity of polyaniline emeraldine salt (PANI-ES) was revealed in the aqueous solution of Al-salt, which makes this polymer attractive as an electrode material for aqueous aluminum electrochemical storage devices. Its redox behavior in $Al(NO_3)_3$, $Al(NO_3)_3$+HCl, $AlCl_3$ and HCl was investigated by Cyclic Voltammetry and Chronopotentiometry. While the proton exchange determines PANI's redox behavior in strong acidic solutions, anion doping/dedoping is a more dominant process in less acidic Al-salt solutions. The formation/dissolution of solid-state nitrate complexes is proposed to happen during PANI's redox switching in $Al(NO_3)_3$, which causes disappearance and reappearance of grain boundaries, as revealed by AFM. Combined experimental and DFT approaches identify Al-salt as a secondary dopant of protonated PANI-ES (by Lewis acid-base complexation), which causes polaron→bipolaron conversion. The change in the redox mechanism of PANI-ES, caused by the substitution of HCl with $Al(NO_3)_3$, did not attenuate its charge storage ability. Moreover, PANI-ES delivers a higher capacitance in $Al(NO_3)_3$, amounting to 269 $F g^{-1}$ at 10 $A g^{-1}$. Furthermore, the use of $Al(NO_3)_3$ results in attenuated electrochemical PANI overoxidation, when compared to HCl, thus providing better capacitance retention upon potentiodynamic cycling. The results open novel perspective of using PANI-based materials for more suitable energy storage devices.

* Corresponding author. University of Belgrade, Faculty of Physical Chemistry, Studentski trg 12–14, 11158, Belgrade, Serbia.
E-mail address: milica.vujkovic@ffh.bg.ac.rs (M.J. Vujković).

1. Introduction

Due to the high energy and power density Li-ion batteries and Li-ion hybrid systems dominate contemporary energy storage science and technology [1–3]. However, the awareness of restricted lithium resources on Earth has initiated the shifting of research beyond the Li-ion technology. Development of alternative systems is of great significance in order to save lithium resources, at least in the fields where the high current applications are not required. Furthermore, the use of aqueous instead of organic electrolyte would be the ideal solution in terms of the ionic conductivity of electrolyte as well as from the economic, safety and environmental aspects. On the other hand, the replacement of organic with an aqueous electrolyte is quite a big challenge due to limited electrochemical stability window of aqueous electrolyte [4–6].

Among various post-lithium rechargeable systems (Na, Mg, Ca, Zn, Al …), those based on aluminum charge storage have been studied to a lesser extent, despite the fact that the aluminum is the most abundant metal element in the Earth's crust with one of the highest gravimetrical and volumetric energy density due to its three-electron electrochemical reaction [3]. The reason for that lies in the lack of electrode materials capable of storing large amount of Al-ions. Let us outline the structures that can accumulate Al ions either through the intercalation or pseducoapacitance processes. Gogotsi at al [7] demonstrated the capability of two-dimensional Ti_3C_2 MXene layers to intercalate aluminium ions from the aqueous solutions. A relatively small intercalation capacitance of Ti_3C_2 in aqueous $Al_2(SO_4)_3$ solution amounted only to 5–30 F g^{-1} depending on the scan rate ranging from 2 to 100 mV s^{-1}. The reversible intercalation of trivalent aluminum ions into several oxides such as V-, Ti-, and Mo-based (followed by the appearance of redox peaks) was demonstrated not only in organic [8], but also in the aqueous electrolytic solution [3,9–17]. For example, TiO_2 nanoleaves were able to deliver a reversible capacity of 270.7 mAh g^{-1} at 0.05 A g^{-1} in 1 M Al $(NO_3)_3$, with an excellent stability [9]. Interestingly, TiO_2 nanotubes can show not only the typical intercalation/deintercalation process in an aqueous 1 M $AlCl_3$ solution [11] (the potential range from −0.3 V to −1.5 V vs. SCE), but also pure double layer capacitive response in the same electrolytic solution (the potential range from −0.8 V to −0.4 V vs. SCE) [19]. VO_2 nanorods, capable of intercalating Al ions, have also been proposed as the cathode for Al-ion non-aqueous rechargeable batteries [20]. The Al/VO_2 cell can deliver the initial discharge capacity of 165 mAh g^{-1}, thus retaining the value of 116 mAh g^{-1} after 100 cycles. By combining different graphite materials (carbon paper [21], graphitic-foam [22] and natural graphite flakes [23]) as cathode with aluminum as an anode in an ionic liquid (IL) electrolyte, new AlB systems have been developed. The best performance was achieved with the natural graphite (NG) cathode which delivered high chloroaluminate anions intercalation capacity (100 mA hg^{-1} at 198 mA g^{-1} or 60 mAh g^{-1} at 6C over 6000 cycles).

According to the best of our knowledge and in spite of numerous investigations of PANI, there is no report on the comprehensive study of the charge storage behavior of this polymer in the Al-containing aqueous solution. Redox activity of PANI film was observed in both aluminum sulphate and aluminium chloride solutions [24,25], but these studies were focused on electrochromic properties. The electron and proton transfer reactions of PANI in acidic solutions other than aluminum salt ones (HCl, H_2SO_4, $HClO_4$ …) are widely discussed [26–33], revealing the complexity of the mechanism itself. In this study, the high and stable redox activity of conductive PANI emeraldine salt form was evidenced in the aluminum-nitrate aqueous solution. New data are gathered by electrochemical and ex-situ spectroscopic methods as well as by DFT. This study complements the existing knowledge about PANI redox activity in electrolytes of lower pH values. The results hint that PANI-ES has potential to be used as an electrode for Al-ion supercapacitors and hybrid batteries.

2. Experimental

2.1. Synthesis procedure of polyaniline emeraldine salt (PANI-ES)

PANI-ES was synthesized using the typical chemical polymerization of aniline in the presence of hydrohloric acid, with the $((NH_4)_2SO_4$ (Sigma Aldrich) as an oxidant, according to the procedure described in our recent paper [34]. Briefly, the volume (0.18 mL) of two times distilled aniline monomer was injected into 7 mL of 2 M HCl solution. Then, 0.45 g $(NH_4)_2SO_4$, previously dissolved in 2 mL of deionized water, was added in the drops to the solution and stirred magnetically at ambient temperature (25 °C). The obtained filtrate was washed (with 2 M HCl and deionized water followed by ethanol) and dried at 60 °C in the oven for 36 h.

2.2. Measurements and calculations

Electrochemical measurements by Cyclic Voltammetry and Chronopotentiometry were performed in the typical three-electrode cell using Gamry PCI4/300 Potenciostat/Galvanostat. The saturated calomel electrode (SCE) was served as the reference one, while the wide Platinum foil was the counter electrode. Galvanostatic measurements were performed in two-electrode configuration using Arbin charging/discharging battery device. The self-discharge measurements were performed for both full and half cells. Both systems were first charged to the desired potential of 0.7 V (for the full cell), 0.5 V vs. SCE (for the positive) and −0.4 V vs. SCE (for the negative electrode) and then left to undergo self-discharge over 9 h. The potential is kept for 1 h. For all electrochemical measurements, working electrode was prepared in the same way. The examined PANI-ES powder was mixed with the 5 wt% Nafion binder (Sigma Aldrich) in ethanol/water, to achieve the 95:5 ratio. A certain microliter volume of ethanol was added to obtain a desired viscosity of the slurry. After its homogenization, in an ultrasonic bath, the thin layer was deposited over the rectangular glassy carbon support and allowed to stand at room temperature until ethanol evaporated. Four different solutions were used as electrolytes: 1 M aqueous solutions of $Al(NO_3)_3$ and $AlCl_3$, 1 M HCl, as well as 1 M solution of Al $(NO_3)_3$ dissolved in 1 M HCl. The electrolytes are labeled as Al $(NO_3)_3$_H_2O, $AlCl_3$_H_2O, HCl and $Al(NO_3)_3$_HCl, respectively. The mass loading amounts to ~2.5 mg/cm^2.

The Infrared transmission spectra (FTIR) of the samples were recorded on an Avatar System 370 spectrometer (Thermo Nicolet), with 64 scans per sample and 2 cm^{-1} resolution, in the wavenumber range 4000–400 cm^{-1}. The technique of KBr pellet was used. The Raman spectra of samples were recorded at room temperature, using a DXR Raman microscope (Thermo Scientific) with a research optical microscope and a CCD detector. A HeNe gas laser with 0.5 mW of power (to prevent the carbonization of PANI-ES) and an excitation wavelength of 633 nm was used for all measurements. An exposure time of the sample was 30 s using 20 scan repetitions. The scattered light was analyzed by the spectrograph with 600 lines mm^{-1} and aperture of 50 μm slit.

Atomic force microscopy (AFM) measurements were performed ex-situ, using NT-MDT Ntegra Prima system at ambient conditions. Morphology of samples was measured in tapping AFM mode. At the same time, the phase lag of AFM cantilever was measured. The phase is very sensitive to abrupt changes of sample topography. Therefore, it can be used in order to resolve tiny features on the sample surface. The phase signal is proportional to the dissipation of the mechanical energy during the interaction between AFM tip and the sample surface [35]. Although there are several dissipation channels, the most dominant one in the case of polymers is the viscoelastic damping [36]. In the considered case, variations in the phase contrast imply changes in the viscoelastic properties of the sample surface.

In order to correlate actual electrochemical potential during charging/discharging process to the local electrical surface potential, we employed Kelvin probe force microscopy (KPFM). In KPFM, the

electrical surface potential is measured as contact potential difference (CPD) between AFM tip and the sample surface which is equal to their work function (WF) difference, $CPD=WF_{tip}-WF_{sample}$. Measurements were done by a standard two-pass technique with the amplitude modulation and Pt coated NSG01/Pt probes from NT-MDT. In the first pass, the sample topography was measured in tapping mode. In order to measure just electrostatic interaction and avoid van der Waals forces, in the second pass, the AFM probe was lifted by 30 nm and scanned along the topographic line measured in the first pass. Simultaneously, a sum of AC and variable DC voltage was applied between the sample and the AFM probe. Finally, the CPD between the AFM tip and sample surface is equal to the value of the DC voltage which cancels AFM probe oscillations at the frequency of the applied AC voltage. Therefore, by measuring the sample surface by the same AFM tip, KPFM measurements provide information about changes in the local Fermi level position (where WF_{sample} is equal to the difference between the vacuum and Fermi level).

For ex-situ FTIR, Raman and AFM observations, the PANI-ES powder deposited on supporting Pt foil using the procedure above (pristine) has been modified in the following ways: 1. By the only immersion in Al $(NO_3)_3\_H_2O$ (open circuit conditions); 2. By charging up to 0.2 V and 0.5 V vs. SCE in $Al(NO_3)_3\_H_2O$ solution; 3. By discharging from 0.5 to −0.2 V vs. SCE in $Al(NO_3)_3\_H_2O$ solution. Each step (1, 2, and 3) was finalized in the same way: the rinsing of the modified electrode by the double immersion in deionized water (for ~10 min and for 1 h) and its drying at 60 °C. Dried PANI samples were stripped in powdery form from the Pt support, and used for further analysis. Energy Dispersive Spectroscopy (EDS) is performed by means of the Scanning Electron Microscope (Phenom ProX). Before EDS measurements, the device was calibrated against Al standard. The PANI attached on the conductive support is previously polarized to the desired potentials of −0.4 V, 0.5 V and 1 V (vs. SCE), double-rinsed with water and stripped from the electrode to be subjected for the EDS analysis.

Quantum-chemical calculations were performed by using density functional theory implemented in Turbomole program package [37]. We employed M06–2X functional [38], which correctly describes non-covalent interactions. Geometry optimizations were performed with SVP basis set, whereas larger TZVP basis set was employed for single point energy calculations [39,40]. We employed a continuum solvation model (COSMO) [41,42] with dielectric constant of water (e = 78). This model accounts for implicit solvation in which polarizable environment mimics water molecules.

3. Results and dissusion

The characterization of PANI-ES in terms of thermal/vibrational/ electrical properties was thoroughly described in our previous paper [34]. Its electrochemical behavior in 1 M HCl was also examined [34]. Herein, the electrochemical study is extended to aqueous solutions containing trivalent Al-ions with higher pH, which opens novel

perspectives of using PANI-based materials for more suitable electrochemical storage systems.

3.1. Electrochemical study in aluminum-based electrolytes

Cyclic voltammograms of PANI-ES, measured in 1 M $Al(NO_3)_3$ aqueous solution ($Al(NO_3)_3\_H_2O$), at different scan rates in the narrow voltage range, −0.4 to +0.8 V vs. SCE, are shown in Fig. 1a. The redox pair, which is positioned at 0.16 V/-0.03 V vs. SCE at 20 mV s^{-1}, is associated with leucomeraldine base↔emeraldine salt (LB↔ES) transition (observed through the pale yellow↔green color), which is well known redox process of PANI in an acidic solution. The observed redox activity is enabled by the acidity of aluminum nitrate solution, arising from the binding of the protons in the polarized water molecules of aluminum aqueous complex ion to another water molecule of solvent, according to the equilibrium reaction (equation (1)).

$$[Al(H_2O)_6]^{3+} + H_2O \leftrightarrow [Al(H_2O)_5(OH)]^{2+} + [H-H_2O]^+ \quad 1$$
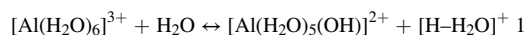
As a result, pH of the 1 M $Al(NO_3)_3$ was measured to be ~2. The difficulties in the understanding of the mechanism of PANI's redox behavior in the acidic solutions persist since its discovery [26–28,32,33, 43]. The main issue has been related to the participation of protons in the LB-ES redox process, which is recognized by a sharp anodic peak and smaller broader cathodic peak in the cyclic voltammogram. Let us express discrepancies in the explanation of the ion-exchange mechanism of PANI by virtue of electrochemical behavior in an acidic solution within the stable potential interval, where only the first redox process (LB-ES) appeared. Some studies [26,28,32,33] showed that the ES can be formed by the oxidation without the change in the number of hydrogen atoms attached to nitrogen atoms (the proton transfer is not involved). It happens through the formation of a radical cation at N-position which is accompanied by the anions insertion to maintain the electroneutrality [26,33]. On the other hand, the proton transfer was shown to be included in the mentioned redox process, alone or together with the anion exchange [26,27,29,30,43]. Co-insertion of water with the anions is also possible [30,43]. As suggested by MacDiarmid [26] and Barbero [27], the mechanism depends on the degree of protonation of reduced PANI (i.e. on the establishment of acid-base equilibrium between amino or imino groups and protons in the solution), which is primarily determined by the pH of electrolytic solution, but depends also on the nature of specific anion. The release of protons, upon anodic oxidation (as a result of charge compensation), occurs in the solutions of pH < 1 solutions (in Cl⁻-containing solutions this occurs at pH of 0.5) [27]. When pH ranges from 1 to 4, the oxidation reaction is independent of pH while anions, from the supporting electrolyte, compensate positive polaron charge induced by anodic polarization, thus participating in the formation of the double layer as well [26]. Still, Orata et al. [30] showed that the reduced form could be partially protonated, even at pH = 1, so that the proton expulsion during oxidation may occur. Actually, the
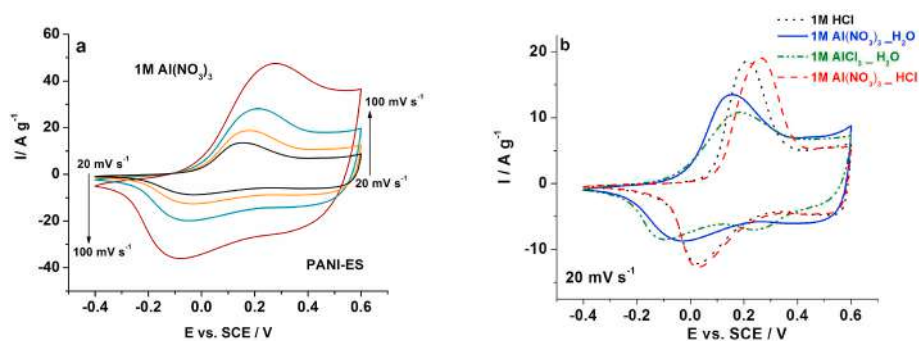

Fig. 1. a) CVs of PANI-ES measured in 1 M $Al(NO_3)_3\_H_2O$ at different scan rates; b) the comparison of CVs measured in 1 M $Al(NO_3)_3\_H_2O$, 1 M $Al(NO_3)_3\_HCl$ and 1 M HCl at a scan rate of 20 mV s^{-1}.

relative proportion of protons (their expulsion) and anions (their insertion) during the oxidation depends on the degree of protonation of reduced form, which is higher at lower pH. When the reduced form is fully protonated only protons are released during oxidation, while for the completely deprotonated reduced form only anions are inserted [27].

Based on these foundations, we can conclude that the proton doping/dedoping process dominates the redox process of PANI-ES in 1 M HCl (Fig. 1b). Besides, it should be kept in mind that H_3O^+ ions are electrostatically attracted by PANI surface upon negative polarization and can participate in the formation of electrical double layer (EDL). In Al(NO$_3$)$_3$_H$_2$O solution with a pH of 2, the process of protons expulsion during oxidation (LB→ES) is reduced while the transference number for larger highly charged Al complex is low. That is why the anion transport is dominant process for the charge compensation. Interestingly, the similar surface area under CV curve of PANI in 1 M Al(NO$_3$)$_3$_H$_2$O, with the corresponding one in 1 M HCl, indicates that the change of the redox mechanism of PANI does not decrease its capacitance. Lower conductivity of Al(NO$_3$)$_3$ than HCl (as demonstrated by the larger frequency intercepts in impedance diagrams shown in Fig. S1) results in CVs broadening, but not in the capacitance decrease of the polymer. This may be explained by the fact that the doping/dedoping of anions takes over the role of compensating charge (concentration of anions is not decreased as the proton concentration decreased), while Al^{3+} ions most likely play the role of protons, since their concentration in this solution is significantly higher than that of protons. Al^{3+} ions can also be involved in the formation of EDL upon negative potentiostatic regime. In conclusion, the charge storage ability of PANI in 1 M Al(NO$_3$)$_3$ solution has been preserved as well, in spite of both lower acidity and lower ionic conductivity of this solution compared to 1 M HCl.

The potentials of redox peaks in Al(NO$_3$)$_3$_H$_2$O are shifted towards lower values with respect to those in HCl, while the peak currents are slightly lower. The potential shifting is influenced by the solution's pH [26,44], which fits into the reported potential-pH dependence. When the 1 M HCl was used as a solvent for aluminum nitrate salt (1 M Al(NO$_3$)$_3$_HCl), the redox peaks move back towards more positive potentials (0.26/0.03 V vs. SCE in Al(NO$_3$)$_3$_HCl against 0.16/-0.03 V vs. SCE in Al(NO$_3$)$_3$_H$_2$O), due to the abatement of pH. Actually, if we add Al-nitrate in 1 M HCl, the position of cathode peak remains the same as in the pure 1 M HCl, while the anodic peak shifts for 30 mV towards higher potentials. One say that the adsorption of anions, upon positive anodic sweep of PANI in Al(NO$_3$)$_3$_HCl (the AlCl$_3$ is essentially formed), required higher energy activation than in HCl. It can be attributed to inductive effect of highly charged Al cation, which can make the bond between polymer and anion weaker. It results in the decrease of the site adsorption energy and the increase of the redox potential.

The redox behavior of PANI in the solution of higher pH depends on the type of anion, as shown by additional measurement of CVs in an aqueous solution of AlCl$_3$ (AlCl$_3$_H$_2$O). It can be seen in Fig. 1b that CVs recorded under common conditions of close pH values, in the electrolytes with a common cation (Al^{3+} ion) and different anions (Cl$^-$ and NO$_3^-$) are somewhat different. A little higher peak potential separation and the noticeably lower anodic response were observed when the AlCl$_3$_H$_2$O solution was used (note that in nitrate solution the cathodic peak current remains identical). One can conclude that the process of NO$_3^-$ doping (to compensate positive charge of chain induced by negative polarization) is faster than the process of Cl$^-$ ions doping. It can be attributed to higher ionic conductivity of Al(NO$_3$)$_3$_H$_2$O solution (Fig. S1) and easier NO$_3^-$ than Cl$^-$ desolvation due to the difference in hydrophobicity [45].

A comparison of galvanostatic curves of PANI recorded in various electrolytic solutions (Fig. 2a) enables to perceive favorable effect of Al^{3+} ions on the capacitance of PANI. Specific capacitance in Al(NO$_3$)$_3$_H$_2$O, Al(NO$_3$)$_3$_HCl and 1 M HCl, measured at 1 A g^{-1}, amounts to ~318/317 F g^{-1}, ~311/310 F g^{-1} and ~291/301 F g^{-1}, respectively. Additionally, Al(NO$_3$)$_3$_H$_2$O is the least corrosive among these

electrolytes due to the lowest concentration of released protons. Therefore, it makes Al(NO$_3$)$_3$_H$_2$O the best candidate for PANI-based aqueous supercapacitor.

The capacitance, measured in Al(NO$_3$)$_3$_H$_2$O, is slightly higher than the one in AlCl$_3$_H$_2$O. Also, Al(NO$_3$)$_3$ is more suitable than AlCl$_3$ for practical use, since dried AlCl$_3$ reacts easily with the moisture releasing gaseous HCl. Furthermore, Fig. 2b illustrates the low sensitivity of aluminum-storage capacitance on both charging and discharging current density when it changes for one order of magnitude. Explicitly, the values measured in Al-nitrate aqueous solution amount to 303, 293, 276 and 265 F g^{-1} (charging) and 302, 293, 278 and 254 (discharging) at 2, 3, 5 and 10 A g^{-1}, respectively (Fig. 2c).

The main drawback of PANI-based supercapacitors using an aqueous electrolytic solution is the low operating voltage. As already observed elsewhere [34,46], and confirmed in Fig. 3a–c, if in HCl one expands working voltage of cyclic polarization of PANI over 0.6–0.7 V vs. SCE, its over-oxidation occurs, resulting in the irreversible formation of electrochemically inactive structures and consequently capacitance decrease. Whether the same PANI's redox behavior holds in the Al-salt solution? In order to answer this question, ten successive CVs of PANI-ES in Al(NO$_3$)$_3$_H$_2$O, in an extended operating voltage, were registered (Fig. 3a). The corresponding cyclic behavior of this material in the Al(NO$_3$)$_3$_HCl, is also shown in Fig. 3b. One can perceive common redox processes characteristic of PANI. The first redox pair, corresponding to LB ↔ ES transition, is positioned at ~0.16/-0.01 V vs. SCE in Al(NO$_3$)$_3$_H$_2$O and 0.26/0.02 V vs. SCE in Al(NO$_3$)$_3$_HCl, while the third redox pair, corresponding to ES ↔ pernigraniline (PN) transition, is placed at 0.69/0.52 V vs. SCE in Al(NO$_3$)$_3$_H$_2$O and 0.85/0.67 V vs. SCE in Al(NO$_3$)$_3$_HCl (the potentials refer to the first cycle). By comparing all CVs, the current changes during cycling are more pronounced for HCl-based solution. The activity of the PN formation in an Al(NO$_3$)$_3$ solution, relative to the formation of emeraldine phase upon the first redox transition, is suppressed. On the other hand, when the electrolyte includes HCl (with or without aluminum salts), the anodic current responses of I and III processes are quite similar (Fig. 3b,d). These differences are the result of the higher fraction of protons in HCl than in Al(NO$_3$)$_3$, since it is known that protons participate in the third redox process [47]. Specifically, the ES-PN redox transition is more pronounced in concentrated acids and suffers greater capacitance abatement throughout cycling.

In summary, the processes including both over-oxidation of polyaniline and formation of electrochemically inactive structures, observed during cycling of PANI-ES electrode in Al-based aqueous nitrate solution show slower kinetics than in HCl-based aqueous solution. Consequently, the slower capacity decrease was observed throughout consecutive cycling in an extended voltage interval (Fig. 3c).

The irreversible capacity loss of PANI-ES, in the first cycle, amounts to ~86 F g^{-1} in 1 M HCl and 72 F g^{-1} in Al(NO$_3$)$_3$_HCl, while this value is noticeably lower (~39 F g^{-1}) in Al(NO$_3$)$_3$_H$_2$O. Also, the capacity retention of PANI-ES, after 60 repeated cycles in Al(NO$_3$)$_3$_H$_2$O, with respect to the first cycle, was found to be 61% for anodic scan and 68% for cathodic scan, which is higher than the corresponding values obtained in HCl (which amount to 47% and 59%) and in Al(NO$_3$)$_3$_HCl amounting to 32% and 48% (see inset in Fig. 3c). Therefore, the use of the Al-nitrate solution as an electrolyte for PANI electrode offers greater advantage by enabling higher operating voltage.

The middle redox pair (denoted as II) appears during PANI cycling in Al(NO$_3$)$_3$_H$_2$O, as well as in a strong acidic solution. Analogously with the pure acidic solution [34], this peak is generally attributed to the formation of both benzoquinone degradation products and cross-linked polyaniline chains formed by a direct reaction between their parts. Since the appearance of this middle peak is correlated to the third redox process which is sensitive to the pH solution [47], one may expect different cyclic behavior of this peak in Al(NO$_3$)$_3$_H$_2$O and HCl-based solutions. In the strong acidic solution, the gradual decrease of the first and third redox pair was followed by the gradual increase of the
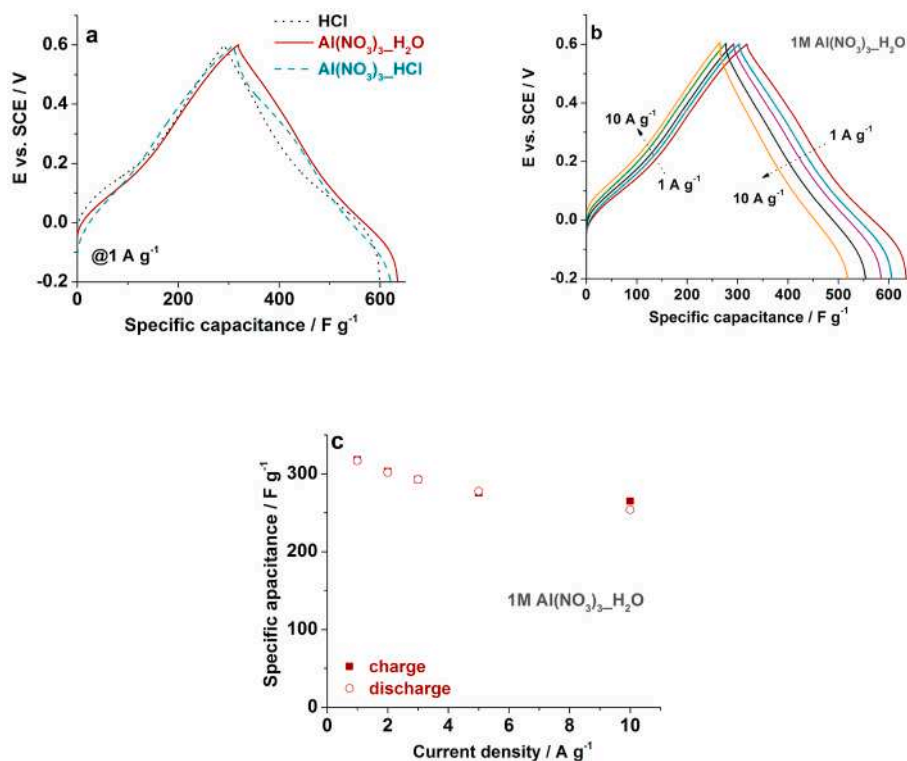
Fig. 2. a) CPs curves of PANI-ES in 1 M $Al(NO_3)_3\_H_2O$, 1 M $Al(NO_3)_3\_HCl$ and 1 M HCl, at a common current density. b) CPs curves of PANI-ES measured in 1 M Al $(NO_3)_3\_H_2O$ at different current densities and c) corresponding capacitance values.
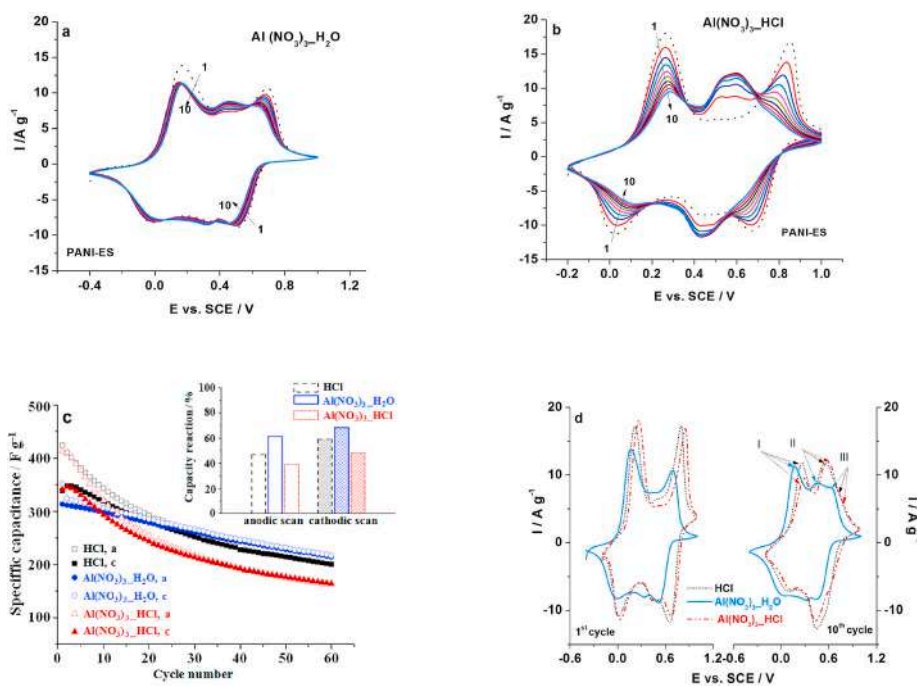

Fig. 3. a,b) Cyclovoltammetric behavior of PANI-ES in $Al(NO_3)_3$-based solution during 10 cycles; c) The capacitance vs. scan rate dependence obtained during 60 cycles in $Al(NO_3)_3\_H_2O$, $Al(NO_3)_3\_HCl$ and HCl; inset in c shows the capacity retention of PANI-ES in the corresponding electrolytes relative to the initial capacitance; d) The first (left) and tenth (right) CVs of PANI-ES in each of investigated electrolyte. Scan rate was 20 mV s^{-1}.

middle pair, upon initial cycling until it became stabilized. These changes are less pronounced in the case of $Al(NO_3)_3\_H_2O$. After 10 cycles (Fig. 3d), the peaks corresponding to the middle redox process, are noticeable lower in $Al(NO_3)_3\_H_2O$ than in $Al(NO_3)_3\_HCl$ and HCl, while in $Al(NO)_3\_H_2O$ solution the peak of the third redox process keeps better

its height. This could be attributed to the different proton concentration in these electrolytes. As mentioned, the protons are involved in PANI's redox reactions II and III. The lower concentration of protons in Al $(NO_3)_3$ solution could be the reason of slower kinetics of these processes (causing also slowing down of PANI's degradation during cycling).

However, the question arises whether the Al^{3+} ions can participate in these reactions and contribute to the slower degradation of PANI?

We have noticed, when the certain amount of 1 M HCl was gradually added to the Al $(NO_3)_3$ solution (after 60 cycles of charging/discharging), the current response (61st-63rd cycle) got higher (Fig. 4). Interestingly, if Al-nitrate solution is completely replaced by 1 M HCl solution the peak current of PANI-ES electrode even increased (see pink dot-dashed 64th CV in Fig. 4). In this way, the proton concentration was increased in the system and the redox reaction II became faster.

However, this (64th) CV in Fig. 4, is significantly higher than those obtained with the fresh PANI electrode upon 60 cycles in 1 M HCl or Al $(NO_3)_3$_HCl (dotted and dashed curves in Fig. 4). It reveals the active role of Al^{3+} ions in the third redox reaction occurring at higher potentials, as shown by EDS which confirms the presence of Al on the PANI surface upon electrochemical reactions. One can still notice the Al content decreases in the following order −0.4 V, 0.5 V and 1 V vs. SCE (Figs. S3–S5). It is in accordance with our assumption about the expulsion of Al ions during oxidation, which, together with the anions adsorption, occurs to balance the polarization-induced charge.

3.2. High-rate performance and self-discharge of Al-based supercapacitor

PANI-ES sample was used to make a symmetric two-electrode capacitor using Al$(NO_3)_3$_H$_2$O as an electrolyte. The constructed capacitor showed a high-rate performance (Fig. 5) and, in the voltage range 0–0.8 V, delivered capacitances of 290 F g^{-1}, 287 F g^{-1} and 269 F g^{-1} at charging/discharging current densities 1, 2 and 10 A g^{-1}, respectively. Very high value was measured at 10 A g^{-1}, under which the stability of capacitor was tested. After 1000 charging/discharging cycles the capacitance kept 90% of its initial value. By the way, in lower voltage range 0–0.6 V, no capacity fade was observed. The measured capacitance is higher than that obtained for PANI-derived carbon capacitor reported in our previous paper [48].

The self-discharge profile of two-electrode supercapacitor cell, after its charging at 0.7 V in an ambient atmosphere over 1 h, is shown in Fig. 5c (solid grey line). One can see that the voltage decreases rapidly in the first 3 h (up to the potential of 0.43 V) and moderately during the next 6 h, thus reaching 0.25 V. To evaluate the contribution of individual cathodic and anodic processes to the self-discharge, the voltage profile is also measured for individual electrodes in a three-electrode arrangement, under the air atmosphere (dashed purple and orange curve). One can notice that the self-discharge is higher at negative than positive
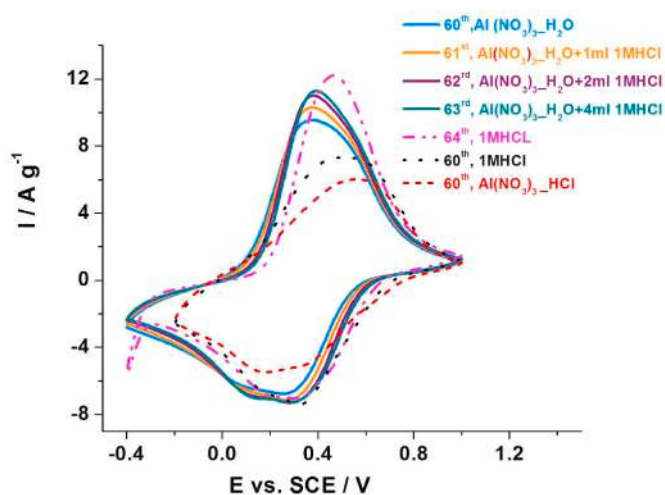

Fig. 4. CVs of the fresh PANI-ES electrode, corresponding to 60th cycle, measured in Al$(NO_3)_3$_H$_2$O, Al$(NO_3)_3$_HCl and HCl as well as CVs of the PANI-ES electrode, previously cycled in Al$(NO_3)_3$_H$_2$O during 60 cycles, after adding of certain amounts of HCl in Al$(NO_3)_3$_H$_2$O and its replacement with 1 M HCl.

electrode. To see whether the oxygen reduction reaction (ORR) influences the discharge rate of negative electrode, its self-discharge profile was also measured when the electrolyte was purged by the nitrogen flow. As a result, the self-discharge was significantly reduced (dotted green line), thus indicating the influence of the parasitic ORR. Namely, in an aerated electrolyte, the adsorbed oxygen on the PANI surface imposes a mixed potential of the negative electrode. After oxygen elimination, the electrode maintains its own potential during the discharge experiment.

Also, the slower self-discharge rate of the full cell was observed when its electrolyte was purged by the nitrogen (solid green line). In this case, after 9 h the voltage dropped to 0.4 V, thus showing the charge loss of 39% in comparison to the charge loss of 69% in the air atmosphere. It is worth noting that the capacity of PANI-ES electrode does not depend on the presence of the oxygen in the electrolyte (the same CV was measured at 20 mV s^{-1} with and without N_2). Actually, the charge of the oxidized PANI electrode (which is polarized from −0.4 to 0.6 V vs. SCE at a certain scan rate), during the subsequent cathodic reaction (from 0.6 V to −0.4 V), is not consumed by the oxygen, but exclusively by the emeraldine salt reduction. This can be attributed to the faster ES-LB redox reaction under cathodic regime.

Last but not least, if someone applies two Conway models (Eqs. S1 and S2) [49] on the measured self-discharged profile of the capacitor cell, it can be expected, in the examined supercapacitor, that the rate-limiting step of self-discharge reactions is the diffusion removal of electrolytes ions from electrical double layer (producing linear V- $t^{1/2}$ dependence) rather than the ohmic leakage over the resistance (producing non-linear lnV-t dependence), as can be seen in Figs. S6a,b,d,e. The diffusion-limited charge redistribution is assumed to be the responsible for this behavior. However, if we look at the plot of V = f (logt) (Figs. S6c and f, equation S(3)), we can notice that the curve (over 9 h) also follows the Conway model for the activation-controlled process [49]. Still, if the open-circuit self-discharge measurement is extended to 24 h, the influence of the charge distribution is clearly evidenced by the change of the curve linearity after 9 h (the presence of two linear regions in the graph of V = logt, as shown in Fig. S7) [50].

Furthermore, the constructed Al-ion supercapacitor shows better gravimetric capacitance than other reported aqueous asymmetric capacitors such as AC//Al$_2$(SO$_4$)$_3$//PPy@MoO$_3$ (~78 F g^{-1} at 2 A g^{-1}) [51], SCNT/W$_{18}$O$_{49}$NW//AlCl$_3$//SCNTPANI (~30 F g^{-1} at 6 mA cm^{-2}) [52], but still inferior to asymmetric MnO$_2$//AlCl$_3$//TiO$_2$ capacitor (~544 F g^{-1} at 10 mV s^{-1}) [19]. Table 1 provides the literature survey of the electrochemical behavior of both intercalation [9,11,13–18,53–55] and capacitive electrodes in Al-based aqueous solutions [7,19,51,52, 56]. Among different Al-intercalation electrodes, the best capacity measured in the half-cell configuration (based on the Al^{3+} and H^+ intercalation) was achieved for TiO$_2$ material in AlCl$_3$ solution, while the PANI-ES used in our study ranks among the best capacitive electrodes available. By the way, the capacity of the aqueous full-cell battery is still inferior when compared to the state of-the art Al-ion batteries [20–23], which are based on the intercalation/deintercalation of Al ions and/or aluminum chloride coordination [Al$_a$Cl$_b$] anions.

3.3. On the redox mechanism of polyaniline in an aluminum-based aqueous solution

To address the role of Al^{3+} ions in the process of PANI-ES oxidation/reduction, either charged or discharged in Al$(NO_3)_3$_H$_2$O, was examined by means of ex-situ methods such as FTIR, RAMAN and AFM. Besides, DFT study has been carried out to supplement the knowledge on the underlying redox processes.

3.3.1. Spectroscopic study

FTIR spectra of the pristine powder (PANI-ES) and its modifications described in experimental section (the short-term rinsing) are shown in Fig. 6a in a comparative way. For the sake of the charge balancing, the
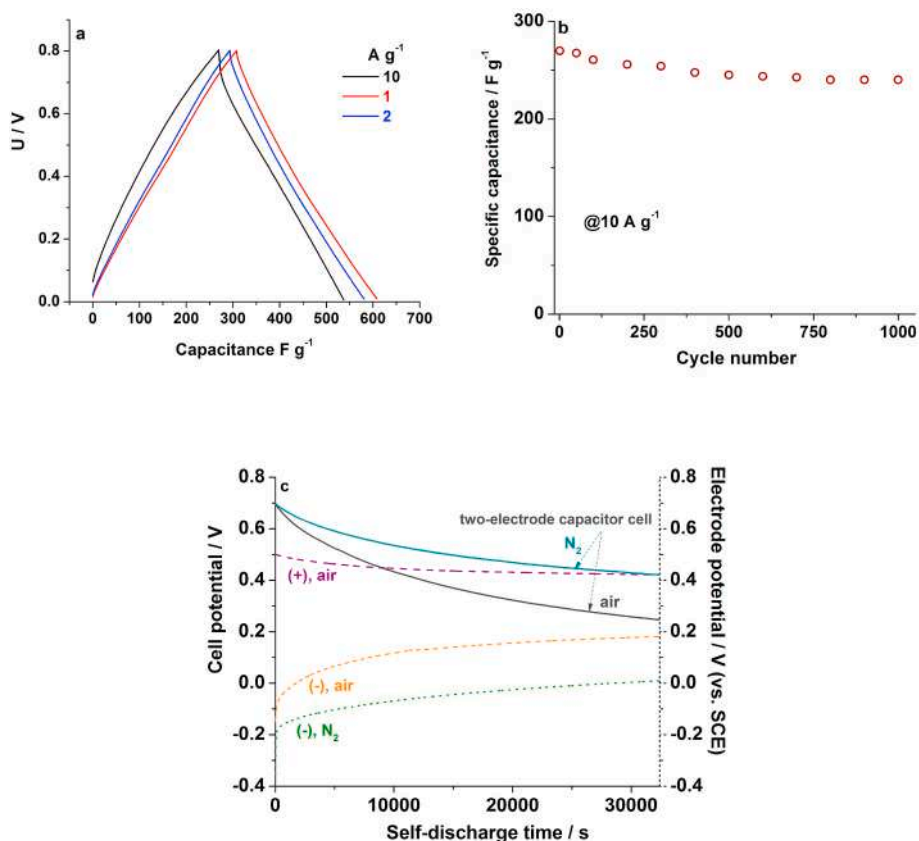
Fig. 5. a) Galvanostatic charge/discharge profile at different current rates, b) the cyclic performance at a current density of 10 A g^{-1} in the 0–0.8 V voltage range and c) self-discharge profile of two-electrode PANI-ES capacitor in Al(NO$_3$)$_3$_H$_2$O. The solid line at Fig. 5c refers to the voltage curve of the full cell, while the dashed lines belong to the profiles of individual electrodes, respectively.

electrode which is polarized at +0.5 V vs. SCE (charged) became doped with nitrate ions, while dedoping of anions is expected to occur when the electrode is polarized at −0.2 V vs. SCE (in the discharged state). Besides, positive/negative electrolyte ions probably contribute to the EDL formation during cathodic/anodic polarization. At + 0.5 V vs. SCE, the polyaniline is in the emeraldine salt form, while the leucoemeraldine base [47,57] is formed at −0.2 V vs. SCE, which is experimentally confirmed by the yellowish-green change of the electrode powder during oxidation/reduction. The yellowish color of the leucoemeraldine base preserves itself very shortly after the electrode removal from the electrolyte. The rinsing and drying of such electrode in water resulted in change of its yellow color to the dark one. It can be attributed to the chemical oxidation of leucoemeraldine to emeraldine base, as confirmed by shown FTIR and Raman spectra (see below).

Let us first consider spectral changes of the PANI-ES sample modified by mere immersion in Al-nitrate solution (labeled by OCP). The immersion of the PANI-ES electrode in Al(NO$_3$)$_3$ caused some changes of PANI vibrational modes, visible as the shift of Q and B bands' positions (1559 cm^{-1}→ 1572 cm^{-1} and 1475 → 1488 cm^{-1}, respectively) and the slight increase of Q/B ratio bands (the intensity of these bands became more equal). This indicates a certain degree of PANI's oxidation under open circuit conditions, evidenced by the oxidation of benzenoid rings to more quinonoid distortion structure. The sharp band at 1381 cm^{-1}, followed by the shoulder at 1375 cm^{-1} (which is more visible under magnification), can be seen additionally in the spectrum of the PANI-ES_OCP with respect to the spectrum of the pristine PANI-ES powder. The sharp band belongs to surface-adsorbed nitrate ions, which are not removed from the electrode by the short-term electrode rinsing. The accompanied band (observed as a shoulder of nitrate-assigned band) can be attributed to the appearance of the small amount of imine structure in PANI-ES_OCP sample [58,59]. This could be the consequence of the

slight oxidation of amine to imine units (i.e. the transition of polaron to the bipolaron structure) upon immersion in the aqueous nitrate solution. The similar changes (the appearance of 1375 cm^{-1} band and the equalization of Q/B ratio), were observed upon aging of partially protonated emeraldine salt, where the color of powder was changed from green to black [58].

The nitrates' doping into PANI under its simple immersion into electrolyte provides the positive value of OCP amounting to ~0.3 V vs. SCE. This process is intensified during oxidation up to 0.5 V vs. SCE for the sake of compensating induced positive charge. Also, there is a possibility for water molecules to co-intercalate, being involved in the oxidation process. On the other hand, nitrates' dedoping occurs upon cathodic polarization. Whether the nitrates are doped/undoped alone or in the form of complex is questionable. Besides, we assume that the process of Al^{3+} exchange during the redox switching of PANI-ES happens additionally to compensate the positive charge, but to a lesser extent than the doping/dedoping of nitrate ions. Doping of Al^{3+} ions upon cathodic polarization can maintain a certain level of electrical conductivity of PANI in the reduction process required for a high reversible storage capacitance (pseudoprotonation). This process is more dominant with respect to the protonation due to significantly higher concentration of Al^{3+} ions than protons.

The blue shifting of Q and B bands is even more pronounced in the case of the discharged electrode, where the corresponding bands are positioned at ~1580 cm^{-1} and ~1496 cm^{-1}. The position of these bands in the discharged state is actually indication of the emeraldine base formation [60]. The appearance of 1381 cm^{-1} and 1375 cm^{-1} bands, in the discharged sample, could be the consequence of the presence of doped nitrate ions. However, the characteristic band of emeraldine base, originating from C–N stretching vibration in the neighborhood of a quinonoid ring (assigned at 1379 cm^{-1} in Ref. [60]) can contribute to

Table 1
Literature survey of electrode materials in aqueous Al-based electrolytes.

Electrode material	The initial specific discharge capacity (mAh g^{-1} or F/g)	The capacity fade	ΔV (ref.pot.) /redox behavior
Al-ion intercalation electrodes (C$_{spec}$ in mAh g^{-1})			
Anatase TiO$_2$ nanoleaves, 1 M Al(NO$_3$)$_3$ [9]	~278 mAh g^{-1} at 0.05 A g^{-1} ~141 mAh g^{-1} at 2 A g^{-1} for the half-cell	~8% over 300 cycles at 0.05A g^{-1}	−1.5 to - 0.3 V, red. pair: 1.27/-0.82 V (SCE) @1 mV s^{-1}
Anatase TiO$_2$ nanotube arrays, 1 M AlCl$_3$ [11]	~50 mA h g^{-1} at 4 mA cm^{-2}, for the half-cell	No capacity fade (50% increase after 13 cycles at 4 mA cm^{-2})	- 1.5 to −0.3 V (SCE), red. pair: −1.26/-0.84 V @ 20 mV s^{-1}
Anatase mesoporous TiO$_2$ nanospheres 1 M AlCl$_3$ [14]	~183 mA h g^{-1} at ~ 0.05 A g^{-1} ~108 mA h g^{-1} at ~ 2 A g^{-1}, for the half-cell	~5% after 25 cycles at various current rates	−1.5 to −0.4 V, red.pair.: 1.25/-0.87 V (Ag/AgCl) @10 mV s^{-1}
TiO$_2$-graphene nanoparticles 0.25–1 M AlCl$_3$ [15]	~50 mAh g^{-1} at 6.25 A g^{-1} for the half-cell in 0.25 M AlCl$_3$ ~33 mAh g^{-1} at 6.25 A g^{-1} for the half-cell in 1 M AlCl$_3$	~30% over 120 cycles at 6.25 A g^{-1} in 0.25 M AlCl$_3$	−1.5 to – 0.4 red. pair: 1.27/-0.99 V (Ag/AgCl) @ 5 mVs^{-1}
MoO$_3$ 1 M AlCl$_3$ [16]	~680 mAh g^{-1} at 2.5 A g^{-1} or 5 mA cm^{-2} for the half-cell	75% after 20 and 300 cycles (i.e. 170 mA h g^{-1})	- 1 to 0.6 V, red. pair −0.86/-0.62 V, −0.61/-0.38 V, −0.4/0.11 V (Ag/AgCl) @ 2.5 mVs^{-1}
MoO$_3$-graphene [17], 1 M AlCl$_3$	590 mA h g^{-1} at 2.5 A g^{-1} for the half-cell 236 mA h g^{-1} at 2.5 A g^{-1} for the half-cell (DG:H$_2$O = 50:50), DG is dyglime	87% over 100 cycles (DG = 0) 32% over 100 cycles (DG/H$_2$O = 50/50)	−1 V–0.6 V red. pair: 0.4/-0.18 V, −0.66/-0.32 V, −0.66/-0.57 V (Ag/AgCl) @ 2.5 mVs^{-1}
TiO$_2$ nanotube arrays 1 M AlCl$_3$ [18]	75 mAh g^{-1} at 4 mA cm^{-2} (maximum discharge capacity)	/	−1.4 to −0.4 V, red. Pair: ~ −1.2/ ~ −1 V (Ag/AgCl), @10 mV s^{-1}
K$_{0.02}$Cu[Fe (CN)$_6$]$_{0.7}$ · 3.7H$_2$O (CuFe-PBA), 1 M (Al (NO$_3$)$_3^{54}$	50 mAh g^{-1} at 0.05 A g^{-1} for 3-electrode AC/Al$_{0.2}$CuFePBA full cell 37 mA hg^{-1} at 0.05 A g^{-1} for 2-electrode AC/Al$_{0.2}$CuFePBA full cell	~10% over 1000 cycles (2-electrode full cell) at 0.25 A g^{-1}	0.2–0.7 V for 3-electrode cell. red. pair ~0.38/0.39 V and ~0.53/0.57 V (Ag/AgCl), @1 mV s^{-1} 0–1 V for two -electrode full cell
KCu[Fe(CN)$_6$] xH$_2$O (CuHCF), 0.5 M Al$_2$(SO$_4$)$_3$ [55]	~63 mA h g^{-1} at 0.05 A g^{-1} ~47 mA hg^{-1} at 0.4 A g^{-1} for the half-cell	~45% over 1000 cycles at 0.4 A g^{-1}	0.2–1.2 V, red.pair: 0.53/0.79 V and 0.8/0.9 V(SCE) @ 1 mV s^{-1}
V$_2$O$_5$ xerogel 1 M AlCl$_3$ [10]	120 mAh g^{-1} at 0.06 A g^{-1} ~20 mAh g^{-1} 0.2 A g^{-1}	~40% at 0.06 A g^{-1}, ~25% at 2 A g^{-1}, over 12–13 cycles	−0.6 to 0.5 V, red. pair: 0.3/-0.03 V (Hg/Hg$_2$SO$_4$) @10 mV s^{-1}
WO$_3$ 1 M AlCl$_3$ [53]	140 mAh g^{-1} at 2.5 A g^{-1} for the half-cell	50% increase over 100 cycles at 2.5 A g^{-1}	−0.9 to 0.5 V, red. pair: 0.7/-0.3 V, −0.4/-0.01, (Ag/AgCl) @ 2.5 mVs^{-1}
TiO$_2$ and CuHCF, 1 M AlCl$_3$ [13]	14.5 mA h g^{-1} at 0.33 A g^{-1} (20C) for the TiO$_2$/CuHCF full cell (limited by TiO$_2$) 50 mA h g^{-1} at 0.1 A g^{-1} for the TiO$_2$/CuHCF full cell (limited by CuHCF) 10.5 mA hg^{-1} at 0.33 A g^{-1} (20C) for the balanced TiO$_2$/CuHCF full cell	7% after 1000 cycles for TiO$_2$-limited cell. Stable over 1000 cycles for CuHCF-limited cell. 5% over 1814 cycles for the balanced cell	−1.5 to 0 V, red. pair: 1.31/-0.85 V for TiO$_2$ (SCE), @ 10 mV s^{-1} 0 V to 1.4 V, red. pair:0.6/1.05 V for CuHCF (SCE) @ 20 mVs^{-1}

Table 1 (*continued*)

Electrode material	The initial specific discharge capacity (mAh g^{-1} or F/g)	The capacity fade	ΔV (ref.pot.) /redox behavior
Al-ion capacitive electrodes (C$_{spec}$ in F/g or F/cm^2)			
2D Ti$_3$C$_2$Tx layers, 1 M Al (NO$_3$)$_3$ or Al$_2$(SO$_4$)$_3$ [7]	~30 F g^{-1} @ 20 mV s^{-1} for Al(NO$_3$)$_3$ ~25 F g^{-1} @ 20 mV s^{-1} for Al$_2$(SO$_4$)$_3$	/	−0.8 to −0.15 V for the half-cell in Al (NO$_3$)$_3$ or −0.95 to 0.15 V in Al$_2$(SO$_4$)$_3$, (Ag/AgCl), EDLC.
Al–TiO$_2$ nanotubes, 1 M AlCl$_3$ [19]	~3.5 mF cm^{-2} at 10 mV s^{-1} for the half-cell ~544 F g^{-1} at 10 mV s^{-1} for MnO$_2$/ Al–TiO$_2$ full cell (based on the mass of MnO$_2$)	~2.5% over 200 cycles at 100 mV s^{-1}	- 0.8 to −0.4 V for the half-cell, (Ag/AgCl) EDLC 0–0.8 V for the full cell
PPY@MoO$_3$ nanotubes 0.5 M Al$_2$(SO$_4$)$_3$ [51]	693 F g^{-1} at 1 A g^{-1} for the half cell 78 F g^{-1} at 2 A g^{-1} for the AC// PPy@MoO$_3$ full cell	~7% over 1800 cycles at 2 A g^{-1} for the full Al-ion capacitor	−0.4 to 0.5 V for the half-cell, intercal. pseudocap. 0–1.5 V for the full cell.
SCNT/ W$_{18}$O$_{49}$NW 1 M AlCl$_3$ [52]	~1.1 F cm^2 or ~216 F g^{-1} at 2 mA cm^{-2} or 453 F cm^{-3} for the half-cell ~0.8 F cm^2 or ~ 30 F g^{-1} or ~52 F cm^{-3} at 6 mA cm^{-2} and ~21 F g^{-1} at 26 mA cm^{-2} for the balanced asymmetric full cell SCNT/W$_{18}$O$_{49}$NW// SCNTPANI	0.7% at 100 mVs^{-1} and 5% a 5 mVs^{-1} for the half-cell 9.9% over 500 cycles at 100 mV s^{-1}	−0.7 to 0.6 V (Ag/ AgCl), pseudocap 0–1.8 V for the balanced full cell
2D h-MoO$_3$ Al$_2$(SO$_4$)$_3$ [56]	300 F cm^3 at 5 mV s^{-1}	/	−0.3 to 0.4 V (Ag/ AgCl), EDLC
PANI_ES 1 M Al (NO$_3$)$_3^{here}$	317 F g^{-1} at 1 A g^{-1} for the half-cell 290 F g^{-1} at 1 A g^{-1} and 269 F g^{-1} at 10 A g^{-1}, for the PANI// PANI symmetrical full cell.	10% over 1000 cycles (the stable in the interval 0–0.6 V)	−0.4 V–0.6 V, (SCE), pseudocap., for the half-cell 0–0.8 V for the Al-ion capacitor.

these modes as well.

Interestingly, when the polarized electrodes (both charged and discharged) were rinsed longer (by keeping them in water for a longer period of 1 h) the surface-adsorbed nitrates became removed, as evidenced by disappearance of the sharp, nitrate-belonging band (Fig. S2). However, the band at 1375 cm^{-1}, as the consequence of conformation changes of polymer chain, still remains in the FTIR spectrum of samples. Maintenance of the new conformation change, upon removal of nitrates, indicates the role of aluminum-nitrate as a secondary dopant [61,62]. Since the nitrate ions are present in the polymer chains upon charging/discharging, it is more realistic that the structural changes of polyaniline upon charging/discharging would be observed in the presence of nitrates, as performed further by Raman spectroscopy.

Raman spectra of the pristine powder and polarized PANI-ES samples are shown in Fig. 6b. The assignment of all Raman modes of pristine PANI-ES powder, based on the literature [63–66], is summarized in our previous paper [34]. After immersing the electrode into Al(NO$_3$)$_3$ solution and rinsing (labeled by ocp), some changes of PANI surface can be perceived (Fig. 7). Namely, one can see a high frequency widespread of the C~N$^+$ band (at ~ 1336 cm^{-1}) due to the appearance of one additional mode. This change is intensified upon further polarization at positive potentials, due to the formation of radical cation at N-atom and consequent insertion of nitrates ions. On the other hand, the steadiness of 718 and 585 cm^{-1} bands, which correspond to the amine deformation of the ES bipolaronic form [64], can be noticed upon the oxidation process (although the 585 cm^{-1} band can also be attributed to the
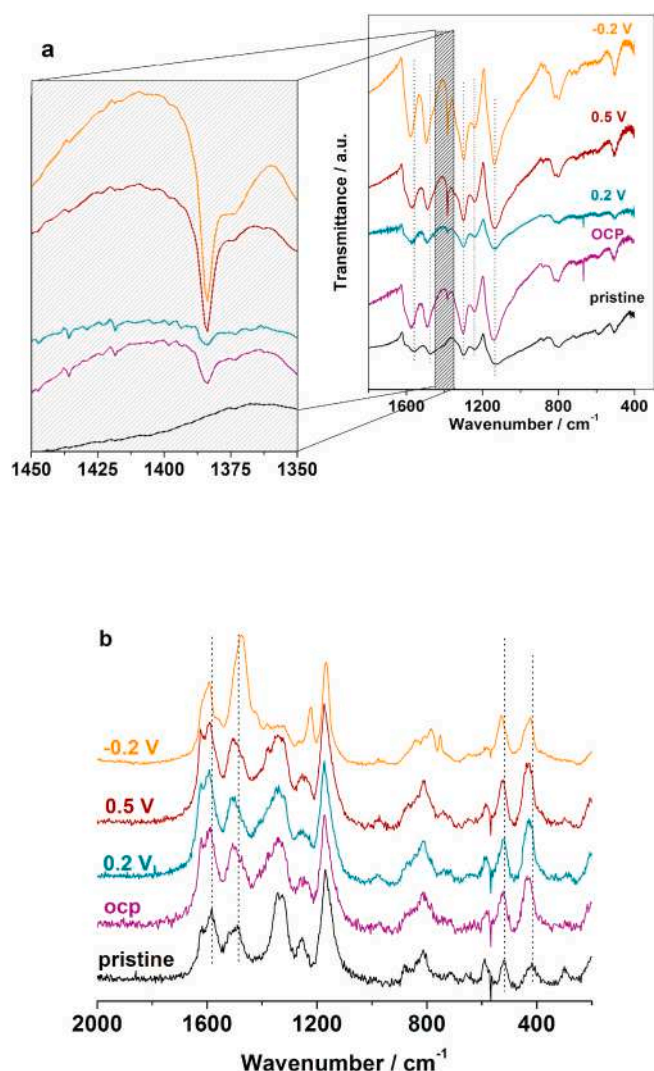
Fig. 6. FTIR (a) and Raman (b) spectra of the PANI-ES electrode polarized at different potentials in Al(NO$_3$)$_3$_H$_2$O.

phenoxazine-type units [67]), while the extra small band (at ~740 cm^{-1}) is detected only in the spectra of the modified samples (OCP, 0.2 V and 0.5 V). It seems that the anions' doping occurs on protonated imine sites rather than on amine sites. Furthermore, bands at ~1584 cm^{-1} (related to the C═C stretching vibrations of the quinonoid ring and correspond to the protonation of polymer and the semiquinonoid-ring formation), ~1490 cm^{-1} (ascribed to the C═N stretching vibration of the quinonoid unit), ~519 cm^{-1} and ~419 cm^{-1} (belong the ring out-of-plane deformations) are shifted towards higher frequencies (~1592, ~1506, ~523 and ~432 cm^{-1}, respectively) when the PANI-ES was immersed in Al-nitrate solution. These blue-shifted bands kept the same position upon anodic polarization. The relative intensity of all these modes (when compared to the most pronounced 1172 cm^{-1} band related to C–H bending vibrations of semi-quinonoid rings) is also increased under open circuit condition and preserved upon anodic polarization. All these changes can be attributed to the slight oxidation process, as shown by FTIR. An increase in the relative intensity of the low-frequency bands (~523 cm^{-1} and ~432 cm^{-1}) is a more pronounced upon anodic polarization, due to an additional nitrate ion doping.

The spectrum of PANI polarized up to −0.2 V vs. SCE, differs from all other spectra in Fig. 6b. The characteristic modes are ~1592 cm^{-1} (along with the shoulders at ~1620 cm^{-1} and at 1560 cm^{-1}), ~1475 cm^{-1} (along with the shoulder at ~1420 cm^{-1}), 1320 cm^{-1}, ~1220

cm^{-1}, ~1166 cm^{-1}, ~841 cm^{-1}, ~813 cm^{-1}, ~785 cm^{-1}, ~750 cm^{-1}, ~528 cm^{-1} and ~422 cm^{-1}. Relying on the literature [67], these modes belong to deprotonated PANI, more precisely emeraldine base, as in accordance with FTIR finding. The ~1475 cm^{-1} assigned band, associated with C═N vibration of quinoid unit, dominates the spectrum. The shoulder at 1420 cm^{-1}, can be most probably connected with cross-linked phenazine-like structures [67]. As we mentioned, the formation of PANI-EB after electrochemical reduction at −0.2 V vs. SCE is the consequence of the fact that the electrochemically reduced LB form became oxidized upon exposing of the electrode to water/air during washing/drying.

Based on all the above, we assume that the Lewis acid (i.e. aluminum-nitrate) doping of ES (acting as a Lewis base) occurred through the complexation with Cl$^-$ anions on protonated nitrogen carrying radical cation (ex-imine sites). It was also shown that FeCl$_3$ could be doped to the protonated form of polyaniline through the acid-base reaction with Cl$^-$ anions thus transforming into FeCl$_4^-$ [68]. Herein, Al (NO$_3$)$_3$ acts as a mild oxidizing agent, thus leading to the conformation change of PANI's chain. Interestingly, it has been predicted that nitrate anions can act as a Lewis acid by forming complexes with electron-rich partners [69]. One can conclude that the mechanism of nitrate's doping/dedoping (alone or in the form of complex anion) dominates the redox switching of ES in an aluminum nitrate aqueous solution, thus causing the formation/breaking of solid state nitrate complex. This process is probably accompanied by the expulsion/injection of Al^{3+} ions (most likely hydrated), which is similar to the protons' behavior during redox process of ES in the moderate acidic electrolyte [30,43,70]. Actually, the reduced PANI is poorly protonated in the electrolyte of lower acidity [30,43,70], but we believe that the Al^{3+} ions can take the role of protons due to their higher concentration. The presence of Al^{3+} ions in the electrolyte prevents the capacity decline which can be caused by the acidity decrease of the electrolyte solution [44].

3.3.2. AFM study

In order to observe the conformational changes of PANI-ES induced by charging/discharging process, AFM measurements were performed. Two-dimensional (2D) and three-dimensional (3D) topography of discharged sample are depicted in Fig. 7 (a$_1$ and a$_2$, respectively). As can be seen, the sample consists of small grains with an average diameter in the range of 100–200 nm. These grains are even better visualized in the phase image in Fig. 7b, where abrupt changes, in the phase signal, correspond to grain boundaries. Apart from these changes along the grain boundaries, the phase contrast is rather constant, indicating homogeneous viscoelastic properties. Similar measurements were done on the charged sample and these results are given in the second row of Fig. 7, where the parts (c1) and (c2) present 2D and 3D topography. Contrary to the discharged state, now there are two distinct structural features. First, as in the previous case, the middle part has grain structure with a similar grain size of 100–200 nm. On the other hand, the grain structure disappeared in the top and bottom part of the figures which are now characterized with smooth and large, micron-size domains. Therefore, during the charging process small grains were merged together into a single domain. Similar changes have been recently observed in the case of conductive polymers such as poly(3,4-ethylenedioxythiophene) (PEDOT) [71].

In addition to the observed morphological changes, there is a huge difference in the phase contrast between two areas with distinct morphology. As shown in the phase image in Fig. 7d, the middle part with a grain structure is dark, while the top and bottom regions with large and smooth domains are bright. The observed phase contrast indicates different viscoelastic damping during the interaction between oscillating AFM tip and the sample surface during the imaging in tapping AFM mode. Therefore, the charging process results in merging of grains into larger domains with a modified viscoelasticity.

The local electrical surface potential of both charged and discharged samples were studied by Kelvin probe force Microscopy (KPFM).
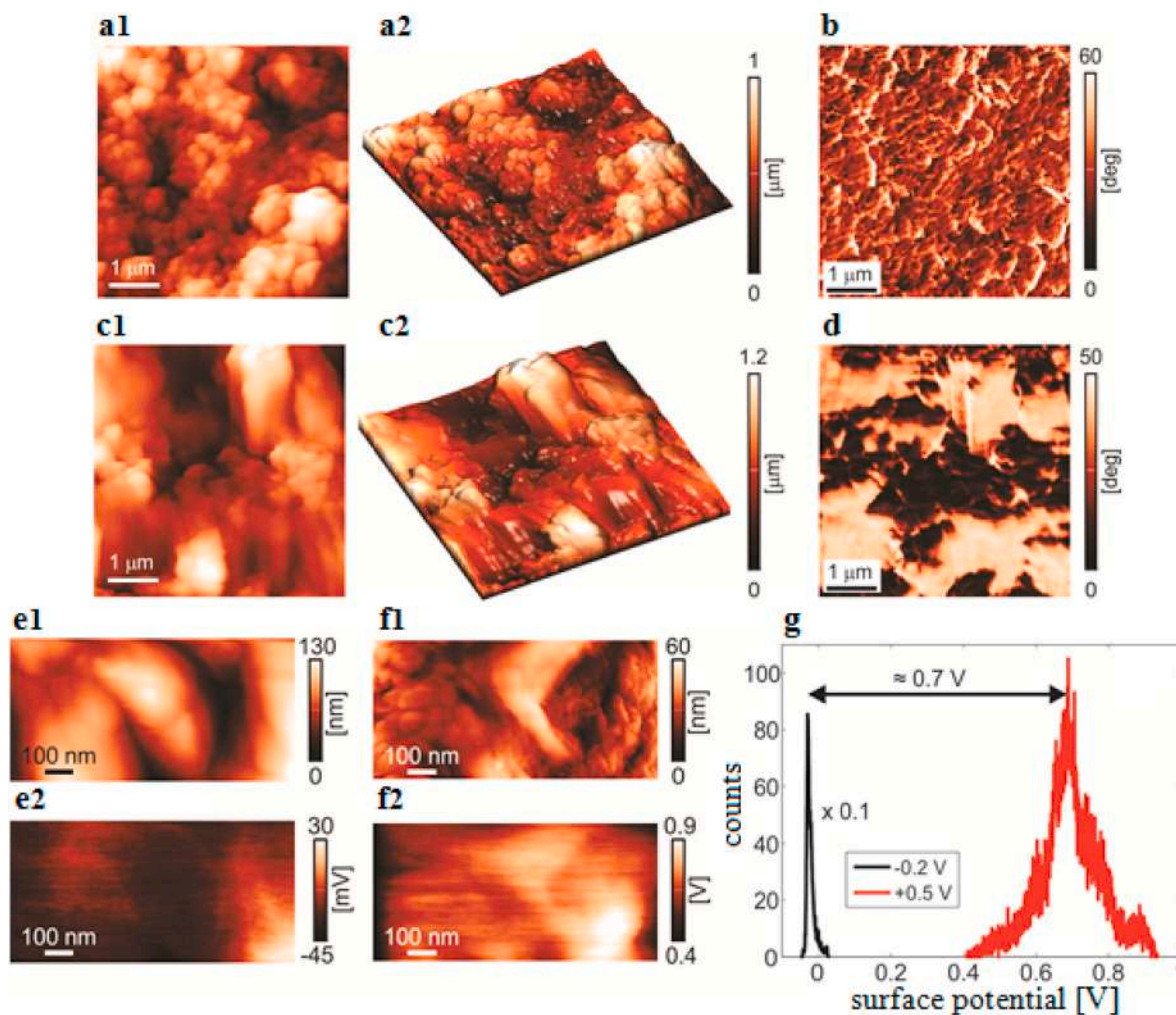
Fig. 7. Sample morphology after discharging (at −0.2 V vs. SCE): (a1) 2D and (a2) 3D topography, and (b) phase map. Sample morphology after charging (at + 0.5 V): (c1) 2D and (c2) 3D topography, and (b) phase map (top); AFM topography and electrical surface potential of discharged (e₁,e₂) and charged sample (f₁,f₂). (g) Histograms of the electrical surface potential maps from parts (e2) and (f2) indicating that the average difference of the surface potential between two states is around 0.7 V. For the sake of clarity and better visibility, the peak for the discharged sample is scaled by ten times (bottom).

Fig. 7e1 and 7e2 show the morphology and surface potential, respectively, measured on the same area of discharged sample. Similarly, the topography and potential of the charged sample are presented in Fig. 7f₁ and Fig. 7f₂, respectively. By comparing the absolute values of the surface potential of the charged and discharged sample, there is a significant difference. It is better represented in Fig. 7g which displays histograms of the surface potential for both cases. Although the surface potential for the charged sample is rather inhomogeneous, in the range from 0.4 V to 0.9 V, the peaks between charged and discharged cases are separated by around 0.7 V. This is exactly the same value as the difference between the electrochemical potentials during the charging (+0.5 V) and discharging (−0.2 V). Therefore, the changes in the surface potential measured ex-situ correspond quite well to the electrochemical potential during charging/discharging. Recently, this correlation has been demonstrated for $LiNi_{0.80}Co_{0.15}Al_{0.05}O_2$ cathode at different state of charge [72].

3.3.3. DFT calculations

Doping of PANI base by strong acids leads to formation of polarons and bipolarons. In the former structural form, only one nitrogen atom in the oxidized unit accumulates positive charge, which results in a radical open-shell specie. In the later form, both imine nitrogen atoms are protonated creating a spinless state. Although the relative stability of these forms is still under debate [73], they are interconvertible, i.e. a

bipolaron might rearrange into two polarons, Previous computational studies revealed that effects associated with the doping process are localized around the binding site [74] and that electronic structure of the bipolaron and polaron forms does not depend on the kind of protonating agent [61]. Also, the solvent polarity was attributed to be the major factor responsible for the energy difference between the polaron and bipolaron forms [61]. These findings led us to study to what extent hydrated Al^{3+} cation might modify electronic properties of emeraldine PANI salt. To this end, we examined PANI salt model consisted of a tetramer protonated with HCl and HNO_3 acids.

We examined its polaron (two polarons in the lowest triplet state) and bipolaron (in the singlet state) forms. The optimized geometries and selected bond length of these forms are provided in Fig. 8. The electronic energy difference between the polaron and bipolaron forms are 21 and 26 kJ/mol for structures doped with HCl and HNO_3 acids, respectively. Thus, we find that in our model, the polaron form is more stable than the bipolaron form. Similarly as in the other study [61], the doping agent does not considerably modify the energy difference between the two electronic forms. We find that the lowest singlet state of polaron form is approximately 40 kJ/mol less stable than the triplet state and thus it does not play a significant role in charge transport. Highly charged aluminum cation might be attracted by the anions in the PANI salt. We considered a configuration in which the Al^{3+} cation is positioned 3 Å away from the Cl^- anion along the H–Cl direction (Fig. 8). The
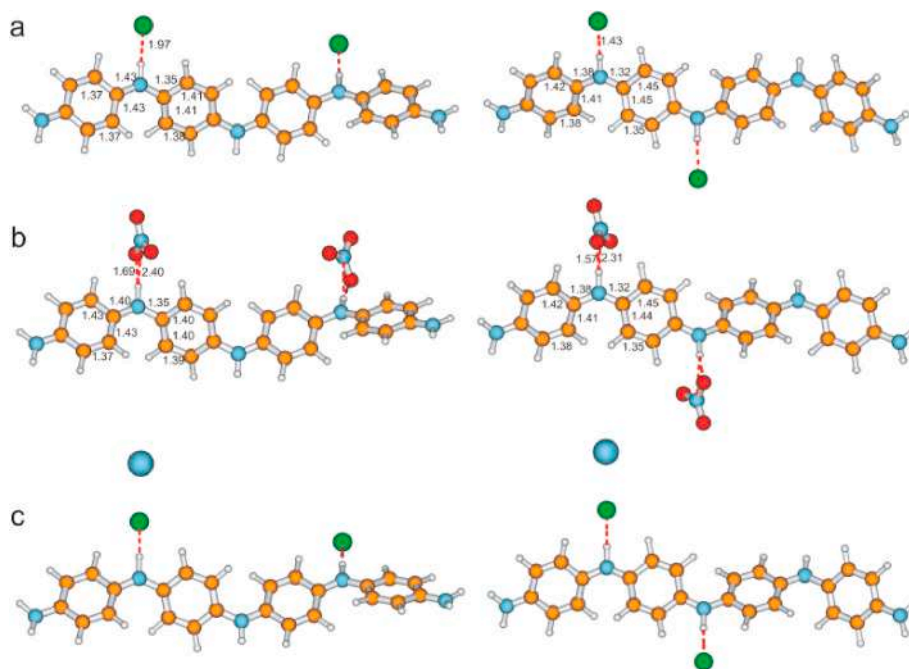
Fig. 8. The optimized geometries and selected bond lengths (in Å) of the PANI model protonated with HCl (a), HNO_3 (b) and HCl and Al^{3+} cation (c). Polaron and bipolaron forms are given in left and right columns, respectively. The geometry of the structure with the Al^{3+} cation was created by using the optimized PANI model doped with HCl acid and positioning the Al^{3+} cation 3 Å away from the Cl^- anion along the H–Cl direction.

computed energy difference between the polaron and bipolaron forms was −26 kJ/mol. Hence, the Coulomb interaction between the PANI salt and the aluminum cation was sufficient to reverse the relative stability of the electronic forms. This result shed light that the aluminum cation is able to alter electronic properties of PANI even it is not primary doping agent. We tentatively refer this effect to the secondary doping, which is in agreement with the experiment [62].

4. Conclusions

The highly conductive polyaniline-emeraldine salt (PANI-ES) was synthesized, using the typical acidic polymerization of aniline, in order to be thoroughly examined as supercapacitor electrode in an aqueous solution of aluminium salt. The typical, leucoemeraldine ↔emeraldine (the first one) and emeraldine ↔ pernigranilin (the second one) redox processes were observed in all examined electrolytes (1 M HCl, 1 M aluminum-nitrate in water and in 1 M HCl as well as 1 M aluminum-chloride in water). However, their mechanism strongly depends on the used electrolyte, which determines specific charge storage ability of the polymer. Unlike the strong acidic solution, where the proton deinsertion/insertion dominates the first redox process, anion doping/dedoping mostly compensates the charge, induced by the PANI's redox switching in an Al-based aqueous solution, while Al^{3+} ions do not behave only as spectators. They can also be interchanged during the redox reaction of the PANI's electrode likely to protons in the acidic solutions. The redox behavior of PANI, in an Al-containing aqueous solution, was found to induce the swelling/shrinking of its grain size structure.

Furthermore, Lewis acid $Al(NO_3)_3$ doping into emeraldine (thus oxidizing some reduced parts of polymer), is exerted through the complexation with Cl-anions bonded to N-atom (from radical cation) rather than with protonated amine sites. The formation of nitrates complexes and their breaking follows the redox reaction of polymer in the $Al(NO_3)_3$. Theoretical modeling showed that the primary doping of PANI with protonic agents (HCl and HNO_3) stabilized its polaron form. However, Al-salt doping results in the formation of bipolaron lattice,

which can be attributed to the secondary doping.

As the consequence of the particular redox mechanism, the slightly higher capacitance in $Al(NO_3)_3$ (amounting to 317 F g^{-1} at 1 A g^{-1}) than in 1MHCl (amounting to 301 Fg^{-1} at 1 A g^{-1}) was measured. PANI-ES symmetrical two-electrode capacitor, with the $Al(NO_3)_3\_H_2O$ as an electrolyte, could deliver the discharge capacitance of 269 F g^{-1} at 10 Ag^{-1}, in the voltage range $\Delta V = 0.8$ V. Under the same conditions, the capacitance retained 88% of its initial value after 1000 cycles.

Furthermore, it was shown that the electrochemical overoxidation of PANI within voltage window $\Delta E = 1.4$ V is significantly influenced by the electrolytic composition, more precisely, by the protons' concentration in the electrolyte. Due to lower protons' concentration in $Al(NO_3)_3$, the capacitance retention during cycling in an extended potential range is significantly better (which amounts to 61% after 60 cycles) in 1 M $Al(NO_3)_3$ than in 1 M HCl (which amounts to 47% after 60 cycles). The aluminum ions do not behave passively in the emeraldine ↔ pernigranilin redox process, but they decelerate over-oxidation of emeraldine salt more effectively than protons in the pure acidic solution do.

The obtained results opened the way for the development of a new generation of more suitable charge storage devices, based on well-known polymer material.

CRediT authorship contribution statement

Milica J. Vujković: Conceptualization, Methodology, Investigation, Writing - original draft. **Mihajlo Etinski:** Investigation, Formal analysis, Writing - original draft. **Borislav Vasić:** Investigation, Formal analysis, Writing - original draft. **Bojana Kuzmanović:** Investigation, Data curation, Formal analysis. **Danica Bajuk-Bogdanović:** Investigation, Data curation, Formal analysis. **Robert Dominko:** Conceptualization, Writing - review & editing. **Slavko Mentus:** Conceptualization, Supervision, Writing - review & editing.

Declaration of competing interest

The authors declare that they have no known competing financial interests or personal relationships that could have appeared to influence the work reported in this paper.

Acknowledgments

Appendix A. Supplementary data

Supplementary data to this article can be found online at https://doi.org/10.1016/j.jpowsour.2020.228937.

References

[1] A. Ponrouch, J. Bitenc, R. Dominko, N. Lindahl, P. Johansson, M.R. Palacin, Multivalent rechargeable batteries, Energy Storage Mater 20 (2019) 253–262, https://doi.org/10.1016/j.ensm.2019.04.012.

[2] G.A. Elia, K. Marquardt, K. Hoeppner, S. Fantini, R. Lin, E. Knipping, W. Peters, J. F. Drillet, S. Passerini, R. Hahn, An overview and future perspectives of aluminum batteries, Adv. Mater. 28 (2016) 7564–7579, https://doi.org/10.1002/adma.201601357.

[3] J. Huang, Z. Guo, Y. Ma, D. Bin, Y. Wang, Y. Xia, Recent progress of rechargeable batteries using mild aqueous electrolytes, Small Methods 3 (2019) 1800272, https://doi.org/10.1002/smtd.201800272.

[4] M. Vujković, S. Mentus, Potentiodynamic and galvanostatic testing of $NaFe_{0.95}V_{0.05}PO_4$/C composite in aqueous $NaNO_3$ solution, and the properties of aqueous $Li_{1.2}V_3O_8$/$NaNO_3$/$NaFe_{0.95}V_{0.05}PO_4$/C battery, J. Power Sources 325 (2016) 185–193, https://doi.org/10.1016/j.jpowsour.2016.06.031.

[5] M. Vujković, M. Mitrić, S. Mentus, High-rate intercalation capability of $NaTi_2(PO_4)_3$/C composite in aqueous lithium and sodium nitrate solutions, J. Power Sources 288 (2015) 176–186, https://doi.org/10.1016/j.jpowsour.2015.04.132.

[6] M. Vujković, S. Mentus, Fast sodiation/desodiation reactions of electrochemically delithiated olivine $LiFePO_4$ in aerated aqueous $NaNO3$ solution, J. Power Sources 247 (2014) 184–188, https://doi.org/10.1016/j.jpowsour.2013.08.062.

[7] M.R. Lukatskaya, O. Mashtalir, C.E. Ren, Y. Dall'Agnese, P. Rozier, P.L. Taberna, M. Naguib, P. Simon, M.W. Barsoum, Y. Gogotsi, Cation intercalation and high volumetric capacitance of two-dimensional titanium carbide, Science 341 (2013) 1502–1505, https://doi.org/10.1126/science.1241488.

[8] S.K. Das, S. Mahapatra, H. Lahan, Aluminium-ion batteries: developments and challenges, J. Mater. Chem. A. 5 (2017) 6347–6367, https://doi.org/10.1039/c7ta00228a.

[9] Y.J. He, J.F. Peng, W. Chu, Y.Z. Li, D.G. Tong, Black mesoporous anatase TiO_2 nanoleaves: a high capacity and high rate anode for aqueous TiO_2 batteries, J. Mater. Chem. A. 2 (2014) 1721–1731, https://doi.org/10.1039/c3ta13906a.

[10] J.R. González, F. Nacimiento, M. Cabello, R. Alcántara, P. Lavela, J.L. Tirado, Reversible intercalation of aluminium into vanadium pentoxide xerogel for aqueous rechargeable batteries, RSC Adv. 6 (2016) 62157–62164, https://doi.org/10.1039/c6ra11030d.

[11] S. Liu, J.J. Hu, N.F. Yan, G.L. Pan, G.R. Li, X.P. Gao, Aluminum storage behavior of anatase TiO_2 nanotube arrays in aqueous solution for aluminum ion batteries, Energy Environ. Sci. 5 (2012) 9743–9746, https://doi.org/10.1039/c2ee22987k.

[12] J. Liu, C. Xu, Z. Chen, S. Ni, Z.X. Shen, Progress in aqueous rechargeable batteries, Green Energy Environ 3 (2018) 20–41, https://doi.org/10.1016/j.gee.2017.10.001.

[13] A. Holland, R.D. Mckerracher, A. Cruden, R.G.A. Wills, An aluminium battery operating with an aqueous electrolyte, J. Appl. Electrochem. 48 (2018) 243–250, https://doi.org/10.1007/s10800-018-1154-x.

[14] M. Kazazi, P. Abdollahi, M. Mirzaei-Moghadam, High surface area TiO_2 nanospheres as a high-rate anode material for aqueous aluminium-ion batteries, Solid State Ionics 300 (2017) 32–37, https://doi.org/10.1016/j.ssi.2016.11.028.

[15] H. Lahan, R. Boruah, A. Hazarika, S.K. Das, Anatase TiO_2 as an anode material for rechargeable aqueous aluminum-ion batteries: remarkable graphene induced aluminum ion storage phenomenon, J. Phys. Chem. C 121 (2017) 26241–26249, https://doi.org/10.1021/acs.jpcc.7b09494.

[16] H. Lahan, S.K. Das, Al^{3+} ion intercalation in MoO_3 for aqueous aluminum-ion battery, J. Power Sources 413 (2019) 134–138, https://doi.org/10.1016/j.jpowsour.2018.12.032.

[17] H. Lahan, S.K. Das, Graphene and diglyme assisted improved Al^{3+} ion storage in MoO_3 nanorod: steps for high-performance aqueous aluminum-ion battery, Ionics 25 (2019) 3493–3498, https://doi.org/10.1007/s11581-019-03058-6.

[18] Y. Liu, S. Sang, Q. Wu, Z. Lu, K. Liu, H. Liu, The electrochemical behavior of Cl^- assisted Al^{3+} insertion into titanium dioxide nanotube arrays in aqueous solution for aluminum ion batteries, Electrochim. Acta 143 (2014) 340–346, https://doi.org/10.1016/j.electacta.2014.08.016.

[19] W. Zhong, S. Sang, Y. Liu, Q. Wu, K. Liu, H. Liu, Electrochemically conductive treatment of TiO_2 nanotube arrays in $AlCl_3$ aqueous solution for supercapacitors, J. Power Sources 294 (2015) 216–222, https://doi.org/10.1016/j.jpowsour.2015.06.052.

[20] W. Wang, B. Jiang, W. Xiong, H. Sun, Z. Lin, L. Hu, J. Tu, J. Hou, H. Zhu, S. Jiao, A new cathode material for super-valent battery based on aluminium ion intercalation and deintercalation, Sci. Rep. 3 (2013) 3383, https://doi.org/10.1038/srep03383.

[21] H. Sun, W. Wang, Z. Yu, Y. Yuan, S. Wang, S. Jiao, A new aluminium-ion battery with high voltage, high safety and low cost, Chem. Commun. 51 (2015) 11892–11895, https://doi.org/10.1039/c5cc00542f.

[22] M.C. Lin, M. Gong, B. Lu, Y. Wu, D.Y. Wang, M. Guan, M. Angell, C. Chen, J. Yang, B.J. Hwang, H. Dai, An ultrafast rechargeable aluminium-ion battery, Nature 520 (2015) 325–328, https://doi.org/10.1038/nature14340.

[23] D.Y. Wang, C.Y. Wei, M.C. Lin, C.J. Pan, H.L. Chou, H.A. Chen, M. Gong, Y. Wu, C. Yuan, M. Angell, Y.J. Hsieh, Y.H. Chen, C.Y. Wen, C.W. Chen, B.J. Hwang, C. C. Chen, H. Dai, Advanced rechargeable aluminium ion battery with a high-quality natural graphite cathode, Nat. Commun. 8 (2017), https://doi.org/10.1038/ncomms14283.

[24] P. Yao, M. Ye, W. Guo, X. Liu, Aluminum ion electrolyte for enhanced electrochromism of polyaniline, AIP Conf. Proc. 1864 (2017) 10–15, https://doi.org/10.1063/1.4992880.

[25] R. Prakash, Electrochemistry of polyaniline: study of the pH effect and electrochromism, J. Appl. Polym. Sci. 83 (2002) 378–385, https://doi.org/10.1002/app.10025.

[26] A.G.M. Wu-Song Huang, Brian D. Humphrey, A.G. Macdiarmid, Polyaniline, a novel conducting polymer, J. Chem. SOC., Faraday Trans. 82 (1986) 2385–2400, https://doi.org/10.1007/s12043-006-0044-7.

[27] C. Barbero, M.C. Miras, O. Haas, R. Kotz, Direct in situ evidence for proton/anion exchange in polyaniline films by means of probe beam deflection, J. Electrochem. Soc. 138 (1991) 669–672, https://doi.org/10.1149/1.2085655.

[28] E.M. Genies, M. Lapkowski, Polyaniline films. Electrochemical redox mechanisms, Synth. Met. 24 (1988) 61–68, https://doi.org/10.1016/0379-6779(88)90595-4.

[29] L.P. Bauermann, P.N. Bartlett, EQCM measurements of the ion and solvent flux in thin poly(aniline)- poly(styrenesulfonate) films during redox switching, Electrochim. Acta 50 (2005) 1537–1546, https://doi.org/10.1016/j.electacta.2004.10.011.

[30] D. Orata, D.A. Buttry, Determination of ion populations and solvent content as functions of redox state and pH in polvaniline, J. Am. Chem. Soc. 109 (1987) 3574–3581, https://doi.org/10.1021/ja00246a013.

[31] Z. Ping, G.E. Nauer, H. Neugebauer, J. Theiner, A. Neckel, Protonation and electrochemical redox doping processes of polyaniline in aqueous solutions: investigations using in situ FTIR-ATR spectroscopy and a new doping system, J. Chem. Soc. - Faraday Trans. 93 (1997) 121–129, https://doi.org/10.1039/a604620g.

[32] A. Watanabe, K. Mori, Y. Iwasaki, Y. Nakamura, S. Niizuma, Electrochromism of polyaniline film prepared by electrochemical polymerization, Macromolecules 20 (1987) 1793–1796, https://doi.org/10.1021/ma00174a015.

[33] A. Watanabe, K. Mori, M. Mikuni, Y. Nakamura, M. Matsuda, Comparative study of redox reactions of polyaniline films in aqueous and nonaqueous solutions, Macromolecules 22 (1989) 3323–3327, https://doi.org/10.1021/ma00198a022.

[34] B. Kuzmanović, M.J. Vujković, N. Tomić, D. Bajuk-Bogdanović, V. Lazović, B. Šljukić, N. Ivanović, S. Mentus, The influence of oxygen vacancy concentration in nanodispersed non-stoichiometric $CeO_{2-δ}$ oxides on the physico-chemical properties of conducting polyaniline/CeO_2 composites, Electrochim. Acta 306 (2019) 506–515, https://doi.org/10.1016/j.electacta.2019.03.135.

[35] R. Garcia, C.J. Gómez, N.F. Martinez, S. Patil, C. Dietz, R. Magerle, Identification of nanoscale dissipation processes by dynamic atomic force microscopy, Phys. Rev. Lett. 97 (2006) 1–4, https://doi.org/10.1103/PhysRevLett.97.016103.

[36] D. Wang, X. Bin Liang, Y.H. Liu, S. Fujinami, T. Nishi, K. Nakajima, Characterization of surface viscoelasticity and energy dissipation in a polymer film by atomic force microscopy, Macromolecules 44 (2011) 8693–8697, https://doi.org/10.1021/ma201148f.

[37] V.7 Turbomole, University of Kalsrue and Forschungszentrum Karlsrue GmbH, 2015, 1989-2007.

[38] Y. Zhao, D.G. Truhlar, The M06 suite of density functionals for main group thermochemistry, thermochemical kinetics, noncovalent interactions, excited states, and transition elements : two new functionals and systematic testing of four M06-class functionals and 12 other functional, Theor Chem Account 120 (2008) 215–241, https://doi.org/10.1007/s00214-007-0310-x.

[39] A. Schäfer, C. Huber, R. Ahlrichs, A. Schafer, C. Huber, R. Ahlrichs, Fully Optimized Contracted Gaussian Basis Sets of Triple Zeta Valence Quality for Atoms Li to Kr Fully Optimized Contracted Gaussian Basis Sets of Triple Zeta Valence Quality for Atoms Li to Kr, 1994, p. 5829, https://doi.org/10.1063/1.467146.

[40] A. Schäfer, H. Horn, R. Ahlrichs, Fully optimized contracted Gaussian basis sets for atoms Li to Kr, J. Chem. Phys. 97 (1992) 2571–2577, https://doi.org/10.1063/1.463096.

[41] A. Klamt, G. Schuurmann, COSMO : a new approach to dielectric screening in solvents with explicit expressions for the screening energy and its gradient, J. Chem. Soc.Perkin Trans. 2 (1993) 799–805.

[42] A. Schäfer, A. Klamt, D. Sattel, C.W. Lohrenz, F. Eckert, COSMO Implementation in TURBOMOLE : extension of an efficient quantum chemical code towards liquid systems, Phys. Chem. Chem. Phys. 2 (2000) 2187–2193.

[43] J. Desilvestro, W. Scheifele, O. Haas, In situ determination of gravimetric and volumetric charge densities of battery electrodes polyaniline in aqueous and nonaqueous electrolytes, J. Electrochem. Soc. 139 (1992) 2727–2736.

[44] T. Kobayashi, H. Yoneyama, H. Tamura, Electrochemical reactions concerned with electrochromism of polyaniline film-coated electrodes, J. Electroanal. Chem. 177 (1984) 281–291, https://doi.org/10.1016/0022-0728(84)80229-6.

[45] X. Yang, Q. Xie, S. Yao, A comparative study on polyaniline degradation by an electrochemical quartz crystal impedance system : electrode and solution effects, Synth. Met. 143 (2004) 119–128, https://doi.org/10.1016/j.synthmet.2003.10.027.

[46] R. Pauliukaite, C.M.A. Brett, A.P. Monkman, Polyaniline fibres as electrodes . Electrochemical characterisation in acid solutions, Electrochim. Acta 50 (2004) 159–167, https://doi.org/10.1016/j.electacta.2004.07.034.

[47] E. Song, J. Choi, Conducting polyaniline nanowire and its applications in chemiresistive sensing, Nanomaterials 3 (2013) 498–523, https://doi.org/10.3390/nano3030498.

[48] N. Garilov, I.A. Pašti, M. Vujković, J. Travas-Sejdić, G. Ćirić -Marjanović, S.V. Mentus, High-performance charge storage by N-containing nanostructured carbon derived from polyaniline, Carbon 50 (2012) 3915–3927, https://doi.org/10.1016/j.carbon.2012.04.045.

[49] J. Niu, W.G. Pell, B.E. Conway, Requirements for performance characterization of C double-layer supercapacitors : applications to a high specific-area C-cloth material, J. Power Sources 156 (2006) 725–740, https://doi.org/10.1016/j.jpowsour.2005.06.002.

[50] J. Black, H.A. Andreas, Prediction of the self-discharge profile of an electrochemical capacitor electrode in the presence of both activation-controlled discharge and charge redistribution, J. Power Sources 195 (2010) 929–935, https://doi.org/10.1016/j.jpowsour.2009.08.040.

[51] F. Wang, Z. Liu, X. Wang, X. Yuan, X. Wu, A conductive polymer coated MoO_3 anode enables an Al-ion capacitor with high performance, J. Mater. Chem. 4 (2016) 5115–5123, https://doi.org/10.1039/c6ta01398h.

[52] K. Li, Y. Shao, S. Liu, Q. Zhang, H. Wang, Y. Li, R.B. Kaner, Aluminum-Ion-Intercalation Supercapacitors with Ultrahigh Areal Capacitance and Highly Enhanced Cycling Stability : Power Supply for Flexible Electrochromic Devices, 2017, p. 1700380, https://doi.org/10.1002/smll.201700380. Small.

[53] H. Lahan, S.K. Das, Reversible Aluminium-ion insertion into tungsten trioxide (WO_3) for aqueous aluminum-ion batteries, Dalton Trans. 48 (2019) 6337–6340, https://doi.org/10.1039/c9dt00844f.

[54] Z. Li, K. Xiang, W. Xing, W.C. Carter, Y.M. Chiang, Reversible aluminum-ion intercalation in prussian blue analogs and demonstration of a high-power aluminum-ion asymmetric capacitor, Adv. Energy Mater. 5 (2015) 1–6, https://doi.org/10.1002/aenm.201401410.

[55] S. Liu, G.L. Pan, G.R. Li, X.P. Gao, Copper hexacyanoferrate nanoparticles as cathode material for aqueous Al-ion batteries, J. Mater. Chem. 3 (2015) 959, https://doi.org/10.1039/C4TA04644G.

[56] X. Xiao, H. Song, S. Lin, Y. Zhou, X. Zhan, Z. Hu, Q. Zhang, J. Sun, B. Yang, two-dimensional transition metal oxides, Nat. Commun. 7 (2016) 1–8, https://doi.org/10.1038/ncomms11296.

[57] M.M. Gvozdenović, B.Z. Jugović, J.S. Stevanović, B.N. Grgur, Electrochemical synthesis of electroconducting polyanilines, Chem. Ind. 68 (2014) 673–684, https://doi.org/10.2298/HEMIND131122008G.

[58] E.T. Kang, K.G. Neoh, T.C. Tan, Structural studies of poly(ppheny1eneamine) and its oxidation, Macromolecules 23 (1990) 2918–2926.

[59] E.T. Kang, K.G. Neoh, K.L. Tan, Polyaniline : a polymer with many ineresting intrinsic redox states, Prog. Polym. Sci. 23 (1998) 277–324.

[60] M. Trchová, J. Stejskal, Polyaniline : The infrared spectroscopy of conducting polymer nanotubes, IUPAC Technical Report)* 83 (2011) 1803–1817, https://doi.org/10.1351/PAC-REP-10-02-01.

[61] J. Romanova, G. Madjarova, A. Tadjer, Solvent polarity and dopant effect on the electronic, Structure of the Emeraldine Salt 111 (2011) 435–443, https://doi.org/10.1002/qua.

[62] A.G. Macdiarmid, A.J. Epstein, Secondary doping in polyaniline 69 (1995) 85–92.

[63] G. Ćirić-Marjanović, M. Trchová, J. Stejskal, The chemical oxidative polymerization of aniline in water, Raman spectroscopy 39 (2008) 1375–1387, https://doi.org/10.1002/jrs.

[64] M. Trchová, Z. Moravkova, I. Šeděnková, J. Stejskal, Spectroscopy of thin polyanilin films deposited during chemical oxidation of aniline, Chem. Pap. 66 (2012) 415–445, https://doi.org/10.2478/s11696-012-0142-6.

[65] G.M. Nascimento, V.R.L. Constantino, R. Landers, M.L.A. Temperini, Aniline polymerization into montmorillonite Clay : a spectroscopic investigation of the intercalated conducting polymer, Macromolecules 37 (2004) 9373–9385.

[66] B.Z. Wei, M. Wan, T. Lin, L. Dai, Polyaniline nanotubes doped with sulfonated carbon nanotubes made via a self-assembly process, Adv. Mater. 15 (2003) 136–139.

[67] M. Trchová, Z. Morávková, M. Bláha, J. Stejskal, Raman spectroscopy of polyaniline and oligoaniline thin films, Electrochim. Acta 122 (2014) 28–38, https://doi.org/10.1016/j.electacta.2013.10.133.

[68] F. Genoud, I. Kulszewicz-Bajer, A. Bedel, J.L. Oddou, C. Jeandey, A. Pron, Lewis acid doped polyaniline. Part II: spectroscopic studies of emeraldine base and emeraldine hydrochloride complexation with $FeCl_3$, Chem. Mater. 12 (2000) 744–749, https://doi.org/10.1021/cm990485u.

[69] A. Bauzá, A. Frontera, T.J. Mooibroek, NO_3 anions can act as Lewis acid in the solid state, Nat. Commun. 8 (2017) 1–6, https://doi.org/10.1038/ncomms14522.

[70] K. Shimazu, K. Murakoshi, H. Kita, Quantitative and in-situ measurements of proton transport at polyaniline film electrodes, J. Electroanal. Chem. 277 (1990) 347–353.

[71] T. Schoetz, M. Kurniawan, M. Stich, R. Peipmann, I. Efimov, A. Ispas, A. Bund, C. Ponce De Leon, M. Ueda, Understanding the charge storage mechanism of conductive polymers as hybrid battery-capacitor materials in ionic liquids by: in situ atomic force microscopy and electrochemical quartz crystal microbalance studies, J. Mater. Chem. A. 6 (2018) 17787–17799, https://doi.org/10.1039/c8ta06757k.

[72] X. Zhu, R.I. Revilla, A. Hubin, Direct correlation between local surface potential measured by Kelvin probe force microscope and electrochemical potential of $LiNi_{0.80}Co_{0.15}Al_{0.05}O_2$ cathode at different state of charge, J. Phys. Chem. C 122 (2018) 28556–28563, https://doi.org/10.1021/acs.jpcc.8b10364.

[73] A. Varela-Álvarez, J.A. Sordo, G.E. Scuseria, Doping of polyaniline by acid-base chemistry: density functional calculations with periodic boundary conditions, J. Am. Chem. Soc. 127 (2005) 11318–11327, https://doi.org/10.1021/ja051012t.

[74] J. Casanovas, M. Canales, C.A. Ferreira, C. Alemán, A first principle analysis of the structure of oligoanilines doped with alkylsulfonic acids, J. Phys. Chem. 113 (2009) 8795–8800, https://doi.org/10.1021/jp904618a.

Laser-Tunable Printed ZnO Nanoparticles for Paper-Based UV Sensors with Reduced Humidity Interference

Georges Dubourg [1,*] ![ORCID]**, Marko Radović** [1] **and Borislav Vasić** [2]

1 Center for Sensor Technologies, BioSense Institute, University of Novi Sad, Zorana Đinđića, 21101 Novi Sad, Serbia; marrad@biosense.rs
2 Institute of Physics Belgrade, University of Belgrade, Pregrevica 118, 11080 Belgrade, Serbia; bvasic@ipb.ac.rs
* Correspondence: georges.dubourg@biosense.rs

Abstract: Development of paper-based sensors that do not suffer with humidity interference is desirable for practical environmental applications. In this work, a laser processing method was reported to effectively modulate the cross-sensitivity to humidity of ZnO-based UV (Ultraviolet) sensors printed on paper substrate. The results reveal that the laser induced zinc oxide (ZnO) surface morphology contributes to the super-hydrophobicity of the printed ZnO nanoparticles, reducing humidity interference while enhancing UV sensitivity. Herein, this conducted research highlights for the first time that laser processing is an attractive choice that reduces the cross-sensitivity to water vapor in the UV sensing response of ZnO-based devices printed on paper, paving the way to low-cost and sophisticated paper-based sensors.

Keywords: paper-based device; UV sensors; ZnO nanoparticles; humidity resistance

1. Introduction

For a long time, cellulose fiber paper has been used as the main support for storing, displaying, transferring information and connecting people in the form of missives, flyers or books. In recent years, however, its function as a writing medium has been declining with the evolution of information and communication technologies. This evolution drastically changed how people work, communicate and learn, gradually replacing the paper substrate with electronic support, such as computer, TV, e-book and e-library. Nevertheless, this has generated a considerable amount of electronic waste resulting in severe environmental issues. In order to address the environmental concerns and end-of-life disposal challenges, paper was reinvented as a building component in flexible electronics because it is disposable, recyclable, inexpensive and one of the most abundant organic materials. Therefore, paper-based substrate has been explored with the aim of developing a variety of components, such as electronic and optoelectronic devices [1,2], electrochemical biosensors [3–5] and physical sensors [6,7]. Among them, physical sensors which transduce physical parameters, such as mechanical and optical signals, into processable electrical signals represent a major category of paper-based devices and might play an important role in the upcoming era of wearable electronics.

Various functional nanomaterials have been employed in order to enhance the paper-based sensor performance. Among them, the zinc oxide (ZnO) nanostructures are a popular choice due to their multiple sensing modalities [8–10]. For instance, its direct wide bandgap and 60 meV high exciton energy make ZnO nanostructures the ideal materials for UV sensing applications [11,12]. Due to the growing importance of detecting/protecting UV light application in various fields, various reports have been published on the fabrication of low-cost ZnO-based UV sensors on paper substrate [13–16]. Although many of the reported paper-based UV sensors work very well in laboratory scale proof of principle experiments, they are still limited by their cross-sensitivity to background conditions, such as relative humidity than can vary in outdoor conditions, impeding their practical use in applications

such as environmental monitoring. Indeed, it has been demonstrated that water vapor, present in the real environment for monitoring, strongly interacts with the surface or interface of a ZnO nanostructure, which leads to a significant fluctuation of its electrical and UV sensing properties [17–19]. Although the effect of humidity on UV sensing properties of ZnO nanostructure has been investigated [20–22], the elimination of cross-sensitivity of ZnO-based UV sensors to environmental humidity is still a major challenge. This is even more critical when they are made on paper substrate. As the paper is hygroscopic, the effect of moisture can cause additional significant fluctuations in the conductivity of paper-based devices. So far, the most applicable approaches to reduction of the influence of humidity include either coating paper with a superhydrophobic layer [23–27] or its chemical modification [28,29]. Even though those approaches are effective, they require additional processing steps, making the overall process more time-consuming and costlier. One interesting route to process paper substrate is by use of laser processing technique, which represents a simple, fast and scalable alternative to coating and chemical modification techniques and offers many advantages because of its capability of selective treatment and its fine spatial resolution [30–32]. It has been used to control the wetting properties of paper substrate for microfluidic applications [32–34]. In this work, we introduce the laser irradiation post-processing technique to withstand the influence of humidity and to improve the electrical properties of ZnO based UV detectors and screen-printed devices printed on paper substrate. Effects of the laser irradiation on the conductivity and UV sensing performance of the screen-printed ZnO nanoparticles (NPs) were studied in detail. Afterwards, both dark current and UV photocurrent of the laser treated ZnO UV sensors were measured in air with varied relative humidity (RH) to investigate the effect of water vapor on the ZnO film devices. Basic mechanisms for the observed behavior were discussed and correlated with results from structural analysis of the ZnO film. The results showed that the laser treated UV sensor had excellent compatibility between stability and sensitivity, response and recovery time, and reducing the impact of humidity.

2. Materials and Methods

The concept of the paper-based UV sensor is based on the resistive transduction principle, consisting of a nanostructured ZnO photosensitive layer deposited on interdigitated electrodes (IDE) that are printed on paper substrate, as shown in the Figure 1a.
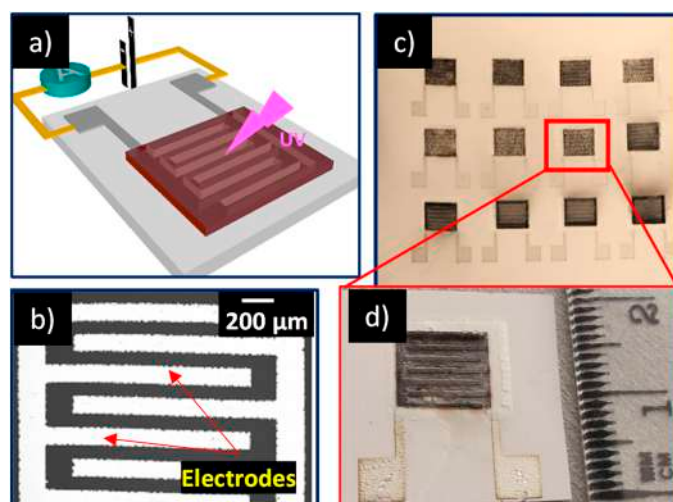

Figure 1. (**a**) Process sequence for fabrication of the paper-based devices; (**b**) SEM (Scanning electron microscope) image of the silver interdigitated electrodes; (**c**,**d**) Optical images of laser sintered devices fabricated on a paper substrate.

2.1. Device Fabrication

A simple, economic and scalable technological process, consisting of two screen-printing steps and a laser-postprocessing step, was used for the fabrication of the paper-based UV sensors. A schematic representation of the fabrication steps is described in the Figure S1. Firstly, a commercial silver paste (HPS-021LV, Novacentrix, Austin, TX, USA) was screen-printed with a semi-automatized screen-printer (EKRA 2H screen-printer, Dornstadt, Germany) on the paper substrate to design the IDEs and baked in an oven at 110 °C for 15 min. An individual digit of the IDE structure was 4 mm long and 170 μm wide. It was separated by a gap of 100 μm from the next digit, as shown in the Figure 1b exhibiting SEM (Scanning electron microscope, HITACHI TM3030, Tokyo, Japon) image of Ag interdigitated electrodes.

In order to fabricate the sensitive layer, based on commercial ZnO nanoparticles (Alfa Aesar™, particle size <25 nm, Kandel, Germany), a functional paste was developed [35]. The paste composition was optimized to meet the criteria: (i) used chemicals should be cost-efficient and environmentally friendly; (ii) paste components should be suitable for laser treatment (boiling point <500 °C); and (iii) paste should produce thick uniform film on top of the electrodes, with preserved properties of ZnO nanomaterial. Main components of the paste were solvent, binder, dispersant and the nanomaterial. Water as solvent was not suitable for final application of printed structure, so ethanol was used as solvent. Since the conducted research was focused on design of sensors with minimum humidity interference, we used PVP (Poly vinyl pyrrolidone) as binder because of its slightly better stability in higher humidity conditions in comparison to other commonly used binders, such as cellulose [36]. For the dispersant, we opted to use alpha-terpineol, which is environmentally friendly, has a relatively low boiling point and is suitable for laser treatment. First, 2 g of PVP (Sigma-Aldrich, St. Louis, MO, USA) was dissolved in 10 mL of ethanol. Afterwards, 1 g of ZnO nanopowder was dispersed in 400 μL of terpineol (Sigma-Aldrich, St. Louis, MO, USA), followed by the addition of 600 μL of PVP solution. High loading ratio of nanomaterial has proven to be optimal for the screen-printing of the sensitive layer, providing desired film thickness and uniformity.

Obtained suspensions were treated with ultrasonic homogenizer (Bandelin HD-70, Berlin, Germany), operating in continuous mode at 40% of total power. Duration of ultrasonic homogenization was 10 min.

2.2. Laser Treatment

The laser treatment of printed films was carried out by using a diode-pumped Nd:YAG laser cutter Rofin-Sinar Power Line D–100, operating in the NIR (Near-infrared) range at 1064 nm. Frequency of the laser pulse was set at 65 kHz, and the speed of the displacement was adjusted to 500 mm s^{-1} in order to obtain sufficient pulse overlapping. The laser fluence was varied by adjusting the laser current. One sample was kept untreated to be used as a reference, and two samples were treated with the input current values of 29 A and 30 A, corresponding to laser fluences of 0.21 J cm^{-2} and 0.23 J cm^{-2}, respectively. The Figure 1d shows the laser treated films sample with laser treated screen-printed ZnO nanoparticles. Figure 1c exhibits a matrix of laser treated samples, providing clear evidence that the developed process can be easily scaled-up for the large-scale fabrication of paper-based electronic devices.

2.3. Device Characterization

The morphology of the screen-printed ZnO film was examined by atomic force microscopy (AFM) in tapping mode. In order to precisely resolve grain boundaries, magnitude of AFM cantilever was recorded during the tapping mode imaging as well, since this signal is very sensitive to abrupt changes in the morphology. Surface roughness was calculated as a root mean square of the height distribution. The wetting characteristic of the sample was carried out by measuring contact angles using the sessile drop technique. A liquid droplet of about 2 μL in volume was dropped on the sample's surface with a micropipette.

The image of the liquid droplet was captured by a digital camera (uEye, IDS, Obersulm, Germany) attached to a microscope (Microzoom, Bausch and Lomb, Rochester, NY, USA) with 2.25× magnification and computed with the IDS camera manager software (IDS, Obersulm, Germany). The recorded droplet images were analyzed with the DropSnake Java plug-in for the ImageJ software (1.8.0, Wayne Rasband, Bethesda, MD, USA) based on B-spline snakes (active contours) to shape the drop [37].

3. Results and Discussion

3.1. Characterization of Laser-Treated ZnO Surface

Figure 2 exhibits top- and side-view SEM images of the ZnO film before and after laser treatment at 0.21 and 0.23 J cm^{-2} laser fluences, which clearly demonstrates that laser irradiation induces significant modifications of the film morphology. From SEM imaging of the untreated film, it can be established that nano-sized particles packed together by the dried organic additives formed a flat and uniform surface layer. When irradiated at 0.21 J cm^{-2}, the film exhibited bigger pores due to the formation of melted droplets. These droplets were formed during the breaking of the large agglomerates accomplished by laser thermal evaporation of organic components. With further increase of the laser fluence at 0.23 J cm^{-2}, the screen-printed film was transformed into solidified and dense ceramic material due to the complete release of the organic components and the sintering effect.
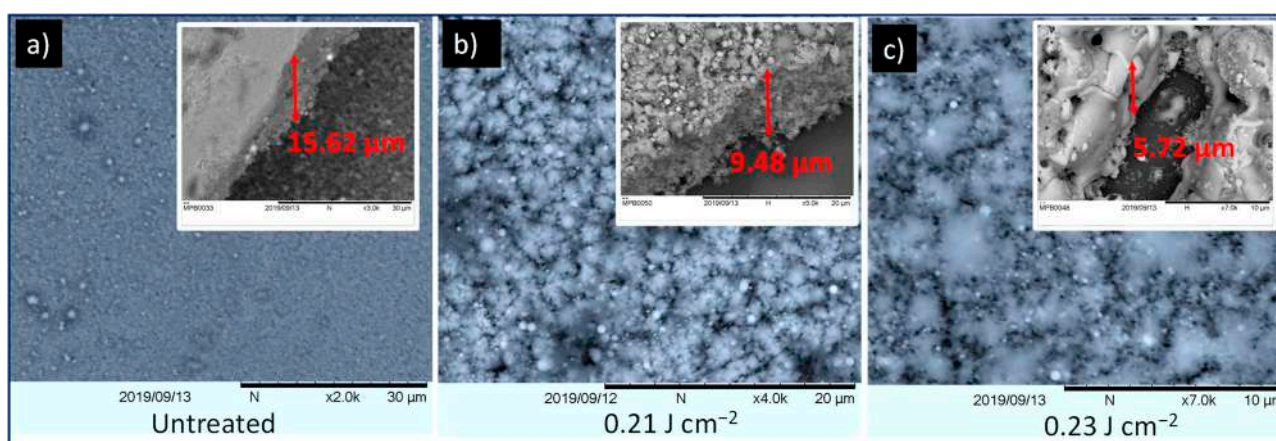

Figure 2. SEM images of (**a**) untreated screen-printed ZnO film, and laser-treated at (**b**) 0.21 J cm^{-2} and (**c**) 0.23 J cm^{-2}. Inset: side view of untreated and treated samples.

Additionally, the presented results demonstrate that the film thickness reduced from 15.6 μm to 9.5 μm and 6 μm after irradiation at 0.21, and 0.23 J cm^{-2}, respectively, which is in agreement with the profile analysis provided in the supporting information (Figure S2). This reduction in film thickness can be directly correlated to the removal of organic binder components with laser radiation and the densification of the screen-printed ZnO film during the sintering process. Furthermore, it can be noticed from the EDX (Energy-dispersive X-ray) characterization, shown in Figure S3, that the Zn and O signatures are present in the untreated and laser treated samples, while carbon signature is considerably reduced in the laser treated sample. This confirms that the laser irradiation does not change the chemical composition of the ZnO nanoparticles or remove organic components of the printed paste matrix.

Therefore, additional investigations were performed by atomic force microscopy (AFM) in tapping mode to explore the change of surface morphology in the laser sintered samples. Figure 3a presents images of the AFM magnitude of the untreated and all treated samples, which emphasize grains and grain boundaries. As can be seen, the morphology significantly changes from a flat surface with small grains in the case of the untreated sample, to very rough surfaces with large grains in the case of the treated samples.

Therefore, these images clearly represent the sintering process where small grains are merged into bigger ones. The underlying morphological changes during the sintering are summarized in the bottom row of Figure 3, in which Figure 3b shows characteristic height profiles from topographic images, while Figure 3c displays the surface roughness. An average grain diameter of the selected grains (encircled by dashed lines in the magnitude images) is presented partly in Figure 3d. The height profile of the untreated sample was a rather flat line, the surface roughness was around 30 nm, while the diameter of the selected grain was around 270 nm. On the other hand, the surface roughness of the treated samples were in the range of 200–300 nm, with some grains being larger than 2 μm.
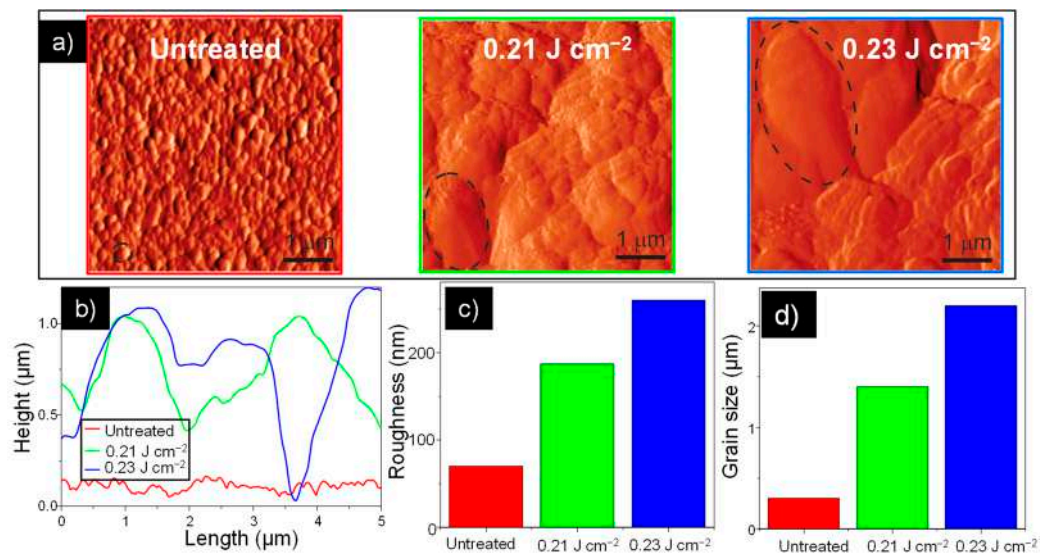
Figure 3. (**a**) AFM characterization of the untreated sample and samples treated at 0.21 and 0.23 J cm^{-2}. Inset: Corresponding 3D morphologies. (**b**) Surface profile from AFM analysis of the untreated and laser treated samples. (**c**) Roughness measurement of the investigated screen-printed films. (**d**) Grain size measurement of the investigated screen-printed films.

Figure 4 shows the contact angle of the untreated sample and samples treated with 0.21 and 0.23 J cm^{-2} laser fluence, where it can be noticed that hydrophobicity of the ZnO film increases with increase in the laser fluence. Clearly, a water droplet stands stable on the laser treated films, while it spreads out on the untreated sample. The wettability behavior of a surface is strongly related to the surface morphology [38]. From the AFM measurements, we established that morphology and roughness of the film surfaces change with the increase of the laser fluence. The surface of the untreated film (Figure 4a) with low surface roughness shows a low contact angle with hydrophilic behavior. With the rise of the surface roughness the contact angle increased, indicating a hydrophobic behavior for the sample treated at 0.21 J cm^{-2} and super hydrophobic behavior for the sample treated with higher laser fluence 0.23 J cm^{-2}. For porous nanostructured surfaces, the Cassie and Baxter (CB) model is usually applied for the description of wetting properties [39]. According to the CB model, the water contact angle on the porous surface is greatly influenced by the surface fraction of solid–liquid and liquid–air interfaces on the solid surface. In the CB wetting state, the large volume of air trapped between the grains prevents the water droplet from penetrating into the free space and the water droplet is suspended above the substrate unstably. Within such a framework, a hydrophilic surface can be modified into a hydrophobic one, and the contact angle increases with the ratio of water–air interface to the total area because air pockets formed below the water droplet minimize the interfacial energy. Considering that surface roughness of ZnO films increase with laser treatment, the fraction of interfacial area between air and liquid also increases. For highly rough surfaces, more air can be trapped within the interstices, increasing measured contact angle. The increased surface roughness and additional trapped air prevent further penetration of the

water droplet into the solid surface, giving rise to the observed shift from hydrophilicity to super-hydrophobicity.
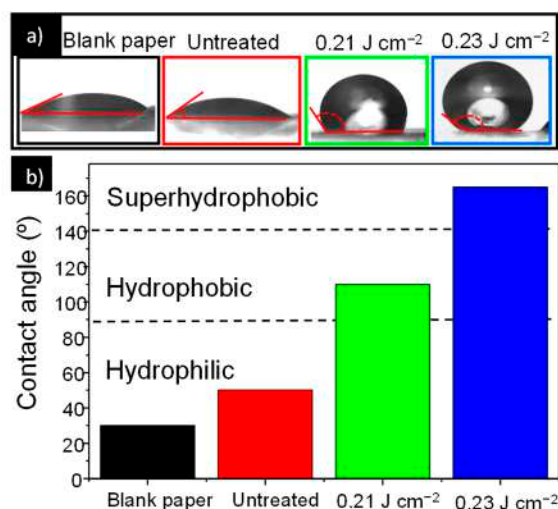

Figure 4. (**a**) Photographs of water droplet shape on the untreated and laser treated ZnO screen printed films. (**b**) Contact angle measured for untreated and laser treated samples.

3.2. UV Detection Performances

Figure 5a displays the dark current–voltage (I–V) characteristics, together with the photocurrent of the untreated samples and samples sintered with 0.21 J cm^{-2} and 0.23 J cm^{-2} laser fluences, measured in the -5 V to 5 V range at ambient humidity of 45%. Analysis of the obtained results clearly reveals that increase in laser fluence induces a significant increase in the dark current values, thus improving the conductivity of the printed ZnO film. Indeed, for the untreated sample, the profile of the I(V) curve corresponds to that of the material with poor conductivity with 3.42 nA at 5 V, whereas the I(V) curve of the sample treated with 0.23 J cm^{-2} has 5 orders of magnitude higher current (935 μA at 5 V). For porous nanomaterials, where nanoparticles are packed together, the conductivity is greatly affected by a mechanism governed by the grain-boundary resistance, since the resistance at these contacts is much higher than the resistance across the grains. The conduction channels in the ZnO–NP film include NP–NP junctions, and electrons must overcome the junction barriers to pass from one nanoparticle to another. Using AFM measurements, it was determined that during the sintering process, most of these grain boundaries vanished as the nanoparticles form neck like structures and the grains connected, reducing the junction barrier and creating a conductive path for electron transfer. In this case, the grain conductivity becomes dominant, leading to an observed increase in the current value.

Figure 5a also demonstrated that there was a significant increase in the photocurrent of all the samples when they were exposed to 360 nm wavelength at 10 mW cm^{-2}. This excitation wavelength was chosen to be in the vicinity of the optical band gap of ZnO (Eg = 305–395 nm) [40]. Moreover, it was noticed that a relatively high photocurrent ($\approx$300 nA) was obtained at zero bias for the sample treated at 0.23 J cm^{-2}, offering the possibility to use this laser treated device as a self-powered, paper-based photodetector system. The Figure 5b depicts the photocurrent-to-dark current ratio (called the photoresponse) as a function of the time, which compares the switching characteristics of the investigated samples under a bias of 5 V. Figure 5b demonstrated that a significant increase in the photoresponse was observed under UV light illumination for the untreated samples, as well as for the samples treated at 0.21 and 0.23 J cm^{-2}, confirming the results from Figure 5a.
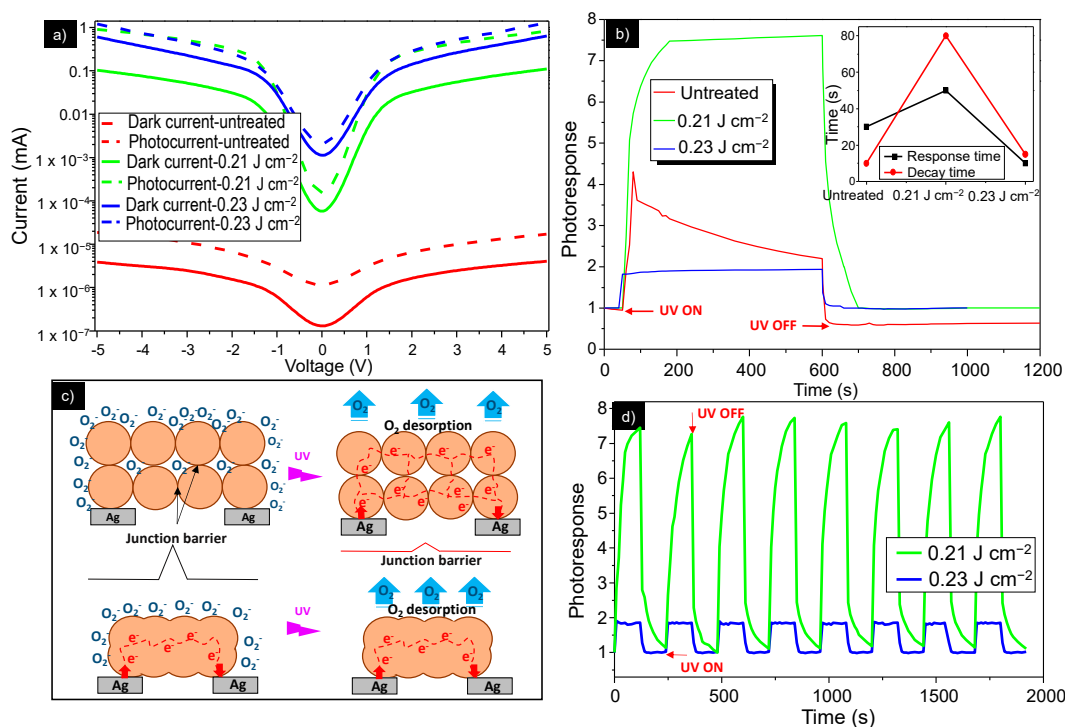
Figure 5. (**a**) I–V curves for uncoated and untreated samples and samples sintered at 0.21, and 0.23 J cm^{-2} with and without UV illumination. (**b**). Dynamic response behavior (response/recovery times) for the untreated and laser treated samples under UV illumination (**c**) Schematic diagram of the NP–NP junctions. (**d**) Time-resolved photoresponse of the ZnO device treated at 0.21 and 0.23 J cm^{-2} under a continuous UV light rectangle pulse.

However, the untreated device showed poor stability, with photoresponse decreasing gradually after the light source was switched on, while the laser treated samples showed good stability with constant photocurrent values under UV illumination, and a return to the initial value after switching off the light source. This can be attributed to some residual organic additives in the untreated screen-printed film, resulting in a poor conducting path for the electron transfer between nanoparticles, thus generating unstable conductivity. During the sintering process, the organic additives were removed from the film, creating better ZnO nanoparticle interconnection and thus the conducting path for electron transfer.

The device sintered at 0.21 J cm^{-2} shows better photosensitivity than the film sintered at 0.23 J cm^{-2}, which is due to its more efficient structure and morphology. The processes of generating and transporting carriers in the laser sintered devices are illustrated in the schematic diagram shown in Figure 5c. The photodetection property of the ZnO NPs-based screen-printed film is strongly influenced by two mechanisms: the adsorption and desorption of oxygen in the air. In the absence of photons, oxygen molecules adsorb on the surface of the ZnO nanoparticles as negatively charged ions, by capturing free electrons from the n-type ZnO. This process creates a low-conductivity depletion layer near the surface of the NPs. When the film was irradiated with UV light, electron-hole pairs were created in the depletion region and the negatively charged surface species traps the holes and releases the electrons into the conduction band of ZnO, so the current gradually increases until saturation. The conduction channels in the ZnO NPs detectors also include NP–NP junctions. Electrons must get over the junction barrier to pass from one NP to another. These barriers formed by the surface depletion layers can govern the charge transport within the film under UV illumination.

When treated at 0.23 J cm^{-2}, the film becomes more compact and bulkier, with bigger grains, lower porosity and thickness reducing surface-to-volume ratio of the film structure compared with the structure of the film treated at 0.21 J cm^{-2}. This facilitates the penetration of oxygen species into the inner film layers, ensuring the participation of the nanoparticles

from whole film in the UV sensing mechanism. Therefore, under illumination, the film treated with 0.23 J cm^{-2} fluence provides less active surface area and lower rate of oxygen desorption, resulting in a lower photocurrent. Additionally, the structure of the NP–NP junction is beneficial for the electrons to flow through the nanoparticle networks under UV light illumination, giving rise to the increase in photocurrent.

The inset in Figure 5b shows decay and rise time of the untreated and laser treated devices, defined respectively as the time required for photocurrent to drop from 90% to 10% and rise from 10% to 90% of its maximum value. The sample treated at 0.23 J cm^{-2} had a shorter response time than the sample treated at 0.21 J cm^{-2}, with decay and rise time of 10 s, which is comparable with other paper-based UV-detectors [8,41].

Furthermore, in order to examine the repeatability of the screen-printed paper-based ZnO UV detectors, the time-resolved photoresponse at 5 V bias with multiple UV on/off cycles was measured, in which both the turn-on and turn-off times of the UV light equaled 2 min. The Figure 5d shows height cycles of photocurrent switching, demonstrating very good repeatability and sensitivity of the two laser treated photodetectors.

3.3. Suppressed Response to Humidity by Laser-Post Processing Treatment

The influence of humidity was evaluated by calculating the device's response given by the ratio of the initial electrical resistance (R_0) at zero humidity, used as a baseline, to the electrical resistance when humidity is introduced (R_m), measured between the IDE. The inclusion of an uncoated paper allowed us to assess whether the ZnO screen printed film coating suppresses the water vapor absorption. The results shown in Figure 6a disclose the strong response differences between different samples, clearly indicating the effects of the screen-printed films and laser surface modification. For the uncoated paper, an important rise of the response is observed when humidity increases, with two times increased response with increasing RH from 0 to 10%, and at 3 orders of magnitude higher at moderate humidity levels (60%) than at 0% RH. The untreated ZnO sample shows a lower sensitivity to humidity than the uncoated sample. However, the sensitivity to humidity of the untreated sample was still significant, at 2 orders of magnitude higher at moderate humidity levels (60%) than at 0% RH. It was evident that the samples treated with laser exhibit a negligible response to humidity, revealing a very poor sensitivity to humidity of the laser treated ZnO films. This difference in humidity sensitivity between the untreated and laser treated samples can be directly correlated to their different surface wettability properties. The inset in Figure 6a depicts the relationship of the contact angle and response to humidity in the investigated samples. It was noticed that the samples with hydrophobic surfaces were sensitive to humidity, while humidity did not affect the laser treated samples with hydrophilic surfaces. Indeed, when the sensor film was hydrophilic, the water nucleation barrier was low, yielding high nucleation rate due to the strong attraction forces between the surface and the water molecules. This implies that water vapor is strongly adsorbed onto the sample surface, resulting in high humidity response. When the sensor film was hydrophobic, the energy barrier was high, thus minimizing the water vapor adsorption onto the film surface, which resulted in roughness induced non-wetting properties and no humidity interference.

Figure 6b showed the UV photoresponse of the investigated samples cross-linked with different humidity levels of 0%, 45% and 80%. It was noticed that the photoresponse of the untreated samples were greatly affected by the presence of water molecules, whereas the effect of the humidity on the photoresponse of the laser treated samples can be neglected. Indeed, the photoresponse of the untreated sample decreased with the humidity increase. This was due to the fact that water molecules replaced the previously surface adsorbed ionized oxygen species, and hence released electrons into the conduction band, a process which partially annihilates the depletion layer, leading to a rise in the dark current, as shown in the Figure 6a. Under the UV illumination, the dissociated H_2O molecules on the surface of the ZnO film capture both electrons and holes generated by UV light, leading to a decrease of carrier density and thus lower photoconductivity. At low RH <50%, the effect

of O_2 desorption is more pronounced, so that the photoresponse slightly decreased with the humidity but it was still detectable. At high RH, around 80%, the effect of the dissociated H_2O capturing electrons and holes becomes more significant due to a discrete water layer formed on the ZnO film surface, which generates a humidity-induced degradation of ZnO-based photodetector with a photoresponse almost undetectable. As seen in Figure 6c, in the case of the laser treated samples, the photoresponse does not change with the humidity level, due to the roughness engineered hydrophobic surface that hampers water molecules to be absorbed at the surface of the ZnO film, as previously explained.
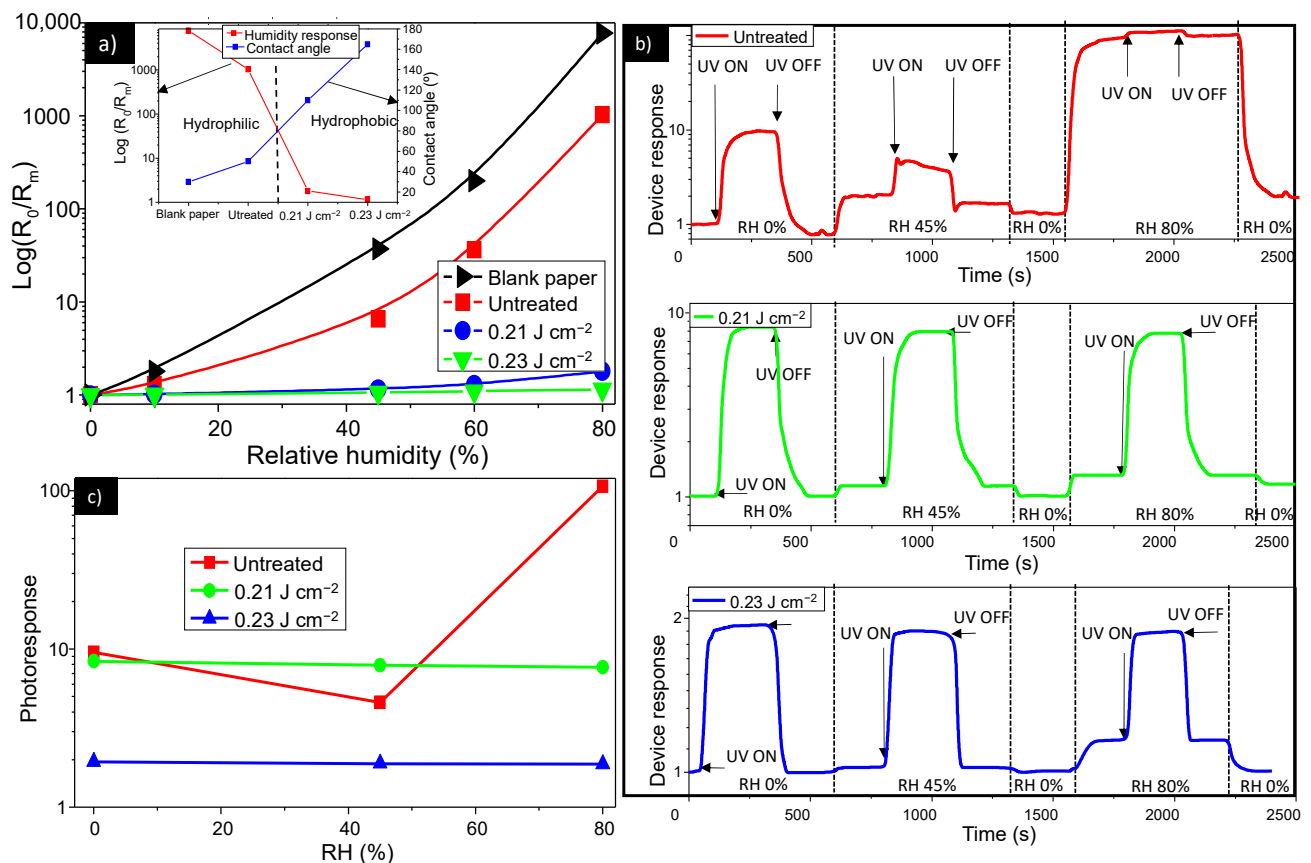
Figure 6. (**a**) Electrical resistance changes for the untreated and laser treated devices as a function of RH (Relative Humidity). Inset: Humidity response at 60% and contact angle as a function of the laser fluence. (**b**) Dynamic response of untreated and treated ZnO sensor to UV light at various humidity levels. (**c**) Photoresponse of the untreated and laser treated samples as a function of RH.

The laser-profiling of the sensitive layer surface roughness provides us with a powerful tool for the management of the film wettability properties, with high impact on tuning of the device sensitivity toward humidity. The undertaken approach can be easily optimized for fabrication of humidity-sensitive ZnO film that can be used for humidity sensors or for fabrication of paper-based ZnO film with no humidity interference that can be used for other electronic devices like UV detectors.

4. Conclusions

In summary, we developed a new strategy to reduce humidity interference on paper-based UV sensor. The proposed approach is fast, cost-effective, scalable, easy-to-operate and paper-friendly, since they do not require annealing steps at high temperatures. The effects of the laser fluence on morphology, electrical properties, UV and humidity sensing properties were disclosed. The ZnO film conductivity and UV photoresponse were improved and the influence of the humidity was considerably reduced by properly adjusting

the laser fluence. It was found that this phenomenon is correlated to the change of the morphology and structure of the ZnO film generated by the laser irradiation. Additionally, the resulting UV sensors showed good repeatability and relatively short response time. Therefore, the possibility of fabricating paper-based sensing devices with no humidity impact in a rapid and large-scale manner paves the way to low-cost solutions of sophisticated paper-based electronics with low environmental footprint.

Supplementary Materials: The following are available online at https://www.mdpi.com/2079-4991/11/1/80/s1, Figure S1: Process sequence of the humidity sensors, Figure S2: Thickness profile of the ZnO films, Figure S3: EDX profiles of the untreated and treated ZnO films.

Author Contributions: Conceptualization, G.D.; data curation, G.D. and B.V.; formal analysis, G.D., M.R. and B.V.; investigation, G.D.; methodology, G.D. and M.R.; resources, M.R. and B.V.; supervision, G.D.; validation, G.D. and M.R.; visualization, G.D., M.R. and B.V.; writing—original draft preparation, G.D.; writing—review and editing, M.R. and B.V. All authors have read and agreed to the published version of the manuscript.

Data Availability Statement: The data presented in this study are available on request from the corresponding author.

Conflicts of Interest: The authors declare no conflict of interest.

References

1. Ha, D.; Fang, Z.; Zhitenev, N.B. Paper in Electronic and Optoelectronic Devices. *Adv. Electron. Mater.* **2018**, *4*, 1700593. [CrossRef]
2. Bordbar, M.M.; Tashkhourian, J.; Hemmateenejad, B. Structural Elucidation and Ultrasensitive Analyses of Volatile Organic Compounds by Paper-Based Nano-Optoelectronic Noses. *ACS Sens.* **2019**, *4*, 1442–1451. [CrossRef] [PubMed]
3. Ratajczak, K.; Stobiecka, M. High-performance modified cellulose paper-based biosensors for medical diagnostics and early cancer screening: A concise review. *Carbohydr. Polym.* **2020**, *229*, 115463. [CrossRef] [PubMed]
4. Samir Kamel, S.; Khattab, T.A. Recent Advances in Cellulose-Based Biosensors for Medical Diagnosis. *Biosensors* **2020**, *10*, 67. [CrossRef] [PubMed]
5. Pradela-Filho, L.A.; Noviana, E.; Araújo, D.A.G.; Takeuchi, R.M.; Santos, A.L.; Henry, C.S. Rapid Analysis in Continuous-Flow Electrochemical Paper-Based Analytical Devices. *ACS Sens.* **2020**, *5*, 274–281. [CrossRef]
6. Ummartyotin, S.; Manuspiya, H. A critical review on cellulose: From fundamental to an approach on sensor technology. *Renew. Sustain. Energy Rev.* **2015**, *41*, 402–412. [CrossRef]
7. Vicente, A.T.; Araújo, A.; Mendes, M.J.; Nunes, D.; Oliveira, M.J.; Sanchez-Sobrado, O.; Ferreira, M.P.; Águas, H.; Fortunato, E.; Martins, R.J. Multifunctional cellulose-paper for light harvesting and smart sensing applications. *Mater. Chem. C* **2018**, *6*, 3143–3181. [CrossRef]
8. Sahoo, K.; Mohanty, B.; Biswas, A.; Nayak, J. Role of hexamethylenetetramine in ZnO-cellulose nanocomposite enabled UV and humidity sensor. *Mater. Sci. Semicond. Process.* **2020**, *105*, 104699. [CrossRef]
9. Zhang, G.; Liao, Q.; Ma, M.; Gao, F.; Zhang, Z.; Kang, Z.; Zhang, Y. Uniformly assembled vanadium doped ZnO microflowers/bacterial cellulose hybrid paper for flexible piezoelectric nanogenerators and self-powered sensors. *Nano Energy* **2018**, *52*, 501–509. [CrossRef]
10. Chen, L.; Cui, J.; Sheng, X.; Xie, T.; Xu, T.; Feng, X. High-performance photoelectronic sensor using mesostructured ZnO nanowires. *ACS Sens.* **2017**, *2*, 1567–1572. [CrossRef]
11. Martinez, A.G.; Santana, G.; Güell, F.; Martínez-Alanis, P.R.; Dutt, A. Photoluminescence of ZnO Nanowires: A Review. *Nanomaterials* **2020**, *10*, 857. [CrossRef] [PubMed]
12. Lee, M.E.; Armani, A.M. Flexible UV exposure sensor based on UV responsive polymer. *ACS Sens.* **2016**, *1*, 1251–1255. [CrossRef]
13. Carvalho, J.T.; Dubceac, V.; Grey, P.; Cunha, I.; Fortunato, E.; Martins, R.; Clausner, A.; Zschech, E.; Pereira, L. Fully Printed Zinc Oxide Electrolyte-Gated Transistors on Paper. *Nanomaterials* **2019**, *9*, 169. [CrossRef] [PubMed]
14. Liao, Q.; Zhang, Z.; Zhang, X.; Mohr, M.; Zhang, Y.; Fecht, H.J. Flexible piezoelectric nanogenerators based on a fiber/ZnO nanowires/paper hybrid structure for energy harvesting. *Nano Res.* **2014**, *7*, 917. [CrossRef]
15. Gullapalli, H.; Vemuru, V.S.M.; Kumar, A.; Botello-Mendez, A.; Vajtai, R.; Terrones, M.; Nagarajaiah, S.; Ajayan, P.M. Flexible piezoelectric ZnO–paper nanocomposite strain sensor. *Small* **2010**, *6*, 1641. [CrossRef]
16. Pimentel, A.; Samouco, A.; Nunes, D.; Araújo, A.; Martins, R.; Fortunato, E. Ultra-Fast Microwave Synthesis of ZnO Nanorods on Cellulose Substrates for UV Sensor Applications. *Materials* **2017**, *10*, 1308. [CrossRef]

17. Hsu, C.L.; Li, H.H.; Hsueh, T.J. Water-and humidity-enhanced UV detector by using p-type La-doped ZnO nanowires on flexible polyimide substrate. *ACS Appl. Mater. Interfaces* **2013**, *5*, 11142–11151. [CrossRef]

18. Li, Y.B.; Valle, F.D.; Simonnet, M.; Yamada, I.; Delaunay, J. Competitive surface effects of oxygen and water on UV photoresponse of ZnO nanowires. *J. Appl. Phys. Lett.* **2009**, *94*, 023110. [CrossRef]

19. Qiu, X.; Tang, R.; Zhu, J.; Oiler, J.; Yu, C.; Wang, Z.; Yu, H. The effects of temperature, relative humidity and reducing gases on the ultraviolet response of ZnO based film bulk acoustic-wave resonator. *Sens. Actuators B* **2011**, *151*, 360–364. [CrossRef]

20. Liu, Y.-J.; Zhang, H.-D.; Zhang, J.; Li, S.; Zhang, J.-C.; Zhu, J.-W.; Gong, M.-G.; Wang, X.-X.; Long, Y.-Z. Effects of Ce doping and humidity on UV sensing properties of electrospun ZnO nanofibers. *J. Appl. Phys.* **2017**, *122*, 105102. [CrossRef]

21. Lai, C.; Wang, X.X.; Zhao, Y.; Fong, H.; Zhu, Z.T. Effects of humidity on the ultraviolet nanosensors of aligned electrospun ZnO nanofibers. *RSC Adv.* **2013**, *3*, 6640–6645. [CrossRef]

22. Nobbs, J. The effect of water vapour on the photoconductivity of zinc oxide. *J. Phys. Chem. Solids* **1968**, *29*, 439–450. [CrossRef]

23. Gao, L.; Chao, L.; Hou, M.; Liang, J.; Chen, Y.; Yu, H.-D.; Huang, W. Flexible, transparent nanocellulose paper-based perovskite solar cells. *NPJ Flex. Electron.* **2019**, *3*, 4. [CrossRef]

24. Mates, J.E.; Schutzius, T.M.; Bayer, I.S.; Qin, J.; Waldroup, D.E.; Megaridis, C.M. Water-Based Superhydrophobic Coatings for Nonwoven and Cellulosic Substrates. *Ind. Eng. Chem. Res.* **2014**, *53*, 222–227. [CrossRef]

25. Bollstrom, R.; Pettersson, F.; Dolietis, P.; Preston, J.; Oster-backa, R.; Toivakka, M. Impact of humidity on functionality of on-paper printed electronics. *Nanotechnology* **2014**, *25*, 094003. [CrossRef]

26. Ren, F.; Guo, H.; Guo, Z.; Jin, Y.; Duan, H.; Ren, P.; Yan, D. Highly Bendable and Durable Waterproof Paper for Ultra-High Electromagnetic Interference Shielding. *Polymers* **2019**, *11*, 1486. [CrossRef]

27. Ogihara, H.; Xie, J.; Okagaki, J.; Saji, T. Simple Method for Preparing Superhydrophobic Paper: Spray-Deposited Hydrophobic Silica Nanoparticle Coatings Exhibit High Water-Repellency and Transparency. *Langmuir* **2012**, *28*, 4605–4608. [CrossRef]

28. De Medeiros, M.S.; Chanci, D.; Martinez, R.V. Moisture-insensitive, self-powered paper-based flexible electronics. *Nano Energy* **2020**, *78*, 105301. [CrossRef]

29. Baidya, A.; Ganayee, M.A.; Jakka Ravindran, S.; Tam, K.C.; Das, S.K.; Ras, R.H.A.; Pradeep, T. Organic Solvent-Free Fabrication of Durable and Multifunctional Superhydrophobic Paper from Waterborne Fluorinated Cellulose Nanofiber Building Blocks. *ACS Nano* **2017**, *11*, 11091–11099. [CrossRef]

30. Yao, Y.; Duan, X.; Niu, M.; Luo, J.; Wang, R.; Liu, T. One-Step Process for Direct Laser Writing Carbonization of $NH_4H_2PO_4$ Treated Cellulose Paper and Its Use for Facile Fabrication of Multifunctional Force Sensors with Corrugated Structures. *Cellulose* **2019**, *26*, 7423–7435. [CrossRef]

31. Khan, M.; Chantal, G. Laser processing for bio-microfluidics applications (part I). *Anal. Bioanal. Chem.* **2006**, *385*, 1351–1361. [CrossRef] [PubMed]

32. Balliu, E.; Andersson, H.; Engholm, M.; Ohlund, T.; Nilsson, H.E.; Olin, H. Selective laser sintering of inkjet-printed silver nanoparticle inks on paper substrates to achieve highly conductive patterns. *Sci. Rep.* **2018**, *8*, 10408. [CrossRef] [PubMed]

33. Hiep, D.H.; Tanaka, Y.; Matsubara, H.; Ishizaka, S. Fabrication of paper-based microfluidic devices using a laser beam scanning technique. *Anal. Sci.* **2020**, *36*, 1275–1278. [CrossRef] [PubMed]

34. Le, S.; Zhou, H.; Nie, J.; Cao, C.; Yang, J.; Pan, H.; Li, J.; Zhang, Y. Fabrication of paper devices via laser-heating-wax-printing for high-tech enzyme-linked immunosorbent assays with low-tech pen-type pH meter readout. *Analyst* **2017**, *142*, 511–516. [CrossRef]

35. Dubourg, G.; Radović, M. Multifunctional Screen-Printed TiO_2 Nanoparticles Tuned by Laser Irradiation for a Flexible and Scalable UV Detector and Room-Temperature Ethanol Sensor. *ACS Appl. Mater. Interfaces* **2019**, *11*, 6257–6266. [CrossRef]

36. Barański, A.; Dutka, D.; Dziembaj, R.; Konieczna-Molenda, A.; Łagan, J.M. Effect of Relative Humidity on the Degradation Rate of Cellulose. Methodology Studies. *Restaurator* **1970**, *25*, 68–74. [CrossRef]

37. Stalder, A.F.; Kulik, G.; Sage, D.; Barbieri, L.; Hoffmann, P. A snake-based approach to accurate determination of both contact points and contact angles. *Colloid Surf. A* **2006**, *286*, 92–103. [CrossRef]

38. Li, S.; Huang, J.; Chen, Z.; Chen, G.; Lai, Y. A review on special wettability textiles: Theoretical models, fabrication technologies and multifunctional applications. *J. Mater. Chem. A* **2017**, *5*, 31. [CrossRef]

39. Cassie, A.B.D.; Baxter, S. Wettability of porous surfaces. *Trans. Faraday Soc.* **1944**, *40*, 546–551. [CrossRef]

40. Tan, S.T.; Chen, B.J.; Suna, X.W.; Fan, W.J. Blueshift of optical band gap in ZnO thin films grown by metal-organic chemical-vapor deposition. *J. Appl. Phys.* **2005**, *98*, 013505. [CrossRef]

41. Fang, F.; Futter, J.; Markwitz, A.; Kennedy, J. UV and humidity sensing properties of ZnO nanorods prepared by the arc discharge method. *Nanotechnology* **2009**, *24*, 245502. [CrossRef] [PubMed]

Tunable Beam Steering at Terahertz Frequencies Using Reconfigurable Metasurfaces Coupled With Liquid Crystals

Borislav Vasić ⓘ, Goran Isić ⓘ, Romeo Beccherelli ⓘ, *Member, IEEE*, and Dimitrios C. Zografopoulos ⓘ

Abstract—**Metasurfaces with a spatially varying phase profile enable the design of planar and compact devices for manipulating the radiation pattern of electromagnetic fields. Aiming to achieve tunable beam steering at terahertz frequencies, we numerically investigate metasurfaces consisting of one dimensional arrays of metal-insulator-metal (MIM) cavities infiltrated with liquid crystals (LCs). The spatial phase profile is defined by a periodic voltage pattern applied on properly selected supercells of the MIM-cavity array. By means of the electro-optic effect, the voltage controls the orientation of LC molecules and, thus, the resulting effective LC refractive index. Using this approach, the spatial phase profiles can be dynamically switched among a flat, binary, and gradient profile, where the corresponding metasurfaces function as mirrors, beam splitters or blazed gratings, respectively. Tunable beam steering is achieved by changing the diffraction angle of the first diffraction order, through the reconfiguration of the metasurface period via the proper adjustment of the applied voltage pattern.**

Index Terms—**Beam steering, tunable metasurfaces, liquid crystals, terahertz frequencies.**

I. INTRODUCTION

TUNABLE beam-splitting and steering devices are integral components of terahertz (THz) systems that are required for wireless communications, measurements, imaging and sensing [1]–[3]. In addition to common electromechanical scanning and phased-array systems [4], there are several proposals for

dynamically tunable THz beam steering utilizing wedge-shaped devices [5] and leaky-wave antennas [6] with liquid crystals (LCs), gratings with semiconductors [7], [8] and specially designed THz systems [9]. Still, further developments are needed in order to engineer more compact and faster devices with increased efficiency and advanced functionalities.

One promising approach in this direction is the application of metasurfaces, namely planar and periodic arrays of subwavelength electromagnetic resonators which strongly enhance light-matter interaction [10], [11] and have been demonstrated to facilitate the design of efficient THz modulators [12]–[17]. Gradient metasurfaces [18]–[22] are a natural choice for beam-steering applications since they introduce a spatially varying phase shift at the interface between two media thus providing additional opportunities for wavefront shaping [23]–[26]. In the case of gradient metasurfaces with linear phase shift profile, the beam-steering angle is dictated by the gradient of the linear phase profile [23]–[25]. Therefore, tunable beam steering with such metasurfaces can be realized by dynamically varying the phase gradient [27]–[32], which is a known concept applied in tunable microwave reflectarrays [33]–[35] and optical phased arrays [36]. However, the rigorous approach requires changing the period of the metasurface with simultaneous readjustment of the phase in order to keep the linear phase shift from 0° to 360° within each period [37]–[40], which is challenging for practical realizations. The 360° phase-shift requirement is relaxed in binary metasurfaces, periodic structures with just two spatial zones introducing phase shifts of either 0° or 180°. They operate as beam splitters like classical binary optical gratings [41]. Tunable beam splitting with adjustable diffraction angles can be then realized by less demanding phase modulation between 0° and 180° [27], [42], [43].

The phase modulation is the underlying physical foundation for tunable beam steering with both gradient and binary metasurfaces. The modulation efficiency strongly depends on the selection of the tunable elements and their applicability for a specified frequency range. So far, semiconductors [7], [8], [31] and graphene [37], [44] have been mostly employed at THz frequencies. However, they are Drude materials with tunable absorption which makes them more suitable not for phase, but amplitude THz modulators [45], [46]. On the other hand, recently it has been demonstrated that the large inherent birefringence of LCs combined with the possibility for electrical
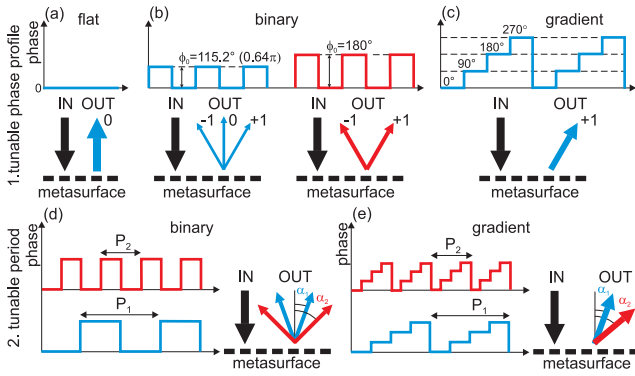
Fig. 1.   Principles of tunable beam steering: 1. control of DE for zero and first order is achieved by modulation of the phase profile from (a) flat to (b) binary, or to (c) gradient, 2. tunable angle α of the first diffraction order is obtained by changing the period of either (d) binary or (e) gradient metasurfaces.
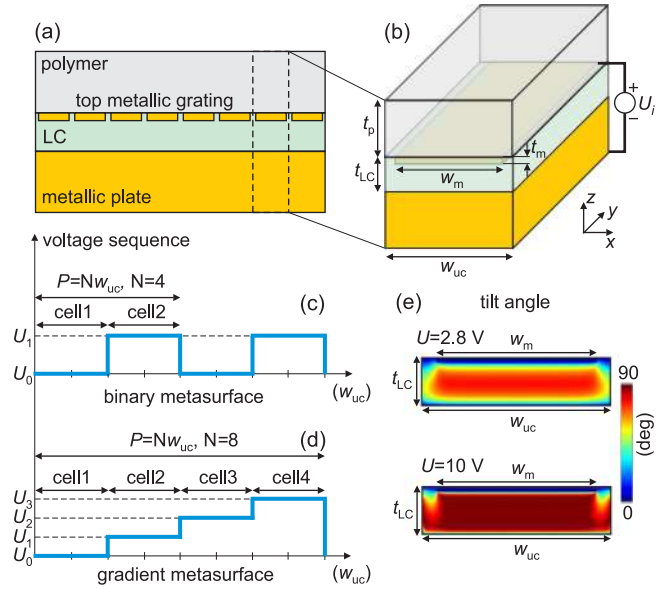

Fig. 2.   (a) Cross-section of considered metasurfaces and (b) unit cell. Voltage patterns for (c) binary and (d) gradient metasurfaces. (e) Tilt angle of LC molecules within in a single unit cell for two chracteristic bias voltages.

modulation of their refractive index render them promising for frequency tunable THz metamaterials, which can provide both amplitude [14], [47], [48] and phase [49] modulation. Still, the interplay between amplitude and phase modulation needs careful design.

In this paper, we investigate one-dimensional arrays of metal-insulator-metal (MIM) cavities infiltrated with LCs targeting the design of tunable binary and gradient metasurfaces at THz frequencies working in reflection mode. Compared to conventional LC cells, such MIM resonant cavities have been previously [14], [49] found particularly promising for LC-based technology as the enhanced light-matter interaction allows an orders of magnitude speedup in LC switching. The phase tuning is achieved by the electro-optic modulation of the spatial profile of the LC refractive index. The same metallic stripes that form the MIM resonant cavities are also employed for the application of the low-frequency LC control voltage. In binary metasurfaces, the LC refractive index is periodically varied in order to achieve periodic phase gratings with either $0°$ or ϕ_0 phase zones, where $\phi_0 \in [0°, 180°]$. Beam splitters with tunable diffraction efficiency (DE) are implemented by modulating the LC refractive index in the zones with non-zero phase ϕ_0 thus controlling the interplay of the DEs for the $0°$ and ± 1 orders. Next, we design gradient metasurfaces with a four-level discretized linear phase profile ($0°$, $90°$, $180°$, $270°$) that behave like blazed gratings thus allowing for switchable beam steering of the impinging THz beam between the $0°$ and $+1$ diffraction order. A routine for the maximization of DE in real lossy systems is also presented, leading to significant improvement in the grating's performance. In the case of both binary and gradient metasurfaces, the beam splitting/steering angle can be dynamically adjusted by reconfiguring the grating period, thanks to the subwavelength dimensions of the employed MIM resonant cavities.

II. Modulation Principles and Modeling

The physical principles for tunable beam steering of the proposed devices are illustrated in Fig. 1. The metasurface acts as a phase grating with tunable phase profile. DEs for a

grating with symmetrical rectangular phase profile are given by: $\cos^2(\phi_0/2)$ for zero order, $(2/\pi m)^2 \sin^2(\phi_0/2)$ for odd orders ($m = \pm 1, \pm 3, \ldots$), and zero for even orders ($m = \pm 2, \pm 4, \ldots$), where ϕ_0 is the phase difference between two levels as depicted in Fig. 1(b) [50]. A metasurface with flat phase ($\phi_0 = 0°$) operates as a mirror which just reflects an incoming wave (zero order) as depicted in Fig. 1(a). On the other hand, metasurfaces with the binary phase profiles presented in Fig. 1(b) act as beam splitters. If $\phi_0 = 115.2°$ (0.64π), the outgoing wave is split into three diffraction orders, 0 and ± 1, with same DE (higher orders are neglected due to low DE). Furthermore, the zero-order beam can be suppressed when the phase difference is exactly $\phi_0 = 180°$, leaving just the ± 1 diffraction orders.

Blazed gratings are realized by gradient metasurfaces with the sawtooth phase profile depicted in Fig. 1(c). They provide an additional option to single out just $+1$ (-1) diffraction order (for the positive (negative) phase slope with respect to the x-axis). For the sake of simplicity and practical realization, here the sawtooth profile is discretized into four phase levels $0°$, $90°$, $180°$, $270°$.

By changing the phase profile from flat to binary or gradient as presented in Figs. 1(a-c), it is possible to control the DE of zero and first order. In order to achieve beam steering with the same amplitude, but at a tunable angle, it is necessary to control the diffraction angle as shown in Figs. 1(d) and 1(e). The diffraction angle of the first order is $\alpha = \arcsin(\lambda/P)$, where λ is the wavelength and P is the grating period. Therefore, a tunable diffraction angle can be achieved by changing the metasurface period with simultaneous readjustment of the phase in order to keep either the binary or gradient profile.

The cross section of the considered metasurface is presented in Fig. 2(a), whereas its three-dimensional unit cell with indicated geometrical parameters is depicted in Fig. 2(b). The metasurfaces consist of a bottom gold plate, a layer of the nematic liquid

crystal with thickness t_{LC}, a top metallic grating made of parallel gold ribbons with width w_{m}, and a polymer layer with thickness t_{p} which serves as a substrate for the grating and simultaneously encapsulates the LC. The unit cell size is w_{uc}.

The phase profile of the metasurfaces is controlled by the pattern of voltage control signals U_i applied between the back-reflector ground plane and each one of the unit cells. The applied voltage controls the orientation of LC molecules and the spatial variation of the effective LC refractive index. The pattern of the LC bias voltages produces the desired phase profile along the x-axis of the metasurface. In the case of binary metasurfaces, this pattern consists of two voltage levels U_0 and U_1, with the low level U_0 fixed to zero, as schematically depicted in Fig. 2(c). The number of voltage levels in the pattern for gradient metasurfaces in Fig. 2(d) is defined by the number of discrete phase levels chosen for the approximation of the sawtooth phase profile, which is four in this study. We define a phase cell as series of k adjacent unit cells that have the same bias voltage and hence same phase value. The metasurface period/supercell in binary structures consists of 2 phase cells (2 k unit cells) corresponding to phase levels $0°$ and ϕ_0, whereas in gradient metasurfaces, it consists of 4 phase cells (4 k unit cells) implementing the phase levels $0°$, $90°$, $180°$, $270°$. Therefore, the metasurface period is defined as $P = Nw_{\mathrm{uc}}$, where N is the number of unit cells per period, 2k and 4k in the case of binary and gradient metasurfaces, respectively. Two examples for a binary metasurface with N = 4 and gradient metasurface with N = 8 are schematically shown in Figs. 2(c) and 2(d), respectively.

Numerical calculations of both the LC studies and full-wave propagation of the THz waves were done by means of the finite-element method using COMSOL Multiphysics. The voltage-dependent LC orientation and switching dynamics were solved by the Q-tensor implementation of the Landau-de Gennes theory for uniaxial nematics, a powerful tool capable of resolving biaxial solutions, nematic order variations and defects in complex LC systems [51]. The spatial profile of the local molecular orientation, which coincides with the optical axis of the unixial anisotropic LC, was calculated by minimizing the total energy in the LC bulk, composed by thermotropic, elastic, and electrostatic energy contributions. Once the LC orientation is known, the complex permittivity tensor which describes the LC dielectric properties in the THz spectrum was calculated and fed into an electromagnetic full-wave solver, using the same finely-resolved mesh employed in the LC studies. This way, the spatial variation of the LC anisotropic permittivity was rigorously taken into account in our analysis [14], [49]. The Drude model [52] was employed for gold permittivity. For both the equations governing LC orientation and electromagnetic wave propagation, periodic boundary conditions were imposed on lateral boundaries of the supercell. Our numerical model thus cannot account for the effects of the finite device surface area. However, all devices considered in this work are designed for steering well collimated incoming THz beams with millimeter-scale waists, meaning that the device active area will in practice extend laterally at least a couple of millimeters or circa 50 - 100 unit cells, so the edge effects will always be negligible.

The profile of the tilt angle, defined as the angle between the x-y plane and the LC local optical axis, for the nematic mixture 1825 [53] is given for two characteristic voltage levels in Fig. 2(e) ($t_{\mathrm{LC}} = 3.35\,\mu\mathrm{m}$). For zero voltage, the in-plane orientation of the molecules (xy-plane) is provided by well-established LC alignment layers, e.g. rubbed polymer such as Nylon-6 with negligible thickness as far as the electromagnetic problem is concerned. Strong anchoring along the y-axis with a pretilt angle of $1°$ was considered for the top and bottom aligning surfaces of the LC cell. The dielectric permittivity of the LC layer in the z-direction (which determines the spectral position of MIM cavity resonances) is then equal to the ordinary permittivity ε_o. Due to the electro-optic effect, the applied bias voltage (the example for $U = 2.8\,\mathrm{V}$ is given) and resulting electric field lead to the reorientation of the LC molecules. Finally, for 10 V, practically all LC molecules in the volume of the LC cell beneath the top metallic ribbon are oriented vertically (the tilt angle is $90°$) thus giving the extraordinary permittivity ε_e in z-direction. According to measurement results, the refractive indices of the highly birefringent nematic mixture 1825 around the working frequency of 2.5 THz are $n_o = 1.54 + \mathrm{j}0.013$ and $n_e = 1.911 + \mathrm{j}0.018$ [53] which gives a large change of the LC refractive index of around 0.37 for a low voltage sweep of 10 V only.

The metasurface shown in Fig. 2 operates as a tunable phase shifter when the MIM resonators are in the overcoupled regime [49], defined by the requirement that the resonant mode radiative decay rate γ_{rad} is larger than absorption decay rate γ_{abs} [14]. When $\gamma_{\mathrm{rad}} \gg \gamma_{\mathrm{abs}}$, the metasurface simultaneously provides both a large phase change and high reflection in the vicinity of resonance. By tuning the LC refractive index from n_o to n_e, the resonance is spectrally shifted producing a phase shift $\Delta\Phi$ at the fixed operating frequency f_{op}. The LC thickness t_{LC} is the main geometrical parameter which determines the relative magnitude of γ_{rad} and γ_{abs} and, consequently, the achievable phase shift. Therefore, in order to find the optimal structure, the reflectance and phase are calculated as a function of t_{LC} while other geometrical parameters are fixed. The unit cell size and metallic ribbon width in all binary and gradient metasurfaces considered here, are $w_{\mathrm{uc}} = 32\,\mu\mathrm{m}$ and $w_{\mathrm{m}} = 28\,\mu\mathrm{m}$, respectively. Such values provide the resonant frequency around the targeted $f_{\mathrm{op}} \approx 2.5$ THz. The top substrate is Zeonor, a cyclo-olefin polymer with very low losses at THz, with layer thickness of $40\,\mu\mathrm{m}$ and refractive index $1.518 + \mathrm{j}0.0009$, respectively [54]. Metallic ribbon arrays similar to those considered here have been experimentally patterned on Zeonor substrates by standard photolithography [55].

The power reflectance for zero voltage applied to all unit cells is given in Fig. 3(a). The resonance can be identified by the dip in the reflectance map which is red-shifted for a thicker LC layer while simultaneously the reflectance becomes higher. For 10 V of applied voltage, the resonance is significantly red-shifted compared to the previous case owing to the higher LC refractive index that interacts with the z-polarized resonant mode, while the overall reflectance is a bit lower as depicted in Fig. 3(b). The phase difference $\Delta\Phi$ between these two states is displayed in Fig. 3(c) indicating a large phase change across the resonance.
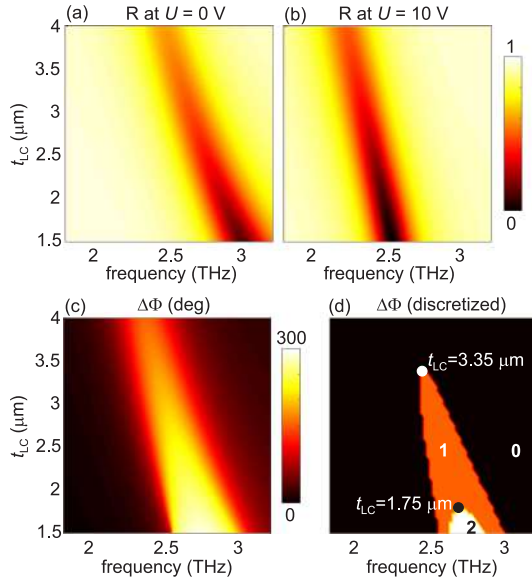
Fig. 3. The reflectance as a function of frequency and LC thickness t_{LC} for two voltages (the same voltage applied to all unit cells): (a) $U = 0\,V$ and (b) $U = 10\,V$. (c) Phase difference $\Delta\Phi$ between the cases for 0 V and 10 V, and (d) its discretized representation (for sake of better visibility), where the area with $\Delta\Phi \geq 180°$ ($\Delta\Phi \geq 270°$) is represented by 1 (2).

Fig. 4. The reflectance as a function of frequency and polymer layer thickness t_p for two voltages (the same voltage applied to all unit cells): (a) $U = 0\,V$ and (b) $U = 10\,V$. (c) Phase difference $\Delta\Phi$ between the cases for 0 V and 10 V.

Fig. 5. (a) Diffraction efficiency for 0th, 1st, and 2nd order as a function of frequency and voltage U_1 of the investigated binary metasurface for N = 8. (b) Diffraction efficiencies as a function of the voltage for the fixed operating frequency 2.42 THz.

Larger values of $\Delta\Phi$ are obtained with thinner LC cells because the decrease of t_{LC} in overcoupled MIM cavities reduces the total resonance linewidth $\gamma_{rad} + \gamma_{abs}$. However, this comes at the expense of bringing the resonant mode closer to critical coupling which implies a lower reflectance [14].

Areas with desired $\Delta\Phi$ are represented in the discretized phase map in Fig. 3(d) with three levels: "1" if $\Delta\Phi \geq 180°$ needed for binary metasurfaces, "2" if $\Delta\Phi \geq 270°$ needed for four-level gradient metasurfaces (this area is a subset of domain 1), whereas the rest of the phase map is not of interest and it is represented with "0" level. In order to design efficient metasurfaces, reflectance should be as high as possible. Therefore, the maximum LC thickness is selected to provide the maximum phase difference required for binary 180° and gradient metasurfaces 270°. These are found along the boundaries of domain 0 and 1 and a the boundaries between domain 1 and 2, respectively. It is worth noting that the choices for t_{LC} are in general, not unique for a single frequency. However we choose for the highest possible values of t_{LC}, such that the device does not suffer from additional losses. These values are $t_{LC} = 3.35\,\mu m$ for binary and $t_{LC} = 1.75\,\mu m$ for gradient metasurfaces, for an operating frequency $f_{op} = 2.42$ THz and 2.7 THz, respectively. The reflectance of the unit cell at $U = 0\,V$ and 10 V for the binary (gradient) grating is 0.71 and 0.62 (0.7 and 0.73), respectively.

Although the role of the top polymer layer is to act as a mechanical support for the proposed LC-based beam steering devices, it also influences both reflectance and phase difference because of Fabry-Pérot resonances. The power reflectance for two voltages $U = 0\,V$ and $U = 10\,V$ (the same voltage applied to all unit cells) and the phase difference between these two states are presented in Figs. 4(a-c), respectively, as a function of frequency and polymer layer thickness. As can be seen, both the
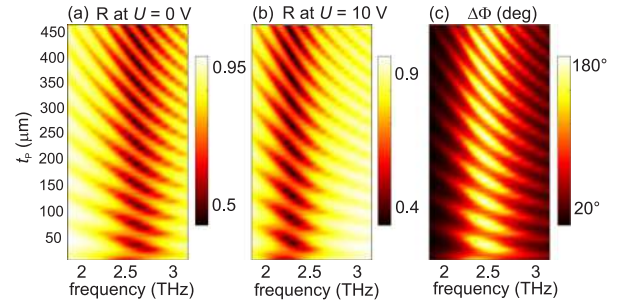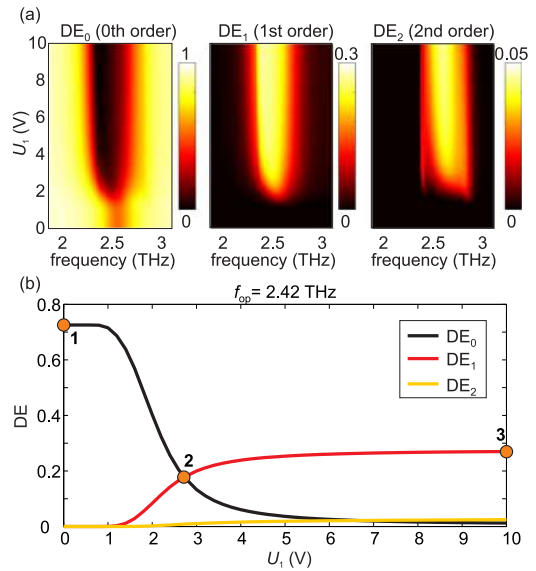
reflectance and phase difference are characterized with fringes due to Fabry-Perot resonances in the polymer layer. Therefore, the polymer thickness influences the device performance and it has to be taken into account. The chosen polymer is commercialized in foils with a set of thickness values. In the the current design, we have have selected $t_p = 40\,\mu m$, a value that does not deteriorate the operation of the device and that we already found suitable for the microfabrication of metallic structures [55].

III. TUNABLE BEAM SPLITTERS WITH BINARY METASURFACES

Having selected the LC thickness, all geometrical parameters of the investigated metasurfaces are defined. The analysis starts with a reference case of the binary metasurface with N = 8 unit cells per period, which acts as a beam splitter with tunable diffraction efficiency. The level U_1 in the voltage pattern shown in Fig. 2(c) is varied in the range 0–10 V. The maps for the voltage dependence of DEs for three lowest orders are depicted in Fig. 5(a), whereas the cross-sections of these maps for the
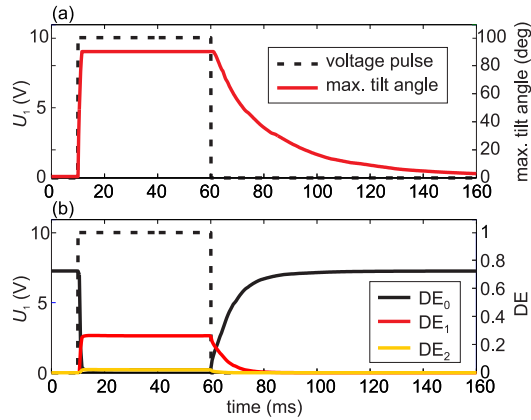
Fig. 6.   The transient response of the binary metasurface for a 50 ms and 10 V rectangular pulse: (a) the maximum tilt angle, and (b) DEs for three lowest diffraction orders.

Fig. 7. DE_1 as a function of frequency for the binary metasurface at $U_1 = 10\,V$. The bandwidth is defined as FWHM of DE_1.

operating frequency $f_{op} = 2.42$ THz are shown in Fig. 5(b). As can be seen, for zero voltage (working point 1), just zero order is reflected and the binary metasurface operates as a mirror, with a reflectance of 0.71, namely that of the unit cell in the case of $U = 0$ V, as calculated in Fig. 3(a). For $U_1 = 2.8$ V (working point 2), the metasurface divides an incoming wave into three beams, corresponding to $-1, 0, +1$ orders with the same DE of around 0.18. For sufficiently high voltage (working point 3 at $U_1 = 10$ V), the zeroth order is practically suppressed (DE is just 0.01). The metasurface then splits an incoming beam into -1 and $+1$ diffraction orders with the same DE of around 0.27. DE for the second order mode is low in the whole frequency range under investigation.

The transient response of the binary metasurface was investigated by applying a rectangular voltage pulse (with a duration of 50 ms and amplitude of 10 V). Results for the maximum tilt angle of LC molecules and DEs for the three lowest orders are illustrated in Figs. 6(a) and 6(b), respectively. The voltage is turned-on at $t = 10$ ms. As a result of the biasing electric field, LC molecules are vertically reoriented in a few ms and the tilt angle reaches $90°$. DE_0 simultaneously falls down while DE_1 rises. Inverse processes take place at $t = 60$ ms when the voltage is turned-off. As can be seen, the response speed is limited by the fall time starting at $t = 60$ ms during which LC molecules undergo elastic relaxation back into the initial state dictated by the orientation of the planar alignment. The resulting switch-off time for the LC molecules is around 50 ms. Please note, that DE_1, which is the key property of interest, switches notably faster, in less than 20 ms. The switching times of LC-based devices scale with the inverse square of the LC thickness. In this work, the LC-infiltrated resonant MIM cavities feature a deeply subwavelength thickness ($\lambda/36$), which results in two orders of magnitude faster switching compared with non-resonant LC-THz modulators that employ LC cells with a thickness comparable to the wavelength.

The modulation speed is compatible with several applications such as THz time-domain imaging and spectroscopy [61]. A few times improvement could be expected by exploiting the expertise
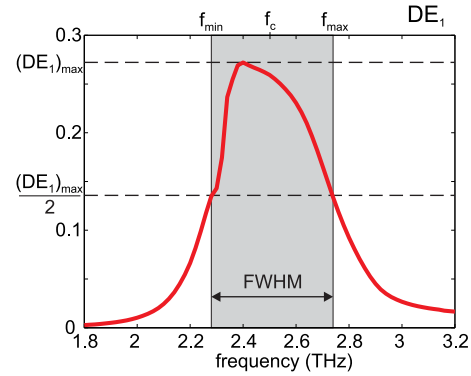
accrued in LC display technology on the synthesis of novel LC molecules with low-viscosity and high-$\Delta\varepsilon$ at THz frequencies. Another technique to increase the switching speed of nematic LC cells is by using a polymer network to stabilize the LC molecules [62], [63]. Finally, one of the most promising ways to increase the device speed is by employing dual-frequency nematic mixtures [64], thus equalizing the switch on and off times and pushing the overall response time of the beam steerer towards 1 ms, which is practically a fundamental limit of nematic LC-based devices.

The proposed beam-steering devices belong to the class of diffractive optics elements which inherently have a narrow bandwidth. Here it is defined as the full width at half maximum (FWHM) or 3-dB attenuation in DE_1 which is presented in Fig. 7 as a function of frequency for $U_1 = 10$ V. The absolute value of the bandwidth is 0.46 THz, while the relative bandwidth, namely the FWHM over its central frequency f_c, is 18%.

IV. TUNABLE BLAZED GRATINGS WITH GRADIENT METASURFACES

The geometry of the gradient metasurface is essentially the same as for the binary structure, except the LC thickness is reduced to 1.75 μm. The period of the considered metasurface consists of N = 4 unit cells. The metasurface with zero voltage applied to all cells behaves as a flat mirror just reflecting an normally-incident beam with $DE_0 = 0.73$ at the operating frequency 2.7 THz. The four-level gradient phase profile $0°$, $90°$, $180°$, $270°$ given in Fig. 1(c) is provided by the corresponding voltage pattern from Fig. 2(c) with $U_0 = 0$ V, $U_1 = 1.8$ V, $U_2 = 2.2$ V, $U_3 = 10$ V. The reflectance and phase for four cells with the specified voltages are given in Figs. 8(a) and 8(b), respectively. As can be seen, the phase is linearly changing across the cells from $0°$ to $270°$. The reflectance is high, above 0.7 for cells 1 and 4, since they implement the phase levels $0°$ and $270°$, respectively, which are away from the MIM cavity resonance. On the other hand, the inner cells 2 and 3 implement the phase levels $90°$ and $180°$, which are located in close vicinity to the cavity resonance, so the resulting reflectance for these cells is very low, around 0.1. DEs for the gradient metasurface are shown in Fig. 8(c). DE_{+1} is just slightly above 0.3. This low
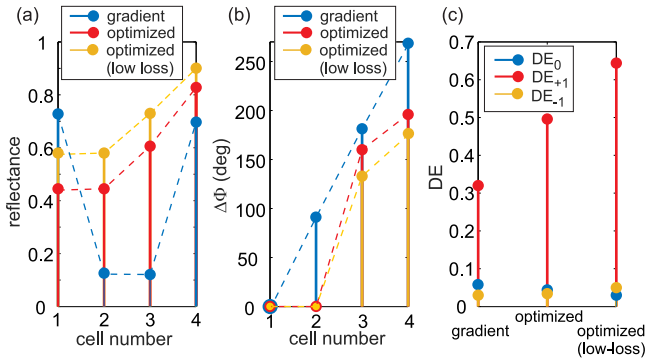
Fig. 8. (a) Reflectance and (b) phase for cells 1–4 in the gradient, optimized gradient, and optimized gradient metasurface with lower loss LC. (c) DEs (−1, 0, +1 orders) for the gradient, optimized gradient, and optimized gradient metasurface with low losses.
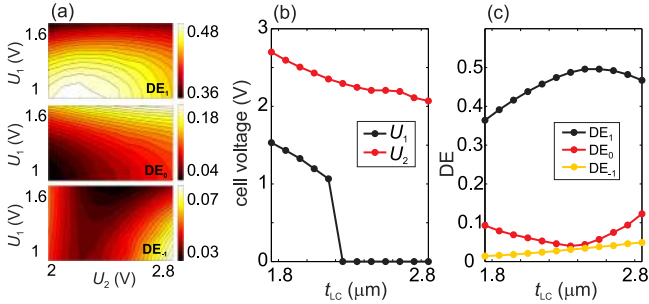

Fig. 9. The optimization procedure performed in order to maximize DE_{+1}: (a) DEs for varying voltages U_1 and U_2 with fixed $U_0 = 0$ V and $U_3 = 10$ V, (b) the evolution of U_1 and U_2 which give maximum DE_{+1} as a function of LC thickness, and (c) DEs as a function of t_{LC}.

efficiency is the result of high absorption in cells 2 and 3. At the same time, 0 and −1 orders are suppressed with DEs less than 0.05.

Such large variations of the reflectance among the four cells can lead to sub-optimal performance, even if the implemented discretized phase profile is linear. This is a general issue of beam steering gratings that involve lossy resonators [40]. In order to maximize DE_{+1}, a simple optimization procedure was performed. Bias voltages for cells 1 and 4 were kept constant at $U_0 = 0$ V and $U_3 = 10$ V, respectively, while the voltages applied on cells 2 and 3 were swept from 0 to 10 V. The same procedure was repeated for the LC thickness in the range from the initial value $1.75\,\mu$m to $2.85\,\mu$m. Thicker LC layers were considered in order to enhance overall reflection and DE_{+1} by reducing the absorption losses in the overcoupled MIM cavities. The results of the optimization procedure are presented in Fig. 9. DE maps for $t_{LC} = 2.45\,\mu$m are given in Fig. 9(a). The evolution of the bias voltages for cells 2 and 3 which give maximum DE_{+1} is depicted in Fig. 9(b). DEs as a function of LC thickness are presented in Fig. 9(c). As can be seen, the maximum DE_{+1} is achieved for $U_1 = 0$ V, $U_2 = 2.2$ V, and $t_{LC} = 2.45\,\mu$m. The results for the optimized gradient structure are presented in Fig. 8. The reflectance is increased for all cells except for cell 1, the phase is not linear anymore, whereas DE_{+1} is increased

to around 0.5, which is a significant improvement compared to 0.3 for the non-optimized structure.

The main source of losses in the considered metasurfaces is the field absorption within the LC layer. Therefore, further improvement in DE can be achieved by considering LCs with lower losses. The results for the optimized gradient metasurface (with $t_{LC} = 2.55\,\mu$m) infiltrated with a speculated LC with the same real part of the refractive index, but with one order of magnitude lower losses (imaginary part of the refractive index) are given in Fig. 8 as well, to compare with previous structures. Such low-loss LCs have been recently realized and characterized at millimeter waves [56], and it can be expected that they could retain such low amounts of absorption losses also in the THz spectrum, given the material dispersion behaviour of most nematic LCs [57]. As can be seen, the reflectance is increased in all cells 1-4 compared to the optimized structure while the phase profile stays almost the same. DE_{+1} increases to around 0.65 which is quite close to the theoretical maximum of around 0.8 for a 4-level reflective grating. It can be remarked in Fig. 8(b) that the phase profiles of the optimized structures deviate significantly from the predefined $0° − 90° − 180° − 270°$ values. Therefore, in order to maximize the DE_{+1} of the investigated beam steering metasurface, it is crucial to increase and equalize the reflectance of each unit cell within a metasurface period.

V. TUNABLE BEAM STEERING

Beam steering with a tunable diffraction angle is achieved by varying the metasurface period as schematically represented in Figs. 1(d) and 1(e). Results for the beam steering with a binary metasurface are depicted in Fig. 10(a). The number of unit cells per period is varied from N = 4 to N = 20, which corresponds to P varying in the range $128 − 640\,\mu$m. Simultaneously, the voltage pattern from Fig. 2(b) is modified accordingly with voltage levels $U_0 = 0$ V and $U_1 = 10$ V, such that each grating is composed of two phase cells of total width $Nw_{uc}/2$ with values 0 and 180°. As can be seen in Fig. 10(a), the diffraction angle of the first order changes from 75.6° to 11.2° in accordance with the well-known formula $\alpha = \arcsin(\lambda/P)$. Diffraction angle for −1 order changes in the same way for the negative angles. The highest $DE_{\pm1}$ of 0.31 is achieved for the smallest period (N = 4), whereas $DE_{\pm1}$ slightly falls down with increasing P down to around 0.25 for N = 20. The binary metasurface was designed with the phase difference $\Delta\Phi_0 = 180°$. Therefore, it acts as a beam splitter with just ±1 diffraction orders, while other orders can be neglected since their DEs are below 0.05.

The results for the beam steering with gradient metasurfaces are depicted in Fig. 10(b). Here N changes from 4 to 12, while P is in the range $128 − 384\,\mu$m. The optimized phase profile for N = 4 was applied in other two cases as well. In all cases, the voltage pattern was the same: $U_0 = 0$ V, $U_1 = 0$ V, $U_2 = 2.2$ V, $U_3 = 10$ V. Diffraction angle for the first order changes from 60.2° (N = 4) to 25.7° (N = 8) and 16.8° (N = 12). DE_{+1} is high, around 0.5 for N = 4, but it falls down for larger periods, so it is around 0.4 for N = 8, and around 0.35 for N = 12. Other diffraction orders are quite well suppressed for N = 4, however they become more pronounced for larger
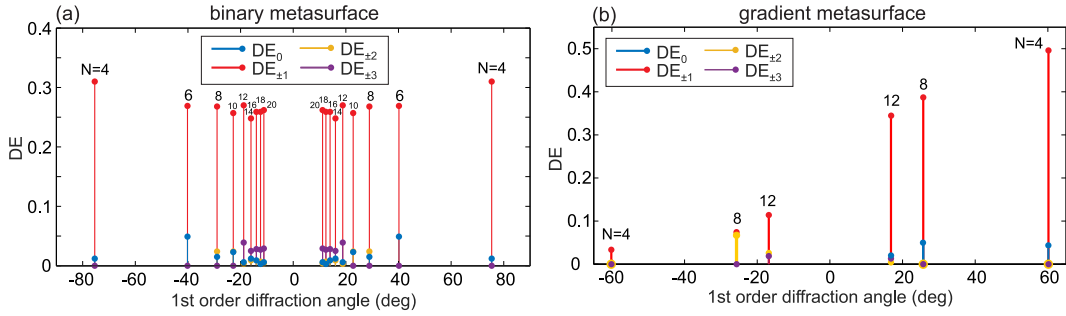
Fig. 10.   DEs with a variable period as a function of the first order diffraction angle: (a) binary (the phase difference is $\Delta\Phi_0 = 180°$,) and (b) gradient metasurface. The period is represented by the number N of unit cells per period and it varies (a) from $128\,\mu m$ (for N = 4) to $640\,\mu m$ (for N=20) and (b) from $128\,\mu m$ (for N = 4) to $384\,\mu m$ (for N=12). Geometrical parameters are the following: the unit cell size $w_{uc} = 32\,\mu m$, the metallic ribbon width $w_m = 28\,\mu m$, and the LC thickness (a) $t_{LC} = 3.35\,\mu m$) and (b) $t_{LC} = 2.45\,\mu m$.

periods. Better performance, i.e. higher DE of the dominant beam and higher suppression of undesired orders, are expected by following an optimization procedure as described for the case N = 4.

The accuracy of the reported beam-steering angles depends only on the metasurface period for a given wavelength of operation. The considered metal stripe array can be readily fabricated by standard photolithography with resolution better than $1\,\mu m$ and accuracy of the pitch value better than 100 nm [55]. Therefore, without resorting to more sophisticated nanofabrication processes, the tolerance of the period value in the considered metasurfaces would be less than 0.5%, which translates in a maximum deviation of approximately 1 degree for the steering angle for N = 4, and vanishing for larges pitch values.

VI. DISCUSSION

Standard tunable elements for beam-steering devices, such as diodes employed for microwave coding metasurfaces [27] and reflectarrays [33], [34], and ITO commonly used at near-infrared frequencies [38], [42], are not applicable for THz devices. Phase-change materials [58] require the temperature tuning which limits achievable modulation speed. Electromechanical metasurfaces [32] could be utilized for efficient beam steering, but they require more sophisticated fabrication and control, and they are prone to faster degradation of their moving parts, especially at THz frequencies.

On the other hand, LCs as low-loss dielectrics with a continuous tuning of dielectric permittivity are simple and efficient tunable elements. For the LC mixture 1825, the achieved DE is 0.5–0.6. Further improvement of DEs can be achieved by using LCs with lower losses, as demonstrated in the case of the optimized gradient structure (Fig. 8(c)) whose DE reaches around 0.65 when infiltrated with a novel LC mixture having an order of magnitude lower losses [56]. Such high DE is quite close to the theoretical limit of around 0.8.

The achieved DEs are higher than those obtained in THz beam-steering devices with semiconductors as tunable elements [7], [8], [31]. These were made from thin semiconductor films [8] or from metasurfaces coupled with thin semiconductor layers [31]. In both cases, the modulation principle is based

on the control of free charge carries in semiconductors. Although this provides efficient modulation of the real part of semiconductors' permittivity, a significant imaginary part leads to a pronounced absorption and limits achievable efficiency to around 0.2–0.3 [31].

Graphene-based metasurfaces are also appealing for beam steering at THz frequencies [37], [44]. They are also made of MIM-cavity based resonators. Still, very high voltages of around 1 kV are needed because of thick insulating layers of MIM cavities at THz frequencies. Such high voltages are not suitable for practical applications because of huge power consumption and safety issues. At the same time, THz devices require large-area graphene, dominantly fabricated by chemical vapour deposition. Losses in such graphene at THz frequencies are several times higher [59] than the ones theoretically predicted and used for numerical calculations [37]. At the same time, the conductivity of chemical vapour deposition graphene is spatially inhomogeneous [60], which also induces significant constraints for making THz modulators.

MIM metasurfaces enhance the efficiency of THz beam-steering devices compared to LC based wedge-shaped devices [5] and Fabry-Perot cavities with LC layers [6]. MIM cavities provide very compact devices since the thickness of the active LC layer is decreased by orders of magnitude, from millimiters [5] and hundreds of microns [6], to just several microns in the case considered here. Since the speed scales with the square of the LC thickness [14], the modulation speed in LC devices with MIM cavities is greatly improved to a few tens of milliseconds. Moreover, such thickness values for the LC cell are fully compatible with the mature technology used in the fabrication of LC displays.

DEs for considered metasurfaces are around 0.6 for binary, and 0.5 for gradient metasurfaces. As already mentioned, absorption within the LC layer is the main source of losses. The LC layer is thinner in gradient metasurfaces because a larger phase difference is required, which implies a higher absorption and a slightly lower DE compared to binary metasurfaces. In order to increase DE, low-loss LCs are one possible solution. Another approach can be the utilization of metasurfaces with simultaneous control of both amplitude and phase [65]. This could be implemented by two-dimensional arrays of MIM

cavities and by angular reorientation of top metallic elements of different shapes. In this way, it could be possible to achieve required phase difference and retain high reflection amplitude.

VII. CONCLUSION

In a summary, we demonstrated that the functionality of beam-steering metasurfaces based on one dimensional arrays of MIM cavities infiltrated with LCs can be adjusted by dynamically controlling the spatial voltage pattern. As a result, the metasurfaces can be switched from a mirror, to beam splitter and blazed grating, while the angle of the diffracted beam can be adjusted by reconfiguring the metasurface period. DE in the range 0.5–0.6 can be further increased by using novel LC mixtures with low losses. The proposed components can find direct application in THz systems, as they feature i) flat profile and compact dimensions with a subwavelength thickness, ii) fast switching speed of around 20 ms, iii) continuous control of the LC effective index with a low power consumption and driving voltages not higher than 10 V, and iv) technological scalability of their design and working frequency up to several THz. The last point is particularly relevant as the performance of other standard approaches for tunable THz devices using e.g. electronics (PIN diodes, varactors) or MEMS rapidly degrades or becomes impractical above 1 THz. Together with previously demonstrated LC based tunable metasurfaces for the amplitude [14] and polarization modulation [49], they provide a multifunctional platform for tunable THz devices.

REFERENCES

[1] M. Tonouchi, "Cutting-edge terahertz technology," *Nature Photon.*, vol. 1, pp. 97–105, 2007.

[2] T. Kleine-Ostmann and T. Nagatsuma, "A review on Terahertz communications research," *J. Infrared Millimeter THz Waves*, vol. 32, pp. 143–171, 2011.

[3] P. U. Jepsen, D. G. Cooke, and M. Koch, "Terahertz spectroscopy and imaging—Modern techniques and applications," *Laser Photon. Rev.*, vol. 5, pp. 124–166, 2011.

[4] X. Fu, F. Yang, C. Liu, X. Wu, and T. J. Cui, "Terahertz beam steering technologies: From phased arrays to field-programmable metasurfaces," *Adv. Opt. Mater.*, 2019, Art. no. 1900628.

[5] B. Scherger *et al.*, "Discrete terahertz beam steering with an electrically controlled liquid crystal device," *J. Infrared Millimeter THz Waves*, vol. 33, pp. 1117–1122, 2012.

[6] W. Fuscaldo *et al.*, "Tunable Fabry-Perot cavity THz antenna based on leaky-wave propagation in nematic liquid crystals," *IEEE Antennas Wireless Propag. Lett.*, vol. 16, pp. 2046–2049, 2017.

[7] S. Busch, B. Scherger, M. Scheller, and M. Koch, "Optically controlled terahertz beam steering and imaging," *Opt. Lett.*, vol. 37, pp. 1391–1393, 2012.

[8] T. P. Steinbusch, H. K. Tyagi, M. C. Schaafsma, G. Georgiou, and J. Gómez Rivas, "Active terahertz beam steering by photo-generated graded index gratings in thin semiconductor films," *Opt. Exp.*, vol. 22, pp. 26 559–26 571, 2014.

[9] K.-i. Maki and C. Otani, "Terahertz beam steering and frequency tuning by using the spatial dispersion of ultrafast laser pulses," *Opt. Exp.*, vol. 16, pp. 10 158–10 169, 2008.

[10] A. P. Hibbins, J. R. Sambles, C. R. Lawrence, and J. R. Brown, "Squeezing millimeter waves into microns," *Phys. Rev. Lett.*, vol. 92, 2004, Art. no. 143904.

[11] Y. Todorov *et al.*, "Strong light-matter coupling in subwavelength metal-dielectric microcavities at terahertz frequencies," *Phys. Rev. Lett.*, vol. 102, 2009, Art. no. 186402.

[12] H.-T. Chen *et al.*, "Active terahertz metamaterial devices," *Nature*, vol. 444, pp. 597–600, 2006.

[13] H.-T. Chen *et al.*, "A metamaterial solid-state terahertz phase modulator," *Nature Photon.*, vol. 3, pp. 148–151, 2009.

[14] G. Isić, B. Vasić, D. C. Zografopoulos, R. Beccherelli, and R. Gajić, "Electrically tunable critically coupled terahertz metamaterial absorber based on nematic liquid crystals," *Phys. Rev. Appl.*, vol. 3, 2015, Art. no. 064007.

[15] M. Rahm, J.-S. Li, and W. J. Padilla, "THz wave modulators: A brief review on different modulation techniques," *J. Infrared Millimeter THz Waves*, vol. 34, pp. 1–27, 2013.

[16] M. R. Hashemi, S. Cakmakyapan, and M. Jarrahi, "Reconfigurable metamaterials for terahertz wave manipulation," *Rep. Prog. Phys.*, vol. 80, 2017, Art. no. 094501.

[17] W. J. Padilla and R. D. Averitt, "Properties of dynamical electromagnetic metamaterials," *J. Opt.*, vol. 19, 2017, Art. no. 084003.

[18] N. Yu *et al.*, "Light propagation with phase discontinuities: Generalized laws of reflection and refraction," *Science*, vol. 334, pp. 333–337, 2011.

[19] C. Pfeiffer *et al.*, "Efficient light bending with isotropic metamaterial huygens' surfaces," *Nano Lett.*, vol. 14, pp. 2491–2497, 2014.

[20] H.-T. Chen, A. J. Taylor, and N. Yu, "A review of metasurfaces: Physics and applications," *Rep. Prog. Phys.*, vol. 79, 2016, Art. no. 076401.

[21] N. M. Estakhri and A. Alù, "Recent progress in gradient metasurfaces," *J. Opt. Soc. Amer. B*, vol. 33, pp. A21–A30, 2016.

[22] F. Ding, A. Pors, and S. I. Bozhevolnyi, "Gradient metasurfaces: A review of fundamentals and applications," *Rep. Prog. Phys.*, vol. 81, 2017, Art. no. 026401.

[23] S. Sun *et al.*, "High-efficiency broadband anomalous reflection by gradient meta-surfaces," *Nano Lett.*, vol. 12, pp. 6223–6229, 2012.

[24] T. Niu *et al.*, "Experimental demonstration of reflectarray antennas at terahertz frequencies," *Opt. Exp.*, vol. 21, pp. 2875–2889, 2013.

[25] Z. Wei, Y. Cao, X. Su, Z. Gong, Y. Long, and H. Li, "Highly efficient beam steering with a transparent metasurface," *Opt. Exp.*, vol. 21, pp. 10 739–10 745, 2013.

[26] M. Farmahini-Farahani, J. Cheng, and H. Mosallaei, "Metasurfaces nanoantennas for light processing," *J. Opt. Soc. Amer. B*, vol. 30, pp. 2365–2370, 2013.

[27] T. J. Cui, M. Q. Qi, X. Wan, J. Zhao, and Q. Cheng, "Coding metamaterials, digital metamaterials and programmable metamaterials," *Light Sci. Appl.*, vol. 3, 2014, Art. no. e218.

[28] M. Maasch, M. Roig, C. Damm, and R. Jakoby, "Voltage-tunable artificial gradient-index lens based on a liquid crystal loaded fishnet metamaterial," *IEEE Antenn. Wireless Propag. Lett.*, vol. 13, pp. 1581–1584, 2014.

[29] L. Zou, M. Cryan, and M. Klemm, "Phase change material based tunable reflectarray for free-space optical inter/intra chip interconnects," *Opt. Exp.*, vol. 22, pp. 24 142–24 148, 2014.

[30] G. Kaplan, K. Aydin, and J. Scheuer, "Dynamically controlled plasmonic nano-antenna phased array utilizing vanadium dioxide," *Opt. Mater. Exp.*, vol. 5, pp. 2513–2524, 2015.

[31] X. Su *et al.*, "Active metasurface terahertz deflector with phase discontinuities," *Opt. Exp.*, vol. 23, pp. 27 152–27 158, 2015.

[32] L. Cong *et al.*, "Active multifunctional microelectromechanical system metadevices: Applications in polarization control, wavefront deflection, and holograms," *Adv. Opt. Mater.*, vol. 5, 2017, Art. no. 1600716.

[33] D. Sievenpiper and J. Schaffner, "Beam steering microwave reflector based on electrically tunable impedance surface," *Electron. Lett.*, vol. 38, pp. 1237–1238, 2002.

[34] T. H. Hand and S. A. Cummer, "Reconfigurable reflectarray using addressable metamaterials," *IEEE Antennas Wireless Propag. Lett.*, vol. 9, pp. 70–74, 2010.

[35] S. Bildik, S. Dieter, C. Fritzsch, W. Menzel, and R. Jakoby, "Reconfigurable folded reflectarray antenna based upon liquid crystal technology," *IEEE Trans. Antennas. Propag.*, vol. 63, no. 1, pp. 122–132, Jun. 2015.

[36] P. F. McManamon *et al.*, "Optical phased array technology," *Proc. IEEE*, vol. 84, no. 2, pp. 268–298, Feb. 1996.

[37] T. Yatooshi, A. Ishikawa, and K. Tsuruta, "Terahertz wavefront control by tunable metasurface made of graphene ribbons," *Appl. Phys. Lett.*, vol. 107, 2015, Art. no. 053105.

[38] A. Forouzmand and H. Mosallaei, "Tunable two dimensional optical beam steering with reconfigurable indium tin oxide plasmonic reflectarray metasurface," *J. Opt.*, vol. 18, 2016, Art. no. 125003.

[39] P. P. Iyer, M. Pendharkar, and J. A. Schuller, "Electrically reconfigurable metasurfaces using heterojunction resonators," *Adv. Opt. Mater.*, vol. 4, pp. 1582–1588, 2016.

[40] F. Liu *et al.*, "Intelligent metasurfaces with continuously tunable local surface impedance for multiple reconfigurable functions," *Phys. Rev. Appl.*, vol. 11, 2019, Art. no. 044024.

[41] D. C. O'Shea, T. J. Suleski, and D. W. Kathman, A. D. Prather, *Diffractive Optics: Design, Fabrication, and Test*. Bellingham, WA, USA: SPIE, 2004.

[42] Y.-W. Huang *et al.*, "Gate-tunable conducting oxide metasurfaces," *Nano Lett.*, vol. 16, pp. 5319–5325, 2016.

[43] M. Kim, J. Jeong, J. K. S. Poon, and G. V. Eleftheriades, "Vanadium-dioxide-assisted digital optical metasurfaces for dynamic wavefront engineering," *J. Opt. Soc. Amer. B*, vol. 33, pp. 980–988, 2016.

[44] E. Carrasco, M. Tamagnone, and J. Perruisseau-Carrier, "Tunable graphene reflective cells for THz reflectarrays and generalized law of reflection," *Appl. Phys. Lett.*, vol. 102, 2013, Art. no. 104103.

[45] G. Isić *et al.*, "Electrically tunable metal-semiconductor-metal terahertz metasurface modulators," *IEEE J. Sel. Topics Quantum Electron.*, vol. 25, no. 3, May/Jun. 2019, Art. no. 8500108.

[46] B. Vasić, M. M. Jakovljević, G. Isić, and R. Gajić, "Tunable metamaterials based on split ring resonators and doped graphene," *Appl. Phys. Lett.*, vol. 103, 2013, Art. no. 011102.

[47] D. Shrekenhamer, W.-C. Chen, and W. J. Padilla, "Liquid crystal tunable metamaterial absorber," *Phys. Rev. Lett.*, vol. 110, 2013, Art. no. 177403.

[48] R. Kowerdziej, M. Olifierczuk, J. Parka, and J. Wróbel, "Terahertz characterization of tunable metamaterial based on electrically controlled nematic liquid crystal," *Appl. Phys. Lett.*, vol. 105, 2014, Art. no. 022908.

[49] B. Vasić, D. C. Zografopoulos, G. Isić, R. Beccherelli, and R. Gajić, "Electrically tunable terahertz polarization converter based on overcoupled metal-isolator-metal metamaterials infiltrated with liquid crystals," *Nanotechnology*, vol. 28, 2017, Art. no. 124002.

[50] M. A. Golub, "Laser beam splitting by diffractive optics," *Opt. Photon. News*, vol. 15, no. 2, pp. 36–41, 2004.

[51] D. C. Zografopoulos, R. Beccherelli, and E. E. Kriezis, "Beam-splitter switches based on zenithal bistable liquid-crystal gratings," *Phys. Rev. E*, vol. 90, 2014, Art. no. 042503.

[52] M. A. Ordal, R. J. Bell, J. R. W. Alexander, L. L. Long, and M. R. Querry, "Optical properties of fourteen metals in the infrared and far infrared: Al, Co, Cu, Au, Fe, Pb, Mo, Ni, Pd, Pt, Ag, Ti, V, and W," *Appl. Opt.*, vol. 24, pp. 4493–4499, 1985.

[53] M. Reuter *et al.*, "Highly birefringent, low-loss liquid crystals for terahertz applications," *APL Mater.*, vol. 1, 2013, Art. no. 012107.

[54] P. A. George, W. Hui, F. Rana, B. G. Hawkins, A. E. Smith, and B. J. Kirby, "Microfluidic devices for terahertz spectroscopy of biomolecules," *Opt. Exp.*, vol. 16, pp. 1577–1582, 2008.

[55] A. Ferraro, D. C. Zografopoulos, R. Caputo, and R. Beccherelli, "Guided-mode resonant narrowband terahertz filtering by periodic metallic stripe and patch arrays on cyclo-olefin substrates," *Sci. Rep.*, vol. 8, 2018, Art. no. 17272.

[56] V. Lapanik, G. Sasnouski, S. Timofeev, E. Shepeleva, G. Evtyushkin, and W. Haase, "New highly anisotropic liquid crystal materials for high-frequency applications," *Liquid Crystals*, vol. 45, pp. 1242–1249, 2018.

[57] D. C. Zografopoulos, A. Ferraro, and R. Beccherelli, "Liquid-crystal high-frequency microwave technology: Materials and characterization," *Adv. Mater. Technol.*, vol. 4, 2019, Art. no. 1800447.

[58] M. R. M. Hashemi, S.-H. Yang, T. Wang, N. Sepúlveda, and M. Jarrahi, "Electronically-controlled beam-steering through vanadium dioxide metasurfaces," *Sci. Rep.*, vol. 6, 2016, Art. no. 35439.

[59] C. Lee, J. Y. Kim, S. Bae, K. S. Kim, B. H. Hong, and E. J. Choi, "Optical response of large scale single layer graphene," *Appl. Phys. Lett.*, vol. 98, 2011, Art. no. 071905.

[60] J. L. Tomaino *et al.*, "Terahertz imaging and spectroscopy of large-area single-layer graphene," *Opt. Exp.*, vol. 19, pp. 141–146, 2011.

[61] H. Guerboukha, K. Nallappan, and M. Skorobogatiy, "Toward real-time terahertz imaging," *Adv. Opt. Photon.*, vol. 10, pp. 843–938, 2018.

[62] Y. Utsumi, T. Kamei, K. Saito, and H. Moritake, "Increasing the speed of microstrip-line-type polymer-dispersed liquid-crystal loaded variable phase shifter," *IEEE Trans. Microw. Theory Tech.*, vol. 53, no. 11, pp. 3345–3353, Nov. 2005.

[63] K. Altmann, M. Reuter, K. Garbat, M. Koch, R. Dabrowski, and I. Dierking, "Polymer stabilized liquid crystal phase shifter for terahertz waves," *Opt. Exp.*, vol. 21, pp. 12 395–12 400, 2013.

[64] T. Kuki, H. Fujikake, and T. Nomoto, "Microwave variable delay line using dual-frequency switching-mode liquid crystal," *IEEE Trans. Microw. Theory Tech.*, vol. 50, no. 11, pp. 2604–2609, Nov. 2002.

[65] L. Liu *et al.*, "Broadband Metasurfaces with Simultaneous Control of Phase and Amplitude," *Adv. Mater.*, vol. 26, pp. 5031–5036, 2014.

Borislav Vasić was born in Vinkovci, Croatia, in 1982. He received the Diploma in microcomputer electronics from the Faculty of Technical Sciences, University of Novi Sad, Novi Sad, Serbia, in 2005, and the Ph.D. degree in nanoelectronics and photonics from the Faculty of Electrical Engineering, University of Belgrade, Beograd, Serbia, 2012. His research interests include design of tunable photonics devices based on metamaterials and plasmonic structures.

Goran Isić was born in Subotica, Yugoslavia, in 1982. He received the Diploma in physical electronics from the School of Electrical Engineering, University of Belgrade, Beograd, Serbia, in 2006 and the Ph.D. degree in quantum electronics from the School of Electronic and Electrical Engineering, University of Leeds, Leeds, U.K., in 2011. His research interest include nano-optics, nanospectroscopy, plasmonics, metamaterials and resonant optical systems in general.

Romeo Beccherelli (M'12) was born in Plovdiv, Bulgaria, in 1969. He received the Laurea (*cum laude*) and Ph.D. degrees in electronic engineering from the Sapienza University of Rome, Rome, Italy, in 1994 and 1998, respectively. In 1997, he joined as a Postdoctoral Research Assistant with the Department of Engineering Science, University of Oxford, Oxford, U.K. In 2001, he was appointed Researcher and a Senior Researcher with the National Research Council of Italy, Institute for Microelectronics and Microsystems, Rome, in 2006. He has invented two patents and authored more than 90 scientific papers in international journals, more than 110 conference proceedings papers, and 4 book chapters. His current research interests include sensor arrays, photonics and plasmonics based on liquid crystals, and metamaterial and metasurface devices and systems for processing microwaves and terahertz waves. His doctoral thesis was awarded the International Otto Lehman Prize 1999 in liquid crystal technology by the University of Karlsruhe (Germany) and the Otto Lehmann Foundation.

Dimitrios C. Zografopoulos was born in Thessaloniki, Greece, in 1980. He received the Diploma in electrical and computer engineering and the Ph.D. degree from the Aristotle University of Thessaloniki, Thessaloniki, Greece, in 2003 and 2009, respectively. In 2011, he was a Postdoctoral Research Fellow with the Greek States Scholarship Foundation and a Visiting Research Fellow with the Department of Electronics Technology, Carlos III University of Madrid, Madrid, Spain. He subsequently moved under a two-year Intra-European Marie-Curie Fellowship to the Institute for Microelectronics and Microsystems, Italian National Research Council of Italy, Rome, where he is currently a Researcher. He has authored or coauthored more than 70 scientific papers in international journals and two book chapters. His current research interests include the investigation of photonic/plasmonic waveguides, tunable metamaterials and metasurfaces, and the interaction between electromagnetic waves and liquid crystals.

SCIENTIFIC REPORTS

natureresearch

Check for updates

OPEN

Single-step fabrication and work function engineering of Langmuir-Blodgett assembled few-layer graphene films with Li and Au salts

Ivana R. Milošević[1✉], Borislav Vasić[1], Aleksandar Matković[2✉], Jasna Vujin[1], Sonja Aškrabić[3], Markus Kratzer[2], Thomas Griesser[4], Christian Teichert[2] & Radoš Gajić[1]

To implement large-area solution-processed graphene films in low-cost transparent conductor applications, it is necessary to have the control over the work function (WF) of the film. In this study we demonstrate a straightforward single-step chemical approach for modulating the work function of graphene films. In our approach, chemical doping of the film is introduced at the moment of its formation. The films are self-assembled from liquid-phase exfoliated few-layer graphene sheet dispersions by Langmuir-Blodgett technique at the water-air interfaces. To achieve a single-step chemical doping, metal standard solutions are introduced instead of water. Li standard solutions (LiCl, $LiNO_3$, Li_2CO_3) were used as n-dopant, and gold standard solution, $H(AuCl_4)$, as p-dopant. Li based salts decrease the work function, while Au based salts increase the work function of the entire film. The maximal doping in both directions yields a significant range of around 0.7 eV for the work function modulation. In all cases when Li-based salts are introduced, electrical properties of the film deteriorate. Further, lithium nitrate ($LiNO_3$) was selected as the best choice for n-type doping since it provides the largest work function modulation (by 400 meV), and the least influence on the electrical properties of the film.

Graphene, consisting of a single layer carbon arranged in a hexagonal lattice, has attracted extensive interest because of the excellent mechanical and electrical properties associated with its two dimensional structure[1–4]. Chemical vapor deposition (CVD) method has become the most common method for production of large-area graphene films[5]. Still, simple and low-cost methods are needed for mass production especially when considering the cases where high-quality films are not needed for the desired functionality, as in low-power lighting, sensors, transparent heating, and de-icing applications[6]. In that context, liquid-phase exfoliation (LPE) is a perspective way of obtaining large quantities of exfoliated graphite in solution. LPE of graphite results in a dispersion of few-layer graphene sheets (GSs) in the solvent. However, in order to access the full potential of LPE-processed graphene, thin-films needs to be controllably fabricated utilizing techniques capable to introduce self-ordering of GSs[7]. One such example is Langmuir-Blodgett assembly (LBA). Based on surface-tension induced self-assembly of nanoplatelets at the liquid-air interface or the interface of two liquids, LBA is a good method for production of large-scale, highly transparent, thin solution-processed graphene films[8–11].

Excellent electrical conductivity, flexibility and transparency in the visible domain make graphene a natural choice for ultrathin, flexible and transparent electrodes in electronic devices[10,12–19]. Still, a significant work function difference between graphene and frequently employed active layers of photovoltaic and light-emitting diode (LED) devices gives rise to a high contact resistance. Contact resistance can have a significant impact on overall efficiency and performance of the devices[20]. This is of a particular technological relevance considering that any realistic application of graphene based transparent electrode must compete against those based on indium tin

¹Laboratory for Graphene, other 2D Materials and Ordered Nanostructures of Center for Solid State Physics and New Materials, Institute of Physics, University of Belgrade, Pregrevica 118, 11080, Belgrade, Serbia. ²Institute of Physics, Montanuniversität Leoben, Franz Josef Str. 18, 8700, Leoben, Austria. ³Nanostructured Matter Laboratory of Center for Solid State Physics and New Materials, Institute of Physics, University of Belgrade, Pregrevica 118, 11080, Belgrade, Serbia. ⁴Institute of Chemistry of Polymeric Materials, Montanuniversität Leoben, Otto-Gloeckel-Straße 2, 8700, Leoben, Austria. ✉e-mail: novovic@ipb.ac.rs; aleksandar.matkovic@unileoben.ac.at

oxide (ITO) or fluorine-doped tin oxide (FTO), which have already gone through decades of interfacial optimization in order to deliver todays' performance[21–23]. Therefore, the understanding of the efficient ways for modulation of the graphene work function is crucial for improving device performances[21,22,24]. In order to enhance the charge injection, the work function of the graphene electrode should be optimized to better match WF of the adjacent layer in order to form an ohmic contact[24].

Recently, the chemical doping has been reported to be an effective method for doping of CVD graphene and tuning its work function by charge transfer between the graphene sheet and metal salts, organic dopants, or metal oxide layers[12,14,21–28]. Such surface charge transfer induced by chemical doping is expected to efficiently control the Fermi level of graphene sheets without introducing substitutional impurities or basal plane reactions, thus, preventing any damage to the carbon networks and not introducing scattering centres that would lower carrier mobility[21]. Kwon *et al.* reported n-type chemical doping of CVD graphene with alkali metal carbonates by soaking in appropriate solutions[23] and alkali metal chlorides by spin-coating of appropriate solutions on the transferred graphene substrates[25]. So far, doping of Langmuir-Blodgett graphene films prepared from LPE dispersions has been done with nitric acid and ozone after the film was formed using the drop-casting method and UV/ozone treatment[9,29]. Chemical doping is especially attractive for LPE-based graphene films since many exposed edges of GSs are expected to enable very efficient functionalization through charge transfer doping. However, the chemical doping with metal salt solutions has not been used to control the work function of LBA graphene films so far. In this work LBA graphene films obtained from LPE dispersion were doped during the process of film formation. Therefore, the formation and doping of the LBA graphene films in our work represent a single-step process. This is a significant improvement compared to previous works where the chemical doping was applied only after the graphene fabrication.

In the present work, we systematically investigated single-step work function modulation (increase and decrease) of the LPE GS films achieved by chemical doping. In particular, using Li standard solutions (LiCl, LiNO$_3$ and Li$_2$CO$_3$) as n-dopant, and gold standard solution H(AuCl$_4$) as p-dopant was investigated. In contrast to previous methods for chemical doping of CVD graphene which can be applied only after the graphene films fabrication, here we described the method for the production and doping of LPE graphene films in a single-step. Single-step work function modulation means doping of the film at the moment of its formation from the LPE graphene dispersion by LBA technique at the air-metal standard solution interface. We have demonstrated tunability of the WF in the range of almost 1 eV, making these metal-salt treated LPE-based graphene electrodes suitable candidates for both electron and hole injection interfaces.

Results and discussion

Morphology of LPE GS films.   Fabrication and doping of the GS films is schematically represented in Fig. 1(a): air-metal standard solution interface, introduction of LPE dispersion and formation of the LPE GS film at the interface, scooping of the doped film on the target substrate and finally, obtained doped LPE GS film which is further investigated with different techniques.

Morphology of LPE GS films is depicted in Fig. 1 consisting of both optical (Fig. 1(b1-f1)) and Atomic Force Microscopy (AFM) topographic images (Fig. 1(b2-f2)) for both undoped and metal doped LPE GS films. As can be seen from AFM images, the doping process does not change morphology of LPE films, except that the doped films contain more agglomerates (visible as bright particle-like domains). The following values for the surface roughness were obtained by AFM measurements averaged on ten $50 \times 50\,\mu m^2$ areas: (a) 11.9 ± 1.5 nm for undoped LPE GS film, (b) 11.5 ± 3.5 nm for Li$_2$CO$_3$ doped, (c) 13.3 ± 2 nm for H(AuCl$_4$) doped, (d) 13.7 ± 1.6 nm for LiCl doped, and (e) 13.8 ± 1.2 nm for LiNO$_3$ doped LPE GS films. Therefore, the surface roughness sligtly increases by around 2 nm after the doping, while for Li$_2$CO$_3$ doped LPE GS film is practically the same as for the undoped film. Still, optical images recorded on larger scale depict formation of agglomerates in doped films which could degraded their optical (leading to an increased scattering and/or absorption of incoming lights on these clusters) and electrical properties (due to enhanced scattering of charge carriers).

The observed formation of the agglomerates is most likely not an inherent property of the particular metal-salt doping. Overcoming this would likely require further optimization of the LBA process. However, as a benchmark the LBA process in this study was optimized for an undoped film and was left unchanged for all of the metal-salt doped films.

Transmittance measurements.   Using the different doping metal standard solution during LBA of graphene films was found to result in different transparency. In the UV region, the transmittance of graphene is dominated by an exciton-shifted van Hove peak in absorption[9,30]. Transmittance at 550 nm was 82% for undoped and 80%, 76%, 74%, 68% for H(AuCl$_4$), LiCl, LiNO$_3$, Li$_2$CO$_3$ doped LPE GS films, respectively (Fig. 2). It can be seen that transmittance decreases for doped LPE GS films. Metal salts decrease the transmittance of the graphene films regardless the type of the present metal (gold or lithium). The degree of the transmittance decrease was related to not only the metal cations but also the anions. Different lithium salts decrease transmittance in different amounts. Transmittance decrease of 14% was the highest for the LPE GS film doped with lithium carbonate (Li$_2$CO$_3$). Similar results of the transmittance decrease for metal doped CVD graphene films were obtained in studies of Kwon *et al.*[22,23,25]. Transmittance decrease could be a consequence of the metal particles adsorption and agglomeration on doped films after the solvent evaporation process. Changes in the thickness of LPE GS films with doping could not be excluded because LBA process in this study was optimized for an undoped film and was left unchanged for all of the metal-salt doped films.

Raman measurements.   Raman spectra for undoped and H(AuCl$_4$), LiCl, LiNO$_3$, Li$_2$CO$_3$ doped LPE GS films are given in Fig. 3(a). The four basic graphene/graphite peaks D (~1348 cm^{-1}), G (~1579 cm^{-1}), D' (1614
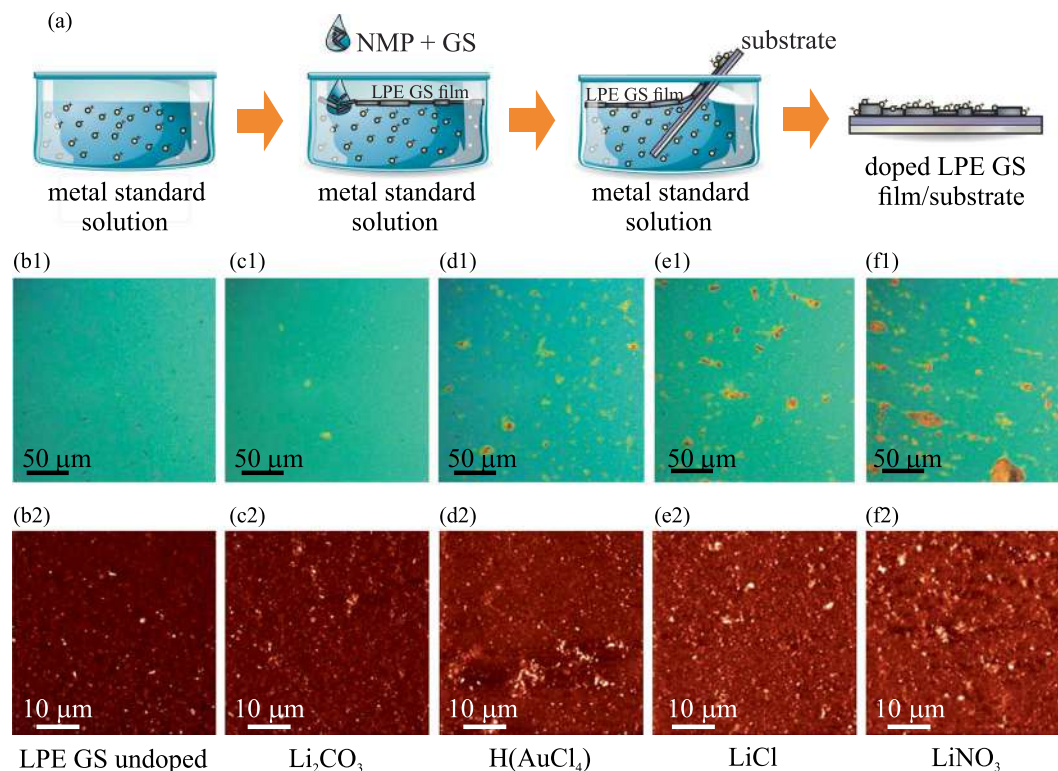
Figure 1. (**a**) Schematic representation of the LPE GS film formation and its doping in the single-step process. (**b1–f1**) Optical images are shown in the top row, whereas (**b2–f2**) AFM topographic images are shown in the bottom row for the following cases: (**b**) undoped LPE GS film, and (**c**) Li_2CO_3, (**d**) $H(AuCl_4)$, (**e**) LiCl, (**f**) $LiNO_3$ doped LPE GS films. z-scale in all AFM images is 100 nm.
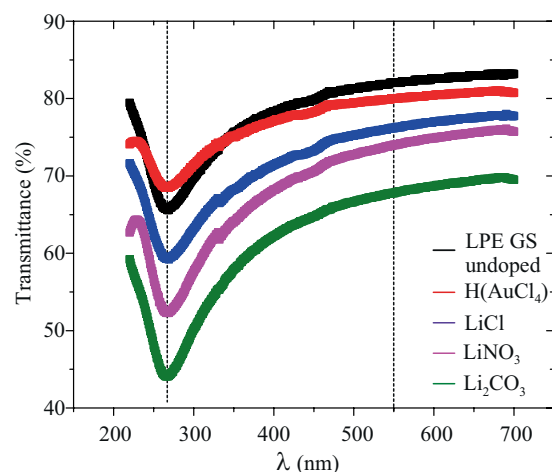

Figure 2. Transmittance spectra of undoped and $H(AuCl_4)$, LiCl, $LiNO_3$, Li_2CO_3 doped LPE GS films.

cm^{-1}) and 2D (2700 cm^{-1}) are observed for all the samples. No significant shifts of any characteristic Raman peaks of graphene were detected after chemical doping (Fig. 3(a)).

The change of the full weight at half-maximum (FWHM) of the Raman modes after doping with metal standard solutions was negligible Fig. 3(b). The only notably change of the Raman spectra was the increase of the intensity ratio of D to G peaks, I(D)/I(G) (Fig. 3(c)). The quantity of defects has been shown to be related to the ratio between the D and G peaks, I(D)/I(G); the larger the ratio, the larger the defect density[31]. We observe increase of the defect density with $H(AuCl_4)$, LiCl, $LiNO_3$, Li_2CO_3 doping in relation to the undoped film and the amount of the increase expressed in percent was 37%, 24%, 29% and 21%, respectively.

All self-assembled films suffer from a large defect density that often leads to a high sheet resistance of deposited film. Therefore, the nature and density of defects in any thin film transparent conductor is important, especially when chemical treatment was used to enhance films' performance. The intensity ratio between the D and
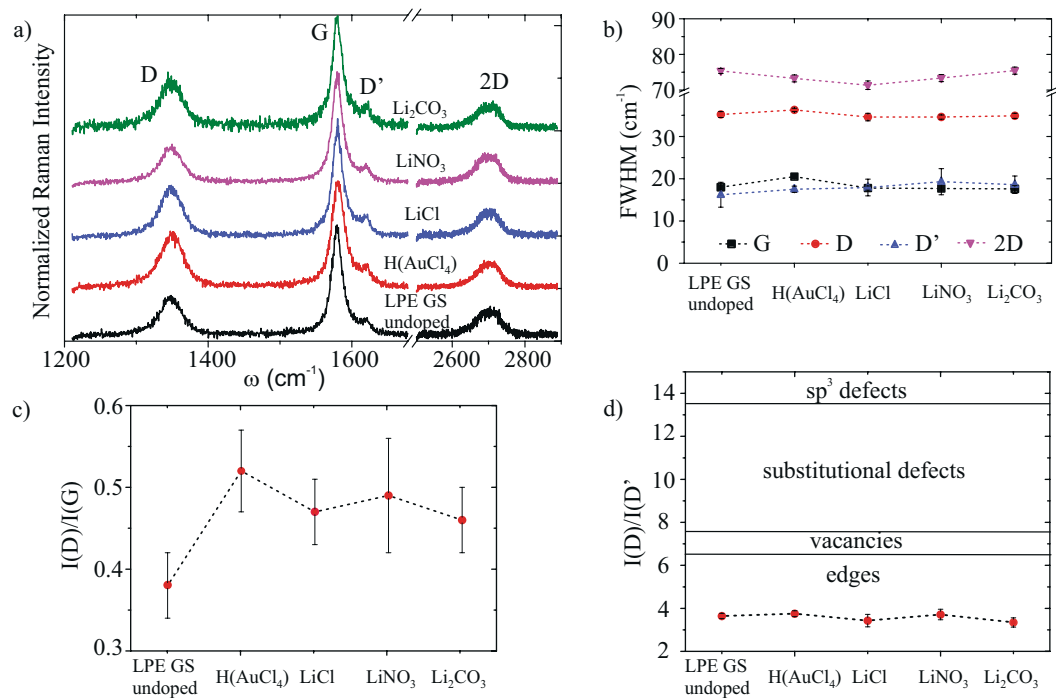
Figure 3. (**a**) Raman spectra of the undoped LPE GS film and films doped with Li and Au salts, (**b**) FWHM of the four basic Raman peaks (**c**) The intensity ratio of D to G peak for different doping metal salts, I(D)/I(G), (**d**) The intensity ratio of D to D' peak, I(D)/I(D'), for different doping metal salts. We refer to peak intensity as the height of the peaks as proposed by Eckmann *et al.*[32].
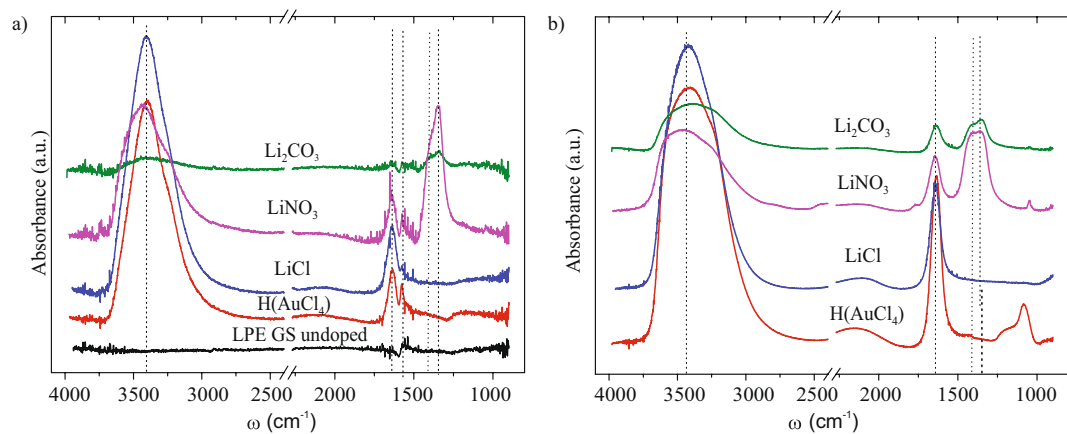

Figure 4. FT-IR spectra of (**a**) undoped and H(AuCl$_4$), LiCl, LiNO$_3$, Li$_2$CO$_3$ LPE GS doped films, (**b**) metal standard solutions (0.1 mg/mL) used for doping processes.

D' peak can be used to get information on the nature of defects in graphene[32,33]. I(D)/I(D') was calculated, and the obtained results were presented in Fig. 3(d). Topological defects (like pentagon-heptagon pairs), boundaries, vacancies, substitutional impurities and sp^3 defects are possible defects in graphene[31]. Studies reporting a ratio of 3.5 for boundaries, 7 for vacancies, 13 for sp^3 and values in-between those for vacancies and sp^3 for substitutional impurities can be found in the literature[31,32,34]. From Fig. 3(d) it can be observed that the D to D' intensity peak ratio is nearly constant in our samples regardless of the doping solution, and the value of the ratio indicates that the edges are the dominant type of defects in our LPE GS films.

Fourier transform infrared absorbance (FT-IR) measurements. FT-IR spectra of undoped and LiCl, LiNO$_3$, Li$_2$CO$_3$, H(AuCl$_4$) doped LPE GS films, as well as FT-IR spectra of corresponding metal standard solutions are shown in Fig. 4.

For the undoped LPE GS film FT-IR spectra is simple. It can be seen only a small peak assignable to C=C skeletal vibration[35–37] of the graphene basal planes at ~1560 cm^{-1}. This peak can also be seen in FT-IR spectra for
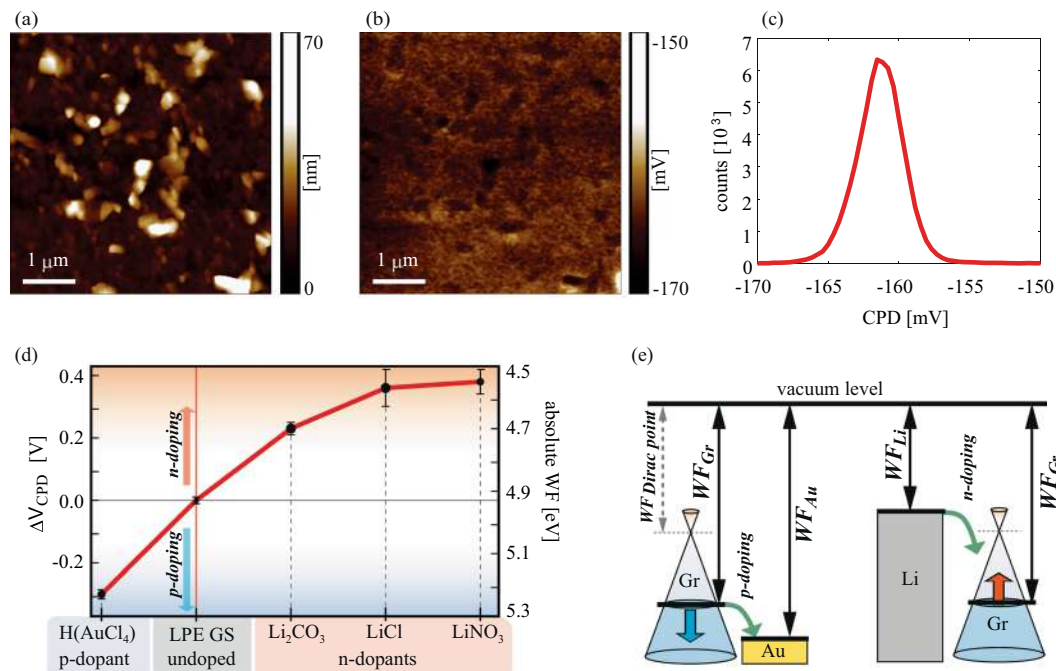
Figure 5. (**a**) AFM topography, (**b**) CPD map measured by KPFM, and (**c**) histogram of (**b**) shown for H(AuCl$_4$) doped LPE GS film as an example. (**d**) Change in WF for doped LPE GS films for different dopants, in comparison to the undoped LPE GS film. Solid red line in (**d**) is only a guide for the eye. (**e**) Schematic representation of the work functions prior to the interaction (equal vacuum levels) for Au-based salt/graphene and Li-based salt/graphene. The green arrows indicate direction of electron flow showing that in the case of Li (Au) based salts, electrons are transferred to (from) graphene.

all investigated doped films at the same wavenumber indicating that graphene basal planes were not interrupt by doping. The strong peak at around ~3400 cm^{-1} and another, smaller one, near ~1630 cm^{-1} can be seen in all doped LPE GS films (Fig. (4a)) and corresponding metal standard solutions (Fig. (4b)). They are attributed to the water molecules and are assignable to the O-H stretching vibrations (~3400 cm^{-1}) and H-O-H bending mode (~1630 cm^{-1})[38,39]. In the case of FT-IR spectra for LPE GS film doped with LiNO$_3$ the peak at ~1340 cm^{-1} and ~1390 cm^{-1} are assignable to the vibration mode of the NO$_3^-$ ions and asymmetric stretch of O-NO$_2$, respectively[38,40]. Similar vibration modes can be observed in the case of FT-IR spectra for LPE GS film doped with Li$_2$CO$_3$ and can be assigned to the vibration mode of the CO$_3^-$ ions (1340 cm^{-1}) and asymmetric stretch of O-CO$_2$ (~1390 cm^{-1})[41]. The same vibrational modes could be seen for LiNO$_3$ and Li$_2$CO$_3$ standard solutions (Fig. (4b)).

From the observed FT-IR results (Fig. 4(a)) it is clear that additional peaks appear with LPE GS film chemical doping. These additional peaks match with vibrational modes of the anions in solution (Fig. 4(b)). Considering that no new peaks are visible in the given spectra (which would indicate the formation of chemical bonds) the present peaks could be a consequence of the metal salts adsorption to the graphene lattice during the doping. In order to understand Li and Au doping mechanisms XPS measurements were performed and they are presented in separate section.

Work function modulation. Results for the work function dependent on the different metal standard solution used in the LBA process are summarized in Fig. 5. The top row depicts an example with the topography (Fig. 5(a)), corresponding contact potential difference (CPD) map measured by Kelvin probe force Microscopy-KPFM (Fig. 5(b)), and the histogram of the CPD distribution measured on H(AuCl$_4$) doped graphene film (Fig. 5(c)). The histogram is characterized with a single peak, which is used for the averaging and calculation of the absolute value of work function. The same procedure was done for all considered films. More details about the measurements of CPD and WF calculations are given in Supplementary information in Supplementary Figs. S3-S5. As a result, the values of the absolute work function are presented in Fig. 5(d) for both, doped and undoped LPE GS films. As can be seen, n-doping of graphene films is achieved by Li-based salts, whereas Au-based salt leads to p-doping.

The change of the WF due to the doping can be explained according to the schematic presentation in Fig. 5(e), illustrating that Li (Au) as a lower (higher) work function material compared to GS films. Therefore, presence of Li-based salts into the graphene film results in a reduction of the work function of the entire film. This behavior can be interpreted as an increase in the Fermi level of GSs – compared to the value for the undoped films – indicating predominantly a charge transfer from Li-based salts to graphene (n-doping), as expected when considering that Li has lower WF than graphene (graphite). In contrast to Li-based salts, the Au-based salt shows an opposite trend for the relative change of the work function. This indicates charge transfer from graphene to
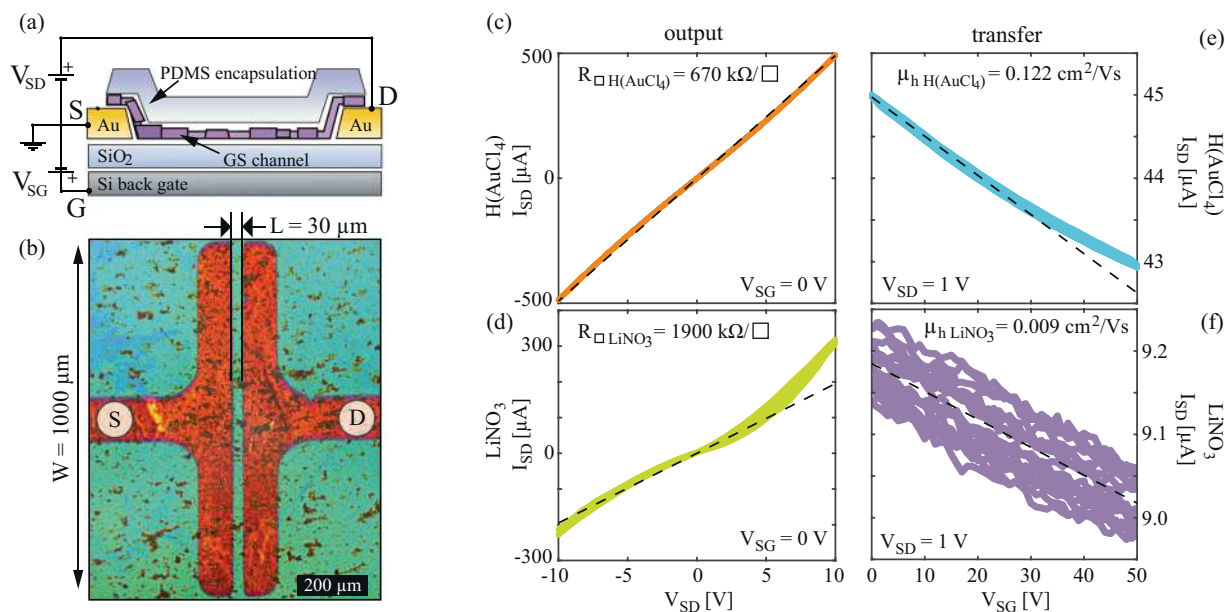
Figure 6. (**a**) Schematic cross-section of the bottom-contacted back-gated FET devices, also indicating electrical connections. (**b**) Optical microscopy image of one of the devices, without PDMS capping (for clarity). LBA GS film covers the entire sample surface. (**c,d**) Output curves of $H(AuCl_4)$ and $LiNO_3$ doped samples, and (**e,f**) transfer curves of $H(AuCl_4)$ and $LiNO_3$ doped samples, respectively. Dashed lines represent least squares linear fits (to selected regions) that were used to extract sheet resistance and linear mobility.

Au-based salt and a relative reduction of the Fermi level in GSs (p-doping). It is also worth mentioning that poly-crystalline nature of LPE based GS films, large amount of sheet edges and presence of the residual solvent (NMP) results in p-doped films[9], as was also observed in the electrical measurements presented in the following subsection. Therefore, WF values are lower for the LPE-based films by at least 200 meV, than for the pristine exfoliated single-crystals[42]. p-type doping is also reflected on the WF of the reference samples (undoped LPE GS), and therefore on the whole accessible range for the WF modulation by this method. This was also highlighted in Fig. 5(e), where the $WF_{Dirac\ point}$ depicts the case of undoped graphene[42].

According to Fig. 5(d), the maximal doping in both directions is similar, around 0.3–0.4 eV, finally providing a significant range of around 0.7 eV for the work function modulation of LPE GS films. The achieved range was obtained for 0.1 mg/mL concentration of dopants. For smaller concentrations (one order of magnitude lower, 0.01 mg/mL), the observed changes in CPD were in the order of 10 mV. On the other hand, for higher concentrations (for one order of magnitude higher, 1 mg/mL) gave rise to the problems related to the formation of continuous, large-area LPE GS films, and were therefore excluded from this study. The reported shift of the Fermi level is very similar to the other (comparable) systems in the literature. WF values change of 0.3 eV in our experiment (chemical doping by Au ions) are the same order of magnitude as in Kwon *et al.* manuscripts for gold-chloride (WF change of 0.6 eV[21], 0.6 eV[22], 0.4 eV[25]). Compared with Kwon *et al.* alkali carbonate[23] and chloride[25] graphene chemical doping data (0.4 eV and 0.3–0.4 eV, respectively) WF values change for Li in our manuscript (0.2 eV and 0.4 eV) are in the same order of magnitude. Compared with literature data the same effect can be achieved but advantages of our approach is fast and simple solution-based method for one-step fabrication and WF control of large-area graphene films.

Sheet resistance. The schematic cross-section of the devices used for the electrical characterization is shown in Fig. 6(a), also indicating electrical connections. An optical microscopy image for one of the devices without PDMS encapsulation (for clarity) is shown in Fig. 6(b) illustrating source (S) and drain (D) contact geometries. One characteristic set of transport and output curves for $H(AuCl_4)$ and $LiNO_3$ doped film is presented in Fig. 6(c–f). Here linear fits were used to extract sheet resistances and apparent linear hole mobilities. Transfer curves for all four salt-treatments and for the reference LPE GS film are presented in the Supplementary information (Supplementary Fig. S1).

In the cases of a reference (undoped) and $H(AuCl_4)$ doped LPE GS samples, output curves barely deviate from a perfect linear behavior in a rather large bias range, indicating that the contact resistance is negligible in comparison to the channel. This is in contrast to all samples doped with Li-based salts, where a significant deviation from the linear output curves were observed at higher bias, indicating non-negligible contact resistance. This can be attributed to large WF differences with Au bottom contacts in the case of Li-based salt doping of the films. Furthermore, while $H(AuCl_4)$ doping enhances electrical performance of the films, a significant increase of the resistivity and reduction of the mobility was observed in the case of all Li-based salt dopings.

The slope of the transfer curves indicates that holes are the majority carriers for all samples, including both the undoped (reference) and all metal salt doped films. Linear fits to the transfer curves were used to estimate
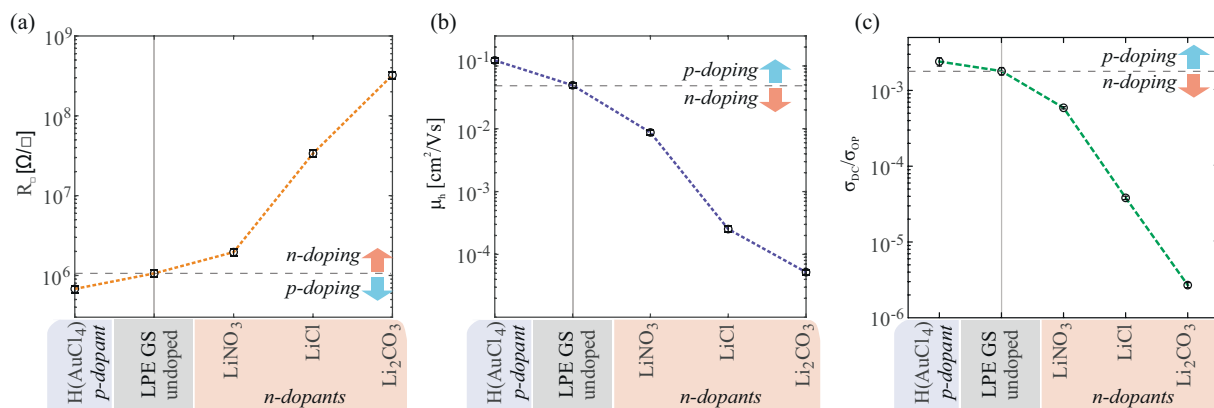
Figure 7. The dependence of the electrical properties of LBA graphene films on the type of metal standard solution based doping; (**a**) sheet resistance, and (**b**) apparent linear hole mobility, and (**c**) direct current conductivity to optical conductivity ratio (σ_{DC}/σ_{OP}). Dashed lines in (**a**–**c**) serve only as a guide for the eye.

apparent hole mobility of the devices. While the type of majority carriers was not affected by the doping, a significant (over one order of magnitude) suppression of the field-effect was observed for Li salt dopings of the films.

Figure 7 summarizes electrical properties obtained for all of the measured devices as a function of the different metal based doping.

The results indicate that anions also play a significant role. In the case of Li-based salts, a large variation of the electrical properties was obtained by the different choice of the anion species. Nonetheless, the experiments point out that metal cations dictate the direction of the WF shift (see Fig. 5), as is apparent in the case of H(AuCl$_4$) and LiCl where only cation species is varied. Our results of metal based doping of LPE graphene films demonstrate a tradeoff between enhancement of the electrical performance and modulation of the WF. Similar results were obtained for CVD doping with Li and Au salts[23,25]. Of a particular technological relevance is large reduction of the WF of graphene. While many methods for chemical modulation of graphene result in p-type doping[43–46], stable and simple n-type doping is much harder to achieve[47–49]. For an efficient electron injection, a significant reduction of graphene's WF is required. As pointed out by WF measurements and electrical characterization, LiNO$_3$ is the best choice from the tested Li-based salts with respect to both the largest WF reduction (by 400 meV) and least deterioration of the electrical properties of the films with ~2–3 times increase in sheet resistance compared to the reference (undoped LPE GS).

In contrast, doping of LPE GS films by HNO$_3$ vapor results in an increase of the apparent mobility[9]. However, using a LiNO$_3$ solution reduces the mobility by one order of magnitude. Therefore, Li$^+$ cations – and not anions – are likely responsible for the deterioration of the electrical properties upon n-doping. An increase of sheet resistance was observed in doping of CVD graphene with alkali metal carbonates and chlorides[23,25]. There, a significant increase in the sheet resistance was related to the combination of carbon atoms and dopant metals because electron donation occurred[23,25]. Also, Chen *et al.* observed that the mobility of the charge carriers decreases with the increase of the potassium doping concentration which they attributed to additional scattering caused by ionized potassium atoms[49,50]. It is most likely that Li$^+$ cations are acting as scattering centers for the carriers, or provide traps at the boundaries between neighbouring GSs and effectively increase contact resistance between the overlapping GSs.

Finally, considering that the main potential application of these LPE GS films lies in transparent electrodes, direct current conductivity to optical conductivity ratio (σ_{DC}/σ_{OP}) is presented in Fig. 7(c) for all metal standard solution doping cases and for the reference (undoped). σ_{DC}/σ_{OP} is a parameter frequently reported in order to characterize the relative performance of the films in terms of transparency and sheet resistance[11,33,51]. The higher the ratio the better the quality of transparent electrodes[33]. Compared to the changes in the electrical properties (Fig. 7(a)) the changes in the optical properties (Fig. 2) are minor. Therefore, the dependence of the σ_{DC}/σ_{OP} on the type of the metal-ion doping clearly follows the trend set by $1/R_\square$.

X-ray Photoemission Spectroscopy (XPS) measurements. In order to understand Au and Li ion doping mechanisms XPS measurements were performed. C 1 s, Au 4 f and Li 1 s core-level XPS spectra are shown in Fig. 8. N 1 s, Cl 2p and O 1 s spectra are presented as Supplementary Fig. S2. The C 1 s peak of undoped and LiCl, LiNO$_3$, Li$_2$CO$_3$, H(AuCl$_4$) doped LPE GS films is shown on Fig. 8(a). The C 1 s peak is deconvoluted using Gaussian profile into 4 components for undoped and doped films: C=C/C–C in aromatic rings (284.5 eV); C–C sp^3 (285.4 eV); C–O (286.6 eV) and C=O (289 eV)[23,52]. In the case of Li$_2$CO$_3$ we can see a small additional peak at 289.2–291.0 eV[53] which can be assigned to carbonate. Detected oxygen peak (C=O) is likely due to the residual of NMP and oxygen functionalized edges (C–O) on graphene[54,55]. The C=C/C–C peak was shifted to a lower binding energy by about 0.16, 0.48, 0.10 and 0.83 eV for H(AuCl$_4$), LiCl, LiNO$_3$ and Li$_2$CO$_3$ doping process, respectively. The C=C/C–C peak shifts in present work are a consequence of doping by different metal standard solutions. Kwon *et al.* have shown that degree of doping was related to the electronegativity of the anion in the Au complex where anions with a high electronegativity and high bond strength are adequate for use as a p-type
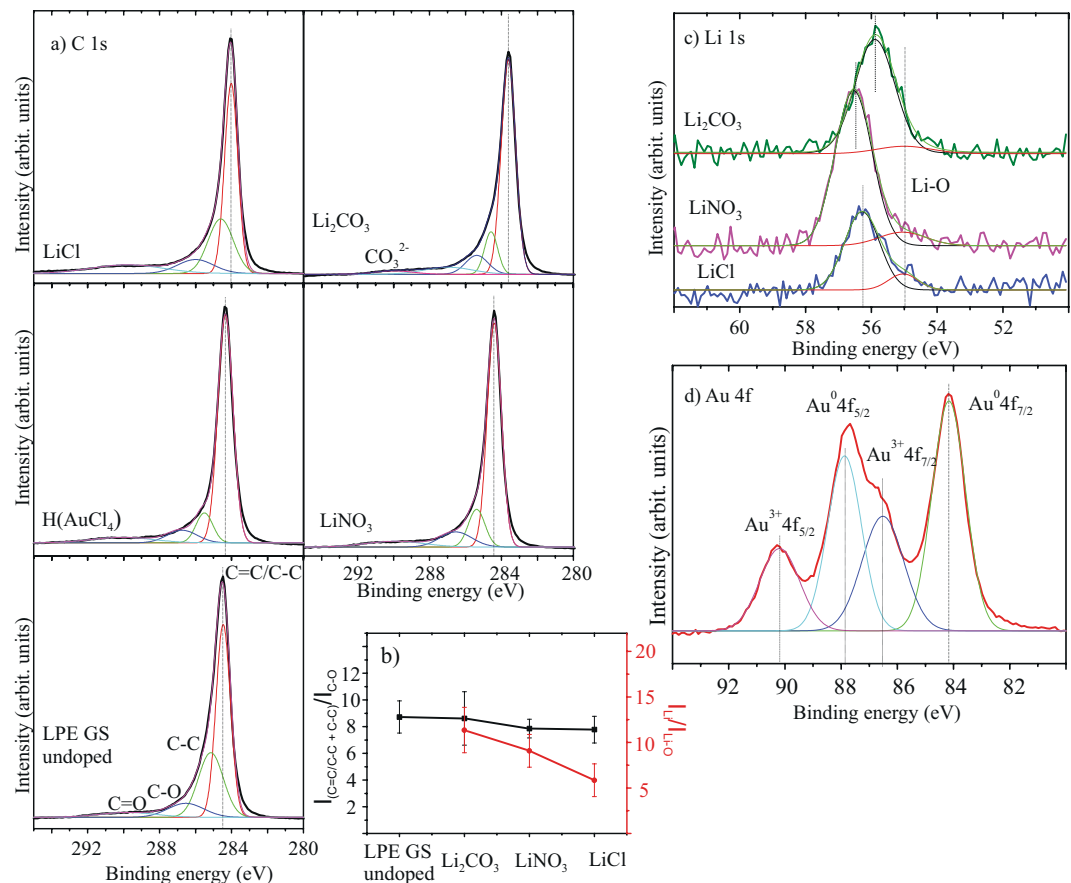
Figure 8. (**a**) XPS C 1 s spectra of undoped and H(AuCl$_4$), LiCl, LiNO$_3$, Li$_2$CO$_3$ doped LPE GS films. C=C/C–C in aromatic rings (284.5 eV); C–C sp^3 (285.4 eV); C–O (286.6 eV) and C=O (289 eV) were considered. For Li$_2$CO$_3$ a small additional peak at 289.2–291.0 eV can be assigned to carbonate. (**b**) Peak intensity ratio for the sum of C=C/C-C and C-C peaks intensities, and the intensity of C-O, I$_{(C=C/C-C+C-C)}$/I$_{(C-O)}$ (black line) and the ratio of Li 1 s intensity from Li salts to Li-O intensity, I$_{Li}$/I$_{Li-O}$ (red line). (**c**) XPS Li 1 s spectra for different Li compounds and for Li–O. (**d**) The Au 4 f peak in the XPS data of H(AuCl$_4$).

dopant in graphene[21]. Thus, different shifts of C=C/C–C peak for different metal-salt doping materials could be also a consequence of anions influence on graphene films.

Figure 8(c) show the Li 1 s core-level XPS spectra. Literature values for Li 1 s core-level for different Li compounds are: LiCl (56.2 eV), Li$_2$CO$_3$ (55.5 eV) and LiNO$_3$ (55.8 eV)[56] and they correspond well to the values obtained in this work. Li 1 s peak at 55.0 eV is assigned to Li–O bond[57]. Vijayakumar and Jianzhi have shown that lithium ion tends to bind with the oxygen rather than the carbon on graphene surface, and interacts by forming Li-O ionic bond[58]. Also Kwon *et al*. have proposed that C–O–X complexes can be formed during doping treatment and can act as an additional dipole to further reduce the value of WF[23–25,59]. The intensity ratio between sum of the intensities of C=C/C-C and C-C peaks, and the intensity of C-O (I$_{(C=C/C-C+C-C)}$/I$_{(C-O)}$) is shown in Fig. 8(b). Also, the ratio of Li 1 s intensity from Li salts to Li-O intensity (I$_{Li}$/I$_{Li-O}$) can be seen in Fig. 8(b). In both cases, intensity ratios decrease for Li$_2$CO$_3$, LiNO$_3$, LiCl, respectively and this implies increased formation of C–O and Li–O bonds. Increased number of Li-O bonds follow the increasing trend of C–O bonds, which is in correlation with the WF change (Fig. (5d)). The above mentioned results strongly suggest that the mechanism of n-type doped LPE GS films with lithium-salts could be explained with formation of Li complexes (C–O–Li).

Figure 8(d) show the Au 4 f peak of gold-chloride doped LPE GS film. The peak is composed of metal (Au^0) and metal ion (Au^{3+}). The peaks at 84.2 eV and 87.9 eV are assigned to neutral Au (Au^0 4f$_{7/2}$ and Au^0 4f$_{5/2}$, respectively), and the peaks at 86.5 eV and 90.2 eV are assigned to Au ion (Au^{3+} 4f$_{7/2}$ and Au^{3+} 4f$_{5/2}$, respectively). Au ions (Au^{3+}) have positive reduction potential and have tendency to spontaneously accept charges from other materials (graphene) and reduce to Au^0 [21,22,25,60]. Therefore, the mechanism of p-doped LPE GS film can be explained as spontaneous electron transfer from graphene film to Au^{3+}, resulting in depletion of electrons in the graphene networks, thus increasing the WF of doped graphene.

Conclusion

We demonstrate a straightforward single-step method for forming and doping of LPE GS films by metal standard solutions through charge transfer processes. Chemical doping of graphene allows to modulate its WF in a very large range, and therefore potentially enables to use the same electrode material for both, the injection and for the extraction of the electrons. n-doping of graphene films is achieved by Li-based salts, whereas Au-based salt leads

to p-doping. Furthermore, solution-processed graphene films are in particular suited for the chemical modulations, since a large number of the sheet edges opens up many adsorption sites and enhances the doping effects when compared to many other types of graphene.

The morphology of the LPE GS films does not change with the doping process, except that doped films contain agglomerates. FT-IR measurements point out that graphene basal planes stay chemically unchanged with metal doping and the charge transfer process is enabled with adsorption of the metal salts. Li-based salts decrease the WF, while Au-based salts increase the WF of the entire film. The maximal doping in both directions gives a significant range of around 0.7 eV for the work function modulation. Changing the dopant (Au or Li based salts) significantly affects the electrical properties of the films. In the case of the Li-based salts doping of the film, a significant suppression of the field-effect mobility and the increase of the sheet resistance was observed. This indicates that adsorbed Li-anions act as scattering centers for the charges. XPS data indicated that different mechanisms exist in the case of Au and Li doping. For Au ions spontaneous charge transfer occurred from graphene, thus increasing WF. In the case of Li doping, potential adsorption sites are a large number of the sheet edges where C-O bonds are preferential sites for lithium ions and for forming of C-O-Li complexes. In all cases graphene films are p-type, which is in accordance with KPFM measurements. Also, tradeoff between Li complex which reduce the value of WF and anion which increase the value of WF could be a reason of such a doping.

Metal salts charge transfer doping – which happens with this single-step method – provides a facile and effective method to tune the WF of LPE graphene therefore extending the potential use of these materials in low-cost transparent electrode applications.

Methods

Preparation of GS dispersion and doping solutions. A dispersion of GS in N-methyl-2-pyrrolidone (NMP, Sigma Aldrich, product no. 328634) has been used. GS dispersion was prepared from graphite powder (Sigma Aldrich, product no. 332461) of initial concentration 18 mg/mL. The solution was sonicated in a low-power ultrasonic bath for 14 h. The resulting dispersion was centrifuged for 60 min at 3000 rpm immediately after the sonication.

Stock standard solutions used in our work for n-doping are 1 mg/mL LiCl, $LiNO_3$ and Li_2CO_3 and for p-doping is 1 mg/mL gold standard solution (Merck, $H(AuCl_4)$, product no. 170216). Lithium standard solutions were prepared from originated Li salts (LiCl, $LiNO_3$ and Li_2CO_3, Merck, product no. 105679, 105653 and 105680, respectively). By appropriate dilution of the stock solution with deionized water we obtained 0.1 mg/mL metal water solution which is then used in doping process.

Deposition on a substrate and doping of LPE GS films. GS dispersion in NMP was used to fabricate transparent and conductive films by LBA technique at a water-air interface, like in our previous work[9,29,61]. A small amount of GS dispersion was added to the water-air interface and after the film was formed it was slowly scooped onto the target substrate. Applying the same process of fabricating the GS films and using the appropriate metal standard solution instead of water, chemical doping was achieved. As substrates SiO_2/Si wafer were used for electrical and WF measurements, while quartz and CaF_2 substrates were chosen for optical and FT-IR spectroscopy, respectively.

Characterization of undoped and doped LPE GS films. The Morphology of LPE GS films was studied by optical and atomic force microscopy (AFM). Topographic AFM measurements were done by NTEGRA Prima AFM system and NSG01 probes with a typical tip radius of around 10 nm. The surface roughness of LPE GS films was calculated as a root-mean square of the height distribution and averaged on ten 50×50 μm² areas.

Kelvin probe force microscopy (KPFM) – established almost three decades ago[62] and in the meantime frequently applied to graphene[42,63–65] – was employed in order to characterize changes in the electrical surface potential and corresponding Fermi level shifts due to doping. For this purpose, we measured the contact potential difference (CPD) between AFM tip and the sample surface[66] by using Pt covered NSG01/Pt probes with a typical tip curvature radius of 35 nm. In the first pass of KPFM, the sample topography was measured in tapping AFM mode. In the second pass, the probe was lifted by 20 nm, and moved along the trajectory measured in the first pass. Simultaneously, the sum of AC and DC voltage was applied between the sample and the probe. The AC voltage excites AFM probe oscillations during its movement, while the CPD between AFM tip and the sample surface in every point is then equal to the value of variable DC voltage which cancels the AFM probe oscillations. For all samples, the CPD was measured on five 5×5 μm² areas, and then averaged. In order to obtain the absolute value of the work function, the following procedure was applied[42]. The CPD is equal to the work function difference between AFM tip (WF_t) and sample (WF_s), $CPD = WF_t\text{-}WF_s$. The calibration of the WF_t was done by a standard procedure consisting of KPFM measurements on a freshly cleaved HOPG with a well known work function of 4.6 eV[42]. Finally, the sample work function was calculated as $WF_s = WF_t$ - CPD, where CPD is measured by KPFM for all, undoped and doped LPE GS films.

The effect of chemical doping on optical properties of LBA GS films was investigated with measurements of optical transmittance, using UV-VIS spectrophotometer (Beckman Coulter DU 720 UV-VIS Spectrophotometer).

Electrical measurements were performed under ambient conditions in a standard field-effect device configuration with Si substrate acting as a back gate electrode, using Keithley 2636 A SYSTEM SourceMeter. Devices were based on bottom-contact gold pads defined by a shadow mask with L/W = 30 μm/1000 μm, and SiO_2 as a gate dielectric with thickness of 285 nm. Graphene films were deposited using the same LBA method as described above. The top surface of the devices was encapsulated by polydimethylsiloxane (PDMS) films (GelPak X4) to ensure stable performance and minimize any adsorption/desorption during electrical measurements that could occur from the surroundings (e.g. water vapor). Electrical characterization was performed on several devices of each doping with metal standard solution, and for undoped films as a reference. For each device ten subsequent forward and

backward transfer and output curves were measured, using low sweeping rate (~0.005–1 Hz per point in a voltage sweep) to minimize parasitic capacitance. Sheet resistance and apparent linear field-effect mobility were extracted using fits to output and transfer curves, respectively. For the output measurements source-drain bias was varied in a range between $-10\,V$ and $+10\,V$, with the gate electrode grounded. For transfer measurements, the gate voltage was varied between $0\,V$ and $50\,V$, with source-drain bias at $1\,V$ in all cases except for Li_2CO_3 where due to a very weak field-effect (very low mobility) $10\,V$ bias was used.

The room-temperature micro-Raman spectra of undoped and metal salt doped LPE GS films were collected using Tri Vista 557 triple spectrometer coupled to the liquid nitrogen-cooled CCD detector. Nd:YAG laser line of 532 nm was used for the excitation and 50 magnification objective was used for focusing the beam onto the sample. Low laser power (less than 1 mW) was applied to prevent the thermal degradation of the sample. Each LPE GS film sample was measured at eight different positions.

Fourier transform infrared absorbance spectra (FT-IR spectra) of undoped and metal salt doped LPE GS films were measured over a range of $400–4000\,cm^{-1}$ with Nicolet Nexus 470 FT-IR spectrometer. Standard solutions which were used for the preparation of doped films were measured too and they were prepared by drop casting method on the CaF_2 substrate.

XPS spectra were recorded using a Thermo Scientific instrument (K-Alpha spectrometer, Thermo Fisher Scientific, Waltham, USA) equipped with a monochromatic Al Kα X-ray source (1486.6 eV). High-resolution scans were performed with a pass energy of 50 eV and a step size of 0.1 eV. All analyses were performed at room temperature.

Data availability
The datasets obtained and analysed during the current study that are not included in this article are available from the corresponding authors on reasonable request.

References
1. Geim, A. K. Graphene: Status and prospects. *Science* **324**, 1530–1534 (2009).
2. Geim, A. K. & Novoselov, K. S. The rise of graphene. *Nat. Mater.* **6**, 183–191 (2007).
3. Novoselov, K. S. *et al.* Room-temperature quantum hall effect in graphene. *Science* **315**, 1379–1379 (2007).
4. Bonaccorso, F., Sun, Z., Hasan, T. & Ferrari, A. C. Graphene photonics and optoelectronics. *Nat. Photonics* **4**, 611–622 (2010).
5. Kwon, K. C., Kim, B. J., Lee, J. L. & Kim, S. Y. Role of ionic chlorine in the thermal degradation of metal chloride-doped graphene sheets. *J. Mater. Chem. C* **1**, 253–259 (2013).
6. Ferrari, A. C. *et al.* Science and technology roadmap for graphene, related two-dimensional crystals, and hybrid systems. *Nanoscale* **7**, 4598–4810 (2015).
7. Backes, C. *et al.* Guidelines for exfoliation, characterization and processing of layered materials produced by liquid exfoliation. *Chem. Mater.* **29**, 243–255 (2017).
8. Li, X. *et al.* Highly conducting graphene sheets and Langmuir-Blodgett films. *Nat. Nanotechnol.* **3**, 538–542 (2008).
9. Matković, A. *et al.* Enhanced sheet conductivity of Langmuir-Blodgett assembled graphene thin films by chemical doping. *2D Mater* **3**, 015002 (2016).
10. Lee, S. K. *et al.* All graphene-based thin film transistors on flexible plastic substrates. *Nano Lett.* **12**, 3472–3476 (2012).
11. Zheng, Q. *et al.* Transparent conductive films consisting of ultralarge graphene sheets produced by Langmuir-Blodgett assembly. *ACS Nano* **5**, 6039–6051 (2011).
12. Park, J. *et al.* Work-function engineering of graphene electrodes by self-assembled monolayers for high-performance organic field-effect transistors. *J. Phys. Chem. Lett.* **2**, 841–845 (2011).
13. Tong, S. W., Wang, Y., Zheng, Y., Ng, M. F. & Loh, K. P. Graphene intermediate layer in tandem organic photovoltaic cells. *Adv. Funct. Mater.* **21**, 4430–4435 (2011).
14. Wang, Y., Tong, S. W., Xu, X. F., Özyilmaz, B. & Loh, K. P. Interface engineering of layer-by-layer stacked graphene anodes for high-performance organic solar cells. *Adv. Mater.* **23**, 1514–1518 (2011).
15. Wu, J. *et al.* Organic light-emitting diodes on solution-processed graphene transparent electrodes. *ACS Nano* **4**, 43–48 (2010).
16. Wang, X., Zhi, L. & Mullen, K. Transparent, conductive graphene electrodes for dye-sensitized solar cells. *Nano Lett.* **8**, 323–327 (2008).
17. Alfano, B. *et al.* Modulating the sensing properties of graphene through an eco-friendly metal-decoration process. *Sensors Actuators, B Chem.* **222**, 1032–1042 (2016).
18. Lynch, P., Khan, U., Harvey, A., Ahmed, I. & Coleman, J. N. Graphene-MoS2 nanosheet composites as electrodes for dye sensitised solar cells. *Mater. Res. Express* **3**, 035007 (2016).
19. Mosciatti, T. *et al.* A multifunctional polymer-graphene thin-film transistor with tunable transport regimes. *ACS Nano* **9**, 2357–2367 (2015).
20. Giubileo, F. & Di Bartolomeo, A. The role of contact resistance in graphene field-effect devices. *Prog. Surf. Sci.* **92**, 143–175 (2017).
21. Kwon, K. C., Kim, B. J., Lee, J. L. & Kim, S. Y. Effect of anions in Au complexes on doping and degradation of graphene. *J. Mater. Chem. C* **1**, 2463–2469 (2013).
22. Kwon, K. C., Choi, K. S. & Kim, S. Y. Increased work function in few-layer graphene sheets via metal chloride doping. *Adv. Funct. Mater.* **22**, 4724–4731 (2012).
23. Kwon, K. C., Choi, K. S., Kim, B. J., Lee, J. L. & Kim, S. Y. Work-function decrease of graphene sheet using alkali metal carbonates. *J. Phys. Chem. C* **116**, 26586–26591 (2012).
24. Huang, J. H., Fang, J. H., Liu, C. C. & Chu, C. W. Effective work function modulation of graphene/carbon nanotube composite films as transparent cathodes for organic optoelectronics. *ACS Nano* **5**, 6262–6271 (2011).
25. Kwon, K. C., Choi, K. S., Kim, C. & Kim, S. Y. Role of metal cations in alkali metal chloride doped graphene. *J. Phys. Chem. C* **118**, 8187–8193 (2014).
26. Wang, X., Xu, J. B., Xie, W. & Du, J. Quantitative analysis of graphene doping by organic molecular charge transfer. *J. Phys. Chem. C* **115**, 7596–7602 (2011).
27. Shin, H. J. *et al.* Control of electronic structure of graphene by various dopants and their effects on a nanogenerator. *J. Am. Chem. Soc.* **132**, 15603–15609 (2010).
28. Shi, Y. *et al.* Work function engineering of graphene electrode via chemical doping. *ACS Nano* **4**, 2689–2694 (2010).

29. Tomašević-Ilić, T. *et al*. Reducing sheet resistance of self-assembled transparent graphene films by defect patching and doping with UV/ozone treatment. *Appl. Surf. Sci.* **458**, 446–453 (2018).

30. Matković, A. *et al*. Spectroscopic imaging ellipsometry and Fano resonance modeling of graphene. *J. Appl. Phys.* **112**, 123523 (2012).

31. Bracamonte, M. V., Lacconi, G. I., Urreta, S. E. & Foa Torres, L. E. F. F. On the nature of defects in liquid-phase exfoliated graphene. *J. Phys. Chem. C* **118**, 15455–15459 (2014).

32. Eckmann, A. *et al*. Probing the nature of defects in graphene by Raman spectroscopy. *Nano Lett.* **12**, 3925–3930 (2012).

33. Rytel, K. *et al*. Ultrasonication-induced sp3 hybridization defects in Langmuir-Schaefer layers of turbostratic graphene. *Phys. Chem. Chem. Phys.* **20**, 12777–12784 (2018).

34. Eckmann, A., Felten, A., Verzhbitskiy, I., Davey, R. & Casiraghi, C. Raman study on defective graphene: Effect of the excitation energy, type, and amount of defects. *Phys. Rev. B - Condens. Matter Mater. Phys.* **88**, 035426 (2013).

35. Drewniak, S. *et al*. Studies of reduced graphene oxide and graphite oxide in the aspect of their possible application in gas sensors. *Sensors* **16**, 103 (2016).

36. Kim, W. J., Basavaraja, C., Thinh, P. X. & Huh, D. S. Structural characterization and DC conductivity of honeycomb-patterned poly(ε-caprolactone)/gold nanoparticle-reduced graphite oxide composite films. *Mater. Lett.* **90**, 14–18 (2013).

37. Ţucureanu, V., Matei, A. & Avram, A. M. FTIR spectroscopy for carbon family study. *Crit. Rev. Anal. Chem.* **46**, 502–520 (2016).

38. Wu, X. *et al*. One-step freezing temperature crystallization of layered rare-earth hydroxide (Ln2(OH)5NO3·nH2O) nanosheets for a wide spectrum of Ln (Ln = Pr-Er, and Y), anion exchange with fluorine and sulfate, and microscopic coordination probed via photoluminescence. *J. Mater. Chem. C* **3**, 3428–3437 (2015).

39. Nakamoto, K. Infrared and Raman Spectra of Inorganic and Coordination Compounds. Part A: Theory and Applications in Inorganic Chemistry; Part B: Application in Coordination, Organometallic, and Bioinorganic Chemistry, 5th Edition (Nakamoto, Kazuo). *John Wiley and Sons* (John Wiley and Sons, 2009).

40. Geng, F. *et al*. New layered rare-earth hydroxides with anion-exchange properties. *Chem. Eur. J.* **14**, 9255–9260 (2008).

41. Lefèvre, G. *In situ* Fourier-transform infrared spectroscopy studies of inorganic ions adsorption on metal oxides and hydroxides. *Adv. Colloid Interface Sci.* **107**, 109–123 (2004).

42. Yu, Y. *et al*. Tuning the graphene work function by electric field effect. *Nano Lett.* **9**, 3430–3434 (2009).

43. Levesque, P. L. *et al*. Probing charge transfer at surfaces using graphene transistors. *Nano Lett.* **11**, 132–137 (2011).

44. Kuruvila, A. *et al*. Organic light emitting diodes with environmentally and thermally stable doped graphene electrodes. *J. Mater. Chem. C* **2**, 6940–6945 (2014).

45. Meyer, J. *et al*. Metal oxide induced charge transfer doping and band alignment of graphene electrodes for efficient organic light emitting diodes. *Sci. Rep* **4**, 5380 (2014).

46. Matković, A. *et al*. Probing charge transfer between molecular semiconductors and graphene. *Sci. Rep* **7**, 9544 (2017).

47. Sanders, S. *et al*. Engineering high charge transfer n-doping of graphene electrodes and its application to organic electronics. *Nanoscale* **7**, 13135–13142 (2015).

48. Han, K. S. *et al*. A non-destructive n-doping method for graphene with precise control of electronic properties via atomic layer deposition. *Nanoscale* **8**, 5000–5005 (2016).

49. Chen, J. H. *et al*. Charged-impurity scattering in graphene. *Nat. Phys.* **4**, 377–381 (2008).

50. Pinto, H. & Markevich, A. Electronic and electrochemical doping of graphene by surface adsorbates. *Beilstein J. Nanotechnol* **5**, 1842–1848 (2014).

51. De, S. & Coleman, J. N. Are there fundamental limitations on the sheet resistance and transmittance of thin graphene films? *ACS Nano* **4**, 2713–2720 (2010).

52. Benayad, A. *et al*. Controlling work function of reduced graphite oxide with Au-ion concentration. *Chem. Phys. Lett.* **475**, 91–95 (2009).

53. López, G. P., Castner, D. G. & Ratner, B. D. XPS O 1s binding energies for polymers containing hydroxyl, ether, ketone and ester groups. *Surf. Interface Anal.* **17**, 267–272 (1991).

54. Hernandez, Y. *et al*. High-yield production of graphene by liquid-phase exfoliation of graphite. *Nat. Nanotechnol* **3**, 563–568 (2008).

55. Kim, H. *et al*. Optoelectronic properties of graphene thin films deposited by a Langmuir-Blodgett assembly. *Nanoscale* **5**, 12365–12374 (2013).

56. Naumkin, A. V., Kraut-Vass, A., Gaarenstroom, S. W. & Powell, C. J. NIST X-ray photoelectron spectroscopy database. Available at: https://srdata.nist.gov/xps/EngElmSrchQuery.aspx?EType=PE&CSOpt=Retri_ex_dat&Elm=Li. (2019).

57. Moulder, J. F., Stickle, W. F., Sobol, P. E. & Bomben, K. D. *Hanbook of X-ray photoelectron spectroscopy. Reference book of standard spectra for indentification and interpretation of XPS data* (Perkin-Elmer Corporation, Physical Electronic division, 1992).

58. Vijayakumar, M. & Jianzhi, H. Exploring the interaction between lithium ion and defective graphene surface using dispersion corrected DFT studies. *ECS Trans* **53**, 23–32 (2013).

59. Pickett, W. E. Negative electron affinity and low work function surface: Cesium on oxygenated diamond (100). *Phys. Rev. Lett.* **73**, 1664–1667 (1994).

60. Syu, J. Y. *et al*. Wide-range work-function tuning of active graphene transparent electrodes via hole doping. *RSC Adv.* **6**, 32746–32756 (2016).

61. Tomašević-Ilić, T. *et al*. Transparent and conductive films from liquid phase exfoliated graphene. *Opt. Quantum Electron.* **48**, 319 (2016).

62. Nonnenmacher, M., O'Boyle, M. P. & Wickramasinghe, H. K. Kelvin probe force microscopy. *Appl. Phys. Lett.* **58**, 2921–2923 (1991).

63. Vasić, B. *et al*. Atomic force microscopy based manipulation of graphene using dynamic plowing lithography. *Nanotechnology* **24**, 015303 (2013).

64. Vasić, B. *et al*. Low-friction, wear-resistant, and electrically homogeneous multilayer graphene grown by chemical vapor deposition on molybdenum. *Appl. Surf. Sci.* **509**, 144792 (2020).

65. Panchal, V., Pearce, R., Yakimova, R., Tzalenchuk, A. & Kazakova, O. Standardization of surface potential measurements of graphene domains. *Sci. Rep* **3**, 2597 (2013).

66. Udum, Y. *et al*. Inverted bulk-heterojunction solar cell with cross-linked hole-blocking layer. *Org. Electron.* **15**, 997–1001 (2014).

Acknowledgements

Author contributions

I.M. devised the concept of LPE GS films doping with metal standard solutions in the single-step method. I.M. and J.V. prepared LPE dispersions and fabricated undoped and doped LPE GS films on different substrates. B.V. did AFM and KPFM measurements, A.M. performed electrical measurements, I.M. and J.V. did FTIR measurements, S.A. and I.M. performed Raman measurements and I.M., T.G, M.K., S.A. and J.V. performed and

processed XPS measurements. C.T. and R.G. oversaw the study. I.M., A.M. and B.V. wrote the manuscript. All authors discussed and analysed the results and reviewed the manuscript.

Competing interests

The authors declare no competing interests.

Additional information

Supplementary information is available for this paper at https://doi.org/10.1038/s41598-020-65379-1.

Correspondence and requests for materials should be addressed to I.R.M. or A.M.

Reprints and permissions information is available at www.nature.com/reprints.

Publisher's note Springer Nature remains neutral with regard to jurisdictional claims in published maps and institutional affiliations.

PAPER

Pseudo-refractive index and excitonic features of single layer CdSe/CdS core–shell nanoplatelet films

View the article online for updates and enhancements.

Pseudo-refractive index and excitonic features of single layer CdSe/CdS core–shell nanoplatelet films

Milka M Jakovljević[1,4] ⬥, **Sonja Aškrabić**[1] ⬥, **Goran Isić**[1,2] ⬥, **Borislav Vasić**[1] ⬥, **Radoš Gajić**[1] **and Mikhail Artemyev**[3] ⬥

[1] Institute of Physics Belgrade, University of Belgrade, Pregrevica 118, 11080 Belgrade, Serbia
[2] Texas A & M University at Qatar, PO Box 23874 Education City, 23874 Doha, Qatar
[3] Research Institute for Physical Chemical Problems of the Belarusian State University, Leningradskaya str. 14, 220030 Minsk, Belarus

E-mail: milka@ipb.ac.rs

CrossMark

Abstract
Semiconductor CdSe/CdS core–shell nanoplatelets exhibit narrow and intense absorption and photoluminescence spectra in the visible range, which makes them suitable for numerous applications in optoelectronics. Of particular interest is the preparation and optical characterization of thin films with an accurately controlled amount of nanoplatelets. Here we report on the use of spectroscopic ellipsometry for investigating the optical properties of ultrathin films composed of a single layer of negatively charged CdSe/CdS core–shell nanoplatelets prepared by the electrostatic layer-by-layer deposition on SiO$_2$/Si substrates. Combining the ellipsometric spectra with atomic force microscopy measurements, we were able to infer the nanoplatelet film extinction spectra which was found to exhibit the two characteristic exciton peaks albeit blueshifted relative to the colloidal nanoplatelets.

Keywords: semiconductor core–shell nanoplatelets, single-layer electrostatic deposition, spectroscopic ellipsometry, refractive index

(Some figures may appear in colour only in the online journal)

1. Introduction

Nanoplatelets (NPLs) or colloidal quantum wells have an atomically flat surface [1]. Their thickness is quantized to an integer number of monolayers, which enables thickness tunable emission. NPLs made of A^{II}B^{VI} semiconductors such as CdS, CdSe, and CdTe are especially interesting because their absorption and photoluminescence (PL) bands lie in the visible range and because of very high absorption and PL excitation efficiency [1–3]. The optical properties of core only NPLs such as quantum yield [4], photostability [5], and reduced fluorescence emission blinking [6, 7] are greatly improved by epitaxial growth of semiconductor shells [8]. All these properties make NPLs good candidates for applications

in optoelectronics. Compared to quantum dots or nanorods, NPLs exhibit extremely narrow intense bands on both absorption and PL spectra, which is essential for color purity of light-emitting diodes [9–11]. They have directed emission and polarization, fast radiative lifetimes related to the giant oscillator strength effect allowing high quantum yields, and promising lasing properties [12, 13].

An important part of nanodevice design is the formation of high quality nanostructured films. Numerous techniques are used for nanoparticle deposition on various substrates, including spin-coating, drop-casting, doctor-blading, self-assembling, etc Although these techniques lead to formation of relatively thick films, their precise composition is hard to control [14]. One of the bottom-up methods for creating well-organized, layer-by-layer assemblies of nanoparticles is based on electrostatic interactions [15–17]. It

---

allows the assembly of ultrathin nanoparticle films by exposing a charged substrate to alternating solutions of polymer molecules and nanoparticles charged with opposite signs, with a single polymer molecule-nanoparticle stack representing the smallest building block in the deposition procedure.

UV–vis absorption spectroscopy exhibiting a linear relationship between the absorption coefficient in the region of the first absorption maximum and the number of nanoparticle monolayers is the standard technique for monitoring the growth of layered structures, and for their optical characterization [18]. It is, however, inadequate when the layers are extremely thin or if the substrate is opaque. One way to overcome this issue is to use spectroscopic ellipsometry (SE) in reflection mode. Owing to its high surface sensitivity, SE has an important role in optical characterization of ultrathin nanostructured films, and various relevant characteristics such as optical functions, film thickness, surface roughness etc can be determined [19]. The key aspect of SE is an appropriate model, capable of accounting for all relevant structural elements of multilayer samples, especially close to material interfaces.

SE was used to measure the dielectric function of thin semiconductor nanocomposite films formed by spin-coating [20–22], but the thicknesses of these films were of the order of tens of nanometers. SE of somewhat thinner HgTe nanocrystal film, self-assembled by a tenfold repetition of layer-by-layer electrostatic deposition showed that the dispersion relation of nanocrystals can be modeled by critical points [23]. However, the investigation of optical properties of a single layer composed of charged layer and oppositely charged nanocrystals on the top is very challenging, due to the strong correlation between the thickness of the film and its refractive index [24, 25].

In this work, we performed the extraction of pseudo refractive index of a NPL monolayer, whose thickness is around 5 nm and which consists of a single layer of negatively charged CdSe/CdS core–shell NPLs deposited on the top of the positively charged molecular layer on a SiO_2(85 nm)/Si(bulk) substrate. Real and imaginary parts of refractive index of the composite film and the substrate were extracted using point-by-point inversion from the SE experimental data [26]. In this procedure, all the parameters of the model including refactive indicies (Si, SiO_2, and positively charged molecular layer) and thicknesses (SiO_2, positively charged molecular layer and NPLs film) must be fixed except for n and k of the NPLs film. Then n and k values are allowed to vary independently at each wavelength, and are results of this analysis. This is quite effective procedure for determining the complex refractive index of a sample, particulary when dielectric function modeling is difficult in some specific regions. Atomic force microscopy (AFM) analysis of morphology and measured thickness of the NPL film are used to interpret the data obtained by SE measurements.

2. Material and methods

2.1. Sample preparation

Hydrophobic CdSe/CdS core–shell NPLs with 4.5 ML CdSe core were synthesized according to a published procedure
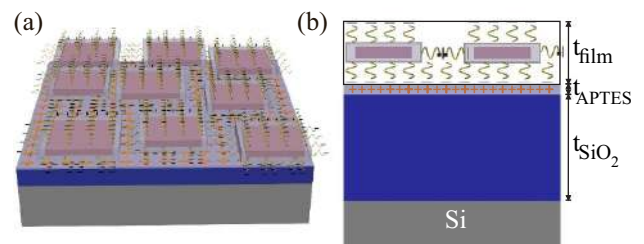

Figure 1. Film formed by close packed CdS/CdSe NPLs on the substrate schematics: (a) 3D view and (b) vertical cross section.

[27]. In order to make NPLs solubilized and negatively charged, hence suitable for electrostatic self-assembly, the hydrophobic NPLs were functionalized with mercaptoacetic acid (MAA). The surface of a commercial highly n-doped Si wafer covered with SiO_2 film (of nominal thickness ∼ 85 nm), was treated in aqueous solution of aminopropyl trietoxy silane (APTES) dissolved in toluene in order to charge SiO_2 positively. After being left in solution for 20 min, the substrate was rinsed with toluene. Finally, the wafer with a monolayer of APTES was treated in a colloidal solution of negatively charged CdSe/CdS NPLs to form a 2D layer of close-packed NPLs on SiO_2 film surface. The schematics of the structure is shown in figure 1.

2.2. Characterization

2.2.1. Spectroscopic ellipsometry.
Spectroscopic ellipsometry measures the change in the state of polarization of the incident light upon reflection from the sample. It gives the ratio of the two complex Fresnel reflection coefficients, $\widetilde{r}_p$ and $\widetilde{r}_s$, for light polarized parallel and perpendicular to the plane of incidence, respectively, $\rho = \widetilde{r}_p/\widetilde{r}_p = \tan\Psi e^{i\Delta}$.

SE measurements were performed using rotating-polarizer spectroscopic ellipsometer (SOPRA GES5E-IRSE VASE). The measured quantities were the two ellipsometric parameters, tan Ψ and cos Δ, and the spectral range was 200–700 nm (with step size 2 nm). During the measurements 'previous tracking mode' is used. This means that the angle of non-rotating exit polarizer in the setup, often called analyzer, at one point (energy or wavelength) is set to the value of Ψ attained at the previous point. This is done in order to keep the reflected beam close to being circularly polarized and measurements at optimal sensitivity [28]. We measured the SE spectra of both the bare SiO_2(85 nm)/Si substrate and the substrate with the NPL monolayer on top. The dielectric function of highly doped Si substrate does not necessarily coincide with spectra found in the literature, therefore bare substrate characterization is important to minimize potential errors in the extraction procedure. The final SE spectra of the film were obtained by averaging over 10 consecutive measurements of 10 s duration for each point in spectra, in order to minimize random errors and to improve signal to noise ratio. All the calculations were performed using home-developed code in MATLAB.

2.2.2. AFM characterization.
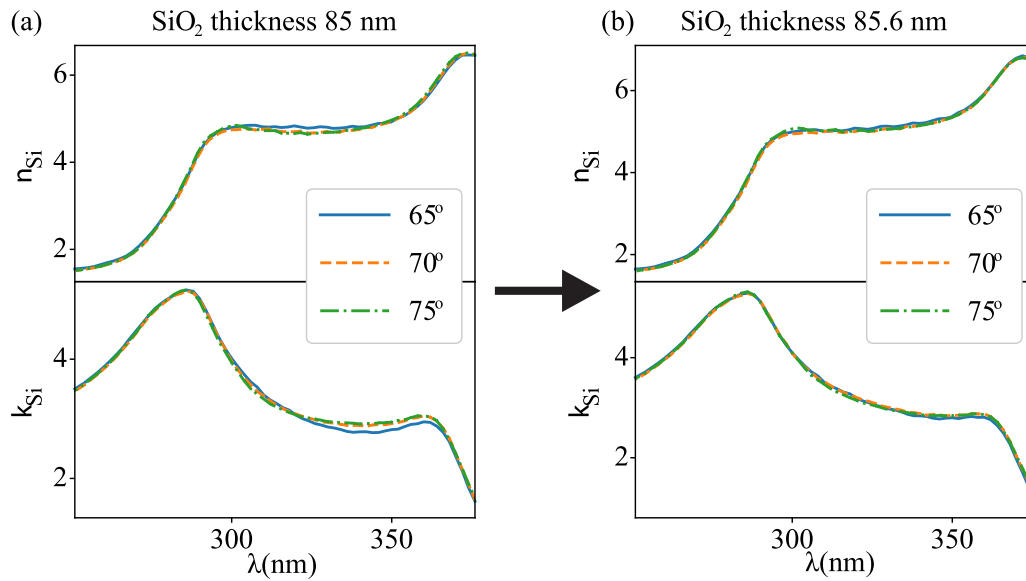The morphological characterization of CdSe/CdS core–shell NPL films was performed

Figure 2. Real (top) and imaginary (bottom) part of the Si refractive index retrieved assuming the SiO_2 layer thickness is (a) 85 nm and (b) 85.6 nm.

by AFM, using the NTEGRA Prima system in ambient conditions. Topographic imaging was carried out in tapping AFM mode using NSG01 probes from NT-MDT. The main aim of the morphological characterization was to measure the thickness of the CdSe/CdS core–shell film, the value which was further included in the fitting procedure of ellipsometric spectra. The film thickness was determined by the following procedure. Topography was measured on five $2 \times 2\ \mu m^2$ areas. For every scan area, an average height and surface roughness were calculated. Both values were further averaged across all considered areas. The final film thickness was calculated as a sum of the averaged height and averaged roughness.

2.3. Ellipsometry data analysis

The initial step in the NPL film refractive index (point-by-point) extraction is to properly characterize the substrate. Commercially made Si wafer was used with nominally 85 nm thick SiO_2 obtained using thermal oxidation. The Si wafer has $< 001 >$ orientation, and is n-type semiconductor highly doped with P (concentration $\sim 10^{15}$ cm^{-3}, resistivity 3–5 Ω cm), therefore it differs from the intrinsic Si, and has slightly different optical properties [29].

The SE spectra of the substrate were measured at three different angles of incidence (AOI) 65°, 70°, and 75°. Typically, there is a strong correlation between the data at different AOI, especially when the overlayer is thin [30]. However, when the SE spectra are measured over the energy range where the substrate has a sharp optical structure (like critical points) the spectra of extracted data at different AOI do not coincide if the thickness of SiO_2 is not properly determined [31]. This property was used to extract the optical function of Si in the wafer and oxide thickness with assumption that the dielectric function of SiO_2 is known and equivalent to the one from SOPRA refractive index base [32]. Once the substrate optical properties are known, direct extraction (or point-by-point inversion)
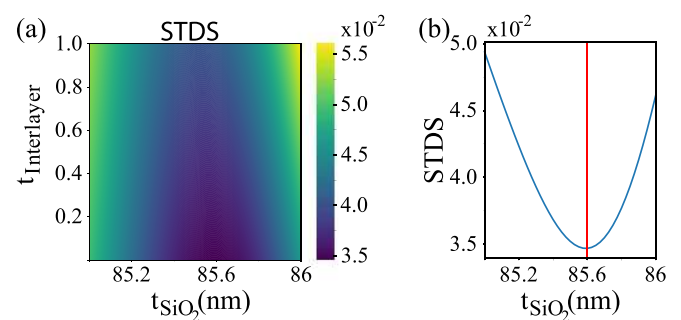

Figure 3. (a) Mapped error function for thicknesses of the SiO_2 layer in range 85–86 nm and interlayer thickness in range 0–1 nm. (b) Selected error function for different SiO_2 thickness without interlayer.

of index of refraction of the composite (mixture) consisting of the CdSe/CdS core–shell NPLs with ligands and air was performed. Here we refer to refractive index of composite as pseudo refractive index of the NPL film, assuming that the film is effectively uniform in its volume. Refractive index of APTES was taken from the literature [33], and its monolayer thickness is estimated to be 0.6 nm based on the length of the molecule. The SE measurements of the sample with film were analyzed at single angle, 75°, since the measurements at different angles did not provide any additional information.

3. Results and discussion

3.1. Substrate characterization

Ellipsometric measurements of the substrate were performed at three different AOI 65°, 70° and 75°. Assuming that the optical model used here is SiO_2(85 nm)/Si, the extracted refractive indices of Si from three different AOI ellipsometric measurements coincide almost perfectly, except
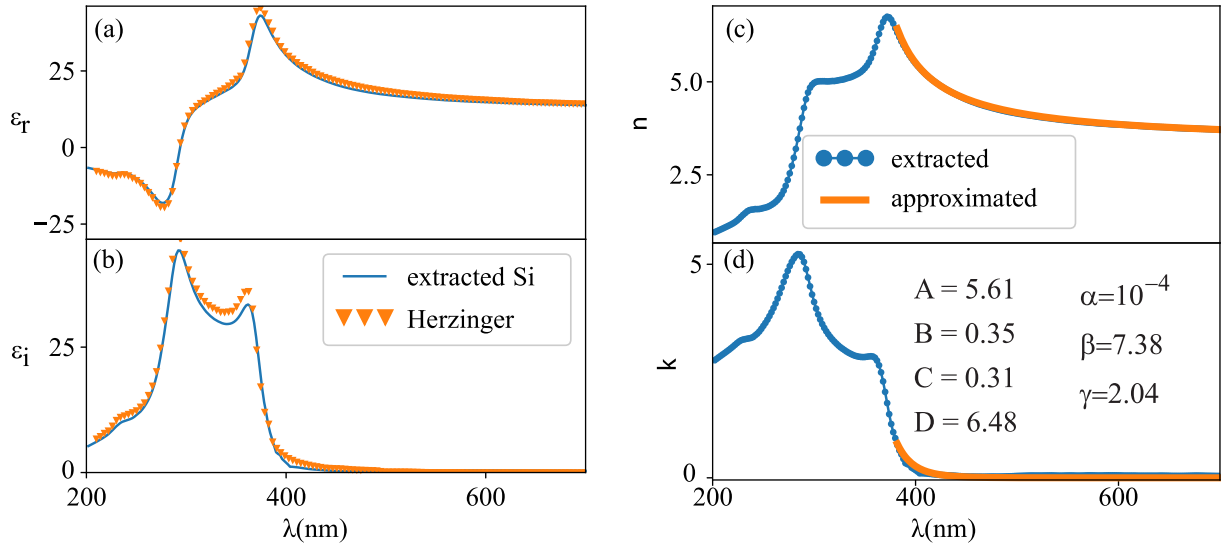
Figure 4. (a) Real and (b) imaginary part of extracted dielectric function of highly doped Si and lightly doped Si (taken from Herzinger *et al* [34]). (c) Real and (d) imaginary part of refractive index of highly doped Si substrate extracted from the measurements (dotted line) and approximated with analytical function to minimize the noise.

at wavelengths that are close to the critical points of Si 2(a). Arwin and Aspnes showed that owing to the sharp features in the dielectric function of Si near the critical points, it is possible to unambiguously determine the thickness and dielectric function of thin films on Si substrate [31]. Here, a part of spectra close to critical points is used for calculation of oxide thickness and dielectric function of Si. We quantify the spectral overlap by the standard deviation of the three spectra (STDS):

$$STDS = \sqrt{\frac{\sum_{i=1}^{N_\lambda} \sum_{j=1}^{N_{AOI}} \left[(n_{ij} - \bar{n}_i)^2 + (k_{ij} - \bar{k}_i)^2\right]}{2N_\lambda N_{AOI} - 1}}, \quad (1)$$

where n_{ij} and k_{ij} are real and imaginary parts of refractive index at λ_i and angle j, $\bar{n}_i$ and $\bar{k}_i$ are the mean values for the three AOI at λ_i, N_λ is the number of wavelengths, and N_{AOI} is the number of angles of incidence (AOI = 65°, 70°, 75°). The initial model with only substrate and SiO$_2$ film was extended by adding an interlayer between SiO$_2$ and Si, to test how its presence influences the STDS. A commonly used model to describe this layer assumes that its dielectric permittivity is a 50% mixture of both materials, and is approximated with Bruggeman effective medium formula. The STDS was calculated in range 252–376 nm at 63 points, for thickness of SiO$_2$ layer in range 85–86 nm, while the interface layer thickness was in range 0–1 nm. The map of the error function is shown in figure 3(a). The minimum value of STDS is at 85.6 nm, with no interface layer figure 3(b). The extracted refractive indices at three different AOI for the thickness of 85 and 85.6 nm are shown in figure 2, and at thickness of SiO$_2$ 85.6 nm when STDS is minimal, three spectra are almost identical, figure 2(b).

The real and imaginary parts of dielectric function of calculated mean spectra, for the three spectra obtained by direct inversion at 65°, 70°, and 75° of highly doped Si in range 200–700 nm are shown in figures 4(a) and (b). They are plotted

together with results from Herzinger [34]. The differences in the spectra originate from the fact that there is a difference between the doping levels and type of dopants (here highly P-doped, in the Herzinger paper slightly B-doped), and potentially from the method of Si crystal growth.

In point-by-point extraction, calculated refractive indices at different wavelengths do not directly depend on each other and the measurement noise is directly transferred to the extracted optical data [30]. Eventually, all the measurement noise, including that from the substrate optical constants, is propagated into the extracted data of the film. To avoid this effect, in the 380–700 nm range the real part of silicon refractive index, obtained by direct extraction, is fitted to the Sellmeier empirical formula [34], while the imaginary part is approximated by an exponential tail [30]:

$$n^2 = D + A\frac{\lambda^2}{\lambda^2 - B^2} - C\lambda^2, \quad (2)$$

$$k = \alpha e^{\beta(hc/\lambda - \gamma)}. \quad (3)$$

The seven model parameters are: *D*, *A*, *B*, *C* for approximation of *n*, and the extinction amplitude α, the exponent factor β, and the band edge γ for approximation of *k*. The fitted refractive index of Si, and thickness of SiO$_2$ layer in range 380–700 nm, figures 4(c) and (d), were further used in extraction of optical properties of NPL film.

3.2. Surface morphology and thickness of the NPL film

The typical topography of a $2 \times 2 \, \mu m^2$ area of the CdSe/CdS core–shell NPL film is depicted in figures 5(a) and (b). NPLs are represented by bright grains with an effective diameter of around several tens of nanometers. NPLs are well deposited onto SiO$_2$ substrate, they are separated from each other and
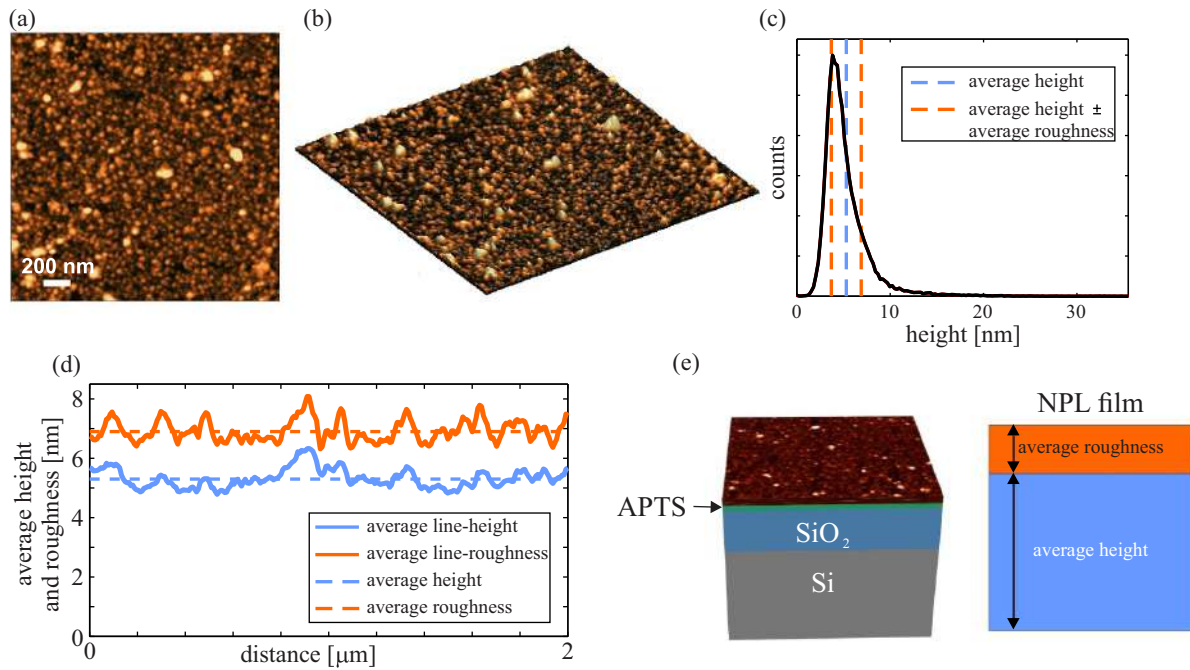
Figure 5. (a) CdSe/CdS core–shell NPL film topography colormap and (b) its three-dimensional rendering. The scan area is $2 \times 2 \ \mu m^2$, whereas the height scale is 12 nm and brightness is linearly proportional to height. (c) Height distribution of the topographic image in part (a). (d) Average line-height and line-roughness for the topographic image in part (a). (e) Model of the considered film: it is a two-component structure with the bottom layer having the thickness of the average height and the top layer with the thickness equal to the average roughness.

form a monolayer. A small number of clusters represented by wider and higher grains and depicted by brighter grains can also be observed. Histogram of the height distribution is given in figure 5(c). The average height of 5.3 nm and the average roughness of 1.6 nm are indicated by dashed lines. In the calculation of the film thickness, the zero-thickness which corresponds to the substrate was taken from narrow air gaps (represented with a dark colour) between neighboring NPLs. The histogram is characterized by a single and narrow peak indicating a good uniformity of the film thickness. According to AFM images, the film roughness mainly originates from narrow air gaps between neighboring NPLs, from their not-flat orientation and formation of small local clusters.

In order to better represent the film morphology, the average height and roughness profiles (called average line-height and line-roughness respectively) of the topographic image in figure 5(a) are shown in figure 5(d). Here the averaging was done along the vertical lines. Dashed lines in figure 5(d) represent the height and roughness averaged over the entire topographic image and they correspond to the dashed lines in figure 5(c). The average height profile represents the layer comprised of NPLs, whereas the roughness profile represents a mixture of NPLs and air. According to these results, the film can be represented by a combination of two layers having the thickness equal to the average height (the bottom layer) and roughness (the top layer). This model is schematically represented in figure 5(e). Finally, the whole film can be approximated as a single layer with the effective thickness equal to the sum of the average height and roughness. After the averaging over five different areas, the calculated film thickness was 5.3 ± 1.6 nm.
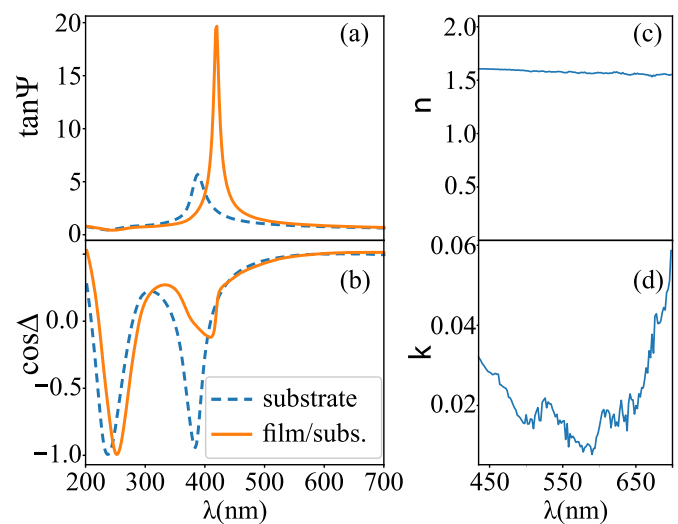

Figure 6. (a) $\tan\Psi$ and (b) $\cos\Delta$ at 75° for bare substrate (dashed line) and substrate with NPLs on it (full line) at range from 200 to 700 nm. (c) n and (d) k of extracted refractive index of the film at shortened range 430–700 nm.

3.3. Extraction of NPL film's refractive index

SE spectra of bare substrate and substrate with APTES and NPLs on the top are shown in figures 6(a) and (b). The shifts in the SE spectra of the film compared to the SE spectra of the bare substrate confirm the presence of an overlayer. When the film thickness is in the nanometer range, the thickness, constituent volume ratios and the mixture's refractive index are correlated, so the modeling procedure with all these
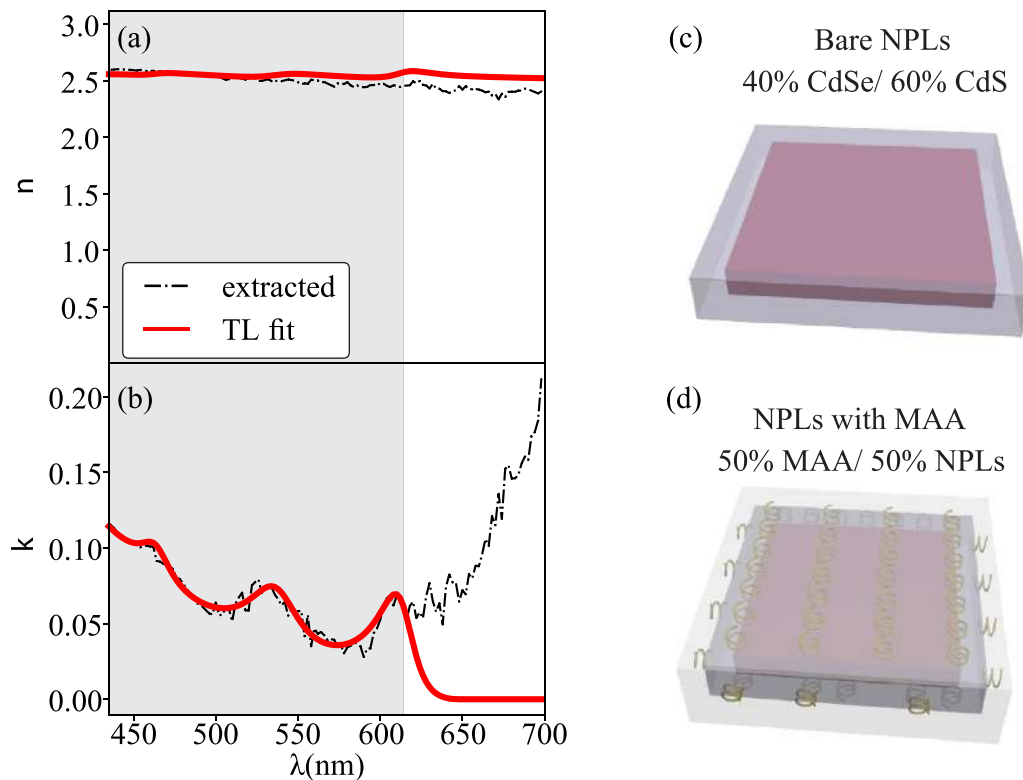
Figure 7. (a) Real and (b) imaginary part of extracted refractive index of NPLs. Dash-dot lines represent values obtained by direct extraction, while full lines represent TL fits. The greyed area denotes part of extracted spectra used in TL fitting, while the rest of the spectra is extrapolation by the model. (c) Schematic of bare NPLs, where estimated volume ratio of bulk CdSe and CdS is 40%/60%. (d) Schematic of MAA covered NPLs, where estimated volume ratios of MAA and NPLs is 50%/50%.

parameters included and fitting directly to the SE curve is very delicate. Therefore, we are extracting the refractive index of the film (mixture) by direct inversion according to the model shown in figure 5(e). AFM-deduced values for thickness of closely packed NPL film (5.3 nm) and roughness (1.6 nm) were used in the ellipsometric model. Since the NPL film is not a bulk material, its roughness can be incorporated as the less dense NPL film (50% air and 50% film). It originates from the fact that surface of NPLs is not completely flat, NPLs do not form closely packed monolayer, as well as from deposition of NPL clusters that appear as bright spots in AFM topographic images, figures 5(a) and (b).

The detailed description of the film includes NPLs covered with MAA and mixed with air at some ratios. The lateral size of the NPLs, deduced from high resolution AFM measurements [35] is around 30 nm, so 10–30 times smaller than the wavelengths of the incident light, and effective medium approximation would be a natural choice for calculation of their optical properties [19]. Estimated thickness of the MAA on the NPLs is approximately 1 nm. This means that the volume fraction of the bare NPLs in MAA covered NPLs is around 50% ($28 \times 28 \times 3.1/30 \times 30 \times 5.1$), figure 7(d). Assuming that the refractive index of the NPLs is close to the one of the mixture of bulk CdSe [32] 40% and CdS [36] 60%, figure 7(c), covered with MAA, the estimated fraction of the air is around 40%.

Going backward, assuming the same coverage of MAA, and fraction of air in the film whose optical properties were

extracted, figures 6(c) and (d), the real and imaginary parts of extracted refractive index of NPLs are shown in figures 7(a) and (b). The SE measurement noise is directly transferred to the spectra of *n* and *k*, and an unexpected increase in *k* and decrease in *n* at wavelengths greater than 610 nm are a consequence of approaching the end of the measuring range of the ellipsometer used in the experiment. The extracted dielectric function (refractive index) is further parametrized using Tauc–Lorentz (TL) oscillator model given by:

$$
\varepsilon_{i,TL}(E) = \begin{cases} \sum_{i=1}^{N} \frac{1}{E} \frac{A_i \cdot E_i \cdot C_i \cdot (E - E_g)^2}{(E^2 - E_i^2)^2 + C_i^2 \cdot E^2}, & E \geq E_g \\ 0, & E < E_g \end{cases} \tag{4}
$$

where A_i is the strength, C_i is the broadening, and E_i is the peak central energy of the *i*th oscillator, while E_g is the gap energy. The real part of the dielectric function is derived from the expression of ε_i using Kramers–Kronig integration. This model accounts for the band gap of the NPLs, and prevents absorption contributions below the band gap that appear due to the decreased measurement sensitivity. The TL model is fitted in range 430–610 nm, while the upturn in the extracted *k* above 610 nm is attributed to the experimental artefact, and extrapolated by the TL model [30].

The absorbance of the NPLs in chloroform solution shows two characteristic excitonic resonances at 560 and 620 nm (figure 8). The extinction coefficient of the NPLs in the film is evaluated from the absorption coefficient *k* through $\alpha = 4\pi k/\lambda$. The total absorption in the free-standing NPL film (mixture) is
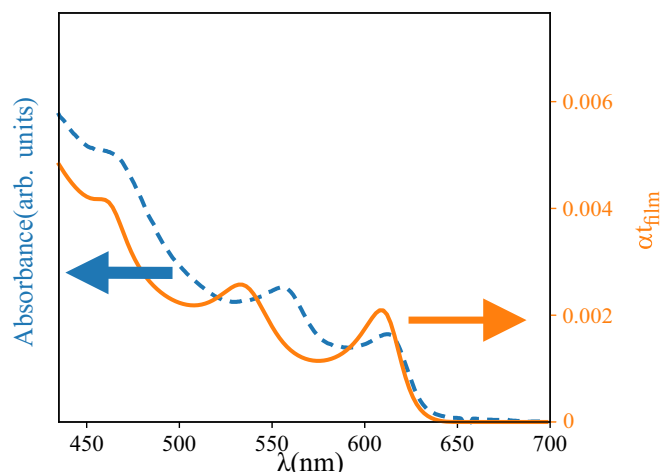
Figure 8. Absorbance (arbitrary units) spectra of CdSe/CdS core–shell NPLs in a chloroform solution (dashed line), and estimated absorption in the 5.3 nm NPLs film (full line).

then approximately αt_{film}, where t_{film} is the film thickness. The exciton peaks of the NPLs in the film are slightly blueshifted compared to the ones in the solution. This shift could be caused by a strain induced by the ligand exchange of oleic acid, used in the solution, by MAA during the electrostatic deposition [37], decrease of the refractive index of surrounding media, or by the interaction of the NPLs with substrate and/or APTES film.

Another important aspect of figure 8 is the very low magnitude (below 0.5%) of the estimated NPL film absorption even if it was free-standing or deposited on a weakly reflecting substrate. It proves that the standard optical characterization involving transmission spectrophotometry would be very difficult to realize for the investigated monolayer NPL films and thus stands in favor of the appropriateness of the method used in this article.

4. Conclusion

CdSe/CdS core–shell nanoplatelet films prepared on SiO_2/Si substrates by electrostatic single-layer deposition have been investigated. We have found that the presence of a monolayer NPL film on optically opaque SiO_2/Si substrates can be established using SE in combination with AFM measurements. While AFM provides the film thickness and demonstrates its surface morphology, the appearance of excitonic signatures in the NPL film extinction spectrum inferred from ellipsometry confirms the presence of CdSe/CdS core–shell NPLs. The two exciton peaks are found to be slightly blueshifted compared to the excitonic peaks in the absorption spectra of colloidal NPLs, which can be explained by the ligand exchange, interaction of NPLs with the SiO_2 substrate and the APTES film and/or by the decrease of the refractive index of the surrounding. These results assert SE as a promising tool for probing the optical properties of monolayer NPL films on arbitrary substrates, which is hardly possible using standard optical absorption measurements.

Direct extraction or point-by-point inversion is highly reliant on the exact knowledge of the refractive indices and thicknesses in the underlying structure, so it is important to characterize the substrate before measuring NPL films and extracting their optical parameters. Here we determined the refractive index of highly doped Si while the thickness of the SiO_2 layer was determined by exploiting the fact that the regions of the spectra close to the sharp optical structure (at critical points of Si) are more sensitive to change of the angle of incidence.

ORCID iDs

Milka M Jakovljević https://orcid.org/0000-0002-8536-3796
Sonja Aškrabić https://orcid.org/0000-0003-1945-040X
Goran Isić https://orcid.org/0000-0002-6841-9356
Borislav Vasić https://orcid.org/0000-0002-1575-8004
Mikhail Artemyev https://orcid.org/0000-0002-6608-0002

References

[1] Ithurria S, Tessier M D, Mahler B, Lobo R P S M, Dubertret B and Efros A L 2011 *Nat. Mater.* **10** 936–41
[2] Achtstein A W, Antanovich A, Prudnikau A, Scott R, Woggon U and Artemyev M 2015 *J. Phys. Chem. C* **119** 20156–61
[3] Pedetti S, Nadal B, Lhuillier E, Mahler B, Bouet C, Abécassis B, Xu X and Dubertret B 2013 *Chem. Mater.* **25** 2455–62
[4] Tessier M D, Mahler B, Nadal B, Heuclin H, Pedetti S and Dubertret B 2013 *Nano Lett.* **13** 3321–8
[5] Talapin D V, Mekis I, Götzinger S, Kornowski A, Benson O and Weller H 2004 *J. Phys. Chem. B* **108** 18826–31
[6] Chen Y, Vela J, Htoon H, Casson J L, Werder D J, Bussian D A, Klimov V I and Hollingsworth J A 2008 *J. Am. Chem. Soc.* **130** 5026–7
[7] Mahler B, Spinicelli P, Buil S, Quelin X, Hermier J and Dubertret B 2008 *Nat. Mater.* **7** 659–64
[8] Mahler B, Nadal B, Bouet C, Patriarche G and Dubertret B 2012 *J. Am. Chem. Soc.* **134** 18591–8
[9] Chen Z, Nadal B, Mahler B, Aubin H and Dubertret B 2014 *Adv. Funct. Mater.* **24** 295–302
[10] Vitukhnovsky A G, Lebedev V S, Selyukovm A S, Vashchenko A A, Vasiliev R B and Sokolikova M S 2015 *Chem. Phys. Lett.* **619** 185–8
[11] Zhang F *et al* 2016 *Nanoscale* **8** 12182–8
[12] Grim J Q, Christodoulou S, Stasio F, Krahne R, Cingolani R, Manna L and Moreels I 2014 *Nat. Nanotechnol.* **9** 891–5
[13] She C, Fedin I, Dolzhnikov D S, Dahlberg P D, Engel G S, Schaller R D and Talapin D V 2015 *ACS Nano* **9** 9475–85

[14] Talapin D V, Lee J S, Kovalenko M V and Shevchenko E V 2010 *Chem. Rev.* **110** 389–458

[15] Zucolotto V, Gattas-Asfura K, Tumolo T, Perinotto A, Antunes P, Constantino C, Baptista M, Leblanc R and Oliveira J O 2005 *Appl. Surf. Sci.* **246** 397–402

[16] Gao M, Zhang X, Yang B, Li F and Shen J 1996 *Thin Solid Films* **284-285** 242–5

[17] Franzl T, Shavel A, Rogach A L, Gaponik N, Klar T A, Eychmüller A and Feldmann J 2005 *Small* **1** 392–5

[18] Peng W, Rupich S M, Shafiq N, Gartstein Y N, Malko A V and Chabal Y J 2015 *Chem. Rev.* **115** 12764–96

[19] Losurdo M and Hingerl K 2013 *Ellipsometry at Nanoscale* (Berlin: Springer)

[20] Dement D B, Puri M and Ferry E 2018 *J. Phys. Chem.* C **122** 21557–68

[21] Diroll B T, Gaulding E A, Kagan C R and Murray C B 2015 *Chem. Mater.* **27** 6463–9

[22] Malak S T, Lafalce E, Jung J, Lin C H, Smith M J, Yoon Y J, Lin Z, Vardeny Z V and Tsukruk V V 2016 *J. Mater. Chem.* C. **4** 10069–81

[23] Rinnerbauer V, Hingerl K, Kovalenko M and Heiss W 2007 *Appl. Surf. Sci.* **254** 291–4

[24] Isić G *et al* 2011 *J. Nanophotonics* **5** 051809

[25] Matković A, Ralević U, Chhikara M, Jakovljević M M, Jovanović D, Bratina G and Gajić R 2013 *J. Appl. Phys.* **114** 093505

[26] Tompkins H G and Irene E A 2005 *Handbook of Ellipsometry* (New York: William Andrew, Inc.)

[27] Antanovich A, Prudnikau A and Artemyev M 2016 *Optical Properties of Semiconductor Colloidal Quantum Wells*, in: A, S A (eds.) *Fundamental and Applied Nano-Electromagnetics* (Netherlands: Springer) p 220

[28] Aspnes D A 1974 *J. Opt. Soc. Am.* **64** 639–46

[29] Aspens D E, Studna A A and Kinsbron E 1984 *Phys. Rev.* B **29** 768–79

[30] Herzinger C M, Snyder P G, Johs B and Woollam J A 1995 *J. Appl. Phys.* **77** 1715–24

[31] Arwin H and Aspnes D E 1984 *Thin Solid Films* **113** 101–13

[32] Palik E D 1985 *Handbook of Optical Constants of Solids* (New York: Academic)

[33] Goyal D K, Pribil G K, Woollam J A and Subramanian A 2008 *Mat. Sci. Eng.* B **149** 26–33

[34] Herzinger C M, Johs B, McGahan W A and Woollam J A 1998 *J. Appl. Phys.* **83** 3323–36

[35] Vasić B, Askrabić S, Jakovljević M M and Artemyev M 2020 *Appl. Surf. Sci.* **513** 145822

[36] Ninomiya S and Adachi S 1995 *J. Appl. Phys.* **78** 1183–90

[37] Atanovich A, Achtstein A W, Matsukovich A, Prudnikau A, Bhaskar P, Gurin V, Molinari M and Artemyev M 2017 *Nanoscale* **9** 18042–53

Check for updates
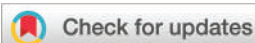
Combined Raman and AFM detection of changes in HeLa cervical cancer cells induced by CeO₂ nanoparticles – molecular and morphological perspectives†

Mirjana Miletić,[a] Sonja Aškrabić, [ID] *[a] Jan Rüger,[b] Borislav Vasić, [ID] [c]
Lela Korićanac, [ID] [d] Abdullah Saif Mondol,[b] Jan Dellith,[b] Jürgen Popp,[b]
Iwan W. Schie[b,e] and Zorana Dohčević-Mitrović[a]

The design of nanoparticles for application in medical diagnostics and therapy requires a thorough understanding of various aspects of nanoparticle–cell interactions. In this work, two unconventional methods for the study of nanoparticle effects on cells, Raman spectroscopy and atomic force microscopy (AFM), were employed to track the molecular and morphological changes that are caused by the interaction between cervical carcinoma-derived HeLa cells and two types of cerium dioxide (CeO₂) nanoparticles, ones with dextran coating and the others with no coating. Multivariate statistical analyses of Raman spectra, such as principal component analysis and partial least squares regression, were applied in order to extract the variations in the vibrational features of cell biomolecules and through them, the changes in biomolecular content and conformation. Both types of nanoparticles induced changes in DNA, lipid and protein contents of the cell and variations of the protein secondary structure, whereas dextran-coated CeO₂ affected the cell-growth rate to a higher extent. Atomic force microscopy showed changes in cell roughness, cell height and nanoparticle effects on surface molecular layers. The method differentiated between the impact of dextran-coated and uncoated CeO₂ nanoparticles with higher precision than performed viability tests. Due to the holistic approach provided by vibrational information on the overall cell content, accompanied by morphological modifications observed by high-resolution microscopy, this methodology offers a wider picture of nanoparticle-induced cell changes, in a label-free single-cell manner.

1. Introduction

Nanoparticles (NPs) occupy an important place in the field of biomedicine, having potential in the diagnostics[1,2] and therapy[3–5] of a wide range of diseases. In order to design NPs for targeting a specific cell population and/or specific subcellu-

lar compartments, to enhance NP delivery and to achieve an adequate balance between cytotoxic and cytoprotective effects, it is crucial to explore molecular interactions between NPs and cells at different levels.[6] Methods generally used for the investigation of NP–cell interactions are based on a multitude of specific biochemical assays that target one parameter/property per assay and need to employ labels. Screening of the effects of NPs as anticancer agents on the tumor cells *in vitro* is standardly performed using viability/cytotoxicity tests such as trypan blue staining, LDH, SRB, MTT assays and others.[7–10] As mentioned previously, these tests are effect-specific, *i.e.* the trypan blue test dyes the cells only if a membrane is damaged in a way that it becomes permeable, very similar to LDH that detects permeated membranes by measuring the level of lactated hydrogenase released into a culture medium. The SRB test registers the changes in the cell number through the changes in total protein mass and MTT measures the degree of preserved mitochondrial activity. Sometimes changes manifested through a different effect than the one measured by a

[a]*Nanostructured Matter Laboratory, Center for Solid State Physics and New Materials, Institute of Physics Belgrade, University of Belgrade, Pregrevica 118, 11080 Belgrade, Serbia. E-mail: sonask@ipb.ac.rs*
[b]*Leibniz Institute of Photonic Technology, Albert-Einstein-Straße 9, 07745 Jena, Germany*
[c]*Graphene Laboratory, Center for Solid State Physics and New Materials, Institute of Physics Belgrade, University of Belgrade, Pregrevica 118, 11080 Belgrade, Serbia*
[d]*Department of Molecular Biology and Endocrinology, Vinča Institute of Nuclear Sciences, University of Belgrade, P.O. Box 522, 11001 Belgrade, Serbia*
[e]*Department of Medical Engineering and Biotechnology, University of Applied Science Jena, Carl-Zeiss-Promenade 2, 07745 Jena, Germany*
†Electronic supplementary information (ESI) available. See DOI: 10.1039/c9an02518a

particular test can remain undetected. For instance, live and metabolically active cells can experience reversible damage of their membranes, while, inversely, dying cells at the initial stages of apoptosis can still have their membranes intact.[7] The most common viability test, trypan blue staining, in these two cases will give false positive or false negative results, respectively. Multiple tests are often needed to detect NP-induced changes and to choose an appropriate approach for the study of the mechanisms behind them most often requires expertise in various analytical techniques. There is a need for methodologies that would enable the extraction of comprehensive data on induced cell changes and detect non-function-specific cellular molecular changes in a single, label-free experiment.

Raman spectroscopy, based on the inelastic scattering of light on molecular vibrations, allows for a label-free and non-destructive way to probe the underlying molecular fingerprint of biological samples.[11] Through the modulations of the corresponding vibrational mode frequencies, linewidths and intensities, characteristics of the transformations of large molecules such as DNA, proteins and lipids can be followed. These changes are of importance because *i.e.* DNA damage can be correlated to cellular processes such as inflammation and oxidative stress,[12] the endocytotic pathway of NP entrance is related to the phospholipid concentration,[13] and the change of the protein secondary structure can mark, for instance, unfolding or aggregation of proteins, or a change in cytoskeleton organization.[14–16] Based on this, Raman spectroscopy represents a tool with potential for fast screening of total biomolecular changes induced in the cells by treatment with NPs and with a possibility of higher sensitivity to the transformations that the cells undergo under the influence of NPs, compared to the tests carried out for the evaluation of individual properties such as cell membrane integrity, protein quantity, mitochondrial activity, *etc.* In the field of biomedical application of NPs, Raman spectroscopy has been mostly employed as an imaging technique for tracing NP intake and subcellular localization.[13,17] Although a few of the studies investigated physiological or pathological changes of the cells induced by drugs and chemicals,[18–21] to our knowledge, there are very few studies that explore the use of Raman spectroscopy for the study of cell changes induced by NPs,[22,23] none of which perform strict multivariate analysis of the entire spectral region of interest for a large number of cells. In addition to the molecular characterization performed by Raman spectroscopy, AFM can be used for the examination of morphology, roughness and composition of particular cell structures, such as cell membrane protrusions, filopodia and lamellipodia, cytoskeleton or sub-membranous cytoplasmatic structures.[24,25] This allows for a more complete and detailed cell morphology investigation and membrane characterization than the one that can be provided by biochemical assays targeting membrane structures.

Among different nanoparticles that have been tested as therapeutic agents, rare-earth oxide CeO_2 NPs are found to be interesting for their therapeutic potential and proposed cell-selective activity: while usually being toxic to cancer cells and

sensitizing cancerous tissues to radiotherapy, CeO_2 NPs are often non-toxic to normal healthy cells and even compensate for the negative effects of the radiotherapy on healthy tissues.[26,27] The reason for such a dual activity of CeO_2 NPs lies in their nonstoichiometric nature characterized by the presence of both Ce^{4+} and Ce^{3+} oxidation states and high content of oxygen vacancies. Thus, through oxidation/reduction changes of $Ce^{3+} - Ce^{4+}$, CeO_2 NPs can mediate both oxygen release and intake. Dispersions of powdered CeO_2 NPs in cell medium can be troublesome, which is the case with the majority of oxide nanoparticles, and results in the agglomeration of NPs.[28] Biocompatible coatings such as hydrocarbons, dextran and glucose have been used to coat ceria nanoparticles. By coating with dextran molecules, dispersions of CeO_2 NPs become stable and the controlled application of NPs in cell treatment is enabled.[29] These NPs have been rarely tested as cytotoxic agents[30,31] whereas their interaction with the cells and the influence of the coating on their activity remain unclear. The interaction of CeO_2 NPs with the cells from different cell lines has been evaluated using standard biological assays,[27,32] but their influence on the molecular content and morphology of the cells has not been investigated so far.

In this work, we aimed to investigate the susceptibility of combined Raman and AFM analysis in the detection and discrimination of the effects of two types of oxide NPs of the same crystalline structure and similar composition, but with different coating and redox activities, on HeLa cells, a cervical carcinoma derived cell line. Special attention was dedicated to the analysis of the possible advantages of this methodology over standard biological cytotoxicity assays. The effects of dextran-coated (CD) CeO_2 NPs on HeLa cells were studied for the first time, to our knowledge, and compared to the effect of uncoated CeO_2 NPs. Changes in the vibrational features of intracellular biomolecules induced by NPs were investigated by high-throughput Raman spectroscopy of control cells and two NP-treated cell groups and analyzed by principal component analysis (PCA) and partial least squares regression (PLS). AFM microscopy was used to provide a characterization of NP-induced morphological changes, *i.e.* an increase in the cell roughness, decrease in the cell height and appearance of depressions. The cytotoxicity of CeO_2 NPs was tested *via* trypan blue staining and SRB assay. The combination of Raman spectroscopy and AFM enabled the detection of degrading changes of the nuclear material and cell membrane in the cells induced by both types of NPs. It was shown that group-discriminating spectral modes characteristic of DNA, lipids and proteins experience changes and that the effects of CD NPs are more pronounced compared to those of SPRT NPs. In contrast to the biological cytotoxicity tests, Raman spectroscopy and AFM showed that uncoated CeO_2 NPs also led to a deterioration of cell status. In light of this, our study suggests that Raman spectroscopy, independently or combined with AFM, can be used for the fast and sensitive screening of negative effects that oxide NPs can produce in human cells.

2. Materials and methods

2.1 Nanoparticle synthesis

Two types of CeO_2 NPs were used for the experiments. Uncoated ceria NPs in the powder form, abbreviated in the text as SPRT, were obtained by self-propagating room temperature synthesis, as described in Boskovic et al.[33] Dextran-coated NPs (CD in further text) are synthesized in the form of dispersions, based on the synthesis procedure given by Karakoti et al.,[29] using ammonia mediated oxidation and dextran T40 for coating.

2.2 Characterization of nanoparticles

The crystalline structure of CeO_2 NPs was investigated by X-ray diffraction (XRD) with a Panalytical X'Pert Pro instrument (PANalytical, Almelo, the Netherlands). Diffraction spectra were recorded in the 2θ interval (20–60)°, with a step size of 0.5°. The X-ray radiation Cu $K\alpha_{1,2}$ line ($K\alpha_1$: transition KLIII; λ = 1.54056 Å) was employed. The Scherrer equation was used for the determination of the crystallite size. TEM (transmission electron microscopy) images were acquired using a JEOL JEM-3010 (300 keV). The average hydrodynamic particle diameter was measured using a Zetasizer Nano ZS90 (Malvern Instruments) apparatus. UV-VIS spectra of NP dispersions were recorded using a Varian Super Scan 3 UV-vis spectrophotometer.

2.3 Cell culture

HeLa cells (ATCC-CCL-2) were grown under standard cell culture conditions (37 °C, 5% CO_2) in DMEM liquid medium with stable glutamine, 3.7 g l^{-1} $NaHCO_3$, and 4.5 g l^{-1} D-glucose (Biochrom AG, Germany) supplemented with 10% fetal calf serum (Merck Millipore, Germany) and 1× penicillin/streptomycin (Sigma Aldrich, Germany). Trypsin/EDTA (0.05%, Biochrom AG, Germany) was employed to detach the cells from the flask, either for passaging, trypan blue assay, Raman imaging or Raman spectroscopy. The seeding density in all cases was 300 000 cells per 25 mm^2 flask or 2000 per well in a 96-well plate.

2.4 Cell treatment with nanoparticles

The cells were treated with NPs 24 hours after seeding in 25 mm^2 flasks (6 batches for CD and 4 batches for SPRT). The starting seeding density, before treatment with NPs, was equal in all batches. CD NPs were added into cell culture medium, to achieve a total concentration of 400 μg ml^{-1}. A stock solution of SPRT NPs has been prepared in sterile deionized water (volume equal to the volume of the applied CD NP solution) and then mixed with cell culture medium in order to reach the final concentration of 400 μg ml^{-1}. Dissolution was aided using an ultrasonic probe system (Bandelin SONOPULS HD 2070), with a power of 15 W, in 3 cycles of 15 s each and 5 s break in between. The medium from the cell flasks was discarded and replaced with the obtained medium with NPs (6 replicates for CD and 4 for SPRT). Proportional volumes of sterile deionized water were added to culture medium in flasks containing control cells. The cells were incubated with NPs for 48 hours, then washed with PBS and detached with trypsin/EDTA. The cells were fixed for 20 min at room temperature in Roti®-Histofix 4% (Roth, Germany), washed twice and re-suspended in PBS. The obtained cell suspensions were used for trypan blue assay, Raman imaging and Raman spectroscopy. In the case of Raman measurements poly-L-lysine was used to immobilize the fixed cells on CaF_2 coverslips. For AFM measurements, the cells were grown on glass coverslips and fixed afterwards in the same manner as described above.

2.5 Trypan blue viability test

Trypan blue at 0.4% (Sigma-Aldrich, Germany) was added to the cell suspension in equal volumes (to obtain a 1 to 2 dilution). Stained and unstained cells were counted within 2–3 minutes using a Neubauer chamber (0.0025 mm^2; Marienfeld, Germany). The percentage of viable (unstained) cells among the total cell population was calculated. Tests were done in 6 replicates for control and CD-treated and in 4 replicates for SPRT-treated cells. The statistical significance of cell number/viability differences between treated and untreated cells was estimated by the one-way ANOVA and post hoc Games-Howell test, performed in R.

2.6 Sulforhodamine B assay

The cells were cultured in 96-well plates and treated with NPs (dose and time same as already described). After fixation with trichloroacetic acid, cell cultures were stained for 15 minutes with 0.4% (wt/vol) sulforhodamine B (SRB) (Sigma-Aldrich, Germany) dissolved in 1% acetic acid, according to the procedure given in Skehan et al.[9] The unbound dye was removed by four washing steps with 1% acetic acid. SRB which stayed bound to cell proteins was extracted with a 10 mM unbuffered Tris base (Sigma-Aldrich, Germany). The absorbance of the extracted dye solution was measured at 550 nm with a reference wavelength of 690 nm in a microplate reader (Wallac, VICTOR2 1420 Multilabel counter, PerkinElmer, Turku, Finland). The results were presented as the percentage of cell growth determined from the relative ratio between the measured absorbance of the treated sample and absorbance of the control. The assay was performed in 8 replicates for every experimental group. The statistical significance of differences between the treated and untreated cells was estimated by the one-way ANOVA and post hoc Games-Howell test, performed in R.

2.7 Raman imaging

Raman imaging was performed on a CRM200 and alpha300 confocal Raman microscope (WITec GmbH, Ulm, Germany). A 785 nm cw diode laser (Toptica Photonics, Gräfelingen, Germany) was used as an excitation source. The laser beam is coupled into the microscope through a single mode optical fiber. The incident laser beam is collimated via an achromatic lens and passed through a holographic band pass filter or a dichroic mirror, before it is focused onto the sample through the microscope objective lens. A Nikon Fluor (60×/1.00 NA,

WD = 2.0 mm) water immersion objective was used. The spatial resolution was 0.5 μm, exposure time 0.5 s and a 300 gr mm^{-1} grating was used as a dispersive element. Raman maps of the cells were obtained from focal points in the horizontal plane (*XY*) at different depths and also in the vertical plane (*ZY*), with *XY* being the plane orthogonal to the incident beam direction, and *Z* being the axis parallel to the incident beam direction. Raman spectra were collected from each pixel at different cell depths distanced 1–2.5 μm, and the corresponding maps are made for each plane. The pixel size was 0.5 μm.

2.8 Atomic force microscopy

For AFM measurements, the cells were grown on glass coverslips, treated with NPs and fixed afterwards in the same manner as described above, but without detaching them from the coverslips, and then kept in PBS. Before the experiment they were rinsed twice with water, left to dry at room temperature and then investigated by AFM. AFM measurements of control and treated HeLa cells were performed using an NT-MDT system NTEGRA Prima under ambient conditions (air at the humidity of around 30–40%). Topographic imaging was done in AFM tapping mode, using NSG01 probes from NT-MDT with a typical force constant of 5.1 N m^{-1} and a typical resonant frequency of 150 kHz. Simultaneously with topographic images, the magnitude of AFM cantilever oscillations was recorded as well. In order to make statistical analysis, the AFM measurements were performed on around 15 cells from each group (control, SPRT-treated and CD-treated cells). Two morphological parameters were followed, the cell height and surface roughness. The height was calculated as a maximum height across each cell. The surface roughness was calculated as a root-mean-square deviation of the height distribution of the cell body. Before roughness calculations, all AFM images were flattened by fitting all lines by 2nd order curves.

2.9 Raman spectroscopy

Cell Raman spectra were recorded using a custom-built upright Raman microscopy setup,[34] equipped with a fiber-coupled laser with an excitation wavelength of 532 nm (DPPS, Lasos) and with a power at the sample plane of approximately 50 mW. The excitation light is coupled into a 60× water-immersion objective lens (NA 1.0; Nikon, Japan). The excitation fiber is re-imaged into the sample plane, resulting in a focal spot diameter of approximately 10 μm. The generated Raman signal is collected by the same objective lens and focused using a 60 mm achromatic lens onto the multimodal core, which guides the signal to a spectrometer (IsoPlane160, Princeton Instruments) equipped with a 400 grooves mm^{-1} grating, and detected using a charge-coupled device (CCD) (PIXIS-400BReXcelon; Princeton Instruments). A spectral resolution of 9 cm^{-1} was achieved and spectra were obtained in the interval (400–3300) cm^{-1}. For all experimental groups of cells, *i.e.* control, SPRT-treated, and CD-treated, Raman spectra were recorded and analyzed from 200–250 cells per cell group and the whole experiment was done in duplicate.

2.10 Spectral preprocessing and multivariate data analysis

The processing of Raman spectra was performed in the R environment, using the hyperSpec package. The spectra of a calibration lamp (KOSI, USA) and powdered 4-acetamidophenol (Sigma-Aldrich) were used for intensity and wavenumber calibration, respectively. The spectra were corrected for spectral contributions from water by extended multiplicative scatter correction (EMSC), which is implemented in the cbmodels package.[35,36] The known component spectra of water and cells were used. The spectra obtained entirely from the CaF$_2$ substrate were excluded from the dataset by k-means clustering. The remaining spectra were normalized relative to the area of spectral ranges of interest (400–1800) cm^{-1} and (2800–3200) cm^{-1}. In order to avoid the influence of CeO$_2$ mode at 453 cm^{-1}, the spectra were cut below 700 cm^{-1} and used for further analysis. Principal component analysis (PCA) was performed using the prcomp function implemented in R. PLS-LDA analysis was performed in R using widekernelpls.fit and lda functions.

3. Results and discussion

3.1 Characterization of nanoparticles

Two different kinds of CeO$_2$ NPs were synthesized: uncoated SPRT particles, in nano-powder form, and coated with T40 dextran, CD, in dispersive form. Their crystalline structure and crystallite size were obtained from the analysis of X-ray diffraction patterns. XRD confirmed the fluorite *Fm*$\bar{3}$*m* crystalline structure of CeO$_2$ both in SPRT and CD NPs. Due to very small sizes of the crystallites, both, the SPRT and CD XRD spectra exhibited broad CeO$_2$ peaks, Fig. 1(a). The CD spectra, however, had a lower intensity due to much lower sampling mass. The crystallite size calculated from the Scherrer formula was 4 nm for SPRT and 3.5 nm for CD NPs (Table 1).

It is known from previous studies that SPRT NPs have a larger grain size than crystallite size, their average grain size deduced from modeling Raman F$_{2g}$ mode and low-frequency modes is 8–10 nm (ref. 37) and according to the AFM image from Fig. S1(a)† their grain size takes a range of values below ∼20 nm. The size of the grains of CD NPs was deduced from transmission electron microscopy, Fig. 1(b). TEM micrographs showed an average grain size of 3–4 nm and confirmed the stability of CD dispersion, with no aggregates and agglomerates observed. In addition to XRD, UV-VIS absorbance measurements of CD and SPRT CeO$_2$ NPs have been performed, confirming that both types of NPs are CeO$_2$. The UV-VIS spectra are presented in Fig. S2 of the ESI.† The hydrodynamic radius of NPs obtained by DLS measurements emphasized better stability of CD NPs in water dispersion, compared to SPRT, represented by almost 20 times lower average hydrodynamic radius (Table 1). The results indicate that no aggregates are formed by CD NPs. DLS analysis demonstrated the tendency of SPRT NPs to form agglomerates, and for this reason, an ultrasonic probe system was used for the preparation of SPRT dispersions later in the study. The TEM
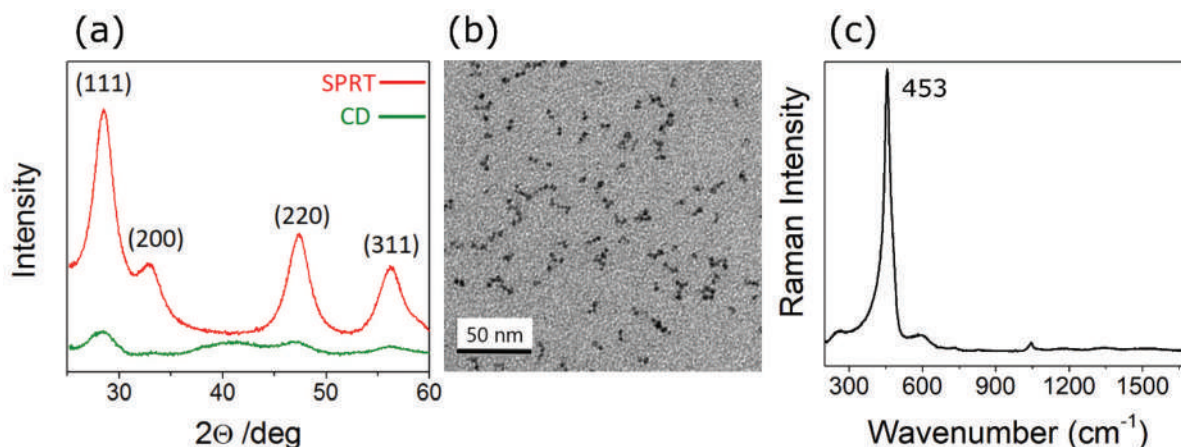
Fig. 1   Characterization of NPs: (a) XRD pattern of SPRT (red) and CD (green) CeO_2 NPs. (b) TEM of CD CeO_2 NPs. (c) Raman spectrum of SPRT CeO_2, showing the characteristic band at 453 cm^{-1}.

Table 1   Crystallite size and average hydrodynamic radius of CeO_2 NPs

	Crystallite size (XRD)	Hydrodynamic radius (DLS)
SPRT (uncoated CeO_2 NPs)	4 nm	849 nm
CD (coated CeO_2 NPs)	3.5 nm	47 nm

image of SPRT NPs in Fig. S1(b)† shows one such agglomerate. Finally, a Raman spectrum of SPRT NPs showed a characteristic CeO_2 Raman F_{2g} mode at 453 cm^{-1}, Fig. 1(c). The Raman mode of CeO_2 was not observed in the spectra of CD NPs, due to the low concentration of small-sized CeO_2 NPs in the dispersion and their very small grain size.

3.2   Cell growth and viability assays

In order to estimate the cell growth changes induced by NPs, both cells attached and cells detached from the flask surface, *i.e.* floating in cell medium, have been counted after incubation with NPs. The results showed an unequivocally significant decrease in cell growth (cell number), following treatment with CD NPs, with $P < 0.01$, Fig. 2(a).

There was, however, a significantly increased number of detached cells for samples treated with these NPs, on average 23% of the total cell number, Fig. 2(g). Considering the detached cells, the total cell number was still significantly lower compared to the control, Fig. 2(b). It can be concluded that CD NPs reduced the growth rate of HeLa cells *in vitro* by five times, presenting around 18% of untreated cell growth. The average cell growth after SPRT NP treatment was also decreased compared to the control (64%), Fig. 2(a) and (b), yet statistically insufficient to confirm the effects of SPRT NPs. A decrease in the growth of CD-treated cells was also evident by simple microscopic observations during experiments, Fig. 2(c) and (d).

To confirm the observed changes in cell growth, a sulforhodamine B (SRB) assay has been used. The test is based on the ability of SRB to bind to proteins' amino acid residues in the cells. The measured absorption of the protein-binding dye is considered to be a measure of cell growth. The results of the SRB assay are shown in Fig. 2(e). The mean growth of control cells is taken as full growth, *i.e.* 100%, whereas the growth of the treated cells was normalized to the mean of control.

The SRB assay was performed in eight batches per three sample groups (one control and two treated), showing a significant decrease of the CD-treated cell growth rate compared to control cells, with $p < 0.05$. It appeared to be reduced on average to 46% regarding the control. Statistical significance for the growth decrease of SPRT-treated cells was below a threshold p value, though a decreasing trend was noticed. The results of SRB growth tests are therefore in accordance with the results obtained by simple cell counting, showing inhibitory effects of CD NPs on HeLa cell growth.

The cell viability was assayed by trypan blue staining, which was chosen because it gives the ratio of the number of dead cells and the number of total cells in the same sample, whereas the majority of viability tests, which are mostly based on colorimetric or fluorescence detection of different reagents, actually normalize the number of dead cells in one sample to the total number of cells in another (control) sample.[8,10] Cell viability tests performed by trypan blue staining are summarized in Fig. 2(f). Although some slightly decreasing trend of the viability of treated cells (especially SPRT-treated cells) can be observed, one-way analysis of variance did not confirm its statistical significance and in conclusion, neither type of CeO_2 NPs influence the cell viability.

Effects of doses of 40 $\mu g\ ml^{-1}$ and 100 $\mu g\ ml^{-1}$ NPs, as well as exposure times of 24 h and 72 h, are also studied by the SRB test which preceded the tests described above and the results are presented in the ESI (Fig. S3 and S4†). In those experiments, treatment with 400 $\mu g\ ml^{-1}$ NPs and exposure of 48 h was chosen as optimal for use in further AFM and Raman experiments.
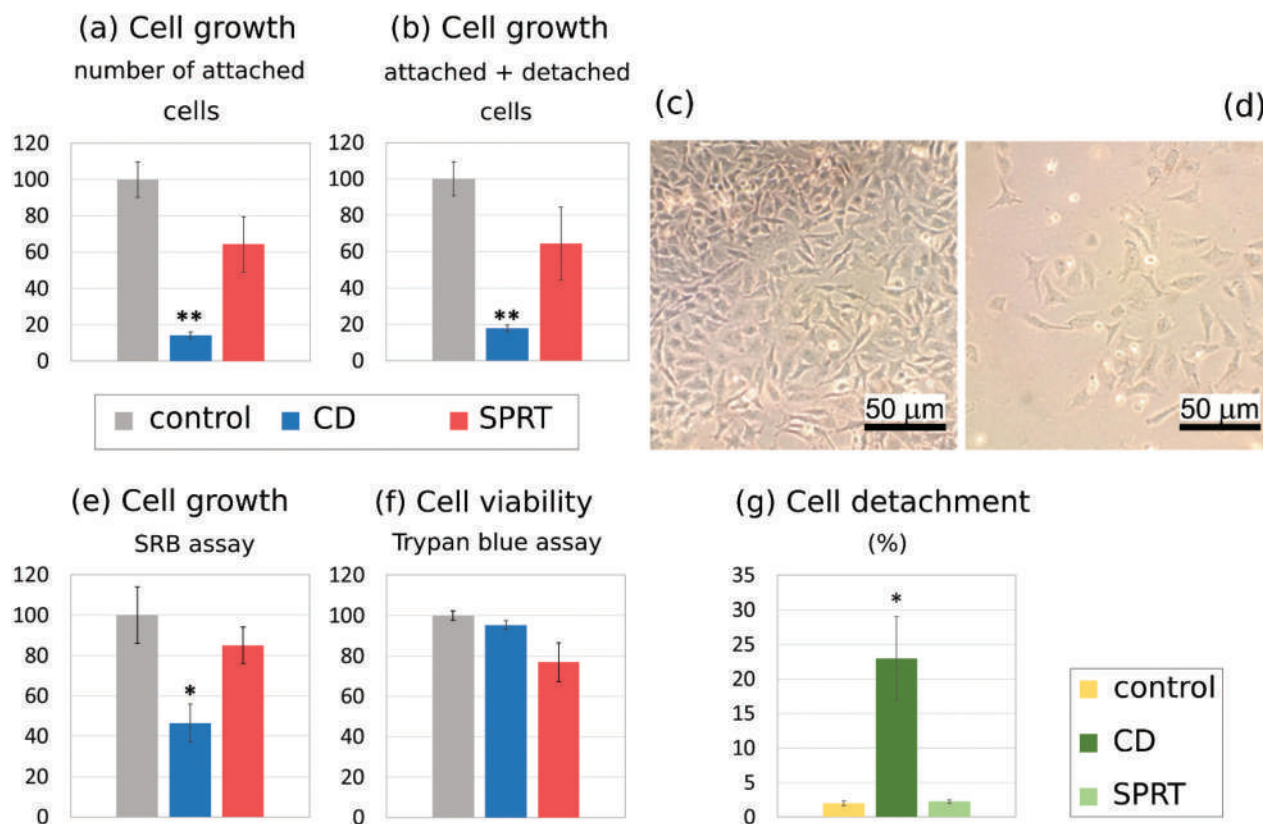
Fig. 2 Results of viability/growth assays. Data presented as mean ± standard error. Statistical significance legend: *$P < 0.05$, **$P < 0.01$, *vs.* control group. (a), (b), (f) and (g) number of replicates $N = 6/6/4$, for untreated/CD-treated/SPRT-treated cells, respectively. (e) $N = 8$, for every group. (a), (b), (e) and (f) Mean of control group is given as 100%, while values for treated groups are expressed related to the mean of control. Statistical significance estimated by one-way ANOVA. (g) Data expressed as the percentage of total number of cells in culture. Statistical significance estimated by one-way non-parametric ANOVA. (c) Microscopy image of control cells. (d) Microscopy image of CD-treated cells. Scale bar on images (c) and (d) is approximate and reflects an order of magnitude.

3.3 Raman imaging

Raman imaging was used to confirm the intracellular localization of SPRT NPs. Due to the small size and surface stability of CD NPs, their Raman signal was too weak to be detected not only in the cells but in the CD NP solution as well. In contrast, SPRT NPs form large aggregates, which results in a strong Raman peak at ~453 cm⁻¹ in the spectra of treated cells. Raman maps were reconstructed based on the intensity mapping of the integrated peak area of the Raman mode at 453 cm⁻¹, Fig. 3(a). Fig. 3(b) shows maps obtained according to the Raman intensity in another region of the same spectra, between 1400 and 1500 cm⁻¹. This region is chosen due to a strong signal of characteristic cell Raman features (CH_2 and CH_3 deformation vibrations in proteins and lipids[38]).

At all measured depths, both modes of cell molecules and NPs are present in the Raman spectra. Bright spots on the maps in Fig. 3(a) correspond to dark spots in Fig. 3(b), *i.e.* where the NP mode is more pronounced, the intensity of cell modes is reduced. Considering the confocality of the system, it appears that the NPs are distributed throughout the cytoplasm, and are not only located at the surface of the cell membrane. The Raman images obtained in the vertical plane per-

pendicular to the previous planes and marked as the *ZY* plane, Fig. 3(c) and (d), confirm the intracellular localization of SPRT NPs. It should be noted that similar Raman maps were made for multiple cells, all showing the presence of NPs throughout the cell.

3.4 Atomic force microscopy (AFM)

The AFM images of control and treated HeLa cells are depicted in Fig. 4. The top, middle and bottom rows display images of control: Fig. 4(a–d), CD-treated: Fig. 4(e–h) and SPRT-treated cells: Fig. 4(i–l), respectively. Going from left to right, the first and the second columns show two-dimensional (2D), Fig. 4(a), (e), and (i), and three-dimensional (3D), Fig. 4(b), (f), and (j), topographic images, respectively. As can be seen, the control cell is characterized with a well-defined nucleus and nucleolus, cell edges and lamellipodia. The surface of the cell is rather smooth, especially on the nucleus. On the other hand, the surface of the cell treated with CD NPs is rough, with pronounced depressions. The nucleus is not well differentiated from the rest of the cell. Several nucleoli are visible, but some of them seem to be fragmented. Finally, the nucleus and nucleoli of the cell treated with SPRT
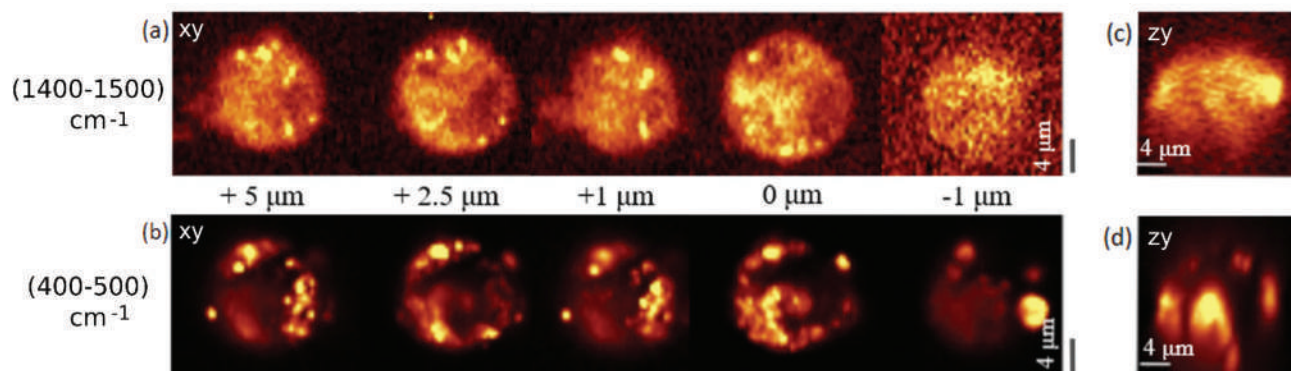
Fig. 3 Raman images of HeLa cells treated with SPRT CeO_2 NPs. (a) and (b) measured in the *XY* plane, (c) and (d) in the *ZY* plane. (a) and (c) made according to the intensity of cell Raman modes in the interval $(1400-1500)$ cm^{-1}. (b) and (d) made according to the integral intensity of NP Raman mode in the range $(400-500)$ cm^{-1}.
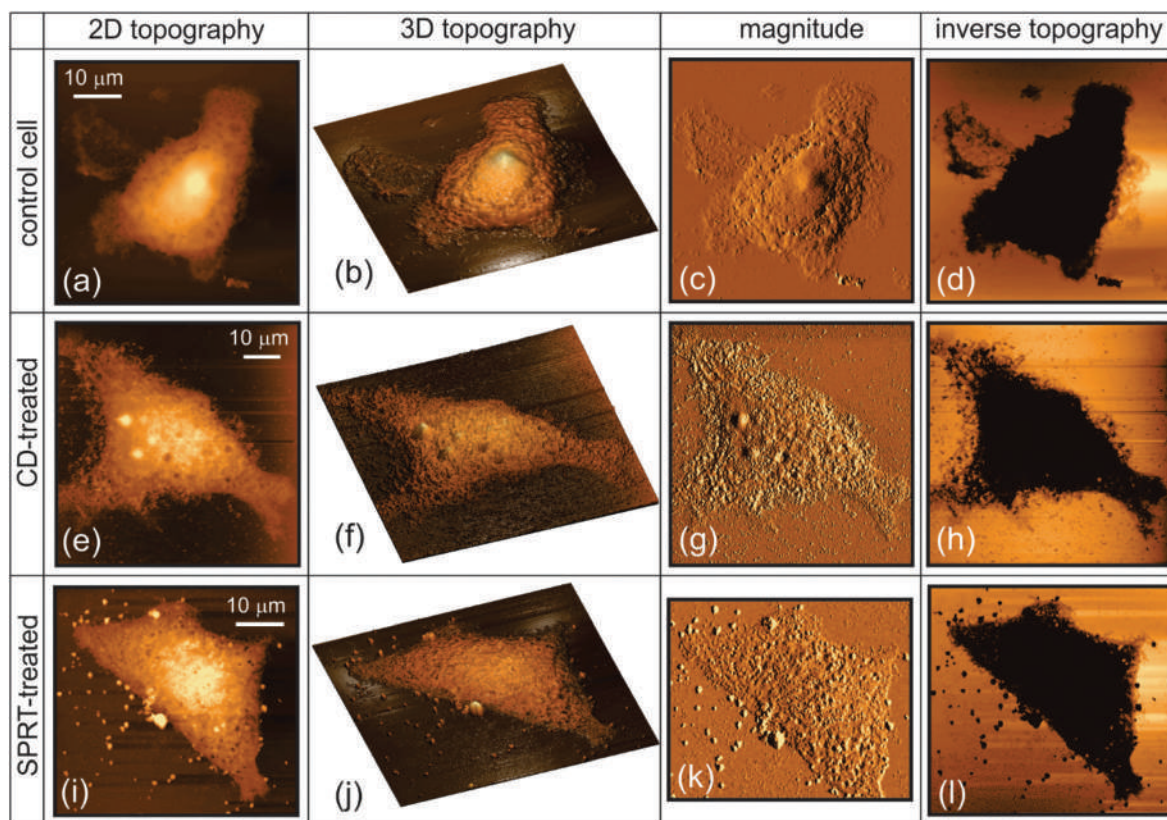

Fig. 4 AFM images of HeLa cells: control (top row), CD-treated (middle row), and SPRT-treated cells (bottom row). The first and the second column (going from the left) show 2D (a, e and i) and 3D (b, f and j) topographical images. The third column shows the AFM magnitude signal (c, g and k). 2D topographical images with inverted contrast emphasizing cell borders are depicted in (d, h and l). Height scales: (a) 1000 nm, (e) and (i) 700 nm.

NPs cannot be recognized and differentiated from the rest of the cell. The cell surface is characterized with large corrugations and many clusters of adsorbed NPs. The visibility of the adsorbed NP clusters is one of the main difference compared to the cells treated with smaller CD NPs, where NPs are hardly visible since they probably penetrated inside cells. The high-resolution AFM images of cell membranes are given in Fig. S5 of the ESI,† showing the appearance of local depressions, 50–100 nm in diameter, in the membranes of treated cells.

The third column of Fig. 4 contains AFM magnitude images, Fig. 4(c), (g), and (k). The magnitude signal is a kind of an error signal with respect to the predefined set-point in AFM tapping mode imaging. Therefore, smooth variations of the magnitude signal across the control cell in Fig. 4(c), especially across the nucleus, indicate a uniform cell surface

without pronounced wrinkles. On the other hand, the magnitude images of the cells treated with NPs in Fig. 4(g) and (k) are very noisy due to the corrugated cell surface. The magnitude image in Fig. 4(c) also shows well defined lamellipodia in the case of the control cell. In order to single out and better emphasize cell edges and lamellipodia, the inverse topographic images in Fig. 4(d), (h), and (l) are given in the most right column. As can be seen, edges of the control cell contain an abundant network of cell brushes. They are fragmented in the cell treated with CD NPs. On the other hand, the cell brushes are rarely seen along the edge of the SPRT-treated cell. The images with the AFM magnitude signal and inverse topography show that there are many small agglomerates around the treated cells which probably originate from the fragmentation of the cell edges and lamellipodia or from NPs, in the case of SPRT NPs.

Fig. 5(a) and (b) present changes of two main morphological parameters, cell height and surface roughness, respectively, due to treatment with NPs. As can be seen, the height of treated cells is decreased in comparison to control cells, and the change is slightly more pronounced for the cells treated with SPRT NPs. As confirmed by the one-way ANOVA test, this change is statistically significant for both types of CeO_2 NPs compared to control, but there is no statistically significant difference between the heights of CD- and SPRT-treated cells. The roughness of CD-treated cells increased to around 13 nm compared to 8 nm measured on the control cells. Increased roughness is a result of many depressions on the cell surface produced by interaction with NPs. The roughness of cells treated with SPRT NPs is not considered due to big adsorbed clusters of NPs, which prevent correct roughness calculation. According to topographic images of control and treated cells, it can be deduced that NPs lead to partial cell damage. This is mainly represented by a decreased height and volume of treated cells, increased surface roughness/corrugations, and not well defined cell elements, such as nucleus, nucleolus, lamellipodia and cell brushes. Overall cell shapes seem to be not influenced by the treatment with NPs, but mainly determined by a local adhesion of cells to the substrate.
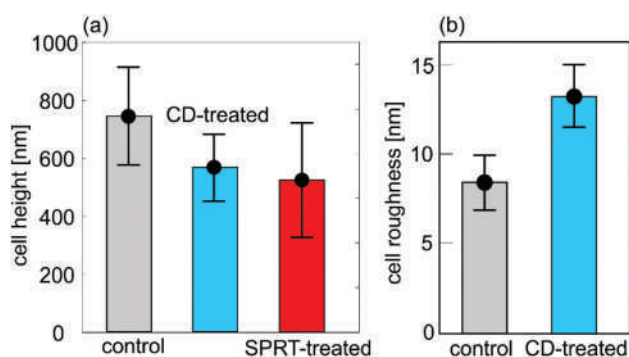
3.5 Raman spectroscopy

The obtained Raman spectra from single cells were analyzed in order to correlate spectral feature changes with NP-induced biomolecular changes. In Fig. 6, the Raman spectra of HeLa cells treated with SPRT NPs, the cells treated with CD NPs and untreated (control) cells are presented as mean ± standard deviation, in the spectral range (700–1800) cm^{-1} and (2800–3200) cm^{-1}. These are the regions where the majority of biomolecules' vibrational peaks are positioned. The obtained Raman spectra were analyzed by PCA, an unsupervised multivariate method used to extract the spectral features, which captures the variance of the analyzed group of spectra. PCA represents the spectra by a linear combination of new, mutually orthogonal vectors, *i.e.* PC loading vectors, which can be multiplied by the corresponding coefficients, PC scores, to reconstruct the original spectra. The first PC loading vector (PC1) carries the largest variance of the entire spectral dataset (control, SPRT-treated and CD-treated, altogether). The amount of variance that PC loading vectors carry decreases with an increasing order of PC loadings and the maximum order is equal to the number of all the Raman spectra subjected to PCA analysis. Generally, for the analysis it is sufficient to use the first few PC components as higher PCs usually absorb more noise.

Local extrema in a PC loading vector can be interpreted as a relative increase/decrease of the intensity of certain vibrational modes. If a PC loading vector contains a maximum at a certain wavenumber and the PC score sign of a spectrum is positive, it suggests that the intensity of the vibrational mode at that particular wavenumber has increased. If, however a PC score sign of the spectrum is negative, the intensity of the particular vibrational mode decreases in this spectrum. Fig. 7 shows PC
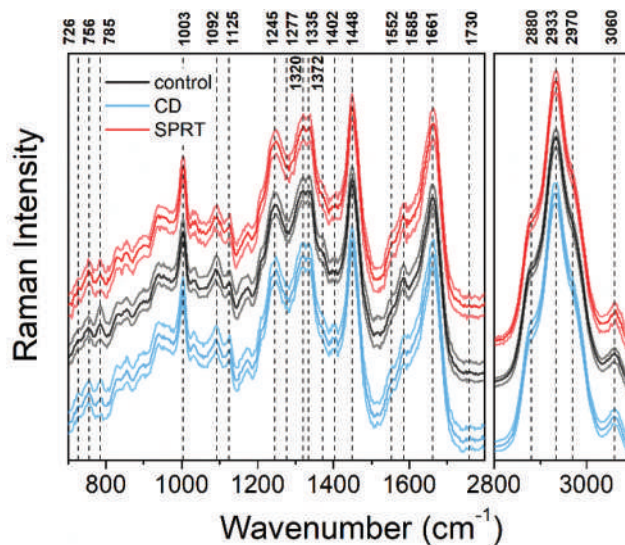

Fig. 5 Morphological changes due to the treatment with NPs: (a) cell height and (b) surface roughness. Roughness of SPRT-treated cells is not considered due to big adsorbed clusters of NPs which prevent correct roughness calculation.

Fig. 6 Raman spectra of control (black), SPRT-treated (red) and CD-treated (blue) cells, presented as mean ± standard deviation. Raman intensity in a high-wavenumber region was rescaled with a factor of 1/3 for presentation purpose.
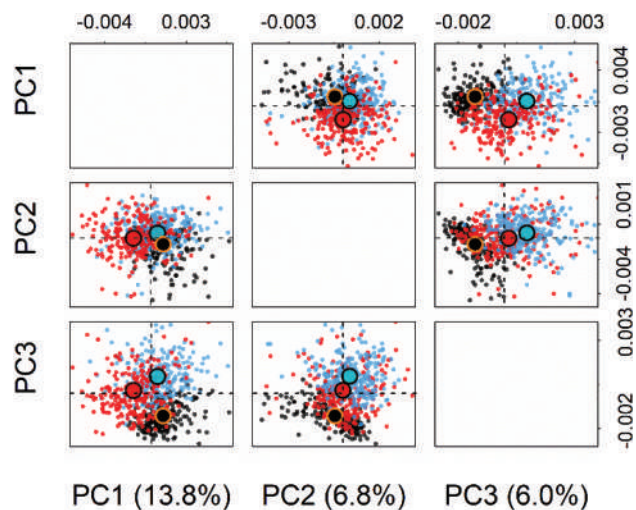
Fig. 7 Score plots of principal component analysis (PCA). Score plots comparing Raman spectra of control (black), SPRT-treated (red) and CD-treated (blue) HeLa cells. Centroids are marked with large bordered circles where circle core colors match the score plot colors of individual groups.

score plots for the first three components, whereas Fig. 8 shows the first three loading vectors (PC1, PC2, PC3) in comparison with two difference spectra (D1/D2), obtained as the

difference in control mean spectrum and NP-treated cell mean spectrum (SPRT/CD respectively). According to the PC scores shown in Fig. 7, the PC1 component that carries 13.8% of the total spectral variance separates best SPRT-treated cell spectra from control cell spectra. The PC3 component accounting for 6.0% of spectral variance separates best CD-treated cell spectra from control cell spectra. Since we aim to find the changes between three groups of cells, we choose to analyze the PC1 and PC3 components that separate best the spectra of the three studied cell groups, as presented in Fig. 8. Afterward, these features are related to the molecular changes in the cells induced by SPRT and CD NPs. Score values of the second principal component, PC2, Fig. 7, do not show observable separation between three studied groups of cells and are not analyzed in further text.

The Raman modes present in measured spectra and their assignment to particular biomolecular vibrations are listed in Table 2. In Fig. S6 from the ESI† first three PC loadings in the range (700–1800) cm^{-1} are shown for better clarity.

In the low-wavenumber region (700–1800 cm^{-1}), the PC1 loading does not exhibit particularly prominent features. Still, several peaks can be distinguished. That is the case with a positive peak at 785 cm^{-1}, negative extrema at 1003 cm^{-1} and 1670 cm^{-1}, and few peaks in the region from 1300 to 1515 cm^{-1}. The Raman mode positioned at 785 cm^{-1} is a
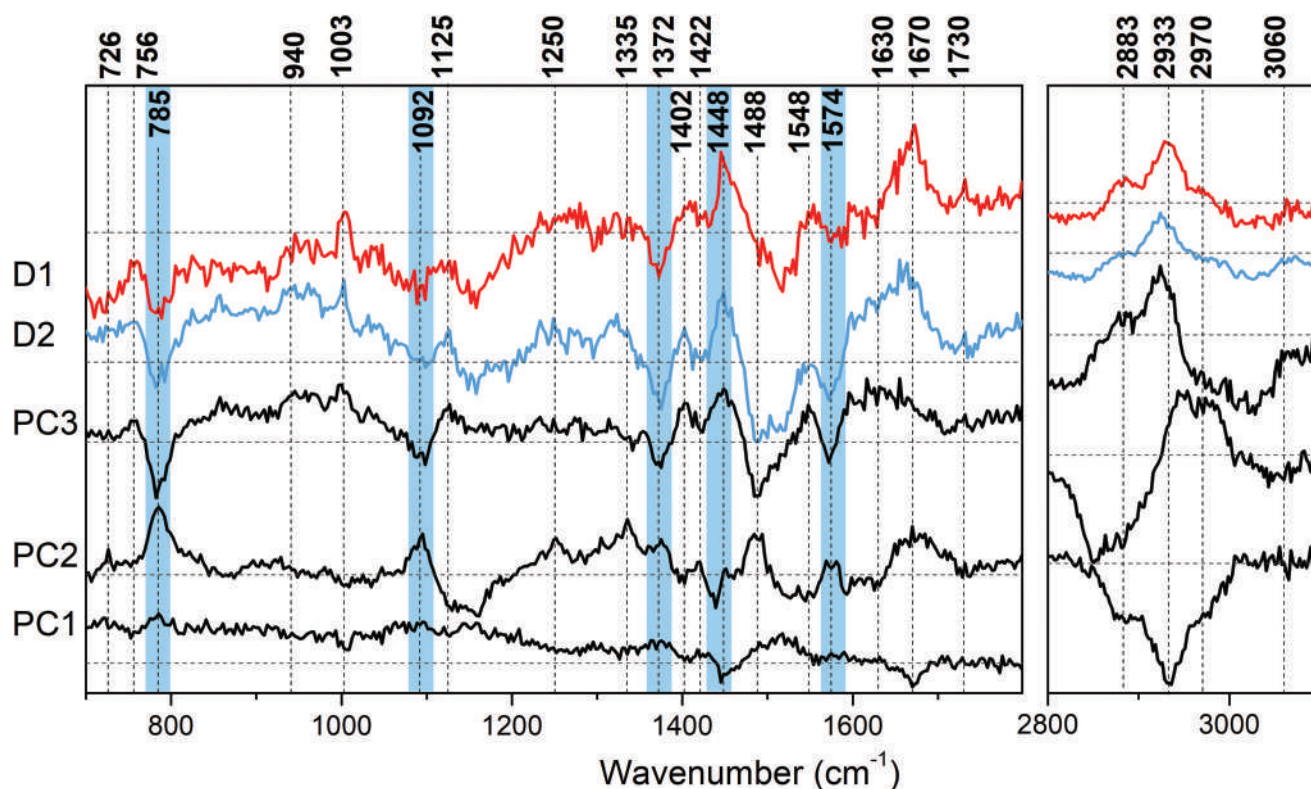

Fig. 8 First three loading spectra (PC1–PC3, from bottom to top), exhibiting Raman spectral differences between cells treated with two types of CeO$_2$ NPs and untreated (control) cells. Difference spectra (D1, D2), obtained by subtracting the mean spectrum of control cells from the mean spectra of NP-treated cells, are shown at the top of the plot (blue for CD-treated cells, red for SPRT-treated cells). Most prominent modes assigned to nucleic acids are marked with blue shading.

Paper

Table 2 Raman modes in the measured cell spectra and their possible assignations

Mean spectra	PC1	PC2	PC3	
Raman bands (cm^{-1})				Related macromolecule
726	720	726		Nucleic acids
756	756	756	756	Tryptophan
785	785	785	785	Nucleic acids
830/853				Tyrosine
940			940	Proteins
1003	1003	1003	1003	Phenylalanine
1092	1092	1092	1092	Nucleic acids
1125	1125	1125	1125	Lipids, proteins
1245		1250		Amide III
1277				Amide III
1320				Proteins, nucleic acids
1335		1335		Proteins, nucleic acids
1372	1372	1372	1372	Nucleic acids
1402	1402	1402	1402	Proteins
	1422	1420	1422	Nucleic acids
1448	1448		1448	Proteins, lipids
		1488	1488	Nucleic acids
1552		1552	1548	Tryptophan
1585		1574	1574	Nucleic acids
	1630	1630	1630	Amide I
1661	1670	1670		Amide I
1730		1730	1730	Lipids
2880	2883		2883	Proteins, lipids
2933	2933		2924	Proteins, lipids
2970				Lipids
3060		3060	3060	Proteins, lipids

typical marker of nucleic acids (ring breathing mode in DNA and RNA bases[39]). Along with less prominent peaks at 726 cm^{-1} and 1092 cm^{-1}, also positive in PC1 loading, as well as the ring-breathing DNA mode at 1372 cm^{-1} and deoxyribose mode at 1422 cm^{-1}, it indicates a decrease in nucleic acid content in SPRT-treated cells (due to negative PC1 scores), when compared to control cells.[39–41] The protein and lipid signals in a Raman spectrum cannot be clearly distinguished, sharing often the same spectral frequencies. Nevertheless, these modes in the PC1 loading spectrum are negative, indicating an increase in total protein and lipid content in SPRT-treated cells. Protein modes at 756 cm^{-1} and 1003 cm^{-1} are assigned to aromatic amino acids, tryptophan and phenylalanine, respectively,[42,43] while the mode at 1402 cm^{-1} (ref. 44) arises from protein methyl groups. The prominent mode at 1670 cm^{-1} represents the amide I band. Its precise spectral position depends on the type of protein secondary structure. Modes at 1448 cm^{-1} and 1125 cm^{-1} could arise from both proteins and lipids.[42,45] Those peaks are, as mentioned above, negative in PC1 loading, having greater contribution in the SPRT-treated cell spectra.

Although the high-wavenumber region of PC1 loading exhibits only a few peaks, those are very pronounced. It therefore demonstrates large differences in this spectral region between groups of cells and seems to be the most important discriminating feature for SPRT-treated cells. Modes in this region originate from protein and lipid vibrations. Although individual contributions of proteins and lipids cannot be clearly distinguished, it was established in the literature that the CH$_2$ stretching vibration at 2851 cm^{-1} is more of lipid character and that the symmetric CH$_3$ stretching vibration at 2928 cm^{-1} is more of protein character.[46] Since negative peaks positioned at 2883 cm^{-1} and 2933 cm^{-1} were observed in PC1 loading, this region indicates a higher global lipid and protein content in SPRT-treated cells, which is in accordance with the lower wavenumber region data.

As previously said, PC3 represents spectral changes that help to separate the spectra of CD-treated cells from those of control cells. Score values for PC3 are positive for CD-treated cells and negative for control cells. When it comes to SPRT-treated cells, it can be observed that roughly one half of cell spectra have negative and the other half have positive values of PC3 scores. In accordance with that, the positive peaks in PC3 loading denote a relative increase in the corresponding molecules in CD-treated cells. Contrary to PC1 loading, PC3 loading is more similar to D2, the difference spectrum of CD-treated cells.

Most prominent bands in the PC3 loading are those assigned to nucleic acids. That group consists of already mentioned 785 cm^{-1} mode along with modes at 1092 cm^{-1}, 1488 cm^{-1} and 1574 cm^{-1}.[42,47–49] A negative sign of these peaks in PC3 loading leads to the conclusion that CD-treated cells carry the smallest DNA content, while SPRT-treated cells also have smaller DNA content compared to control, but larger compared to CD-treated cells. Slightly less prominent negative peaks at 1372 cm^{-1} and 1422 cm^{-1} can also be assigned to nucleic acid vibrations.[40] The decreased DNA content is, therefore, the main characteristic of CD-treated HeLa cells.

Except nucleic acid Raman modes, PC3 loading contains two positive peaks: at 1402 cm^{-1}, assigned to proteins, and at 1448 cm^{-1}, assigned to proteins and lipids. The feature at 1730 cm^{-1} cannot be definitely included into the analysis due to its very low intensity, but it should be mentioned that the mode at this position represents a typical lipid spectral marker, while the peak at 1125 cm^{-1} can arise both from lipids and proteins.[42,44,45] The increased lipid content is, therefore, a discriminating feature also for CD-treated cells (not only SPRT-treated, shown by PC1).

More protein Raman modes in PC3 loading are represented with positive peaks at 756 cm^{-1}, 1003 cm^{-1} and 1630 cm^{-1}. The first two originate from aromatic amino acids, tryptophan and phenylalanine,[43] respectively, while the feature at 1630 cm^{-1} belongs to the amide I band. The amide I band in protein Raman spectra can be observed as a broad peak covering frequencies from 1600 cm^{-1} to 1690 cm^{-1}, approximately.[50] It has been used for studies of the protein secondary structure,[42] being highly sensitive to changes in the molecular geometry and hydrogen binding of peptide groups. In both difference spectra as well as in PC1 and PC3 loadings a feature at ~1670 cm^{-1} is present, which can be related to the relative increase of the protein content. In PC3 loading, as well as in CD-cell difference spectrum, a low-wavenumber wing of the amide I band, centered around 1630 cm^{-1}, is more pronounced than in PC1 loading and SPRT-treated cell difference spectrum. This indicates changes in the protein secondary

structure specific for the cells treated with CD NPs. However, this spectral region also contains some water vibration modes[51] which were subtracted during spectra preprocessing, but some artifacts due to this can appear.

A similar conclusion about the increase of total protein and lipid content in NP-treated cells can be derived analyzing the high-wavenumber region of PC3 loading. All modes in this region, at 2883 cm^{-1}, 2924 cm^{-1} and 3060 cm^{-1}, can be assigned to proteins and lipids, though the band at 2883 cm^{-1} is more of lipid character, while the one at 2924 cm^{-1} is more of protein character mode.[46,52] It should be noticed that the peak at 2924 cm^{-1} in PC3 loading is shifted when compared to the 2933 cm^{-1} peak in the original mean cell spectra, as well as compared with the corresponding peak in the PC1 loading spectrum.

To summarize, PC3 indicates a decrease in nucleic acid and an increase in protein and lipid content of NP-treated cells, with observable differences in the relative ratio of features in the amide I band region for SPRT- and CD-treated cell spectra, suggesting changes in the protein secondary structure for the latter.

Contrary to the expectations that uncoated NPs affect the cells more strongly than coated NPs, due to their free surface accessible to the cell molecules, the results from conventional biological assays and Raman measurements lead to the conclusion that dextran-coated CD NPs had a higher impact on cells. The reason for that could be found in the stability *i.e.* the size of NPs. Coated CD NPs, being smaller in size (3–4 nm), can affect the cells more successfully than large aggregates of uncoated SPRT NPs, as the coated particles pass through cell structures more easily. Our AFM measurements showed that a portion of SPRT NPs rest on the cell surface, in the form of large clusters, which interferes with the AFM characterization of the cell membrane surface. However, the Raman imaging results indicate that at least part of the SPRT NPs passes the cell membrane and are located within the cytoplasm and possibly other cell organelles, except the nucleus. Still, the level of activity of those intracellular NP aggregates is lower than the activity of CD NPs, as has been shown by the SRB assay. In order to ensure that the observed changes in the growth of CD-treated cells are caused by CeO$_2$ and not by dextran itself, we tested for potential interfering effects of a dextran solution on cell culture. A 48 hour treatment with the aqueous dextran solution of the concentration equal to the one used in NP synthesis showed no effect on the growth of cell culture. We thereby confirmed that the effect is due to ceria solely and that dextran itself does not affect the growth, viability and detaching of the cells from the surface.

Conventional biological assays showed that effects of NPs were represented mainly by cell growth inhibition, *i.e.* by a decrease of the overall cell number in treated cell samples. Based on the literature data, most typical Raman spectral markers for reduced cell growth are changes in nucleic acids' Raman modes. In our experiments, the most pronounced differences between the treated and control Raman spectra are also nucleic acids' peaks, indicating the reduced quantity of cell nucleic acids and/or nuclear condensation level. An

increase in the overall quantity of proteins and lipids in NP-treated cells points out the effects caused primarily by CD NPs. This could be associated with the enlargement of the overall cell membranous area, due to vacuolization processes, often following NP internalization in the cell.[53]

AFM showed the depletion of lamellipodia and increased levels of cell surface corrugation, as well as poorly defined nuclei borders and partly fragmented nucleoli, in NP-treated cells compared to control cells. Those features are already studied as potential mechanical biomarkers for monitoring antitumor drug effects.[54] It has been shown that the surface roughness of HeLa cells is increased after treatment with some antitumor drugs, which act as proliferation inhibitors.[55] Protein-related changes represented by the features in the amide I band region in the cell Raman spectra could be related to the reorganization of cytoskeletal elements and membrane proteins, causing cell surface modulations.

It was shown that nanoceria interfere with the cytoskeletal organization of neural stem cells.[15] It was also observed that
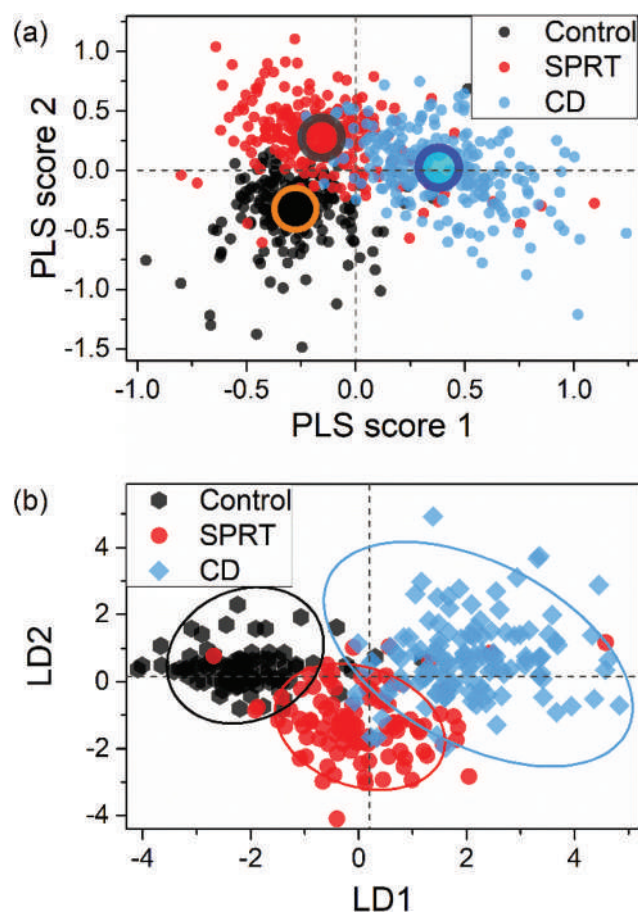

Fig. 9 (a) PLS score plot of first two components. Black dots represent control cells, red SPRT-treated cells and blue dots CD-treated cells, centroids are marked with large bordered circles where circle core colors match the score plot colors of individual groups. (b) LDA projections on LD1 and LD2 for a tested set of spectra. Black hexagons represent control cells, red circles SPRT-treated cells and blue rhombuses CD-treated cells.

gold NPs inhibit the polymerization of cytoskeletal protein tubulin, inducing amide bands' shifts.[14] These NPs induce cell cycle arrest and apoptosis of human lung and breast cancer cells, as shown in the same study. In our experiments, CeO_2 NPs affected the cells by decreasing the cell growth, that could be a consequence of apoptosis or cell cycle arrest.

3.6 Classification of the cells treated with nanoparticles

Partial least squares regression (PLS) analysis is, unlike PCA, a supervised multivariate method and takes into account prior knowledge on the group association of spectra. It is used to decompose the spectral variance in such a way that it optimally separates the spectra from different groups of samples. PLS analysis was performed on all three groups of spectra. PLS scores spanning the space of first two PLS components are shown in Fig. 9(a). A PLS-LDA model was built using a share of total spectral dataset and then tested on the remaining spectra. Linear discriminant analysis (LDA) using first five PLS components was trained on random 360 spectra (training set), 120 from each cell group, and the model was tested on the remaining spectra from the total of 683.

LD1/LD2 scores for the tested spectra are shown in Fig. 9(b) demonstrating good separation and enabling good prediction for spectra membership in each of three groups. The sensitivity of the LDA prediction was 88% and specificity was 92%. The quality of spectra separation shows a potential for the method application in the separation of cells of the same type treated with different kinds of NPs.

4.   Conclusions

AFM and Raman spectroscopy were used to study the morphological and molecular changes of HeLa cells exposed to dextran-coated (CD) CeO_2 NPs and uncoated (SPRT) CeO_2 NPs. AFM showed degrading changes of the cell membrane and lamellipodia and an increase of surface roughness in the treated cells. Raman spectroscopy showed that coated CD NPs have a higher impact on HeLa cells, observed through the decrease of DNA content and the increase of the lipid/protein content. Furthermore, modifications in the spectral region characteristic of the protein secondary structure, induced by coated CD NPs, were detected in their Raman spectra. These changes could be connected with cytoskeleton reorganization, causing morphological modifications of the cell surface.

Based on the results of this study, single-cell Raman spectroscopy performed fast and on a large number of cells has potential for quick screening of cell DNA content changes resulting from NP exposure. Raman analysis demonstrated that the two types of ceria NPs both affect DNA, while standard biological assays had been able to confirm only the effects of CD NPs. The formation of lipid structures and the modification of cell proteins can sometimes signal the mechanism of the NP–cell interaction, and these changes are also observable by Raman spectroscopy, as demonstrated in this work. The AFM investigation of surface cell properties combined with

Raman spectral fingerprinting of surface molecular structures might be used to extract information on the effect of NPs on the cell–cell and the cell–environment communication. In general, the results obtained by Raman spectroscopy provide guidelines for a more detailed characterization of NP–cell interactions. Finally, multivariate PLS-LDA modeling marked the potential of Raman spectroscopy for the classification of the cells of the same origin in different physiological statuses caused by NPs.

Conflicts of interest

There are no conflicts to declare.

Acknowledgements

References

1 X. Huang, R. O'Connor and E. A. Kwizera, *Nanotheranostics*, 2017, **1**, 80–102.

2 H. Jo, J. Her and C. Ban, *Biosens. Bioelectron.*, 2015, **71**, 129–136.

3 K. Kalimuthu, B.-C. Lubin, A. Bazylevich, G. Gellerman, O. Shpilberg, G. Luboshits and M. A. Firer, *J. Nanobiotechnol.*, 2018, **16**, 34.

4 S. S. Lucky, K. C. Soo and Y. Zhang, *Chem. Rev.*, 2015, **115**, 1990–2042.

5 O. Lushchak, A. Zayachkivska and A. Vaiserman, *Oxid. Med. Cell. Longevity*, 2018, **2018**, 9.

6 A. Gallud, K. Kloditz, J. Ytterberg, N. Ostberg, S. Katayama, T. Skoog, V. Gogvadze, Y. Z. Chen, D. Xue, S. Moya, J. Ruiz, D. Astruc, R. Zubarev, J. Kere and B. Fadeel, *Sci. Rep.*, 2019, **9**, 4366.

7 M. Wunsch, R. Caspell, S. Kuerten, P. Lehmann and S. Sundararaman, *Cells*, 2015, **4**, 40–55.

8 P. Kumar, A. Nagarajan and P. D. Uchil, *Cold Spring Harb. Protoc.*, 2018, **2018**, 465–468.

9 P. Skehan, R. Storeng, D. Scudiero, A. Monks, J. McMahon, D. Vistica, J. T. Warren, H. Bokesch, S. Kenney and M. R. Boyd, *J. Natl. Cancer Inst.*, 1990, **82**, 1107–1112.

10 T. L. Riss, R. A. Moravec, A. L. Niles, S. Duellman, H. A. Benink, T. J. Worzella and L. Minor, in *Assay Guidance Manual*, ed. G. S. Sittampalam, A. Grossman, K. Brimacombe, M. Arkin, D. Auld, C. Austin, J. Baell, B. Bejcek, J. M. M. Caaveiro, T. D. Y. Chung, N. P. Coussens, J. L. Dahlin, V. Devanaryan, T. L. Foley, M. Glicksman, M. D. Hall, J. V. Haas, S. R. J. Hoare, J. Inglese, P. W. Iversen, S. D. Kahl, S. C. Kales, S. Kirshner, M. Lal-Nag, Z. Li, J. McGee, O. McManus, T. Riss, O. J. Trask Jr., J. R. Weidner, M. J. Wildey, M. Xia and X. Xu, Eli Lilly & Company and the National Center for Advancing Translational Sciences, Bethesda (MD), 2004, https://www.ncbi.nlm.nih.gov/books/NBK144065/.

11 D. W. Shipp, F. Sinjab and I. Notingher, *Adv. Opt. Photonics*, 2017, **9**, 315–428.

12 T. A. J. de Souza, T. L. Rocha and L. P. Franchi, *Adv. Exp. Med. Biol.*, 2018, **1048**, 215–226.

13 M. P. Harvanova, J. Jiravova, J. Malohlava, K. B. Tomankova, D. Jirova and H. Kolarova, *Int. J. Pharm.*, 2017, **528**, 280–286.

14 D. Choudhury, P. L. Xavier, K. Chaudhari, R. John, A. K. Dasgupta, T. Pradeep and G. Chakrabarti, *Nanoscale*, 2013, **5**, 4476–4489.

15 A. R. Gliga, K. Edoff, F. Caputo, T. Källman, H. Blom, H. L. Karlsson, L. Ghibelli, E. Traversa, S. Ceccatelli and B. Fadeel, *Sci. Rep.*, 2017, **7**, 9284.

16 R. Parveen, T. N. Shamsi and S. Fatima, *Int. J. Biol. Macromol.*, 2017, **94**, 386–395.

17 L. Ahlinder, B. Ekstrand-Hammarström, P. Geladi and L. Österlund, *Biophys. J.*, 2013, **105**, 310–319.

18 E. Brauchle, S. Thude, S. Y. Brucker and K. Schenke-Layland, *Sci. Rep.*, 2014, **4**, 4698.

19 A. S. Mondol, N. Töpfer, J. Rüger, U. Neugebauer, J. Popp and I. W. Schie, *Sci. Rep.*, 2019, **9**, 12653.

20 A. Pliss, A. N. Kuzmin, A. V. Kachynski and P. N. Prasad, *Biophys. J.*, 2010, **99**, 3483–3491.

21 I. W. Schie, L. Alber, A. L. Gryshuk and J. W. Chan, *Analyst*, 2014, **139**, 2726–2733.

22 E. Fazio, A. Speciale, S. Spadaro, M. Bonsignore, F. Cimino, M. Cristani, D. Trombetta, A. Saija and F. Neri, *Colloids Surf., B*, 2018, **170**, 233–241.

23 M. Lasalvia, G. Perna and V. Capozzi, *Sensors*, 2019, **19**, 2418.

24 F. Braet, C. Seynaeve, R. De Zanger and E. Wisse, *J. Microsc.*, 2001, **190**, 328–338.

25 H. A. McNally, B. Rajwa, J. Sturgis and J. P. Robinson, *J. Neurosci. Methods*, 2005, **142**, 177–184.

26 G.-M. Lyu, Y.-J. Wang, X. Huang, H.-Y. Zhang, L.-D. Sun, Y.-J. Liu and C.-H. Yan, *Nanoscale*, 2016, **8**, 7923–7932.

27 S. Rajeshkumar and P. Naik, *Biotechnol. Rep.*, 2018, **17**, 1–5.

28 L. Benameur, M. Auffan, M. Cassien, W. Liu, M. Culcasi, H. Rahmouni, P. Stocker, V. Tassistro, J.-Y. Bottero, J. Rose, A. Botta and S. Pietri, *Nanotoxicology*, 2014, **9**, 696–705.

29 A. S. Karakoti, S. V. N. T. Kuchibhatla, K. S. Babu and S. Seal, *J. Phys. Chem. C*, 2007, **111**, 17232–17240.

30 E. Alpaslan, H. Yazici, N. H. Golshan, K. S. Ziemer and T. J. Webster, *ACS Biomater. Sci. Eng.*, 2015, **1**, 1096–1103.

31 J. M. Perez, A. Asati, S. Nath and C. Kaittanis, *Small*, 2008, **4**, 552–556.

32 S. Mittal and A. K. Pandey, *BioMed Res. Int.*, 2014, **2014**, 891934.

33 S. Boskovic, D. Djurovic, Z. Dohcevic-Mitrovic, Z. Popovic, M. Zinkevich and F. Aldinger, *J. Power Sources*, 2005, **145**, 237–242.

34 I. W. Schie, J. Rüger, A. S. Mondol, A. Ramoji, U. Neugebauer, C. Krafft and J. Popp, *Anal. Chem.*, 2018, **90**, 2023–2030.

35 E. Cordero, F. Korinth, C. Stiebing, C. Krafft, I. Schie and J. Popp, *Sensors*, 2017, **17**, 1724.

36 C. Stiebing, I. W. Schie, F. Knorr, M. Schmitt, N. Keijzer, R. Kleemann, I. J. Jahn, M. Jahn, A. J. Kiliaan, L. Ginner, A. Lichtenegger, W. Drexler, R. A. Leitgeb and J. Popp, *Neurophotonics*, 2019, **6**, 1–9.

37 R. Kostić, S. Aškrabić, Z. Dohčević-Mitrović and Z. V. Popović, *Appl. Phys. A*, 2007, **90**, 679–683.

38 C. Matthäus, T. Chernenko, J. A. Newmark, C. M. Warner and M. Diem, *Biophys. J.*, 2007, **93**, 668–673.

39 J. W. Chan, D. S. Taylor, T. Zwerdling, S. M. Lane, K. Ihara and T. Huser, *Biophys. J.*, 2006, **90**, 648–656.

40 A. J. Ruiz-Chica, M. A. Medina, F. Sánchez-Jiménez and F. J. Ramírez, *J. Raman Spectrosc.*, 2004, **35**, 93–100.

41 I. W. Schie and T. Huser, in *Comprehensive Physiology*, ed. R. Terjung, American Physiological Society, 2013, vol. 3, pp. 941–956.

42 Z. Movasaghi, S. Rehman and I. U. Rehman, *Appl. Spectrosc. Rev.*, 2007, **42**, 493–541.

43 N. Stone, C. Kendall, N. Shepherd, P. Crow and H. Barr, *J. Raman Spectrosc.*, 2002, **33**, 564–573.

44 R. K. Dukor, in *Handbook of Vibrational Spectroscopy*, ed. J. M. Chalmers and P. R. Griffiths, John Wiley & Sons, Ltd., 2006, pp. 3335–3361, DOI: 10.1002/0470027320.s8107.

45 K. Czamara, K. Majzner, M. Z. Pacia, K. Kochan, A. Kaczor and M. Baranska, *J. Raman Spectrosc.*, 2015, **46**, 4–20.

46 N. J. Kline and P. J. Treado, *J. Raman Spectrosc.*, 1997, **28**, 119–124.

47 I. Notingher, I. Bisson, J. M. Polak and L. L. Hench, *Vib. Spectrosc.*, 2004, **35**, 199–203.

48 V. V. Pully, A. T. M. Lenferink and C. Otto, *J. Raman Spectrosc.*, 2011, **42**, 167–173.

49 N. Stone, C. Kendall, J. Smith, P. Crow and H. Barr, *Faraday Discuss.*, 2004, **126**, 141–157.

50 A. Rygula, K. Majzner, K. M. Marzec, A. Kaczor, M. Pilarczyk and M. Baranska, *J. Raman Spectrosc.*, 2013, **44**, 1061–1076.

51 D. M. Carey and G. M. Korenowski, *J. Chem. Phys.*, 1998, **108**, 2669–2675.

52 K. Czamara, K. Majzner, A. Selmi, M. Baranska, Y. Ozaki and A. Kaczor, *Sci. Rep.*, 2017, **7**, 40889.

53 D. Septiadi, F. Crippa, T. L. Moore, B. Rothen-Rutishauser and A. Petri-Fink, *Adv. Mater.*, 2018, **30**, e1704463.

54 X. Yun, M. Tang, Z. Yang, J. J. Wilksch, P. Xiu, H. Gao, F. Zhang and H. Wang, *RSC Adv.*, 2017, **7**, 43764–43771.

55 K. S. Kim, C. H. Cho, E. K. Park, M.-H. Jung, K.-S. Yoon and H.-K. Park, *PLoS One*, 2012, **7**, e30066.

Electrically Tunable Metal–Semiconductor–Metal Terahertz Metasurface Modulators

Goran Isić ⬤, Georgios Sinatkas ⬤, *Student Member, IEEE*, Dimitrios C. Zografopoulos ⬤, Borislav Vasić, Antonio Ferraro ⬤, *Member, IEEE*, Romeo Beccherelli ⬤, *Member, IEEE*, Emmanouil E. Kriezis ⬤, *Senior Member, IEEE*, and Milivoj Belić ⬤

Abstract—We propose metal–semiconductor–metal cavity arrays as active elements of electrically tunable metasurfaces operating in the terahertz spectrum. Their function is based on reverse biasing the Schottky junction formed between top metal strips and the n-type semiconductor buried beneath. A gate bias between the strips and a back metal reflector controls the electron depletion layer thickness thus tuning the Drude permittivity of the cavity array. Using a rigorous multiphysics framework which combines Maxwell equations for terahertz waves and the drift-diffusion model for describing the carrier behavior in the semiconductor, we find a theoretically infinite extinction ratio, insertion loss of around 10%, and picosecond intrinsic switching times at 1 THz, for a structure designed to enter the critical coupling regime once the depletion layer reaches the bottom metal contact. We also show that the proposed modulation concept can be used for devices operating at the higher end of the terahertz spectrum, discussing the limitations on their performance.

Index Terms—Terahertz metasurfaces, tunable metamaterials.

G. Isić is with the Graphene Laboratory of Center for Solid State Physics and New Materials, Institute of Physics Belgrade, University of Belgrade, Belgrade 11080, Serbia, and also with the Texas A&M University at Qatar, Doha 23874, Qatar (e-mail: isicg@ipb.ac.rs).

G. Sinatkas and E. E. Kriezis are with the School of Electrical and Computer Engineering, Aristotle University of Thessaloniki, Thessaloniki 54124, Greece (e-mail: gsinatka@auth.gr; mkriezis@auth.gr).

D. C. Zografopoulos, A. Ferraro, and R. Beccherelli are with the Consiglio Nazionale delle Ricerche, Istituto per la Microelettronica e Microsistemi, Rome 00133, Italy (e-mail: dimitrios.zografopoulos@artov.imm.cnr.it; antonio.ferraro@artov.imm.cnr.it; romeo.beccherelli@artov.imm.cnr.it).

B. Vasić is with the Graphene Laboratory of Center for Solid State Physics and New Materials, Institute of Physics Belgrade, University of Belgrade, Belgrade 11080, Serbia (e-mail: bvasic@ipb.ac.rs).

M. Belić is with the Texas A&M University at Qatar, Doha 23874, Qatar (e-mail: milivoj.belic@qatar.tamu.edu).

Color versions of one or more of the figures in this paper are available online at http://ieeexplore.ieee.org.

Digital Object Identifier 10.1109/JSTQE.2019.2893762

I. INTRODUCTION

TERAHERTZ science has been steadily attracting a growing interest over the past decades. Lying above the upper limit of frequencies attainable in electronic devices and yet below frequencies at which light can be efficiently generated and detected, the current terahertz technology is faced with many challenges [1]. Among them, the development of fast electro-optic modulators for free-space terahertz signals, exhibiting low insertion loss and high modulation depth, has been gaining in importance over the past years considering the rapidly growing demands of wireless communications [2].

Following initial successful demonstrations of electro-optic modulation in terahertz [3], [4], the culprit of the very low modulation efficiency has been identified as the incompatibility of submillimeter wavelengths with much smaller features of the underlying electronic system [5]. A substantial increase in modulation efficiency has since been provided by various metallic structures [6], [7] whose resonant response translates into a stronger light-matter interaction helping bridge the two scales. Devices combining semiconductors (mainly gallium arsenide, GaAs) with metasurfaces have been of particular interest [8] as they offer high-speed modulation, a perspective of on-chip integration using established semiconductor technologies [9] and are fully compatible with quantum cascade lasers [1], the most promising source of terahertz radiation. Other material systems, such as liquid crystals [10]–[12] and graphene [13]–[15] more recently, have also been considered in depth, each presenting its own set of comparative advantages.

After the first prototype was introduced [6], a number of semiconductor-based terahertz metasurface modulators have been considered [7], [16]–[20] with widely ranging performance parameters. Perhaps the most convincing demonstration so far has been the double-channel heterostructure modulator [18] achieving modulation speed above 1 GHz and a modulation depth of 85%. Leaving important technical details aside, the above devices all derive their operation principle from the original work [6]. It involves a cut metal wire taking various shapes (e.g. a split-ring resonator or a dipole antenna) placed on top of a semiconductor, in which modulation occurs as a result of tuning the semiconductor conductivity beneath the gap, since a high conductivity effectively short-circuits the two parts.

Here we consider an alternative device concept whose main characteristic is that the tunable resonant element is buried
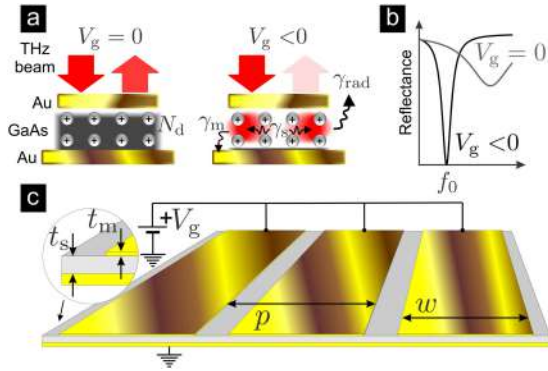
Fig. 1. (a) Operation principle, (b) Typical bias-dependent reflectance spectra, (c) A section of the device shown in real scale (in the actual device, the strips are repeated periodically). The epitaxial GaAs layer is selectively n-doped beneath the strips.

into the semiconductor akin to the one recently used in electrically tunable infrared polaritonic metasurfaces [21]. It comprises a metal-semiconductor-metal cavity of deeply subwavelength thickness known for providing a substantial light-matter interaction enhancement [22]. Such cavities have recently been employed in electrical control of intersubband polaritons [23], terahertz [24], [25] and infrared quantum detectors [26] and vertical-external-cavity surface-emitting quantum cascade lasers [27], [28]. In contrast to the listed examples which all rely on AlGaAs quantum heterostructures, the active region in our case is simply a single n-doped epitaxial layer of GaAs forming a Schottky contact at the interface with the top metal layer, allowing for tuning the n-GaAs permittivity by applying a gate voltage.

II. OPERATION PRINCIPLE AND DEVICE GEOMETRY

The basic element of the device is a metal-semiconductor-metal cavity array depicted in Fig. 1(a). A Schottky junction is formed between the top electrode (gate) and the epitaxial semiconductor layer while the contact to the bottom electrode (ground) is ohmic. The gold and GaAs combination of materials is considered because its optical properties in metal-semiconductor-metal cavities [29] as well as the relevant Schottky [30], [31] and ohmic contact [32] characteristics are well documented, however a range of other materials may suffice as well. At zero bias, the electron concentration n_e in each cavity (gray shading) is considered equal to the fully ionized donor concentration N_d (small spheres). If the doping is very high, so that the plasma oscillation frequency ω_p is above the incoming field frequency, the Drude response will be fast enough to screen the external fields out of the cavities and the device will act as a mirror. Upon applying a sufficiently large reverse voltage, the depletion layer of the Schottky junction extends over the entire cavity which now supports a photonic mode with eigenfrequency $\omega_0 = 2\pi f_0$ and is characterized by a radiative decay rate γ_{rad} and a non-radiative decay rate γ_0, the latter being the sum of the rate of photon absorption in the metal γ_m and semiconductor γ_s. If the geometrical parameters of the cavity

are chosen appropriately [11], the critical coupling condition

$$\gamma_{rad} = \gamma_0, \tag{1}$$

may be reached, ensuring the total absorption of an externally incident terahertz beam. Therefore, by switching V_g, a large reflectance modulation may be achieved in a band of frequencies around f_0, as depicted in Fig. 1(b).

In fact, the analysis below shows that efficient modulation does not strictly require a sub-plasma frequency operation ($\omega_p/\omega_0 > 1$), as long as the free carriers are able to blueshift ω_0 enough. Formally, one may analyze the eigenfrequency $\omega_0(V_g)$ and decay rates $\gamma_m(V_g)$, $\gamma_s(V_g)$, $\gamma_{rad}(V_g)$ as functions of V_g. However, since the quantitative connection between such a dependence and the modulation efficiency is not straightforward, here a direct approach is adopted whereby the decay rates are analyzed only for fully depleted cavities after which the modulation efficiency is evaluated without further reference to them.

For convenience, here the simplest implementation of the described concept is considered, as depicted in realistic scale in Fig. 1(c). The device represents a periodic array of long rectangular strips of width w and pitch p, connected to a common potential V_g at the far end. It is operative for one polarization (across the strips) only, but polarization-insensitive variants [11] can be straightforwardly devised by replacing the strips with symmetrical patches (e.g. circular or square-shaped). Invoking the temporal coupled-mode theory (TCMT) formalism [33], [34], the complex reflection coefficient of metal-semiconductor-metal cavity arrays with fundamental optical modes in the terahertz range [22] can, to an excellent approximation, be written as [35]

$$r(\omega) = \frac{\omega - \omega_0 + i(\gamma_0 - \gamma_{rad})}{\omega - \omega_0 + i(\gamma_0 + \gamma_{rad})}. \tag{2}$$

We use the TCMT formalism in conjunction with rigorous numerical simulations (see Appendix IV), whereby the three parameters ω_0, γ_0 and γ_{rad} are extracted by fitting Eq. (2) to the numerically calculated $r(\omega)$. While useful in providing a simple way of parametrizing the optical response of the device, the real advantage of the TCMT formalism stems from the fact that γ_0 and γ_{rad} are physically meaningful quantities which can be related to the cavity geometry and eigenmode field distribution, thus facilitating the design of cavities with desired $r(\omega)$.

The process of identifying a geometry which yields a critically coupled optical mode at a desired frequency f_0 can be illustrated on the example of $f_0 = 1$ THz. According to Fig. 1(c), it involves deciding on values of three geometrical parameters, w, p and t_s. Here the gold strip thickness t_m is set to 0.3 μm instead of being considered as a free parameter because its exact value is insignificant, as long as it is much smaller than the wavelength but large enough to ensure optical opacity. The cavity width w is determined from the target f_0 because the fundamental optical mode is a transverse-magnetic standing wave [22] whose eigenfrequency is only weakly affected by changing t_s and p (see Figs. 2(a,b) below). A slight lateral spill of the standing wave fields beyond the strip edges implies that the half-wavelength in the semiconductor $\lambda_{0,GaAs}/2$ is slightly larger than w.
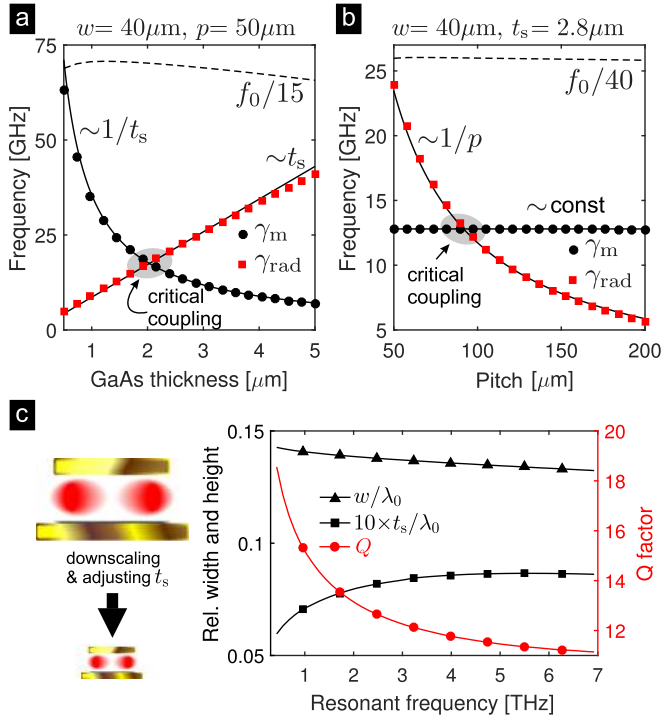
Fig. 2. TCMT parameters as a function of (a) semiconductor layer thickness, (b) pitch. (c) Geometrical parameters yielding critical coupling at full depletion (p is fixed at $1.25\,w$).

Assuming $n_{\mathrm{GaAs}} = 3.3$ at 1 THz, yields $\lambda_{0,\mathrm{GaAs}}/2 \approx 45.45\,\mu\mathrm{m}$, starting from which we easily find $w = 40\,\mu\mathrm{m}$ to yield $f_0 \approx 1$ THz.

To establish the role of GaAs thickness, in Fig. 2(a) we fix $p = 50\,\mu\mathrm{m}$ and plot the TCMT parameters as a function of t_{s}. Since the cavity is assumed to be fully depleted, the absorption rate in the semiconductor layer γ_{s} will be negligible while γ_0 becomes equal to the metal absorption rate γ_{m} plotted in Fig. 2(a). The numerically calculated values of γ_{m} and γ_{rad}, represented by circles and squares respectively, are seen to fit very well to a t_{s}^{-1} and t_{s} curve (solid lines). The origin of the observed scaling of γ_{m} and γ_{rad} has been examined in Appendix C of [11] for the mathematically analogous case of circular patch cavities filled with a liquid crystal. This scaling follows from a straightforward consideration of how the modal fields are redistributed when the cavity height is changed, with the only subtlety being the eigenmode field normalization. Here we limit the discussion to noting that the observed trend is what one would expect: compressing the eigenmode into a thinner cavity causes the fields to penetrate more into the cladding on top and bottom, implying higher absorption in the metal and, therefore, the increase of γ_{m} with decreasing t_{s}. On the other hand, the radiation loss of a cavity must be proportional to the fraction of its surface not covered by metal and since the latter is proportional to t_{s}, we infer that γ_{rad} should decrease as t_{s} is decreased. In Fig. 2(a), adjusting t_{s} alone is found to be sufficient for achieving critical coupling, seen as the crossing of γ_{m} and γ_{rad} curves in Fig. 2(a). In fact, since two curves proportional to $\sim t_{\mathrm{s}}^{-1}$ and $\sim t_{\mathrm{s}}$ always have an intersection, we infer that adjusting t_{s} alone will be sufficient to fulfill Eq. (1) for any reasonable cavity. Meanwhile, the dashed

line depicting $f_0/15$ shows that f_0 undergoes only a small relative variation over the considered t_{s} interval, meaning that once t_{s} is fixed, w may be readjusted to set f_0 exactly to the desired value.

The effect of changing the pitch is considered in Fig. 2(b) where t_{s} is set to a representative value of 2.8 $\mu\mathrm{m}$. For p below 50 $\mu\mathrm{m}$, the strips spacing becomes too small, leading to the hybridization of adjacent cavity modes and their delocalization [29]. At the higher end, p is limited by the requirement that only the zeroth diffraction order is propagative. The calculated γ_{m} datapoints (circles) fit very well to the constant line. This follows from the fact that once adjacent cavities become sufficiently separated, the field of their eigenmodes becomes identical to the field of an isolated cavity. Since γ_{m} is determined by field penetration into the metal, it cannot depend on p. On the other hand, γ_{rad} is seen to decrease rapidly with p, which might appear surprising because it implies that the power emitted by each cavity is affected by p. This, however, is a natural consequence of the fact that the cavities represent an array of mutually coherent emitters. In Appendix IV we give a short proof that $\gamma_{\mathrm{rad}} \sim p^{-1}$ approximately. This is confirmed in Fig. 2(b), with the $\sim p^{-1}$ fit (full line) matching the numerical data very well over the entire considered range of p. In this case, the dashed line representing $f_0/40$ shows that f_0 is virtually independent of p. Since γ_{m} remains invariant, there will be cases in which changing p alone will not be sufficient to reach critical coupling. For example, cavities with higher aspect ratios (t_{s}/w) will be highly overcoupled $\gamma_{\mathrm{m}} \ll \gamma_{\mathrm{rad}}$, so even at $p \approx \lambda_0$, γ_{rad} might still be substantially larger than γ_{m}. The reverse problem occurs with very small aspect ratios (highly undercoupled cavities), as in that case even for $p \approx w$, γ_{rad} might still be well below γ_{m}.

Now, consider a cavity with eigenfrequency ω_0 in which Eq. (1) is fulfilled for given t_{s} and p. If we decrease p, in order to retain critical coupling, we also have to decrease t_{s}. Since p does not affect it, γ_{m} is modified only because t_{s} was decreased, meaning that we end up with a cavity having both γ_{m} and γ_{rad} larger than in the initial cavity. Therefore, decreasing p increases the bandwidth $\Delta f = (\gamma_{\mathrm{m}} + \gamma_{\mathrm{rad}})/\pi$ of the device. A shorter p is also important as it allows smaller values for t_{s}, translating into lower operation voltage and higher speed. For these reasons, in what follows we set the pitch to $p = 1.25\,w$, (a value close to the onset of cavity mode hybridization) and adjust t_{s} until critical coupling is reached.

The above procedure may be repeated for an arbitrary frequency f_0. However, in order to find w and t_{s} that ensure critical coupling over the entire terahertz spectrum, it is more straightforward to employ geometrical scaling. Downscaling all geometrical parameters of a cavity array by a factor, upscales the TCMT parameters approximately by the same factor. However, small deviations from linear scaling due to material dispersion result in a cavity that does not meet the critical coupling condition exactly [35], meaning that t_{s} will have to be slightly adjusted to restore it. Figure 2(c) shows the values of w and t_{s} that yield critically coupled cavities, for resonant frequencies ranging from 0.3 THz up to 7 THz, beyond which GaAs cannot be used for this purpose, due to its optical phonons and onset of the reststrahlen band [29]. The plotted quantities are actually
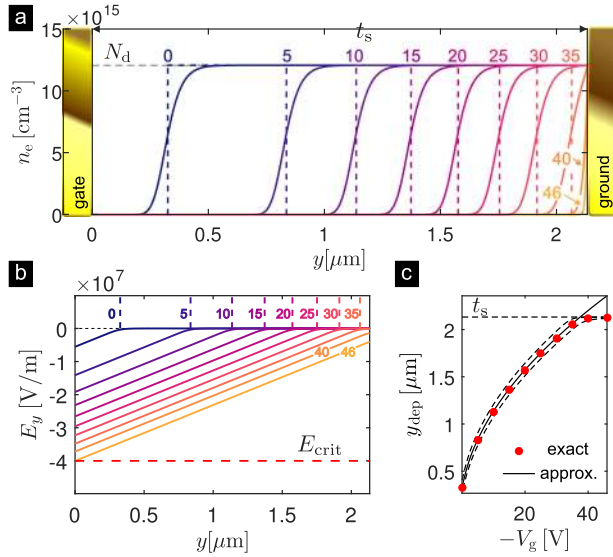
Fig. 3. Schottky junction under reverse bias showing the depletion layer reach-through effect. The profiles are drawn along the symmetry axis of a cavity with $p = 52.72\,\mu\text{m}$, $w = 42.18\,\mu\text{m}$, $t_\text{s} = 2.13\,\mu\text{m}$, $t_\text{m} = 0.3\,\mu\text{m}$ and $N_\text{d} = 1.2 \times 10^{16}\,\text{cm}^{-3}$, designed to operate at 1 THz. (a) Electron concentration (solid line - rigorous model, dashed - FDA) parametrized by $-V_\text{g}$, (b) Corresponding electric field profiles, (c) Depletion layer width with dashed lines indicating the transition width, defined as location where n_e reaches the $0.1\,N_\text{d}$ and $0.9\,N_\text{d}$ marks.

normalized to the free-space wavelength λ_0, demonstrating the mentioned deviation from the linear scaling law. For the same reason, the Q factor $Q = \omega_0/2(\gamma_\text{m} + \gamma_\text{rad}) = \omega_0/4\gamma_\text{rad}$ is seen to decrease slowly going towards higher frequencies.

III. DOPING CONCENTRATION AND PERFORMANCE ANALYSIS

A nonzero concentration $n_\text{e}(\mathbf{r})$ of free electrons in the cavity introduces a Drude term to the optical permittivity ε_opt of GaAs. The total permittivity becomes inhomogeneous and is given by [36], [37]

$$\varepsilon_\text{s}(\mathbf{r}, \omega) = \varepsilon_\text{opt}\left(1 - \frac{\omega_\text{p}^2(\mathbf{r})}{\omega(\omega + i\gamma_\text{c})}\right), \tag{3}$$

where the plasma frequency ω_p and intraband electron collision rate γ_c read

$$\omega_\text{p}(\mathbf{r}) = \sqrt{\frac{n_\text{e}(\mathbf{r})q^2}{\varepsilon_\text{opt}\varepsilon_0 m_c^*}}, \quad \gamma_\text{c} = \frac{q}{\mu_n m_c^*}, \tag{4}$$

while the realistic doping-dependent conduction band electron mobility μ_n is evaluated following [38]. At zero gate bias, $n_\text{e} \approx N_\text{d}$ in the entire cavity, except in a thin depletion layer beneath the gate. It is thus clear that the higher N_d is, the greater the voltage-induced change of permittivity will be, resulting in more effective modulation. The upper limit on N_d is set by the requirement that the cavity can be fully depleted before the avalanche breakdown of the Schottky junction.

To estimate the highest possible value of N_d, we consider the characteristic Schottky junction behavior under reverse bias illustrated in Fig. 3(a), where $n_\text{e}(\mathbf{r})$ is plotted along the vertical

axis going through the center of the cavity, with $-V_\text{g}$ as a parameter. The profiles drawn by solid lines are obtained using a rigorous solid-state physics framework based on a majority-carrier solution scheme (for details see Appendix B). For comparison, the step-like n_e profiles of the full depletion approximation (FDA) [39] are indicated by dashed lines. Apart from being abrupt, the FDA curves are a rather good match to the rigorous ones. This is demonstrated in Fig. 3(c) where the depletion layer width y_dep, defined as the distance from the junction at which n_e reaches $0.5\,N_\text{d}$, is drawn against $-V_\text{g}$ for both the rigorous (circular datapoints) and FDA model (solid line), the latter being given by

$$y_\text{dep} = \sqrt{\frac{2\varepsilon_\text{stat}\varepsilon_0(\psi_\text{bi} - V_\text{g})}{qN_\text{d}}}, \tag{5}$$

where $\psi_\text{bi} = 0.9\,\text{V}$ is the Schottky barrier height of the n-GaAs/Au interface, q the elementary charge and $\varepsilon_\text{stat} = 12.9$ the electrostatic dielectric permittivity of GaAs. With increasing reverse voltage, the depletion layer expands until it reaches the ground gold layer. In itself, the reach-through phenomenon is not associated with critical behavior [40], as a further increase of $-V_\text{g}$ merely causes a charge buildup on the gold side of the contact. To simplify the evaluation of the breakdown voltage, we employ the commonly-used critical field approximation [40], whereby the avalanche breakdown is assumed to occur once the electric field passes a critical value E_crit. The latter is dependent on the doping concentration, but for simplicity we take $E_\text{crit} = 4 \times 10^7\,\text{V/m}$ as a representative value [30] for the range of N_d considered in this work.

Neglecting the effect of strip edges, the only nonzero component of the static electric field is E_y and it reaches its highest value at the Schottky junction. According to FDA, $-E_\text{max} = qN_\text{d}y_\text{dep}/\varepsilon_\text{stat}\varepsilon_0$, from which we find the highest doping for $E_\text{max} = E_\text{crit}$ when $y_\text{dep} = t_\text{s}$

$$N_\text{d,max} = \frac{\varepsilon_\text{stat}\varepsilon_0 E_\text{crit}}{qt_\text{s}}. \tag{6}$$

This value, however, is arrived at neglecting the tail of the actual n_e profile. To see this, note that in the Fig. 3 example, FDA predicts $-V_\text{g} = 37.48\,\text{V}$ as the reach-through voltage, while the actual n_e profiles in Fig. 3 show that even at $-V_\text{g} = 40\,\text{V}$, there is still a non-negligible concentration of electrons in the cavity. To reduce the remanent n_e at the ground contact, the cavity should be biased slightly above the reach-through voltage and to achieve this without avalanche breakdown, a slightly lower doping concentration is used, $N_\text{d} = 0.9 \times N_\text{d,max}$. The cavity shown in Fig. 3 has $t_\text{s} = 2.13\,\mu\text{m}$, giving $N_\text{d,max} = 1.34 \times 10^{16}\,\text{cm}^{-3}$, so the actual value used is $N_\text{d} = 1.2 \times 10^{16}\,\text{cm}^{-3}$. The numerically calculated electric field profiles $E_y(y)$ are shown in Fig. 3(b). On this scale, the latter virtually overlap with the field profiles predicted by FDA. From these, we find that the breakdown occurs around $-V_\text{g} \approx 46\,\text{V}$.

As a proof of concept, in Fig. 4 we analyze the switching of a device designed to operate at 1 THz. The first four panels, (a)–(d), depict $n_\text{e}(\mathbf{r})$, the normalized terahertz field magnitude $|\mathbf{E}(\mathbf{r})|/E_0$ excited by an incoming linearly polarized plane wave
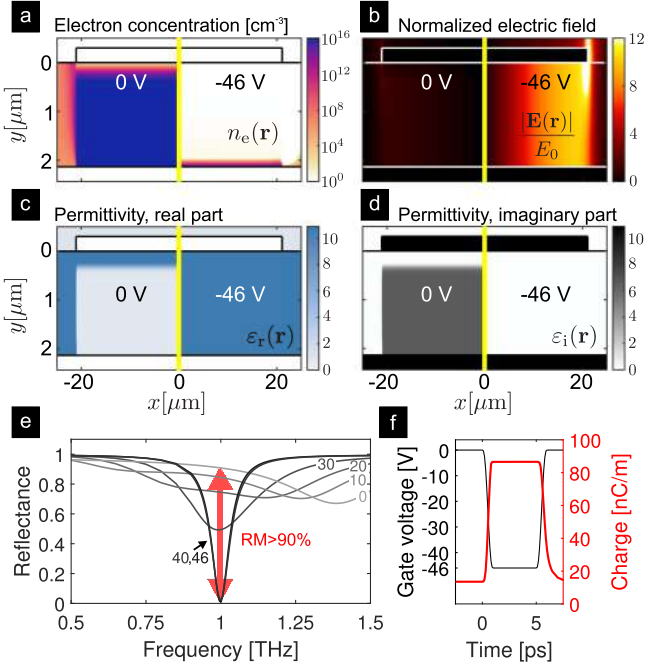
Fig. 4. Proof of concept simulation for the 1 THz device (for details, see Appendix IV and B). (a) Electron concentration, (b) High-frequency electric field distribution resulting from illumination at 1 THz, (c) Real and (d) imaginary part of permittivity at 1 THz. For better contrast, the range used in colormaps of panels (b)–(d) is saturated by cutting out the high electric field values at strip corners in (b), and gold permittivity values in (c) and (d). (e) Reflectance spectra parametrized by $-V_{\rm g}$, (f) Transient response of the total charge in cavity to a 5 ps reverse bias pulse. (All the colormaps used in this article have been produced by a source code kindly provided by Peter Kovesi, see [41].)

with field amplitude E_0 falling perpendicularly onto the strip array, as well as the real $\varepsilon_{\rm r}(\mathbf{r})$ and imaginary $\varepsilon_{\rm i}(\mathbf{r})$ parts of $\varepsilon_{\rm s}(\mathbf{r})$ given by Eq. (3). For conciseness in illustrating the switching effect of the gate voltage, we exploit the mirror symmetry of the problem. Noting that the calculated distributions exhibit this symmetry, in Figs. 4(a)–(d) we use the left half of the unit cell to plot the quantities calculated at $V_{\rm g} = 0\,\text{V}$ while those corresponding to $V_{\rm g} = -46\,\text{V}$ are shown in the right half.

The depleted cavity ($V_{\rm g} = -46\,\text{V}$) is seen to be virtually free of electrons, except at the bottom contact (note the logarithmic scale of the colormap). Consequently, $\varepsilon_{\rm s}$ is very close to $\varepsilon_{\rm opt}$ practically everywhere, thus justifying the assumptions made in designing the cavities in previous section. At the microscopic scale, the efficiency of the device is demonstrated by the huge difference in the electromagnetic field intensity evident from Fig. 4(b), where the field is seen to hardly penetrate the cavity at $V_{\rm g} = 0\,\text{V}$, while at $V_{\rm g} = -46\,\text{V}$ the field enhancement in the cavity is around 10.

Figure 4(e) shows the calculated reflectance spectra $R(\omega) = |r(\omega)|^2$ parametrized by $-V_{\rm g}$. At f_0 we have $R(\omega_0; 0\,\text{V}) \approx 90\%$ and $R(\omega_0; -46\,\text{V}) \approx 0\%$. Introducing the reflectance modulation (RM), and insertion loss (IL) as

$$\text{RM} = R(\omega_0; 0\,\text{V}) - R(\omega_0; V_{\rm g,min}),$$
$$\text{IL} = 1 - R(\omega_0; 0\,\text{V}), \tag{7}$$

with $V_{\rm g,min}$ denoting the avalanche breakdown voltage, we find RM and IL to be approximately 90% and 10%, respectively, which is excellent for solid-state terahertz modulators [5]. Since $R(\omega_0; V_{\rm g,min}) \approx 0\%$ by design, the proposed modulator will have a very high (theoretically infinite) extinction ratio which will in practice be limited by device fabrication tolerance. Previously considered Schottky junction based modulators [6], [7] used similar doping concentrations and, consequently, similar gate-induced permittivity changes. The origin of the increased modulation efficiency of the proposed device is the almost complete overlap of the resonant terahertz fields with the region in which $\varepsilon_{\rm s}$ is modified, which is known to be proportional to the change in resonant frequency and decay rates [42]. Finally, we note that the fact that the 40 V and 46 V reflectance curves almost overlap, indicates that the critical coupling effect is rather robust to the presence of the remanent electron concentration at the bottom electrode. It further implies that meeting the $\gamma_0 \approx \gamma_{\rm rad}$ condition reasonably well should not be particularly difficult in practice, especially considering that various post-processing steps might also help [34].

Switching times in the subnanosecond range are among the key advantages of solid-state terahertz modulators over those based on liquid crystals, phase change or thermal tuning [8] where the switching time is in the millisecond range at best [11]. In recently demonstrated semiconductor-based terahertz modulators [16], [21] with $\sim 10\,\text{MHz}$ operating frequencies, the speed has been found to be limited not by the inherent response time of the device but by the driving circuit. More recently, however, modulation above 1 GHz has been demonstrated [18]. Therefore, with driving circuits being perfected, the inherent switching time of terahertz modulators might become the limiting factor.

An important aspect of the proposed device is its very high intrinsic speed, as a consequence of the ultrathin active region. This is demonstrated by numerical simulations of the cavity charge $Q(t)$ (per unit length along the strip axis) transient upon applying a rectangular pulse of reverse bias shown in Fig. 4(f). The $-V_{\rm g}(t)$ pulse duration is set to 5 ps, with 0.5 ps 10%–90% rise and fall times. The corresponding rise time of $Q(t)$ is well below 1 ps, while the fall time is somewhat longer and calculated to be around 1 ps.

Such a short intrinsic response time originates from the very small distance $t_{\rm s}$ between the contacts, which is well below $\lambda_0/100$ as shown in Fig. 2(c). Here, as well as in [21], it is achieved by using a deeply-subwavelength cavity, while in [16], [18] the small distance between the electrodes is achieved at the expense of device complexity. Devices with laterally arranged contacts are likely to have a much longer intrinsic response time, increasing with the distance between the electrodes, as demonstrated in [43].

Having seen that the proposed device performs very well at $f_0 = 1\,\text{THz}$, we now examine how changing f_0 affects the modulator performance. The above procedure for determining the appropriate donor concentration in conjuction with cavity parameters shown in Fig. 2(c) can be repeated to obtain the $N_{\rm d}$ values shown in Fig. 5(a). The corresponding inverse gate voltages required for full depletion are shown in panel (b), while
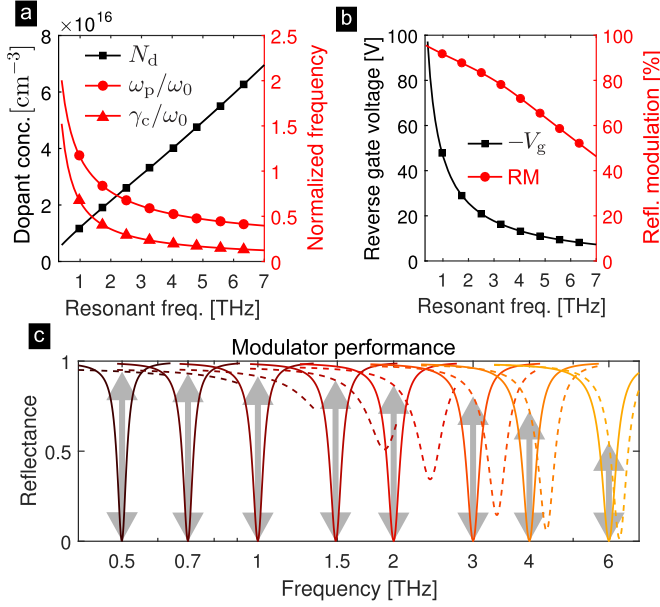
Fig. 5. Device parameters for operation across the terahertz spectrum, to be combined with geometrical parameters in Fig. 2(c). (a) Doping and normalized Drude parameters, (b) Gate voltage required for full cavity depletion and reflectance modulation. (c) Characteristic reflectance spectra for devices operating across the terahertz spectrum (solid line - biased, dashed line - no bias). The vertical gray arrows indicate the reflectance modulation.

the reflectance spectra for eight modulators with f_0 ranging over the terahertz spectrum are depicted in (c). In the latter, solid lines depict $R(\omega)$ in fully depleted state and the dashed lines the zero bias state. Note that the horizontal axis in Fig. 5(c) is shown in logarithmic scale, in order to better resolve all the depicted spectra. The thick vertical gray arrows indicate RM for each of the depicted modulators.

Extracting RM for spectra at various f_0, we obtain the curve in Fig. 5(b) showing the gradual decline of RM from more than 95% at 0.3 THz to around 46% at 7 THz. The reason for such behavior can be understood by noting that, because the electrostatic field at the junction must be less than $E_{\rm crit}$, the surface density σ of the total charge in the cavity remains invariant with respect to f_0 and equals $N_{\rm d} t_{\rm s}$. This implies that as $t_{\rm s}$ is decreased, $N_{\rm d}$ and $\omega_{\rm p}$ increase, but so that $\omega_{\rm p}$ scales (roughly) as $\sim f_0^{1/2}$. Meanwhile, the modulation efficiency is determined by the change of permittivity in the cavity which can be effected by bias, which is equal to the Drude term contribution and proportional to $\omega_{\rm p}/\omega_0$. The latter is drawn in Fig. 5(a) and, as expected, found to scale (roughly) as $\sim f_0^{-1/2}$.

Another feature arising at high f_0 is the change of the character of the cavity tuning. At 1 THz, the Drude contribution to $\varepsilon_{\rm s}$ has comparable real and imaginary parts, which is apparent in Fig. 4(c) and (d) and a consequence of the ratio $\gamma_{\rm c}/\omega_0$ being close to unity. Plotting this ratio in Fig. 5(a), we find that it also decreases at higher f_0, meaning that the voltage-induced change of permittivity becomes mainly real. The imaginary part of $\varepsilon_{\rm s}$ implies absorption in the semiconductor, introducing the semiconductor absorption term $\gamma_{\rm s}$ to the nonradiative decay rate. In terms of the reflectance spectra, this means that the cavity designed to be critically coupled at full depletion, is driven further

away from this condition at zero bias and has a significant amount of reflection at resonance (slightly shifted though). Such a behavior is nicely seen in the Fig. 4(e) plot. As f_0 approaches 7 THz, this changes significantly, as $\gamma_{\rm s}$ at zero bias remains rather small so the reflectance at cavity resonance remains close to zero, as seen in the $f_0 = 6$ THz modulator example in Fig. 5(c).

IV. SUMMARY

This article proposes a terahertz electro-optic modulator comprising an array of metal-semiconductor-metal cavities of deeply subwavelength thickness. The modulator operates by depleting the carriers from the doped semiconductor layer buried beneath a Schottky junction. Combining the extremely high terahertz field confinement with a reversely-biased Schottky junction in the reach-through regime, allows for a modulation performance that is predicted to match or even surpass existing devices. The proof of concept analysis presented for the modulator operating at 1 THz, based on a rigorous multiphysics framework incorporating Maxwell equations for terahertz waves and the drift-diffusion model describing carriers in the cavity, predicts an insertion loss around 10%, reflectance modulation of 90% and a theoretically infinite extinction ratio associated with cavities designed to work in the critically coupled regime. The performance is found to decrease in modulators designed to operate in the higher end of the terahertz spectrum, reaching insertion loss of 54% and reflectance modulation falling to 46% at 7 THz. This decline has been shown to be an inherent characteristic of the Drude response in which the plasma frequency scales as the square root of carrier concentration. In addition to forging strong light-matter interaction, the ultrathin cavity has been shown to allow for ultrafast intrinsic response times, which have been shown to be in the picosecond range.

APPENDIX A
LIGHT SCATTERING ANALYSIS

To obtain $r(\omega)$, the Maxwell equations are solved in frequency domain using the scattered field formulation with the background field $\mathbf{E}_{\rm b}(\mathbf{r})$ being the sum of the incoming and the plane wave reflected from the opaque back metal electrode (normal incidence is assumed), and the scattered field $\mathbf{E}_{\rm s}(\mathbf{r})$ being induced by the presence of the inhomogeneously doped semiconductor and the array of metal strips. The problem is represented by a two-dimensional model with a rectangular simulation domain, where the side boundaries are related with periodic conditions on $\mathbf{E}_{\rm s}(\mathbf{r})$, while the air superstrate above the structure is represented by a few-wavelength-thick domain terminated by a perfectly matched layer. The solution at both the top and bottom boundaries is set by the zero-field (Dirichlet) boundary condition. $r(\omega)$ is obtained from $\mathbf{E}_{\rm s}(\mathbf{r})$ as the complex coefficient of the zeroth diffraction order (the only propagating one in all considered cases).

The gold permittivity $\varepsilon_{\rm m}(\omega)$ was assumed to have the Drude form

$$\varepsilon_{\rm m}(\omega) = 1 - \frac{\omega_{\rm p,Au}^2}{\omega(\omega + i\gamma_{\rm c,Au})}, \qquad (8)$$

with the gold plasma $\omega_\mathrm{p} = 1.37 \times 10^{16}$ rad/s and collision frequency $\gamma_\mathrm{c,Au} = 4.05 \times 10^{13}$ rad/s taken from [44].

The reasoning in the article relies on the concept of a leaky eigenmode whose interaction with the environment is quantified by its radiative γ_rad and non-radiative γ_0 decay rates. These may be introduced in an intuitive manner by assuming that both the dissipative effects (absorption in metal and semiconductor) and the coupling between the eigenmode and environment are weak enough to be treated perturbatively. In that case, the eigenmode energy U exhibits an exponential temporal decay with a decay rate equal to $\gamma_\mathrm{rad} + \gamma_0$, whereby the total loss power $P_\mathrm{loss} = P_\mathrm{rad} + P_0$ is broken down into the radiation P_rad and absorption P_0 terms so that $\gamma_\mathrm{rad} = P_\mathrm{rad}/2U$ and $\gamma_0 = P_0/2U$. A deeper analysis employing TCMT [45] reveals a general connection between the decay rates of a weakly coupled resonant system and its scattering matrix [46] which, in case of a single-port system with one eigenmode, implies Eq. (2). For sufficiently high quality factors, the TCMT parameters are directly related to the complex eigenfrequency $\tilde{\omega} = \omega_0 + \mathrm{i}\omega_\mathrm{I}$ of the associated cavity quasi-normal mode [47], with $\omega_\mathrm{I} = \gamma_0 + \gamma_\mathrm{rad}$. As TCMT itself is not the focus of this work, the reader is referred to [35] and [11] for further details on the formalism in the current context.

To explain the dependence of γ_rad on p, let us assume that the cavity array eigenmode is excited and allowed to decay both radiatively and via absorption, and let $H(x) = H(x, y_0)$ denote the magnetic field phasor (only the z-component is nonzero) along a horizontal line $y = y_0$ chosen at an arbitrary height above the cavity array. Assuming the spacing between adjacent cavities is large enough, the total field $H(x)$ may be represented as a sum of fields emitted by individual cavities, $H(x) = \sum_{n=-\infty}^{\infty} H_\mathrm{uc}(x - np)$, where $H_\mathrm{uc}(x) = H_\mathrm{uc}(x, y_0)$ is the magnetic field profile of an eigenmode of a single cavity centered at $x = 0$. Since $H(x)$ is periodic in x, it can be expanded into a Fourier series $H(x) = \sum_{m=-\infty}^{\infty} H^{(m)} \exp(\mathrm{i}m\Delta k)$ where $\Delta k = 2\pi/p$ and m is the diffraction order. The dependence of $H^{(m)}$ on p is seen after introducing the Fourier transform of the single-cavity field by $h_\mathrm{uc}(k) = \int_{-\infty}^{\infty} H_\mathrm{uc}(x) \exp(-\mathrm{i}kx)\mathrm{d}x$ and noting that $H^{(m)} = h_\mathrm{uc}(m\Delta k)/p$, while $h_\mathrm{uc}(m\Delta k)$ is obviously independent on p. In the considered spectral range, only the zeroth diffraction order is propagative so the radiated power flux through a unit cell equals $P_\mathrm{uc,rad} = z_0 p |H^{(0)}|^2/2 = z_0 |h_\mathrm{uc}(0)|^2/2p$, with z_0 denoting the free-space impedance. Finally, denoting by U_uc the energy contained in one cavity, and by N the total number of cavities in the array (formally $N \to \infty$) we have

$$\gamma_\mathrm{rad} = \frac{P_\mathrm{rad}}{2U} = \frac{N P_\mathrm{uc,rad}}{2N U_\mathrm{uc}} = \frac{z_0 |h_\mathrm{uc}(0)|^2}{4 U_\mathrm{uc}} p^{-1}, \qquad (9)$$

thus proving the $\sim p^{-1}$ scaling stated in the article.

APPENDIX B
SOLID-STATE ANALYSIS

The gate bias effect on the carrier distribution is described using a rigorous solid-state physics framework based on a majority-carrier solution scheme, consisting in the conservation

TABLE I
SOLID-STATE PHYSICS PARAMETERS FOR GaAs [51]

Parameter	GaAs
Static permittivity, $\varepsilon_\mathrm{stat}$	12.90
High-frequency permittivity, ε_opt	10.89
Effective electron mass, m_c^*/m_0	0.067
Energy band gap, E_g (eV)	1.424
Electron affinity, χ_0 (eV)	4.07
Conduction band density of states, N_c (cm^{-3})	4.7×10^{17}
Valence band density of states, N_v (cm^{-3})	9.0×10^{18}

law for charge (Poisson equation) and the time-dependent current continuity equations [48], [49]. The current density is expressed by the drift-diffusion expressions, while the simplified Maxwell-Boltzmann energy distribution is used for the carrier concentration, allowed by the moderate doping level of the n-GaAs cavity. The Schottky contact is described as a source/sink for carriers, treated as a surface recombination mechanism [50]. The Schottky barrier height of the n-GaAs/Au interface is considered 0.9 V, while the effective Richardson's constant for the n-doped GaAs is set equal to 4.4 Acm^{-2}K^{-2} [39]. The lateral intrinsic GaAs sections are interfaced to the central n-GaAs (under the strips) using quasi-Fermi level continuity boundary conditions. The resulting system of partial differential equations is set to additionally satisfy insulating conditions at the external metamaterial unit-cell boundaries and the thermodynamic equilibrium at the back contact, considered ideal ohmic. It is highlighted that, even though both contacts can be indiscriminately represented as Au layers from an electromagnetic standpoint, suitable Au-based alloys should be used in practice to ensure ohmic conditions at the back contact [32], having, though, marginal effect on the electromagnetic analysis.

The GaAs semiconductor parameters are listed in Table I, while the carrier mobility is calculated using [38]. The Au workfunction is set equal to 5.1 eV.

REFERENCES

[1] M. Tonouchi, "Cutting-edge terahertz technology," *Nature Photon.*, vol. 1, pp. 97–105, 2007.

[2] D. M. Mittleman, "Perspective: Terahertz science and technology," *J. Appl. Phys.*, vol. 122, no. 23, 2017, Art. no. 230901.

[3] R. Kersting, G. Strasser, and K. Unterrainer, "Terahertz phase modulator," *Electron. Lett.*, vol. 36, no. 13, pp. 1156–1158, Jun. 2000.

[4] T. Kleine-Ostmann, P. Dawson, K. Pierz, G. Hein, and M. Koch, "Room-temperature operation of an electrically driven terahertz modulator," *Appl. Phys. Lett.*, vol. 84, no. 18, pp. 3555–3557, 2004.

[5] R. Degl'Innocenti, S. J. Kindness, H. E. Beere, and D. A. Ritchie, "All-integrated terahertz modulators," *Nanophotonics*, vol. 7, pp. 127–144, 2018.

[6] H.-T. Chen *et al.*, "Active terahertz metamaterial devices," *Nature*, vol. 444, pp. 597–600, 2006.

[7] H.-T. Chen *et al.*, "A metamaterial solid-state terahertz phase modulator," *Nature Photon.*, vol. 3, pp. 148–151, 2009.

[8] M. Rahm, J.-S. Li, and W. J. Padilla, "THz wave modulators: A brief review on different modulation techniques," *J. Infrared Millimeter Terahertz Waves*, vol. 34, no. 1, pp. 1–27, 2013.

[9] J. Yoon *et al.*, "GaAs photovoltaics and optoelectronics using releasable multilayer epitaxial assemblies," *Nature*, vol. 465, pp. 329–334, 2010.

[10] D. Shrekenhamer, W.-C. Chen, and W. J. Padilla, "Liquid crystal tunable metamaterial absorber," *Phys. Rev. Lett.*, vol. 110, Apr. 2013, Art. no. 177403.

[11] G. Isić, B. Vasić, D. C. Zografopoulos, R. Beccherelli, and R. Gajić, "Electrically tunable critically coupled terahertz metamaterial absorber based on nematic liquid crystals," *Phys. Rev. Appl.*, vol. 3, Jun. 2015, Art. no. 064007.

[12] B. Vasić, D. C. Zografopoulos, G. Isić, R. Beccherelli, and R. Gajić, "Electrically tunable terahertz polarization converter based on overcoupled metal-isolator-metal metamaterials infiltrated with liquid crystals," *Nanotechnology*, vol. 28, no. 12, 2017, Art. no. 124002.

[13] B. Sensale-Rodriguez *et al.*, "Extraordinary control of terahertz beam reflectance in graphene electro-absorption modulators," *Nano Lett.*, vol. 12, no. 9, pp. 4518–4522, 2012.

[14] W. Gao *et al.*, "High-contrast terahertz wave modulation by gated graphene enhanced by extraordinary transmission through ring apertures," *Nano Lett.*, vol. 14, no. 3, pp. 1242–1248, 2014.

[15] S.-F. Shi *et al.*, "Optimizing broadband terahertz modulation with hybrid graphene/metasurface structures," *Nano Lett.*, vol. 15, no. 1, pp. 372–377, 2015.

[16] D. Shrekenhamer *et al.*, "High speed terahertz modulation from metamaterials with embedded high electron mobility transistors," *Opt. Express*, vol. 19, no. 10, pp. 9968–9975, May 2011.

[17] N. Karl *et al.*, "An electrically driven terahertz metamaterial diffractive modulator with more than 20 dB of dynamic range," *Appl. Phys. Lett.*, vol. 104, no. 9, 2014, Art. no. 091115.

[18] Y. Zhang *et al.*, "Gbps terahertz external modulator based on a composite metamaterial with a double-channel heterostructure," *Nano Lett.*, vol. 15, no. 5, pp. 3501–3506, 2015.

[19] M. T. Nouman *et al.*, "Terahertz modulator based on metamaterials integrated with metal-semiconductor-metal varactors," *Sci. Rep.*, vol. 6, 2016, Art. no. 26452.

[20] Z. Zhou, S. Wang, Y. Yu, Y. Chen, and L. Feng, "High performance metamaterials-high electron mobility transistors integrated terahertz modulator," *Opt. Express*, vol. 25, no. 15, pp. 17832–17840, Jul. 2017.

[21] J. Lee *et al.*, "Ultrafast electrically tunable polaritonic metasurfaces," *Adv. Opt. Mater.*, vol. 2, no. 11, pp. 1057–1063, 2014.

[22] Y. Todorov *et al.*, "Strong light-matter coupling in subwavelength metal-dielectric microcavities at terahertz frequencies," *Phys. Rev. Lett.*, vol. 102, May 2009, Art. no. 186402.

[23] A. A. Anappara, A. Tredicucci, G. Biasiol, and L. Sorba, "Electrical control of polariton coupling in intersubband microcavities," *Appl. Phys. Lett.*, vol. 87, no. 5, 2005, Art. no. 051105.

[24] A. Benz *et al.*, "Resonant metamaterial detectors based on THz quantum-cascade structures," *Sci. Rep.*, vol. 4, 2014, Art. no. 4269.

[25] D. Palaferri *et al.*, "Patch antenna terahertz photodetectors," *Appl. Phys. Lett.*, vol. 106, no. 16, 2015, Art. no. 161102.

[26] D. Palaferri *et al.*, "Ultra-subwavelength resonators for high temperature high performance quantum detectors," *New J. Phys.*, vol. 18, no. 11, 2016, Art. no. 113016.

[27] L. Xu *et al.*, "Terahertz metasurface quantum-cascade VECSELs: Theory and performance," *IEEE J. Sel. Topics Quantum Electron.*, vol. 23, no. 6, pp. 1–12, Nov. 2017.

[28] L. Xu *et al.*, "Metasurface quantum-cascade laser with electrically switchable polarization," *Optica*, vol. 4, no. 4, pp. 468–475, Apr. 2017.

[29] Y. Todorov *et al.*, "Optical properties of metal-dielectric-metal microcavities in the THz frequency range," *Opt. Express*, vol. 18, no. 13, pp. 13886–13907, Jun. 2010.

[30] B. J. Baliga, R. Ehle, J. R. Shealy, and W. Garwacki, "Breakdown characteristics of gallium arsenide," *IEEE Electron Device Lett.*, vol. EDL-2, no. 11, pp. 302–304, Nov. 1981.

[31] M. Hudait and S. Krupanidhi, "Breakdown characteristics of MOVPE grown Si-doped GaAs Schottky diodes," *Solid-State Electron.*, vol. 43, no. 12, pp. 2135–2139, 1999.

[32] A. Baca, F. Ren, J. Zolper, R. Briggs, and S. Pearton, "A survey of ohmic contacts to III-V compound semiconductors," *Thin Solid Films*, vol. 308/309, pp. 599–606, 1997.

[33] S. Fan, W. Suh, and J. D. Joannopoulos, "Temporal coupled-mode theory for the Fano resonance in optical resonators," *J. Opt. Soc. Amer. A*, vol. 20, no. 3, pp. 569–572, Mar. 2003.

[34] J.-M. Manceau, S. Zanotto, I. Sagnes, G. Beaudoin, and R. Colombelli, "Optical critical coupling into highly confining metal-insulator-metal resonators," *Appl. Phys. Lett.*, vol. 103, no. 9, 2013, Art. no. 091110.

[35] G. Isić, and R. Gajić, "Geometrical scaling and modal decay rates in periodic arrays of deeply subwavelength terahertz resonators," *J. Appl. Phys.*, vol. 116, no. 23, 2014, Art. no. 233103.

[36] R. Ulbricht, E. Hendry, J. Shan, T. F. Heinz, and M. Bonn, "Carrier dynamics in semiconductors studied with time-resolved terahertz spectroscopy," *Rev. Mod. Phys.*, vol. 83, pp. 543–586, Jun. 2011.

[37] D. Lockwood, G. Yu, and N. Rowell, "Optical phonon frequencies and damping in AlAs, GaP, GaAs, InP, InAs and InSb studied by oblique incidence infrared spectroscopy," *Solid State Commun.*, vol. 136, no. 7, pp. 404–409, 2005.

[38] M. Sotoodeh, A. H. Khalid, and A. A. Rezazadeh, "Empirical low-field mobility model for III-V compounds applicable in device simulation codes," *J. Appl. Phys.*, vol. 87, no. 6, pp. 2890–2900, 2000.

[39] S. Sze and K. N. Kwok, *Physics of Semiconductor Devices*. Hoboken, NJ, USA: Wiley, 2007.

[40] C. Bulucea, "Breakdown voltage of diffused epitaxial junctions," *Solid State Electron.*, vol. 34, no. 12, pp. 1313–1318, 1991.

[41] P. Kovesi, "Good colour maps: How to design them," 2015, arXiv/1509.03700.

[42] G. Isić, R. Gajić, and S. Vuković, "Plasmonic lifetimes and propagation lengths in metallodielectric superlattices," *Phys. Rev. B*, vol. 89, Apr. 2014, Art. no. 165427.

[43] H.-T. Chen *et al.*, "Hybrid metamaterials enable fast electrical modulation of freely propagating terahertz waves," *Appl. Phys. Lett.*, vol. 93, no. 9, 2008, Art. no. 091117.

[44] M. A. Ordal, R. J. Bell, R. W. Alexander, L. L. Long, and M. R. Querry, "Optical properties of fourteen metals in the infrared and far infrared: Al, Co, Cu, Au, Fe, Pb, Mo, Ni, Pd, Pt, Ag, Ti, V, and W," *Appl. Opt.*, vol. 24, no. 24, pp. 4493–4499, Dec. 1985.

[45] H. A. Haus and W. Huang, "Coupled-mode theory," *Proc. IEEE*, vol. 79, no. 10, pp. 1505–1518, Oct. 1991.

[46] W. Suh, Z. Wang, and S. Fan, "Temporal coupled-mode theory and the presence of non-orthogonal modes in lossless multimode cavities," *IEEE J. Quantum Electron.*, vol. 40, no. 10, pp. 1511–1518, Oct. 2004.

[47] P. Lalanne, W. Yan, K. Vynck, C. Sauvan, and J.-P. Hugonin, "Light interaction with photonic and plasmonic resonances," *Laser Photon. Rev.*, vol. 12, no. 5, 2018, Art. no. 1700113.

[48] G. Sinatkas, A. Pitilakis, D. C. Zografopoulos, R. Beccherelli, and E. E. Kriezis, "Transparent conducting oxide electro-optic modulators on silicon platforms: A comprehensive study based on the drift-diffusion semiconductor model," *J. Appl. Phys.*, vol. 121, no. 2, 2017, Art. no. 023109.

[49] G. Sinatkas and E. E. Kriezis, "Silicon-photonic electro-optic phase modulators integrating transparent conducting oxides," *IEEE J. Quantum. Electron.*, vol. 54, no. 4, pp. 1–8, Aug. 2018.

[50] C. Crowell and S. Sze, "Current transport in metal-semiconductor barriers," *Solid State Electron.*, vol. 9, no. 11, pp. 1035–1048, 1966.

[51] V. Agranovich and Y. Gartstein, "Gallium arsenide (GaAs)," in *Handbook Series on Semiconductor Parameters*, vol. 1, M. Levinshtein, S. Rumyantsev, and M. Shur, Eds. Singapore: World Scientific, 2000.

Authors' photographs and biographies not available at the time of publication.

RESEARCH ARTICLE

Influence of laser-induced heating on MnO nanoparticles

B. Hadžić[1] | B. Vasić[1] | B. Matović[2] | I. Kuryliszyn-Kudelska[3] | W. Dobrowolski[3] |
M. Romčević[1] | N. Romčević[1]

[1]Institute of Physics, University of
Belgrade, Pregrevica 118, Belgrade 11 080,
Serbia

[2]Vinča Institute of Nuclear Sciences,
University of Belgrade, P.O. Box 522,
Belgrade 11000, Serbia

[3]Institute of Physics, Polish Academy of
Science, al. Lotnikow 32/46, Warsaw
02-668, Poland

Correspondence
B. Hadžić, Institute of Physics, University
of Belgrade, Pregrevica 118, Belgrade 11
080, Serbia.
Email: branka@ipb.ac.rs

Funding information
Serbian Ministry of Education, Science
and Technological Development, Grant/
Award Number: 45003

Abstract

The phase changes of MnO nanoparticles under laser-induced heating have
been studied. Previous confirmation of the existence of MnO phase was based
on the X-ray diffraction measurements. Here, we report the experimental spec-
tra of nonresonant Raman scattering in the range between 100 and 1,600 cm^{-1},
for a sample irradiated with 8 different laser powers. The laser-induced heating
has produced change in existing phases in sample, destruction of MnO phase,
and creation of MnO_2, Mn_3O_4, and $MnOOH$ phases along with formation of
Mn^{2+} on the sample surface. These phase changes have been confirmed by
X-ray diffraction and atomic force microscopy measurements.

KEYWORDS
heating, irradiation, nanostructures, properties, spectroscopy

1 | INTRODUCTION

Manganese oxide (MnO) belongs to an important group
of materials, transition metal oxides, with many interest-
ing chemical and physical properties and numerous
applications. Transition metal oxides have, in majority,
a cubic rock-salt structure, merely ZnO and CoO possess
a stable hexagonal structure, as well as majority of
transition metal oxides MnO have cubic rock-salt crystal
structure, with energy gap between 2.43 and 3.6 eV
depending from calculation type. Due to its unique
properties and large possibility of applications as
catalysts, lithium-ion battery materials, energy storage,
ion exchange, and magnetic resonance imaging,
MnO has attracted significant attention. Nowadays,
MnO is widely used as electrode materials, rechargeable
batteries, electrochemical capacitors, catalysts, sensors,
and magnetoelectronic devices, and it also has triggered
optoelectronic application.[1–5]

In the investigation of MnO, its related compounds,
and different oxides of manganese such as MnO_2,

Mn_2O_4, and Mn_3O_4 exist two basic trends. In the first
one, laser power density has been kept as low as possible
to avoid changes in samples,[6–12] or in the second one,
the influence of laser-induced heating (with constant laser
power and elongated time exposure) has been investi-
gated on samples characteristics in MnO_2, Mn_3O_4, and
Mn_5O_8,[8,11,13–17] whereas in the paper of Buciuman
et al.,[16] three different laser lines are used.

Among the different experimental techniques, vibra-
tional spectroscopy such as Raman spectroscopy has
attracted significant attention. It provides unique struc-
tural information at atomic scale such as sample quality,
to study local atomic arraignment, chemical composition,
dopant incorporation, and molecular structure. As rapid,
sensitive, and nondestructive tool, with minimal or no
sample preparation, Raman spectroscopy can solve the
problem of phase identification. Sensitivity of the relative
intensities and wavenumbers of the Raman bands to the
crystal symmetry, coordination geometry, and oxidation
states allows distinction of different kinds of metal oxides
whose atomic arrangements are closely related to one

another. Raman spectroscopy has been a method of choice for analysis of manganese oxide and its related compounds because it can distinguish between different metal oxide compounds having the same elementary analysis.[4,8,16,18]

In our previous paper, we have investigated influence of locally induced heating with increasing laser power densities on stable hexagonal transition oxides, ZnO doped with CoO.[19] The aim of this work is to continue our research with investigation influence of locally induced heating with increasing laser power densities on cubic rock-salt MnO using complementary techniques such as X-ray diffraction (XRD) and Raman spectroscopy along with atomic force microscopy (AFM).

2 | EXPERIMENTAL

Polycrystalline MnO sample powder was of >99.9% purity of analytical grade, purchased from Sigma-Aldrich Co., and for more convenient use was pressed into a pellet.

The sample was characterized first by XRD, with the Rigaku Ultima IV Multipurpose XRD system. The system was operated at 40 kV and 40 mA to produce nickel-filtered CuKa1 X-ray with l = 0.1540 nm. To discriminate phase content in sample, the 2θ scan was performed in the range between 20° and 70° at the scanning rate of 5°/min. The phase analysis was performed using the PDXL2 software, version 2.0.3.0,[20] with reference to the patterns of the International Centre for Diffraction Database, version 2012.[21] Second, samples has been investigated by AFM. AFM measurements were done using NT-MDT system NTEGRA Prima at ambient conditions. AFM images were recorded in tapping mode using NSG01 probes from NT-MDT.

In situ investigation of laser-induced heating influence on sample characteristics was performed by micro-Raman spectroscopy, which was taken in the backscattering configuration, analyzed by Jobin-Yvon T6400 spectrometer equipped with nitrogen-cooled charge couple device detector. Verdi G optically pumped semiconductor laser operating on 532 nm laser line was used as excitation source. The spectra were taken using eight different laser powers whose intensity in front of the microscope was from 3 to 24 mW with 3 mW step.

After Raman measurements, sample was investigate once more with XRD and AFM for better understanding of the changes produced by laser-induced heating effects.

3 | RESULTS AND DISCUSSION

MnO sample pressed into a pellet was investigated with Raman spectroscopy and analyzed assuming that all phonon lines are of Lorentzian type.[22] In Figure 1, the obtained and fitted characteristic of Raman spectra in eight different laser powers with induced laser local heating effects are presented.

Due to the facile phase transformation of MnO during preparation, several oxides can be formed and coexist, or can progressively change one into the other, especially under influence of laser-induced local heating effect. That is why Raman spectroscopy was a method of choice for observing this transformation in our sample. Its sensitivity for crystals as well as amorphous components along with those for short-range order gives a more complete and reliable description of this kind of materials. With all this in mind, we will start the analysis of spectra shown in Figure 1 with few remarks about structure and vibrational properties of MnO. Vibrational properties of bulk material are crucial for understanding vibrational properties of small particles. At room temperature, MnO has face-centered cubic structure (space group *Fm3m*, lattice parameter a_o ~ 4.43 Å).[23,24] In MnO-related publications, there have been reported up to five Raman peaks with large variation in peak position, such as Buciuman et al. reported peaks at 595 cm^{-1} whereas other two peaks have few possible positions 544 (or 537 or 521) cm^{-1} and 648 (or 645) cm^{-1},[16] Julien et al. reported peaks at 523, 574, and 647 cm^{-1},[12] whereas in their other publication, they have reported peaks at 250, 531, 591, and 654 cm^{-1},[25] and Mironova-Ulmane et al. reported two broad asymmetric bands at about 530 and 1050 cm^{-1}.[4] Pandey et al. for MnO colloidal nanoparticles suspended in double distilled water at room temperature reported peaks at 358, 405, 525, 559, and 660 cm^{-1}.[2]

In Raman spectra for lowest laser power on the sample surface of 3 mW MnO phase are represented with peaks at approximately 250, 535, 591 and 659 cm^{-1}, which are in good agreement with MnO peaks reported
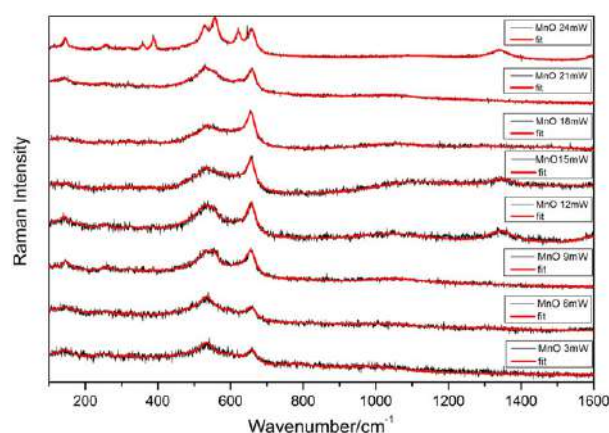

FIGURE 1 Fitted Raman spectra of MnO heated with increasing laser power [Colour figure can be viewed at wileyonlinelibrary.com]

by Julien et al.[25] Besides, these peaks whose presence were predicted by XRD in Raman spectra are also notable peaks at 323, 448, and 490 cm^{-1} that, according to papers,[25–27] belongs to βMnO$_2$ phase, as well as peak at 146 cm^{-1} that belongs to αMnOOH, peak at 386 cm^{-1} that belongs to αMnO$_2$ phase, and peak at 620 cm^{-1} that belongs to γMnOOH phase according to papers,[8,28] respectively. With increase of laser power to 6 mW, intensity of all peaks grow. With further increase in laser power on 9 mW, spectra of MnO appear two additional peaks. Peak at 556 cm^{-1} belongs to MnOOH phase. Here, we have first of many situation in which it is difficult to precisely determine the exact origin of the peak. Mn oxides have many phases and reported peaks that represent these phases that are close to each other in Raman shift. In this case, γMnOOH has reported peak at 558 cm^{-1},[8] whereas Cheng et al.[28] have reported αMnOOH peak at 549 cm^{-1} as well as at 552 cm^{-1}. Peak at 651 cm^{-1} by Julien et al.[10] and papers cited there belongs to MnO$_2$ phase. Intensity of all previously reported peaks continued their increase. In Raman spectra of continuously increased laser power to 12 mW on sample surface appears one new peak at 178 cm^{-1}, by Cheng et al.,[28] that belongs to αMnO$_2$ phase, whereas intensity of all other peaks keep increasing. With further increase of laser power on sample surface at 15 mW in Raman spectra appears one new peak at 117 cm^{-1} that according to paper[28] belongs to αMnOOH phase. Intensity of all peaks keep increasing except peak at approximately 530 cm^{-1} whose intensity abruptly decreases. This decrease will be discussed later. Further continuous increase of laser power to 18 mW proceeds increase in peak intensity of all peaks, whereas intensity of peak at approximately 530 cm^{-1} increases as well comparing with its value at 15 mW of laser power but it is lower comparing with its value at 12 mW. Similar situation is for 21 mW of laser power, intensity of all peaks increases, whereas peak at 530 cm^{-1} has abrupt increase of peak intensity with value higher than it was at 12 mW. Finally, reaching 24 mW of laser power on sample surface situation becomes more complex. In this spectra, we have notice peaks at 117, 144, 174, 218, 257, 318, 359, 388, 434, 467, 495, 528, 556, 587, 621, 649, and 659 cm^{-1}. According to Cheng et al.,[28] peaks at 117 and 144 cm^{-1} belongs to αMnOOH phase, and peaks at 359, 388, 528, 556, and 621 cm^{-1} belong to γMnOOH phase, whereas peak at 174 cm^{-1} belongs to αMnO$_2$ phase. Gao et al. have reported αMnO$_2$ phase peak at 467 cm^{-1} as well as βMnO$_2$ phase peaks at 495, 587, 649, and 659 cm^{-1}.[8] According to Julien et al., peaks at 218 and 257 cm^{-1} belong to MnOOH phase, whereas for peak at 318 cm^{-1} can belong to βMnO$_2$ or αMn$_2$O$_3$ phase.[25] In our case, we think that it is more

likely that peak at 318 cm^{-1} belongs to βMnO$_2$ phase. Julien et al. in their other paper confirm that peak at 495 cm^{-1} belongs to βMnO$_2$ phase[26] or in case of peak at 649 cm^{-1} belongs to MnO$_2$ phase.[10] According to Lutz et al.[29] and Bernard et al.,[30] peak at 434 cm^{-1} can belong to Mn(OH)$_2$ phase. Generally speaking, there has been a big lack in reported peaks of MnO and its related compounds in region from 400 to 480 cm^{-1}, what makes analysis of this region more complicated. What make analysis of obtained results more interesting is that Gao et al.[31] reported peaks at 173, 263, 535, and 622 cm^{-1} that belong to amorphous Mn$_5$O$_8$ phase, which are in good agreement with our obtained peaks. Their Mn$_5$O$_8$ powder is obtained by thermal annealing of Mn$_3$O$_4$ in the air and contained a mix of crystalline Mn$_5$O$_8$ and Mn$_3$O$_4$. Have Mn$_3$O$_4$ phase been formed in our sample under induced laser local heating is hard to tell. Peaks at 318 and 659 cm^{-1} according to Kim et al.[15] might belong to Mn$_3$O$_4$ phase, but Gao et al.[8] have reported that heating γMnOOH in air at temperature higher than 200 °C results in its transformation to βMnO$_2$ phase, whereas at about 500 °C goes to αMn$_2$O$_3$ phase, and finally, at about 1000 °C reaches Mn$_3$O$_4$ phase. It is hard to believe that by locally induced laser heating we could reach 1000 °C. All registered peaks have their maximal intensity on this, biggest used, laser power.

As it was clearly visible from our analysis till now, MnO as well as many of its related compounds has peaks approximately at 530 cm^{-1} such as MnO, Mn$_5$O$_8$, βMnO$_2$, γMnOOH, and MnO$_2$. According to Buciuman et al.[16] the peak at 530 cm^{-1} has been attributed even to isolated Mn^{2+}. Peak at 530 cm^{-1} is the most intense peak in spectra on lower laser powers. After abrupt decrease at 15 mW and slow increase at 18 mW, at higher laser powers such as 21 mW and the highest 24 mW become once again the most intense peak in spectra. We assume that on crucial laser power of 15 mW occurs breaking MnO bonds, formation of Mn^{2+} and O^{2-} in major part of the MnO particles, and migration of Mn^{2+} and O^{2-} on sample surface where oxygen evaporate, resulting in decrease of 530 cm^{-1} peak intensity. With further increase of laser power interaction of Mn^{2+} with atoms in the air takes place and forming and formatting new phases, such as Mn$_5$O$_8$, βMnO$_2$, γMnOOH, which result in increase of 530 cm^{-1} peak intensity. This process in sample, although less intense, continues to be played out on the higher laser powers as well.

In this research as well as in others is evident transformation of manganese oxide under laser-induced heating in the samples and formation of new phases. That is why we can say that these results are in good agreement with laser heating structural changes reported for MnO$_2$ with fixed laser power and increased laser power by Widjaja et al.[13] and Froment et al.,[32] or with increasing laser power by
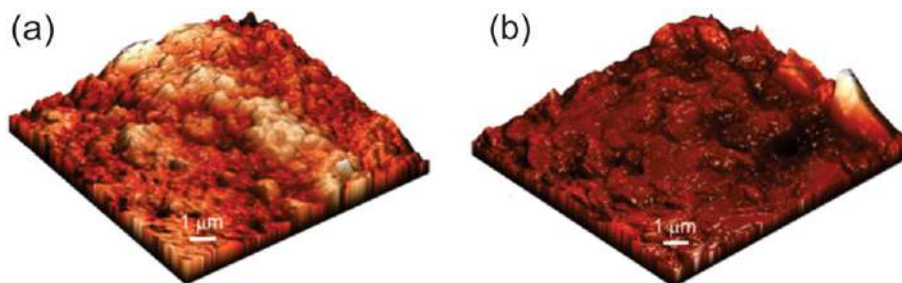
FIGURE 2 Three-dimensional atomic force microscopy topography of the sample irradiation: (a) before and (b) after irradiation [Colour figure can be viewed at wileyonlinelibrary.com]

Caggiani et al.[33] and other manganese oxide-related compounds in other papers already cited here.

Topography of the sample was investigated by AFM measurements. This investigation was performed two times, before and after laser irradiation to examine changes in sample topography. Three-dimensional topography results, before and after irradiation, for better understanding, are shown in Figure 2, whereas two-dimensional AFM results before (a) and after (b) irradiation are available in Figure S1. Before the irradiation, the sample has grain structure with grain size below 1 μm (Figure 2a). On the other hand, after the irradiation, as it is clearly visible in Figure 2b, this grain structure disappears. Aggregates of adjacent grains are then transformed to either larger bump or rather flat surface. This result is in good agreement with obtained Raman spectra for 24 mW laser power.

To confirm changes in sample structure and phase composition produced by laser irradiation, sample was firstly and finally investigated by XRD spectroscopy. The obtained results are shown in Figure 3. For easier comparison in Figure 3, blue line shows XRD results before laser irradiation, whereas with red and black lines represent XRD results after laser irradiation in two different points on sample surface. Before irradiation, this analysis reveals only presence of MnO phase. The mean crystalline size D, the microstrain ε, and lattice parameter a_o in sample were determined, by use of Scherrer's formula and Williamson-Hall method,[34,35] to be 44.42 nm for D, 0.002303 for ε, and 0.44389 nm for a_o. In this way, we confirm that process of pressing in pellet has not influence on sample structure and phase composition. The mean crystalline size after laser irradiation was between 18.7 and 25.6 nm. XRD spectra peak list after laser irradiation contains 10 peaks, which reveals presence of MnO, MnO_2, and Mn_3O_4 phases and α-phase of elemental Mn. Obtained XRD results confirm that laser irradiation produced permanent change in sample structure and are in good agreement with Raman spectroscopy results. Existence of Mn_5O_8 phase by XRD cannot be confirmed due to amorphous nature of this phase. Presence of MnO phase in XRD spectra indicates two things. First that
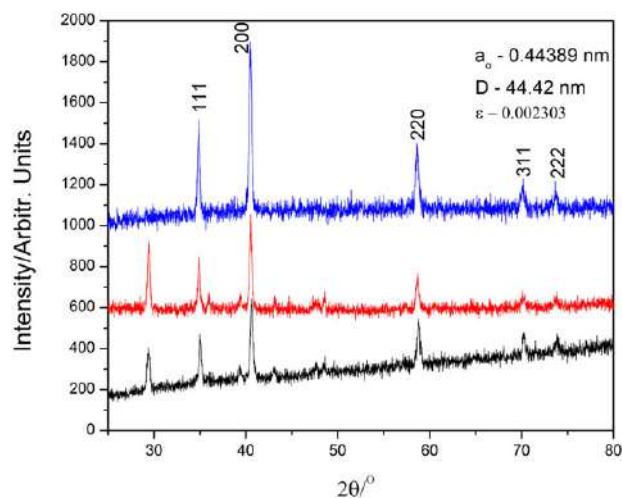
FIGURE 3 X-ray diffraction spectra of MnO sample before and after laser irradiation [Colour figure can be viewed at wileyonlinelibrary.com]

changes in sample structure are local in the area affected by laser spot as well as conductivity of sample and second that it is difficult to find and make measurements on the exact same place on the sample surface when you change the instrument and experiment. From existence of α-phase elemental Mn after laser irradiation, we can conclude that laser-induced local heating on sample surface has not raised temperature on sample surface over 1000 K.[36]

4 | CONCLUSION

Influence of laser power-induced heating effects on sample characteristics and changing in existing phases has been investigated. The use of XRD, AFM, and in situ non-resonant Raman spectroscopy allowed us to follow all processes in sample step by step. We have shown that intensity of registered peaks increases with increase of laser power and that change in phase compositions is continuous. Crucial laser power in phase transformation is 15 mW, in which major part of MnO bonds is destroyed and followed by strong recombination and formation of

new phases. That is confirmed with existence of Mn^{2+} phase in sample after the treatment. Besides, this phase in sample has been formed phases of MnO_2, Mn_3O_4, MnOOH, and even Mn_5O_8 phase. Temperature on sample surface due to laser-induced heating did not exceed 1000 K. The above investigation clarifies MnO nanoparticles behaving under strong laser powers and can provide important information for further use and investigation with MnO and its related compounds.

ACKNOWLEDGEMENTS

REFERENCES

[1] K. M. Nam, Y.-I. Kim, Y. Jo, S. M. Lee, B. G. Kim, R. Choi, S.-I. Choi, H. Song, J. T. Park, *J. Am. Chem. Soc.* **2012**, *134*, 8392.

[2] B. K. Pandey, A. K. Shahi, R. Gopal, *Mater. Focus* **2013**, *2*, 221.

[3] Collaboration: Authors and editors of the volumes III/17G-41D, Landolt-Börnstein-Group III Condensed Matter, in *Non-Tetrahedrally Bonded Binary Compounds II*, (Eds: O. Madelung, U. Rossler, M. Schulz) Vol. 41D, Springer, Berlin, Heidelberg, Germany **2000** 1.

[4] N. Mironova-Ulmane, A. Kuzmin, M. Grube, *JALLCOM* **2009**, *480*, 97.

[5] M. A. Langell, C. W. Hutchings, G. A. Carson, M. H. Nassir, *J. Vac. Sci. Technol., A* **1996**, *14*, 1656.

[6] W. Kiefer, H. J. Bernstein, *Chem. Phys. Lett.* **1971**, *8*, 381.

[7] F. Kapteijn, A. D. van Langeveld, J. A. Moulijn, A. Andreini, M. A. Vuurman, A. M. Turek, J.-M. Jehng, I. E. Wachs, *J. Catal.* **1994**, *150*, 94.

[8] T. Gao, H. Fjellvåg, P. Norby, *Anal. Chim. Acta* **2009**, *648*, 235.

[9] M. Richter, A. Trunschke, U. Bentrup, K.-W. Brzezinka, E. Schreier, M. Schneider, M.-M. Pohl, R. Fricke, *J. Catal.* **2002**, *206*, 98.

[10] C. Julien, M. Massot, S. Rangan, M. Lemal, D. Goyomard, *J. Raman Spectrosc.* **2002**, *33*, 223.

[11] T. Byrum, S. L. Gleason, A. Thaler, G. J. MacDougall, S. L. Cooper, *Phys. Rev. B* **2016**, *93*, 184418.

[12] C. Julien, M. Massot, R. Baddour-Hadjean, S. Franger, S. Bach, J. P. Pereira-Ramos, *Solid State Ionics* **2003**, *159*, 345.

[13] E. Widjaja, J. T. Sampanthar, *Anal. Chim. Acta* **2007**, *585*, 241.

[14] C. B. Azzoni, M. C. Mozzati, P. Galinetto, A. Paleari, V. Massarotti, D. Capsoni, M. Bini, *Solid State Commun.* **1999**, *112*, 375.

[15] M. Kim, X. M. Chen, X. Wang, C. S. Nelson, R. Budakian, P. Abbamonte, S. L. Cooper, *Phys. Rev. B* **2011**, *84*, 174424.

[16] F. Buciuman, F. Patcas, R. Cracium, D. R. T. Zahn, *Phys. Chem. Chem. Phys.* **1999**, *1*, 185.

[17] J. Luo, H. T. Zhu, H. M. Fan, J. K. Liang, H. L. Shi, G. H. Rao, J. B. Li, Z. M. Du, Z. X. Shen, *J. Phys. Chem. C* **2008**, *112*, 12594.

[18] R. Baddour-Hadjean, J. P. Pereira-Ramos, *Chem. Rev.* **2010**, *110*, 1278.

[19] B. Hadžić, N. Romčević, D. Sibera, U. Narkiewicz, I. Kuryliszyn-Kudelska, W. Dobrowolski, M. Romčević, *J. Phys. Chem. Solids* **2016**, *91*, 80.

[20] PDXL Version 2.0.3.0 Integrated X-ray Powder Diffraction Software, Rigaku Corporation, Tokyo, Japan, **2011**, 196–8666.

[21] Powder Diffraction File, PDF-2 Database, announcement of new database release **2012**, International Centre for Diffraction Data (ICDD).

[22] H. Idink, V. Srikanth, W. B. White, E. C. Subbarao, *J. Appl. Phys.* **1994**, *76*, 1819.

[23] L. Laffont, P. Gibot, *Mat. Char.* **2010**, *61*, 1268.

[24] H. Shaked, J. Faber Jr, R. L. Hitterman, *Phys. Rev. B* **1988**, *38*, 11901.

[25] C. M. Julien, M. Massot, C. Poinsignon, *Spectrochim. Acta A* **2004**, *60*, 689.

[26] C. M. Julien, M. Massot, Proceedings of the International Workshop Advanced Techniques for Energy Sources Investigation and Testing, Sofia, Bulgaria, September **2004**, 1–17.

[27] S. Kumar, A. K. Ojha, R. K. Singh, *J. Raman Spectrosc.* **2014**, *45*, 717.

[28] S. Cheng, L. Yang, D. Chen, X. Ji, Z.-J. Jiang, D. Ding, M. Liu, *Nano Energy* **2014**, *9*, 161.

[29] H. D. Lutz, H. Möller, M. Schmidt, *J. Mol. Struct.* **1994**, *328*, 121.

[30] M.-C. Bernard, A. Hugot-Le Goff, B. V. Thi, S. Cordoba de Torresi, *J. Electrochem. Soc.* **1993**, *140*, 3065.

[31] J. Gao, M. A. Lowe, H. D. Abruña, *Chem. Mater.* **2011**, *23*, 3223.

[32] F. Froment, A. Tournie, P. Colomban, *J. Raman Spectrosc.* **2008**, *39*, 560.

[33] M. C. Caggiani, P. Colomban, *J. Raman Spectrosc.* **2011**, *42*, 839.

[34] A. L. Patterson, *Phys. Rev.* **1939**, *56*, 978.

[35] G. K. Williamson, W. H. Hall, *Acta Metall.* **1953**, *1*, 22.

[36] J. R. Stewart, R. Cywinski, *J. Phys.:Condens. Matter.* **1999**, *11*, 7095.

SUPPORTING INFORMATION

Additional Supporting Information may be found online in the supporting information tab for this article.

PAPER

Design of hollow metasurfaces for absorption sensors and surface enhanced infrared absorption

To cite this article: Borislav Vasić 2022 *J. Phys. D: Appl. Phys.* **55** 315105

View the article online for updates and enhancements.

Design of hollow metasurfaces for absorption sensors and surface enhanced infrared absorption

Borislav Vasić

Institute of Physics Belgrade, University of Belgrade, Pregrevica 118, 11080 Belgrade, Serbia

E-mail: bvasic@ipb.ac.rs

Abstract

Absorption sensors detect variations in the imaginary part of refractive index with selectivity in sensing since analytes can be distinguished according to their characteristic absorption bands. In this study we combine the theoretical analysis based on temporal coupled mode theory and numerical calculations in order to derive design principles of optimal metasurfaces aimed for absorption sensing and surface enhanced infrared absorption (SEIRA). We consider hollow metal–insulator-metal metasurfaces with an empty space between two metallic layers. This space acts as a channel for the infiltration of fluid analytes in the region with the maximal electric field enhancement, which provides high sensitivity. We demonstrate that optimal metasurfaces operate in overcoupled regime where radiative decay rate of the resonant mode is larger than non-radiative decay rate. The operation in this regime is adjusted by choosing appropriate channel thickness (the vertical distance between two metallic layers), which should be around three times larger than the channel thickness at the critical coupling point, associated with equal decay rates and zero reflectance. Metasurface period should be as large as possible, whereas the operating frequency should be equal to the resonant frequency of metasurfaces. The same conclusions hold for hollow metasurfaces aimed for SEIRA, while in addition, their resonant frequency should match the vibrational frequency of an analyte under investigation. The absorption sensitivity (reflectance change divided by the change in the imaginary part of refractive index) of an optimal metasurface is larger than $10\,\mathrm{RIU}^{-1}$, which provides detection of the imaginary part of refractive index below 10^{-3}.

Supplementary material for this article is available online

Keywords: metasurface, metal–insulator-metal structure, absorption sensing,
surface enhanced infrared absoprtion (SEIRA)

(Some figures may appear in colour only in the online journal)

1. Introduction

Plasmonic structures and metamaterials aimed for refractive index sensing commonly detect variations in the real part $n_{a,r}$ of refractive index. Typically this is achieved by recording the spectral shifts of resonant modes upon changes of $n_{a,r}$ [1–3]. Still, when variations in the imaginary part of refractive index $n_{a,i}$ are dominant, absorption measurements are more

appropriate for sensing [4]. In addition to improved sensitivity, the absorption measurements provide selectivity since various analytes can be distinguished according to their characteristic absorption bands. Typically, in the mid-infrared domain, the absorption bands arise due to vibrational modes of molecules.

Absorption spectroscopy and sensing are based on Beer–Lambert law which states that the absorbance is proportional to the optical path length. Therefore, in the case of very thin

molecular films or liquid layers with a subwavelength thickness, the resulting absorption is very low which often makes detection impossible. Standard solution to solve this problem is to use optical cavities and resonant structures where absorption is increased due to very long effective optical paths and/or due to enhanced electric fields [5–10]. In this context, surface enhanced infrared absorption (SEIRA) [4, 11] is one of the most widespread techniques, where the infrared absorption is enhanced by metallic substrates. At the beginning, SEIRA substrates were made as thin films consisting of close, but separated metallic nanoparticles acting as plasmonic resonators [12–16]. Still, since metal island films are disordered structures, their reproducibility and electric field enhancement are not well controlled.

Further improvement of SEIRA substrates was achieved by metasurfaces. These planar structures consist of periodic and ordered arrays of metallic resonators. By scaling of their dimensions, it is straightforward to spectrally shift metasurface resonances and overlap them with vibrational modes to be detected. At the same time, geometry of the metallic resonators can be tailored practically at will in order to achieve large and well controlled electric field enhancement. Initial metasurface based SEIRA substrates were made of planar metallic resonators on dielectric substrates [17–22]. Additional bottom metallic background plate improved absorption enhancement and their sensitivity due to constructive interference [23–26]. SEIRA substrates consisting of a layer with metallic resonators, dielectric layer and metalic plate resemble typical metal–insulator-metal (MIM) metasurfaces which gained a lot of attention last years because of numerous possible applications and straightforward fabrication [27].

The main issue in the application of MIM metasurfaces for refractive index sensing is a low overlap between analytes and spatial domains with a large electric field enhancement. Namely, in the standard configuration, the analytes are deposited on the top of metasurfaces, while the maximal field enhancement is achieved in the insulating layer between two metallic layers. This issue was solved by using hollow metasurfaces which proved themselves as very efficient refractometric sensors (sensors of the real part of refractive index) [28–32] as well as SEIRA substrates [33–35]. In this configuration, the empty space between two metallic layers serves as a nanofludic channel which can be easily infiltrated by a fluid analyte. As a result, hollow metasurfaces provide excellent overlap between the channel with an analyte and regions with a high field enhancement.

Although initial experimental results were promising [33–35], design principles of optimal hollow MIM metasurfaces for absorption sensors and SEIRA substrates have not been established yet. The aim of this study is to close this gap and to find an optimal geometry and working regime which give maximal sensitivity. The manuscript organization is the following. In section 2 we explain the considered structure, the model based on temporal coupled mode theory (TCMT) and numerical calculations of decay rates (radiative and non-radiative). In section 3, optimal geometry (channel thickness and metasurface period), operating regime (governed

by the ratio between radiative and non-radiative decay rates of the resonant mode) and working frequency are derived from the TCMT model. Numerical results for absorption sensors and SEIRA are presented in sections 4 and 5, respectively. Additional interpretations of obtained numerical results, the analysis of sensitivity enhancement provided by hollow metasurfaces, discussions on dynamic range and limits of detection, possible applications, concluding remarks and prospects for future works are given in sections 6 and 7.

2. Sensing structure and modeling

Hollow MIM metasurface and the unit cell are schematically depicted in figure 1. The structure is periodic along x-direction with period P. The top metallic layer consists of a periodic array of parallel stripes of width w_m and thickness t_m. Thick metallic plate at the bottom acts as a back reflector and prevents transmission of the incident field coming from the top. Nanofluidic channel between two metallic layers is filled with a fluid analyte. The channel thickness is denoted by t_c. The top encapsulating layer serves as a substrate for the deposition of metallic stripes and encloses whole fluid cell. The incident beam propagates from the top along z-direction (the normal incidence), while it is polarized along x-direction.

Numerical calculations were performed using RETICOLO electromagnetic solver based on rigorous coupled wave analysis [36]. In order to find an optimal structure with maximal sensitivity, the reflectance was calculated for variable geometrical parameters of metasurfaces, period P and channel thickness t_c. The third geometrical parameter, the width of metallic stripes w_m dominantly determines the resonant frequency. Although it is influenced by other geometrical parameters as well [37], a simple standing-wave model [38] gives a good estimate of the resonant frequency and can be used as a starting point in metasurface design. In this study w_m was fixed to 2.5 μm which provided the operation in the mid-infrared domain, at wavelengths around 10 μm. Thickness of metallic stripes was $t_m = 80$ nm. The maximal period in the study was set to $P = 5$ μm in order to avoid diffraction.

Water was considered as a fluid carrying analytes through the channel between two metallic layers [33]. At selected wavelengths around 10 μm, the water is almost dispersionless with a refractive index $n_w \approx 1.3$. Analytes were modeled with a complex refractive index $n_a = n_{a,r} + jn_{a,i}$ (which corresponds to the refractive index of metasurface channel as well). Since their amount is small in realistic cases, the real part of their refractive index was taken as constant and equal to the refractive index of water $n_{a,r} = 1.3$. Absorption sensitivity was then calculated by varying the imaginary part $n_{a,i}$ of analyte (channel) refractive index as specified below in the text.

In the case of SEIRA, molecules of interest are commonly associated with many vibrational modes active at mid-infrared frequencies. Here, for the sake of simplicity, we consider the case with single vibrational mode. Dielectric permittivity is then represented by the following Lorentz model
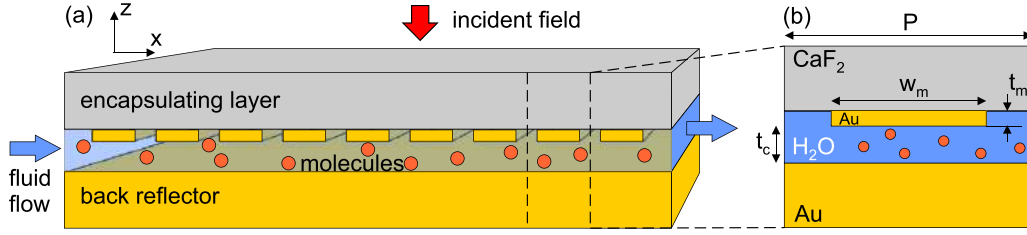
Figure 1. Geometry of absorption sensors based on hollow metasurfaces with a nanofluidic channel: (a) schematic representation and (b) the unit cell.

$$\varepsilon_a(\omega) = \varepsilon_\infty + \frac{S_v}{\omega_v^2 - \omega^2 - j\gamma_v\omega}, \qquad (1)$$

where ε_∞ stands for high-frequency permittivity, S_v is oscillator strength, ω_v is vibrational frequency and γ_v is damping term. Usually, the concentration of molecules is very small, therefore the high-frequency permittivity is practically defined with the refractive index of water, $\varepsilon_\infty = n_w^2$. ω_v is variable (specified below in the text), but approximately matched with resonances of considered metasurfaces (around 10 μm). The values chosen for the oscillator strength $S_v = (9.77 \times 10^{12} \, \mathrm{rad\,s^{-1}})^2$ and damping term $\gamma_v = 3 \times 10^{12} \, \mathrm{rad\,s^{-1}}$ are typical for protein permittivity [20].

Dielectric permittivity of metallic parts was calculated using Drude model for gold with the following parameters: the plasma frequency $\omega_p = 1.32 \times 10^{16} \, \mathrm{rad\,s^{-1}}$ and collision frequency $\gamma_{\mathrm{Au}} = 1.2 \times 10^{14} \, \mathrm{rad\,s^{-1}}$ [20]. CaF$_2$ is taken as the encapsulating layer and substrate for metallic stripes [33]. At mid-infrared frequencies, it is transparent and practically lossless, and therefore it was modeled with a refractive index of 1.4.

Theoretical analysis provides deeper insight into physical principles of metasurfaces working as absorption sensors and SEIRA substrates and it gives an initial estimate of optimal geometrical parameters. The analysis was performed within TCMT model [39–41] which very nicely reproduces reflectance spectra of low-loss metasurfaces and which was already applied to analyse metasurfaces aimed for refractometric sensing (real part of refractive index) [38]. According to TCMT, the reflectance of MIM metasurfaces is given by the following expression

$$R(\omega) = 1 - \frac{4\gamma_r\gamma_0}{(\omega - \omega_0)^2 + (\gamma_r + \gamma_0)^2}, \qquad (2)$$

where ω_0 is the resonant frequency, whereas γ_0 and γ_r are non-radiative and radiative decay rates of the resonant mode, respectively. According to the ratio between these two decay rates, we distinguish three operating regimes of MIM metasurfaces: undercoupled regime when $\gamma_0 > \gamma_r$, the critically coupled regime with equal decay rates $\gamma_0 = \gamma_r$, and overcoupled regime when $\gamma_0 < \gamma_r$. The non-radiative decay rate describes dissipative processes in metasurfaces related to the dissipation either in metallic parts or in analyte. Therefore, γ_0 can be expressed as,

$$\gamma_0 = \gamma_m + \gamma_a, \qquad (3)$$

where γ_m and γ_a are absorption rates in metallic parts and analyte, respectively.

Radiative and non-radiative decay rates were calculated by fitting numerically calculated reflectance to the TCMT model given by equation (2). Contributions of metal and analyte absorption rates to total non-radiative decay rate were then separated in the following way [40]. Small absorption in the channel was treated as a perturbation. In the first step, the imaginary part of the analyte refractive index was set to zero, $n_{a,i} = 0$. γ_m was then equal to non-radiative decay rate γ_0^I for this case: $\gamma_m = \gamma_0^I$. In the second step, analyte losses were included, therefore $n_{a,i} > 0$, whereas non-radiative decay rate was γ_0^{II}. Since the metallic absorption rate is independent on the losses in the channel and determined in the first step, the analyte absorption rate was obtained as $\gamma_a = \gamma_0^{II} - \gamma_m$ (or $\gamma_a = \gamma_0^{II} - \gamma_0^I$).

In order to find an optimal geometry of absorption sensors, it is necessary to relate decay rates from equation (2) with geometrical parameters of metasurfaces, channel thickness and period. Numerically calculated decay rates as functions of t_c and P, as well as corresponding fitting curves are displayed in figures 2(a) and (b), respectively. Decay rates as function of t_c can be expressed in the following way:

$$\gamma_m = \alpha_m/t_c, \; \gamma_a = \mathrm{const.}, \; \gamma_r = \beta t_c. \qquad (4)$$

As can be seen, the metallic absorption rate is inversely proportional to t_c, the analyte absorption rate is practically constant and independent on t_c, while the radiative decay rate linearly increases with t_c. Accordingly, the total non-radiative decay rate is $\gamma_0 = \gamma_m + \gamma_a = \alpha_m/t_c + \mathrm{const.}$ In the case of small analyte losses, they can be treated as perturbations from the lossless case. Then the total non-radiative decay rate γ_0 is still approximately inversely proportional to t_c and can be expressed as

$$\gamma_0 \approx \alpha/t_c. \qquad (5)$$

Hereafter, the channel thickness for the MIM cavities at the critically coupled point ($\gamma_0 = \gamma_r$) is denoted with t_{cc} and according to equations (4) and (5), $t_{cc} = \sqrt{\alpha/\beta}$. Then, for $t_c < t_{cc}$ ($t_c > t_{cc}$), MIM metasurfaces operate in undercoupled (overcoupled) regime as indicated in figure 2(a).

According to figure 2(b), metallic and analyte absorption rates (as well as total non-radiative decay rate) are practically independent on period. On the other hand, the radiative decay rate approximately linearly decreases with P.
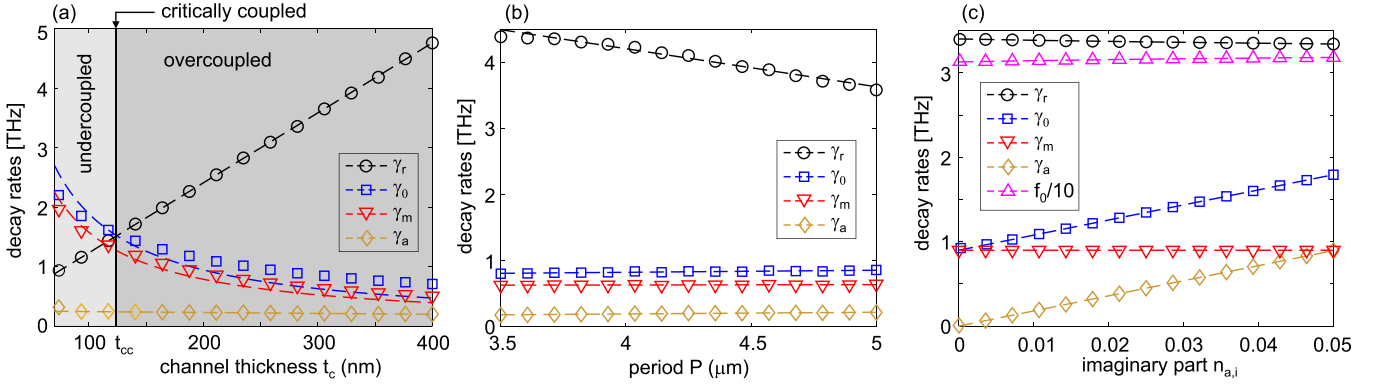
Figure 2. Decay rates as function of geometrical parameters: (a) channel thickness t_c ($P = 5 \mu$m) and (b) period P ($t_c = 300$ nm). (c) Decay rates and resonant frequency $f_0 = \omega_0/(2\pi)$ (divided by 10 for better visibility) as function of the imaginary part of analyte refractive index $n_{a,i}$ ($t_c = 200$ nm, $P = 3.5 \mu$m). Operating regimes (undercoupled and overcoupled) are indicated in part (a) by dashed regions.
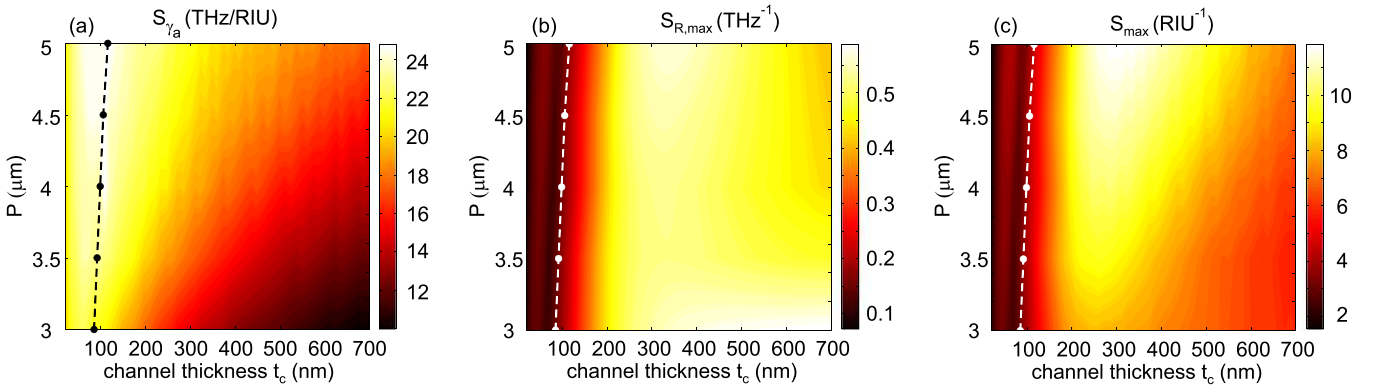

Figure 3. Sensitivities (a) S_{γ_a}, (b) $S_{R,\text{max}}$ and (c) S_{max} as function of geometrical parameters, metasurface period P and channel thickness t_c. Dashed line connects (t_c, P) points where metasurfaces are critically coupled.

3. Design principles of absorption sensors

Sensing mechanism of absorption sensors is based on the measurement of variations in reflectance/transmittance magnitude. In our case, the output signal is reflectance since the transmission channel of MIM metasurfaces is blocked. The sensitivity S can be then defined as a variation of reflectance R with respect to small changes in the imaginary part of analyte refractive index $n_{a,i}$ (unit for S is RIU^{-1}, where RIU stands for refractive index unit):

$$S(\omega) = \frac{dR(\omega)}{dn_{a,i}}. \tag{6}$$

According to equation (2), the reflectance of MIM metasurfaces depends on the resonant frequency and decay rates. Therefore, the sensitivity can be calculated as

$$S(\omega) = \frac{\partial R}{\partial \omega_0}\frac{\partial \omega_0}{\partial n_{a,i}} + \frac{\partial R}{\partial \gamma_r}\frac{\partial \gamma_r}{\partial n_{a,i}} + \frac{\partial R}{\partial \gamma_0}\frac{\partial \gamma_0}{\partial n_{a,i}}. \tag{7}$$

Resonant frequency ($\omega_0/(2\pi)$) and decay rates ($\gamma_r, \gamma_0, \gamma_m, \gamma_a$) as functions of $n_{a,i}$ are plotted in figure 2(c). As can be seen, the resonant frequency, radiative decay rate and metal

absorption rate are represented by almost flat lines meaning that $\partial \omega_0/\partial n_{a,i} \approx 0$, $\partial \gamma_r/\partial n_{a,i} \approx 0$, and $\partial \gamma_m/\partial n_{a,i} \approx 0$. As a result, $\partial \gamma_0/\partial n_{a,i} = \partial(\gamma_m + \gamma_a)/\partial n_{a,i} \approx \partial \gamma_a/\partial n_{a,i}$ whereas the expression for the sensitivity becomes

$$S(\omega) \approx \frac{\partial R}{\partial \gamma_0}\frac{\partial \gamma_a}{\partial n_{a,i}} = S_R(\omega) \cdot S_{\gamma_a}. \tag{8}$$

Let's first consider sensitivity $S_{\gamma_a} = \partial \gamma_a/\partial n_{a,i}$. For a structure with a fixed geometry, the analyte absorption rate γ_a approximately linearly increases with $n_{a,i}$ as shown in figure 2(c). S_{γ_a} can be therefore obtained as a slope of the corresponding linear fit. Using this procedure, S_{γ_a} was calculated as a function of P and t_c and the corresponding two dimensional map is displayed in figure 3(a).

Sensitivity $S_R(\omega)$ is derived from equation (2) as

$$S_R(\omega) = \frac{\partial R}{\partial \gamma_0} = -4\gamma_r \frac{(\omega - \omega_0)^2 + \gamma_r^2 - \gamma_0^2}{((\omega - \omega_0)^2 + (\gamma_0 + \gamma_r)^2)^2}. \tag{9}$$

The sensitivity $S_{R,\text{max}} = \max|S_R(\omega)|$ as a function of P and t_c is depicted in figure 3(b). In the calculations, radiative and non-radiative decay rates were obtained by fitting numerically calculated reflectance to the TCMT model given by equation (2).

Total sensitivity based on the theoretical model was obtained by multiplying S_{γ_a} and $S_{R,\max}$ and it is presented in figure 3(c). As can be seen, the total sensitivity increases with period, while it is maximized in the overcoupled regime for channel thickness around 300 nm.

By comparing maps from figure 3, it is clear that the total sensitivity $S_{\max}$ is dominantly determined by $S_{R,\max}$. Therefore, the following analysis is focused on this term. Optimal working frequency and geometrical parameters are defined as the parameters for which $S_R(\omega)$ is maximized. The working frequency ω_W is defined by $S_{R,\max} = |S_R(\omega_W)|$ and it can be determined from equation $\partial S_R(\omega)/\partial\omega = 0$ which has the following solutions:

$$\omega_{W1} = \omega_0, \tag{10}$$

$$\omega_{W2\pm} = \omega_0 \pm \sqrt{3\gamma_0^2 - \gamma_r^2 + 2\gamma_0\gamma_r}, \ \gamma_0 > \gamma_r/3. \tag{11}$$

The previous equations define two branches of sensitivity $S_{R,\max}$ which are given by the following expressions:

$$S_{R,\max1} = |S_R(\omega_{W,1})| = 4\gamma_r \frac{|\gamma_r - \gamma_0|}{(\gamma_0 + \gamma_r)^3}, \tag{12}$$

$$S_{R,\max2} = |S_R(\omega_{W,2})| = \frac{\gamma_r}{2\gamma_0(\gamma_0 + \gamma_r)}, \ \gamma_0 > \gamma_r/3. \tag{13}$$

In order to find optimal geometrical parameters from equations (12) and (13), it is necessary to include equations (4) and (5) which give relations between decay rates and channel thickness. As a result, the expressions for two branches as function of t_c become

$$S_{R,\max1} = \frac{4\beta t_c^3 |\beta t_c^2 - \alpha|}{(\beta t_c^2 + \alpha)^3}, \tag{14}$$

$$S_{R,\max2} = \frac{\beta t_c^3}{2\alpha(\beta t_c^2 + \alpha)}. \tag{15}$$

Optimal channel thickness was then found from expressions $\partial S_{R,\max1}/\partial t_c = 0$ and $\partial S_{R,\max2}/\partial t_c = 0$. For working frequency ω_{W1}, this condition gives two values (derivations given in section S1 of supplementary material available online at stacks.iop.org/JPhysD/55/315105/mmedia): $t_{c1} = k_1 t_{cc}$ $(k_1 = \sqrt{(8 - \sqrt{52})/2} \approx 0.63)$ where $S_{R,\max1}$ is $0.22/\sqrt{\alpha\beta}$ and $t_{c3} = k_3 t_{cc}$ $(k_3 = \sqrt{(8 + \sqrt{52})/2} \approx 2.8)$ where $S_{R,\max1}$ is $0.87/\sqrt{\alpha\beta}$. For working frequency ω_{W2}, $S_{R,\max2}$ is maximized at $t_{c2} = k_2 t_{cc}$ $(k_2 = \sqrt{3})$ (derivations given in section S1 of supplementary material) where $S_{R,\max2} \approx 0.65/\sqrt{\alpha\beta}$. Therefore, the maximum of $S_{R,\max}$ is achieved at $t_{c3} \approx 2.8t_{cc}$ which implies that optimal MIM metasurfaces should operate in the overcoupled regime, with a channel thickness around three times larger than at the critical coupling point. At the same time, an optimal working frequency is the resonant one.

Two branches of $S_{R,\max}$ from equations (12) and (13) as function of channel thickness are displayed in figure 4. In the
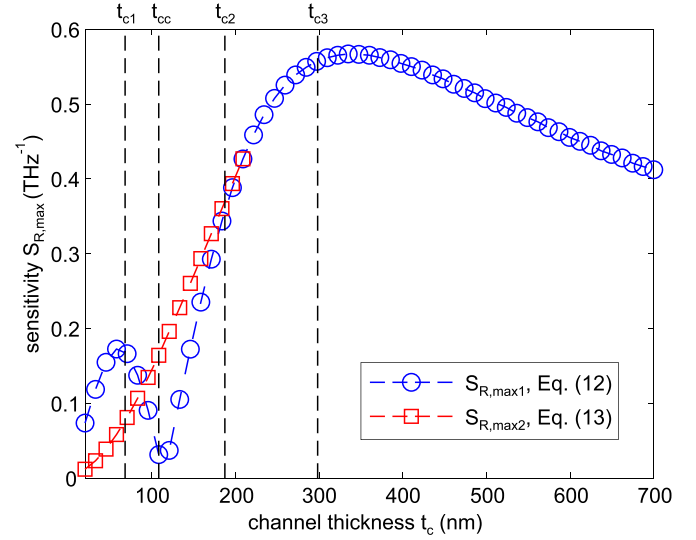

Figure 4. Two branches of sensitivity $S_{R,\max}$ defined by equations (12) and (13) as function of channel thickness ($P = 5 \ \mu$m). Dashed lines stand for t_c where two branches have maxima: $t_{c1} \approx 0.63t_{cc}$ and $t_{c3} \approx 2.8t_{cc}$ for the first branch, and $t_{c2} \approx 1.73t_{cc}$ for the second branch. t_{cc} is numerically calculated as a value where $\gamma_r = \gamma_0$.

undercoupled regime ($t_c < t_{cc}$), $S_{R,\max}$ follows the first branch defined by equation (14) which has a local maximum at t_{c1}. In the intermediate regime around the critical coupling point (for t_c around t_{cc}), the first branch goes through zero. In this case, larger sensitivity is achieved by the second branch defined by equation (15). For $t_c > t_{c2}$, the condition $\gamma_0 > \gamma_r/3$ is not fulfilled and there are no real solutions for the second branch anymore. Thereafter, the sensitivity is again defined by the first branch and maximized in the overcoupled regime at t_{c3}.

Let's consider now dependence of decay rates on period. According to figure 2(b), the non-radiative decay rate is practically independent on P, while the radiative decay rate approximately linearly decreases with P (except for small periods close to metallic stripe width). Therefore, in order to take into account dependences on both t_c and P, the radiative decay rate from equation (4) can be expressed as $\gamma_r = \beta(P)t_c$, where factor $\beta(P)$ decreases with P. Since the previous analysis demonstrated that $S_{R,\max} \sim 1/\sqrt{\beta}$ (for both branches), sensitivities $S_{R,\max}$ and $S_{\max}$ increase with period.

4. Numerical results

In order to illustrate the operation of absorption sensors, we study two cases, without analyte losses ($n_{a,i1} = 0$) and with losses included ($n_{a,i2} = 0.02$). Figures 5(a)–(c) depict corresponding reflectance spectra R_1 and R_2, together with their difference $\Delta R = R_2 - R_1$ for three different operating regimes (undercoupled (a), near critically coupled (b), and overcoupled (c)). As can be seen, $|\Delta R|$ for the undercoupled and overcoupled system is maximized at $\omega_{W1} = \omega_0$, whereas in the case of near-critically coupled system, $|\Delta R|$ reaches the maximum around $\omega_{W2\pm}$. At the resonant frequency, $\Delta R(\omega_0)$ is positive (negative) in undercoupled (overcoupled) regime. This is explained by the inspection of $R(\omega_0)$ as a function of the imaginary part $n_{a,i}$ of analyte refractive index as depicted in
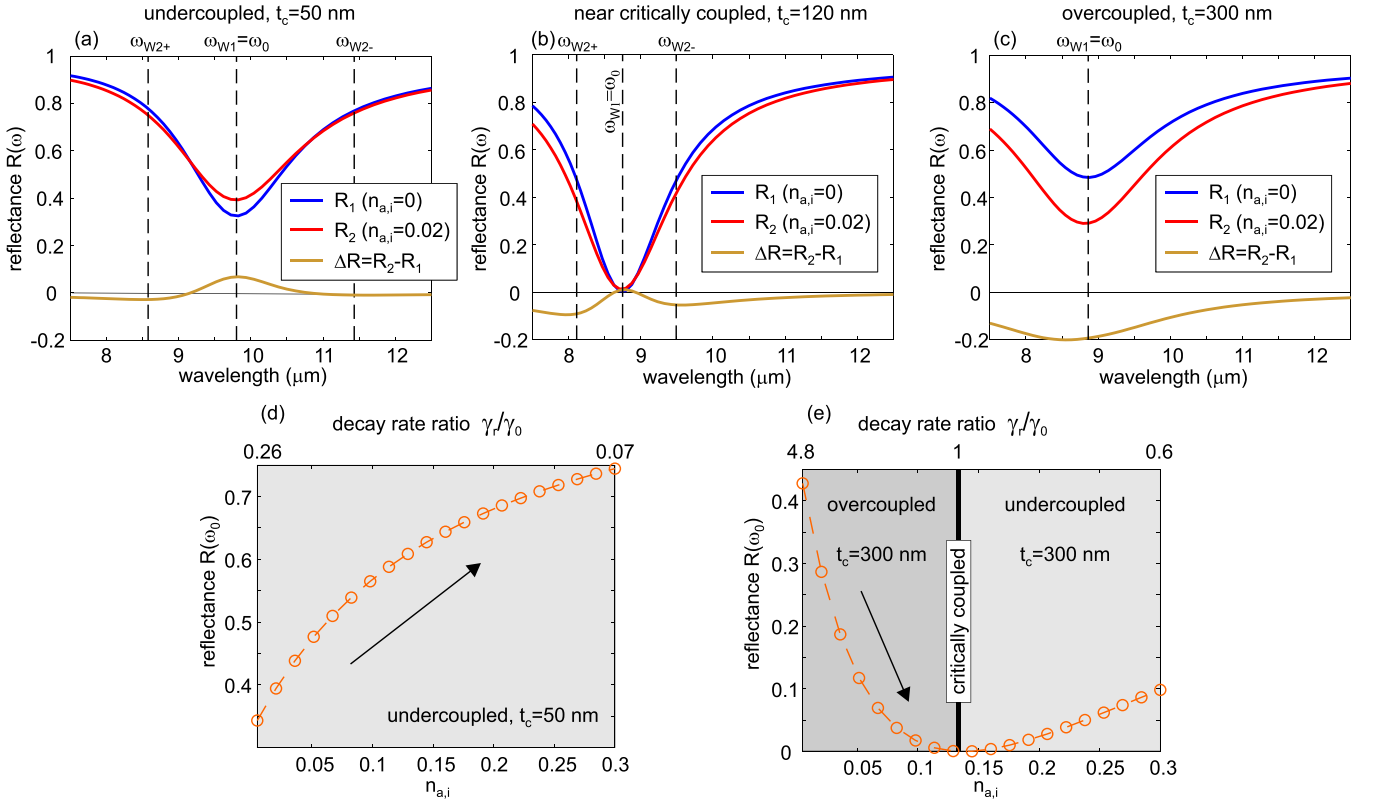
Figure 5. Reflectance spectra of a metasurface for $n_{a,i} = 0$ (R_1) and $n_{a,i} = 0.02$ (R_2) as well as their difference $\Delta R = R_2 - R_1$ for three different operation regimes: (a) undercoupled ($t_c = 50$ nm), (b) near to critically coupled ($t_c = 120$ nm), and (c) overcoupled regime ($t_c = 300$ nm). Period is $P = 5$ μm. Reflectance at the resonant frequency $R(\omega_0)$ as a function of the imaginary part of analyte refractive index $n_{a,i}$ for initially (d) undercoupled ($t_c = 50$ nm) and (e) overcoupled system ($t_c = 300$ nm). The arrows in (d) and (e) show the movement of the system with increasing $n_{a,i}$.

figures 5(d) and (e). Generally, larger $n_{a,i}$ and losses imply increased non-radiative decay rate γ_0. As a result, an initially undercoupled system is shifted further away from the critical coupling point associated with zero reflectance (denoted by the arrow in figure 5(d)). At the same time, the reflectance increases with $n_{a,i}$ and ΔR is positive. On the other hand, increased losses and non-radiative decay rate shift an initially overcoupled system toward the critical coupling point. Therefore, the reflectance decreases thus giving negative ΔR (denoted by the arrow in figure 5(e)).

Total sensitivity $S_{\max}$ was numerically calculated as $S_{\max} = \max|\Delta R(\omega)|/\Delta n_{a,i}$ ($\Delta R(\omega) = R_2(\omega) - R_1(\omega)$, $\Delta n_{a,i} = n_{a,i2} - n_{a,i1}$) and displayed in figure 6(a) as a function of channel thickness and period. The overall maximum of $S_{\max}$ is achieved for the channel thickness around 300 nm. The sensitivity profile as a function of t_c is depicted in figure 6(b). The profile exhibits two maxima, the lower one in the undercoupled regime for $t_c \approx t_{c1}$ and the higher one in the overcoupled regime for $t_c \approx t_{c3}$. Around the critical coupling point $t_c \approx t_{cc}$, the sensitivity has a local minimum. After the reaching of the maximum for $t_c \approx 300$ nm, $S_{\max}$ decreases with channel thickness since an incident field does not couple efficiently with MIM cavities. Generally, higher sensitivity is obtained for larger periods, which is further illustrated in the inset of figure 6(b) depicting the profile of $S_{\max}$ as a function of P.

Numerical results for $S_{\max}$ agree quite well with the theoretical results from figure 3(c). This is further illustrated in figure S1 of supplementary material which displays the comparison between the model and numerics as a function of channel thickness only and for fixed period. According to both approaches, an optimal metasurface has period $P = 5$ μm and channel thickness $t_c \approx 300$ nm. The numerics confirms that the sensitivity increases with period, while it is maximized in the overcoupled regime. The profile of $S_{\max}$ from figure 6(b) is similar to the profile of $S_{R,\max}$ in figure 4 obtained from the theoretical model. Simple approximate expression $t_{c3} \approx 2.8 t_{cc}$ quite well matches an optimal channel thickness providing maximal sensitivity. Therefore, the theoretical model well predicts optimal geometry and operating regime and gives a good prediction of total absorption sensitivity.

Next we consider working frequency of absorption sensors. Two dimensional map of the normalized working frequency ω_W/ω_0 obtained as a function of metasurface period and channel thickness is given in figure 7(a). The working frequency ω_W was calculated as a frequency where the sensitivity $S(\omega)$ reaches maximal value. The resonant frequency ω_0 was calculated as a frequency of the reflectance dip for $n_{a,i} = 0$. As can be seen, the normalized working frequency is equal to 1 in the undercoupled regime since the peak of $|\Delta R|$ is achieved exactly at the resonant frequency (figure 5(a)). In
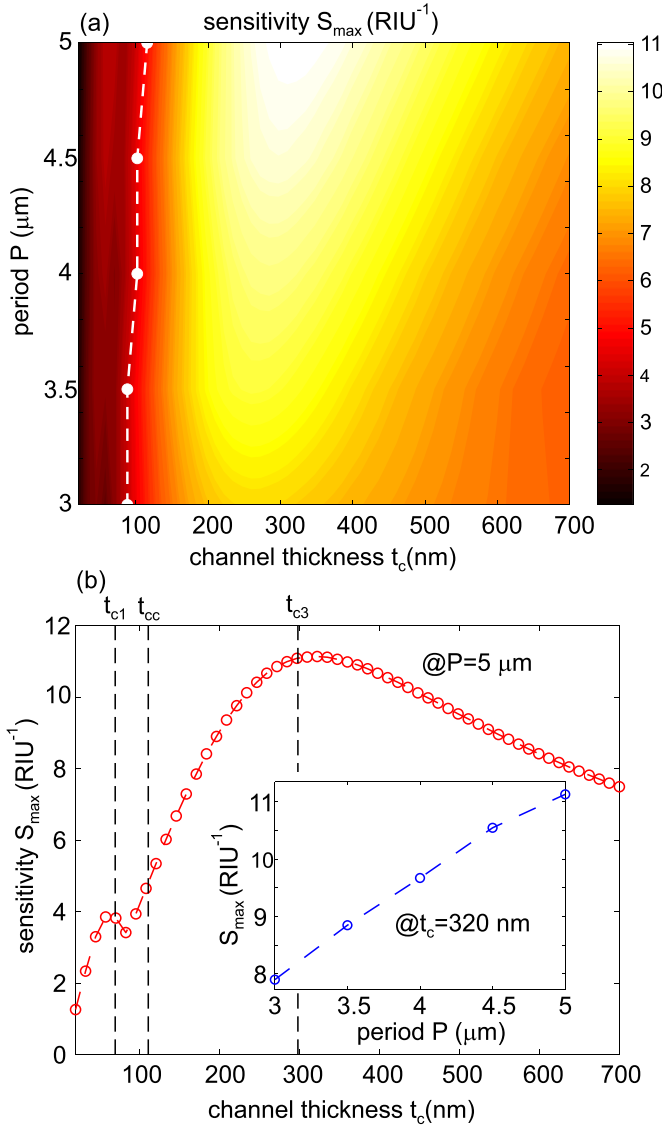
Figure 6. (a) Numerically calculated sensitivity S_{max} of absorption sensors as a function of metasurface period P and channel thickness t_c. Dashed line connects (t_c, P) points where metasurfaces are critically coupled. (b) Sensitivity profile as a function of t_c for fixed $P = 5$ μm. The inset depicts the sensitivity profile as a function of P for fixed $t_c = 320$ nm. Vertical dashed lines stand for characteristic values of channel thickness (t_{c1}, t_{cc}, and t_{c3}) obtained from the theoretical analysis.

Figure 7. (a) Numerically calculated normalized working frequency ω_W/ω_0 a function of metasurface period P and channel thickness t_c. Dashed line connects (t_c, P) points where metasurfaces are critically coupled. (b) Comparison between the numerically calculated working frequency as a function of t_c and the theoretical model given by equations (10) and (11) ($P = 5$ μm).

the overcoupled regime ω_W/ω_0 is increased to around 1.04 since the peak of $|\Delta R|$ is slightly shifted from the resonant frequency toward higher frequencies (figure 5(c)) due to losses. The normalized working frequency is around 1.1 in the area around the critical coupling point since $|\Delta R|$ is maximized not at the resonance, but at two side lobes around $\omega_{W2\pm}$ as depicted in figure 5(b).

The theoretical model predicts two working frequencies $\omega_{W,1}$ and $\omega_{W,2}$ given by equations (10) and (11). Solution of these equations are compared with numerical calculations in figure 7(b). As can be seen, the theoretical model well predicts the evolution of the working frequency. In the undercoupled and overcoupled regime, $\omega_W \simeq \omega_0$ is defined by equation (10),

while in the intermediate regime around the critical coupling point, ω_W is defined by equation (11) and the top branch

$$\omega_{W2+} = \omega_0 + \sqrt{3\gamma_0^2 - \gamma_r^2 + 2\gamma_0\gamma_r}.$$

5. Surface enhanced infrared absorption

According to TCMT model, the reflectance from a hollow metasurface containing an analyte with vibrational frequency ω_v and damping rate γ_v is [42]

$$R(\omega) = 1 - \frac{4\gamma_r(\gamma_0 + \gamma_\mu)}{(\omega - \omega_0 - \omega_\mu)^2 + (\gamma_r + \gamma_0 + \gamma_\mu)^2}. \tag{16}$$

γ_μ and ω_μ are effective decay rate and modified vibrational frequency of the vibrational mode, respectively, which are given with the following expressions: $\omega_\mu = \mu^2(\omega - \omega_v)/((\omega - \omega_v)^2 + \gamma_v^2)$ and $\gamma_\mu = \mu^2\gamma_v/((\omega - \omega_v)^2 + \gamma_v^2)$. Here μ is
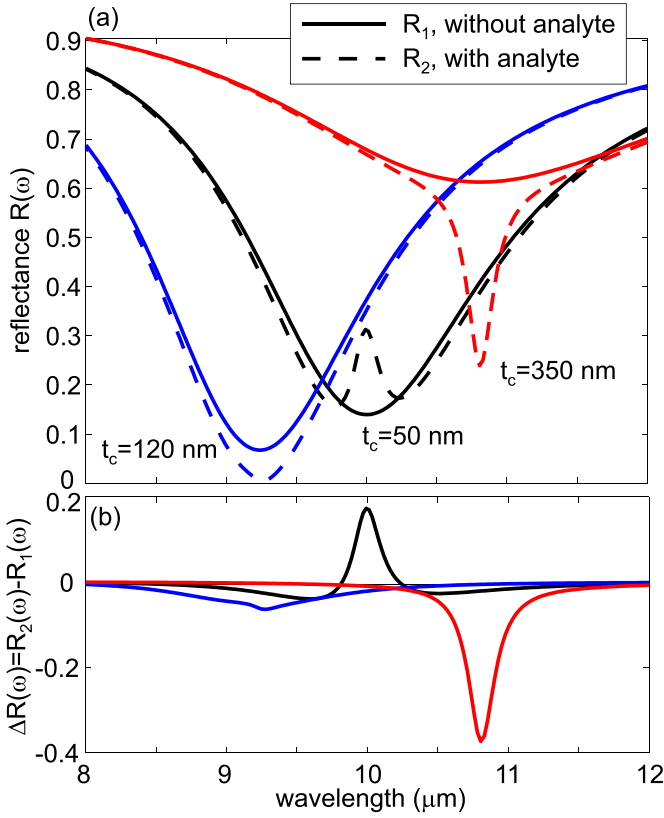
Figure 8. Metasurfaces for SEIRA: (a) reflectance spectra for the case with and without analyte and for three value of channel thickness: $t_c = 50$ nm (undercoupled), $t_c = 120$ nm (near critically coupled), and $t_c = 300$ nm (overcoupled operational regime). (b) The corresponding reflectance change ΔR.

the coupling rate which describes energy exchange between metasurface and vibrational modes. It is reasonable to expect that the maximal absorption and reflectance change is achieved at the vibrational frequency ω_v. Then, $\omega_\mu|_{\omega=\omega_v} = 0$ and $\gamma_\mu|_{\omega=\omega_v} = \mu^2/\gamma_v$, whereas the expression from equation (16) becomes

$$R|_{\omega=\omega_v} = 1 - \frac{4\gamma_r\gamma_0'}{(\omega_v - \omega_0)^2 + (\gamma_r + \gamma_0')^2}, \qquad (17)$$

where $\gamma_0' = \gamma_0 + \mu^2/\gamma_v$ is the effective non-radiative decay rate of metasurface coupled with an analyte containing vibrational mode. The previous equation has the same form as equation (2). Therefore, according to conclusions previously derived for absorption sensors, an optimal metasurface aimed for SEIRA should operate in the overcoupled regime with a period as large as possible, while the resonant frequency of the metasurface should be matched with the vibrational one, $\omega_0 = \omega_v$.

The operation of metasurface based SEIRA substrates is illustrated in figure 8(a). Reflectance spectra are displayed for the case with (R_2) and without (R_1) analyte and for different operating regimes (determined by t_c). Vibrational frequencies were equal to the resonant frequencies of the metasurfaces
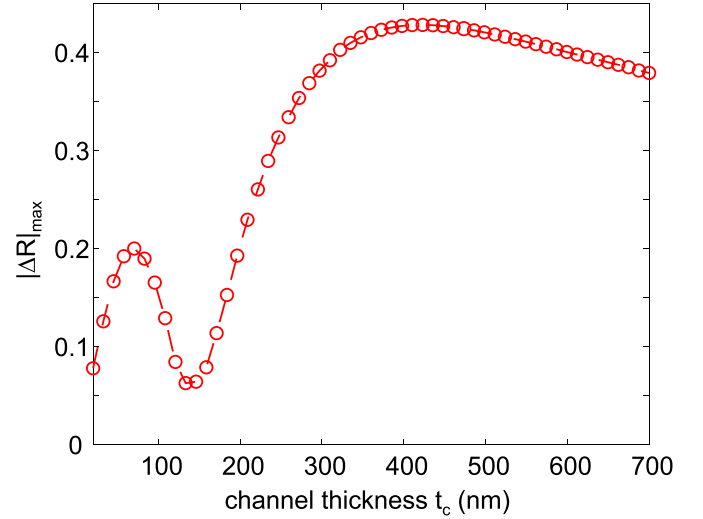
Figure 9. Metasurfaces for SEIRA: change of the reflectance $|\Delta R|_{\max} = \max|\Delta R(\omega)|$ as a function of channel thickness and for fixed period $P = 5$ μm.

without analyte. As can be seen, the reflectance change $|\Delta R| = |R_2 - R_1|$ is maximized at the vibrational frequencies, while ΔR changes its sign depending on operational regime. According to figures 5(d) and (e), in the undercoupled (overcoupled) regime, the reflectance at the resonance increases (decreases) due to additional losses introduced by the analyte. As a result, $\Delta R(\omega_0)$ is positive (negative) for undercoupled (overcoupled) metasurfaces.

Optimal geometry of hollow metasurfaces aimed for SEIRA is determined from the plot of $|\Delta R|_{\max} = \max|\Delta R(\omega)|$ as a function of channel thickness depicted in figure 9. As can be seen, it is qualitatively very similar to the corresponding sensitivity profile for absorption sensors in figure 6(b). $|\Delta R|_{\max}$ is associated with a local maximum (for $t_c \sim 70$ nm) in the undercoupled regime and with a local minimum around the critical coupling point ($t_c \sim 150$ nm). Finally, the maximal $|\Delta R|_{\max}$ is achieved in the overcoupled regime for t_c around 400 nm, which represents and optimal channel thickness. Therefore, the overcoupled regime is the optimal working regime in this case as well.

In order to calculate optimal working frequency, vibrational frequencies ω_v were swept in a frequency range $0.9\omega_0 - 1.1\omega_0$ around the metasurface resonant frequency ω_0. Corresponding $R(\omega)$ and $\Delta R(\omega)$ spectra are plotted in figure 10(a), whereas the maximal $|\Delta R|_{\max} = \max|\Delta R(\omega)|$ as a function of the normalized frequency ω_v/ω_0 is given in figure 10(b). $|\Delta R|_{\max}$ is maximized at the normalized frequency close to 1. Therefore, the resonant frequency of an optimal metasurface based SEIRA substrate should be equal to the vibrational frequency ω_v of analyte. The peak of $|\Delta R|_{\max}$ is slightly shifted and therefore reached for $\omega_v/\omega_0 > 1$ since the resonance is shifted toward higher frequencies when losses are included. As can be seen, for lower oscillator strength, $|\Delta R|_{\max}$ moves to $\omega_v/\omega_0 = 1$.
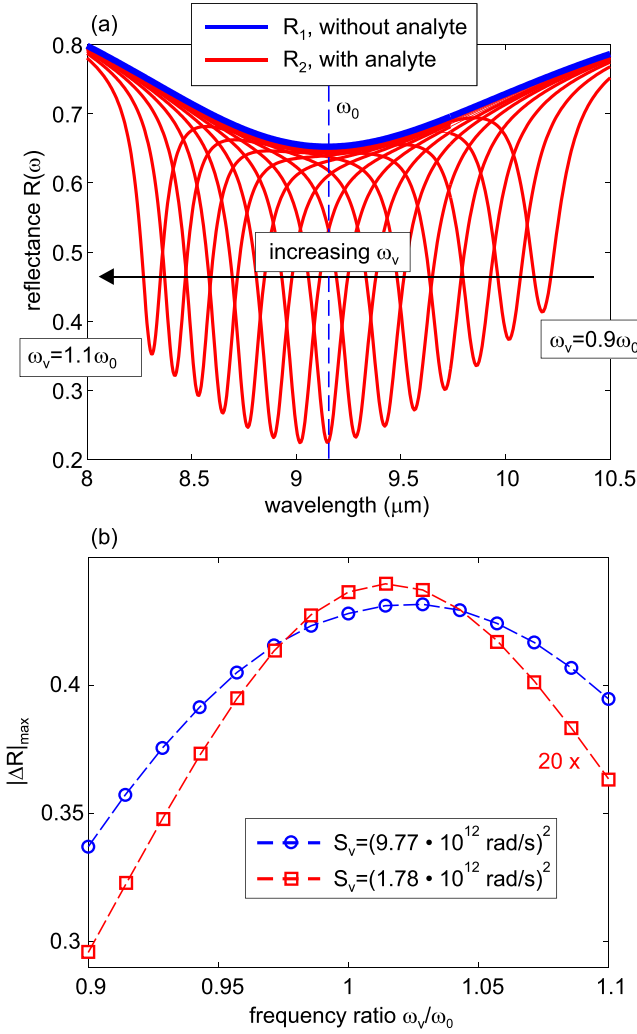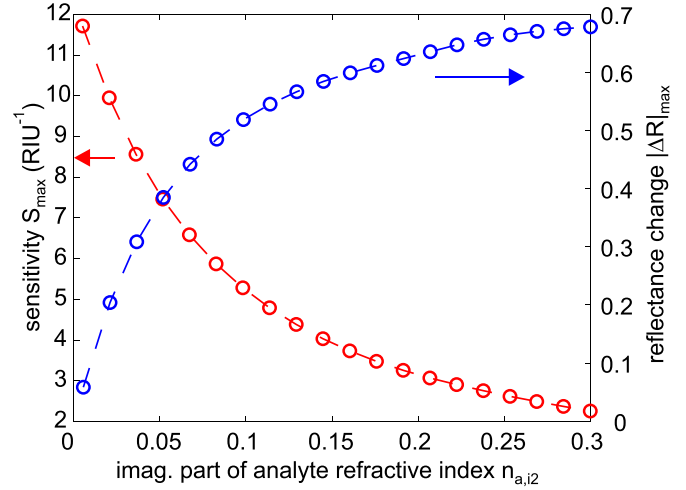
Figure 11. Dynamic range of absorption sensors: sensitivity S_{max} and reflectance change $|\Delta R|_{max}$ as function of analyte losses (the imaginary part of analyte refractive index $n_{a,i2}$). The metasurface considered in this case is the optimal one, with $t_c = 300$ nm and $P = 5$ μm, while $n_{a,i1} = 0$.

The sensitivity as a function of channel (analyte) thickness is associated with a maximum in the overcoupled regime as demonstrated in figure 6(b). Generally, the absorption sensitivity increases with analyte thickness due to larger optical path. As a result, the sensitivity of hollow metasurfaces increases for small values of channel thickness. However, at some point, it starts to decrease since an incident field does not couple efficiently with the metasurfaces (reflectance increases in overcoupled regime with increasing t_c) and therefore, does not reach the channel with analyte. The channel thickness around 300–400 nm is then an optimal value which gives both high absorption as well as efficient penetration of the incident field into the channel. As a result, this is the point with the maximal sensitivity.

In the system with a fixed geometry (t_c and P), the operational regime is controlled by analyte losses as illustrated in figure 5(e). In the considered case for $n_{a,i} < 0.13$, non-radiative decay rate is lower than radiative decay rate ($\gamma_r/\gamma_0 > 1$), and the system is in overcoupled regime. Higher analyte losses ($n_{a,i} > 0.13$) increases non-radiative decay rate and shift the system into undercoupled regime ($\gamma_r/\gamma_0 < 1$). As can be seen in figure 5(e), the curve of $R(\omega_0)$ as a function of $n_{a,i}$ is steeper in the overcoupled regime meaning that $|\Delta R|$ is larger in the overcoupled system for the same change of $n_{a,i}$. In this regime, metasurfaces are associated with lower losses and larger electric field enhancement which leads to larger absorption and sensitivity.

Sensitivity enhancement provided by hollow metasurfaces is explained in figure 12 where they are compared with standard metasurfaces and the case with a bare analyte (without metasurface) just deposited on a gold film. In the latter case, as expected, the sensitivity increases with the analyte thickness. When the analyte is placed on a top of the standard metasurface, the sensitivity increases with the analyte thickness as
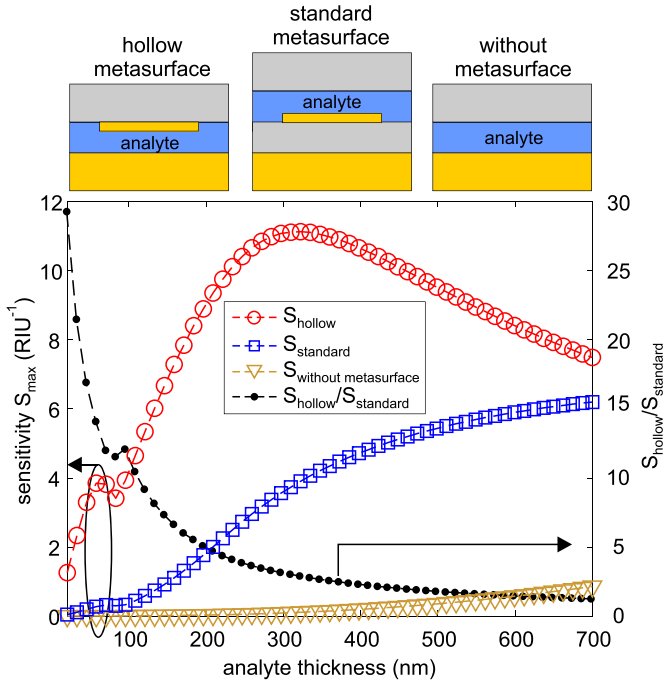

Figure 10. (a) Reflectance spectra for an analyte with varying vibrational frequency ω_v in the range $0.9\omega_0 - 1.1\omega_0$ ($t_c = 400$ nm, $P = 5$ μm). (b) The maximal reflectance change $|\Delta R|_{max}$ as a function of the normalized frequency ω_v/ω_0 for two values of the oscillator strength $S_v = (9.77 \times 10^{12} \text{ rad s}^{-1})^2$ and $S_v = (1.78 \times 10^{12} \text{ rad s}^{-1})^2$. In the latter case, $|\Delta R|_{max}$ is multiplied by 20 for better visibility.

6. Discussion

So far, the sensitivity of absorption sensors was considered for small values of the imaginary part of analyte refractive index ($n_{a,i2} \sim 0.01$). In order to assess dynamic range, properties of absorption sensors were analyzed for $n_{a,i2}$ from 0.01 up to 0.3 ($n_{a,i1} = 0$). Results in figure 11 display that the reflectance change $|\Delta R|_{max}$ saturates, while the sensitivity S_{max} decreases with $n_{a,i2}$. For $n_{a,i2} = 0.3$, S_{max} falls down by more than five times compared to the case with $n_{a,i2} = 0.01$. The sensing mechanism is based on absorption of an incident electromagnetic field within MIM cavities, whereas the absorption efficiency depends on the electric field enhancement in the cavities. Analytes with higher losses decrease the field enhancement which therefore results in a lower sensitivity for larger $n_{a,i2}$.

Figure 12. Sensitivity as a function of analyte thickness for three structures: hollow metasurface where the analyte is placed between two metallic layers in MIM metasurface, standard metasurface where the analyte is placed on the top of MIM metasurface, and bare analyte (without metasurface) placed just on thick metallic film. Considered structures are schematically depicted at the top.

well, while it is magnified due to improved absorption caused by the electric field enhancement generated by the metasurface. Finally, in the case of the hollow metasurface, the achieved magnification is further increased due to improved coupling between the analyte and the region with a high electric field enhancement. Still, in this case, the sensitivity has a peak at an analyte thickness of around 300 nm. In this case, the absorption is not simply increased for thicker analyte since the analyte thickness strongly influences the operational regime of metasurface, as previously explained. As displayed in figure 12, the sensitivity provided by the hollow metasurface operating in undercoupled regime (analyte thickness less than ∼100 nm) is enhanced by more than order of magnitude compared to the standard metasurface. The enhancement is decreased for thicker analytes, but still it is around four times at the optimal channel thickness of ∼300 nm.

Although in the previous analysis we focused on finding of an optimal regime of hollow metasurfaces, the comparison with standard metasurfaces demonstrates that undercoupled hollow metasurfaces are also very efficient absorption sensors, especially in cases when very thin analytes (less than ∼100 nm) are considered. Generally, hollow metasurfaces provide cavity enhanced sensing and detection of extremely thin films with a deep subwavelength thickness of only several tens of nanometers while the ratio of wavelength (around 10 μm) and film thickness is in the range 10^2–10^3.

The absorption sensitivity of optimal hollow metasurfaces is larger than 10 RIU^{-1}. The limit of detection of absorption sensors mainly depends on the instrumental resolution for

reflectance measurements σ_R. By considering lossless channel in the initial case ($n_{a,i1} = 0$), the aim was to estimate minimal change in the imaginary part of analyte refractive index $n_{a,i2}$ which led to reflectance change greater than (or at least equal to) the instrumental resolution, $|\Delta R| \geqslant \sigma_R$. By taking $\sigma_R \sim 0.5\%$ [43], considered hollow metasurface based absorption sensors can detect changes in the imaginary part of refractive index of ∼0.5×10^{-3}.

In the previous analysis, only normal incidence was considered. On the other hand, oblique incidence could be more favourable for measurements due to spatially separated incident and reflected beam. Calculation results for maximal reflectance change as a function of the angle of incidence show that ΔR_{max} (presented in figure S2 of supplementary material, calculated for the case from figure 5(c)) is practically constant for angles in the range of 0°–15°. Therefore, the absorption sensitivity stays preserved for small angles of incidence.

In addition to absorption sensing and SEIRA, hollow metasurfaces are very efficient for refractometric sensing as well (the real part of refractive index) [28–32]. Therefore, they provide options for multimode sensing, where the most appropriate sensing mode should be selected according to achievable sensitivity, while in some cases the combinations of both sensing modes [44] could be useful in order to acquire complementary information about analytes under investigation.

Multiband metasurfaces are of special interest for SEIRA in order to provide enhanced absorption of vibrational modes in several spectral ranges [23]. Although here we considered metasurfaces associated with a single resonance, our study can be extended by considering metasurfaces with several metallic stripes of different widths within single unit cell [45], or by designing more complex metasurfaces with two-dimensional periodicity and asymmetric metallic structures at the top [23].

The presented analysis is based on relations between geometrical parameters of MIM metasurfaces and decay rates which appear in the TCMT model. Therefore, similar optimization procedure could be applied to other metasurfaces aimed for SEIRA such as mushroom based MIM structures [42, 46, 47]. The relevance of the ratio between decay rates on achievable sensitivity in SEIRA and optimal sensor geometry was demonstrated in the case of transmissive metasurfaces as well [48]. Since many materials exhibit absorption bands in terahertz range, our approach can be also applied to terahertz metasurfaces [3, 49] aimed for absorption sensing. Since the sensing efficiency decreases with analyte losses (figure 11), hollow metasurfaces would be efficient only for the sensing of low-loss analytes at terahertz frequencies. In this work, we assume that a fluid analyte flows along the channel between two metallic layers of MIM metasurface. Recent work has demonstrated that similar metasurfaces with specially prepared liquid metal as a bottom plate can be used for the sensing and SEIRA of even solid analyte films as well [50].

7. Conclusions

In summary, hollow metasurfaces are efficient absorption sensors and substrates for SEIRA with the absorption

sensitivity larger than 10 RIU^{-1}. They provide cavity-enhanced detection of subwavelength films, with the ratio wavelength/thickness up to 10^3. The optimal metasurfaces with maximal absorption sensitivity should have period as large as possible. Optimal channel thickness (which is equal to analyte thickness) is the one which provides both high absorption and efficient coupling of an incident field into the metasurface channel. In the case of analytes with thicknesses up to ∼300 nm, the hollow metasurfaces operating at mid-infrared frequencies enhance absorption sensitivity by three orders of magnitude compared to the case of bare analyte films, and by around one order of magnitude compared to the case when the analytes are deposited on the top of traditional MIM metasurfaces. The absorption sensitivity decreases with analyte losses which therefore limit dynamic range of the imaginary part of refractive index up to around 10^{-1}. The limit of detection of the imaginary part of refractive index is below 10^{-3}.

Data availability statement

All data that support the findings of this study are included within the article (and any supplementary files).

Acknowledgments

ORCID iD

Borislav Vasić ⬤ https://orcid.org/0000-0002-1575-8004

References

[1] Willets K A and Van Duyne R P 2007 Localized surface plasmon resonance spectroscopy and sensing *Annu. Rev. Phys. Chem.* **58** 267–97

[2] Špačková B, Wrobel P, Bocková M and Homola J 2016 Optical biosensors based on plasmonic nanostructures: a review *Proc. IEEE* **104** 2380–408

[3] Beruete M and Jáuregui-López I 2020 Terahertz sensing based on metasurfaces *Adv. Opt. Mater.* **8** 1900721

[4] Hartstein A, Kirtley J R and Tsang J C 1980 Enhancement of the infrared absorption from molecular monolayers with thin metal overlayers *Phys. Rev. Lett.* **45** 201–4

[5] Brown S S 2003 Absorption spectroscopy in high-finesse cavities for atmospheric studies *Chem. Rev.* **103** 5219–38

[6] Hodgkinson J and Tatam R P 2013 Optical gas sensing: a review *Meas. Sci. Technol.* **24** 012004

[7] Chen Y, Lin H, Hu J and Li M 2014 Heterogeneously integrated silicon photonics for the mid-infrared and spectroscopic sensing *ACS Nano* **8** 6955–61

[8] Shalabney A, George J, Hutchison J, Pupillo G, Genet C and Ebbesen T W 2015 Coherent coupling of molecular resonators with a microcavity mode *Nat. Commun.* **6** 5981

[9] Hertzog M, Munkhbat B, Baranov D, Shegai T and Börjesson K 2021 Enhancing vibrational light-matter coupling strength beyond the molecular concentration limit using plasmonic arrays *Nano Lett.* **21** 1320–6

[10] Oh J, Lee K and Park Y 2021 Enhancing sensitivity in absorption spectroscopy using a scattering cavity *Sci. Rep.* **11** 14916

[11] Osawa M 2001 Surface-enhanced infrared absorption *Near-Field Optics and Surface Plasmon Polaritons* (*Topics in Applied Physics*) ed S Kawata (Berlin: Springer)

[12] Nishikawa Y, Nagasawa T, Fujiwara K and Osawa M 1993 Silver island films for surface-enhanced infrared absorption spectroscopy: effect of island morphology on the absorption enhancement *Vib. Spectrosc.* **6** 43–53

[13] Johnson E and Aroca R 1995 Surface-enhanced infrared spectroscopy of monolayers *J. Phys. Chem.* **99** 9325–30

[14] Jensen T R, Van Duyne R P, Johnson S A and Maroni V A 2000 Surface-enhanced infrared spectroscopy: a comparison of metal island films with discrete and nondiscrete surface plasmons *Appl. Spectrosc.* **54** 371–7

[15] Enders D and Pucci A 2006 Surface enhanced infrared absorption of octadecanethiol on wet-chemically prepared Au nanoparticle films *Appl. Phys. Lett.* **88** 184104

[16] Kundu J, Le F, Nordlander P and Halas N J 2008 Surface enhanced infrared absorption (SEIRA) spectroscopy on nanoshell aggregate substrates *Chem. Phys. Lett.* **452** 115–9

[17] Neubrech F, Pucci A, Cornelius T W, Karim S, García-Etxarri A and Aizpurua J 2008 Resonant plasmonic and vibrational coupling in a tailored nanoantenna for infrared detection *Phys. Rev. Lett.* **101** 157403

[18] Cubukcu E, Zhang S, Park Y-S, Bartal G and Zhang X 2009 Split ring resonator sensors for infrared detection of single molecular monolayers *Appl. Phys. Lett.* **95** 043113

[19] Pryce I M, Kelaita Y A, Aydin K and Atwater H A 2011 Compliant metamaterials for resonantly enhanced infrared absorption spectroscopy and refractive index sensing *ACS Nano* **5** 8167–74

[20] Wu C, Khanikaev A B, Adato R, Arju N, Yanik A A, Altug H and Shvets G 2012 Fano-resonant asymmetric metamaterials for ultrasensitive spectroscopy and identification of molecular monolayers *Nat. Mater.* **11** 69–75

[21] Wang T, Nguyen V H, Buchenauer A, Schnakenberg U and Taubner T 2013 Surface enhanced infrared spectroscopy with gold strip gratings *Opt. Express* **21** 9005–10

[22] D'Andrea C *et al* 2013 Optical nanoantennas for multiband surface-enhanced infrared and Raman spectroscopy *ACS Nano* **7** 3522–31

[23] Chen K, Adato R and Altug H 2012 Dual-band perfect absorber for multispectral plasmon-enhanced infrared spectroscopy *ACS Nano* **6** 7998–8006

[24] Li Y, Su L, Shou C, Yu C, Deng J and Fang Y 2013 Surface-enhanced molecular spectroscopy (SEMS) based on perfect-absorber metamaterials in the mid-infrared *Sci. Rep.* **3** 2865

[25] Ishikawa A and Tanaka T 2015 Metamaterial absorbers for infrared detection of molecular self-assembled monolayers *Sci. Rep.* **5** 12570

[26] Brown L V, Yang X, Zhao K, Zheng B Y, Nordlander P and Halas N J 2015 Fan-shaped gold nanoantennas above reflective substrates for surface-enhanced infrared absorption (SEIRA) *Nano Lett.* **15** 1272–80

[27] Ding F, Yang Y, Deshpande R A and Bozhevolnyi S I 2018 A review of gap-surface plasmon metasurfaces: fundamentals and applications *Nanophotonics* **7** 1129–56

[28] Hu X, Xu G, Wen L, Wang H, Zhao Y, Zhang Y, Cumming D R S and Chen Q 2016 Metamaterial absorber

J. Phys. D: Appl. Phys. **55** (2022) 315105

B Vasić

integrated microfluidic terahertz sensors *Laser Photonics Rev.* **10** 962–9

[29] Soltani A, Neshasteh H, Mataji-Kojouri A, Born N, Castro-Camus E, Shahabadi M and Koch M 2016 Highly sensitive terahertz dielectric sensor for small-volume liquid samples *Appl. Phys. Lett.* **108** 191105

[30] Lan F *et al* 2019 Dual-band refractometric terahertz biosensing with intense wave-matter-overlap microfluidic channel *Biomed. Opt. Express* **10** 3789–99

[31] Shih K, Ren Z, Wang C and Lee C 2019 MIR plasmonic liquid sensing in nano-metric space driven by capillary force *J. Phys. D: Appl. Phys.* **52** 394001

[32] Vasić B and Isić G 2021 Refractive index sensing with hollow metal-insulator-metal metasurfaces *J. Phys. D: Appl. Phys.* **54** 285106

[33] Le T H H and Tanaka T 2017 Plasmonics-nanofluidics hybrid metamaterial: an ultrasensitive platform for infrared absorption spectroscopy and quantitative measurement of molecules *ACS Nano* **11** 9780–8

[34] Le T H H, Morita A, Mawatari K, Kitamori T and Tanaka T 2018 Metamaterials-enhanced infrared spectroscopic study of nanoconfined molecules by plasmonics-nanofluidics hybrid device *ACS Photonics* **5** 3179–88

[35] Xu J, Ren Z, Dong B, Liu X, Wang C, Tian Y and Lee C 2020 Nanometer-scale heterogeneous interfacial sapphire wafer bonding for enabling plasmonic-enhanced nanofluidic mid-infrared spectroscopy *ACS Nano* **14** 12159–72

[36] Hugonin J P and Lalanne P 2005 *RETICOLO Code for Grating Analysis* (Palaiseau: Institute d'Optique)

[37] Hao J, Zhou L and Qiu M 2011 Nearly total absorption of light and heat generation by plasmonic metamaterials *Phys. Rev. B* **83** 165107

[38] Vasić B 2021 Semi-analytical approach for refractive index sensors based on reflective metasurfaces *J. Opt. Soc. Am.* B **38** 1676–83

[39] Fan S, Suh W and Joannopoulos J D 2003 Temporal coupled-mode theory for the Fano resonance in optical resonators *J. Opt. Soc. Am.* A **20** 569–72

[40] Isić G and Gajić R 2014 Geometrical scaling and modal decay rates in periodic arrays of deeply subwavelength terahertz resonators *J. Appl. Phys.* **116** 233103

[41] Qu C *et al* 2015 Tailor the functionalities of metasurfaces based on a complete phase diagram *Phys. Rev. Lett.* **115** 235503

[42] Hwang I, Yu J, Lee J, Choi J-H, Choi D-G, Jeon S, Lee J and Jung J-Y 2018 Plasmon-enhanced infrared spectroscopy based on metamaterial absorbers with dielectric nanopedestals *ACS Photonics* **5** 3492–8

[43] Adato R, Aksu S and Altug H 2015 Engineering mid-infrared nanoantennas for surface enhanced infrared absorption spectroscopy *Mater. Today* **18** 436–46

[44] Chen X, Wang C, Yao Y and Wang C 2017 Plasmonic vertically coupled complementary antennas for dual-mode infrared molecule sensing *ACS Nano* **11** 8034–46

[45] Wu C and Shvets G 2012 Design of metamaterial surfaces with broadband absorbance *Opt. Lett.* **37** 308–10

[46] Miao X, Yan L, Wu Y and Liu P Q 2021 High-sensitivity nanophotonic sensors with passive trapping of analyte molecules in hot spots *Light Sci. Appl.* **10** 5

[47] Hwang I, Kim M, Yu J, Lee J, Choi J-H, Park S A, Chang W S, Lee J and Jung J-Y 2021 Ultrasensitive molecule detection based on infrared metamaterial absorber with vertical nanogap *Small Methods* **5** 2100277

[48] Wei J, Li Y, Chang Y, Hasan D M N, Dong B, Ma Y, Qiu C-W and Lee C 2019 Ultrasensitive transmissive infrared spectroscopy via loss engineering of metallic nanoantennas for compact devices *ACS Appl. Mater. Interfaces* **11** 47270–8

[49] Shen S, Liu X, Shen Y, Qu J, Pickwell-MacPherson E, Wei X and Sun Y 2022 Recent advances in the development of materials for terahertz metamaterial sensing *Adv. Opt. Mater.* **10** 2101008

[50] Miao X, Luk T S and Liu P Q 2022 Liquid-metal-based nanophotonic structures for high-performance SEIRA sensing *Adv. Mater.* **34** 2107950

Semi-analytical approach for refractive index sensors based on reflective metasurfaces

Borislav Vasić

Institute of Physics Belgrade, University of Belgrade, Pregrevica 118, 11080 Belgrade, Serbia (bvasic@ipb.ac.rs)

We present a semi-analytical approach for the analysis and design of refractive index sensors based on metal–insulator–metal (MIM) metasurfaces. While numerical methods require extensive calculations for all values of geometrical parameters, the semi-analytical approach provides straightforward guidelines for a design of optimal metasurfaces with maximized sensitivity. Semi-analytical formulas for refractive index sensitivities are derived from equations of the temporal coupled mode theory and standing-wave resonance model. They require three numerically calculated parameters (resonant frequency and radiative and non-radiative decay rates of the resonant mode), obtained by the fitting of reflectance spectra. Generality of the presented approach allows us to consider the operation of metasurface sensors in three different interrogation methods: spectral (frequency), intensity (reflectance), and phase. Validity of the proposed approach is confirmed by a good agreement with numerical results. Starting from semi-analytical formulas, we derive working frequencies of metasurface based sensors, prove that the critical coupling with equal decay rates of the resonant mode is the optimal working regime, and demonstrate that optimal MIM metasurfaces should have periods as large as possible with the thickness of MIM cavities determined by the critical coupling condition. © 2021 Optical Society of America

https://doi.org/10.1364/JOSAB.422070

1. INTRODUCTION

Metasurfaces are artificial electromagnetic structures consisting of planar arrays of subwavelength metallo–dielectric resonators. Refractive index sensors based on metasurfaces [1–4] belong to the group of resonant and label-free photonic sensors together with surface plasmon resonance [5,6] and localized surface plasmon resonance sensors [7–9], Fabry–Perot [10–13] and photonic crystal cavities [14–17], and whispering gallery mode sensors [18–21]. All these structures generate a large electric field enhancement in the vicinity of their resonances, while the interaction between the enhanced electric field and surrounding medium under investigation results in a spectral shift of the resonances. By measurement of the induced spectral shift, changes in refractive index in the surrounding medium can be detected.

The efficiency of resonant photonic sensors is quantified through the refractive index sensitivity defined as a change of a measured signal for a given refractive index change. Depending on the measured signal, we distinguish the sensing with spectral (wavelength/frequency), intensity (reflectance/transmittance), and phase interrogation. A straightforward way to determine sensitivity is to numerically calculate the sensor response for two refractive index values. Still, the physics behind a sensing mechanism remains unclear with such an approach. Additionally, to find an optimal sensing structure and working regime, it is necessary to sweep through all possible values of geometrical

parameters and find a set of the parameters that provides maximal sensitivity. To avoid such extensive optimization procedures based on numerical calculations, theoretical models are strongly desired. They not only give physical insight, but provide general and quick guidelines for the design and optimization of sensing structures.

So far, theoretical models have been developed for surface plasmon resonance sensors based on flat [22–24] and nanostructured metallic films [25,26], and for sensors based on metallic nanoparticles with localized surface plasmon resonances [27,28] and with surface lattice resonances [29]. While these models are mainly applicable for specific geometry only, the perturbation theory provides the most general model for the spectral sensitivity of plasmonic structures [30–32] and whispering gallery mode sensors [33]. Still, all these models were developed for spectral interrogation only, while a universal model for refractive index sensitivities with intensity and phase interrogation is still lacking.

Metasurface based sensors are especially attractive since their properties can be controlled by reshaping individual resonators, which provides novel functionalities and extends the scope of their applicability. For example, operating frequencies of metasurfaces can be adjusted simply by scaling the geometry of building unit cells, which is especially important when the operation frequency has to overlap with absorption bands of an analyte [34]. Chiral metasurfaces facilitate efficient sensing of chiral analytes [35,36], anisotropic metasurfaces

can be employed for polarization conversion based sensing [37,38], and the deep subwavelength thicknesses of metal–insulator–metal (MIM) cavities provide enhanced light–matter interaction and sensing with MIM metasurfaces [39–42]. Still, due to a more complex geometry of individual resonators, the refractive index sensitivity of metasurfaces is dominantly calculated numerically, while the model based on the standing-wave approach [43,44] is used only for spectral sensitivity and specific geometries.

To fill this gap, here we derive semi-analytical formulas for the reflectance and phase sensitivities of reflective metasurfaces based on MIM cavities. The starting points are general expressions for the reflectance and phase derived from the temporal coupled mode theory (TCMT) [45–49], whereas the equation for spectral sensitivity is derived from the standing-wave resonance model [50–52]. Derived semi-analytical formulas require numerically calculated resonant frequency and radiative and non-radiative decay rates of the resonant mode, obtained by the fitting of reflectance spectra. By analyzing the semi-analytical formulas, we derive guidelines to design optimal metasurfaces and find optimal operating regimes for all three interrogation methods.

2. REFRACTIVE INDEX SENSITIVITIES: A SEMI-ANALYTICAL APPROACH

As an example of reflective metasurfaces, here we consider MIM structures. They are relatively simple for fabrication and scalable, and therefore applicable in a broad frequency range, and they are associated with a very high refractive index sensitivity for analytes infiltrated into MIM cavities, as recently demonstrated [39–42,53]. We investigate the simplest case of a MIM metasurface with one-dimensional periodicity. The cross-section of the unit cell with a period P is given in Fig. 1(a). In this configuration, a fluid analyte with refractive index n_a is placed in the channel (channel thickness denoted by t_c) between parallel gold ribbons at the top (width and thickness of the ribbons denoted by w_m and t_m, respectively) and thick gold plate at the bottom. The channel is the region with an enhanced electric field responsible for a high refractive index sensitivity. The whole metasurface is encapsulated by a polymer layer (with a thickness t_p) that mechanically supports gold ribbons and simultaneously encloses a fluid cell.

The frequency sensitivity S_f is determined by the following expression:

$$S_f = \mathrm{d}f_0/\mathrm{d}n_a, \tag{1}$$
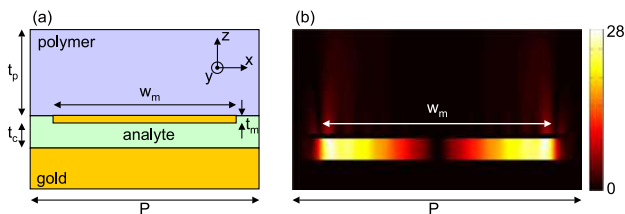
Fig. 1. (a) Cross-section of the unit cell of considered MIM metasurface with indicated all geometrical parameters. (b) Spatial distribution of the electric field enhancement ($|E_z/E_0|$) for the fundamental cavity mode.

where f_0 is the resonant frequency, and n_a is the refractive index of the analyte that infiltrates the MIM cavity. To determine S_f, the cavity or standing-wave resonance model is employed [50–52]. Here the resonant mode is represented as a standing wave with odd multiples N of the half of wavelength along metallic ribbon width w_m. Distribution of the electric field enhancement $|E_z/E_0|$ for the fundamental mode with $N = 1$ is given in Fig. 1(b). The node with zero field is located at the center, whereas two anti-nodes with high fields are located near the edges of the metallic ribbon. The resonant frequency for the fundamental mode is then given by [50]

$$f_0 = \frac{c}{2w_m n_a}, \tag{2}$$

where c is the speed of light in vacuum. According to Eqs. (1) and (2), the expression for frequency sensitivity reads

$$S_f = -\frac{c}{2w_m n_a^2}, \tag{3}$$

which is further simplified to the following form:

$$S_f = -\frac{f_0}{n_a}. \tag{4}$$

According to TCMT [45–49], reflectance R and phase Φ of a reflective, single-channel resonator (transmission channel is disabled, therefore $T = 0$) are

$$R = 1 - \frac{4\gamma_0\gamma_r}{(f - f_0)^2 + (\gamma_0 + \gamma_r)^2}, \tag{5}$$

$$\Phi = \mathrm{a}\tan\left(\frac{-2\gamma_r(f - f_0)}{(f - f_0)^2 + \gamma_0^2 - \gamma_r^2}\right), \tag{6}$$

where γ_r and γ_0 are the radiative and non-radiative decay rates of the resonant mode, respectively. The reflectance and phase sensitivities, S_R and S_Φ, can be obtained as derivatives of R and Φ with respect to n_a in the following way:

$$S_Y = \frac{\mathrm{d}Y}{\mathrm{d}n_a} = \frac{\partial Y}{\partial f_0}\frac{\partial f_0}{\partial n_a} + \frac{\partial Y}{\partial \gamma_r}\frac{\partial \gamma_r}{\partial n_a} + \frac{\partial Y}{\partial \gamma_0}\frac{\partial \gamma_0}{\partial n_a}, \tag{7}$$

where $Y = R, \Phi$. Here we prove that the second and third terms from Eq. (7) are at least an order of magnitude smaller than the first one. Therefore, the second and third terms from Eq. (7) can be neglected, while the formula for the sensitivity simplifies to

$$S_Y \approx \frac{\partial Y}{\partial f_0}\frac{\partial f_0}{\partial n_a} = S_{Y,f}S_f. \tag{8}$$

In the previous formula, S_f is the frequency sensitivity, whereas $S_{Y,f}$ stands for the reflectance and phase sensitivities with respect to frequency given with the following expressions:

$$S_{R,f} = \frac{\partial R}{\partial f_0} = \frac{-8\gamma_r\gamma_0(f - f_0)}{((f - f_0)^2 + (\gamma_0 + \gamma_r)^2)^2}, \tag{9}$$

$$S_{\Phi,f} = \frac{\partial \Phi}{\partial f_0} = \frac{2\gamma_r(\gamma_0^2 - \gamma_r^2 - (f - f_0)^2)}{((f - f_0)^2 + \gamma_0^2 - \gamma_r^2)^2 + 4\gamma_r^2(f - f_0)^2}. \tag{10}$$

Since decay rates and resonant frequency are determined numerically, the model for refractive index sensitivities is semi-analytical.

In order to prove validity of the simplified Eq. (8), first we consider the partial derivatives with respect to the analyte refractive index n_a in Eq. (7): $\partial f_0/\partial n_a$, $\partial \gamma_r/\partial n_a$, and $\partial \gamma_0/\partial n_a$. According to TCMT, the resonance width, defined as the full width at half maximum (FWHM), is FWHM $= 2(\gamma_r + \gamma_0)$. The relation between the resonant frequency and decay rates is then obtained from the formula for the quality factor Q of resonant modes:

$$Q = \frac{f_0}{\text{FWHM}} = \frac{f_0}{2(\gamma_0 + \gamma_r)}, \qquad \textbf{(11)}$$

while the relation between the partial derivatives is the following:

$$\frac{\partial(\gamma_0 + \gamma_r)}{\partial n_a} = \frac{1}{2Q}\left(\frac{\partial f_0}{\partial n_a} - \frac{f_0}{Q}\frac{\partial Q}{\partial n_a}\right). \qquad \textbf{(12)}$$

The non-radiative decay rate γ_0 is related to the losses in metallic layers since analytes in this study are lossless. According to the perturbation theory, the mode profile of the electric field does not change significantly with small changes in the cavity refractive index n_a. As a result, the metallic losses are approximately constant for varying n_a. Therefore, it is reasonable to assume that $\partial \gamma_0/\partial n_a \approx 0$ [proven by numerical results presented in Fig. S1(d) of Supplement 1]. Going back to Eq. (12) and taking into account that quality factors of metasurface resonances are typically around 10 [proven by numerical results given in Fig. S1(c) of Supplement 1], in the first approximation, it is reasonable to neglect the second term from the right-hand side of Eq. (12). Then according to the simplified expression $\partial \gamma_r/\partial n_a \approx (\partial f_0/\partial n_a)/(2Q)$ and again taking into account that Q is around 10, we get the following approximative relation between the partial derivatives with respect to n_a: $|\partial \gamma_r/\partial n_a| \ll |\partial f_0/\partial n_a|$. The previous approximation is confirmed by numerical calculations for decay rates as a function of n_a. The results are presented in Fig. S1(d) of Supplement 1. They also confirm the validity of the initial approximation where the second term from the right-hand side of Eq. (12) was neglected.

Next, we consider the ratios between the partial derivatives of reflectance [full mathematical expressions given in Eqs. (S2)–(S4) of Supplement 1] and phase [full mathematical expressions given in Eqs. (S6)–(S8) of Supplement 1] with respect to the resonant frequency and decay rates. Below, it is demonstrated that the optimal operating frequency for the reflectance interrogation is $f_0 \pm (\gamma_r + \gamma_0)/\sqrt{3}$, whereas the optimal operating regime is achieved at the critical coupling point with equal decay rates $\gamma_r = \gamma_0$. At these conditions, the ratios between $|\partial R/\partial f_0|$ and $|\partial R/\partial \gamma_r|$, and between $|\partial R/\partial f_0|$ and $|\partial R/\partial \gamma_0|$ are $\sqrt{3}$; therefore, $|\partial R/\partial f_0| > |\partial R/\partial \gamma_r|, |\partial R/\partial \gamma_0|$. In the case of the phase interrogation, at the optimal operating frequency f_0, $|\partial \Phi/\partial f_0|$ has some finite value, while both partial derivatives $|\partial \Phi/\partial \gamma_r|$ and $|\partial \Phi/\partial \gamma_0|$ are equal to zero; therefore, $|\partial \Phi/\partial f_0| > |\partial \Phi/\partial \gamma_r|, |\partial \Phi/\partial \gamma_0|$. Numerically calculated partial derivatives of reflectance and phase with respect to the resonant frequency and decay rates and as a function of frequency are presented in Fig. S2 of Supplement 1.

The numerical results confirm relations between the partial derivatives obtained by the previous theoretical analysis.

According to the previous discussion, the absolute value of the partial derivative of the resonant frequency with respect to the analyte refractive index $|\partial f_0/\partial n_a|$ is at least an order of magnitude larger than the corresponding partial derivatives of decay rates $|\partial \gamma_r/\partial n_a|$ and $|\partial \gamma_0/\partial n_a|$. At the same time, the absolute value of the partial derivative of reflectance (phase) with respect to the resonant frequency $|\partial R/\partial f_0|$ ($|\partial \Phi/\partial f_0|$) is greater than or similar to the corresponding derivatives of reflectance (phase) with respect to decay rates $|\partial R/\partial \gamma_r|$ and $|\partial R/\partial \gamma_0|$ ($|\partial \Phi/\partial \gamma_r|$ and $|\partial \Phi/\partial \gamma_0|$). Therefore, the first term in Eq. (7) for the reflectance and phase sensitivity is at least an order of magnitude larger than the other two, which allows us to neglect the second and third terms and use the approximative Eq. (8).

3. VALIDITY OF THE SEMI-ANALYTICAL APPROACH

To test validity of the presented semi-analytical approach, numerical calculations were performed using rigorous coupled wave analysis implemented in Reticolo software [54]. Here the operation at terahertz frequencies is considered since similar structures have been dominantly fabricated at far- and mid-infrared frequencies [39–42]. Reticolo software aims for the analysis of periodic electromagnetic structures. Only the unit cell is defined, which is periodically repeated simulating an infinite structure. We consider a metasurface with one-dimensional periodicity along x axis, while the structure is invariant along the y axis, meaning that the metallic ribbons are infinitely long along this axis. The initial geometrical parameters of the unit cell in Fig. 1(a) are the following: unit cell size (period) $P = 100\ \mu m$, metallic ribbon width and thickness $w_m = 80\ \mu m$ and $t_m = 0.3\ \mu m$, respectively, thickness of the channel with an analyte to be sensed $t_c = 1.3\ \mu m$, and thickness of the encapsulating polymer layer $t_p = 40\ \mu m$. The normal incidence is considered, while the electric field of the incident field is polarized along the x axis. Material parameters for gold (with Drude parameters plasma frequency $\omega_p = 1.37 \cdot 10^{16}$ rad/s and collision frequency $\gamma_c = 4.05 \cdot 10^{13}$ rad/s) and the encapsulating polymer layer (with a refractive index $1.8 + j0.06$) at terahertz frequencies are taken from Refs. [55,56], respectively. The initial refractive index of the analyte placed in the MIM cavity (channel) is $n_a = 1.5$, which is a common refractive index of transparent liquid analytes at terahertz frequencies [40].

Numerically calculated sensitivities are determined as changes in the output signal (resonant frequency, reflectance, or phase) observed for a small variation Δn_a from the initial value of 1.5. The numerically calculated S_f is obtained as the ratio between the frequency shift of the resonant mode $\Delta f_0 = f_0(n_a + \Delta n_a) - f_0(n_a)$ and refractive index change $\Delta n_a = 0.05$. The numerically calculated S_R was obtained as $\Delta R/\Delta n_a$, with $\Delta R = R(n_a + \Delta n_a) - R(n_a)$ and $\Delta n_a = 0.001$. S_f was numerically calculated as the ratio $\Delta \Phi/\Delta n_a$, where $\Delta \Phi = \Phi(n_a + \Delta n_a) - \Phi(n_a)$ and $\Delta n_a = 0.001$.

To semi-analytically calculate S_f [Eq. (4)], $S_{R,f}$ [Eq. (9)], and $S_{\Phi,f}$ [Eq. (10)] as a function of frequency, three parameters that completely describe the resonant mode, f_0, γ_r, and γ_0, were calculated by fitting the formula for the reflectance derived from TCMT [Eq. (5)] to numerically calculated reflectance. A detailed explanation of the fitting procedure is given in Ref. [48]. In Section 3.B an example of the fitting is presented in Fig. 3(a). As can be seen, the fit and the numerically calculated reflectance perfectly agree, which demonstrates that the model based on TCMT well describes the considered metasurface.

A. Frequency Interrogation

A comparison between the resonant frequency f_0 calculated by Eq. (2) and numerically is presented in Fig. 2(a). As can be seen, both curves exhibit the same trend: f_0 is inversely proportional to n_a. Still, the theoretical model overestimates f_0 by around 10%. The observed difference appears due to a small spatial extension of the cavity mode beyond the edges of the metallic ribbon [57], as can be seen in Fig. 1(b). As a result, the cavity is effectively extended, w_m from Eq. (2) is effectively increased, and the resonant frequency is decreased.

The calculation results for the refractive index sensitivity in frequency interrogation are displayed in Fig. 2(b). The theoretically calculated curve for $|S_f|$ using Eq. (3) exhibits a good agreement with the numerics, but still differs by around 10%–15%. Better accuracy is achieved by the semi-analytical Eq. (4), where f_0 is numerically calculated. As can be seen in Fig. 2(b), the difference compared to the numerics is now decreased to around only 5%. Therefore, hereafter $|S_f|$ is calculated as f_0/n_a, with f_0 obtained numerically.

B. Reflectance Interrogation

Semi-analytical results for $|S_{R,f}|$ [Eq. (9)] are compared with numerics in Fig. 3(b), and they exhibit excellent agreement. Since $|\partial R/\partial f_0| = |\partial R/\partial f|$, the numerical calculations for $|S_{R,f}|$ were done by differentiating the reflectance spectrum $R(f)$ in Fig. 3(a). The working frequency f_R for the reflectance interrogation is defined as a frequency where $|S_{R,f}|$ has a maximum. The resonant frequency is obviously not appropriate as a working point since $|S_{R,f}(f = f_0)|$ is zero. On the other hand, the working frequency is located symmetrically around f_0 at

$$f_R = f_0 \pm (\gamma_r + \gamma_0)/\sqrt{3}. \tag{13}$$

The derivation for f_R from Eq. (9) is given in Section 2 of Supplement 1. The validity of Eq. (13) was tested for a resonator with varying decay rates controlled by the channel thickness
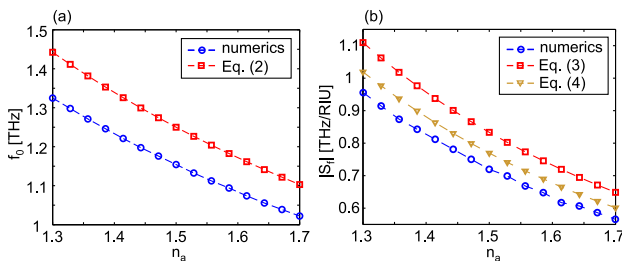
Fig. 2. (a) Resonant frequency f_0 and (b) frequency sensitivity $|S_f|$ as a function of analyte refractive index n_a.
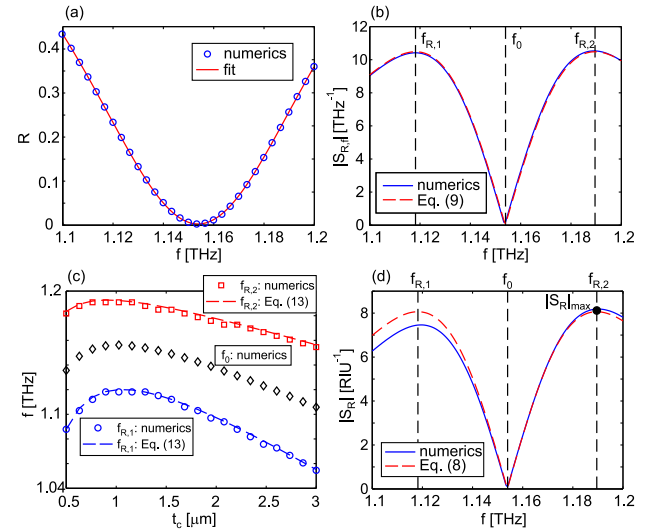
Fig. 3. (a) Reflectance R and (b) sensitivity $|S_{R,f}|$ as a function of frequency. (c) Working frequency f_R as a function of channel thickness t_c ($f_{R,1} = f_0 - (\gamma_r + \gamma_0)/\sqrt{3}$ and $f_{R,2} = f_0 + (\gamma_r + \gamma_0)/\sqrt{3}$) and (d) sensitivity $|S_R|$ as a function of frequency. $|S_R|_{\max}$ marked in (d) stands for the maximal value of $|S_R|$ obtained at the operating frequency: $|S_R|_{\max} = \max\{|S_R(f = f_R)|\}$.

t_c as displayed in Fig. 3(c). The numerically calculated f_R was obtained as a frequency that maximizes $|S_{R,f}|$. As can be seen, the semi-analytical formula perfectly agrees with the numerics and therefore offers a straightforward way to determine the working frequency for the sensing with reflectance interrogation.

The absolute value of reflectance sensitivity $|S_R|$ calculated using the semi-analytical model in Eq. (8) with known $S_{R,f}$ and S_f is given in Fig. 3(d). As in the previous case, the semi-analytical model displays a very good agreement with the numerics, while the peaks of $|S_R|$ are reached at the working frequency f_R.

C. Phase Interrogation

The semi-analytical model for $|S_{\Phi,f}|$ [Eq. (10)] exhibits an excellent agreement with numerical calculations, as depicted in Fig. 4(a). Since $|\partial \Phi/\partial f| = |\partial \Phi/\partial f_0|$, $|S_{\Phi,f}|$ was numerically calculated by differentiating the phase spectrum $\Phi(f)$ [an example given in Fig. 4(a)]. The peak of $|S_{\Phi,f}|$ is reached at the resonant frequency f_0 where the phase curve has maximal slope. Therefore, opposite to the reflectance interrogation, $f_\Phi = f_0$ is the working frequency for the phase interrogation. According to Eq. (8), the sensitivity S_Φ is obtained by multiplying $S_{\Phi,f}$ by S_f. The absolute value $|S_\Phi|$ is presented in Fig. 4(b). It has the same shape as $S_{\Phi,f}$ with the maximum at f_0. As in the previous case of S_R, the semi-analytical formula very well reproduces numerical results.

D. Validity for Wider Range of Refractive Index Change

To calculate refractive index sensitivities numerically, it is necessary to perform calculations for two refractive index values
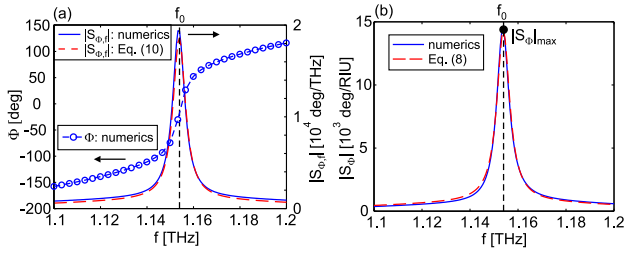
Fig. 4. (a) Phase Φ and sensitivity $|S_{\Phi,f}|$, and (b) sensitivity $|S_\Phi|$ as a function of frequency. $|S_\Phi|_{max}$ marked in (b) stands for the maximal value of $|S_\Phi|$ obtained at the operating frequency: $|S_\Phi|_{max} = \max\{|S_\Phi(f = f_\Phi)|\}$.

of an analyte, n_a and $n_a + \Delta n_a$. On the other hand, the proposed semi-analytical approach provides formulas to determine sensitivities by knowing properties of the resonant mode just for single n_a. Still, the formulas for refractive index sensitivities [Eqs. (1) and (8)] are based on derivatives of f_0 with respect to n_a and R/Φ with respect to f. Therefore, they are per definition valid only for infinitesimally small changes in refractive index around the working point defined with $n_a = 1.5$. To test their validity for a broader range of refractive index values, the semi-analytical results are compared with numerical calculations for Δn_a in the following ranges: -0.2 to $+0.2$ for S_f, -0.3 to $+0.3$ for S_R, and -0.05 to $+0.05$ for S_Φ. The comparison is presented in Fig. 5. Hereafter, $|S_R|_{max}$ [marked in Fig. 3(d)] and $|S_\Phi|_{max}$ [marked in Fig. 4(b)] stand, respectively, for the maximal values of reflectance and phase sensitivities obtained at operating frequencies $|S_R|_{max} = \max\{|S_R(f = f_R)|\}$ and $|S_\Phi|_{max} = \max\{|S_\Phi(f = f_\Phi)|\}$.

Numerically calculated $|S_f|$ approximately linearly increases (decreases) for negative (positive) Δn_a, as depicted in Fig. 5(a). According to the theoretical formula in Eq. (4), the spectral sensitivity is inversely proportional to n_a, which explains the observed increase (decrease) in $|S_f|$ for smaller (larger) values of n_a and negative (positive) values of Δn_a. The semi-analytical formula in Eq. (4) gives a correct value for $|S_f|$ only when $\Delta n_a \to 0$. Still, for $|\Delta n_a| < 0.1$, the deviation compared to the numerics is less than approximately 10%.

Changes in $|S_R|_{max}$ and $|S_\Phi|_{max}$ with Δn_a are presented in Figs. 5(b) and 5(c), respectively. The semi-analytical formula [Eq. (8)] well predicts both reflectance and phase sensitivities when Δn_a is close to zero. Here both sensitivities reach the maximal values. It should be noted that the considered MIM geometry is slightly detuned from the critical coupling point

(achieved by using a channel thickness $t_c = 1.3$ μm, a bit thicker than $t_{cc} = 1.25$ μm for the critically coupled structure). Such a detuned metasurface is more realistic in experiments, while in theoretical/numerical analysis, it allows us to avoid divergence of the phase sensitivity for $\Delta n_a \to 0$. According to numerical results, for larger Δn_a, both sensitivities symmetrically decrease. Still, for $|\Delta n_a| < 0.1$, the reflectance sensitivity decreases by less than approximately 20%. A similar decrease in phase sensitivity is achieved for a much narrower range of $|\Delta n_a| < 0.01$.

More pronounced decay of the phase sensitivity is a result of a much narrower dynamic range of the phase interrogation method. $|S_\Phi|_{max}$ decays faster since $|S_{\Phi,f}|$ diverges at the critical coupling point, while the slope of phase $\Phi(f)$ becomes very large (theoretically infinite), as depicted in Fig. 4(a). Even a small refractive index change then easily shifts the system from the linear regime (the spectral region with the linear slope of $\Phi(f)$ around f_0) to spectral regions where the phase slope is much lower, thus resulting in a smaller phase change (for a given refractive index change) and lower phase sensitivity.

E. Applicability of the Semi-Analytical Approach

The proposed semi-analytical approach for the analysis of refractive index sensitivities of reflective metasurfaces is based on TCMT, which is derived for the case of low-loss electromagnetic resonators. Therefore, the presented approach is valid if the losses in the metallic parts are low (we consider lossless analytes). This condition is fulfilled at terahertz frequencies. Still, at higher frequencies, the losses in metals are increased. In practice, the presented approach is valid as long as numerically calculated reflectance spectra can be fitted by Eq. (5) of the TCMT model, and it was demonstrated that the fitting procedure nicely reproduces reflectance spectra of MIM metasurfaces even at optical frequencies [58]. Possible deviations between the TCMT model and numerics would result in just certain quantitative deviations of the resulting refractive index sensitivity obtained using the semi-analytical model compared to those calculated numerically.

Angular interrogation is also a very common detection method for surface plasmon resonance based sensors [59]. In this method, measurements are performed for a range of angles of incidence. The excitation of surface plasmon polaritons is associated with a dip in the angular reflectance, while the angle of incidence at the reflectance dip is taken as the sensor output. Still, here the presented approach cannot be applied on sensing with angular interrogation due to a lack of formulas connecting
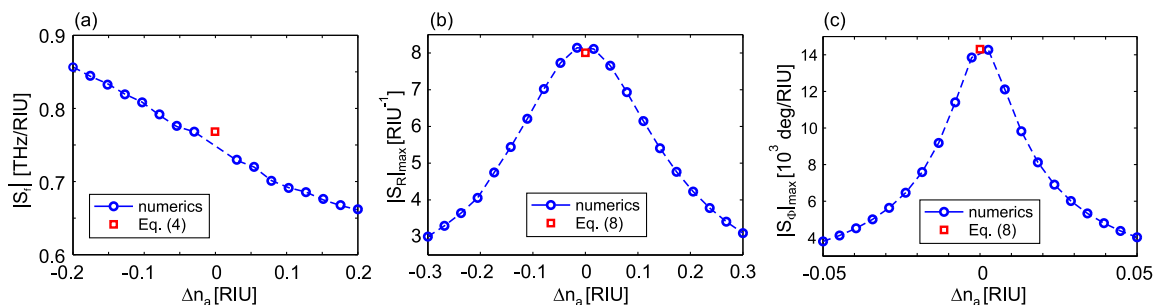

Fig. 5. (a) Spectral sensitivity $|S_f|$, and the maximum of (b) reflectance sensitivity $|S_R|_{max}$ and (c) phase sensitivity $|S_\Phi|_{max}$ as a function of the refractive index change Δn_a with respect to the initial $n_a = 1.5$. The results of the semi-analytical models are given for $\Delta n_a = 0$.

the angle of incidence and three parameters of the TCMT based model: resonant frequency and radiative and non-radiative decay rates. Generally, the angular dispersion in metasurfaces arises due to the coupling between adjacent meta-atoms and due to the radiation property of a single meta-atom [60], and both effects can be studied using only numerical calculations.

4. OPTIMAL STRUCTURE

In this section, optimal working regimes for all three interrogation methods are derived based on the proposed semi-analytical approach. The working regime of MIM based metasurfaces is determined by the ratio between radiative and non-radiative decay rates, which is controlled by two geometrical parameters: channel thickness t_c and period P [47,48]. The third geometrical parameter of MIM cavities, metallic ribbon width w_m, defines the resonant frequency according to Eq. (2). γ_r and γ_0 as a function of t_c and P are plotted in Figs. 6(a) and 6(b), respectively. Dashed lines connect points in the (t_c, P) plane, which are associated with critically coupled metasurfaces having equal decay rates $\gamma_r = \gamma_0$. To further clarify dependence of decay rates on t_c and P, characteristic cross-sections of the previous maps are presented in Figs. 6(c) (γ_r and γ_0 as a function of t_c and for $P = 100 \, \mu m$) and 6(d) (γ_r and γ_0 as a function of P and for $t_c = 1.39 \, \mu m$). As can be seen, γ_r is directly proportional and γ_0 is inversely proportional to t_c. On the other hand, γ_0 is practically independent of P, whereas γ_r is inversely proportional to P. Therefore, dependence of γ_0 and γ_r on t_c and P can be mathematically expressed in the following way:

$$\gamma_0 = \frac{\alpha_0}{t_c}, \tag{14}$$

$$\gamma_r = \alpha_r t_c = \frac{\beta t_c}{P}, \tag{15}$$

where α_0, α_r, and β are fitting constants, while $\alpha_r = \beta/P$. Recently, we numerically demonstrated enhanced refractive index sensitivities of reflective MIM metasurfaces at the critically coupled point associated with equal decay rates $\gamma_r = \gamma_0$ [53]. According to Eqs. (14) and (15), the channel thickness at the critical coupling point t_{cc} is

$$t_{cc} = \sqrt{\alpha_0/\alpha_r} = \sqrt{\alpha_0 P/\beta}. \tag{16}$$

The spectral sensitivity of MIM metasurfaces is independent of their working regime since the sensitivity is determined by the ratio between the resonant frequency and analyte refractive index as given by Eq. (4). The figure of merit (FOM) factor for the spectral interrogation is defined as FOM $= S_f/$FWHM. Since FWHM $= 2(\gamma_0 + \gamma_r)$, the FOM factor obviously depends on the working regime and the ratio between γ_0 and γ_r. By substituting formulas for decay rates [Eqs. (14) and (15)] into the expression for FWHM, it follows that the FWHM is minimized at the critical coupling point for channel thickness equal to t_{cc} (derivations given in Section 3.A of Supplement 1). In that case, FWHM is proportional to $\sqrt{(\alpha\beta)/P}$, and the FOM factor is proportional to $\sqrt{P/(\alpha\beta)}$ (derivations given in Section 3.A of Supplement 1).

The maximal reflectance sensitivity $|S_R|_{max}$ is achieved at $f_w = f_0 \pm (\gamma_r + \gamma_0)/\sqrt{3}$. At that frequency, according to
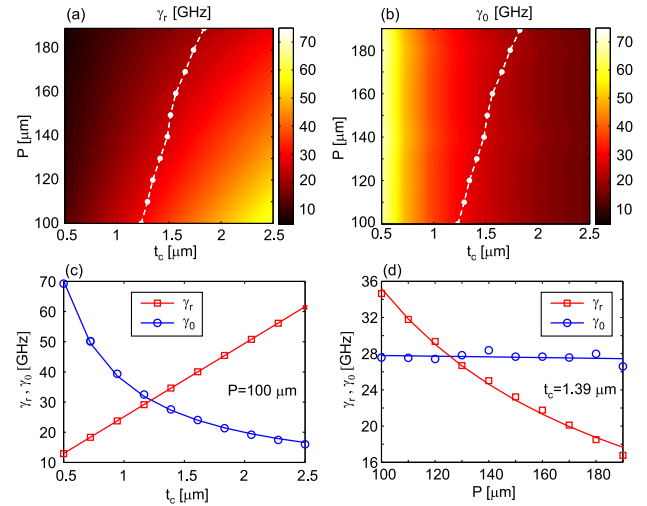

Fig. 6. (a) Radiative decay rate γ_r and (b) non-radiative decay rate γ_0 as a function of channel thickness t_c and period P. Dashed lines connect points associated with critically coupled metasurfaces having equal decay rates $\gamma_r = \gamma_0$. (c) γ_r and γ_0 as a function of t_c and for $P = 100 \, \mu m$, and (d) γ_r and γ_0 as a function of P and for $t_c = 1.39 \, \mu m$.

Eq. (9), $|S_R|_{max}$ is proportional to $\gamma_r \gamma_0/(\gamma_r + \gamma_0)^3|S_f|$. By substituting formulas for decay rates [Eqs. (14) and (15)] into the previous expression, it follows that $|S_R|_{max}$ is maximized exactly at the critical coupling condition for channel thickness equal to t_{cc} (derivations given in Section 3.B of Supplement 1). For that value of the channel thickness, the maximal reflectance sensitivity $|S_R|_{max}$ is proportional to $\sqrt{P/(\alpha\beta)}$ (derivations given in Section 3.B of Supplement 1).

The maximal phase sensitivity $|S_\Phi|_{max}$ is achieved at the resonant frequency f_0. According to Eq. (10), $|S_\Phi|_{max}$ at f_0 is equal to $2\gamma_r/(\gamma_0^2 - \gamma_r^2)|S_f|$. The phase sensitivity is obviously maximized at the critical coupling point for $\gamma_r = \gamma_0$. Still, at this point, $|S_\Phi|_{max}$ diverges. To avoid the singular point, $|S_\Phi|_{max}$ is calculated for $t_c = \rho t_{cc}$, where $\rho = 1 \pm \varepsilon$, while $\varepsilon \to 0$ ($\varepsilon = 0$ exactly at the critical coupling point). Then, $|S_\Phi|_{max}$ becomes proportional to $(2\rho^3/(1 - \rho^4))\sqrt{P/(\alpha\beta)}|S_f|$. Therefore, $|S_\Phi|_{max}$ is proportional to $\sqrt{P/(\alpha\beta)}$.

According to the previous theoretical analysis, at the critical coupling point, the reflectance and phase sensitivities are maximized. At the same time, the resonance width is minimized, thus providing a maximized FOM factor in the spectral interrogation. The reflectance and phase sensitivities as well as the FOM factor in the spectral interrogation are proportional to the same factor $\sqrt{P/(\alpha\beta)}$, which means that they are increased for metasurfaces with larger periods. Therefore, the theoretical analysis indicates that the critical coupling should be an optimal working regime; the channel thickness should be selected to achieve critically coupled metasurfaces ($t_c = t_{cc}$), while at the same time, their period should be as large as possible.

Validity of the previous theoretical analysis and its conclusions were tested by numerical calculations for metasurfaces with varying channel thicknesses and periods. Results of the numerical calculations confirm that FWHM [Fig. 7(a)] is minimized, while the reflectance sensitivity is maximized [Fig. 7(b)] at the critical coupling points for the channel thickness $t_c = t_{cc}$. These points are represented by the dashed lines in
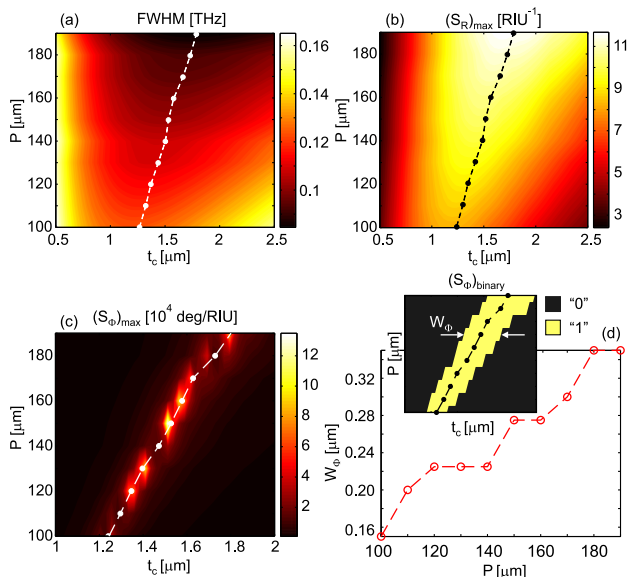
Fig. 7. (a) Resonance width FWHM, (b) reflectance sensitivity $|S_R|_{max}$, and (c) $|S_\Phi|_{max}$ as function of channel thickness t_c and period P. (d) Width W_Φ defined as a range of channel thickness t_c for which $|S_\Phi|_{max} > 10^4$ deg/RIU. The inset depicts the binary image of $|S_\Phi|_{max}$, where area with $|S_\Phi|_{max} < 10^4$ deg/RIU ($|S_\Phi|_{max} > 10^4$ deg/RIU) is represented with "0" ("1").

both Figs. 7(a) and 7(b). At the same time, FWHM decreases while $|S_R|_{max}$ increases with period P. The maximal period of 190 µm was defined by the onset of diffraction after which sensitivities decreased.

Results of the numerical calculations for $|S_\Phi|_{max}$ as a function of channel thickness and period are presented in Fig. 7(c). It clearly demonstrates that the phase sensitivity is maximized at the critical coupling points (represented by the dashed line). Still, due to singularity of the phase sensitivity at critical coupling, dependence of $|S_\Phi|_{max}$ on the period is not clear. To elucidate this dependence, we define the width W_Φ as a range of channel thickness t_c, where $|S_\Phi|_{max} > S_{tr}$, where S_{tr} is a threshold sensitivity taken as 10^4 deg/RIU. W_Φ as a function of period is plotted in Fig. 7(d), while a binary map of the phase sensitivity is given in the inset of Fig. 7(d). Here the area with $|S_\Phi|_{max} < S_{tr}$ ($|S_\Phi|_{max} > S_{tr}$) is represented with "0" ("1"). As can be seen, W_Φ is wider for a larger metasurface period P, which indirectly proves the theoretical prediction that the phase sensitivity increases with P.

Therefore, results of numerical calculations prove that an optimal MIM metasurface has the channel thickness determined by the critical coupling condition, whereas the period should be as large as possible, but beyond the diffraction onset. Since critically coupled points are associated with zero reflectance, realistic structures should always be slightly detuned to provide the output signal needed for measurements and sensing [53].

5. CONCLUSION

In a summary, we derive and validate semi-analytical formulas for spectral, reflectance, and phase sensitivities of MIM metasurfaces based refractive index sensors. The sensitivities are

calculated by knowing properties of the resonant mode (resonant frequency and radiative and non-radiative decay rate) for single values of the refractive index of an analyte under investigation. The model demonstrates that critical coupling with equal decay rates is the optimal working regime for reflectance and phase interrogation, while their optimal working frequencies are $f_0 \pm (\gamma_r + \gamma_0)/\sqrt{3}$ and f_0, respectively. The spectral sensitivity is independent on the working regime, but the corresponding FOM factor is maximized for critically coupled structures. According to the derived semi-analytical formulas, three main geometrical parameters of MIM metasurfaces should be selected in the following way: the metallic ribbon width determines the spectral domain for operation, the channel thickness should provide the critical coupling regime, and the period should be as large as possible, still beyond the onset of diffraction. The model is universal and applicable to any single-mode optical resonator operating in the reflection mode. Possible extensions on sensors operating in transmission mode would require a model based on two-port TCMT [47].

Disclosures. The authors declare no conflicts of interest.

Data Availability. Data underlying the results presented in this paper are not publicly available at this time but may be obtained from the authors upon reasonable request.

Supplemental document. See Supplement 1 for supporting content.

REFERENCES

1. C. Debus and P. H. Bolivar, "Frequency selective surfaces for high sensitivity terahertz sensing," Appl. Phys. Lett. **91**, 184102 (2007).
2. J. F. O'Hara, R. Singh, I. Brener, E. Smirnova, J. Han, A. J. Taylor, and W. Zhang, "Thin-film sensing with planar terahertz metamaterials: sensitivity and limitations," Opt. Express **16**, 1786–1795 (2008).
3. N. Liu, M. Mesch, T. Weiss, M. Hentschel, and H. Giessen, "Infrared perfect absorber and its application as plasmonic sensor," Nano Lett. **10**, 2342–2348 (2010).
4. M. Beruete and I. Jáuregui-López, "Terahertz sensing based on metasurfaces," Adv. Opt. Mater. **8**, 1900721 (2020).
5. J. Homola, "Surface plasmon resonance sensors for detection of chemical and biological species," Chem. Rev. **108**, 462–493 (2008).
6. Y. H. Huang, H. P. Ho, S. K. Kong, and A. V. Kabashin, "Phase-sensitive surface plasmon resonance biosensors: methodology, instrumentation and applications," Ann. Phys. **524**, 637–662 (2012).
7. J. J. Mock, D. R. Smith, and S. Schultz, "Local refractive index dependence of plasmon resonance spectra from individual nanoparticles," Nano Lett. **3**, 485–491 (2003).
8. K. A. Willets and R. P. Van Duyne, "Localized surface plasmon resonance spectroscopy and sensing," Annu. Rev. Phys. Chem. **58**, 267–297 (2007).
9. B. Špačková, P. Wrobel, M. Bocková, and J. Homola, "Optical biosensors based on plasmonic nanostructures: a review," Proc. IEEE **104**, 2380–2408 (2016).
10. J. Han, "Fabry-Perot cavity chemical sensors by silicon micromachining techniques," Appl. Phys. Lett. **74**, 445–447 (1999).
11. T. Zhang, S. Talla, Z. Gong, S. Karandikar, R. Giorno, and L. Que, "Biochemical sensing with a polymer-based micromachined Fabry-Perot sensor," Opt. Express **18**, 18394–18400 (2010).
12. A. A. P. Trichet, J. Foster, N. E. Omori, D. James, P. R. Dolan, G. M. Hughes, C. Vallance, and J. M. Smith, "Open-access optical microcavities for lab-on-a-chip refractive index sensing," Lab Chip **14**, 4244–4249 (2014).

13. H. Kelkar, D. Wang, D. Martn-Cano, B. Hoffmann, S. Christiansen, S. Götzinger, and V. Sandoghdar, "Sensing nanoparticles with a cantilever-based scannable optical cavity of low finesse and sub-λ^3 volume," Phys. Rev. Applied **4**, 054010 (2015).

14. E. Chow, A. Grot, L. W. Mirkarimi, M. Sigalas, and G. Girolami, "Ultracompact biochemical sensor built with two-dimensional photonic crystal microcavity," Opt. Lett. **29**, 1093–1095 (2004).

15. A. Di Falco, L. O'Faolain, and T. F. Krauss, "Chemical sensing in slotted photonic crystal heterostructure cavities," Appl. Phys. Lett. **94**, 063503 (2009).

16. J. Jágerská, H. Zhang, Z. Diao, N. Le Thomas, and R. Houdré, "Refractive index sensing with an air-slot photonic crystal nanocavity," Opt. Lett. **35**, 2523–2525 (2010).

17. D. Yang, S. Kita, F. Liang, C. Wang, H. Tian, Y. Ji, M. Lončar, and Q. Quan, "High sensitivity and high Q-factor nanoslotted parallel quadrabeam photonic crystal cavity for real-time and label-free sensing," Appl. Phys. Lett. **105**, 063118 (2014).

18. F. Vollmer, D. Braun, A. Libchaber, M. Khoshsima, I. Teraoka, and S. Arnold, "Protein detection by optical shift of a resonant microcavity," Appl. Phys. Lett. **80**, 4057–4059 (2002).

19. N. M. Hanumegowda, C. J. Stica, B. C. Patel, I. White, and X. Fan, "Refractometric sensors based on microsphere resonators," Appl. Phys. Lett. **87**, 201107 (2005).

20. A. M. Armani, R. P. Kulkarni, S. E. Fraser, R. C. Flagan, and K. J. Vahala, "Label-free, single-molecule detection with optical microcavities," Science **317**, 783–787 (2007).

21. M. R. Foreman, J. D. Swaim, and F. Vollmer, "Whispering gallery mode sensors," Adv. Opt. Photon. **7**, 168–240 (2015).

22. E. M. Yeatman, "Resolution and sensitivity in surface plasmon microscopy and sensing," Biosens. Bioelectron. **11**, 635–649 (1996).

23. L. S. Jung, C. T. Campbell, T. M. Chinowsky, M. N. Mar, and S. S. Yee, "Quantitative interpretation of the response of surface plasmon resonance sensors to adsorbed films," Langmuir **14**, 5636–5648 (1998).

24. M. Piliarik and J. Homola, "Surface plasmon resonance (SPR) sensors: approaching their limits?" Opt. Express **17**, 16505–16517 (2009).

25. L. Pang, G. M. Hwang, B. Slutsky, and Y. Fainman, "Spectral sensitivity of two-dimensional nanohole array surface plasmon polariton resonance sensor," Appl. Phys. Lett. **91**, 123112 (2007).

26. P. Jia and J. Yang, "Universal sensitivity of propagating surface plasmon resonance in nanostructure arrays," Opt. Express **23**, 18658–18664 (2015).

27. M. M. Miller and A. A. Lazarides, "Sensitivity of metal nanoparticle surface plasmon resonance to the dielectric environment," J. Phys. Chem. B **109**, 21556–21565 (2005).

28. P. Kvasnička and J. Homola, "Optical sensors based on spectroscopy of localized surface plasmons on metallic nanoparticles: sensitivity considerations," Biointerphases **3**, FD4–FD11 (2008).

29. B. Špačková and J. Homola, "Sensing properties of lattice resonances of 2D metal nanoparticle arrays: an analytical model," Opt. Express **21**, 27490–27502 (2013).

30. A. Unger and M. Kreiter, "Analyzing the performance of plasmonic resonators for dielectric sensing," J. Phys. Chem. C **113**, 12243–12251 (2009).

31. J. Yang, H. Giessen, and P. Lalanne, "Simple analytical expression for the peak-frequency shifts of plasmonic resonances for sensing," Nano Lett. **15**, 3439–3444 (2015).

32. W. Zhang and O. J. F. Martin, "A universal law for plasmon resonance shift in biosensing," ACS Photon. **2**, 144–150 (2015).

33. S. Arnold, M. Khoshsima, I. Teraoka, S. Holler, and F. Vollmer, "Shift of whispering-gallery modes in microspheres by protein adsorption," Opt. Lett. **28**, 272–274 (2003).

34. C. Wu, A. B. Khanikaev, R. Adato, N. Arju, A. A. Yanik, H. Altug, and G. Shvets, "Fano-resonant asymmetric metamaterials for ultrasensitive spectroscopy and identification of, molecular monolayers," Nat. Mater. **11**, 69–75 (2012).

35. S. Yoo and Q.-H. Park, "Metamaterials and chiral sensing: a review of fundamentals and applications," Nanophotonics **8**, 249–261 (2019).

36. Y. Y. Lee, R. M. Kim, S. W. Im, M. Balamurugan, and K. T. Nam, "Plasmonic metamaterials for chiral sensing applications," Nanoscale **12**, 58–66 (2020).

37. S.-D. Liu, X. Qi, W.-C. Zhai, Z.-H. Chen, W.-J. Wang, and J.-B. Han, "Polarization state-based refractive index sensing with plasmonic nanostructures," Nanoscale **7**, 20171–20179 (2015).

38. R. Verre, N. Maccaferri, K. Fleischer, M. Svedendahl, N. Odebo Länk, A. Dmitriev, P. Vavassori, I. V. Shvets, and M. Käll, "Polarization conversion-based molecular sensing using anisotropic plasmonic metasurfaces," Nanoscale **8**, 10576–10581 (2016).

39. X. Hu, G. Xu, L. Wen, H. Wang, Y. Zhao, Y. Zhang, D. R. S. Cumming, and Q. Chen, "Metamaterial absorber integrated microfluidic terahertz sensors," Laser Photon. Rev. **10**, 962–969 (2016).

40. A. Soltani, H. Neshasteh, A. Mataji-Kojouri, N. Born, E. Castro-Camus, M. Shahabadi, and M. Koch, "Highly sensitive terahertz dielectric sensor for small-volume liquid samples," Appl. Phys. Lett. **108**, 191105 (2016).

41. T. H. H. Le and T. Tanaka, "Plasmonics-nanofluidics hybrid metamaterial: an ultrasensitive platform for infrared absorption spectroscopy and quantitative measurement of molecules," ACS Nano **11**, 9780–9788 (2017).

42. G. Duan, J. Schalch, X. Zhao, J. Zhang, R. D. Averitt, and X. Zhang, "An air-spaced terahertz metamaterial perfect absorber," Sens. Actuators A, Phys. **280**, 303–308 (2018).

43. Y.-T. Chang, Y.-C. Lai, C.-T. Li, C.-K. Chen, and T.-J. Yen, "A multifunctional plasmonic biosensor," Opt. Express **18**, 9561–9569 (2010).

44. B. Vasić, G. Isić, and R. Gajić, "Localized surface plasmon resonances in graphene ribbon arrays for sensing of dielectric environment at infrared frequencies," J. Appl. Phys. **113**, 013110 (2013).

45. S. Fan, W. Suh, and J. D. Joannopoulos, "Temporal coupled-mode theory for the Fano resonance in optical resonators," J. Opt. Soc. Am. A **20**, 569–572 (2003).

46. C. Wu, B. Neuner, G. Shvets, J. John, A. Milder, B. Zollars, and S. Savoy, "Large-area wide-angle spectrally selective plasmonic absorber," Phys. Rev. B **84**, 075102 (2011).

47. C. Qu, S. Ma, J. Hao, M. Qiu, X. Li, S. Xiao, Z. Miao, N. Dai, Q. He, S. Sun, and L. Zhou, "Tailor the functionalities of metasurfaces based on a complete phase diagram," Phys. Rev. Lett. **115**, 235503 (2015).

48. G. Isić, B. Vasić, D. C. Zografopoulos, R. Beccherelli, and R. Gajić, "Electrically tunable critically coupled terahertz metamaterial absorber based on nematic liquid crystals," Phys. Rev. Appl. **3**, 064007 (2015).

49. J. Park, J.-H. Kang, S. J. Kim, X. Liu, and M. L. Brongersma, "Dynamic reflection phase and polarization control in metasurfaces," Nano Lett. **17**, 407–413 (2017).

50. C. A. Balanis, *Antenna Theory* (Wiley, 2005).

51. Y. Todorov, L. Tosetto, J. Teissier, A. M. Andrews, P. Klang, R. Colombelli, I. Sagnes, G. Strasser, and C. Sirtori, "Optical properties of metal-dielectric-metal microcavities in the THz frequency range," Opt. Express **18**, 13886–13907 (2010).

52. X.-Y. Peng, B. Wang, S. Lai, D. H. Zhang, and J.-H. Teng, "Ultrathin multi-band planar metamaterial absorber based on standing wave resonances," Opt. Express **20**, 27756–27765 (2012).

53. B. Vasić and G. Isić, "Refractive index sensing with hollow metal-insulator-metal metasurfaces," J. Phys. D (in press).

54. J. P. Hugonin and P. Lalanne, *RETICOLO Code for Grating Analysis* (Institute d'Optique, 2005).

55. M. A. Ordal, R. J. Bell, J. R. W. Alexander, L. L. Long, and M. R. Querry, "Optical properties of fourteen metals in the infrared and far infrared: Al, Co, Cu, Au, Fe, Pb, Mo, Ni, Pd, Pt, Ag, Ti, V, and W," Appl. Opt. **24**, 4493–4499 (1985).

56. P. A. George, W. Hui, F. Rana, B. G. Hawkins, A. E. Smith, and B. J. Kirby, "Microfluidic devices for terahertz spectroscopy of biomolecules," Opt. Express **16**, 1577–1582 (2008).

57. M. G. Nielsen, D. K. Gramotnev, A. Pors, O. Albrektsen, and S. I. Bozhevolnyi, "Continuous layer gap plasmon resonators," Opt. Express **19**, 19310–19322 (2011).

58. B. Vasić and R. Gajić, "Optical modulation based on tunable light absorption and amplification in metasurfaces coupled with gain medium," Opt. Lett. **42**, 2181–2184 (2017).

59. J. Homola, *Surface Plasmon Resonance Based Sensors* (Springer, 2006).

60. X. Zhang, Q. Li, F. Liu, M. Qiu, S. Sun, Q. He, and L. Zhou, "Controlling angular dispersions in optical metasurfaces," Light Sci. Appl. **9**, 76 (2020).

Check for updates

Nanoscale mechanical control of surface electrical properties of manganite films with magnetic nanoparticles†

Borislav Vasić, [ID] *a Zorica Konstantinović, [ID] b Elisa Pannunzio-Miner, ‡c
Sergio Valencia, [ID] d Radu Abrudan, [ID] §e Radoš Gajić a and Alberto Pomar [ID] c

Mechanical control of electrical properties in complex heterostructures, consisting of magnetic FeO_x nanoparticles on top of manganite films, is achieved using atomic force microscope (AFM) based methods. Under applied pressure of the AFM tip, drop of the electrical conductivity is observed inducing an electrically insulating state upon a critical normal load. Current and surface potential maps suggest that the switching process is mainly governed by the flexoelectric field induced at the sample surface. The relaxation process of the electrical surface potential indicates that the diffusion of oxygen vacancies from the bulk of the manganite films towards the sample surface is the dominant relaxation mechanism. The magnetic FeO_x nanoparticles, staying attached to the sample surface after the rubbing, protect the underlying manganite films and provide stability of the observed resistive switching effect. The employed mechanical control gives a new freedom in the design of resistive switching devices since it does not depend on the film thickness, and biasing is not needed.

1 Introduction

Further improvement of nanoelectronic devices such as switches and memories, requires development of novel materials as well as advanced mechanisms for the dynamic control of their electrical

aGraphene Laboratory of Center for Solid State Physics and New Materials, Institute of Physics Belgrade, University of Belgrade, Pregrevica 118, 11080 Belgrade, Serbia. E-mail: bvasic@ipb.ac.rs

bCenter for Solid State Physics and New Materials, Institute of Physics Belgrade, University of Belgrade, Pregrevica 118, 11080 Belgrade, Serbia

cInstitut de Ciència de Materials de Barcelona, ICMAB-CSIC, Campus de la UAB, 08193 Bellaterra, Spain

dHelmholtz-Zentrum Berlin für Materialien und Energie, Albert-Einstein-Str. 15, 12489 Berlin, Germany

eInstitut für Experimentalphysik/Festkörperphysik, Ruhr-Universität Bochum, 44780 Bochum, Germany

† Electronic supplementary information (ESI) available: ESI contains the reciprocal space maps of (103) reflections and in-plane magnetization curves of the LSMO film (Fig. S1), the results of XAS measurements and the resulting XMCD for the LSMO film (Fig. S2), the reciprocal space maps of (103) reflections and in-plane magnetization curves of the LSFMO film (Fig. S3), AFM images of the LSFMO film (Fig. S5), the electrical current (C-AFM images in Fig. S5) and surface potential (KPFM images in Fig. S6) distributions after the rubbing of the LSFMO film, and the maps of the electrical surface potential of the LSFMO film after combined rubbing with grounded and biased probe (KPFM images in Fig. S7). See DOI: 10.1039/c8na00301g

‡ Present address: Centro de Investigaciones en Ciencias de la Tierra (CICTERRA-CONICET-UNC), Facultad de Ciencias Exactas, Físicas y Naturales, Av. Velez Sarsfield 1611, X5016GCA, Ciudad Universitaria, Cordoba, Argentina.

§ Present address: Helmholtz-Zentrum Berlin für Materialien und Energie, Albert-Einstein-Str. 15, 12489 Berlin, Germany.

properties. In this context, one of the most studied mechanisms is resistive switching – an electrically induced change of the resistance of various thin metal-oxide films.[1–7] This research is mainly driven by possible applications in new data storage devices such as resistive random access memories.[4–7]

In order to fully understand complex physicochemical processes during resistive switching, investigations at the nanoscale are of particular relevance, where methods based on atomic force microscopy (AFM) are prerequisite.[8–11] At the same time, AFM could provide novel methods for the manipulation of resistive switching. Namely, in addition to the electrical control, strain engineering is a simple approach to tailor the electrical properties of metal oxide films.[12–17] The significant coupling between the strain and the electrical properties is based on flexoelectricity (an internal electric field resulting from a strain gradient) and the inverse Vegard effect (changes of ion concentrations due to a stress).[18] The flexoelectricity is typically small. However, it has recently been shown that stress and stress gradients at the nanoscale can lead to sizable effects.[19–21]

A large nanoscale gradient of stress can be obtained by using the tip of an AFM which has been employed for mechanically induced resistive switching[22–29] and switching of ferroelectric polarization.[30–36] Since purely mechanical control is independent of film thickness and biasing is not needed, it could provide new prospects for the resistive switching. While recent studies[22–29] have been focused on the mechanically induced switching of homogeneous metal-oxide films, it is interesting to investigate the phenomena in the presence of nano-objects on the film surface. In this respect, nanoparticles (NPs) constitute a model system as

they not only improve mechanical properties,[37] but also may provide enhanced functionalities such as novel magnetotransport phenomena[38] or optoelectronic capabilities,[39,40] and they could serve as novel magnetic tunnel junctions[41,42] or memory devices.[43]

Here we investigate the local mechanical control of the surface electrical properties of a heterostructure consisting of a manganite film with magnetic FeO_x NPs. The AFM tip is used to generate a local stress by rubbing the sample surface, and the resulting changes in local conductivity and electrical surface potential are subsequently measured by conductive AFM (C-AFM) and Kelvin probe force microscopy (KPFM), respectively. It is shown that for a high enough normal load, the manganite surface can be switched to an insulating state. At the same time, the sample exhibits weak room-temperature magnetism due to the presence of FeO_x NPs which stay well attached to the sample surface even after the rubbing at a high normal load.

2 Experimental

2.1 Sample preparation

Samples consisting of iron oxide FeO_x NPs assembled onto manganite films, were grown by radio frequency (RF) magnetron sputtering on the top of (001)-oriented $SrTiO_3$ (STO) substrates. Two manganite families were considered with very different properties, fully spin polarized $La_{0.67}Sr_{0.33}MnO_3$ (LSMO) on one side and insulating $La_{0.5}Sr_{0.5}Fe_{0.5}Mn_{0.5}O_3$ (LSFMO) thin film on the other side. Nanostructured thin films were deposited under a pure oxygen partial pressure (0.19 mbar) at a high temperature (850–900 °C) with a wide range of nominal thickness (between 20 nm and 100 nm),[44] while the detailed microstructure of LSMO films can be also found in ref. 44. Iron oxide NPs have been deposited under a pure oxygen pressure of 0.06 mbar at 700 °C.

2.2 Structural and magnetic characterization

The surface morphology of nanostructured thin films was characterized by field emission scanning electron microscopy (SEM) (QUANTA FEI 200 FEG-ESEM). The crystal structure of manganite films was characterized by X-ray diffraction based reciprocal space mapping using a Bruker AXS GADDS system equipped with a 2D X-ray detector.

Magnetic properties were measured with a superconducting quantum interference device magnetometer (SQUID) (Quantum Design). The structural and magnetic nature of iron oxide NPs was studied by X-ray absorption spectroscopy (XAS) and X-ray magnetic circular dichroism (XMCD). The synchrotron experiments were performed at room temperature by using the ALICE chamber[45] at the PM3 beamline of the electron storage ring BESSY II of the Helmholtz-Zentrum Berlin. The radiation impinged on samples at a grazing angle of 30°. The polarization of the incoming radiation was set to circular ($P_c = 0.92(3)$). Data were acquired across the Fe $L_{3,2}$ edges by means of total electron yield. The XMCD spectrum was obtained for a fixed helicity of the incoming polarization by reversing the magnetization direction at every data point from positive to negative by means of an external magnetic field (± 0.1 T). Data were obtained in magnetic remanence. XMCD was defined as the difference in

the absorption for the curves obtained after applying the external magnetic field +0.1 T ($\beta+$) and −0.1 T ($\beta-$), respectively.

2.3 AFM measurements

AFM measurements were performed using an NTEGRA Prima AFM system from NT-MDT under ambient conditions. Tapping AFM mode was used for the topographic imaging. Simultaneously, phase imaging was performed by recording the phase lag of the employed AFM cantilevers.

Electrical measurements were done using C-AFM and KPFM. In C-AFM, local electrical currents were measured in contact mode, while DC voltage was applied between the sample and the AFM tip. KPFM was employed to measure the contact potential difference (CPD) between the AFM tip and the sample surface. The CPD is equal to the difference in the work functions of the tip and sample. KPFM measurements were done using a standard two-pass technique. In the first pass, sample topography was measured in tapping mode. In the second pass, the AFM cantilever was lifted by 30 nm and the sum of AC and variable DC voltage was applied between the cantilever and the sample. In the second pass, the lifted probe, only electrically excited and with a switched-off mechanical feedback loop, followed the topography measured in the first pass. Then, the CPD in every point of a two-dimensional AFM image was the value of the variable DC voltage which canceled the electrically excited oscillations of the AFM cantilever in the second pass.

The procedure for the mechanical control of the surface electrical properties was the following: first, the local electrical current or CPD was measured on an area of 2×2 μm^2, and then we switched to contact AFM mode and only the inner and central part of 1×1 μm^2 was rubbed at an increased normal force (in the order of 1 μN), whereas after the rubbing, we switched back to C-AFM or KPFM mode, and measured either local electrical currents or electrical surface potentials, respectively, on the initial area of 2×2 μm^2. Hereafter, the rubbing will stand for controllable scanning at increased normal load in order to induce local changes of the electrical properties.

Both AFM imaging, rubbing and electrical measurements were done using diamond coated and nitrogen doped DCP20 probes from NT-MDT. They have triangular cantilevers with the typical force constant of 48 N m^{-1} and a resonant frequency of 420 kHz. Diamond coatings make these probes wear resistive, while a high doping with nitrogen provides excellent conductivity. Therefore, these robust and conductive probes are suitable for the rubbing in contact AFM mode at high normal loads (in the order of μN) and subsequent AFM imaging as well as electrical measurements many times. Since C-AFM measurements were done in contact mode as well, in order to avoid any influence of the applied normal force from the AFM tip during the C-AFM scanning, these measurements were done at low normal load from 50–100 nN.

3 Results and discussion

Manganites are an important class of metal oxides, especially in the context of resistive switching, because of both

magnetoresistive[46,47] and electroresistive properties.[48–50] Strain engineering is an additional and simple approach to tailor their properties.[25,51–54] Epitaxial manganite films are usually elastically strained due to a lattice mismatch between the films and underlying substrates (STO in the considered case). This strain facilitates growth of various self-organized morphologies such as pit arrays[55–57] which can serve as templates for subsequent self-assembly of NPs.[44] The strain state in our films is analyzed by the asymmetric reciprocal space mapping of the reflection (103) for the nanostructured 100 nm thick LSMO film grown on top of the STO substrate (Fig. S1(a) of the ESI†). As observed previously,[55] the LSMO film seems to be fully strained with the in-plane lattice constant close to $a_{\parallel,STO} = 3.905$ Å. On the other hand, the estimated out of-plane lattice constant $a_{\perp,LSMO} = 3.882(6)$ Å is slightly smaller than the corresponding bulk value of 3.889 Å, as expected due to presence of a tensile strain.[44,55] Nevertheless, the higher value of the out-of-plane parameter 3.882(6) Å compared with the one of the fully strained films of 3.868 Å (ref. 58) indicates the presence of a small quantity of oxygen vacancies, as previously discussed.[55]

The AFM topographic and the corresponding phase image of the LSMO film with FeO$_x$ NPs are given in Fig. 1(a) and (b), respectively. In the topographic image, NPs are visible as bright domains. They are better resolved in the phase image, where they are dark and with a pronounced contrast compared to the underlying LSMO film. The phase images recorded in forward and backward directions were the same, implying that the observed phase difference was due to the material contrast (not just a topographic artifact) between NPs and the LSMO substrate. As a reference, an array of three NPs is marked by dashed lines in both topographic and phase images. The SEM image of the sample is depicted in Fig. 1(c). According to the SEM images, the surface coverage of the film by NPs was around 50%, while the NP size distribution is presented in Fig. 1(d) showing that the average NP size is around 60 nm.

The magnetic characterization reveals that iron-oxide NPs provide weak room-temperature magnetism as shown in Fig. S1(b) of the ESI.† At 300 K, the magnetization disappears in bare manganite films and remains principally only in the structures with FeO$_x$ NPs as depicted in Fig. S4 of the ESI.† According to the results of XAS and XMCD measurements, the NPs are mostly γ-Fe$_2$O$_3$ (the results of XAS and the fit of the XMCD curve are presented in Fig. S2 of the ESI†).

The influence of the local pressure from the AFM tip on the electrical properties of the manganite film decorated with iron-oxide NPs is presented in Fig. 2(a). The current maps were measured by C-AFM on six different 2×2 μm^2 areas, after the rubbing of inner 1×1 μm^2 domains with the AFM tip at increasing normal force, starting from 0.32 μN to 1.6 μN. As can be seen, after the rubbing, the electrical current of inner square domains is decreased. At a normal load of 1.6 μN, the inner
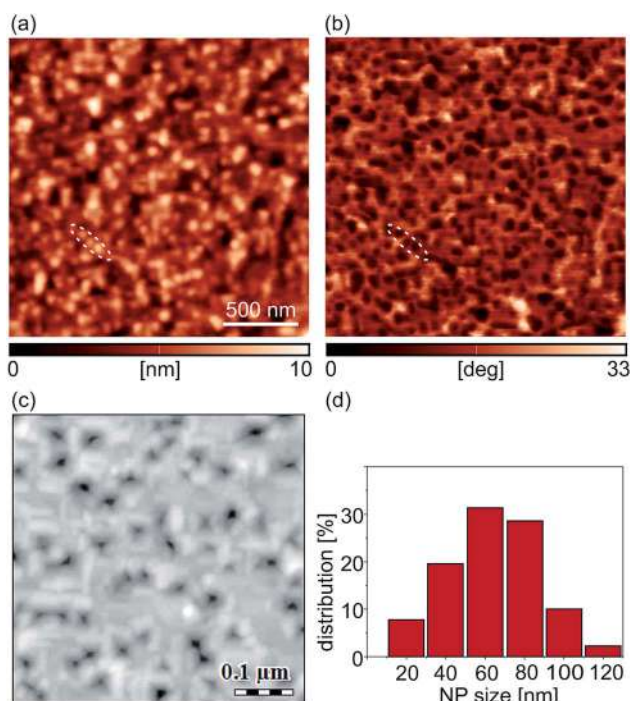
Fig. 1 Sample morphology: (a) AFM topographic image (z-scale is 10 nm), and (b) AFM phase image acquired during the imaging in tapping mode. As an example, an array of three NPs is encircled in both the topographic and phase images. (c) SEM image and (d) the size distribution of iron-oxide NPs.
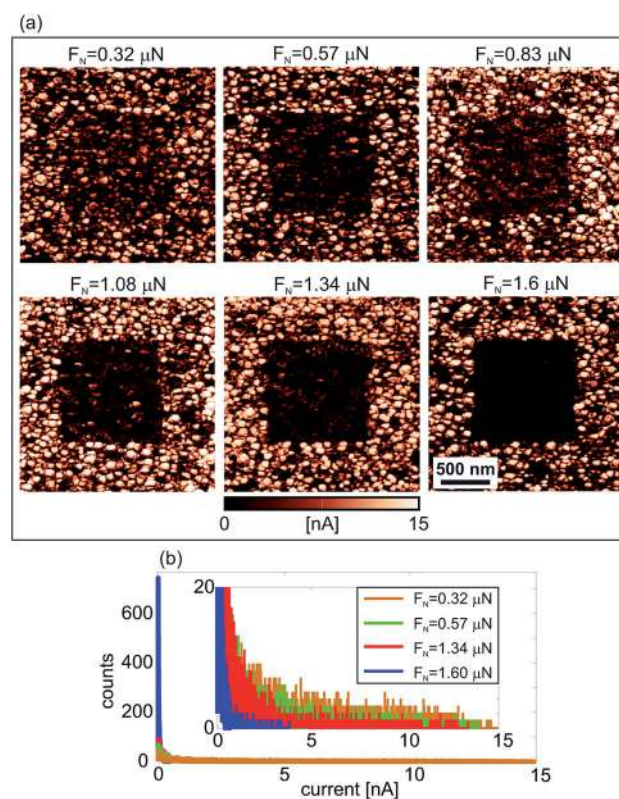
Fig. 2 (a) 2×2 μm^2 current maps measured by C-AFM (at the sample bias voltage $U_s = 2$ V) after the rubbing of inner 1×1 μm^2 domains at specified normal force (from 0.32 μN to 1.6 μN). The results were obtained on six different sample regions. The current scale is 15 nA. (b) Histograms of the current distribution on rubbed domains in (a) for the selected normal forces. In the inset, the histograms are saturated at 20 counts for a better visibility.

square is switched to a practically insulating state (with almost zero electrical current). The histograms of the current distribution measured only on rubbed domains are given in Fig. 2(b). All current peaks are located around zero, but they become much more pronounced with increasing normal load. For the highest load, almost all points in the histogram are located around zero (just few of them with non-zero current) showing that the sample surface is really switched to an insulating state.

Fig. 3(a) presents the CPD maps measured by KPFM on 2×2 μm^2 areas after the rubbing of inner 1×1 μm^2 regions with the AFM tip at an increasing normal force from 0.62 μN to 2.4 μN. As in the previous case, the CPD maps were measured on different sample locations. As can be seen, CPD increases on the rubbed domains. Since the CPD stands for the difference between the work functions of the AFM tip and the sample, an increase in the CPD implies a lower work function of the sample. Therefore, the KPFM results indicate the existence of an electric field originating from negative charges on the sample surface.

The typical histogram of the CPD distribution is depicted in Fig. 3(b) for a normal load of 2.4 μN. There are two clearly resolved peaks corresponding to the rubbed (the peak at a higher CPD) and non-rubbed (the peak at a lower CPD)
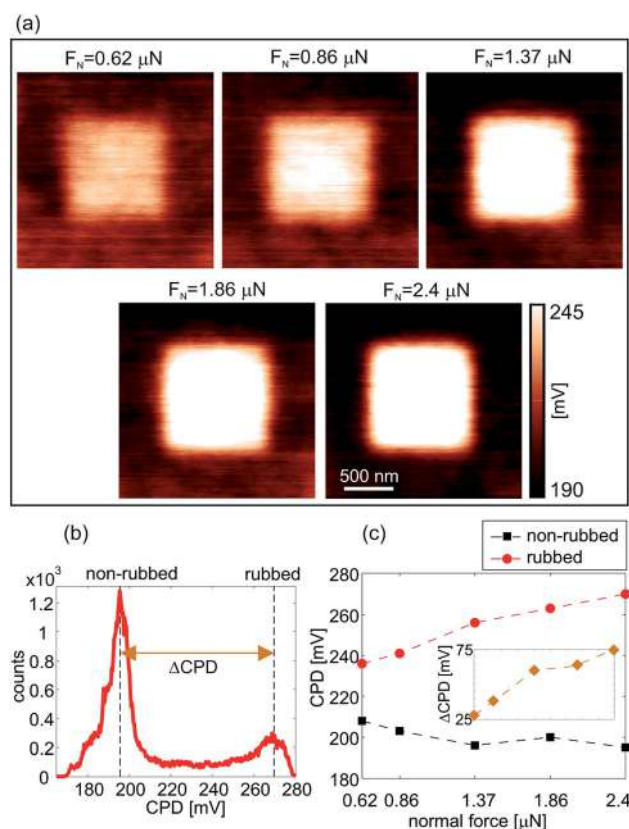
domains. Histograms were calculated for all CPD maps in this manner, whereas the histogram peaks were selected as CPD representatives as a function of a normal load. The corresponding results, together with a difference in the CPD between rubbed and non-rubbed domains (ΔCPD), are given in Fig. 3(c). As can be seen, ΔCPD continuously increases with the normal load from around 25 mV to 75 mV.

The topographic images of the sample surface before and after the rubbing (at a high normal force of 1.6 μN) are given in Fig. 4(a) and (b), respectively. The 1×1 μm^2 rubbed domain is marked by a dashed square. The rubbed region is only slightly darker than the surrounding, non-rubbed part. The histograms and corresponding fits of the height distribution within the square domains before and after the rubbing are given in Fig. 4(c). As can be seen, the mean height is decreased by around 0.3 nm after the rubbing, meaning that the sample surface is locally compressed along the perpendicular direction. Similar results were obtained for the sample with the LSFMO film as depicted in the topographic images in Fig. S6(b) ESI,† again for the cases recorded before and after the rubbing (at a high normal force of 1.34 μN). These topographic images illustrate that NPs were not pushed away by the AFM tip during the rubbing even at very high normal loads. This was confirmed by the absence of accumulated NPs along the rims of the inner 1×1 μm^2 rubbed domains. Still, in addition to the small local compression of the sample surface within the rubbed domains, the topographic images after the rubbing show that the height

Fig. 3 (a) 2×2 μm^2 CPD maps measured by KPFM after the rubbing of inner 1×1 μm^2 domain at specified normal force (from 0.62 μN to 2.4 nN). The CPD scale is 190–245 mV. (b) Histogram of the CPD distribution for a normal load of 2.4 μN. (c) Changes in the CPD and ΔCPD on rubbed and non-rubbed regions in (a) as a function of the normal force.
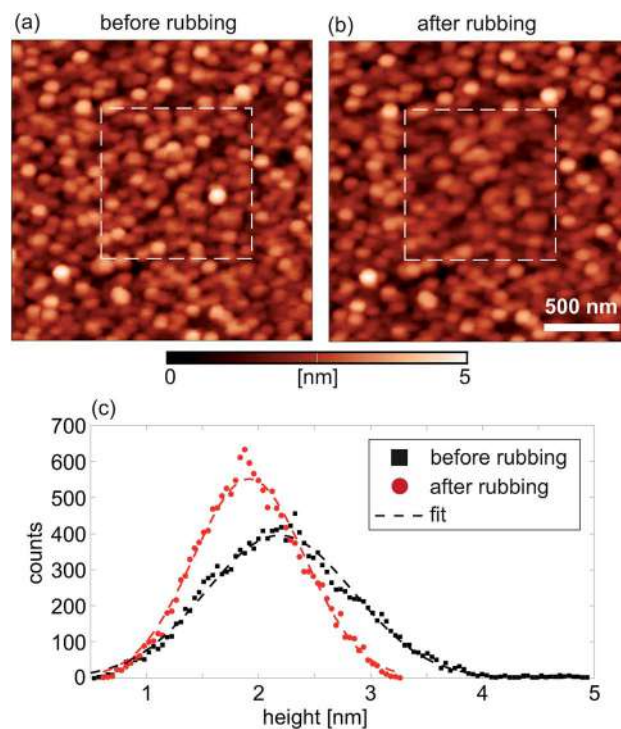
Fig. 4 AFM topographic images of the sample surface acquired (a) before and (b) after the rubbing of the inner 1×1 μm^2 domain (marked by dashed lines) at a normal force of 1.6 μN. z-scale is 5 nm. (c) Histogram of the height distribution within the square domains marked in parts (a) and (b).

of some NPs is slightly decreased. This can be seen by lower brightness and clarity of these NPs. Therefore, NPs stay stable on the film surface and they are not removed, but some of them can be worn since their height is decreased due to local scratching. Still, the most important finding is that the NPs are tightly attached to the underlying film which stays protected.

The protection by NPs is two-fold. They mechanically protect the underlying manganite film from normal load applied by the AFM probe preventing any morphological damage of the film and facilitating a stable and reliable switching process. At the same time, NPs prevent aging of manganite films due to their exposure to the environment. Namely, it is well known that environmental factors deteriorate electrical properties (conductivity for example) of thin metal-oxides, usually due to detrimental reactions with various species from the atmosphere. This is the reason why higher conductivity was usually observed on areas of the manganite film covered by NPs, as can be seen in Fig. 2(a).

In order to further explain the observed effects, the rubbing with a grounded probe at increased normal load was combined with the scanning in contact mode using a biased AFM tip, but at a low normal force. CPD maps after such manipulations are depicted in Fig. 5(a) and (b). In Fig. 5(a), the 2×2 μm^2 square domain was firstly rubbed with the grounded tip, and then the inner 1×1 μm^2 domain was scanned in contact mode with a bias voltage of $U_t = -1$ V applied to the AFM tip. In Fig. 5(b), the order was the opposite, the larger square domain was scanned in contact mode at $U_t = -1$ V, while the inner one was rubbed with the grounded tip. In both cases, the rubbing with the grounded tip and increased normal load leads to an increased CPD. This is exactly the opposite to the case with the applied negative voltage (in this case, the CPD was lowered). Therefore, the local pressure from the AFM probe has a similar

effect as the rubbing with a positive bias voltage applied to the AFM tip.

According to the type of conducting path, there are two resistive switching mechanisms: with a filamentary and an interface-type conducting path.[4] The switching mechanism of LSMO films belongs to the second type and it is based on oxygen vacancy migrations.[59] This mechanism is usually characterized by the formation of a Schottky barrier at the interface between a metal electrode and a semiconducting metal-oxide film.[4,60] The width and height of the barrier can be tuned by applying a bias voltage which controls the oxygen vacancy concentration within the charge depletion layer at the metal–semiconductor interface.

In the considered case of mechanically induced resistive switching, instead of an externally applied bias voltage, the width and height of the Schottky barrier between the AFM tip (DCP20 probes are highly conductive, so they can be considered as metallic ones) and sample surface are controlled by the inverse Vegard effect and flexoelectric field. According to the Vegard law of a chemical expansion, the local stress and strains are proportional to the mobile ion concentration.[18] Generally, the unit cell volume increases with the oxygen vacancy concentration.[26] In the considered case, the sample surface rubbed with the AFM tip is locally compressed along the surface normal, so the oxygen vacancy concentration is decreased. As a result, an excess of negative charges on the sample surface appears. This is in accordance with the results of KPFM measurements, where an increased CPD was observed on rubbed parts, meaning that the Fermi level was locally raised. The electrical transport in LSMO is based on the hopping of electrons between adjacent Mn^{3+} and Mn^{4+} ions across oxygen ions.[61] During the rubbing, the oxygen ion concentration beneath the tip is increased (since the oxygen vacancy concentration is decreased), so this effect does not seem to be a mechanism for the observed decrease of the electrical conductivity.

At the same time, a local and non-uniform compression of a sample surface leads to a strain gradient and a local flexoelectric field. This field is oriented from the sample surface toward the bulk.[31] This pushes oxygen vacancies away from the sample surface, while attracting negative charges toward the sample surface, again in accordance with the KPFM results. Since the C-AFM maps in Fig. 2(a) were measured with a positive bias voltage applied to the sample, the induced flexoelectric field is an obstacle for the electron transport from the AFM tip to the sample. Therefore, the induced flexoelectric field makes an additional potential barrier for the electron transport resulting in lower currents as observed in the C-AFM maps.

The inverse Vegard effect and flexoelectric field can be coupled as well. The LSMO films grown on the STO substrate are under in-plane tensile strain due to a lattice mismatch as can be seen from the asymmetric reciprocal space map given in Fig. S1(a) of the ESI.† This tensile strain can induce an in-built flexoelectric field.[21] The strain can be relaxed by increasing the oxygen vacancy concentration.[21] However, in a sample rubbed with the AFM tip, the oxygen vacancy concentration is further decreased due to the inverse Vegard effect. The strain is then
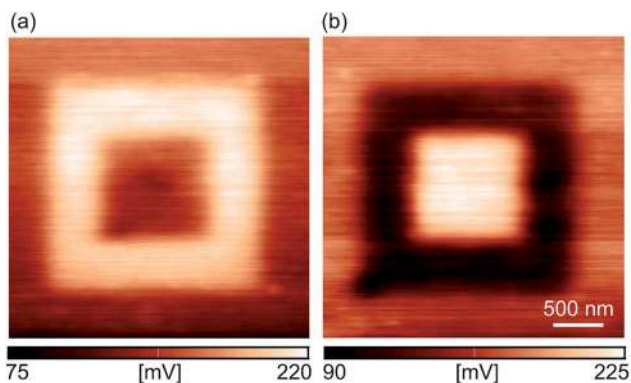

Fig. 5 3×3 μm^2 CPD maps of the sample rubbed with both grounded (at high normal load) and biased (low normal load and negative bias voltage) tips: (a) first, the inner 2×2 μm^2 domain was rubbed with the grounded AFM probe and at a normal force 0.48 μN, and then, the smaller inner 1×1 μm^2 domain was scanned in the contact mode at a low normal force 0.16 μN and with a tip bias voltage of −1 V, and (b) first, the inner 2×2 μm^2 domain was scanned in the contact mode at a low normal force of 0.16 μN and with a tip bias voltage of −1 V, and then the smaller inner 1×1 μm^2 domain was rubbed with the grounded AFM probe and at a normal force of 0.48 μN. The CPD scale is (a) 75–220 mV and (b) 90–225 mV.

even more enhanced, potentially leading to an additional increase of the flexoelectric field. As a result, both the inverse Vegard effect and flexoelectric field could raise the potential barrier supporting the observed changes of the electrical properties.

The efficiency and robustness of the resistive switching process were tested also in the case of an insulating LSFMO thin film with FeO$_x$ NPs on top. At the same time, besides different conductivities of the underlying film (here the measured current on non-rubbed areas was up to 50 pA, that is, three order of magnitude lower than on the LSMO film with NPs), the surface coverage of the LSFMO film by NPs was increased in order to check its influence on the switching process. The asymmetric reciprocal space map and the in-plane magnetization curves for this sample are given in Figs. S3(a) and (b) of the ESI,† respectively. The morphology of the investigated sample is depicted in Fig. S5 of the ESI.† The surface coverage of the LSFMO substrate by FeO$_x$ NPs is more than 80%. As a result, the AFM tip is practically in direct contact only with the NPs (on the other hand, due to a lower surface coverage of the LSMO film, there are parts with a bare LSMO substrate which can be directly probed with the AFM tip). The influence of a local pressure on the surface electrical properties is displayed in Fig. S6 (C-AFM analysis) and S7 (KPFM analysis) of the ESI.† They illustrate that the local electrical current drops, while the local CPD grows with the normal force applied during a rubbing. The CPD maps measured after the combined rubbing with a grounded tip at an increased normal load and a negatively biased tip are given in Fig. S8 of the ESI.† The observed changes in the CPD indicate that the rubbing with the grounded tip is equivalent to the applying a positive bias voltage by the AFM tip.

According to the presented results, the electrical properties were changed in the same way for both samples despite a different surface coverage by NPs. We hence conclude that the observed changes are dominantly related to manganite films since the surface coverage by NPs does not have a significant influence. Therefore, during the rubbing with the AFM tip, the applied mechanical load is transferred across NPs to the underlying manganite films, so the AFM tip does not need to be in direct contact with the films. Since FeO$_x$ NPs are not laterally connected, electrical currents go from the AFM tip across NPs to manganite films, or directly from the tip to the films. After that, charge carriers are transported laterally through the manganite films to an external electrical contact.

The results of KPFM measurements indicate that the rubbing with a grounded AFM tip and increased normal load induce localized charges on a sample surface. In metal-oxides generally, localized charges appear due to local changes in the oxygen vacancy concentration. In order to measure the time evolution of the localized charges, the CPD was measured as a function of a time. The resulting CPD maps after the rubbing of the inner 1×1 μm^2 square domain are given in Fig. 6(a) (immediately after the rubbing, after 2 h and after 3 h) and Fig. 6(b) (immediately after the rubbing, after 3 h and after 6 h) for LSMO and LSFMO films, respectively.

The results for the time-dependent measurements are summarized in Fig. 7(a1) and (b1) for the samples with LSMO

and LSFMO films, respectively, displaying the CPD for both rubbed and non-rubbed regions. The representative values of the CPD were calculated from the corresponding histograms, as in the previous analysis. The CPD on the rubbed regions was decreasing rather slowly. After around 4 h and 6 h for the LSMO and LSFMO films, respectively, the CPD was almost equal on both rubbed and non-rubbed domains. The difference in the CPD between two domains, ΔCPD as a function of time is depicted in Fig. 7(a2) and (b2) for the LSMO and LSFMO films, respectively. The experimental results were fitted with the following curve: $\Delta\text{CPD}(t) = \Delta\text{CPD}(0)\exp(-t/\tau)$ (given by the dashed line), where t is time in hours, while τ is the time constant of the relaxation process. For the sample with the LSMO film, $\tau = 1.75$ h, while for that with the LSFMO film, the relaxation was much slower, with the time constant $\tau = 3.5$ h.

The rate constant of the relaxation of oxygen vacancies can be calculated according to the measured CPD in the following way:[62]

$$\gamma(t) = \frac{\Delta\text{CPD}(t) - \Delta\text{CPD}(0)}{\Delta\text{CPD}(\infty) - \Delta\text{CPD}(0)}, \qquad (1)$$

where $\Delta\text{CPD}(t)$ is the change in the CPD between rubbed and non-rubbed domains, while $\Delta\text{CPD}(0)$ and $\Delta\text{CPD}(\infty)$ stand for ΔCPD at the initial moment and at the end of the relaxation, respectively. Generally, oxygen incorporation into a metal-oxide film can be divided into two processes, the surface reaction and diffusion in the sample bulk,[62–64] so the rate constant can be deduced in the following way:

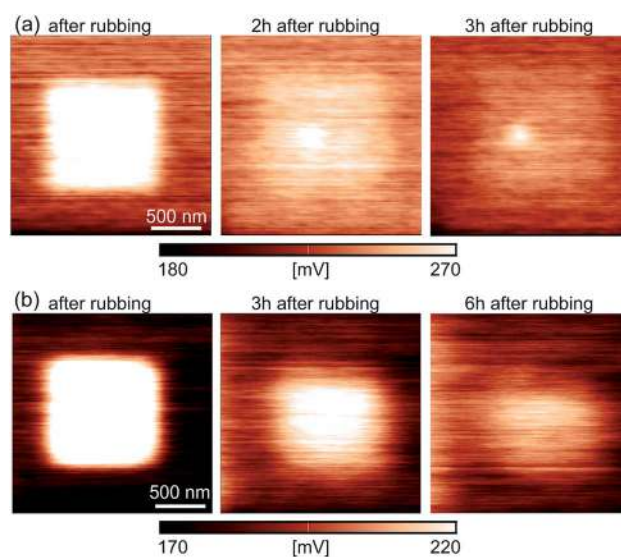$$\gamma(t) = \gamma_{\text{surf}}(t) + \gamma_{\text{diff}}(t), \qquad (2)$$

Fig. 6 Evolution of CPD maps after the rubbing (at a normal force of 0.55 μN) of the inner 1×1 μm^2 domain as a function of time: (a) CPD maps of the sample with a LSMO substrate measured immediately after the rubbing, after 2 h, and after 3 h, (b) CPD maps of the sample with a LSFMO substrate measured immediately after the rubbing, after 3 h, and after 6 h. The CPD scale is (a) 180–270 mV and (b) 170–220 mV.
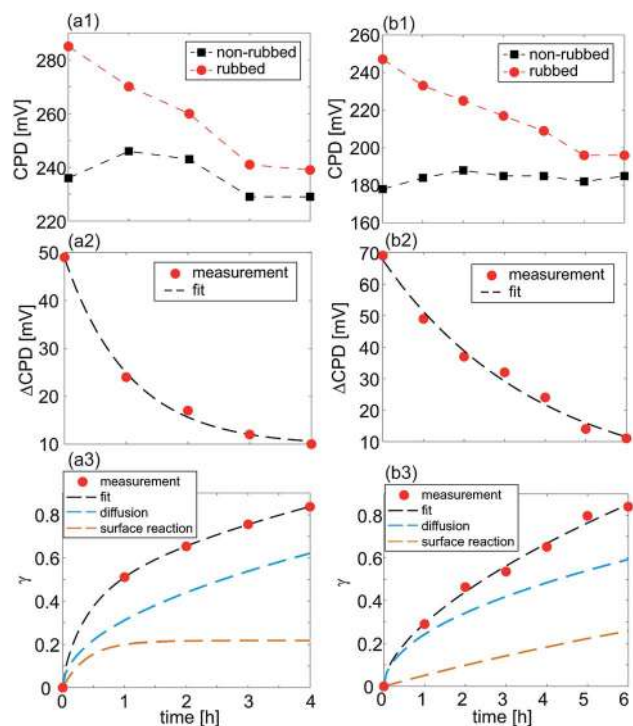
Fig. 7 Evolution of CPD, ΔCPD, and γ as a function of time for the (a) LSMO and (b) LSFMO samples. Top row (a1) and (b1): CPD on rubbed and non-rubbed areas. Middle row (a2) and (b2): CPD difference, ΔCPD, calculated as the difference between CPDs on rubbed and non-rubbed areas. Dashed lines stand for the fit to experimentally obtained points. Bottom row (a3) and (b3): factor γ obtained from the experimental results (points) and the corresponding fit (dashed lines) with the individual contribution of $\gamma_{surf}(t)$ and $\gamma_{diff}(t)$.

where γ_{surf} and γ_{diff} stand for the rate constants of the surface reaction and diffusion, respectively. The surface reaction part can be approximated with an exponential law $\gamma_{surf}(t) \sim 1 - \exp(-k_s t/L)$, where k_s is the surface reaction constant and L is the film thickness. The diffusion part is proportional to $\gamma_{diff}(t) \sim \sqrt{t}$. The overall rate constant $\gamma(t)$ together with the contributions of $\gamma_{surf}(t)$ and $\gamma_{diff}(t)$ are given in Fig. 7(a3) and (b3) for both samples, LSMO and LSFMO films, respectively. As can be seen, the diffusion has larger contribution in the overall relaxation of oxygen vacancies. Accordingly, the relaxation process can be described in the following way. The rubbing with the AFM tip leads to a local sample compression and a decrease of the oxygen vacancy concentration at the sample surface. When the AFM tip is removed, the sample surface relaxes slowly, with a time constant in the order of hours. During that time, oxygen vacancies diffuse from the sample bulk toward the surface in order to reach the initial concentration.

KPFM maps measured after the rubbing suggest that the mechanical interaction AFM tip–sample could induce trapped charges in the sample surface due to either contact charging (local pressure in a single point) or triboelectrification (during AFM tip motion in contact with the sample). However, our measurements were done under ambient conditions at a high humidity around 50%. At such high humidity, it was not

possible to observe any trapped charges induced by either contact charging or triboelectrification. Due to the conductive water layer at a sample surface, the time scale of the relaxation process of the trapped charges is very small (smaller than the time needed to switch to C-AFM (KPFM) mode and make a full scan). At the same time, the relaxation of trapped charges is generally followed by lateral charge spreading. On the other hand, in our case, we didn't observe any spreading of domains with modified surface potential as can be seen in the KPFM images in Fig. 6. In addition, tribocharges generally improve conductivity due to resulting, discharge induced currents, while we observed exactly the opposite behaviour. Therefore, decreased conductivity, the time constant of the relaxation process and clear spatial confinement of domains with the modified electrical surface potential imply that we really induced an internal flexoelectric field, while trapped charges due to triboelectrification can be excluded.

4 Conclusions

In summary, we have demonstrated mechanically induced switching of the electrical conductivity of thin manganite films covered by iron-oxide NPs. The sample surface is switched to an insulating state for a high enough local pressure applied by the AFM tip. The pressure induces the flexoelectric field while the corresponding potential barrier prevents further flow of charge carriers from the AFM tip to the sample. After removing the AFM tip, the sample surface is relaxed slowly, with the time constant in the order of hours. During this time, oxygen vacancies diffuse from the bulk of manganite films towards the surface until the equilibrium electrical surface potential is not reached. Top iron-oxide NPs provide weak room-temperature magnetism, protect the surface of manganite films from aging caused by environmental factors, and assure wear resistance and a reliable switching process of manganite films since the NPs are mechanically stable and tightly attached to the underlying manganite films even after the rubbing at high normal loads. The considered heterostructures are potential candidates for novel multifunctional devices with switchable both electric and magnetic properties. In that sense, in order to reach their full potential, the next step would be to explore the switching of their magnetic properties.

Conflicts of interest

There are no conflicts to declare.

Acknowledgements

References

1 D. B. Strukov, G. S. Snider, D. R. Stewart and R. S. Williams, *Nature*, 2008, **453**, 80–83.

2 J. J. Yang, M. D. Pickett, X. Li, D. A. A. Ohlberg, D. R. Stewart and R. S. Williams, *Nat. Nanotechnol.*, 2008, **3**, 429–433.

3 R. Waser and M. Aono, *Nat. Mater.*, 2007, **6**, 833–840.

4 A. Sawa, *Mater. Today*, 2008, **11**, 28–36.

5 D. S. Jeong, R. Thomas, R. S. Katiyar, J. F. Scott, H. Kohlstedt, A. Petraru and C. S. Hwang, *Rep. Prog. Phys.*, 2012, **75**, 076502.

6 D. B. Strukov and H. Kohlstedt, *MRS Bull.*, 2012, **37**, 108–114.

7 D. Ielmini, *Semicond. Sci. Technol.*, 2016, **31**, 063002.

8 B. J. Choi, D. S. Jeong, S. K. Kim, C. Rohde, S. Choi, J. H. Oh, H. J. Kim, C. S. Hwang, K. Szot, R. Waser, B. Reichenberg and S. Tiedke, *J. Appl. Phys.*, 2005, **98**, 033715.

9 K. Szot, W. Speier, G. Bihlmayer and R. Waser, *Nat. Mater.*, 2006, **5**, 312–320.

10 M. Lanza, U. Celano and F. Miao, *J. Electroceram.*, 2017, **39**, 94–108.

11 Y. Yang, X. Zhang, L. Qin, Q. Zeng, X. Qiu and R. Huang, *Nat. Commun.*, 2017, **8**, 15173.

12 I. Bozovic, G. Logvenov, I. Belca, B. Narimbetov and I. Sveklo, *Phys. Rev. Lett.*, 2002, **89**, 107001.

13 J. H. Haeni, P. Irvin, W. Chang, R. Uecker, P. Reiche, Y. L. Li, S. Choudhury, W. Tian, M. E. Hawley, B. Craigo, A. K. Tagantsev, X. Q. Pan, S. K. Streiffer, L. Q. Chen, S. W. Kirchoefer, J. Levy and D. G. Schlom, *Nature*, 2004, **430**, 758.

14 L. Abad, V. Laukhin, S. Valencia, A. Gaup, W. Gudat, L. Balcells and B. Martínez, *Adv. Funct. Mater.*, 2007, **17**, 3918–3925.

15 A. Tebano, C. Aruta, S. Sanna, P. G. Medaglia, G. Balestrino, A. A. Sidorenko, R. De Renzi, G. Ghiringhelli, L. Braicovich, V. Bisogni and N. B. Brookes, *Phys. Rev. Lett.*, 2008, **100**, 137401.

16 S. Lee, A. Pirogov, M. Kang, K.-H. Jang, M. Yonemura, T. Kamiyama, S.-W. Cheong, F. Gozzo, N. Shin, H. Kimura, Y. Noda and J.-G. Park, *Nature*, 2008, **451**, 805.

17 A. Herklotz, D. Lee, E.-J. Guo, T. L. Meyer, J. R. Petrie and H. N. Lee, *J. Phys.: Condens. Matter*, 2017, **29**, 493001.

18 A. N. Morozovska, E. A. Eliseev, A. K. Tagantsev, S. L. Bravina, L.-Q. Chen and S. V. Kalinin, *Phys. Rev. B*, 2011, **83**, 195313.

19 P. Zubko, G. Catalan and A. K. Tagantsev, *Annu. Rev. Mater. Res.*, 2013, **43**, 387–421.

20 P. Zubko, G. Catalan, A. Buckley, P. R. L. Welche and J. F. Scott, *Phys. Rev. Lett.*, 2007, **99**, 167601.

21 D. Lee, A. Yoon, S. Y. Jang, J.-G. Yoon, J.-S. Chung, M. Kim, J. F. Scott and T. W. Noh, *Phys. Rev. Lett.*, 2011, **107**, 057602.

22 H. Lu, D. J. Kim, C.-W. Bark, S. Ryu, C. B. Eom, E. Y. Tsymbal and A. Gruverman, *Nano Lett.*, 2012, **12**, 6289–6292.

23 D. Lee, S. M. Yang, J.-G. Yoon and T. W. Noh, *Nano Lett.*, 2012, **12**, 6436–6440.

24 Y. Kim, S. J. Kelly, A. Morozovska, E. K. Rahani, E. Strelcov, E. Eliseev, S. Jesse, M. D. Biegalski, N. Balke, N. Benedek, D. Strukov, J. Aarts, I. Hwang, S. Oh, J. S. Choi, T. Choi, B. H. Park, V. B. Shenoy, P. Maksymovych and S. V. Kalinin, *Nano Lett.*, 2013, **13**, 4068–4074.

25 S. J. Kelly, Y. Kim, E. Eliseev, A. Morozovska, S. Jesse, M. D. Biegalski, J. F. Mitchell, H. Zheng, J. Aarts, I. Hwang, S. Oh, J. S. Choi, T. Choi, B. H. Park, S. V. Kalinin and P. Maksymovych, *Nanotechnology*, 2014, **25**, 475302.

26 P. Sharma, S. Ryu, J. D. Burton, T. R. Paudel, C. W. Bark, Z. Huang, Ariando, E. Y. Tsymbal, G. Catalan, C. B. Eom and A. Gruverman, *Nano Lett.*, 2015, **15**, 3547–3551.

27 Y. Wang, K. Zhao, X. Shi, G. Li, G. Xie, X. Lai, J. Ni and L. Zhang, *Sci. Rep.*, 2015, **5**, 10841.

28 S. Das, B. Wang, Y. Cao, M. Rae Cho, Y. Jae Shin, S. Mo Yang, L. Wang, M. Kim, S. V. Kalinin, L.-Q. Chen and T. W. Noh, *Nat. Commun.*, 2017, **8**, 615.

29 A. Gómez, J. M. Vila-Fungueiriño, R. Moalla, G. Saint-Girons, J. Gázquez, M. Varela, R. Bachelet, M. Gich, F. Rivadulla and A. Carretero-Genevrier, *Small*, 2017, **13**, 1701614.

30 G. Catalan, A. Lubk, A. H. G. Vlooswijk, E. Snoeck, C. Magen, A. Janssens, G. Rispens, G. Rijnders, D. H. A. Blank and B. Noheda, *Nat. Mater.*, 2011, **10**, 963–967.

31 H. Lu, C.-W. Bark, D. Esque de los Ojos, J. Alcala, C. B. Eom, G. Catalan and A. Gruverman, *Science*, 2012, **336**, 59–61.

32 Y.-J. Li, J.-J. Wang, J.-C. Ye, X.-X. Ke, G.-Y. Gou, Y. Wei, F. Xue, J. Wang, C.-S. Wang, R.-C. Peng, X.-L. Deng, Y. Yang, X.-B. Ren, L.-Q. Chen, C.-W. Nan and J.-X. Zhang, *Adv. Funct. Mater.*, 2015, **25**, 3405–3413.

33 Y. Gu, Z. Hong, J. Britson and L.-Q. Chen, *Appl. Phys. Lett.*, 2015, **106**, 022904.

34 L. Chen, Z. Cheng, W. Xu, X. Meng, G. Yuan, J. Liu and Z. Liu, *Sci. Rep.*, 2016, **6**, 19092.

35 T. Jia, H. Kimura, Z. Cheng and H. Zhao, *Sci. Rep.*, 2016, **6**, 31867.

36 Z. Lu, Z. Fan, P. Li, H. Fan, G. Tian, X. Song, Z. Li, L. Zhao, K. Huang, F. Zhang, Z. Zhang, M. Zeng, X. Gao, J. Feng, J. Wan and J. Liu, *ACS Appl. Mater. Interfaces*, 2016, **8**, 23963–23968.

37 D. Guo, G. Xie and J. Luo, *J. Phys. D: Appl. Phys.*, 2014, **47**, 013001.

38 K. Yakushiji, F. Ernult, H. Imamura, K. Yamane, S. Mitani, K. Takanashi, S. Takahashi, S. Maekawa and H. Fujimori, *Nat. Mater.*, 2005, **4**, 57–61.

39 H. A. Atwater and A. Polman, *Nat. Mater.*, 2010, **9**, 205–213.

40 X. Yu, T. J. Marks and A. Facchetti, *Nat. Mater.*, 2016, **15**, 383.

41 J.-G. J. Zhu and C. Park, *Mater. Today*, 2006, **9**, 36–45.

42 S. Yuasa, T. Nagahama, A. Fukushima, Y. Suzuki and K. Ando, *Nat. Mater.*, 2004, **3**, 868.

43 Z. Xu, M. Gao, L. Yu, L. Lu, X. Xu and Y. Jiang, *ACS Appl. Mater. Interfaces*, 2014, **6**, 17823–17830.

44 Z. Konstantinović, F. Sandiumenge, J. Santiso, L. Balcells and B. Martínez, *Nanoscale*, 2013, **5**, 1001–1008.

45 R. Abrudan, F. Brüssing, R. Salikhov, J. Meermann, I. Radu, H. Ryll, F. Radu and H. Zabel, *Rev. Sci. Instrum.*, 2015, **86**, 063902.

46 E. Dagotto, T. Hotta and A. Moreo, *Phys. Rep.*, 2001, **344**, 1–153.

47 A.-M. Haghiri-Gosnet and J.-P. Renard, *J. Phys. D: Appl. Phys.*, 2003, **36**, R127.

48 T. Wu, S. B. Ogale, J. E. Garrison, B. Nagaraj, A. Biswas, Z. Chen, R. L. Greene, R. Ramesh, T. Venkatesan and A. J. Millis, *Phys. Rev. Lett.*, 2001, **86**, 5998–6001.

49 C. Moreno, C. Munuera, S. Valencia, F. Kronast, X. Obradors and C. Ocal, *Nano Lett.*, 2010, **10**, 3828–3835.

50 L. Balcells, L. Peña, R. Galceran, A. Pomar, B. Bozzo, Z. Konstantinović, F. Sandiumenge and B. Martínez, *J. Appl. Phys.*, 2013, **113**, 073703.

51 A. Tebano, C. Aruta, P. G. Medaglia, F. Tozzi, G. Balestrino, A. A. Sidorenko, G. Allodi, R. De Renzi, G. Ghiringhelli, C. Dallera, L. Braicovich and N. B. Brookes, *Phys. Rev. B: Condens. Matter Mater. Phys.*, 2006, **74**, 245116.

52 L. Marín, L. A. Rodríguez, C. Magén, E. Snoeck, R. Arras, I. Lucas, L. Morellón, P. A. Algarabel, J. M. De Teresa and M. R. Ibarra, *Nano Lett.*, 2015, **15**, 492–497.

53 J. Ma, Y. Zhang, L. Wu, C. Song, Q. Zhang, J. Zhang, J. Ma and C.-W. Nan, *MRS Commun.*, 2016, **6**, 354–359.

54 R. U. Chandrasena, W. Yang, Q. Lei, M. U. Delgado-Jaime, K. D. Wijesekara, M. Golalikhani, B. A. Davidson, E. Arenholz, K. Kobayashi, M. Kobata, F. M. F. de Groot, U. Aschauer, N. A. Spaldin, X. Xi and A. X. Gray, *Nano Lett.*, 2017, **17**, 794–799.

55 Z. Konstantinović, J. Santiso, L. Balcells and B. Martínez, *Small*, 2009, **5**, 265–271.

56 Z. Konstantinović, J. Santiso, D. Colson, A. Forget, L. Balcells and B. Martínez, *J. Appl. Phys.*, 2009, **105**, 063919.

57 Z. Konstantinović, L. Balcells and B. Martínez, *J. Magn. Magn. Mater.*, 2010, **322**, 1205–1208.

58 A. Tebano, C. Aruta, P. G. Medaglia, F. Tozzi, G. Balestrino, A. A. Sidorenko, G. Allodi, R. De Renzi, G. Ghiringhelli, C. Dallera, L. Braicovich and N. B. Brookes, *Phys. Rev. B: Condens. Matter Mater. Phys.*, 2006, **74**, 245116.

59 L. Yao, S. Inkinen and S. van Dijken, *Nat. Commun.*, 2017, **8**, 14544.

60 Y.-L. Chung, P. Y. Lai, Y.-C. Chen and J.-S. Chen, *ACS Appl. Mater. Interfaces*, 2011, **3**, 1918–1924.

61 J. M. D. Coey, M. Viret and S. von Molnár, *Adv. Phys.*, 2009, **58**, 571–697.

62 M. Andra, F. Gunkel, C. Baumer, C. Xu, R. Dittmann and R. Waser, *Nanoscale*, 2015, **7**, 14351–14357.

63 T. Bieger, J. Maier and R. Waser, *Sens. Actuators, B*, 1992, **7**, 763–768.

64 R. Merkle and J. Maier, *Angew. Chem., Int. Ed.*, 2008, **47**, 3874–3894.

Resistive Switching in Semimetallic SrIrO₃ Thin Films

Víctor Fuentes,[†] Borislav Vasić,[‡] Zorica Konstantinović,[‡] Benjamín Martínez,[†] Lluís Balcells,[†] and Alberto Pomar*,[†]

[†]Institut de Ciència de Materials de Barcelona (ICMAB-CSIC), Campus de la UAB, Bellaterra 08193, Spain
[‡]Center for Solid State Physics and New Materials, Institute of Physics Belgrade, University of Belgrade, Pregrevica 118, 11080 Belgrade, Serbia

Ⓢ *Supporting Information*

ABSTRACT: Local electrical properties, measured by conductive atomic force microscopy, of semimetallic SrIrO₃ thin films are reported. The appearance of an Anderson-type metal−insulator transition (MIT) triggered by disorder and spatial localization due to film thickness reduction is analyzed as well as their influence on the resistive switching behavior. For thin enough films (below ∼3 nm) samples are insulating with hysteretic I−V curves indicative of reversible resistive switching behavior between two states of clearly different resistance at room temperature. A sharp transition into a low resistance state (LRS), i.e., an abrupt increase of the current intensity, is detected above a well-defined threshold voltage indicative of localization of charge carriers. On the other hand, thicker samples exhibit a semimetallic character, and I−V curves show progressive changes of the local resistance without a clearly defined threshold voltage, thus evidencing the absence of a MIT transition with a well-defined resistance jump between the different resistance states.

KEYWORDS: *resistive switching, metal−insulator transition, SrIrO₃, conductive atomic force microscopy, iridate thin films*
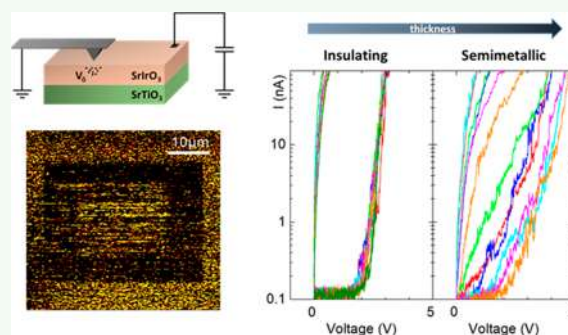
■ INTRODUCTION

In the search for a new generation of faster and more energy efficient electronic devices, the use of reversible resistive switching (RS) phenomena has been proposed as a very appealing solution for the development of nonvolatile memory devices.[1,2] RS is the change of resistance in a reversible manner between two stable states of well-defined resistance by applying voltage pulses. This bistable behavior between high- and low-resistance states can be used as the core of a memory cell to implement a resistive random access memory (Re-RAM). RS behavior, typically observed in metal−insulator−metal (MIM) structures, has been found in a variety of materials, including transition metal oxides (TMOs), chalcogenides, and even organic compounds, and diverse physical mechanisms, mostly based on thermochemical or electrochemical effects, have been invoked to account for the observed experimental behavior.[3−7]

In the case of TMOs one of the most common mechanisms to induce RS is based on modifications of the doping rate by valence change. The migration of oxygen vacancies, or metal cations, under an electric field along defects, grain boundaries, dislocations, and so on induces a valence change of the cations nearby, and therefore a change of the doping rate that may promote strong changes of the resistivity or even to trigger the appearance of a metal-to-insulator transition (MIT).[2,3,8−10] This process of ionic migration can also occur at the interface between the metallic electrode and the active insulating oxide.[8] Among TMOs exhibiting RS behavior, Mott insulators and

strongly correlated systems are of particular interest because they can exhibit different types of MIT transitions, i.e., huge changes of the electrical resistance, in response to a variety of external stimuli, such as temperature, doping rate, or structural strain.[11] The close similarity between electronic correlations and crystal field splitting energies in TMOs provides different mechanism for tuning their electronic properties, and these mechanisms can even be widened by making use of spin−orbit coupling (SOC). In 3d TMOs SOC is not very relevant because being proportional to Z^4, where Z is the atomic number of the element under consideration, is much smaller than crystal field splitting and electronic correlations. However, in the case of 5d elements, such as Ir, SOC reaches values of about 0.5 eV.[12−14] Thus, SOC becomes comparable to crystal field and electronic correlations, giving place to novel physics and exotic properties.[15−17] In particular, the Ruddlesden−Popper series of 5d strontium iridates ($Sr_{n+1}Ir_nO_{3n+1}$) have been investigated in the past years because of the strong interplay between these three contributions. This interplay may trigger different electronic states just by subtle structural or chemical changes. For example, the perovskite-like $n = \infty$ phase (SrIrO₃) presents a semimetallic ground state[18] while on the other extreme of the series, in the $n = 1$ phase (Sr₂IrO₄), a

gap is opened at the Fermi level, leading the system into a Mott insulator state.[19]

As mentioned above, the MIT can be modified by applying different external perturbations, such as pressure[20] or electric field pulses as demonstrated for the $n = 1$ phase[21] and in the $n = 2$ phase.[22] In the case of the perovskite $n = \infty$ phase ($SrIrO_3$, hereafter denoted as SIO) thin films, it was reported that a MIT can be triggered by tuning the compressive strain induced by the substrate or by reducing the film thickness.[23−27] Different studies indicate that the MIT induced in these cases can be either of disorder driven Anderson type or unconventional Mott−Anderson type in which disorder effects and electronic correlations coexist.[24] However, recent results in high quality epitaxial thin films also show a concomitant divergence of the magnetic susceptibility in very thin films (four unit cells) that clearly points to the opening of a Mott gap.[28,29] Besides their fundamental relevance, the ability to modify at wish the material resistivity by inducing a MIT is of strong interest from the application point of view. Even though the appearance of a MIT in SIO has been reported by different groups[23−27] and some results regarding RS effects in the $n = 1$ phase[21,22] have been reported, reports regarding RS in the interesting semimetallic $n = \infty$ phase are very scarce.

In this work we present a systematic study of RS behavior in high quality SIO thin films prepared by RF sputtering on top of (001)-STO substrates, through local $I−V$ curve measurements and current mapping, by using conductive atomic force microscopy (C-AFM). Epitaxial SIO films show semimetallic character, and the appearance of a MIT is triggered by the reduction of film thickness. For film thickness below ∼3 nm an Anderson-type MIT, i.e., induced by disorder, appears, and resistance increases notoriously on lowering temperature. $I−V$ characteristic curves in thin samples exhibiting the MIT show the typical hysteretic behavior associated with RS processes with two well-defined resistance states. $I−V$ curves show directional RS depending on the polarity of the applied voltage; thus, it can be classified as bipolar RS, with an abrupt increase of the current for voltages above a threshold value of around 2 V. Additionally, because of the particular features of the experimental setup, the observed RS is of interface type in which RS takes place at the interface between the metal electrode and the SIO film. Electric field pulses promote oxygen vacancies migration through the interface; then, to maintain electrical neutrality, a valence change of the cations nearby takes place and therefore a modification of the charge carriers' density and of the position of the Fermi level. A redox mechanism based on the band structure of SIO is proposed to account for the observed RS behavior. Current maps performed with voltage values above the threshold value and of different polarity allow demonstrating the writing/erasing processes, making evident the feasibility of the system for the implementation of Re-RAMs. On the other hand, in the case of thicker films, initially in a semimetallic state, $I−V$ curves present a smooth variation of resistance, without a clear threshold voltage, suggesting the absence of two well-defined resistance states separated by an energy jump. In this case, changes of resistance by applying voltage pulses are simply associated with the variation of charge carriers' density due to the migration of oxygen vacancies.

EXPERIMENTAL DETAILS

SIO films were grown by RF magnetron sputtering on top of single crystalline (001)-$SrTiO_3$ (STO) substrates at 900 °C in an oxygen atmosphere at 140 mTorr. STO substrates were treated before deposition to obtain atomically flat surfaces of TiO_2 terraces. The treatment consisted in an ultrasound leaching in deionized water for 10 min followed by an annealing for 2 h at 1000 °C.[30] SIO samples with different thickness ranging between 2 and 26 nm were prepared. X-ray reflectometry (Siemens D-5000 diffractometer) was used to determine the thickness of SIO thick samples and to calibrate the growth rate; then the thickness of the thinnest films was determined by adjusting the deposition time.

X-ray measurements were also used to check phase purity and epitaxial growth quality. For this purpose a high-resolution X-ray $\theta − 2\theta$ scan of the (002) peak was performed by a using a PANalytical X'PERT PRO MRD system. Additionally, reciprocal space maps (RSM) around the (−103) diffraction peak (pseudocubic notation) were also recorded by using a Bruker D8-Discover diffractometer.

The temperature dependence of the resistivity was measured by using a standard four-probe configuration in a PPMS system from Quantum Design. Measurements were performed in 400 μm long × 100 μm wide tracks patterned by UV lithography and physical etching. The surface quality of the samples was studied by using scanning electron microscopy (SEM) (QUANTA FEI 200 FEG-ESEM). An MFP3D system from Asylum was used for the acquisition of topographic images, $I−V$ curves, and current maps. Atomic force microscope (AFM) topography images were recorded in tapping mode by using Sb-doped Si probes (NCHV-A from Bruker). The surface roughness of the topographic images was calculated as a root mean square (rms) of the height distribution of the sample surface. $I−V$ curves and current maps were measured at room temperature by Conductive-AFM (C-AFM) by using doped diamond-coated probes (DDESP-FM-V2 from Bruker), applying voltage to the sample while the tip was grounded. $I−V$ curves were taken on random positions of the bare sample surfaces with a voltage sweep ranging between +5 and −5 V in an ambient atmosphere. As it has been previously reported, the surface of iridates is very sensitive to air exposure, and measurements of surface properties lose reliability a few days after deposition of the film.[27,31] This intrinsic surface instability is very challenging for C-AFM measurements, especially for performing measurements with long exposure times as current maps. To perform C-AFM maps, a noncontinuous layer of platinum nanoparticles was deposited on top of the SIO film. More details on these measurements may be found later and in the Supporting Information.

RESULTS

A high-resolution $\theta−2\theta$ scan corresponding to a 21 nm thick SIO film deposited on (001)-STO substrate is shown in Figure 1a. The epitaxial nature of the SIO film is clearly evidenced by the figure. The (002) reflection peak corresponding to the perovskite structure of the ($n = \infty$) phase is shown. Apart from the (00l) family, no additional peaks were found in the $\theta−2\theta$ scan, making evident the high purity of the $n = \infty$ phase in the
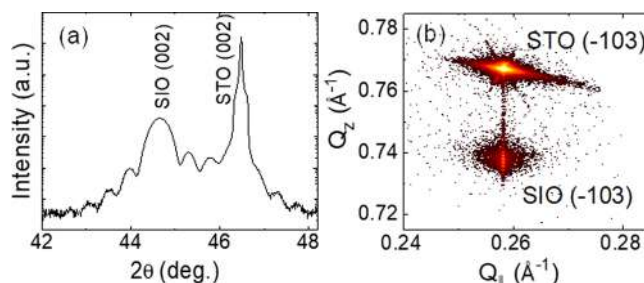

Figure 1. X-ray diffraction measurements of the SIO/STO thin films. (a) High-resolution $\theta−2\theta$ scan around (002) diffraction peaks. (b) Reciprocal space map of the (−103) peaks showing full strained state of the SIO films. For simplicity, all diffraction peaks are indexed in pseudocubic notation.

films. Moreover, satellite fringes can be clearly appreciated at both sides of the SIO Bragg peak. These oscillations, arising from the diffraction of the X-ray beam at film finite planes with coherent thickness, are indicative of the high crystalline quality of the films and of the parallel orientation respect to the substrate. The peak position corresponds to an out-of-plane lattice parameter of 4.056 Å; i.e., the SIO unit cell is slightly elongated with respect to the reported bulk value (a_0 = 3.943 Å).[32] Such a value is in agreement with an elastic behavior governed by the in-plane compressive strain imposed by the smaller STO substrate (a_{STO} = 3.905 Å) as usually reported in the literature.[14,23−25] Figure 1b displays a reciprocal space map around the (−103) reflection. It can be appreciated from the figure that both the substrate and the film peaks are aligned at the same in plane component ($Q_∥$), confirming the fully strained nature of the SIO film.

Surface morphology of SIO films, measured by AFM immediately after the deposition, corresponding to a 2 nm thick and a 26 nm thick samples are depicted in Figures 2a and
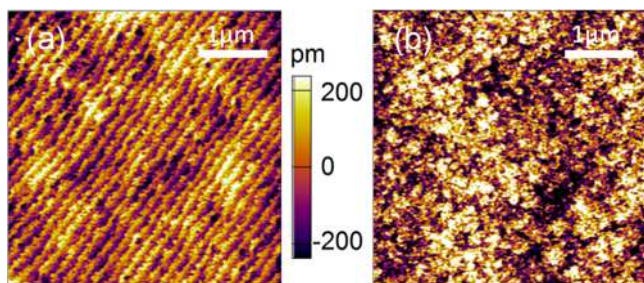
Figure 2. AFM topography images of two SIO thin films on STO with thicknesses of (a) 2 nm and (b) 26 nm. Both films exhibit flat surfaces with low roughness (rms below 0.2 nm). In the case of very thin film, the underlying terraced structure is still observed.

2b, respectively. Both samples show a flat topography with a surface roughness rms below 0.2 nm. In the case of extremely thin samples (rms typically below 0.12 nm) the underlying terrace and steps structure of the STO substrate is replicated on the SIO surface.

Electrical properties of SIO films are clearly thickness-dependent. Figure 3a depicts the temperature dependence of the sheet resistivity for a series of SIO films with thicknesses ranging between 2 and 26 nm. Metallic behavior is observed for film thickness down to ∼3 nm, in agreement with previous results.[23−27,33] However, as thickness decreases a progressive upturn of the resistivity at low temperatures is detected. The temperature at which the minimum in the resistivity is found shifts up in temperature as thickness decreases, and the system exhibits fully insulating behavior for the 2 nm thick sample, thus locating the MIT transition between 3 and 2 nm, in good agreement with previous reports.[24] Discrepancies regarding the actual thickness value at which the MIT takes place are usually attributed to differences in the microstructural quality of the samples.[34] For sample thickness above 10 nm the high-temperature behavior of the resistance is well described by the expression $\rho(T) = \rho_0 + CT^{4/5}$ (see Figure 3b). The value obtained for the residual resistivity, ρ_0, is in all the samples below the so-called Mott−Ioffe−Regel (MIR) limit[35] ($h/e^2 \approx$ 26 kΩ). In the low-temperature regime, the resistivity shows a T^2 dependence down to the lowest temperature measured (∼10 K) indicative of a Fermi liquid behavior (see the inset of Figure 3b). This crossover from a non-Fermi liquid at high T
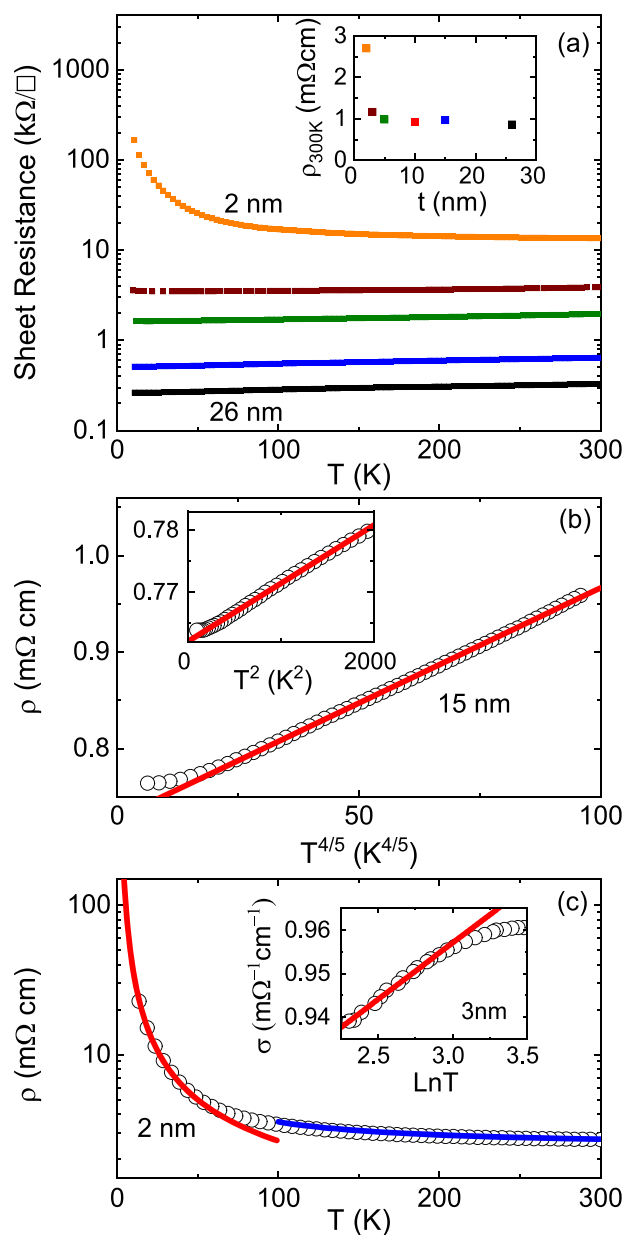
Figure 3. Electric properties of the SIO/STO films. (a) Temperature dependence of the sheet resistance in SIO films with thickness of 2 nm (orange), 3 nm (brown), 5 nm (green), 15 nm (blue), and 26 nm (black). Inset: resistivity of films at 300 K. A change of behavior from a semimetallic state to an insulating state when reducing thickness below 3 nm is clearly observed. (b) Temperature dependence of the resistivity of 15 nm thick SIO film vs $T^{4/5}$. Inset: details of the low-temperature regime to make evident the crossover to a Fermi liquid behavior at low T. (c) Temperature dependence of the resistivity of the 2 nm thick sample. The fittings using the Mott's variable range hopping (VRH) model, $\ln \sigma \propto 1/T^{1/(d+1)}$ (red line), at low T and the Arrhenius equation for thermal activation conduction, $\rho(T) = \rho_0 e^{(\Delta/k_B T)}$, at high T (blue line) are indicated. Inset: details of the low-temperature regime of the sheet conductivity of the 3 nm thick sample showing the ln T dependence indicative of two-dimensional weak localization.

to a Fermi liquid behavior at low T is typically associated with strongly correlated systems;[36] thus, we should conclude that thick SIO samples behave as a three-dimensional correlated metal.

As the critical thickness corresponding to the MIT transition is approached, the low-temperature upturn of the resistivity shifts up to higher temperature and becomes more abrupt, as typically observed when the MIT transition is approached from the metallic side. In the case of the 3 nm thick sample a notable upturn of the resistivity is observed below about 60 K, and the low-temperature regime is well described by a characteristic ln T dependence of the sheet conductance, indicative of two-dimensional weak localization (see the inset of Figure 3c).[37] Once the film thickness is reduced below 3 nm, the transport properties change abruptly. The resistance of the 2 nm thick film presents a typical insulating dependence with $d\rho/dT < 0$ in the whole temperature range. Clues of this transition can also be observed in the inset of Figure 3a, where the resistivity at 300 K is almost constant for the films with thickness between 3 and 26 nm but sharply increases for the 2 nm thick sample.

To clarify the nature of the MIT induced by reducing the film thickness, we have carefully analyzed the temperature dependence of the resistivity of the fully insulating 2 nm thick sample.[38] The low-temperature resistance upturn is well described by using the Mott's variable range hopping (VRH) model: ln $\sigma \propto 1/T^{1/(d+1)}$, with σ being the conductivity and d the dimension.[39] As can be appreciated in Figure 3c, the VRH model with $d = 2$ fits experimental data almost perfectly up to about 40−45 K, while the high-temperature range is properly described by using the Arrhenius equation for thermal activation conduction $\rho(T) = \rho_0 e^{(\Delta/k_B T)}$, with Δ being an activation energy (a value of $\Delta \sim 6$ meV was obtained from the fit) and k_B the Boltzmann's constant (see Figure 3c). Therefore, from the analysis of the $R(T)$ curves we can conclude that the MIT induced in SIO films by reducing the thickness is of Anderson localization type due to disorder, in good agreement with previous reports.[24,26]

The possibility of inducing an Anderson-type MIT by reducing film thickness suggests that resistivity of SIO thin films may be sensitive to different stimuli, especially for a thickness close to the critical one; therefore, it may be a good alternative for obtaining a strong RS response and thus of interest for the implementation of RS devices. For this purpose, we have approached the study of local $I-V$ curves measured at room temperature by C-AFM of SIO thin films. To illustrate our findings, we present in Figure 4 details (below 100 nA) of the $I-V$ curves on samples at both extremes of the thickness series (i.e., 2 and 26 nm). Results at intermediate thickness (5 nm) as well as the full IV curves may be found in the Supporting Information. In all cases hysteretic $I-V$ curves are observed indicative of RS behavior. An anticlockwise behavior, where a positive sample voltage induces the low-resistance state (LRS) and a negative sample voltage induces the high-resistance state (HRS), is found. $I-V$ curves were measured by applying a voltage sweep between +5 and −5 V with no current limitation. Figure 4a displays the $I-V$ curves corresponding to the 2 nm thick film. As it can be seen, the current intensity remains constant and near zero until the threshold voltage value of about 2 V is reached, at which a sudden increase of the current takes place (indicated by arrow 1 in the figure). After reaching +5 V, the sample remains in the LRS returning to 0 V through the superior limit of the graph along the path denoted by arrow 2. In the negative voltage range, the $I-V$ curve starts at the LRS, and the current is continuously increasing for voltages up to −5 V (trajectory marked by arrow 3). Upon reaching this voltage, the $I-V$ curve
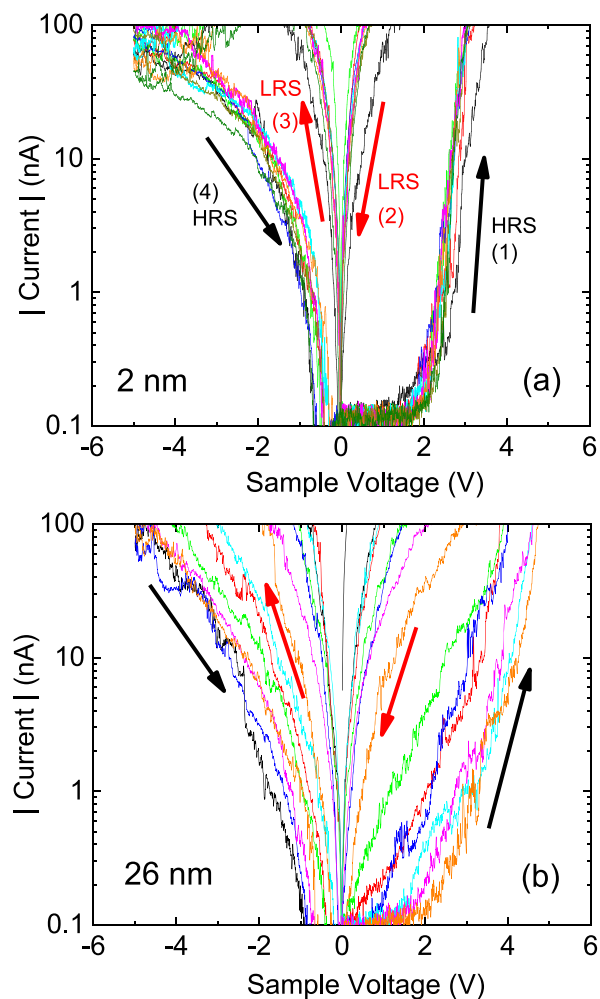

Figure 4. C-AFM $I-V$ curve details in fresh SIO samples: (a) 2 nm thick film; (b) 26 nm thick film. The different colors of the curves represent the different consecutive voltage cycles between +5 and −5 V. The different arrows indicate the direction of the curves and their current resistance state (HRS: black; LRS: red).

returns to the HRS along the path indicated by arrow 4. Figure 4b depicts $I-V$ curves corresponding to the 26 nm thick sample. In this latter case resistance changes in a continuous way, and no well-defined resistance states separated by a clear voltage threshold are observed. The similarity of the measured $I-V$ curves in both samples suggests that the mechanism behind the observed variations of resistance is the same in both cases. However, the absence of a clear voltage threshold in the case of the thick sample suggests the absence of a well-defined energy transition separating the LRS and HRS.

A deeper insight into the RS process in SIO samples may be obtained by performing current maps over extended areas in both HRS and LRS states. Nevertheless, the significant statistical gain has the drawback that measurements are more aggressive and time-consuming than the local $I-V$ curves. Performing a C-AFM map implies to move the AFM tip back and forth several times in the same area of the sample. The continuous scanning deteriorates the electrical tip−sample contact after a few cycles. This well-known drawback in C-AFM analysis of RS phenomena is usually attributed to tip contamination.[40] Experimentally, we have observed that capping of the SIO film surface with a noncontinuous layer of Pt nanoparticles (NPs) is useful to perform the C-AFM

maps. This beneficial effect of the Pt NPs avoids degradation of the tip−sample electrical contact either by reducing the degradation of film surface or by enhancing tip lifetime since brushing with Pt nanoparticles reduces tip contamination. Thus, current maps were performed in 26 nm films with their surface partially covered with platinum NPs (see further details in the Supporting Information). Figure 5a presents a 50 × 50
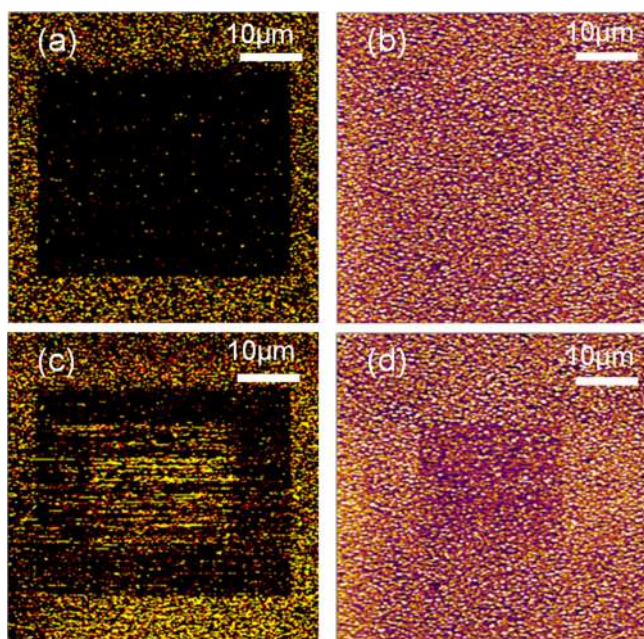

Figure 5. C-AFM current maps (a, c) and topography images (b, d) of a 26 nm SIO/STO sample with Pt NPs on the top obtained simultaneously. (a) Current map showing a 35 × 35 μm^2 zone set into the HRS. (b) Topography of the same zone showing no changes in the surface topography. (c) Current map of the same zone after resetting a 20 × 20 μm^2 zone to the LRS. (d) Topography image of the same zone, where minor changes in the topography can be noticed in the switched area.

μm^2 current map measured at low voltage (0.2 V) and 570 nN of normal load after the scanning of the central 35 × 35 μm^2 area at the negative bias voltage (−5 V) applied to the sample. A clear reduction of the conductivity can be observed in a central square (dark area) that corresponds to the established HRS. In contrast, the surrounded brighter area shows a higher current and corresponds to the pristine state. Figure 5b shows the topography image of the same zone measured simultaneously; no changes in the topography of the area switched into HRS are appreciated. Figure 5c shows a current map of the same zone measured after the scanning of the central 20 × 20 μm^2 area at +3 V applied to the sample. Now three different states can be observed: the pristine state at the outer parts of the current map, the HRS represented as a darker square ring, and finally the LRS depicted by a central bright square. Similar to the I−V curves in Figure 4, HRS was induced by negative sample voltage (−5 V), and it can be reversed to LRS by scanning at positive sample voltage (+3 V). The associated topography measurement is also shown in Figure 5d. Some minor topography changes are detected in the central area switched into LRS. They are represented by a slightly darker contrast, indicating a local decrease of the film height, which, in principle, could be caused by the removal of the Pt NPs or by a local compression of the film. Nevertheless, since accumu-

lations of NPs were not observed along outer rims of the scanning area, and the current intensity in this central zone even increases, NPs removal should be discarded as a possible explanation of the observed changes of the film's topography. On the other hand, because of the difficulties to reset the zone into LRS, a higher normal load (1140 nN) was applied during the scanning performed at +3 V. This increment in the normal load of the AFM tip may well be responsible for the observed local film compression.

Even with the increase of the normal load in the positive voltage scan, the switching into LRS was more difficult to achieve than the switching into HRS. One possible reason for this behavior is the occurrence of undesired reactions at the sample surface for high enough positive voltages due to local anodic oxidation,[38] decreasing the stability of the current measurements. To avoid these reactions, the sample voltage used to reset the surface into the LRS was decreased to a value of +3 V (instead of +5 V). This reduction in the reset voltage is probably the main reason for the less pronounced and stable switching into LRS displayed in Figure 5c.

■ DISCUSSION

There is a large diversity of mechanisms proposed to explain RS phenomena.[3−7] In the particular case of TMOs, redox-based mechanisms, driven by the motion of cations (coming from the electrodes) or defects such as oxygen vacancies, have attracted much attention.[2,3,9] Two different categories can be distinguished: filamentary RS, consisting in the creation of filament of cations or vacancies in a TMO film sandwiched between two electrodes,[1] and interface RS, in which this process of ionic migration occurs at the interface between the metallic electrode and the active insulating oxide.[8] Because of the in-plane geometry used in this study for the I−V measurements (the current path goes from AFM tip, through the sample surface, and finally to a metal contact placed on the sample surface), only interface RS should be considered.

In correlated metals such as SIO, the variation on the concentration of oxygen vacancies can modify the valence of the surrounding metal cations. Because the oxygen vacancies substitute an oxygen position, the surrounding cations must adapt their valence to compensate for the charge variation. Therefore, new electrons would fill Ir orbitals changing the Fermi level and electric properties.[11] Depending on the type of majority charge carriers, this valence change will result in an increase (decrease) of the resistivity in the case of holes (electrons).[2] It is worth noting that the nature of the majority charge carriers in SIO thin films is not clearly established yet. As a semimetal, SIO is expected to have a conduction mechanism that involves both electrons and holes.[19,27] Nevertheless, small differences in the charge carrier density could be critical for the RS mechanism. Recent results based on magnetotransport and thermoelectric measurements suggest that electrons and holes have similar densities and mobilities.[27] However, given the small unbalance between them[27] and the degree of disorder present in our films (considering the appearance of Anderson localization), it seems reasonable to consider that both electrons and holes could be the majority charge carriers in SIO films. Therefore, two similar mechanisms are proposed to explain the observed RS behavior in SIO films.

If electrons are considered the majority charge carriers, the change in the oxygen vacancies' concentration would be driven by their internal migration within a film induced by an

externally applied electric field.[41] When a positive voltage is applied to the sample (negative voltage to AFM tip), oxygen vacancies would migrate toward the AFM tip, thus increasing the Fermi level. The subsequent rise of the electron concentration at the tip—sample interface would decrease the contact resistance and therefore transform the sample surface into the LRS. On the other hand, negative sample voltage (positive voltage at the AFM tip) would act reversely, expelling the vacancies from the tip—sample interface and thus decreasing the electron concentration and conductivity of the sample surface and leading it to HRS. Alternatively, if holes are considered the majority charge carriers, oxygen vacancies could be incorporated or removed from the interface by a redox reaction at the film surface triggered by an externally applied electric field.[42] Contrary to the previous case, vacancies decrease the conductivity in hole-like systems since they are considered as acceptors scavengers. Positive voltage applied to sample would cause the reduction of the atmosphere's oxygen and the incorporation of oxygen anions into the oxide matrix, removing the vacancies from the interface according to eq 1.

$$Sr^{2+}Ir^{4+}O_{3-y}{}^{2-}V_{\ddot{O}y} + 2e_y{}^- + \frac{1}{2}yO_2 \rightarrow Sr^{2+}Ir^{4+}O_3{}^{2-} \tag{1}$$
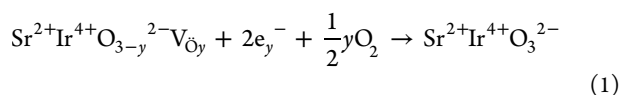
Then, the Fermi level would decrease, while the hole density and the conductivity would increase and transform the sample surface beneath the AFM tip into the LRS. The system can be reversed into the HRS by applying negative voltage to the sample. In this case, the following oxidation reaction takes place:

$$Sr^{2+}Ir^{4+}O_3{}^{2-} \rightarrow Sr^{2+}Ir^{4+}O_{3-y}{}^{2-}V_{\ddot{O}y} + 2e_y{}^- + \frac{1}{2}yO_2 \tag{2}$$
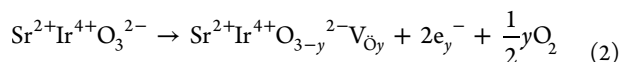
With this reaction oxygen anions would be removed from the matrix, leaving vacancies behind. These vacancies would reduce drastically the number of holes and raise up the Fermi level, reducing this way the conductivity. Although both films seem to follow the same mechanism for the changes of resistance, the two set of I—V curves present notable differences. Figure 4b, corresponding to the 26 nm thick sample, shows smoothly rising I—V curves for the positive voltage range from 0 V to the saturation of the current detector. On the other hand, Figure 4a, corresponding to the 2 nm thick film, which has undergone MIT, shows an almost zero current up to a clear voltage threshold value of about 2 V, when an abrupt increase of the current intensity occurs. This different behavior is closely related to the differences in the band structures of the films that are induced by the MIT. On one hand, it is reported that thick SIO films (such as the employed 26 nm thick one) behave as a semimetal with electrons and holes having similar densities.[18,19,27] On the other hand, even though the band structure of very thin films (such as the 2 nm thick one) has not been measured so far, thickness reduction may trigger the appearance of an Anderson-type MIT transition with strong carriers' localization.[24,26] Furthermore, the aperture of a Mott gap in ultrathin SIO films has been recently documented.[28] With this picture in mind, the behavior of a thick SIO film (26 nm) reflects changes of resistance in a system with continuous energy levels having thus a smooth increase of the current. Moreover, the shift of the Fermi level would bring the system into a state with higher density of states, finally giving higher conductivity and setting it into the LRS. On the other hand, in

the case of the very thin film (2 nm), as long as the Fermi energy lies inside localized states, charge carrier's mobility is seriously hampered or even suppressed, and the current would be almost zero. Nevertheless, when the Fermi level crosses the mobility edge, an energy transition between localized and extended states takes place; for high enough positive voltage, an abrupt increase of the current would be observed, and obviously the system would be switched in the LRS with a higher conductivity.

■ CONCLUSIONS

The local transport properties of SrIrO$_3$ thin films prepared by RF sputtering on top of the (001)-SrTiO$_3$ substrates have been analyzed as a function of the film's thickness. Macroscopic measurements of the film's resistivity as a function of temperature allow demonstrating that an Anderson-type MIT transition can be induced, triggered by thickness reduction, below ∼3 nm. On the other hand, SIO films exhibit hysteretic I—V curves indicative of RS behavior irrespective to their thickness. I—V curves show directional RS depending on the polarity of the applied voltage; thus, it can be classified as bipolar RS. Additionally, because of the particular experimental setup used, it is concluded that the observed RS is of interface type in which RS takes place at the interface between the metal electrode (AFM tip) and the SIO film. Electric field pulses promote oxygen vacancies migration through the interface; then, to maintain electrical neutrality, a valence change of the cations nearby takes place and therefore a modification of the charge carriers' density and of the position of the Fermi level. However, the features of the RS process are clearly different in the case of very thin samples (below 3 nm), where the appearance of the MIT, with the concomitant carriers' localization, is reflected in the existence of a well-defined voltage threshold value separating the low- and high-resistance states. In contrast, in thicker films with semimetallic behavior I—V curves present a continuous smooth variation of resistance, without a clear threshold voltage, making evident the absence of an energy sharp transition separating high- and low-resistance states. In this case, changes of resistance by applying voltage pulses are simply associated with the variation of charge carriers' density due to the migration of oxygen vacancies. In spite of the different behaviors, the same mechanisms involving oxygen vacancies are claimed to explain the observed results irrespective of the nature of the majority charge carriers, electrons or holes. Current maps performed with voltage values above the threshold value and of different polarity allow demonstrating the writing/erasing processes, making evident the feasibility of the system for the implementation of Re-RAMs.

■ ASSOCIATED CONTENT

ⓢ Supporting Information

The Supporting Information is available free of charge on the ACS Publications website at DOI: 10.1021/acsaelm.9b00519.

> nonconformal capping of the SIO surface with Pt nanoparticles to improve C-AFM measurements; complete I—V curves of SIO thin films (2 and 26 nm); details of the I—V curve showing resistive switching for SIO film at intermediate thickness (5 nm) (PDF)

■ AUTHOR INFORMATION

Corresponding Author
*E-mail: apomar@icmab.es.

ORCID 🔘
Benjamín Martínez: 0000-0001-9879-7748
Alberto Pomar: 0000-0002-5855-2356

Notes
The authors declare no competing financial interest.

■ ACKNOWLEDGMENTS

■ ABBREVIATIONS

AFM, atomic force microscopy; C-AFM, conductive atomic force microscopy; MIT, metal−insulator transition; RS, resistive switching; LRS, low-resistance state; HRS, high-resistance state; Re-RAM, resistive random access memory; SIO, $SrIrO_3$; TMO, transition metal oxide; SOC, spin−orbit coupling; RSM, reciprocal space map; rms, root-mean-square; $I−V$, intensity−voltage; MIR, Mott−Ioffe−Regel; MIM, metal−insulator−metal.

■ REFERENCES

(1) Waser, R.; Aono, M. Nanoionics-Based Resistive Switching Memories. *Nat. Mater.* 2007, 6, 833−840.

(2) Sawa, A. Resistive Switching in Transition Metal Oxides. *Mater. Today* 2008, 11, 28−36.

(3) Waser, R.; Dittmann, R.; Staikov, C.; Szot, K. Redox-Based Resistive Switching Memories Nanoionic Mechanisms, Prospects, and Challenges. *Adv. Mater.* 2009, 21, 2632−2663.

(4) Lee, T.; Chen, Y. Organic Resistive Nonvolatile Memory Materials. *MRS Bull.* 2012, 37, 144−149.

(5) Jeong, D. S.; Thomas, R.; Katiyar, R. S.; Scott, J. F.; Kohlstedt, H.; Petraru, A.; Hwang, C. S. Emerging Memories: Resistive Switching Mechanisms and Current Status. *Rep. Prog. Phys.* 2012, 75, No. 076502.

(6) Yang, J. J.; Strukov, D. B.; Stewart, D. R. Memristive Devices for Computing. *Nat. Nanotechnol.* 2013, 8, 13−24.

(7) Scott, J. C.; Bozano, L. D. Nonvolatile Memory Elements Based on Organic Materials. *Adv. Mater.* 2007, 19, 1452−1463.

(8) Bagdzevicius, S.; Maas, K.; Boudard, M.; Burriel, M. Interface-Type Resistive Switching in Perovskite Materials. *J. Electroceram.* 2017, 39, 157−184.

(9) Mehonic, A.; Kenyon, A. J. Resistive Switching in Oxides. In *Springer Series in Surface Sciences*; Jupille, J., Thornton, G., Eds.; Springer International Publishing: Cham, 2015; Vol. 58, pp 401−428.

(10) Peña, L.; Garzón, L.; Galceran, R.; Pomar, A.; Bozzo, B.; Konstantinovic, Z.; Sandiumenge, F.; Balcells, L.; Ocal, C.; Martinez, B. Macroscopic Evidence of Nanoscale Resistive Switching in $La_{2/3}Sr_{1/3}MnO_3$ micro-Fabricated Bridges. *J. Phys.: Condens. Matter* 2014, 26, 395010.

(11) Janod, E.; Tranchant, J.; Corraze, B.; Querré, M.; Stoliar, P.; Rozenberg, M.; Cren, T.; Roditchev, D.; Phuoc, V. T.; Besland, M. P.; Cario, L. Resistive Switching in Mott Insulators and Correlated Systems. *Adv. Funct. Mater.* 2015, 25, 6287−6305.

(12) Zhang, L.; Pang, B.; Chen, Y. B.; Chen, Y. Review of Spin−Orbit Coupled Semimetal $SrIrO_3$ in Thin Film Form. *Crit. Rev. Solid State Mater. Sci.* 2018, 43, 367−391.

(13) Cao, G.; Schlottmann, P. The Challenge of Spin-Orbit-Tuned Ground States in Iridates: A Key Issues Review. *Rep. Prog. Phys.* 2018, 81, No. 042502.

(14) Biswas, A.; Jeong, Y. H. Growth and Engineering of Perovskite $SrIrO_3$ Thin Films. *Curr. Appl. Phys.* 2017, 17, 605−614.

(15) Kim, J.; Casa, D.; Upton, M. H.; Gog, T.; Kim, Y. J.; Mitchell, J. F.; Van Veenendaal, M.; Daghofer, M.; Van Den Brink, J.; Khaliullin, G.; Kim, B. J. Magnetic Excitation Spectra of Sr_2IrO_4 Probed by Resonant Inelastic X-Ray Scattering: Establishing Links to Cuprate Superconductors. *Phys. Rev. Lett.* 2012, 108, 177003.

(16) Wan, X.; Turner, A. M.; Vishwanath, A.; Savrasov, S. Y. Topological Semimetal and Fermi-Arc Surface States in the Electronic Structure of Pyrochlore Iridates. *Phys. Rev. B: Condens. Matter Mater. Phys.* 2011, 83, 205101.

(17) Shitade, A.; Katsura, H.; Kuneš, J.; Qi, X. L.; Zhang, S. C.; Nagaosa, N. Quantum Spin Hall Effect in a Transition Metal Oxide Na_2IrO_3. *Phys. Rev. Lett.* 2009, 102, 256403.

(18) Liu, Z. T.; Li, M. Y.; Li, Q. F.; Liu, J. S.; Li, W.; Yang, H. F.; Yao, Q.; Fan, C. C.; Wan, X. G.; Wang, Z.; Shen, D. W. Direct Observation of the Dirac Nodes Lifting in Semimetallic Perovskite $SrIrO_3$ Thin Films. *Sci. Rep.* 2016, 6, 30309.

(19) Moon, S. J.; Jin, H.; Kim, K. W.; Choi, W. S.; Lee, Y. S.; Yu, J.; Cao, G.; Sumi, A.; Funakubo, H.; Bernhard, C.; Noh, T. W. Dimensionality-Controlled Insulator-Metal Transition and Correlated Metallic State in 5d Transition Metal Oxides $Sr_{n+1}Ir_nO_{3n+1}$ (n = 1, 2, and ∞). *Phys. Rev. Lett.* 2008, 101, 226402.

(20) Domingo, N.; Lopez-Mir, L.; Paradinas, M.; Holy, V.; Zelezny, J.; Yi, D.; Suresha, S. J.; Liu, J.; Rayan Serrao, C.; Ramesh, R.; Ocal, C.; Marti, X.; Catalan, G. Giant Reversible Nanoscale Piezoresistance at Room Temperature in Sr_2IrO_4 Thin Films. *Nanoscale* 2015, 7, 3453−3459.

(21) Wang, C.; Seinige, H.; Cao, G.; Zhou, J. S.; Goodenough, J. B.; Tsoi, M. Electrically Tunable Transport in the Antiferromagnetic Mott Insulator Sr_2IrO_4. *Phys. Rev. B: Condens. Matter Mater. Phys.* 2015, 92, 115136.

(22) Seinige, H.; Williamson, M.; Shen, S.; Wang, C.; Cao, G.; Zhou, J.; Goodenough, J. B.; Tsoi, M. Electrically Tunable Transport and High-Frequency Dynamics in Antiferromagnetic $Sr_3Ir_2O_7$. *Phys. Rev. B: Condens. Matter Mater. Phys.* 2016, 94, 214434.

(23) Zhang, J.; Liang, Q.; Xiong, Y.; Zhang, B.; Gao, L.; Li, H.; Chen, Y. B.; Zhou, J.; Zhang, S. T.; Gu, Z. Bin; Yao, S. H.; Wang, Z.; Lin, Y.; Chen, Y. F. Tunable Semimetallic State in Compressive-Strained $SrIrO_3$ Films Revealed by Transport Behavior. *Phys. Rev. B: Condens. Matter Mater. Phys.* 2015, 91, No. 035110.

(24) Biswas, A.; Kim, K.-S.; Jeong, Y. H. Metal Insulator Transitions in Perovskite $SrIrO_3$ Thin Films. *J. Appl. Phys.* 2014, 116, 213704.

(25) Gruenewald, J. H.; Nichols, J.; Terzic, J.; Cao, G.; Brill, J. W.; Seo, S. S. A. A. Compressive Strain-Induced Metal−Insulator Transition in Orthorhombic $SrIrO_3$ Thin Films. *J. Mater. Res.* 2014, 29, 2491−2496.

(26) Wu, F.-X.; Zhou, J.; Zhang, L Y; Chen, Y B; Zhang, S.-T.; Gu, Z.-B.; Yao, S.-H.; Chen, Y.-F. Metal-Insulator Transition in $SrIrO_3$ with Strong Spin-Orbit Interaction. *J. Phys.: Condens. Matter* 2013, 25, 125604.

(27) Manca, N.; Groenendijk, D. J.; Pallecchi, I.; Autieri, C.; Tang, L. M. K.; Telesio, F.; Mattoni, G.; McCollam, A.; Picozzi, S.; Caviglia, A. D. Balanced Electron-Hole Transport in Spin-Orbit Semimetal $SrIrO_3$ Heterostructures. *Phys. Rev. B: Condens. Matter Mater. Phys.* 2018, 97, No. 081105.

(28) Groenendijk, D. J.; Autieri, C.; Girovsky, J.; Martinez-Velarte, M. C.; Manca, N.; Mattoni, G.; Monteiro, A. M. R. V. L.; Gauquelin, N.; Verbeeck, J.; Otte, A. F.; Gabay, M.; Picozzi, S.; Caviglia, A. D. Spin-Orbit Semimetal $SrIrO_3$ in the Two-Dimensional Limit. *Phys. Rev. Lett.* 2017, 119, 256403.

(29) Schütz, P.; Di Sante, D.; Dudy, L.; Gabel, J.; Stübinger, M.; Kamp, M.; Huang, Y.; Capone, M.; Husanu, M. A.; Strocov, V. N.;

Sangiovanni, G.; Sing, M.; Claessen, R. Dimensionality-Driven Metal-Insulator Transition in Spin-Orbit-Coupled SrIrO$_3$. *Phys. Rev. Lett.* **2017**, *119*, 256404.

(30) Connell, J. G.; Isaac, B. J.; Ekanayake, G. B.; Strachan, D. R.; Seo, S. S. A. Preparation of Atomically Flat SrTiO$_3$ Surfaces Using a Deionized-Water Leaching and Thermal Annealing Procedure. *Appl. Phys. Lett.* **2012**, *101*, 98−101.

(31) Groenendijk, D. J.; Manca, N.; Mattoni, G.; Kootstra, L.; Gariglio, S.; Huang, Y.; Van Heumen, E.; Caviglia, A. D. Epitaxial Growth and Thermodynamic Stability of SrIrO$_3$/SrTiO$_3$ Heterostructures. *Appl. Phys. Lett.* **2016**, *109*, No. 041906.

(32) Zhao, J. G.; Yang, L. X.; Yu, Y.; Li, F. Y.; Yu, R. C.; Fang, Z.; Chen, L. C.; Jin, C. Q. High-Pressure Synthesis of Orthorhombic SrIrO$_3$ Perovskite and Its Positive Magnetoresistance. *J. Appl. Phys.* **2008**, *103*, 103706.

(33) Fruchter, L.; Schneegans, O.; Li, Z. Z. Anisotropy and Interaction Effects of Strongly Strained SrIrO $_3$ Thin Films. *J. Appl. Phys.* **2016**, *120*, No. 075307.

(34) Rondinelli, J. M.; Caffrey, N. M.; Sanvito, S.; Spaldin, N. A. Electronic Properties of Bulk and Thin Film SrRuO$_3$: Search for the Metal-Insulator Transition. *Phys. Rev. B: Condens. Matter Mater. Phys.* **2008**, *78*, 155107.

(35) Hussey, N. E.; Takenaka, K.; Takagi, H. Universality of the Mott-Ioffe-Regel Limit in Metals. *Philos. Mag.* **2004**, *84*, 2847−2864.

(36) Deng, X.; Mravlje, J.; Žitko, R.; Ferrero, M.; Kotliar, G.; Georges, A. How Bad Metals Turn Good: Spectroscopic Signatures of Resilient Quasiparticles. *Phys. Rev. Lett.* **2013**, *110*, No. 086401.

(37) Ramakrishnan, T. V.; Lee, P. A. Disordered Electronic Systems. *Rev. Mod. Phys.* **1985**, *57*, 287.

(38) Kim, K. W.; Lee, J. S.; Noh, T. W.; Lee, S. R.; Char, K. Metal-Insulator Transition in a Disordered and Correlated SrTi$_{1-x}$Ru$_x$O$_3$ System: Changes in Transport Properties, Optical Spectra, and Electronic Structure. *Phys. Rev. B: Condens. Matter Mater. Phys.* **2005**, *71*, 125104.

(39) Mott, N. *Metal-Insulator Transitions*, 2nd ed.; Taylor & Francis: London, 1998.

(40) Lanza, M.; Celano, U.; Miao, F. Nanoscale Characterization of Resistive Switching Using Advanced Conductive Atomic Force Microscopy Based Setups. *J. Electroceram.* **2017**, *39*, 94−108.

(41) Cui, Y.; Peng, H.; Wu, S.; Wang, R.; Wu, T. Complementary Charge Trapping and Ionic Migration in Resistive Switching of Rare-Earth Manganite TbMnO$_3$. *ACS Appl. Mater. Interfaces* **2013**, *5*, 1213−1217.

(42) Lee, H. S.; Choi, S. G.; Park, H. H.; Rozenberg, M. J. A New Route to the Mott-Hubbard Metal-Insulator Transition: Strong Correlations Effects in Pr$_{0.7}$Ca$_{0.3}$MnO$_3$. *Sci. Rep.* **2013**, *3*, 1704.

Research articles

Resistive switching in Strontium iridate based thin films

Víctor Fuentes[a], Borislav Vasić[b], Zorica Konstantinović[b], Benjamín Martínez[a], Lluís Balcells[a], Alberto Pomar[a],*

[a] *Institut de Ciència de Materials de Barcelona, ICMAB-CSIC, Campus de la UAB Bellaterra 08193, Spain*
[b] *Center for Solid State Physics and New Materials, Institute of Physics Belgrade, University of Belgrade, Pregrevica 118, 11080 Belgrade, Serbia*

A B S T R A C T

We report on the local electrical properties, measured by conductive atomic force microscopy, of the Iridate-based $Sr_{n+1}Ir_nO_{3n+1}$ family of thin films, in particular by comparing the n = 1, Sr_2IrO_4, and the n = ∞, $SrIrO_3$, phases. We analyze the different resistive switching behavior as a function of the pristine electronic properties of the films. We will show that, for films exhibiting insulating behavior, i.e., films of the n = 1 phase or films below 3 nm of thickness for the n = ∞ phase, hysteretic I–V curves with a sharp transition into a low resistance state (LRS), i.e. an abrupt increase of the current intensity, is detected above a well-defined threshold voltage. This suggests a resistive switching behavior associated to the jump between two resistance states that may be correlated to the activation energy, Δ, obtained by fitting the temperature dependence of the resistivity to a thermal activated Arrhenius law, ρ (T) ~ $ρ_0$exp(− Δ/k_BT). On the other hand, thicker samples of the n = ∞ phase exhibit a semimetallic character and I–V curves show progressive changes of the local resistance without a clearly defined threshold voltage. Kelvin Probe Force Microscopy based measurements confirmed that, concomitantly to the resistive switching, an evolution of the electronic states at the surface takes place that may be associated to the migration of oxygen vacancies promoted by the electrical fields under the AFM tip.

1. Introduction

Reversible resistive switching (RS), i.e., the change of resistance in a reversible manner between two stable states of well-defined resistance by applying voltages pulses, is considered as one of the most promising solutions for the development of non-volatile memory devices [1,2]. A large variety of materials are known to exhibit RS behavior, including transition metal oxides (TMOs) [3,4]. Although several physical mechanisms have been invoked to account for the observed RS behavior [5–9], modifications of the doping rate by valence change due to the migration of oxygen vacancies is the most common case for TMOs. A broad interest is devoted to RS behavior where the active material is a Mott insulator or a correlated system as the occurrence of a metal-to-insulator transition (MIT) allows generating well defined low and high resistance states [2,5,10–12]. Moreover, various types of MIT may appear in response to variety of external stimuli, such as temperature, doping rate or structural strain [13]. In the case of TMOs, the close similarity between electronic correlations and crystal field splitting energies provides different mechanism for tuning their electronic properties and thus the MIT and, as a consequence, the RS phenomena [13]. Furthermore, in TMOs based on 5d elements, as Ir, spin–orbit

coupling (SOC) reaches values of about 0.5 eV [14–16], and becomes comparable to crystal field and electronic correlations, giving place to novel physics and exotic properties [17–19]. This has been recently manifested in the Ruddlesden-Popper series of 5d Strontium Iridates ($Sr_{n+1}Ir_nO_{3n+1}$) where subtle structural or chemical changes may trigger different electronic states. For example, in the n = 1 phase (Sr_2IrO_4), a gap is opened at the Fermi level, leading the system into a Mott insulator state [20] while the perovskite-like n = ∞ phase ($SrIrO_3$) presents a semimetallic ground state [21]. Nevertheless, in this latter case, a MIT can be also triggered by tuning the compressive strain induced by the substrate or by reducing the film thickness [22–26], although recent studies indicate the coexistence of disorder effects and electronic correlations leading to either disorder driven Anderson MIT or unconventional Mott-Anderson transition [23,27].

In this work we present a study of RS behavior in $Sr_{n+1}Ir_nO_{3n+1}$ thin films of the n = 1 phase (hereafter SIO-214) and of the n = ∞ phase (SIO-113) by means of local I–V curve measurements and current mapping, by using conductive atomic force microscopy (C-AFM). While SIO-214 films are insulating, SIO-113 films present semimetallic behavior but, for film thickness below ~3 nm an Anderson-type MIT i.e., induced by disorder, is triggered. We will show that a sharp RS process,

with an abrupt increase of current at a defined threshold voltage is only attained in the presence of a MIT behavior where two well-defined resistance states separated by an energy jump exist. However, differences in the threshold voltage are observed in the case of both phases due to the different energy barrier to overcome. On the other hand, for thin films in a semimetallic state, I–V curves present a smooth variation of resistance, without a clear threshold voltage. By performing Kelvin Probe Force Microscopy (KPFM), we will show that the RS behavior may be attributed to the variation of charge carriers' density, usually associated to the migration of oxygen vacancies promoted by the electric field pulses. Current maps performed with voltage values above the threshold value and of different polarity allow demonstrating the writing/erasing processes making evident the feasibility of the system for the implementation of Re-RAMs.

2. Experimental details

Sr$_2$IrO$_4$ thin films were grown by Pulsed Laser Deposition on (0 0 1) SrTiO$_3$ (STO) substrates. The growth was carried out in an oxygen atmosphere of 70 mTorr and at a temperature of 850 °C. For the deposition, a KrF excimer laser (248 nm of wavelength) was employed at a frequency of 1 Hz and a laser fluence of 1.25 J/cm^2. On the other hand, SrIrO$_3$ thin films were grown by rf sputtering at 900 °C in 140 mTorr oxygen atmosphere as described elsewhere [27]. In order to achieve single Ti-terminated substrates with well-defined atomic steps, all STO substrates in this work were treated before the film deposition. The treatment consisted of a 10 min bath of ultrasounds in deionized water and a post-annealing of 2 h at 1000 °C [28].

Structural properties of both SrIrO$_3$ and Sr$_2$IrO$_4$ thin films were evaluated by means of X-Ray diffraction. A Bruker D8-Discover diffractometer was employed to measure the Reciprocal Space Map while the High Resolution θ-2θ scan was measured with a PANalytical X'PERT PRO MRD system. The thickness of the films was determined by X-Ray Reflectometry using a D-5000 diffractometer from Siemens.

Resistivity curves of SIO-214 and SIO-113 films were measured in a standard 4 probe configuration by using a Physical Properties Measurement System by Quantum Design. Electrical electrodes were fabricated by depositing a thin layer (~40 nm) of Pt on the surface at room temperature.

RS properties were evaluated by employing an atomic force microscopy (AFM) system in the electrical modes of conducting (C-AFM) and Kelvin Probe (KPFM). The probes used to measure in these modes were DDESP-FM-V2 from Bruker. An AFM MFP3D from Asylum was used to obtain the Current maps (in nitrogen atmosphere) and the I–V curves while an NTEGRA Prima AFM system from NT-MDT was employed to obtain the KPFM data. I–V curves were performed without current compliance. Although it is known that current limitation could prevent sample degradation [29,30], we should note that the current values attained in this work were below typical current compliances used in the literature [31–33]. The KPFM images were recorded by a standard two-pass measurement. In the first step, AFM tapping mode was employed to measure the topography of the film. Then the probe was lifted at a certain height (10–20 nm) and replicated the topography while measuring the Contact Potential Difference (CPD) between the AFM tip and the sample. To obtain the CPD at each point, an AC Voltage was applied to the conducting probe to excite it at its resonance frequency. At the same time, a second DC voltage source was applied in order to nullify the electrical interaction between the tip and the sample. The surface distribution of the CPD can be then mapped by recording the DC voltage which nullifies the electrical tip-sample interaction during scanning [34].

It has been observed that thin films of iridates, such as Sr$_2$IrO$_4$ or SrIrO$_3$ possess a very sensitive surface [26,27,35]. The poor surface stability turns the C-AFM measurements more challenging since high electric fields should be applied between the tip and the iridate surface to obtain the desired switching. With the aim of protecting the films and
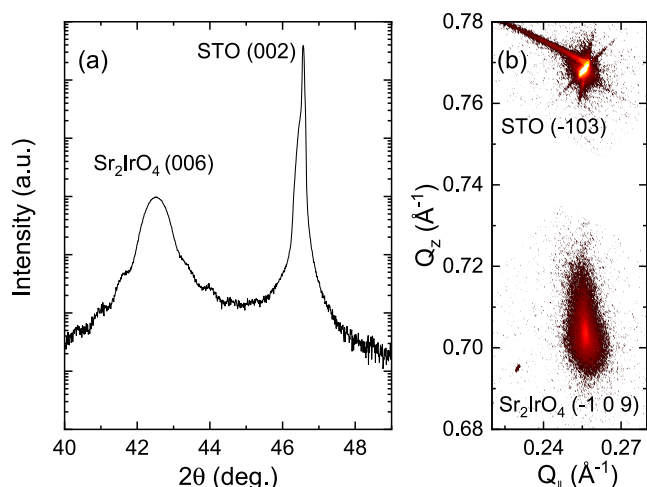

Fig. 1. X-Ray diffraction measurements of SIO-214 films on STO. (a) High-resolution θ–2θ scan around (0 0 6) diffraction peaks. (b) Reciprocal space map of the $(-103)_{STO}$ and $(-109)_{SIO}$ peaks showing full strained state of the SIO-214 films.

stabilize the current, Pt nanoparticles were deposited *in situ* on some of the films after their growth. In the case of SIO-214 films, this deposition was performed with a laser fluence of 2.17 J/cm^2 with pulses at 1 Hz. Details for SIO-113 films may be found elsewhere [27].

3. Results

High resolution θ-2θ x-ray diffraction scans in thin films of both phases confirmed epitaxial growth and high crystallinity evidenced by satellites fringes. Fig. 1(a) shows the result for a SIO-214 sample around the (0 0 6) diffraction peak. In this case, peak position leads to an out-of-plane lattice parameter of c$_{SIO-214}$ ~12.78 Å, i.e. SIO-214 unit cell is slightly shortened with respect to the reported bulk value (a$_0$ = 12.92 Å) [36] in agreement with a small tensile strain [37]. Fig. 1(b) displays a reciprocal space map around (−109) reflection. It can be appreciated from the figure that SIO-214 film is fully strained with the underlying substrate. Similar results were obtained for SIO-113 films grown on STO with c$_{SIO-113}$ ~3.943 Å, i.e., corresponding to compressive strain as it was previously reported [27,38].

As previously mentioned in the Introduction, in the iridate series, strength of spin-orbit coupling competes with crystal field and electronic correlations leading to a rich landscape of electrical properties. This is exemplified by the temperature dependence of electrical resistivity shown in Fig. 2(a). This Figure shows that electrical properties of SIO-113 films are clearly thickness-dependent. Robust metallic behavior is observed for the 26 nm thick film and the resistivity may be well described by the expression $\rho(T) = \rho_0 + CT^{4/5}$ in agreement with previous results [22–26,39]. However, as thickness decreases a progressive upturn of the resistivity at low temperatures is detected and the system exhibits fully insulating behavior for the 2 nm thick SIO-113 sample. The nature of the MIT induced by reducing the film thickness has been previously elucidated by analyzing the temperature dependence of the resistivity of the fully insulating 2 nm thick sample [27,40]. The low temperature regime, up to about 40–45 K, is well described by using the Mott's variable range hopping (VRH) model: Ln$\sigma \propto 1/T^{1/3}$, σ being the conductivity [41], while the high temperature range is properly described by using the Arrhenius equation for thermal activation conduction $\rho(T) = \rho_0 e^{(\Delta/k_B T)}$, Δ being an activation energy (a value of Δ_{123} ~6 meV was obtained from the fit) and k$_B$ the Boltzmann's constant. Fig. 2(b) shows, in typical Arrhenius plot, the quality of this fitting. Therefore, from the analysis of the ρ (T) curves we can conclude that, while for thick SIO-113 films the system behaves as a three dimensional correlated metal, for the thinnest films the MIT is of
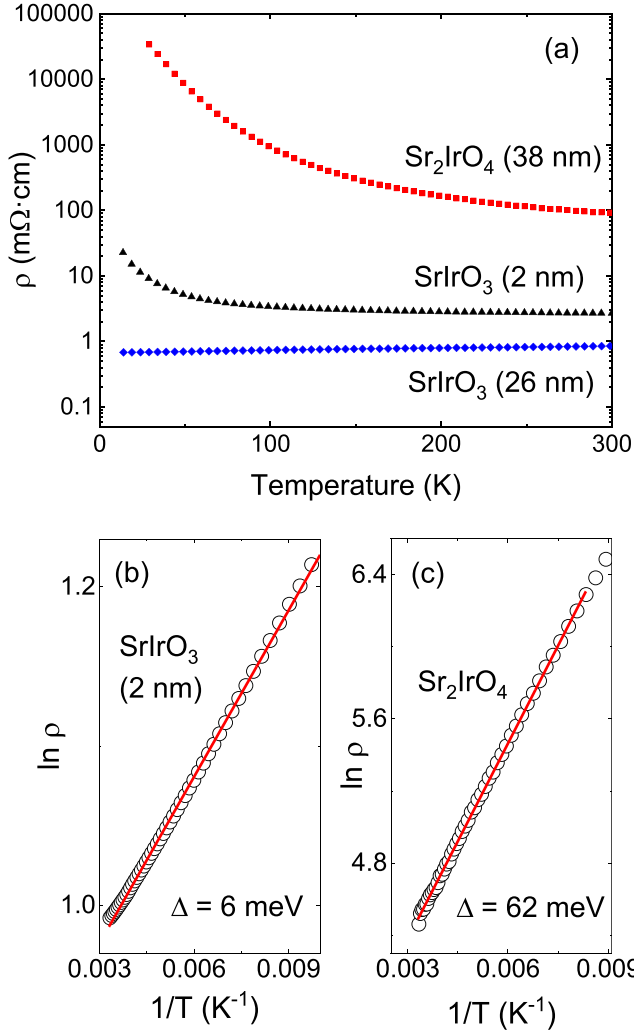
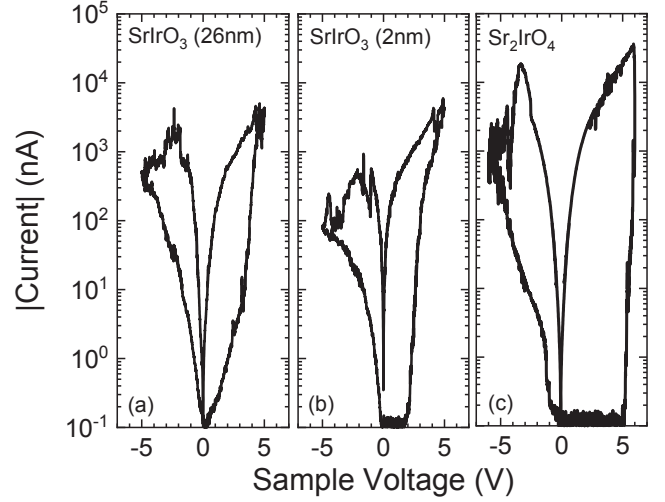**Fig. 3.** C-AFM I–V curves measured on (a) 26 nm thick SIO-113 film; (b) 2 nm thick SIO-113 film and (c) SIO-214 film.

Fig. 2. (a) Temperature dependence of the electrical resistivity of an insulating SIO-214 film (38 nm) an insulating SIO-113 film (2 nm) and a semimetallic SIO-113 film (26 nm). (b) and (c) Arrhenius plot of the high temperature part of the $\rho(T)$ curve for the insulating films shown in (a). The activation energy Δ in each case has been obtained by the fit (solid lines) to the thermal activation law $\rho(T) = \rho_0 e^{(\Delta/k_B T)}$.

Anderson localization type due to disorder, in good agreement with previous reports [23,25,27]. On the other hand, SIO-214 film exhibit a robust insulating behavior with $d\rho/dT < 0$ in the whole temperature range independent of film thickness. Typical results for a 38 nm SIO-214 sample are plotted in Fig. 2(a). This behavior has been usually attributed to the opening of a band-gap in the electronic structure as a result of interplay between strong SOC and electronic correlations [37,42]. Temperature dependence of resistivity is again well described by a thermal activation law, see Fig. 2(c), but, in this case, the fitting leads to an activation energy of $\Delta_{214} \sim 62$ meV, i.e., around one order of magnitude higher than in the precedent case. Both activation energies are in agreement with the expected values reported from numerical simulations [20,43–45].

As resistivity of SIO thin films may be sensitive to different stimuli, iridate films become a promising alternative for obtaining a strong RS response and thus, of interest for the implementation of RS devices. For this purpose, we have studied local I–V curves measured at room temperature by C-AFM of SIO thin films. In Fig. 3 we present the I–V curves on samples with different electronic behavior, i.e., SIO-113 samples at both extremes of the thickness series (i.e. 26 nm and 2 nm), Fig. 3(a) and (b), respectively, and an insulating SIO-214 sample,

Fig. 3(c). In all cases hysteretic I–V curves are observed indicative of RS behavior. These curves are reproducible in the whole sample surface (see current maps below) and identical results were obtained when cycling IV curves over sample surface until sample-tip contact degrades (~10 cycles). An anti-clockwise behavior, where positive sample voltage induces the Low Resistance State (LRS) and negative sample voltage induces the High Resistance State (HRS) is found. From the results in Fig. 3 we observe two clear different RS behaviors if sample is initially in a metallic or in an insulating state. For the samples in an insulating state, SIO-113 (2 nm) and SIO-214, Fig. 3 (b) and (c), the current intensity remains constant and near to zero until a given threshold voltage value is reached after which a sudden increase of the current takes place. This voltage depends on the system and it was found to be around 2 V for the SIO-113 (2 nm) and 4.5 V for SIO-214. These threshold values may be correlated to the activation energy, Δ, obtained above from $\rho(T)$ measurements if we assume that Δ corresponds to the energy barrier needed to bring the system into a conducting state. Thus, the higher threshold voltage observed for the SIO-214 system is just reflecting a higher barrier between insulating and conducting states (remember that $\Delta_{SIO-113} = 6$ meV and $\Delta_{SIO-214} = 62$ meV) as previously observed for other compounds [46,47]. After reaching the maximum voltage, the sample remains in the LRS returning to 0 V through the superior limit of the graph. In the negative voltage range, the I–V curve starts at the LRS and the current is continuously increasing for voltages up to the maximum negative voltage. Once reached this voltage, the I–V curve returns to the HRS along the lower path. On the contrary, for the sample initially in the semimetallic state, SIO-113 (26 nm) shown in Fig. 3(b), the resistance changes in a continuous way and no well-defined resistance states separated by a clear voltage threshold are observed. The similarity of the measured I–V curves in all samples suggests that the mechanism behind the observed variations of resistance is the same in all cases. However, the absence of a clear voltage threshold in the case of the thick sample suggests the absence of a well defined energy transition separating the LRS and HRS.

Although all the films seem to follow the same mechanism for the changes of resistance, the set of I–V curves present notable differences. Fig. 3(a), corresponding to the SIO-113 26 nm thick sample, shows smoothly rising I–V curves for the positive voltage range from 0 V to the maximum of current. On the other hand, Fig. 3(b), corresponding to the SIO-113, 2 nm film and Fig. 3(c), corresponding to the SIO-214 film, show an almost zero current up to a clear voltage threshold value, when an abrupt increase of the current intensity occurs. This different behavior is closely related to the differences in the band structures of the films that are induced by the MIT. On one hand, it is reported that thick

SIO-113 films (such as the employed 26 nm thick one) behave as a semimetal [20,21,26,27] while an Anderson-type MIT transition with strong carriers' localization may be triggered by thickness reduction [23,25,27]. Even more, the aperture of a Mott gap in ultrathin SIO-113 films have been recently documented [44]. In the case of SIO-214, a band gap is expected to appear due to electron-electron correlations [37,42,48,49]. With this picture in mind, the behavior of thick SIO-113 film (26 nm) reflects changes of resistance in a system with continuous energy levels having thus a smooth increase of the current. Moreover, the shift of the Fermi level would bring the system into a state with higher Density of States, finally giving higher conductivity and setting it into the LRS. On the other hand, as long as Fermi energy lies inside localized states or belongs to the energy gap, charge carrier's mobility is seriously hampered or even suppressed and the current would be almost zero. Nevertheless, when the Fermi level crosses the mobility edge for the 2 nm thick SIO-113 or overcome band gap for SIO-214, an energy transition between localized and extended states takes place for high enough positive voltage, an abrupt increase of the current would be observed and obviously the system would be switched in the LRS with a higher conductivity.

Current maps over extended areas in both HRS and LRS states allowed us to obtain a deeper insight into the RS process in SIO samples. Performing a C-AFM map implies to move the AFM tip back and forth several times in the same area of the sample and the continuous scanning deteriorates the electrical tip-sample contact after a few cycles. This well-known drawback in C-AFM analysis of RS phenomena is usually attributed to tip contamination [30,34]. In our experience, current maps cannot be performed in bare iridate thin films due to surface degradation. However, we have found that capping of the SIO film surface with a non-continuous layer of metallic (Pt) nanoparticles (NPs) is useful to perform the C-AFM maps. In this way, quality of the tip-sample electrical contact is improved, while degradation of the electrical contact is avoided thanks to the enhanced tip life time since brushing with Pt nanoparticles removes tip-contaminations. Results for a SIO-214 film are shown in Fig. 4. Fig. 4(a) presents a 50x50 μm^2 current map measured at low voltage (1 V) after the scanning of the central 35x35 μm^2 area at the positive bias voltage ($+4.5$ V) applied to the sample and a further scan of 20x20 μm^2 area at -5 V applied to the sample. The dark outer part corresponds to the pristine state with a low conductivity. Inside, a bright squared ring represents the established LRS with high conductivity, or, as it is usually named, the written area. Finally, the central dark square exhibits again low conductivity and represents the switching back into the HRS, i.e., the erased region. The associated topography measurement is shown in Fig. 4(b). Some minor topography changes are detected in the central area switched into HRS that may be caused by a dragging of the Pt NPs during the scan.
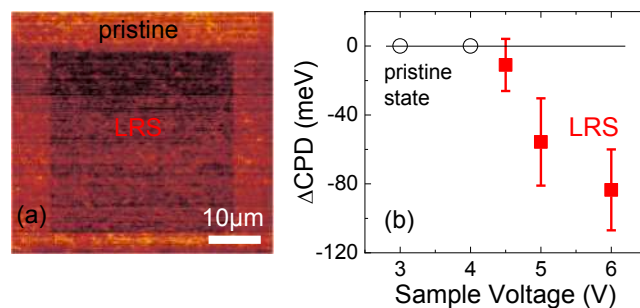
Fig. 5. (a) 50 × 50 μm^2 CPD map measured in the SIO-214 thin film after applying a voltage of 4.5 V to an inner square of 35 × 35 μm^2 (i.e., writing into LRS state). (b) Evolution of ΔCPD defined as the difference of the CPD measured in the inner written area and the CPD measured at the pristine area, ΔCPD = CPD$_{written}$ − CPD$_{pristine}$ as a function of applied voltage.

Nevertheless, as threshold voltage values observed in current maps are identical to those measured from IV curves, influence of Pt nanoparticles in RS may be considered negligible.

Redox based mechanisms, typically driven by the motion of oxygen vacancies, are usually invoked to explain RS phenomena in TMOs [5–9]. In correlated metals such as SIO, the variation of the concentration of oxygen vacancies can modify the valence of the surrounding metal cations. Since the oxygen vacancies substitute an oxygen position, the surrounding cations must adapt their valence to compensate the charge variation. Therefore, new electrons would fill Ir orbitals changing the Fermi level and electric properties [13]. To visualize this modification of Fermi level associated with the RS behavior, KPFM measurements were performed in SIO-214 samples. Fig. 5(a) depicts the CPD map measured by KPFM on a 50x50 μm^2 area after applying a sample voltage of $+4.5$ V on an inner 35x35 μm^2 region, i.e., the same procedure used to perform the above current maps. As can be seen, written region exhibits a decreased CPD. We have performed similar experiments by varying the maximum applied voltage. Fig. 5(b) shows the variation of CPD, Δ CPD, between the one measured in the outer region (i.e., corresponding to the pristine state) and the CPD measured in the square area (i.e., the written region), Δ CPD = CPD$_{written}$ − CPD$_{pristine}$, as a function of maximum applied voltage. We may observe that no modification of CPD is observed until the applied voltage attain the threshold value to switch the sample into a LRS state, around 4.5 V, i.e., the same value as in I–V curves, see Fig. 3(c). Once a LRS is achieved, a reduction of CPD can be measured. As CPD corresponds to the difference between the work function of the AFM tip and the sample, a decrease in CPD implies a higher work function on the LRS state when compared to the pristine sample and thus, the RS may be associated to a change in the electronic properties at the sample surface. Finally, the write-erase cycling was completed by applying a negative voltage of −6 V to a square region of 20 × 20 μm^2. Fig. 6(a) presents the CPD results of the complete cycle. We may see
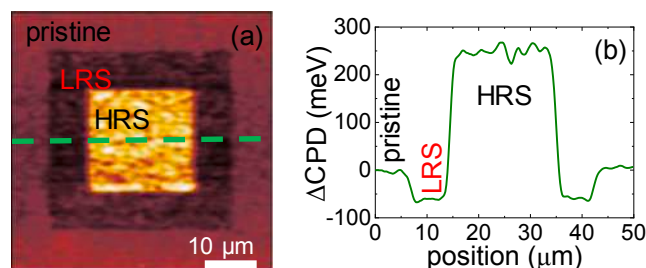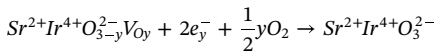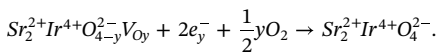

Fig. 4. C-AFM current map (a) and topography image (b) of a SIO-214 film. Current map shows a 35 × 35 μm^2 area set into the LRS state and an inner 20 × 20 μm^2 square reset to the HRS state. Minor changes in the topography associated with the writing-erasing process are noticed in (b).

Fig. 6. (a) 50 × 50 μm^2 CPD map measured in the SIO-214 thin film after applying a voltage of 6 V to an inner square of 20 × 20 μm^2 (i.e., erasing into HRS state) in a previously written sample as in Fig. 5. (b) CPD profile showing the difference between pristine (taken as reference), LRS and HRS states.

that the inner square is much brighter than any of the surroundings areas, i.e., CPD is much higher in this HRS region. A quantification of the values may be followed by the CPD profile presented in Fig. 6(b). This result evidences that the erasing process bring the sample into a HRS state that it is not electronically equivalent to the pristine one.
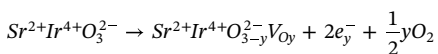
Combining the I–V curves and the KPFM results we may now elaborate a scenario for the RS behavior observed in SIO films. In general, an external applied electric field will promote a redox reaction at the film surface and, as a consequence, oxygen vacancies could be incorporated or removed from the film [50]. In hole-like systems as SIO-214 [51,52], vacancies are considered as acceptors scavengers and they decrease conductivity. The incorporation of oxygen anions into the oxide matrix, removing the vacancies occurs then under positive voltage (applied to sample) according to the following formula for $SrIrO_3$:

$$Sr^{2+}Ir^{4+}O_{3-y}^{2-}V_{Oy} + 2e_y^- + \frac{1}{2}yO_2 \rightarrow Sr^{2+}Ir^{4+}O_3^{2-}$$

and, for Sr_2IrO_4

$$Sr_2^{2+}Ir^{4+}O_{4-y}^{2-}V_{Oy} + 2e_y^- + \frac{1}{2}yO_2 \rightarrow Sr_2^{2+}Ir^{4+}O_4^{2-}.$$

Then, the Fermi level would decrease, as observed in CPD maps, while the hole density and the conductivity would increase and transform the sample surface beneath the AFM tip into the LRS. By applying negative voltage to the sample the system can be reversed into the HRS with the following reaction taking place, for $SrIrO_3$

$$Sr^{2+}Ir^{4+}O_3^{2-} \rightarrow Sr^{2+}Ir^{4+}O_{3-y}^{2-}V_{Oy} + 2e_y^- + \frac{1}{2}yO_2$$

and, for Sr_2IrO_4

$$Sr_2^{2+}Ir^{4+}O_4^{2-} \rightarrow Sr_2^{2+}Ir^{4+}O_{4-y}^{2-}V_{Oy} + 2e_y^- + \frac{1}{2}yO_2.$$
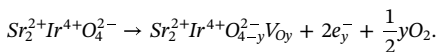
With these reactions, oxygen anions would be removed from the matrix leaving vacancies behind that would reduce drastically the number of holes and raise up the Fermi level, reducing this way the conductivity, in agreement with I–V curves and CPD measurements.

4. Conclusions

The local transport properties of iridate based thin films of the n = 1 phase, Sr_2IrO_4 and n = ∞ phase, $SrIrO_3$ have been analyzed. Macroscopic measurements of the film's resistivity as a function of temperature allow demonstrating that Sr_2IrO_4 films are insulating due to the opening of a gap while $SrIrO_3$ films are either semimetallic (for thickness above 3 nm) or insulating (for thickness below 3 nm), being in this case an Anderson type MIT, i.e., driven by disorder. On the other hand, all the SIO films exhibit hysteretic I–V curves indicative of RS behavior irrespective to their phase or thickness. Due to the particular experimental setup used, the observed RS takes place at the interface between the metal electrode (AFM tip) and the SIO film. Electric field pulses promote oxygen vacancies migration trough the interface then, to maintain electrical neutrality, a valence change of the cations nearby takes place and therefore, a modification of the charge carriers' density and of the position of the Fermi level. However, the features of the RS process are clearly different as a function of their initial conducting state. In the case of Sr_2IrO_4 samples and for very thin samples of $SrIrO_3$ (below 3 nm), where carriers' localization occurs, it is observed the existence of a well-defined voltage threshold value separating the low and high resistance states. This threshold voltage is correlated with the activation energy needed to bring the system into a conducting state. In contrast, in thick $SrIrO_3$ films with semimetallic behavior, (i.e., for thickness above 3 nm) I–V curves present a continuous smooth variation of resistance, without a clear threshold voltage, making evident the absence of an energy sharp transition separating high and low resistance states. In this case, changes of resistance by applying voltage pulses are simply associated to the variation of charge carriers' density

due to the migration of oxygen vacancies. The electronic changes associated with the migration of oxygen vacancies during the electric field pulses were monitored by KPFM and suggested that majority carriers are holes. Current maps performed with voltage values above the threshold value and of different polarity allow demonstrating the writing/erasing processes in a large area of the sample surface.

Authors statement

V.F. and B.V. were responsible for the C-AFM and KPFM measurements and data analysis. V.F, Z.K. and Ll. B. were responsible for film and nanoparticles preparation. V.F., B.M. and A.P. were involved in transport measurements and data analysis.

All authors contributed to discussion, interpretation and manuscript preparation.

Declaration of Competing Interest

The authors declare that they have no known competing financial interests or personal relationships that could have appeared to influence the work reported in this paper.

Acknowledgments

Appendix A. Supplementary data

Supplementary data to this article can be found online at https://doi.org/10.1016/j.jmmm.2020.166419.

References

[1] R. Waser, M. Aono, Nanoionics-based resistive switching memories, Nat. Mater. 6 (2007) 833–840.

[2] A. Sawa, Resistive switching in transition metal oxides, Mater. Today 11 (2008) 28–36.

[3] M.A. Villena, J.B. Roldán, F. Jiménez-Molinos, E. Miranda, J. Suñé, M. Lanza, SIM²RRAM: a physical model for RRAM devices simulation, J. Comput. Electron. 16 (2017) 1095–1120.

[4] M. Lanza, H.S.P. Wong, E. Pop, D. Ielmini, D. Strukov, B.C. Regan, L. Larcher, M.A. Villena, J.J. Yang, L. Goux, A. Belmonte, Y. Yang, Y. Shi, et al., Recommended methods to study resistive switching devices, Adv. Electron. Mater. 5 (2019) 1800143.

[5] R. Waser, R. Dittmann, C. Staikov, K. Szot, Redox-based resistive switching memories nanoionic mechanisms, prospects, and challenges, Adv. Mater. 21 (2009) 2632–2663.

[6] T. Lee, Y. Chen, Organic resistive nonvolatile memory materials, MRS Bull. 37 (2012) 144–149.

[7] D.S. Jeong, R. Thomas, R.S. Katiyar, J.F. Scott, H. Kohlstedt, A. Petraru, C.S. Hwang, Emerging memories: resistive switching mechanisms and current status, Reports Prog. Phys. 75 (2012) 076502.

[8] J.J. Yang, D.B. Strukov, D.R. Stewart, Memristive devices for computing, Nat. Nanotechnol. 8 (2013) 13–24.

[9] J.C. Scott, L.D. Bozano, Nonvolatile memory elements based on organic materials, Adv. Mater. 19 (2007) 1452–1463.

[10] S. Bagdzevicius, K. Maas, M. Boudard, M. Burriel, Interface-type resistive switching in perovskite materials, J. Electroceramics 39 (2017) 157–184.

[11] A. Mehonic, A.J. Kenyon, Resistive Switching in Oxides, in: J. Jupille, G. Thornton (Eds.), Springer Series in Surface Sciences, vol. 58, Springer International Publishing, Cham, 2015, pp. 401–428.

[12] L. Peña, L. Garzón, R. Galceran, A. Pomar, B. Bozzo, Z. Konstantinovic,

F. Sandiumenge, L. Balcells, C. Ocal, B. Martinez, Macroscopic evidence of nanoscale resistive switching in $La_{2/3}Sr_{1/3}MnO_3$ micro-fabricated bridges, J. Phys. Condens. Matter 26 (2014) 395010.

[13] E. Janod, J. Tranchant, B. Corraze, M. Querré, P. Stoliar, M. Rozenberg, T. Cren, D. Roditchev, V.T. Phuoc, M.P. Besland, L. Cario, Resistive switching in mott insulators and correlated systems, Adv. Funct. Mater. 25 (2015) 6287–6305.

[14] L. Zhang, B. Pang, Y.B. Chen, Y. Chen, Review of spin-orbit coupled semimetal $SrIrO_3$ in thin film form, Crit. Rev. Solid State Mater. Sci. 43 (2018) 367–391.

[15] G. Cao, P. Schlottmann, The challenge of spin-orbit-tuned ground states in iridates: a key issues review, Reports Prog. Phys. 81 (2018) 042502.

[16] A. Biswas, Y.H. Jeong, Growth and engineering of perovskite $SrIrO_3$ thin films, Curr. Appl. Phys. 17 (2017) 605–614.

[17] J. Kim, D. Casa, M.H. Upton, T. Gog, Y.J. Kim, J.F. Mitchell, M. Van Veenendaal, M. Daghofer, J. Van Den Brink, G. Khaliullin, B.J. Kim, Magnetic excitation spectra of Sr_2IrO_4 probed by resonant inelastic X-ray scattering: establishing links to cuprate superconductors, Phys. Rev. Lett. 108 (2012) 177003.

[18] X. Wan, A.M. Turner, A. Vishwanath, S.Y. Savrasov, Topological semimetal and fermi-arc surface states in the electronic structure of pyrochlore iridates, Phys. Rev. B 83 (2011) 205101.

[19] A. Shitade, H. Katsura, J. Kuneš, X.L. Qi, S.C. Zhang, N. Nagaosa, Quantum spin hall effect in a transition metal oxide Na_2IrO_3, Phys. Rev. Lett. 102 (2009) 256403.

[20] S.J. Moon, H. Jin, K.W. Kim, W.S. Choi, Y.S. Lee, J. Yu, G. Cao, A. Sumi, H. Funakubo, C. Bernhard, T.W. Noh, Dimensionality-controlled insulator-metal transition and correlated metallic state in 5 d transition metal oxides $Sr_{n+1}Ir_nO_{3n+1}$ (n = 1, 2, and ∞), Phys. Rev. Lett. 101 (2008) 226402.

[21] Z.T. Liu, M.Y. Li, Q.F. Li, J.S. Liu, W. Li, H.F. Yang, Q. Yao, C.C. Fan, X.G. Wan, Z. Wang, D.W. Shen, Direct observation of the Dirac nodes lifting in semimetallic perovskite $SrIrO_3$ thin films, Sci. Rep. 6 (2016) 30309.

[22] L. Zhang, Q. Liang, Y. Xiong, B. Zhang, L. Gao, H. Li, Y.B. Chen, J. Zhou, S.T. Zhang, Z. Gu Bin, S.H. Yao, Z. Wang, Y. Lin, Y.F. Chen, Tunable semimetallic state in compressive-strained $SrIrO_3$ films revealed by transport behavior, Phys. Rev. B 91 (2015) 035110.

[23] A. Biswas, K.-S. Kim, Y.H. Jeong, Metal insulator transitions in perovskite $SrIrO_3$ thin films, J. Appl. Phys. 116 (2014) 213704.

[24] J.H. Gruenewald, J. Nichols, J. Terzic, G. Cao, J.W. Brill, S.S.A.A. Seo, Compressive strain-induced metal-insulator transition in orthorhombic $SrIrO_3$ thin films, J. Mater. Res. 29 (2014) 2491–2496.

[25] F.X. Wu, J. Zhou, L.Y. Zhang, Y.B. Chen, S.T. Zhang, Z. Gu Bin, S.H. Yao, Y.F. Chen, Metal-insulator transition in $SrIrO_3$ with strong spin-orbit interaction, J. Phys. Condens. Matter 25 (2013) 125604.

[26] N. Manca, D.J. Groenendijk, I. Pallecchi, C. Autieri, L.M.K. Tang, F. Telesio, G. Mattoni, A. McCollam, S. Picozzi, A.D. Caviglia, Balanced electron-hole transport in spin-orbit semimetal $SrIrO_3$ heterostructures, Phys. Rev. B 97 (2018) 081105(R).

[27] V. Fuentes, B. Vasić, Z. Konstantinović, B. Martínez, L. Balcells, A. Pomar, Resistive switching in semimetallic $SrIrO_3$ thin films, ACS Appl. Electron. Mater. 1 (2019) 1981–1988.

[28] J.G. Connell, B.J. Isaac, G.B. Ekanayake, D.R. Strachan, S.S.A. Seo, Preparation of atomically flat $SrTiO_3$ surfaces using a deionized-water leaching and thermal annealing procedure, Appl. Phys. Lett. 101 (2012) 98–101.

[29] M. Lanza, A review on resistive switching in high-k dielectrics: a nanoscale point of view using conductive atomic force microscope, Mater. 7 (2014) 2155–2182.

[30] M. Lanza, U. Celano, F. Miao, Nanoscale characterization of resistive switching using advanced conductive atomic force microscopy based setups, J. Electroceramics 39 (2017) 94–108.

[31] M. Lanza, A. Bayerl, T. Gao, M. Porti, M. Nafria, G.Y. Jing, Y.F. Zhang, Z.F. Liu, H.L. Duan, Graphene-coated atomic force microscope tips for reliable nanoscale electrical characterization, Adv. Mater. 25 (2013) 1440–1444.

[32] M.A. Villena, F. Jiménez-Molinos, J.B. Roldán, J. Suñé, S. Long, X. Lian, F. Gámiz, M. Liu, An in-depth simulation study of thermal reset transitions in resistive switching memories, J. Appl. Phys. 114 (2013) 144505.

[33] K.C. Chang, J. Huang Wei, T.C. Chang, T.M. Tsai, K.H. Chen, T.F. Young, J.H. Chen, R. Zhang, J.C. Lou, S.Y. Huang, Y.C. Pan, H.C. Huang, Y.E. Syu, D.S. Gan, S.M. Sze, Space, Electric field concentrated effect for $Zr:SiO_2$ RRAM devices using porous SiO_2 buffer layer, Nanoscale Res. Lett. 8 (2013) 523.

[34] S. Brivio, J. Frascaroli, M.H. Lee, Electrical AFM for the analysis of resistive switching, Electrical Atomic Force Microscopy for Electronics, Springer Nature:, Switzerland, 2019, pp. 205–229.

[35] D.J. Groenendijk, N. Manca, G. Mattoni, L. Kootstra, S. Gariglio, Y. Huang, E. Van Heumen, A.D. Caviglia, Epitaxial growth and thermodynamic stability of $SrIrO_3$/ $SrTiO_3$ heterostructures, Appl. Phys. Lett. 109 (2016) 041906.

[36] J.J. Randall, L. Katz, R. Ward, The preparation of a strontium-iridium oxide Sr_2IrO_4, J. Am. Chem. Soc. 79 (1957) 266–267.

[37] C. Lu, A. Quindeau, H. Deniz, D. Preziosi, D. Hesse, M. Alexe, Crossover of conduction mechanism in Sr_2IrO_4 epitaxial thin films, Appl. Phys. Lett. 105 (2014) 082407.

[38] J.G. Zhao, L.X. Yang, Y. Yu, F.Y. Li, R.C. Yu, Z. Fang, L.C. Chen, C.Q. Jin, High-pressure synthesis of orthorhombic $SrIrO_3$ perovskite and its positive magnetoresistance, J. Appl. Phys. 103 (2008) 103706.

[39] L. Fruchter, O. Schneegans, Z.Z. Li, Anisotropy and interaction effects of strongly strained $SrIrO_3$ thin films, J. Appl. Phys. 120 (2016) 075307.

[40] K.W. Kim, J.S. Lee, T.W. Noh, S.R. Lee, K. Char, Metal-insulator transition in a disordered and correlated $SrTi_{1-x}Ru_xO_3$ system: changes in transport properties, optical spectra, and electronic structure, Phys. Rev. B 71 (2005) 125104.

[41] N. Mott, Metal-Insulator Transitions, second ed., Taylor & Francis, London, 1998 Vol. 70.

[42] B.J. Kim, H. Ohsumi, T. Komesu, S. Sakai, T. Morita, H. Takagi, T. Arima, Phase-sensitive observation of a spin-orbital mott state in Sr_2IrO_4, Science 323 (2009) 1329–1332.

[43] M.A. Villena, B. Magyari-Köpe, Y. Nishi, P.C. McIntyre, M. Lanza, Effect of IrO_2 spatial distribution on the stability and charge distribution of $Ti_{1-x}Ir_xO_2$ alloys, Chem. Mater. 31 (2019) 8742–8751.

[44] D.J. Groenendijk, C. Autieri, J. Girovsky, M.C. Martinez-Velarte, N. Manca, G. Mattoni, A.M.R.V.L. Monteiro, N. Gauquelin, J. Verbeeck, A.F. Otte, M. Gabay, S. Picozzi, A.D. Caviglia, Spin-orbit semimetal $SrIrO_3$ in the two-dimensional limit, Phys. Rev. Lett. 119 (2017) 256403.

[45] B.J. Kim, H. Jin, S.J. Moon, J.Y. Kim, B.G. Park, C.S. Leem, J. Yu, T.W. Noh, C. Kim, S.J. Oh, J.H. Park, V. Durairaj, G. Cao, E. Rotenberg, Novel Jeff=1/2 Mott state induced by relativistic spin-orbit coupling in Sr_2IrO_4, Phys. Rev. Lett. 101 (2008) 076402.

[46] M.-H. Lin, M.-C. Wu, C.-H. Lin, T.-Y. Tseng, Effects of vanadium doping on resistive switching characteristics and mechanisms of $SrZrO_3$-based memory films, IEEE Trans. Electron Devices 57 (2010) 1801–1808.

[47] M.A. Afifi, M.M. Abdel-Aziz, H.H. Labib, M. Fadel, E.G. El-Metwally, Electrical and switching properties of amorphous films based on the Ge-Se-Tl system, Vacuum 61 (2001) 45–53.

[48] A. Biswas, Y.W. Lee, S.W. Kim, Y.H. Jeong, Metal insulator transition and magnetotransport anomalies in perovskite $SrIr_{0.5}Ru_{0.5}O_3$ thin films, J. Appl. Phys. 117 (2015) 115304.

[49] C. Rayan Serrao, J. Liu, J.T. Heron, G. Singh-Bhalla, A. Yadav, S.J. Suresha, R.J. Paull, D. Yi, J.H. Chu, M. Trassin, A. Vishwanath, E. Arenholz, C. Frontera, J. Železný, T. Jungwirth, X. Marti, R. Ramesh, Epitaxy-distorted spin-orbit mott insulator in Sr_2IrO_4 thin films, Phys. Rev. B 87 (2013) 085121.

[50] H.S. Lee, S.G. Choi, H.H. Park, M.J. Rozenberg, A new route to the Mott-Hubbard metal-insulator transition: strong correlations effects in $Pr_{0.7}Ca_{0.3}MnO_3$, Sci. Rep. 3 (2013) 1704.

[51] Y. Klein, I. Terasaki, Transport properties and cationic substitutions in Sr_2IrO_4, J. Electron. Mater. 38 (2009) 1331–1336.

[52] M. Ito, M. Uchida, Y. Kozuka, K.S. Takahashi, M. Kawasaki, Effective carrier doping and metallization in $La_xSr_{2-x-y}Ba_yIrO_{4-\delta}$ thin films, Phys. Rev. B 93 (2016) 045139.

Structural properties of femtosecond laser irradiation induced bismuth oxide based nano-objects in $Bi_{12}SiO_{20}$ (BSO) single crystal

Nebojsa Romcevic, Marina Lekic, Aleksander Kovacevic, Novica Paunovic, Borislav Vasic, Maja Romcevic [*]

Institute of Physics Belgrade, University of Belgrade, 11080, Belgrade, Serbia

ABSTRACT

Single crystal of $Bi_{12}SiO_{20}$ was grown from the melt by Czochralski technique. The crystal growth was in the [111] direction. The surface of the polished sample was irradiated by a femtosecond pulsed laser beam of various power. The influence of laser power on structural properties of $Bi_{12}SiO_{20}$ crystal, as well as on its phase composition, was studied. The surface morphology of our samples was investigated by AFM. The surface of unirradiated sample is rather smooth with no cracks observed. In sample modified by pulsed femtosecond beam, we registered the presence of small spherical islands on the surface. The dimensions of the islands and their density depend on the applied power. There were also significant changes in far-infrared spectra of irradiated sample in comparison to non-irradiated sample. Based on these results, the material obtained after femtosecond pulsed laser irradiation consisting of bismuth oxide based nano-objects, formed as nanocrystals (dimensions below 20 nm in diameter), which are arranged in a matrix of $Bi_{12}SiO_{20}$.

1. Introduction

Sillenites ($Bi_{12}MO_{20}$, M = Si, Ge, Ti) are optically active crystals exhibiting a lot of strong effects (optical rotation, electro-optical (Pockels), magneto-optical (Faraday) and photo-induced effects) and interesting properties such us remarkably large values of dielectric, piezo-electric and elasto-optic constants, very high values of the dark electric resistance, the index of refraction [1] etc. These crystals have application as active elements in many devices [2]. For these applications the materials are bulk single crystal samples.

On the other hand, due to their extremely small sizes, nanomaterials (one, two or three dimensions of less than 100 nm) cannot be used in large scale, particularly as long-bearing materials in engineering applications. For this it has long been a desire to develop bulk composites incorporating these nanomaterials (for example nanocomposites) to harness their extraordinary properties in bulk applicable materials. Initial ideas and principles are given in Ref. [3]. The most important fact is that the characteristics of the nanomaterials are fundamentally different in comparison with the bulk materials [4].

Lasers play an ever expanding role in material processing [5], as is the case with surface treatment of single crystals [6] where the energy of a laser beam interacts with a material to transform it in some way in a thin surface layer. This transformation (or laser process) is controlled by precisely regulating the wavelength, power, duty cycle and repetition rate of the laser beam. All materials have unique characteristics that dictate how the laser beam interacts and consequently modifies the material [7,8].

In our previous papers, we have investigated the influence of locally induced heating with increasing laser power densities on some nanomaterials such as stable hexagonal transition oxides ZnO doped with CoO [9] and cubic rock-salt MnO [10]. The influence of femtosecond pulsed laser power on the quality and optical characteristics of $Bi_{12}GeO_{20}$ single crystal was also studied [11].

The aim of this work is to continue our research with investigation influence of femtosecond pulsed laser irradiation on $Bi_{12}SiO_{20}$ single crystal using FTIR spectroscopy along with atomic force microscopy (AFM), but this time the focus is on modification of material and its structural characterization.

2. Experimental procedure

2.1. Preparation of crystal samples

Czochralski technique was applied to grow $Bi_{12}SiO_{20}$ single crystal,

---

where MSR 2 crystal puller controlled by a Eurotherm was used with temperature fluctuations of the experiment lower than 0.2 °C. Additional weighing set was used to monitor the crucible weight in order to keep a crystal diameter constant (absolute deviation was below 0.1 mm).

A platinum crucible was used to contain the melt, which was placed in an alumina vessel on a zircon – oxide wool. This system was constructed in order to stop the excessive radiation heat losses. Also, a cylindrical silica glass after heater was constructed around the system to reduce the thermal gradients in the crystal and in the melt. Crystal growth was occurred in an air atmosphere while iridium wires were used as initial crystal seeds. Later on, seed cuts from the produced $Bi_{12}SiO_{20}$ crystals were used for the growth of other crystals.

Bi_2O_3 and SiO_2 were used for synthesis of crystals. Starting materials were mixed in 6:1 stoichiometric ratio. Optimal pull rate was chosen in the range 5 – 6 mm/h. Equations of the melt hydrodynamics were used to calculate critical crystal diameter, $d_c = 10$ mm and critical rotation, $\omega_c = 20$ rpm. The crucible was not rotating during crystal growth. The crystal boule was cooled at ~50 °C/h down to a room temperature, after the crystal growth. Crystals grew in [111] direction, without core being observed. Finally, crystals were cut and polished.

2.2. Crystal irradiation and characterization

Crystal samples were exposed to a pulsed femtosecond laser beam (pulse width 90 fs, repetition rate 76 MHz) from Coherent Mira 900 F laser system pumped by a 532 nm continuous wave Coherent Verdi V-10 laser. The irradiating beam wavelength was monitored by an Ocean Optics HR2000CG UV-NIR spectrometer. The samples were irradiated along their longest axis, z, i.e., along the crystal growth direction. During irradiation, the crystal facet was partially exposed due to the oval shape of the beam profile. A graded filter was used to adjust the beam power on the sample from 50 to 800 mW (measured by Ophir Nova II powermeter with thermal and photometric heads), which corresponds to the fluence range of 75–1200 nJ/cm^2. Exposure time of each irradiation power was 3s, measured by a stopwatch of 0.2s of accuracy. The total irradiation time and energy were intentionally kept low to avoid significant contribution of an accumulative process caused by repopulation of the traps [12].

Far-infrared reflection spectra were recorded in the wave number range up to 650 cm^{-1} utilizing an A BOMEM DA - 8 FTIR spectrometer with a deuterated triglycine sulfate (DTGS) pyroelectric detector.

The surfaces of samples were examined in detail using Atomic Force Microscope (AFM), NTEGRA prima from NT-MDT. NSG01 probes with a typical resonant frequency of 150 kHz and 10 nm tip apex curvature radius were used.

The X-ray diffraction (XRD) data for $Bi_{12}SiO_{20}$ single crystals was measured using X-ray diffractometer (XRD) Rigaku Ultima IV, Japan, with filtered CuKα1 radiation ($\lambda = 0.154178$ nm). The X-ray diffraction data were collected over the 2θ range from 20° up to 80° with the step of 0.02° and scanning rate of 2°/min. The PDXL2 v2.0.3.0 software [13], with reference to the diffraction patterns available in the International Center for Diffraction Data (ICDD) [14] was used for the phase identification and data analysis.

3. Results and discussion

3.1. Femtosecond pulsed laser modification

In order to establish the behaviour of the sample material under the influence of femtosecond beam, three wavelengths from the common range of the Mira device (700–900 nm) have been chosen. The samples were exposed to femtosecond beam of 730, 800 and 830 nm, with input powers of 50–700, 50–800, and 50–550 mW, respectively. For each wavelength, the transmitted power vs input power has been monitored. The input power has been gradually increased and in this way the

influence of possible strong modifications by higher power to the results of low power was diminished. Transmitted vs. input power dependency was established (Fig. 1).

Transmitted power dependence on the input power is in fact linear for each chosen wavelengths. The linear dependence shows uniform absorption during the input power change – there were no significant damages in the material of the samples caused by the beam during exposition. If present, strong or large-scale structural changes inside the material would change the absorption coefficient which would lead to the deviation of the Pout vs. Pin (Fig. 1) dependence from the linear one.

Because of that, in the further analysis in this paper, under treated sample we will consider the sample modified with a laser line of 730 nm and a power of 700 mW as a representative one. In Fig. 2, a sample treated with 730 nm and a power of 50 mW was analyzed for comparison.

3.2. AFM

Fig. 2 shows the results of AFM measurements of the $Bi_{12}SiO_{20}$ single crystal and the same sample after being irradiated by a femtosecond pulsed laser beam. The surface of unirradiated sample is rather smooth with no cracks observed, and only traces of mechanical polishing can be seen in Fig. 2a. Fig. 2b and c. Show the surface of the sample after irradiated by a femtosecond pulsed laser with 730 nm and power of 50 mW and 700 mW respectively. Full lines at Fig. 2 a-c present directions in which the structure dimensions were determined. Height prolife on the surface and in the shine dots is shown in Fig. 2 d. For the treated samples, the nanoobject clearly stands out in the selected direction. It could be said that the height of the nano-object for both samples is in the range of about 10–15 nm, and that the height of the nanoobject increases with the increase in the power of the femtosecond laser. On the other hand, the diameter of these nano-objects is about 20 nm (Figs. 2b) and 15 nm (Fig. 2c). In addition, we note that the density of nano-objects is significantly higher in Fig. 2c.

Average roughness (Ra) for the samples shown in Fig. 2 a, b, c is 1.25 nm, 1.57 nm and 1.6 nm, respectively. Although the value for Ra is relatively small, i.e. the surface of the samples is relatively smooth, we can conclude that as a result of the femtosecond laser treatment, as well as when increasing the laser power, the value for Ra also increases, which is expected.

3.3. XRD measurements

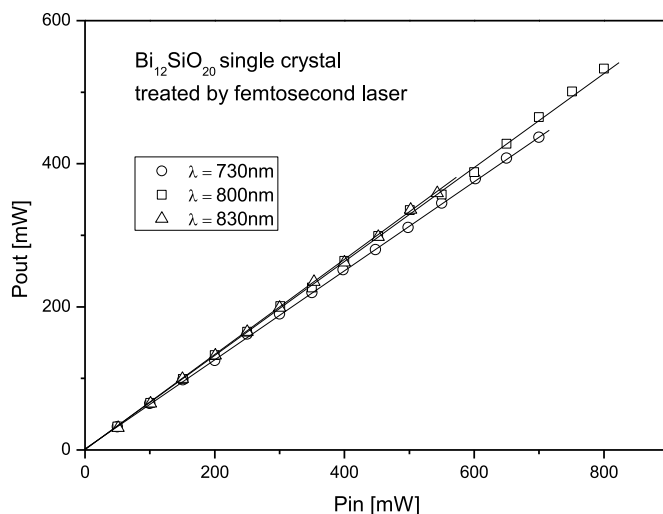Phase analysis using XRD of single crystal BSO samples are presented

Fig. 1. Transmitted (Pout) vs. input (Pin) power for samples exposed to the beam of 730 nm, 800 nm and 830 nm.
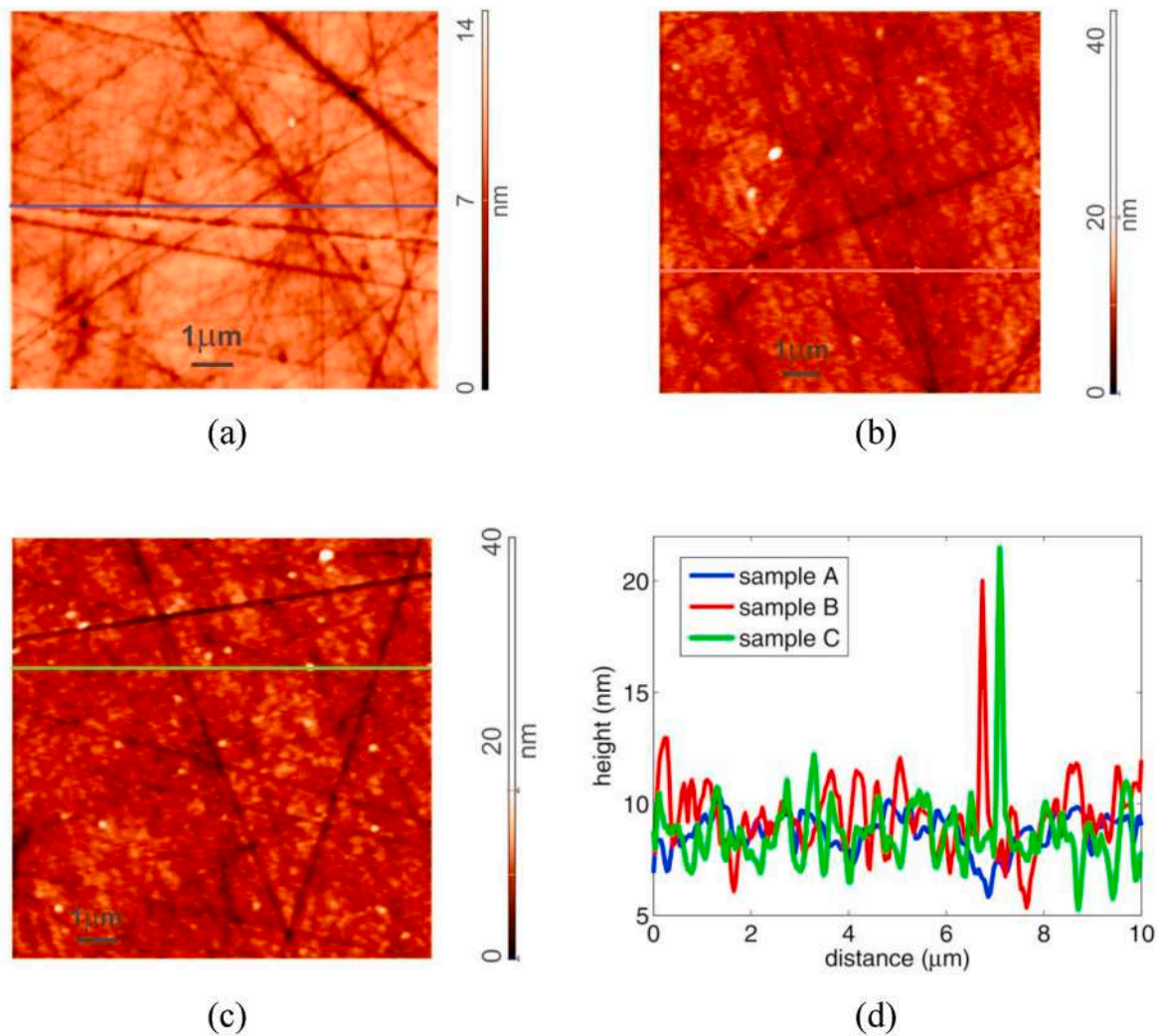
(a)

(b)

(c)

(d)

Fig. 2. AFM results of $Bi_{12}SiO_{20}$ single crystal: untreated (a); femtosecond laser treated sample: 730 nm, 50 mW (b) and 730 nm, 700 mW (c). Height prolife on the surface (d).

in Fig. 3. Phase analysis indicates that all peaks belong to the $Bi_{12}SiO_{20}$ phase, which is in good agreement with the JCPDF Card No. 37–0485.

Fig. 3. X-ray diffraction results of untreated $Bi_{12}SiO_{20}$ single crystal, peaks of $Bi_{12}SiO_{20}$ phase marked with hkl.

The XRD for the treated sample is no different from that for the untreated.

3.4. Far-infrared spectroscopy

The experimental far-infrared spectrum of BSO single crystal was recorded in the spectral range of 70–650 cm^{-1} at room temperature and in Fig. 4 is presented as a blue line. The obtained spectrum shows all characteristics described in the literature [15,16]. The far-infrared spectrum of the femtosecond laser treated BSO, recorded in the spectral range of 70–650 cm^{-1} at room temperature, is presented in Fig. 4 as a red line. Even though the spectra given in Fig. 4 were recorded under the same conditions, differences in the BSO single crystal and femtosecond laser treated BSO spectra are clearly visible at in several places, such as about 130, 180, 280 cm^{-1} ….

$$\Gamma = 8A + 8E + 25F \qquad (1)$$

Among these modes, only the F modes are infrared active.

Fig. 5, lower spectrum, shows the far-infrared spectra of BSO single crystal. The points are given the experimental results, and the solid line is obtained in the standard way by the procedure of fitting parameters [18,19]. Due to the large energy gap (Eg = 2,57eV) and accordingly very low concentrations of free carriers, a dielectric function was used which takes into account only the interaction of electromagnetic radiation with
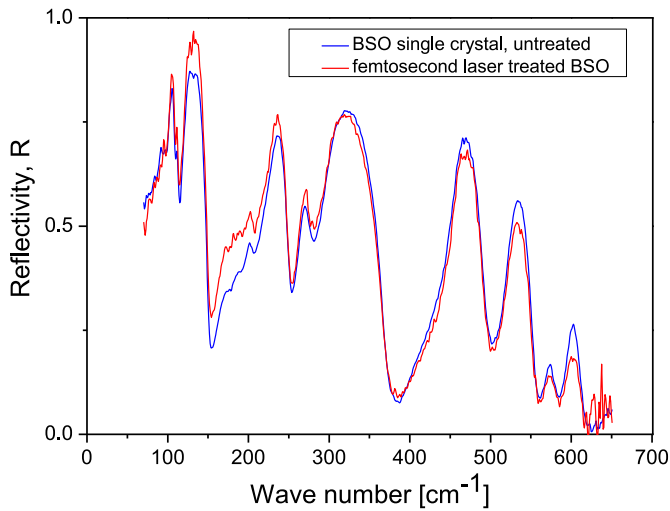
Fig. 4. Experimental far-infrared reflection spectra of $Bi_{12}SiO_{20}$ single crystal untreated (blue line) and treated by femtosecond beam (red line). First, in short about factor group analysis. Crystal BSO has a cubic unit with space group I23 (T3) [17].
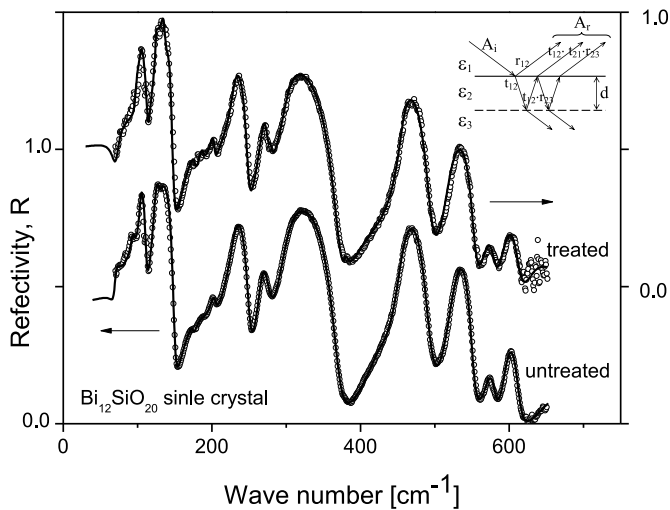
Fig. 5. Far-infrared reflection spectra of $Bi_{12}SiO_{20}$ single crystal and femtosecond laser-treated $Bi_{12}SiO_{20}$ sample. The experimentally obtained data points are depicted as circles. The theoretical spectrum obtained with the model defined by eqs. (2) and (3) and fitting procedure is given as solid line. Insert. Schematic overview of the femtosecond laser-treated $Bi_{12}SiO_{20}$ sample.

phonons:

$$\varepsilon(\omega) = \varepsilon_\infty \prod_{k=1}^{s} \frac{\omega^2 + i\gamma_{kLO} - \omega_{kLO}^2}{\omega^2 + i\gamma_{kTO} - \omega_{kTO}^2} \qquad (2)$$

where ε_∞ is the bound charge contribution and is considered as a constant, ω_{LOk} and ω_{TOk} are the longitudinal and transverse optical – phonon frequencies, and γ_{TOk} and γ_{LOk} are the phonon dampings.

The results obtained for TO/LO frequencies (in cm^{-1}) are: 69/71, 94/95, 104/112, 123/150, 129.5/130, 142/143, 175.2/175.5, 187.5/192.5, 202.5/204.3, 229/251, 267/276.8, 297.5/371, 424/427, 453/494, 520/551.5, 572/581, 594/613, 647/658. The agreement with the literature data [15,16] is excellent. This result serves as an introduction to the spectrum analysis for the femtosecond laser treated BSO sample, where the situation is somewhat more complex. Fig. 5, upper spectrum, shows the far-infrared spectrum of femtosecond laser treated BSO single crystal. The points are given the experimental results, and the solid line

is obtained in the following way.

Namely, as can be seen from Fig. 2b and c, laser treatment leads to a change in the surface of the samples. It seems that its composition changes in a very thin layer, but also that nanoobjects are formed inside the layer and on its surface. Therefore, we decided to use a model that takes into account the existence of a three-layer structure (see insert of Fig. 5), where.

(a) medium 1 is air ($\varepsilon_1 = 1$),
(b) medium 2 is a layer with thickness d present at the sample surface with dielectric constant ε_2 (eq. (2)), and
(c) lower optically thick layer, medium 3, practically single crystal BSO, described with ε_3 (eq. (2)).

In this case, the reflectivity can be determined as described in Ref. [20]:

$$R_A = \frac{A_r}{A_i} = \frac{r_{12}e^{-i\alpha} + r_{23}e^{i\alpha}}{e^{-i\alpha} + r_{12}r_{23}e^{i\alpha}} \qquad (3)$$

where $r_{ij} = (n_i - n_j)/(n_i + n_j) = (\sqrt{\varepsilon_i} - \sqrt{\varepsilon_j})/(\sqrt{\varepsilon_i} + \sqrt{\varepsilon_j})$ are the Fresnel coefficients, A_i and A_r represent amplitudes of the incident and reflection beams, respectively, n is the complex index of refraction, ε is the dielectric constant and $\alpha = 2\pi\omega d\,(\varepsilon_2)^{1/2}$ is the complex phase change related to the absorption in the crystal layer with the thickness d. Reflectance, R, is given as $R = |R_A|^2$.

The parameters of the treated sample were determined by the fitting procedure. In that manner, the parameters for the single crystal BSO layer (medium 3) remained the same as those determined from untreated sample. The surface layer (medium 2), besides them, has additional modes. The layer thickness is d = 1,9 μm. Comparison of our result with the values from the literature for the registered additional phonons is given in Table 1.

Some results from literature, for example [22], show that laser-induced oxidation of bismuth can occur, but the degree of oxidation and the formation of the crystalline phase strongly depend on the laser power. We think that in our case, due to laser heating, on the $Bi_{12}SiO_{20}$ single crystal, the formation of starting material phases occurs. It is known that bismuth oxide can exist in several polymorphic forms: α-Bi_2O_3, the only phase stable at room temperature, and three high-temperature phases, β-, δ- and γ-Bi_2O_3. The orthorhombic phase, α-Bi_2O_3, transforms to cubic δ-Bi_2O_3 at 729 °C, which may transform to tetragonal β-Bi_2O_3 or body-centered cubic γ-Bi_2O_3 upon cooling to 650 and 639 °C, respectively [24–27]. Both of these forms are metastable,

Table 1
Comparison between additional far-infrared frequencies registered in this paper and experimentally and calculated frequencies from the literature.

Phonon peaks This work [cm⁻¹]	Experimental literature values of phonon frequencies [cm⁻¹]	Calculated phonon frequencies [cm⁻¹]	Description
120	120 [21]	120 [21]	Bi_4O_7 [21]
	118 [22]		α-Bi_2O_3 [22]
		124 [21]	β-Bi_2O_3 [21]
161	157 [21]		γ-Bi_2O_3 [21]
	166 [23]		γ-Bi_2O_3 [23]
278	279 [22]		γ-Bi_2O_3 [22]
	281 [21]		γ-Bi_2O_3 [22]
380	381 [21]		γ-Bi_2O_3 [21]
		388 [21]	Bi_4O_7 [21]

but may be stabilized at room temperature by the addition of impurities [25].

Another metastable phase, which was also registered by our measurements, is Bi_4O_7. This phase is a fully chargeordered pseudo-binary bismuth (Bi^{3+}, Bi^{5+}) oxide [28,29]. This mixed valence and the optical gap within the visible range (1.9eV) turns the Bi_4O_7 interesting for applications in photocatalysis. Also, because of strong luminescence at about 420 nm Bi_4O_7 is a candidate as for purplish-blue light emitter [30]. One of the following directions of research can be dedicated to this topic as well.

It seems to us that in this way it is clearly shown that femtosecond laser treating produces nano-objects consisting of different phases based on bismuth oxide in a matrix of $Bi_{12}SiO_{20}$ single crystal. In the future, we will search for new functionalities, which would open up new topics and areas.

4. Conclusions

We used a femtosecond pulsed laser to modify the surface on a $Bi_{12}SiO_{20}$ single crystal growth by Czochralski technique. The treatment led to the formation of bismuth oxide based nanoobjects in the $Bi_{12}SiO_{20}$ matrix. These nanoobjects are formed as nanocrystals with dimensions below 20 nm in diameter and about 15 nm in height. By composition, they are α-, β-, and γ-Bi_2O_3 and Bi_4O_7. The concentration of nanoobjects increases when the power of the femtosecond laser increases. Application in optoelectronics and optical sensor industry is expected.

Author contributions

N. Romcevic: Conceptualization, Methodology, Formal analysis, Writing- Original draft preparation. **N. Paunovic, M. Lekic, A. Kovacevic, B. Vasic:** Investigation, Formal analysis. **M. Romcevic:** Investigation, Formal analysis, Writing—review and editing. All authors have read and agreed to the published version of the manuscript.

Funding

Declaration of competing interest

The authors declare that they have no known competing financial interests or personal relationships that could have appeared to influence the work reported in this paper

Data availability

Data will be made available on request.

References

[1] J.-C. Chen, L.-T. Liu, C.-C. Young, A study of the growth mechanism of bismuth silicon oxide during LHPG method, J. Cryst. Growth 198/199 (1999) 476–481, https://doi.org/10.1016/S0022-0248(98)01142-7.

[2] M.P. Petrov, A.V. Khomenko, in: P. Gunter, J.P. Huignard (Eds.), Photorefractive Materials and Their Applications II, Publicher, Springer, Berlin, 1989, pp. 325–352, https://doi.org/10.1007/BFb0120157.

[3] Y. Dzenis, Structural nanocomposites, Science 319 (2008) 419–420, https://doi.org/10.1126/science.1151434.

[4] T.E. Twardowski, Introduction to Nanocomposites Material Properties, Processing, Characterization, Publicher: Destech Publications, Lancaster, Pa, USA, 2007, pp. 1–532.

[5] P.M. Ossi, M. Dinescu, Laser processing of materials, in: P. Schaaf (Ed.), Springer Series in Materials Science (SSMATERIALS), vol. 139, 2010, pp. 131–167, https://doi.org/10.1007/978-3-642-13281-0.

[6] M.A. Montealegre, G. Castro, P. Rey, J.L. Arias, P. Vazquez, M. Gonzalez, Surface treatments by laser technology, Contemporary Materials I–1 (2010) 19–30, https://doi.org/10.5767/anurs.cmat.100101.en.019M.

[7] A.K. Roy (Ed.), Hybrid Atomic-Scale Interface Design for Materials Functionality, Publicher, Elsevier, 2021, https://doi.org/10.1016/C2018-0-05143-9.

[8] M.V. Shugaev, C. Wu, O. Armbruster, A. Naghilou, N. Brouwer, D.S. Ivanov, T.J.-Y. Derrien, N.M. Bulgakova, W. Kautek, B. Rethfeld, L.V. Zhigilei, Fundamentals of ultrafast laser–material interaction, MRS Bull. 41 (12) (2016) 960–968, https://doi.org/10.1557/mrs.2016.274.

[9] B. Hadzic, N. Romcevic, D. Sibera, U. Narkiewicz, I. Kurylisyn-Kudelska, W. Dobrowolski, M. Romcevic, Laser power influence on Raman spectra of ZnO (Co) nanoparticles, J. Phys. Chem. Solid. 91 (2016) 80–85, https://doi.org/10.1016/j.jpcs.2015.12.008.

[10] B. Hadzic, B. Vasic, B. Matovic, I. Kuryliszyn-Kudelska, W. Dobrowolski, M. Romcevic, N. Romcevic, Influence of laser induced heating on MnO nanoparticles, J. Raman Spectrosc. 49 (5) (2018) 817–821, https://doi.org/10.1002/jrs.5358.

[11] A. Kovacevic, J. Ristic-Djurovic, M. Lekic, B. Hadzic, G. Saleh Isa Abudagel, S. Petricevic, P. Mihailovic, B. Matovic, D. Dramlic, Lj Brajovic, N. Romcevic, Influence of femtosecond pulsed laser irradiation on bismuth germanium oxide single crystal properties, MRS Bull. 83 (2016) 284–289, https://doi.org/10.1016/j.materresbull.2016.06.023.

[12] B. Taheri, S.A. Holmstrom, R.C. Powell, J.J.F. Song, F. Antonio Munoz, I. Földvári, A. Péter, Nonlinear absorption of laser light in $Bi_{12}GeO_{20}$ single crystals, Opt. Mater. 3 (1994) 251–255, https://doi.org/10.1016/0925-3467(94)90037-X.

[13] PDXL Version 2.0.3.0 Integrated X-Ray Powder Diffraction Software, Rigaku Corporation, Tokyo, Japan, 2011, p. 196.

[14] Powder Diffraction File, PDF-2 Database, Announcement of New Database Release, International Centre for Diffraction Data (ICDD), 2012.

[15] A. Golubovic, S. Nikolic, R. Gajic, S. Duric, A. Valcic, The grown and optical properties of $Bi_{12}SiO_{20}$ single crystals, J. Serb. Chem. Soc. 67 (4) (2002) 279–289.

[16] D. Senuliene, G. Babonas, Far infrared reflection spectra of sillenite crystals and their solid solutions, phys. stat. solidi (b) 180 (2) (1993) 541–549, https://doi.org/10.1002/pssb.2221800225.

[17] G.N. Zhizhin, B.N. Mavrin, V.F. Shabanov, Opticheskie Kolebatelnye Spektry Kristallov, Pubisher: Nauka, Moskva, 1984.

[18] J. Trajic, M. Romcevic, N. Romcevic, B. Babic, B. Matovic, P. Balaz, Far-infrared spectra of mesoporous ZnS nanoparticles, Opt. Mater. 57 (2016) 225–230, https://doi.org/10.1016/j.optmat.2016.05.004.

[19] J. Trajic, M. Rabasovic, S. Savić-Sevic, D. Sevic, B. Babic, M. Romcevic, J. Ristic-Durovic, N. Paunovic, J. Krizan, N. Romcevic, Far-infrared spectra of dysprosium doped yttrium aluminium garnet nanopowder, Infrared Phys. Technol. 77 (2016) 226–229, https://doi.org/10.1016/j.infrared.2016.06.003.

[20] M. Gilic, J. Trajic, N. Romcevic, M. Romcevic, D.V. Timotijevic, G. Stanisic, I. S. Yahia, Optical properties of CdS thin films, Opt. Mater. 35 (2013) 1112–1117, https://doi.org/10.1016/j.optmat.2012.12.028.

[21] O. Depablos-Rivera, A. Martinez, S.E. Rodil, Interpretation of the Raman spectra of bismuth oxide thin films presenting different crystallographic phases, J. Alloys Compd. 853 (2021), 157245, https://doi.org/10.1016/j.jallcom.2020.157245.

[22] K. Trentelman, A note on the characterization of bismuth black by Raman microspectroscopy, J. Raman Spectrosc. 40 (2009) 585–589, https://doi.org/10.1002/jrs.2184.

[23] C. Rodriguez-Fernandez, K. Akius, M.M. de Lima Jr., A. Cantarero, J.M. van Ruitenbeek, C. Sabater, Raman signal revels the rhombohedral crystallographic structure in ultra-thin layers of bismut thermally evaporated on amprphous substrate, Maerials Sci. Eng. B 27 (2021), 115240, https://doi.org/10.1016/j.mseb.2021.115240.

[24] S. Venugopalan, A.K. Ramdas, Raman spectra of bismuth germanium oxide and bismut silicon oxide, Phys. Rev. B 8 (10) (1972) 4065–4079, https://doi.org/10.1103/PhysRevB.5.4065.

[25] B. Mihailova, M. Gospodinov, L. Konstantinov, Raman spectroscopy study of silenites. I. Comparasion between $Bi_{12}(Si,Mn)O_{20}$ single crystals, J. Phys. Chem. Solid. 60 (1999) 1821–1827, https://doi.org/10.1016/S0022-3697(99)00194-8.

[26] I.F. Vasconcelos, M.A. Pimenta, A.S.B. Sombra, Optical properties of $Bi_{12}SiO_{20}$ (BSO) and $Bi_{12}TiO_{20}$ (BTO) obtained by mechanical alloying, J. Mater. Sci. 36 (2001) 587–592, https://doi.org/10.1023/A:1004804000723.

[27] J.C. Alonso, R. Diamant, E. Haro-Poniatowski, M. Fernandez-Guasti, G. Munoz, I. Camarillo, M. Jouanne, J.F. Morhange, Raman characterization of $Bi_{12}SiO_{20}$ thin films obtained by pulsed laser deposition, App. Sur. Sci. 109/110 (1997) 359–361, https://doi.org/10.1016/S0169-4332(96)00674-5.

[28] B. Begemann, M. Jansen, Bi_4O_7, das erste definierte binare Bismut (III, V) - oxid, J. Less Common. Met. 156 (1989) 123–135, https://doi.org/10.1016/0022-5088(89)90412-8.

[29] R.E. Dinnebier, R.M. Ibberson, H. Ehrenberg, M. Jansen, The crystal structures of the binary mixed valence compound $Bi(III)_3Bi(V)O_7$ and isotypic Bi_3SbO_7 as determined by high resolution X-ray and neutron powder diffraction, J. Solid State Chem. 163 (2002) 332–339, https://doi.org/10.1006/jssc.2001.9427.

[30] H. Guan, Y. Feng, Facile synthesis and purplish blue luminescence of the binary mixed valence compound Bi_4O_7 microcrystals, Matter. Lett. 143 (2015) 269–272, https://doi.org/10.1016/j.matlet.2014.12.129.

Inducing LIPSS on multilayer thin metal films by femtosecond laser beam of different orientations

Aleksander G. Kovačević[1] · Suzana M. Petrović[2] · Branislav Salatić[1] · Marina Lekić[1] ·
Borislav Vasić[1] · Radoš Gajić[1] · Dejan Pantelić[1] · Branislav M. Jelenković[1]

Abstract

The occurrence of laser-induced periodic surface structures (LIPSS) has been known for a while. Multilayer thin films, like Al/Ti, are suitable for LIPSS formation and attractive for applications—due to their wearing behavior and corrosion resistance; LIPSS generation may improve their properties as well. LIPSS properties depend not only on the material but also on the beam characteristics, like wavelength, polarization and scanning directions, etc. After exposing with NIR femtosecond pulses from Coherent Mira 900 laser system in several beam exposures, we have analyzed the samples of thin metal film systems with Tescan Mira3 SEM and NTegra AFM. The formation of LIPSS is most probably due to the generation of surface plasmon polariton, through the periodic distribution of energy in the interaction zone which lead to thermal processes in layers and interfaces. Two types of LIPSS were generated, which differ in shape, orientation and in ablation pronounced or not. For consecutive interactions in the same direction, LIPSS maintained its orientation, while for orthogonal passes LIPSS with mutually orthogonal orientation were generated. LIPSS period fluctuated between 320 and 380 nm and structures with pronounced ablation have significantly smaller width. Probable mechanism is that for greater accumulated energy pronounced ablation takes place giving LIPSS in the form of trenches or grooves, while for less accumulated energy the buildup of the material—probably due to pronounced oxidation—lead to LIPSS in the form of hills or ridges.

This article is part of the Topical Collection on Advanced Photonics Meets Machine Learning.

Guest Edited by Goran Gligoric, Jelena Radovanovic and Aleksandra Maluckov.

✉ Aleksander G. Kovačević
Aleksander.Kovacevic@ipb.ac.rs

[1] Institute of Physics, University of Belgrade, Belgrade, Serbia

[2] Institute of Nuclear Sciences "Vinča", University of Belgrade, Belgrade, Serbia

1 Introduction

Interaction of pulsed laser beam with surfaces yields the appearance of LIPSS (laser-induced periodic surface structures). The occurrence of LIPSS has long been known and studied (Birnbaum 1965; Van Driel et al. 1982; Sipe et al. 1983; Young et al. 1984; Ursu et al. 1985). It has been studied on variety of materials: metals (Ursu et al. 1985; Wang and Guo 2005; Vorobyev and Makin 2007; Vorobyev and Guo 2008, 2013), semi-conductors (Von der Linde et al. 1997; Bonse and Krüger 2010; Bonse et al. 2011; Varlamova et al. 2014), dielectrics (Reif et al. 2008), graphite (Golosov et al. 2011), compounds (Kautek et al. 2005; Gakovic et al. 2011), diamond (Shinoda et al. 2009), graphene (Beltaos et al. 2014). LIPSS properties depend not only on the material but also on the beam characteristics, like wavelength, polarization and scanning directions, etc. (Kovačević et al. 2017).

Surface morphology is a key factor in controlling the optical, mechanical, wetting, chemical, biological, and other properties of a solid surface. LIPSS may improve material properties by functionalization and may widen applications: structural coloring, absorptance enhancement, antireflective films, biomedical applications, optofluidics applications, holography, anti-counterfeiting, decorating, sensing, catalysis, optical data storage (Vorobyev and Guo 2013).

The occurrence of LIPSS can be viewed as an inherent phenomena of the interaction of the ultrafast beam with solid surface, with main characteristics that the spatial period of LIPSS is less than the beam wavelength. The orientation depends on the incident beam polarization direction. Generation is explained by self-organization or by surface plasmon polaritons (SPP) (Vorobyev and Makin 2007; Reif et al. 2008). Incident wave induces oscillations of charges (surface plasmon) and SPP forms as the coupling between incident and induced waves; in this way periodic distribution of energy is formed on the surface.

Two types of LIPSS are reported: low spatial frequency LIPSS (LSFL) and high spatial frequency LIPSS (HSFL) (Bonse et al. 2005). LSFL period $\lesssim$ wavelength and HSFL period < wavelength/2. Named after their size (magnitude of spatial frequency), their orientation in respect to the polarization direction is not yet fully understood. It seems that LSFL orientation is perpendicular to polarization for metals and semiconductors (Bonse et al. 2012). Due to SPP, periodical distribution of thermal energy on the surface can instigate thermal processes. The occurrence of metal-oxide, or thermochemical type of LIPSS has been reported on Ti, Ni, Cr and NiCr surfaces, as well as ablative LIPSS and models have been proposed (Öktem et al. 2013; Dostovalov et al. 2017, 2019a).

When creating LIPSS on multilayer thin metal films, the underneath layer has an important role. In the example of Al/Ti multilayer film (Kovačević et al. 2015), Ti and Al have different electron heat conductivity and electron–phonon coupling. Top layer (Al) electrons accept energy and quickly transfer to the next layer (Ti). Strong coupling keeps the energy in Ti and away from topmost Al. In this way, the damage threshold for Al increases which preserves LIPSS for longer expositions. In this work, we have examined the LIPSS generated upon consecutive scanning over the same area of same and of different scanning orientations. By changing the parameters of the beam (fluence, scanning speed, scanning number and directions over the same area) the formation of LIPSS was affected. Two types of LIPSS, which differ in shape, orientation to the incoming beam polarization and in ablation pronounced or not, are generated and examined during repeated consecutive scanning of same and orthogonal directions. For lower accumulation on energy, LIPSS in the form of ridges formed while for higher fluences and accumulated energies, the generation of LIPSS gave prevalence to the ablation. After repeated consecutive scanning along the

same trajectory LIPSS preserved to some extent. Also, during scanning along close parallel lines, LIPSS from one line affected generation of LIPSS from neighboring line. Overlapping scanning lines should generate LIPSS mutually perpendicular. We have examined the three cases of LIPSS: repeated consecutive scanning along same trajectory, scanning with close parallel lines, and scanning with perpendicular lines. The results can be of use in functionalization of materials by LIPSS forming with possible impact in wetting and biomedical applications.

2 Experiment and methods

The samples were prepared by D.C. ion sputtering in a single vacuum run, using Ar ions and switching from one target to the other. Targets were 99.9% pure Al and Ti deposited on a Si(100) wafer as a substrate. In this way, 5×(Al/Ti) multilayer structures have been generated, where each layer was 13 nm thick and total thickness of the multilayer structure was 130 nm.

Coherent Mira 900 laser system was a source of NIR femtosecond pulses (wavelength 730–840 nm, repetition rate 76 MHz, fluence 145–260 mJ/cm^2) pumped by Verdi V10 Nd:YVO4 CW laser (wavelength 532 nm, power 10 W) for exposition of the samples. Steering and focusing was a part of a modified optical microscope with 2D mirror scanner (objective 40×, NA 0.65). Ocean optics HR2000CG UV-NIR fiber spectrometer was used for spectral detection. The samples have been analyzed with Tescan Mira3 SEM and NTegra Prima AFM under ambient conditions. The numerical simulations have been performed by COMSOL Multiphysics package, with one-dimensional two-temperature (1D TTM) model. Basic relations underlying the TTM model were proposed by Anisimov (Anisimov et al. 1974). The model observes the electron and lattice subsystems. TTM model has been used for many years to calculate the temperature of the electrons and lattice during interaction of ultrashort laser pulses with different materials. All necessary physical quantities and constants that we used in the simulation can be found in the literature (Majchrzak et al. 2010a, b). The fs beam from laser was introduced into the modified microscope onto the steering two-axis scanning mirror system and transferred through the objective of the microscope to the sample.

Patterns used for interaction are presented in Fig. 1. For consecutive repeated scanning over same trajectory, the pattern in the form of letter "N" is used (Fig. 1a). The laser beam traverses over the sample surface following the pattern of the letter. At first location, it "writes" one letter. At second (neighboring) location, it traverses the same trajectory twice, writing two letters one over another. At third location, it writes three letters, and so on. The pattern used for perpendicular overlapped scanning is composed of set of parallel lines and the sample is rotated by 90° (Fig. 1b).

3 Results and discussion

The samples were exposed to laser beam of 730, 800 and 840 nm of wavelength with different fluences. Irradiated areas were examined by SEM and AFM. For specified parameters, simulations of 1D temperature distribution were performed.

In Fig. 2, the results after beam of 800 nm wavelength and 153 mJ/cm^2 of fluence repeatedly scanned from 1 to 10 times over the surface are presented. The area where beam
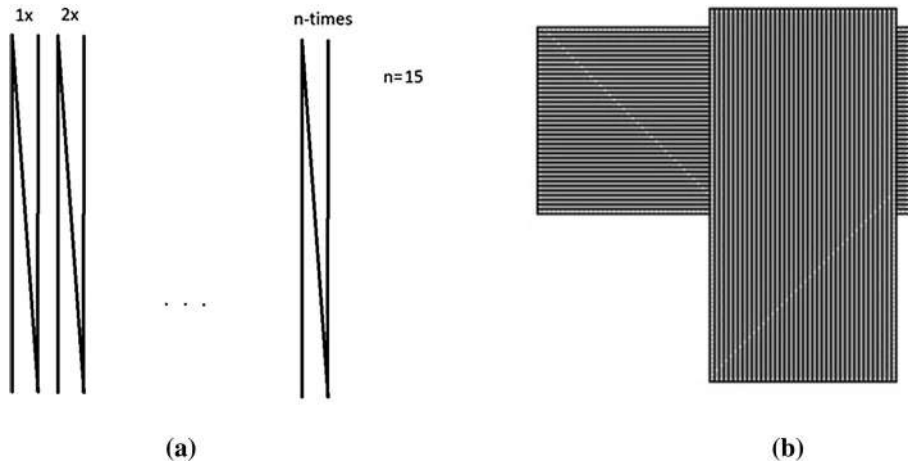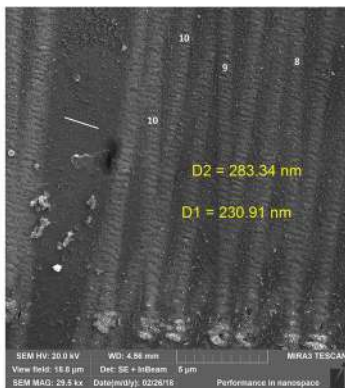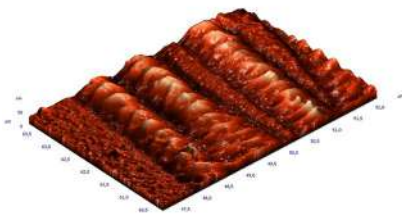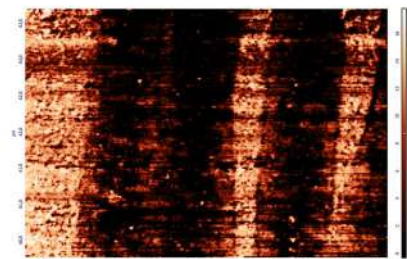
Fig. 1 Implemented patterns of scanning: **a** for consecutive repeated scanning; **b** for perpendicular overlapped scanning

Fig. 2 LIPSS generated after beam of 153 mJ/cm^2 repeatedly scanned over the same trajectory: **a** SEM of the area of 8–10 passes: **b** AFM, detailed portion of the area in **a**—rendered area is (3×5) μm and maximal height is 50 nm; **c** graphical presentation of the AFM current (a.u.) of the area in **b**

scanned 8, 9 and 10 times along the same trajectory, following the shape of the letter "N", is shown in Fig. 2a. White line on the left side of the image presents polarization direction. The beam repetition rate was 76 MHz, diameter ~ 1.2 μm, scanning speed 242 μm/s. Effective number of pulses (number of pulses which affect the area of a beam spot) for one pass is 317,000. LIPSS in the form of ridges parallel to the polarization direction with spatial period of ~ 283 nm are generated and preserved up to 10 passes. In Fig. 2b, detailed AFM view of a part of the area from Fig. 2a which shows 10 passes is presented. AFM current of the area from Fig. 2b is shown in Fig. 2c.

The simulation of the lattice temperature from the surface to the bulk is shown in Fig. 3. Odd layers (Al) are presented with light grey bars, even layers (Ti) are presented with grey bars, while substrate (Si) is presented with dark grey bar. After 1.25 ps (Fig. 3a), the temperature reaches maximum in the second (Ti) layer. After 20 ps (Fig. 3b), the temperature reaches maximum in the first (Al) layer.

In Fig. 4, the results after beam of: (a) 730 nm wavelength and 145 mJ/cm^2 fluence (repetition rate 76 MHz, diameter ~ 1 μm) scanned 15 times (scanning speed 1.14 mm/s, effective number of pulses for one pass 67,000) and (b) 800 nm wavelength and 215 mJ/cm^2 fluence (repetition rate 76 MHz, diameter ~ 1.1 μm) scanned 10 times (scanning speed 24 μm/s, effective number of pulses for one pass 667,000) along the same trajectories are presented. In Fig. 4a, LIPSS are in the form of ridges (spatial period of ~ 278 nm) parallel to the polarization direction. In Fig. 4b, LIPSS are in the form of grooves (spatial period of ~ 370 nm and groove width of ~ 80 nm) perpendicular to the polarization. In both cases LIPSS are preserved up to 15 and 10 passes, consecutively. Higher fluence provoked the appearance of groove-type of LIPSS. Spatial temperature distribution is similar in shape to the distributions shown in Fig. 3.

In order to create structures of mutual perpendicular direction at the same area, we performed perpendicular consecutive scanning of two (same) patterns by sample rotation (Fig. 1b). The beam was of 840 nm wavelength and the fluence was set to ~ 182 mJ/cm^2 in order to generate groove-type of LIPSS. The beam repetition rate was 76 MHz, scanning speed 1.5 mm/s. diameter ~ 1.1 μm, Effective number of pulses for one pass is 51,000.

In Fig. 5a, the interaction area of the sample with two consecutive beam scanning of the same pattern (Fig. 1b) is presented. The right-hand and lower parts of the image present areas where patterns don't overlap, while central, upper and left parts present overlapped patterns. Magnified portion of the right-hand part, Fig. 5b, shows that grooves of two
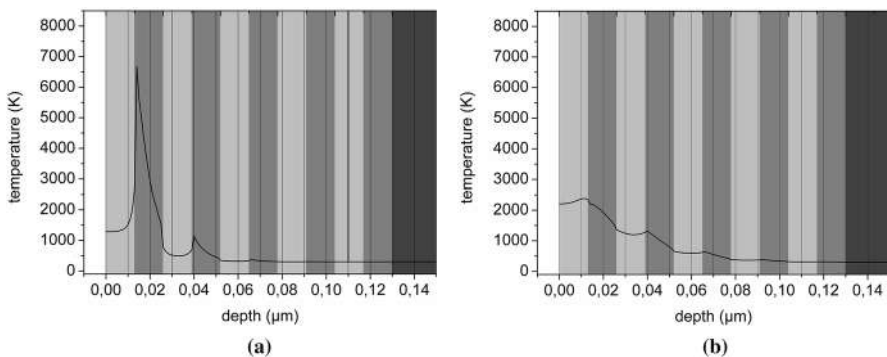

Fig. 3 Spatial temperature distribution from the surface to the bulk after exposition to the beam of 800 nm wavelength and 153 mJ/cm^2 of fluence: **a** after 1.25 ps; **b** after 20 ps
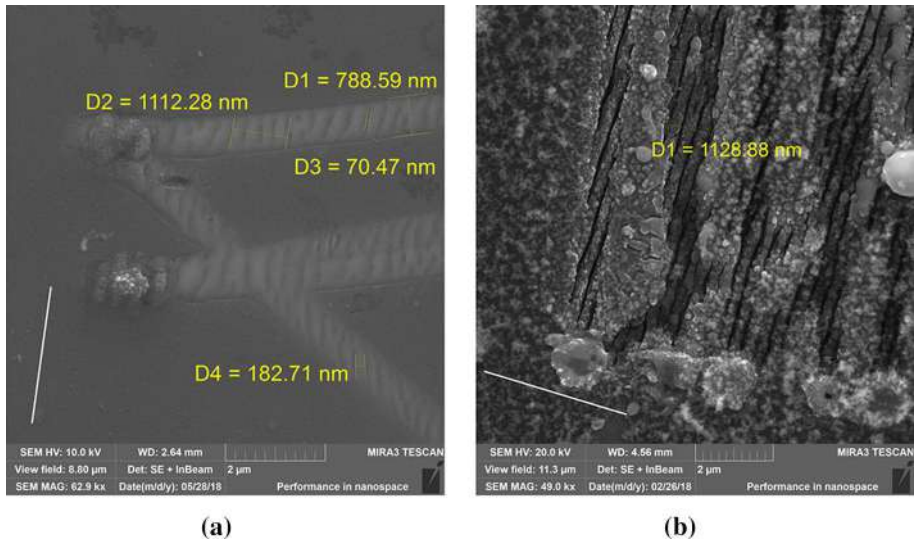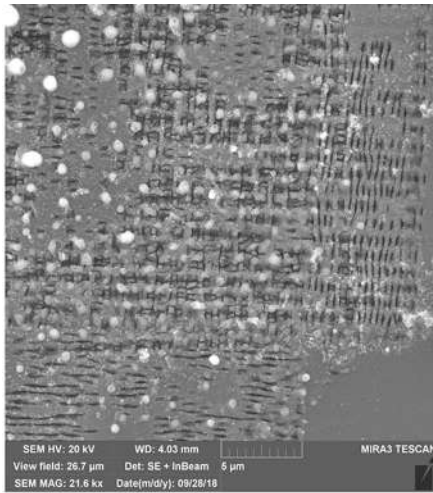
Fig. 4 SEM micrographs of LIPSS generated after beam of: **a** 145 mJ/cm^2 scanned 15 passes and **b** 215 mJ/cm^2 scanned 10 passes. White line on the left side shows polarization orientation

neighboring lines connect when patterns do not overlap. Where patterns overlap, Fig. 5c, grooves don't form in connected perpendicular directions; their width ranges from 98 to 126 nm.

The decrease in the AFM current (Fig. 2c) in the areas of laser exposition could be explained by increased resistivity of the exposed areas. Interaction with the beam fostered the penetration of nitrogen and/or oxygen into the first (Al) layer increasing the resistivity, which goes well with the three-step model (Öktem et al. 2013). The lattice temperature distribution from the surface to the bulk (Fig. 3) shows the influence of the multi-layer structure. After 1.25 ps (Fig. 3a), the temperature reaches maximum in the second layer (Ti). Moreover, the temperatures are higher in Ti layers than in neighboring Al layers. This is explained by the difference between two materials characteristics (Kovačević et al. 2015). Electrons from Al can quickly transfer energy to Ti layer away from the interaction zone due to the difference in electron–phonon coupling. This increases the damage threshold in Al leading to more regular ripples. The repetition rate also influences the regularity of the LIPSS, as noted in (Dostovalov et al. 2019b): higher the repetition rate, more ordered structures are formed.

The LIPSS in the form of ridges (Figs. 2a, 4a) are most probably generated by the penetration of the nitrogen and/or oxygen from the ambient (air) into the material—thermochemical LIPSS (Öktem et al. 2013; Dostovalov et al. 2017). For higher fluences, LIPSS formed in the form of grooves by ablation mechanisms, which can be deduced by scattered ejected material seen in Fig. 4b. Slower scanning speed and low melting point of Al induced energy accumulation sufficient for Al melting and ablation, which gave the prevalence of the generation of grooves (ablative LIPSS) over ridges (thermochemical LIPSS). The comparison of the spatial periods—283 nm (Fig. 2a) and 278 nm (Fig. 4a) for ridges versus 370 nm (Fig. 4b) for grooves—suggests grooves could be classified into LSFL and ridges into HSFL; this could be also supported by their orientation in respect to the beam polarization direction (Bonse et al. 2013).

(a)
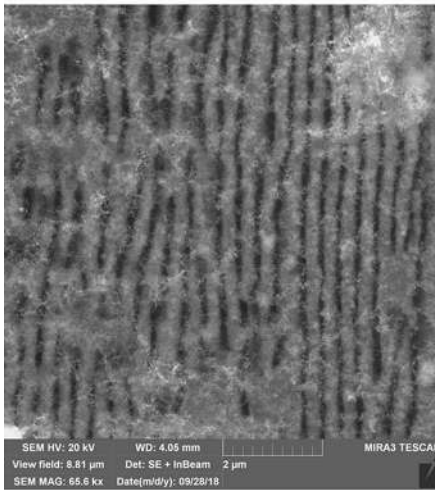
(b)
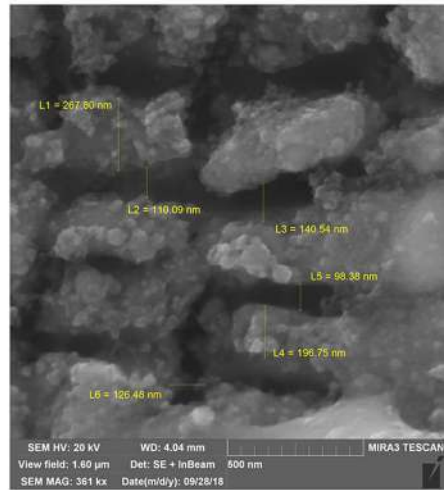
(c)

Fig. 5 SEM micrograph of LIPSS generated by consecutive pattern scanning and sample rotation: **a** wide area; **b** right-hand part of the area in **a**; **c** magnified part of the central area in **a**

The attempt to generate intersecting perpendicular grooves was not successful. The reason is twofold. First generated LIPSS pattern distracts the formation of the second LIPSS pattern. Also, the formation of the second LIPSS pattern smears the first LIPSS pattern due to the accumulation of energy.

4 Conclusion

We have exposed 5×(Al/Ti) multilayer thin film metal structures to fs laser beam of various wavelengths and fluences. Due to differences in materials characteristics, the temperatures are higher in Ti layers than in neighboring Al layers, which was illustrated by simulations. The appearance of LIPSS indicates lateral periodical distribution of temperature in second layer (Ti). Two types of LIPSS emerged depending on the beam fluence. For fluence lower than ~ 170 mJ/cm^2, LIPSS in the form of ridges are generated most probably by the penetration of nitrogen and/or oxygen into the sample material (thermochemical LIPSS), which can be deduced by the decrease in the AFM current indicating the increase in resistivity. For higher fluences (above 170 mJ/cm^2), LIPSS in the form of grooves are generated by ablation mechanisms (ablative LIPSS). Both types are preserved after 10–15 consecutive beam scanning along the same trajectory. Intersecting perpendicular LIPSS can't be successfully formed because of competing influences of perpendicular patterns causing smearing of LIPSS.

References

Anisimov, S.I., Kapeliovich, B.L., Perel'man, T.L.: Electron emission from metal surface exposed to ultrashort laser pulses. Sov. Phys. JETP **39**, 375–377 (1974)

Beltaos, A., Kovačević, A.G., Matković, A., Ralević, U., Savić-Šević, S., Jovanović, Dj, Jelenković, B.M., Gajić, R.: Femtosecond laser induced periodic surface structures on multi-layer graphene. J. Appl. Phys. **116**, 204306 (2014)

Birnbaum, M.: Semiconductor surface damage produced by ruby lasers. J. Appl. Phys. **36**, 3688–3689 (1965)

Bonse, J., Krüger, J.: Pulse number dependence of laser-induced periodic surface structures for femtosecond laser irradiation of silicon. J. Appl. Phys. **108**, 034903 (2010)

Bonse, J., Munz, M., Sturm, H.: Structure formation on the surface of indium phosphide irradiated by femtosecond laser pulses. J. Appl. Phys. **97**, 013538 (2005)

Bonse, J., Rosenfeld, A., Krueger, J.: Implications of transient changes of optical and surface properties of solids during femtosecond laser pulse irradiation to the formation of laser-induced periodic surface structures. Appl. Surf. Sci. **257**, 5420–5423 (2011)

Bonse, J., Krüger, J., Höhm, S., Rosenfeld, A.: Femtosecond laser-induced periodic surface structures. J. Laser Appl. **24**, 042006 (2012)

Bonse, J., Höhm, S., Rosenfeld, A., Krüger, J.: Sub-100-nm laser-induced periodic surface structures upon irradiation of titanium by Ti:sapphire femtosecond laser pulses in air. Appl. Phys. A **110**, 547–551 (2013)

Dostovalov, A.V., Korolkov, V.P., Terentyev, V.S., Okotrub, K.A., Dultsev, F.N., Babin, S.A.: Study of the formation of thermochemical laser-induced periodic surface structures on Cr, Ti, Ni and NiCr films under femtosecond irradiation. Quantum Electron. **47**, 631–637 (2017)

Dostovalov, A.V., Derrien, T.J.-Y., Lizunov, S.A., Přeučil, F., Okotrub, K.A., Mocek, T., Korolkov, V.P., Babin, S.A., Bulgakova, N.M.: LIPSS on thin metallic films: new insights from multiplicity of laser-excited electromagnetic modes and efficiency of metal oxidation. Appl. Surf. Sci. **491**, 650–658 (2019a)

Dostovalov, A.V., Okotrub, K.A., Bronnikov, K.A., Terentyev, V.S., Korolkov, V.P., Babin, S.A.: Influence of femtosecond laser pulse repetition rate on thermochemical laser-induced periodic surface structures formation by focused astigmatic Gaussian beam. Laser Phys. Lett. **16**, 026003 (2019b)

Gakovic, B., Radu, C., Zamfirescu, M., Radak, B., Trtica, M., Petrovic, S., Panjan, P., Zupanic, F., Ristoscu, C., Mihailescu, I.N.: Femtosecond laser modification of multilayered TiAlN/TiN coating. Surf. Coat. Technol. **206**, 411–416 (2011)

Golosov, E.V., Ionin, A.A., Kolobov, Yu.R., Kudryashov, S.I., Ligachev, A.E., Makarov, S.V., Novoselov, Yu.N., Seleznev, L.V., Sinitsyn, D.V., Sharipov, A.R.: Near-threshold femtosecond laser fabrication of one-dimensional subwavelength nanogratings on a graphite surface. Phys. Rev. B **83**, 115426 (2011)

Kautek, W., Rudolph, P., Daminelli, G., Kruger, J.: Physico-chemical aspects of femtosecond-pulse-laser-induced surface nanostructures. Appl. Phys. A **81**, 65–70 (2005)

Kovačević, A.G., Petrović, S.M., Bokić, B.M., Gaković, B.M., Bokorov, M.T., Vasić, B.Z., Gajić, R.B., Trtica, M.S., Jelenković, B.M.: Surface nanopatterning of Al/Ti multilayer thin films and Al single layer by a low-fluence UV femtosecond laser beam. Appl. Surf. Sci. **326**, 91–98 (2015)

Kovačević, A.G., Petrović, S., Lazović, V., Peruško, D., Pantelić, D., Jelenković, B.M.: Inducing subwavelength periodic nanostructures on multilayer NiPd thin film by low-fluence femtosecond laser beam. Appl. Surf. Sci. **417**, 155–159 (2017)

Majchrzak, E., Poteralska, J.: Two-temperature microscale heat transfer model. Part I: determination of electron parameters. Sci. Res. Inst. Math. Comput. Sci. Czestochowa Univ. Technol. **9**, 99–108 (2010a)

Majchrzak, E., Poteralska, J.: Two-temperature microscale heat transfer model Part II: Determination of lattice parameters. Sci. Res. Inst. Math. Comput. Sci. Czestochowa Univ. Technol. **9**, 109–119 (2010b)

Öktem, B., Pavlov, I., Ilday, S., Kalaycıoğlu, H., Rybak, A., Yavaş, S., Erdoğan, M., Ilday, F.Ö.: Nonlinear laser lithography for indefinitely large area nanostructuring with femtosecond pulses. Nat. Photonics **7**, 897 (2013)

Reif, J., Varlamova, O., Costache, F.: Femtosecond laser induced nanostructure formation: self-organization control parameters. Appl. Phys. A **92**, 1019–1024 (2008)

Shinoda, M., Gattass, R.R., Mazur, E.: Femtosecond laser-induced formation of nanometer-width grooves on synthetic single-crystal diamond surfaces. J. Appl. Phys. **105**, 053102 (2009)

Sipe, J.E., Young, J.F., Preston, J.S., van Driel, H.M.: Laser-induced periodic surface structure. I. Theory. Phys. Rev. B **27**, 1141–1154 (1983)

Ursu, I., Mihăilescu, I.N., Prokhorov, A.M., Konov, V.I., Tokarev, V.N.: On the role of the periodical structures induced by powerful laser irradiation of metallic surfaces in the energy coupling process. Phys. B+C **132**, 395–402 (1985)

Van Driel, H.M., Sipe, J.E., Young, J.F.: Laser-induced periodic surface structure on solids: a universal phenomenon. Phys. Rev. Lett. **49**, 1955–1958 (1982)

Varlamova, O., Martens, C., Ratzke, M., Reif, J.: Genesis of femtosecond-induced nanostructures on solid surfaces. Appl. Opt. **53**, I10–I15 (2014)

Von der Linde, D., Sokolowski-Tinten, K., Bialkowski, J.: Laser–solid interaction in the femtosecond time regime. Appl. Surf. Sci. **109–110**, 1 (1997)

Vorobyev, A.Y., Guo, C.: Femtosecond laser-induced periodic surface structure formation on tungsten. J. Appl. Phys. **104**, 063523 (2008)

Vorobyev, A.V., Guo, C.: Direct femtosecond laser surface nano/microstructuring and its applications. Laser Photonics Rev. **7**, 385–407 (2013)

Vorobyev, A.Y., Makin, V.S.: Periodic ordering of random surface nanostructures induced by femtosecond laser pulses on metals. J. Appl. Phys. **101**, 034903 (2007)

Wang, J., Guo, C.: Ultrafast dynamics of femtosecond laser-induced periodic surface pattern formation on metals. Appl. Phys. Lett. **87**, 251914 (2005)

Young, J.F., Sipe, J.E., van Driel, H.M.: Laser-induced periodic surface structure. III. Fluence regimes, the role of feedback, and details of the induced topography in germanium. Phys. Rev. B **30**, 2001–2015 (1984)

Selected transport, vibrational, and mechanical properties of low-dimensional systems under strain 🅕

V. Celebonovic 🆔, J. Pesic 🆔, R. Gajic, B. Vasic, and A. Matkovic 🆔

COLLECTIONS

🅕   This paper was selected as Featured

View Online   Export Citation   CrossMark

ARTICLES YOU MAY BE INTERESTED IN

Selected transport, vibrational, and mechanical properties of low-dimensional systems under strain

View Online   Export Citation   CrossMark

V. Celebonovic,[1,a] J. Pesic,[2] R. Gajic,[2] B. Vasic,[2] and A. Matkovic[2,3]

AFFILIATIONS

[1]LEX Laboratory, Institute of Physics, University of Belgrade, Pregrevica 118, 11080 Belgrade, Serbia
[2]Graphene Laboratory, Center for Solid State Physics and New Materials, Institute of Physics, University of Belgrade, Pregrevica 118, 11080 Belgrade, Serbia
[3]Institute of Physics, Montanuniversität Leoben, Franz Josef Strasse 18, Leoben 8700, Austria

[a]vladan@ipb.ac.rs

ABSTRACT

The aim of the present paper is to discuss some recent results concerning the behavior of low-dimensional materials under strain. This concerns the electrical conductivity calculations of 1D structures under strain, within the Hubbard model, as well as *ab initio* investigations of phonon, electron-phonon, and superconducting properties of doped graphene and MgB_2 monolayer. Two different experimental approaches to strain engineering in graphene have been considered regarding local strain engineering on monolayer flakes of graphene using atomic force microscopy and dynamic plowing lithography technique as well as the effects of mechanical straining on liquid phase exfoliated graphene and change of sheet resistance of graphene films.

I. INTRODUCTION

Strain engineering is widely used in materials science to tune various properties of materials and eventually enhance the performance of devices. Engineering of strain in low-dimensional materials promises to revolutionize the field of nanotechnology with the possibility of creating new artificial materials. Two-dimensional materials are a remarkable ground to study the influence of strain, as they can sustain very large deformations without breaking. The unique mechanical properties of graphene present an excellent opportunity for research of strain-induced modifications; for example, graphene is the strongest 2D material ever measured, with Young's modulus of 1 TPa and an intrinsic strength of 130 GPa.[1] What is more important is its ability to sustain reversible elastic tensile strain as large as 25%[1] and this allows the possibility for strain engineering in order to modify or tune graphene properties for specific applications. Since its discovery in 2004 with the size of a micrometer,[2] graphene has attracted increased attention. It is a truly two-dimensional (2D) plane of sp2-hybridized carbon atoms arranged in a honeycomb lattice. The unit cell has two identical

carbon atoms giving rise to electronic linear dispersion near the Fermi level and peculiar massless electron dynamics governed by the Dirac–Weyl relativistic equations.[3,4] This unique lattice of graphene leads to many extraordinary properties that include exceptionally high charge carrier mobility,[2,3] high mechanical strength and elasticity,[1,5] optical transparency,[6,7] and a wide variety of possible chemical modifications.[8–10] All of these properties make graphene an ideal material to investigate not only fundamental scientific problems in condensed matter physics, but also practically a wide variety of applications including flexible electronics,[11–14] optoelectronics,[15,16] sensors, and transistors.[17,18] The outstanding stretchability of graphene has made it suitable for application in flexible electronic devices as well as in superconducting electronics based on 2D materials since the electron-phonon (e-ph) coupling is greatly enhanced by the biaxial strain causing the change of superconducting critical temperatures.[19–23]

In this paper, we study and discuss selected transport, vibrational, and mechanical properties of low-dimensional systems under strain with the main focus on strain-induced changes on

conductivity. In Sec. II, we present theoretical approaches for strain engineering in low-dimensional systems. Section II A discusses the effects of the application of strain on conductivity studied in the one-dimensional Hubbard model. Section II B presents the *ab initio* study of the effects of the biaxial strain on doped graphene and isostructural new material MgB_2 monolayer, namely, both materials are considered superconducting,[24–26] and here it is demonstrated that biaxial strain can cause softening of the phonons, affecting the total electron-phonon interaction and resulting in a significantly higher critical transition temperature. These two-dimensional materials not only share a similar structure, a hexagonal structure with an adatom in the center of a hexagon, but also have a similar electronic structure, and very interestingly, both are electron-phonon mediated superconductors.[1,34–39] Engineering of strain in those materials opens the road to new artificial structures with the improved electron-phonon coupling and higher critical temperatures.

Application of the strain in graphene and 2D materials is an intensively studied topic, both theoretically and experimentally;[1,40,41] for example, application of the strain on graphene can induce changes in the vibrational properties,[42,43] in the electronic bandgaps[44,45] and significant changes in conductivity at both local and macroscopic levels.[46–48] The type of the strain is a very important feature, since the graphene lattice symmetry determines its band structure. The breaking of the hexagonal symmetry will modify the band structure of graphene,[49,50] causing the opening of the bandgap and many other effects.[51,52]

In intercalated graphene, it is known that not all types of intercalant atoms produce superconductivity or significantly increase T_c. In Li-intercalated graphene (Li-GIC), a strong confinement for electrons along the z-axis exists and it prevents the occupation of the interlayer state. In the monolayer,[24,35] there is a significant reduction of a charge transfer that is beneficial for superconductivity. The charge transfer from the interlayer state formed by the presence of the adatom is a crucial ingredient. Though it is necessary, the completion of the charge transfer is deleterious for the enhancement of the superconductivity.[24,35] For example, in the Li-GIC, a strong confinement along the z-axis exists and it prevents the occupation of the interlayer state. When the quantum confinement is removed as in the monolayer, it results in the reduction of charge transfer which is beneficial for the superconductivity. In Sec. III, we discuss the effects of strain, as shown above, on the most prominent example of low-dimensional materials, graphene.

We present two different experimental approaches to strain engineering in graphene. In Sec. III A, we discuss local strain engineering on monolayer flakes of graphene produced by micromechanical exfoliation using atomic force microscopy (AFM) and dynamic plowing lithography (DPL). In Sec. III B, we present the effects of mechanical straining on the liquid phase exfoliated graphene and the change of sheet resistance graphene films obtained in that way. These two techniques are diametrically different, both in results and in the procedure. Micromechanical exfoliation is a clean technique where high-quality, well-defined monolayer samples are produced using the Scotch tape method.[1] However, samples produced this way though very pure, ideal monolayer without vacancies, are small in scale (maximally, hundreds of micrometers), making this technique excellent for state-of-the-art nanodevices and fundamental research. Nonetheless, for applications, especially macroscopic ones, this kind of production technique is not applicable. Liquid phase exfoliation (LPE) is an alternative where solution processing of graphite flakes breaks van der Waals forces creating liquid graphene dispersion. Samples produced from this dispersion can be very large in scale, macroscopic; however, they are not monolayers, but few-layer graphene flakes overlap in between forming graphene films.[27,28] We study how strain can be engineered in both samples, where in the first experimental section we focus more on a fine technique for the induction of the local strain in monolayer samples, and in the second one, where strain can be induced and engineered in a much more simple way (since we can work with macroscopic samples), the spotlight is on the effect of the strain quality of the film and eventually on sheet resistance, hence conductivity. Straining the monolayer graphene sample shows that a high enough local pressure induced by an AFM tip will result in protrusion at a neighboring point. The generated local strain introduced in this way is well controlled, and it is expected to affect conductivity along protrusion. The other presented case, the sample of which is produced in LPE, shows the change of resistivity with the application of strain, as it is presented that this is not the intrinsic strain of single graphene flakes but is more of a macroscopic effect. The small flakes that the film consists of are deposited onto the elastic substrate, and when mechanical strain is applied, the substrate surface stretches but individual flakes do not get strained. The total resistance of LPE films comes from the points of the overlap between neighboring flakes, and stretching the LPE graphene film results in effective pulling apart of individual flakes, and thus an increase in the sheet resistivity of the whole film (and vice versa).

II. THEORY

A. Effects of strain on the conductivity in 1D system— The Hubbard model study

Toward the middle of the last century, the metal to insulator transition was one of the outstanding problems of condensed matter physics. A general model of the metal to insulator transition was proposed by John Hubbard, in a series of papers starting from Ref. 29. Apart from the metal to insulator transition, the Hubbard model has found applications in studies of transport processes in 1D and 2D correlated electron systems. These calculations have often been performed using the memory function method. A detailed review is available in Ref. 30, while the main results are given in the following.

The initial point for a study of the transport properties of any system is the knowledge of its Hamiltonian. Using the second quantization formalism, the Hamiltonian of the 1D Hubbard model has the following form:

$$H = -t \sum_{i=1,\sigma}^{N} (c_{i+1,\sigma}^{+} c_{i,\sigma} + c_{i,\sigma}^{+} c_{i+1,\sigma}) + U \sum_{l} n_{l,\uparrow} n_{l,\downarrow}. \quad (1)$$

The symbols N, t, and U denote the number of nodes in a lattice, the mean kinetic energy of the electrons (the so-called hopping

energy), and the interaction energy of pairs of electrons with opposing spins on the same lattice node; σ stands for the electron spin. The symbols in the parenthesis denote the creation and annihilation operators.

Calculations of the electrical conductivity have been performed using the memory function method.[30] These basic expressions are

$$\chi_{AB} = \ll A; B \gg = -i \int_0^\infty e^{izt} < [A(t), B(0)] > dt, \quad (2)$$

$$\sigma(\omega) = i \frac{\omega_p^2}{4\pi z} \times \left[1 - \frac{\chi(z)}{\chi(0)} \right]. \quad (3)$$

The symbol $\omega_p^2 = \frac{4\pi n_e e^2}{m_e}$ denotes the square of the plasma frequency

and $\chi_0 = \frac{n_e}{m_e}$ is the zero frequency limit of the dynamical susceptibility.

Expression (2) is the general definition of the linear response of a physical quantity corresponding to operator A to the perturbation by another physical quantity described by operator B. $A(t)$ denotes the Heisenberg representation of operator A. Inserting $A = B = [j, H]$, with j denoting the current operator and H the Hamiltonian, leads to the definition of the current-current correlation function. Details of the calculation of the electrical conductivity are presented in Ref. 30. The final result is

$$\sigma_R(\omega_0) = \left(\frac{1}{2\chi_0} \right) \left(\frac{\omega_p^2}{\pi} \right) \frac{1}{\omega_0^2 - (bt)^2} \left(\frac{Ut}{N^2} \right)^2 \times S, \quad (4)$$

where S denotes the following function:

$$S = \frac{42.49916}{(1 + \exp[\beta(-\mu - 2t)])^2} + \frac{78.2557}{(1 + \exp[\beta(-\mu + 2t)\cos(1 + \pi)])^2} + \frac{bt}{\omega_0 + bt} \left[\frac{4.53316}{(1 + \exp[\beta(-\mu - 2t)])^2} + \frac{24.6448}{(1 + \exp[\beta(-\mu + 2t)\cos(1 + \pi)])^2} \right]. \quad (5)$$

The symbol μ denotes the chemical potential of the electron gas on a 1D lattice, given by the following (Ref. 30 and references therein):

$$\mu = \frac{(\beta t)^6 (ns - 1)|t|}{1.1029 + 0.1694(\beta t)^2 + 0.0654(\beta t)^4}. \quad (6)$$

The practical calculation of the conductivity: Inserting values of material parameters into Eqs. (4)–(6) leads to the electrical conductivity expressed as a function of these parameters. Some examples of such calculations have been discussed in Refs. 32–35 and references therein.

As this paper focuses on nanomaterials under strain, this section considers the problem of treating the material under strain within the Hubbard model. This problem is not only of academic, but also of practical, interest. There already exist examples of stretchable electronics (some examples are given in Refs. 31 and 33). By changing an initial material length from l_0 to l, the strain is defined as

$$\varepsilon = \frac{l - l_0}{l_0}. \quad (7)$$

If a material is subdued to nonzero strain, the overlap between wave functions of electronic wave functions in adjacent atoms changes, leading to changes in the hopping energy and all material parameters which contain the lattice constant. The dependence of the hopping on the interatomic distance is represented by[31]

$$t = t_0 \times \left[1 + r + \frac{1}{3} r^2 \right] \exp[-r], \quad (8)$$

where the distance is expressed in Bohr radii.

All expressions used in the calculations discussed in this section are analytically tractable but too long to be explicitly stated here. Therefore, only a few resulting graphs are presented (Fig. 1).

Figure 1 shows the electrical conductivity of a 1D Hubbard model expressed as a function of the strain to which it is exposed. The data are normalized to 1 at $n = 1.25$, $t = 0.01$, $T = 116$, $\varepsilon = 0$.
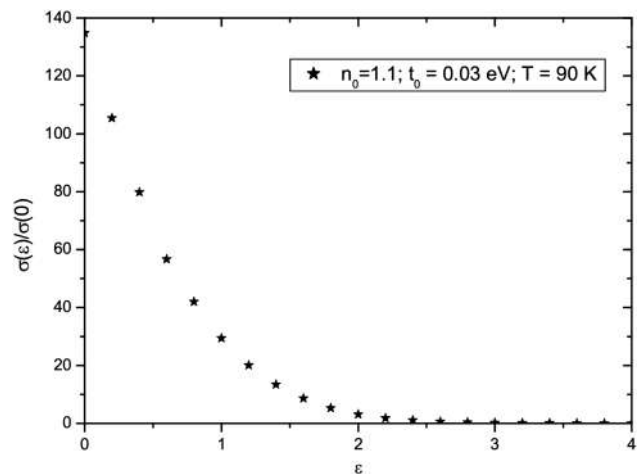

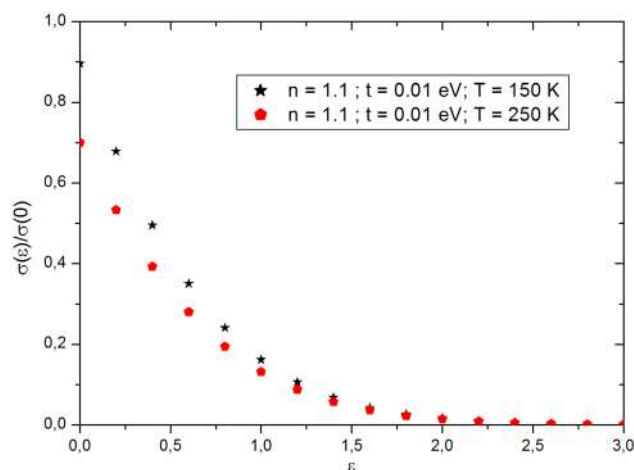**FIG. 1.** Normalized conductivity of 1D HM as a function of strain.

FIG. 2. Normalized conductivity for $T = 150$ K and $T = 250$ K.

Figure 2 taken from Ref. 31 shows the behavior of the conductivity for two values of the temperature T. It could be objected here that extending the value of the strain up to $\varepsilon = 3$ in Fig. 2 is unphysical, as no real material can withstand such a large value of strain. Indeed, this should be understood just as a mathematical extension. The values of various constants needed for the calculation leading to Fig. 2 are given in Ref. 31.

Figure 3 shows the normalized conductivity for a fixed value of the strain, $\varepsilon = 0.05$, and the band filling factor, $n = 0.9$. The conductivity is normalized to 1 at $T = 116$ K, $n = 1.25$.

Note that there is a big difference in the behavior of curves presented in Figs. 2 and 3. The curve in Fig. 3 changes sign at a certain point (at $T \cong 100 - 110 K$).
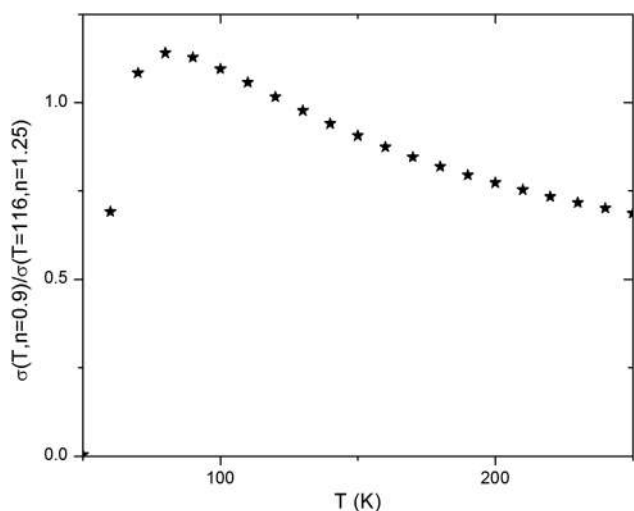

FIG. 3. Normalized conductivity for strain 0.05.

This result has considerable theoretical importance. Namely, practical attempts in applications of stretchable and flexible electronics may require such changes of material characteristics for different sets of material parameters. Therefore, results presented here, and some more which are forthcoming, can contribute to the development of various applications.

B. Strain effects on vibrational properties in 2D structures—*Ab initio* calculations

In this section, we study the effect of strain on vibrational properties and electron-phonon coupling in two-dimensional materials. The low-dimensional materials are characterized by strong covalent in-plane bonds and weak interlayer van der Waals interactions which give them a layered structure. An application of homogenous strain in bulk materials would be practically impossible outside of the theoretical discussion, and in low-dimensional material, it is rather simple.

Based on this concept, we present computational study within the density functional theory framework of the effects of the (equi)biaxial strain on the two isostructural two-dimensional materials, Li-intercalated graphene and magnesium-diboride monolayer. We used Quantum Espresso software package[53] with both local-density approximation (LDA) and generalized gradient approximation (GGA) Perdew-Burke-Ernzerhof (PBE) functionals and vibrational properties and the electron-phonon interaction is calculated using density functional perturbation theory implemented in this software package.

Here, it is shown that tensile biaxial strain causes softening of the phonons, affecting the total electron-phonon interaction and resulting in significantly a higher critical temperature. In particular, in Li-doped graphene, the in-plane phonons will be dramatically softened, whereas the out-of-plane ones will be less affected.[52] By application of strain, we achieve the increase of the density of states at the Fermi level and softening of the modes.[54,55] Without drastically modifying the structure, this results in great effects on the electron-phonon coupling constant.[55,56] In principle, both these effects can be achieved rather easily in low-dimensional systems.

In order to strain the LiC_6-mono and increase the lattice constant, the in-plane distance between C atoms is increased leaving the hexagonal symmetry unaffected. The Li adatom is placed above the H site in graphene (the center of a hexagon). The modification of the lattice constant does not interfere with the Li adatom position which remains fixed in the center of the hexagon, leaving the symmetry unbroken. Due to the expansion of the carbon atom distances and the invariance of the hexagonal symmetry the Li adatom shifts only along the z-axis. The change in the distance between the carbon plane and the Li adatom is presented in Table I. The obtained results are in agreement with other similar studies and experimental results.[24,36,54]

The effects of several values of the strain, which increase the lattice constant by 3%, 5%, 7%, and 10%, are studied. Larger strains are not applied due to the instabilities that occur after the attempt of geometrical optimization and relaxation.[57] The distance between the Li adatom and graphene decreases with the strain, as the Li adatom moves down deeper toward graphene. When the strain is applied, the distance between neighboring C atoms increases and the graphene pi bonds repulse the Li adatom less, which then

TABLE I. Changes of bond lengths in Li-doped graphene with application on tensile equibiaxial strain.

Strain %	Distance between Li adatom and carbon layer (Å)	Carbon-carbon bond length (Å)
0	1.80	1.42
3	1.69	1.46
5	1.64	1.49
7	1.61	1.52
10	1.54	1.57

moves down along the z-axis. The small shift of the Fermi level is observed with the strain.

In the phonon dispersion spectrum of doped graphene, the three regions can be distinguished: the adatom-related modes are associated with low-energy regions (0–400 cm^{-1}), where 300–400 cm^{-1} are Li modes mixed with the out-of-plane carbon modes (C_z), the midregion (400–900 cm^{-1}) can be associated with C_z modes and the high-energy region with carbon-carbon stretching modes.[1]

The main contributions to lambda come from the low-energy lithium modes and the carbon vibrations along the z-axis, with an additional contribution from the C-C stretching modes (in agreement with Refs. 24 and 35). When strain is applied, significant softening of phonons occurs, as shown in Fig. 4. In green color, phonon dispersion is depicted for the 3% strained LiC$_6$-mono and in red for 10%. The softening of the high-energy C-C stretching modes is strongly present with a larger strain. In addition, the consequent increase of the phonon DOS in the low-energy region occurs as well. Although the low-energy modes slightly move upwards in energy, the main effect on the electron-phonon coupling is the softening of graphene high-energy C-C stretching modes.

At the same time, with stretching of C-C bonds, another structural change occurs. For the small strain, the Li adatom drops

down toward the center of a hexagon and its orbitals overlap more with the carbon π orbitals. That causes an increase in charge transfer and emptying of the interlayer band, which reduces λ. When more strain is applied, the carbon bonds are elongated and the π orbitals move away, both from each other and the center of the hexagon. The orbital overlap is reduced, and after the certain critical value, λ increases, following the strain. Figure 5 presents the effects of the different strain on electronic localization function (ELF).

The significant changes for the large strain are presented, depicting the above-described effects. For ELF at 10% of the strain, the electron localization region is greatly lowered as graphene and adatom separate one from another and as a C-C bond are elongated. The critical temperature is enhanced with straining of structure, up to $T_c = 29$ K where the electron-phonon coupling constant is 0.73.[54] It is important to stress that this increase in T_c, achieved by the described mechanism, can be experimentally realized. A pristine graphene is experimentally confirmed to be elastically stretchable up to 25%[1] making here considered strains feasible.

Following structural and electronic similarity we explored the effect of the biaxial strain on the MgB$_2$ monolayer.[25] As in graphene the application of the biaxial strain leaves the symmetry of the system unchanged, yet a tensile (compressive) strain moves boron atoms further (closer) from (to) each other in the same proximity, allowing the Mg atom to move along the z-axis. This causes a change in the charge transfer from the magnesium atoms to the boron plane increasing (decreasing) DOS on the Fermi level. The other effects concern the softening (hardening) of modes of the boron atoms due to an elongation (compression) of the B-B bonds.

We compare phonon dispersion for nonstained MgB$_2$-mono with compressively and tensely strained ones (Fig. 6). Significant softening (hardening) of high-energy modes is present with elongation (compression) of bonds between boron atoms, following the general trend for phonons, as distances between atoms increase, the interatomic bonds become less stiff, resulting in a decrease
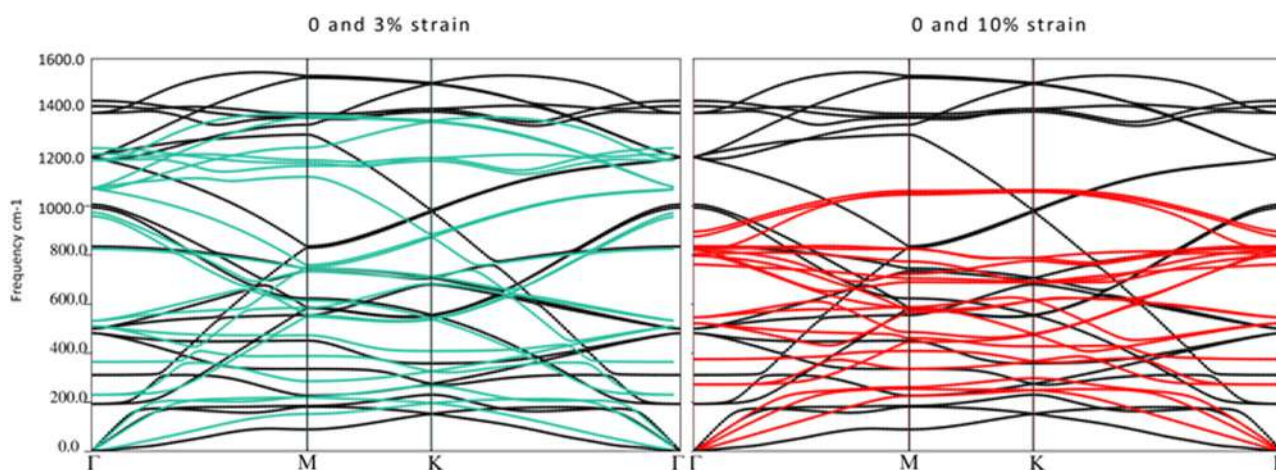
FIG. 4. Phonon dispersion for the LiC$_6$-mono; black lines are for the nonstrained LiC$_6$-mono, and green and red for the 3% and 10% tensile biaxial strain, respectively.
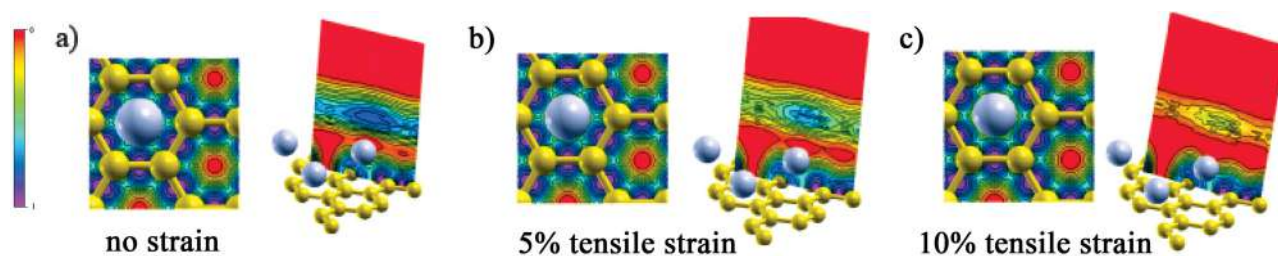
FIG. 5. ELF (electron localization function) for the LiC_6-mono without (a) and with strain [5% (b) and 10% (c)] (first image in pair ELF on the xy direction, second, ELF on the xz direction).

of phonon frequencies (and vice versa). In electron-phonon coupling strongest contribution to coupling comes from E_2 optical mode.[37,38]

In Fig. 6, a significant shift of E_2 mode is visible, it changes frequency for almost $100\,cm^{-1}$ with the application of strain. However straining of structure results same as in graphene, not only in a variation of B-B bonds occurs but as well position of Mg adatom above the center of boron hexagon changes. As the distance between B atoms increases (i.e., for tensile strain) Coulomb repulsion is reduced allowing Mg atom to sink deeper towards the center of the hexagon. For compression opposite situation occurs. The repulsion is stronger and the Mg atom gets more remote. This has an effect on charge transfer from Mg to B layer.

To investigate this we study electron localization function (ELF). It is noticeable that straining not only affects ELF in the B layer but as well on the Mg layer. For both compressive and tensile strain in the Mg layer, ELF becomes denser than in the non-strained case. Due to the closing of B atoms in hexagon ELF increases B plane increases for compression (and vice versa) (Fig. 7). As in LiC_6 mono application of the biaxial strain dramatically increases critical temperature, more than 30 K.[25,26]
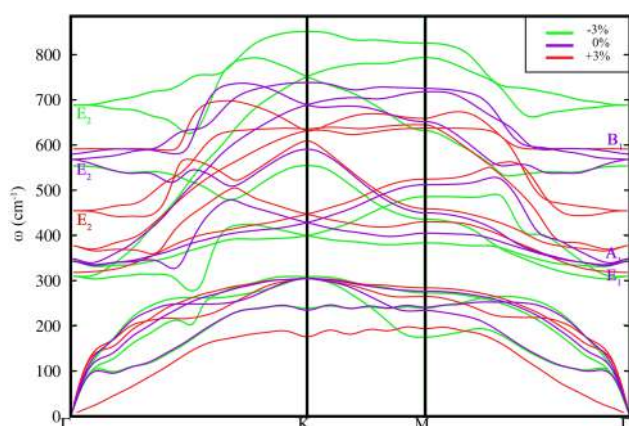
The question of the reduction of dimensionality of superconducting materials to its limit, a truly atomic-scale 2D system and the consequence of this[57–62] are highly relevant not only to fundamental science but to nanotechnology and it will be crucial for the production of superconducting devices in future. Engineering of strain in such systems could lead to significant improvements in their superconducting properties and pave the way toward new applications.

III. EXPERIMENT

A. Local strain engineering of graphene by atomic force microscopy

A typical way to introduce a local strain into graphene is its transfer on a prepatterned substrate, containing, for example, arrays of nanopillars.[63] Atomic force microscopy (AFM) based lithography offers additional possibilities for graphene reshaping and patterning at the nanoscale. The typical curvature radius of AFM tips is around 5–10 nm making them appropriate for the fabrication of various graphene nanostructures, based on either AFM scratching[64] or AFM based local anodic oxidation.[64–66] In a similar way, a local strain can be introduced into the graphene lattice by applying a local pressure from AFM tips without graphene tearing.[67,68]

Our approach to generating a local strain in graphene is based on the AFM dynamic plowing lithography (DPL),[68] employing the so-called tapping AFM mode. In this mode, the AFM cantilever oscillates above a sample during scanning. The amplitude of the cantilever oscillations, represented by the amplitude set-point, is kept constant during scanning in the tapping mode. In order to hold constant the interaction between the AFM tip and the sample, the AFM scanner together with the sample moves up and down, in the z-direction according to the sample topography. Then, the scanner movement in the z-direction is proportional to the sample topography. On the other hand, during DPL, it is necessary to increase the mechanical interaction between the AFM tip and the considered sample in order to induce local changes in morphology. For this purpose, in order to increase a tip-sample interaction needed for graphene deformation, the free oscillation amplitude of the employed AFM cantilevers is first increased by around 10 times. The tip-sample interaction, controlled by the amplitude set-point in the tapping AFM mode, is then additionaly increased by decreasing the set-point by 10–100 times compared to ordinary
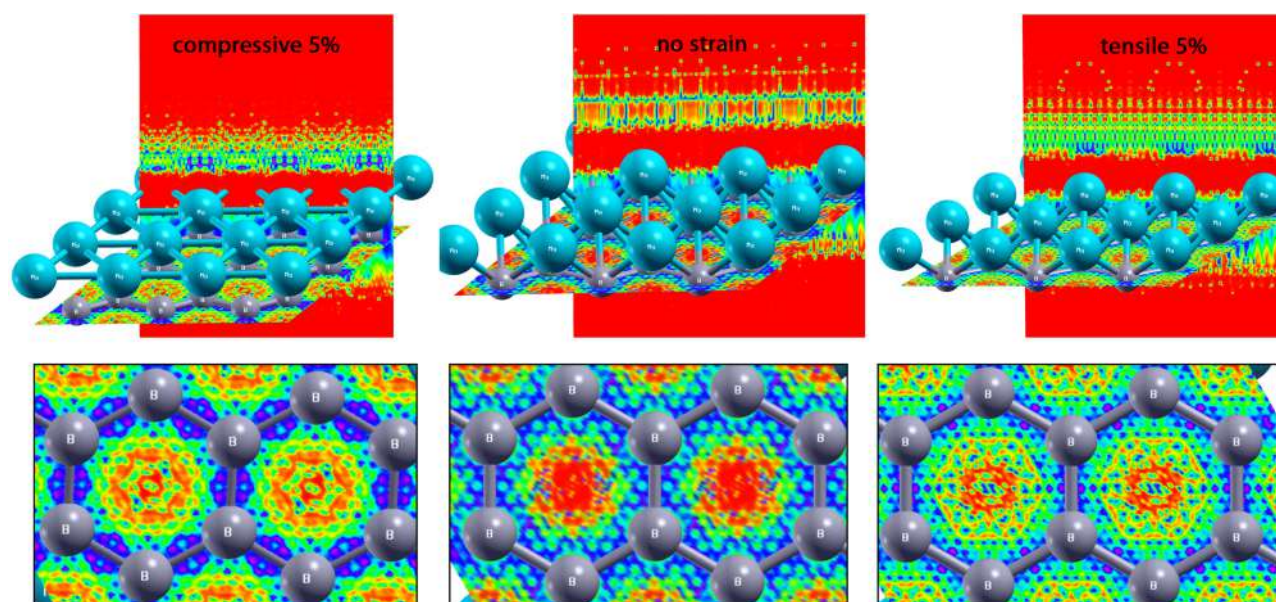

FIG. 6. Comparison of phonon dispersion for nonstrained MgB_2 (violet) and compressively (green) and tensely (red) strained (for 3% each).

FIG. 7. Electron localization function (ELF) for MgB$_2$-mono nonstrained and compressively (left) and tensely (right) strained. Top: 3D projection of ELF with focus on the Mg layer. Bottom: ELF projection on the B layer.

AFM imaging. Benefits of using DPL instead of more traditional AFM scratching lithography stem from the fact that the AFM cantilever is vibrating and not in continuous contact with a sample surface, as in the case of the static plowing (AFM based scratching lithography) employed using the AFM contact mode. As a result, the lateral and friction forces between the AFM tip and the sample surface are minimized, so there is no undesirable dragging, pushing, and pulling of graphene sheet during DPL. At the same time, the AFM cantilever during DPL is free from a torsion caused by lateral forces, which facilitates the fabrication of nanostructures with well-defined edges. AFM imaging and DPL were done using the NTEGRA Prima measuring system, manufactured by NT-MDT (www.ntmdt-si.com). Since the lithography is based on the mechanical tip-sample interaction, we used robust and wear resistive diamond coated DCP20 probes from NT-MDT.

The selected nanostructures fabricated by DPL of graphene are presented in Fig. 8. All graphene samples were made by the standard mechanical exfoliation onto the Si/SiO$_2$ substrate. The local strain in graphene can be generated along straight and curved trenches as depicted in Figs. 8(a) and 8(b), respectively, whereas more complex structures can be made by overlapping basic patterns, as presented in Fig. 8(c). DPL can be also used for the fabrication of point-like deformations of graphene, as shown in Fig. 8(d). These deformations were made by local amplitude-distance curves in the tapping mode, with an increased free oscillation amplitude of the employed AFM cantilever and with decreased set-point in order to increase the tip-sample interaction. During the measurement of the amplitude-distance curves, there is no lateral movement and scanning, just a vertical movement of the AFM scanner holding a sample, which finally gives point-like local strain in graphene.

Common for all fabricated nanostructures is a smooth surface without bumps, protrusions, or cuts, implying that the graphene together with the underlying silicon-dioxide substrate is just locally deformed and strained. The only exception is presented in Fig. 8(c) where a small bump appeared parallel and next to the graphene trench. This example shows that for a high enough local pressure,
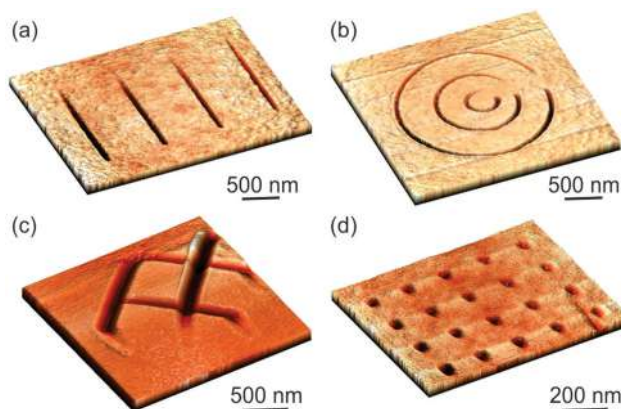

FIG. 8. Local strain in graphene nanostructures generated by DPL: (a) straight (z-height 3 nm) and (b) curved trenches (z-height 7 nm), (c) a more complicated pattern obtained by crossing straight trenches (z-height is 11 nm), and (d) point-like local deformation made by DPL during the measurement of amplitude-distance curves in the tapping AFM mode (z-height is 3.5 nm).

the sample compression at one point inevitably results in a protrusion at an adjacent point.

The local strain generated in graphene sheet in percent can be estimated according to the formula $(L - L_0)/L_0 \times 100\%$,[68] where L_0 and L are the lengths of graphene segments before and after the deformation by DPL, respectively. Therefore, L_0 and L can be then considered as the graphene trench width and perimeter, respectively, and the values of which can be approximately calculated from measured AFM topographic images (the perimeter can be calculated from the measured trench width and perimeter). For the typical trench widths and depths of around 50–100 nm and several nanometers, respectively, the generated local strain in graphene is in the order of 0.1%. The trench width is dominantly determined by the AFM probe width. In the considered case, since we employed DCP20 probes with a rather large tip radius curvature of 50–70 nm, probably it would not be possible to make narrower trenches. Produced trenches in graphene could be an excellent platform in order to study local changes in graphene conductivity due to strain.[87,88]

B. Axial strain in liquid phase exfoliated graphene films

Many potential applications of graphene and other 2D materials[27,69,70] rely on continuous films, either polycrystalline or single crystals. Chemical vapor deposition (CVD) techniques are commonly the fabrication methods of choice when large area graphene is considered.[71–73] However, CVD based films require a transfer from a catalyst on which these are grown onto a targeted substrate for their application. Usually, this step introduces many undesired features in the films, such as cracks, wrinkles, and transfer residues, and hinders intrinsic properties of graphene.[74,75]

A low-cost alternative to large area CVD graphene films is based on solution processing of either graphene oxide or graphite flakes.[28,74–80] In particular, LPE using solvers that do not covalently bond with graphene sheets can result with graphene-based films that are very promising for many applications—as strain gauges— where coatings are needed on an industrial scale.[81] Since these coatings are made out of many overlapping small (100 nm–10 μm) single-crystal sheets of graphene or multilayer graphene, their response to strain is rather different from the case of continuous films. Understanding the strain mechanisms in these complex nanoscaled systems is crucial for their future applications. In this section, we demonstrate how axial strain of the flexible support affects the electrical properties of LPE graphene films, and similar mechanisms are to be expected for the coatings and films of other 2D materials, fabricated via solution processes.

LPE graphene films were prepared following the route described in Ref. 28. 500 μm mesh high purity and high crystallinity graphite powder was dispersed in N-methylpyrrolidone (15–20 mg/ml), sonicated in a low-power ultrasonic bath for 14 h, and finally centrifuged at 300 rpm. The top part of the resulting solution (with 0.3–0.4 mg/ml graphene concentration) was drop casted on the water surface, and the film formed on a water-air interface was transferred to substrates by the Langmuir–Blodgett technique. Figure 9(a) shows an AFM topography of the film's edge deposited on a SiO₂/Si substrate. The film thickness was estimated from the AFM cross-sections [as presented in Fig. 9(b)]), giving (4.0 ± 1.5) nm thick films (including also batch-to-batch variations). Typical Raman spectra of the deposited LPE graphene films on a SiO₂/Si substrate are presented in Fig. 9(c), for comparison also showing the spectra obtained from the starting graphite powder (measured within a single graphite flake). Raman spectra were obtained using a TriVista 557S&I GmbH spectrometer $(\lambda = 532 \text{ nm})$ under ambient conditions. Intensity ratios of Raman active modes can be used to estimate the quality of the film and to point out the types of defects.[82–85] For the samples used in this study, the I(D)/I(G) ratio was found to be (0.6 ± 0.1). In particular, the I(D)/I(D') ratio of (2.8 ± 0.4) was observed, indicating that mainly it is the edges of the flakes that contribute to D mode intensity observed in the spectra.[82]

In order to examine the influence of the uniaxial strain on the electrical conductivity of these LPE graphenes—in the same manner as described above—the films were deposited onto flexible polyethylene terephthalate (PET) foils. Figure 10 gives an example of how LPE graphene films commonly respond to axial strain.
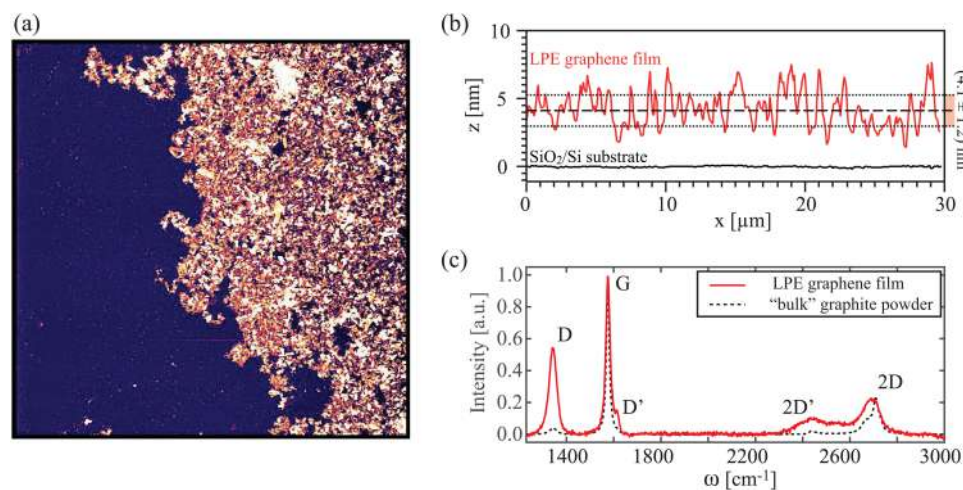

FIG. 9. $50 \times 50 \ \mu m^2$ (z scale 10 nm) of a LPE graphene film edge, deposited on a SiO₂/Si substrate. (b) shows 30 μm long height profiles on the film and on the substrate, averaging 10 μm in width. (c) Raman spectra of the LPE graphene film (solid line) compared with the starting graphite powder (dashed line). Most relevant modes of graphene/graphite are labeled. Spectra are normalized to I(G) = 1.
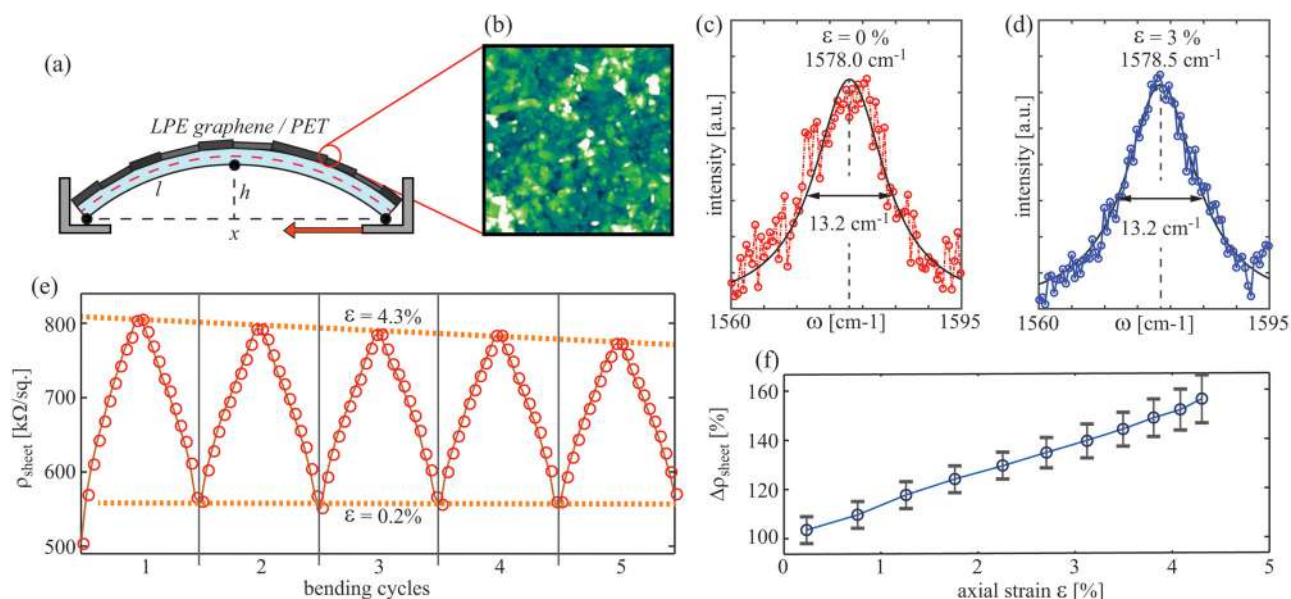
FIG. 10. (a) Scheme of the setup used for stretching of LPE graphene films. (b) Typical surface morphology of the films ($5 \times 5\,\mu m^2$, z scale 40 nm). (c) and (d) Normalized Raman spectra of graphene's G mode without strain, and with 3% of axial strain, respectively. (e) Sheet resistance as a function of alternating axial strain between 0.2% and 4.3%, showing five subsequent bending cycles. (f) Relative sheet resistance (with respect to nominal values) as a function of axial strain, averaged over several LPE films used in this study.

The film was exposed to uniaxial stretching through bending of the PET support, as schematically presented in Fig. 9(a). For this purpose, a micrometer screw was used and controlled by an integrated step motor with the precision down to $10\,\mu m$, thus allowing a precise control over the distance between the two fixed points of the PET support. Axial strain that the LPE graphene film exhibits in such a case depends on the bending curvature of the PET support (expressed through geometrical parameters x, l, and d) and the thickness of PET $(200 \pm 20)\,\mu m$. The structure of the film was investigated using atomic force microscopy [Fig. 9(b)], showing how many small flakes overlap into a continuously conducting film.

A clear fingerprint of stretching the hexagonal lattice of graphene can be obtained from Raman spectroscopy.[82–85] However, in the presented case when many small flakes are deposited onto the PET substrate, the substrate surface stretches but individual flakes are not strained. This can be clearly seen from the lack of both the shift and broadening of graphene's characteristic Raman active mode at $\sim 1580\,cm^{-1}$ (G mode).[82–85] By measuring Raman spectra of graphene on PET, while bending the support, effective axial strain was introduced up to $\sim 3\%$. Higher values of axial strain during Raman spectroscopy measurements were not possible to reach with a particular setup used in this study. Figures 10(c) and 10(d) show examples of the G mode without and upon 3% of axial strain. The presented spectra have been renormalized, and the spectra of clean PET have been deduced. The G mode was fitted by a single Lorentzian function [solid lines in Figs. 10(c) and 10(d)]. No significant shift (above local variations on the sample) or any

trend of either the mode frequency, intensity, or width was detected within the applied stretching range.

Although individual flakes were not exposed to axial strain in the bending experiments, sheet resistivity of the entire film exhibits a strong dependence on axial strain. Since the main contribution to the total resistance of LPE films comes from the points of overlap between neighboring flakes,[28] stretching the LPE graphene film results in effective pulling apart of individual flakes, and thus an increase in the sheet resistivity of the whole film. Figure 10(e) presents five repeated cycles of stretching and relaxing of the LPE graphene film on PET.

Maximal axial strain applied to the films in the case presented in Fig. 10(e) was estimated to be $\sim 4.3\%$. Figure 10(f) shows the dependence of relative sheet resistance increase (with respect to the unstrained value) of the LPE graphene film as a function of axial strain (ϵ). The data were obtained by measuring in a two-point probe configuration by considering several films, with the length of the films varying between 10 mm and 20 mm. The width of the films was fixed to 10 mm. Contact resistance was determined by varying the length of the films and found to be negligible, commonly being over two orders of magnitude smaller than the resistance of LPE graphene films. A strong increase of sheet resistivity was observed upon stretching of the films, increasing linearly by $\sim 10\%$ for 1% of axial strain. These values are much larger than in the case of CVD graphene,[11] as expected, since the mechanism behind the change in sheet resistance is fundamentally different. Such a large change of resistance upon bending, with the opportunity to further optimize the fabrication, opens up many possibilities

to use LPE graphene films in sensing applications such as strain gauges, pressure sensors, e-skin, and touch screens.[86]

IV. CONCLUSION

As we have outlined, strain engineering has an unprecedented ability to manipulate the plethora of properties of low-dimensional materials. Design of new materials with desired features, engineered through the introduction of mechanical deformations, could lead to the production of novel devices and the low-dimensional materials offering a great possibility for manipulation and engineering, especially with techniques that are not available in bulk materials. As demonstrated in this paper, conductivity can be strongly modified with strain. We have shown how electrical conductivity can be tuned with the application of strain in one-dimensional systems. For two-dimensional materials, we demonstrated a significant effect of the biaxial strain on phonons and its drastic modification of superconducting coupling in doped graphene and isostructural MgB_2-monolayer. We showed that critical temperature of the superconducting state can be enhanced up to several times by the application of strain in order to modify the electron-phonon coupling. All proposed strains are within experimental reach; however, they are beyond the scope of techniques used in this research.

To further understand the effects of strain on realistic 2D materials, we experimentally study an introduction of strain on graphene samples. On two essentially different types of samples, we demonstrate strain effects, both locally and macroscopically. This concerns a possible strain engineering of monolayer graphene by atomic force microscopy and the influence of an axial strain in liquid phase exfoliated graphene films. Manipulation of properties of these different nanomaterials in a controllable fashion through strain engineering has been proven achievable and potentially useful for the design of next generation devices. We showed that AFM produced trenches in graphene could be an excellent platform in order to study local changes in graphene conductivity due to strain. Results of such a study could be related to our theoretical prediction on the effects of strain on conductivity in the 1D-like system. This opens the path for further research on this topic. Application of strain of LPE films has a significant effect on their predicted applications. The sheet resistivity in the entire LPE graphene film exhibits a strong dependence on axial strain. Stretching results in effective pulling apart of individual flakes, and thus an increase in the sheet resistivity of the whole film. This could have a significant impact on their use as flexible electrodes; however, it will open the possibility for a new set of applications such as pressure sensors and strain gauges.

All these results together indicate the effects of the application of strain; tensile and compressive and uniaxial and biaxial strains have significant effects on conductivity and have to be carefully considered depending on the application or concept that we are researching for.

REFERENCES

[1]C. Lee, X. Wei, J. Kysar, and J. Hone, "Measurement of the elastic properties and intrinsic strength of monolayer graphene," Science **321**, 385–388 (2008).
[2]K. S. Novoselov, V. I. Falko, L. Colombo, P. R. Gellert, M. G. Schwab, and K. Kim, Nature **490**, 192–200 (2012).
[3]K. S. Novoselov, A. K. Geim, S. V. Morozov, D. Jiang, Y. Zhang, S. V. Dubonos, I. V. Grigorieva, and A. A. Firsov, "Electric field effect in atomically thin carbon films," Science **306**, 666–669 (2004).
[4]M. I. Katsnelson, "Graphene: Carbon in two dimensions," Mater. Today **10**, 1–2 (2007).
[5]S.-K. Lee, H. Y. Jang, S. Jang, E. Choi, B. H. Hong, J. Lee, S. Park, and J.-H. Ahn, Nano Lett. **12**, 3472–3476 (2012).
[6]R. R. Nair, P. Blake, A. N. Grigorenko, K. S. Novoselov, T. J. Booth, T. Stauber, N. M. R. Peres, and A. K. Geim, Science **320**, 1308 (2008).
[7]S. Bae, H. Kim, Y. Lee, X. Xu, J.-S. Park, Y. Zheng, J. Balakrishnan, T. Lei, H. Ri Kim, Y. I. Song, Y.-J. Kim, K. S. Kim, B. Ozyilmaz, J.-H. Ahn, B. H. Hong, and S. Iijima, Nat. Nanotechnol. **5**, 574–578 (2010).
[8]Z. Sun, D. K. James, and J. M. Tour, J. Phys. Chem. Lett. **2**, 2425–2432 (2011).
[9]K. P. Loh, Q. Bao, P. K. Ang, and J. Yang, J. Mater. Chem. **20**, 2277–2289 (2010).
[10]S. Niyogi, E. Bekyarova, J. Hong, S. Khizroev, C. Berger, W. de Heer, R. C. Haddon, and J. Phys, Chem. Lett. **2**, 2487–2498 (2011).
[11]K. S. Kim, Y. Zhao, H. Jang, S. Y. Lee, J. M. Kim, K. S. Kim, J.-H. Ahn, P. Kim, J.-Y. Choi, and B. H. Hong, Nature **457**, 706–810 (2009).
[12]C.-C. Lu, Y.-C. Lin, C.-H. Yeh, J.-C. Huang, and P.-W. Chiu, ACS Nano **6**, 4469–4474 (2012).
[13]B. J. Kim, H. Jang, S.-K. Lee, B. H. Hong, J.-H. Ahn, and J. H. Cho, Nano Lett. **10**, 3464–3466 (2010).
[14]S.-K. Lee, B. J. Kim, H. Jang, S. C. Yoon, C. Lee, B. H. Hong, J. A. Rogers, J. H. Cho, and J.-H. Ahn, Nano Lett. **11**, 4642–4646 (2011).
[15]P. Avouris, Nano Lett. **10**, 4285–4294 (2010).
[16]F. Bonaccorso, Z. Sun, T. Hasan, and A. C. Ferrari, Nat. Photonics **4**, 611–622 (2010).
[17]Y.-M. Lin, C. Dimitrakopoulos, K. A. Jenkins, D. B. Farmer, H.-Y. Chiu, A. Grill, and P. Avouris, Science **327**, 662 (2010).
[18]F. Schwierz, Nat. Nanotechnol. **5**, 487–496 (2010).
[19]G. G. Naumis, S. Barraza-Lopez, M. Oliva-Leyva, and H. Terrones, "Electronic and optical properties of strained graphene and other strained 2D materials: A review," Rep. Prog. Phys. **80**, 096501 (2017).
[20]C. Si, Z. Suna, and F. Liu, "Strain engineering of graphene: A review," Nanoscale **8**, 3207 (2016).
[21]B. Amorim, A. Cortijo, F. de Juan, A. G. Grushin, F. Guinea, A. Gutiérrez-Rubio, H. Ochoa, V. Parente, R. Roldán, P. San-Jose, J. Schiefele, M. Sturla, and M. A. H. Vozmediano, "Novel effects of strains in graphene and other two dimensional materials," Phys. Rep. **617**, 1 (2016).
[22]M. A. Bissett, M. Tsuji, and H. Ago, "Strain engineering the properties of graphene and other two-dimensional crystals," Phys. Chem. Chem. Phys. **16**, 11124 (2014).
[23]D. Akinwande et al., "A review on mechanics and mechanical properties of 2D materials—Graphene and beyond," Ext. Mech. Lett. **13**, 42 (2017).
[24]G. Profeta, M. Calandra, and F. Mauri, "Phonon-mediated superconductivity in graphene by lithium deposition," Nat. Phys. **8**, 131 (2012).
[25]J. Pesic, "Investigation of superconductivity in graphene and related materials, using ab-initio methods," Ph.D. thesis (University of Belgrade, 2017).

[26]J. Bekaert, A. Aperis, B. Partoens, P. M. Oppeneer, and M. V. Milosevic, "Evolution of multigap superconductivity in the atomically thin limit: Strain-enhanced three-gap superconductivity in monolayer MgB_2," Phys. Rev. B **96**, 094510 (2017).

[27]Y. Hernandez et al., Nat. Nanotechnol. **3**, 563–568 (2008).

[28]A. Matkovic et al., 2D Mater. **3**, 015002 (2016).

[29]J. Hubbard, "Electron correlations in narrow energy bands," Proc. R. Soc. Lond. A **276**, 238 (1963).

[30]V. Celebonovic, "Hubbard model in materials science: Electrical conductivity and reflectivity of models of some 2D materials," in *Advanced 2D Materials*, edited by A. Tiwari and M. Syvajarvi (Scrivener Publishing LLC, 2016), pp. 115–144.

[31]V. Celebonovic, "The hubbard model: Useful for stretchable nanomaterials?," J. Phys. Conf. Ser. **558**, 012006 (2014).

[32]V. Celebonovic, "Some calculational improvements in applying the hubbard model to nanomaterials," J. Phys. Conf. Ser. **794**, 012008 (2017).

[33]J. van den Brand, M. de Kok, M. Koetse et al., "Flexible and stretchable electronics for wearable health devices," Solid State Electron. **113**, 116–120 (2015).

[34]K. Szalowski, "Critical temperature of MgB_2 ultrathin superconducting films: BCS model calculations in the tight-binding approximation," Phys. Rev. B **74**, 094501 (2006).

[35]M. Calandra, G. Profeta, and F. Mauri, "Superconductivity in metal-coated graphene," Phys. Status Solidi B **12**, 2544 (2012).

[36]B. M. Ludbrook, G. Levy, P. Nigge, M. Zonno, M. Schneider, D. J. Dvorak, C. N. Veenstra, S. Zhdanovich, D. Wong, P. Dosanjh, C. Strasser, A. Stohr, S. Forti, C. R. Ast, U. Starke, and A. Damascelli, "Evidence for superconductivity in Li-decorated monolayer graphene," Proc. Natl. Acad. Sci. U.S.A. **112**(38), 11795–11799 (2015).

[37]J. Nagamatsu, N. Nakagawa, T. Muranaka, Y. Zentani, and J. Akimitsu, "Superconductivity at 39 K in magnesium diboride," Nature **410**, 63–64 (2001).

[38]J. M. An and W. E. Pickett, "Superconductivity of MgB_2: Covalent bonds driven metallic," Phys. Rev. Lett. **86**, 4366 (2001).

[39]Z. H. Ni, T. Yu, Y. H. Lu, Y. Y. Wang, Y. P. Feng, and Z. X. Shen, "Uniaxial strain on graphene: Raman spectroscopy study and band-gap opening," ACS Nano **11**, 2301 (2008).

[40]M. Huang, H. Yan, C. Chen, D. Song, T. F. Heinz, and J. Hone, "Phonon softening and crystallographic orientation of strained graphene studied by Raman spectroscopy," Proc. Natl. Acad. Sci. U.S.A. **106**, 7304 (2009).

[41]V. M. Pereira, A. H. Castro Neto, and N. M. R. Peres, "A tight-binding approach to uniaxial strain in graphene," Phys. Rev. B **80**, 045401 (2009).

[42]F. Ding, H. Ji, Y. Chen, A. Herklotz, K. Dorr, Y. Mei, A. Rastelli, and O. G. Schmidt, "Stretchable graphene: A close look at fundamental parameters through biaxial straining," Nano Lett. **10**, 3453 (2010).

[43]T. M. G. Mohiuddin, A. Lombardo, R. R. Nair, A. Bonetti, G. Savini, R. Jalil, N. Bonini, D. M. Basko, C. Galiotis, N. Marzari, K. S. Novoselov, A. K. Geim, and A. C. Ferrari, "Uniaxial strainin graphene by Raman spectroscopy: G peak splitting, Grneisen parameters, and sample orientation," Phys. Rev. B **79**, 205433 (2009).

[44]N. Levy, S. A. Burke, K. Meaker, M. L. Panlasigui, A. Zettl, F. Guinea, A. H. C. Neto, and M. F. Crommie, "Strain-induced pseudo-magnetic fields greater than 300 Tesla in graphene nanobubbles," Science **329**, 544–547 (2010).

[45]F. Guinea, M. I. Katsnelson, and A. K. Geim, "Energy gaps and a zero-field quantum Halle effect in graphene by strain engineering," Nat. Phys. **6**, 30–33 (2009).

[46]M. L. Teague, A. P. Lai, J. Velasco, C. R. Hughes, A. D. Beyer, M. W. Bockrath, C. N. Lau, and N.-C. Yeh, "Evidence for strain-induced local conductance modulations in single-layer graphene on SiO_2," Nano Lett. **9**, 2542 (2009).

[47]M. Huang, T. A. Pascal, H. Kim, W. A. Goddard, and J. R. Greer, "Electronic-mechanical coupling in graphene from in situ nanoindentation experiments and multiscale atomistic simulations," Nano Lett. **11**, 1241–1246 (2011).

[48]X.-W. Fu, Z.-M. Liao, J. X. Zhou, Y.-B. Zhou, H.-C. Wu, R. Zhang, G. Jing, J. Xu, X. Wu, W. Guo, and D. Yu, "Strain dependent resistance in chemical vapor deposition grown graphene," Appl. Phys. Lett. **99**, 213107 (2011).

[49]S. Y. Zhou, G. H. Gweon et al., "Substrate-induced band gap opening in epitaxial graphene," Nat. Mater. **6**, 770 (2007).

[50]D. Xiao, W. Yao, and Q. Niu, "Valley-Contrasting physics in graphene: Magnetic moment and topological transport," Phys. Rev. Lett. **99**, 236809 (2007).

[51]G. Gui, J. Li, and J. Zhong, "Band structure engineering of graphene by strain: First-principles calculations," Phys. Rev. B **78**, 075435 (2008).

[52]C. A. Marianetti and H. G. Yevick, "Failure mechanisms of graphene under tension," Phys. Rev. Lett. **105**, 245502 (2010).

[53]P. Giannozzi, A. V. Fedorov, G.-H. Gweon, P. N. First et al., J. Phys.: Condens. Matter **21**, 395502 (2009).

[54]J. Pesic, R. Gajic, K. Hingerl, and M. Belic, "Strain enhanced superconductivity in Li-doped graphene," Europhys. Lett. **108,**, 67005 (2014).

[55]J. Pesic, V. Damljanovic, R. Gajic, K. Hingerl, and M. Belic, "Density functional theory study of phonons in graphene doped with Li, Ca and Ba," Europhys. Lett. **112**, 67006 (2015).

[56]C. Si, Z. Liu, W. Duan, and F. Liu, "First-Principles calculations on the effect of doping and biaxial tensile strain on electron-phonon coupling in graphene," Phys. Rev. Lett. **111**, 196802 (2013).

[57]A. Romero-Bermudez and A. M. Garca-Garca, "Size effects in superconducting thin films coupled to a substrate," Phys. Rev. B **89**, 064508 (2014).

[58]A. Bingyun, Z. Zhengjun, T. Tao, and Z. Yiping, "Potential enhancement of superconductivity in MgB_2 nanosheets: First-principles calculations," Chem. Phys. Lett. **591**, 185 (2014).

[59]C. Zhang, Y. Wang, D. Wang, Y. Zhang, Z.-H. Liu, Q.-R. Feng, and Z.-Z. Gan, "Suppression of superconductivity in epitaxial MgB_2 ultrathin films," J. Appl. Phys. **114**, 023903 (2013).

[60]N. Acharya, M. A. Wolak, T. Tan, N. Lee, A. C. Lang, M. Taheri, D. Cunnane, B. S. Karasik, and X. X. Xi, "MgB_2 ultrathin films fabricated by hybrid physical chemical vapor deposition and ion milling," APL Mater. **4**, 086114 (2016).

[61]A. Romero-Bermudez and A. M. Garca-Garca, "Shape resonances and shell effects in thin-film multiband superconductors," Phys. Rev. B **89**, 024510 (2014).

[62]D. Valentinis, D. van der Marel, and C. Berthod, "Rise and fall of shape resonances in thin films of BCS superconductors," Phys. Rev. B **94**, 054516 (2016).

[63]A. Reserbat-Plantey, D. Kalita, Z. Han, L. Ferlazzo, S. Autier-Laurent, K. Komatsu, C. Li, R. Weil, A. Ralko, L. Marty, S. Guéron, N. Bendiab, H. Bouchiat, and V. Bouchiat, "Strain superlattices and macroscale suspension of graphene induced by corrugated substrates," Nano Lett. **14**, 5044–5051 (2014).

[64]A. J. M. Giesbers, U. Zeitler, S. Neubeck, F. Freitag, K. S. Novoselov, and J. C. Maan, "Nanolithography and manipulation of graphene using an atomic force microscope," Solid State Commun. **147**, 366 (2008).

[65]L. Weng, L. Zhang, Y. P. Chen, and L. P. Rokhinson, "Atomic force microscope local oxidation nanolithography of graphene," Appl. Phys. Lett. **93**, 093107 (2008).

[66]S. Masubuchi, M. Ono, K. Yoshida, K. Hirakawa, and T. Machida, "Fabrication of graphene nanoribbon by local anodic oxidation lithography using atomic force microscope," Appl. Phys. Lett. **94**, 082107 (2009).

[67]P. Nemes-Incze, G. Kukucska, J. Koltai, J. Kürti, C. Hwang, L. Tapasztó, and L. P. Biró, "Preparing local strain patterns in graphene by atomic force microscope based indentation," Sci. Rep. **7**, 3035 (2017).

[68]B. Vasić, M. Kratzer, A. Matković, A. Nevosad, U. Ralević, D. Jovanović, C. Ganser, C. Teichert, and R. Gajić, "Atomic force microscopy based manipulation of graphene using dynamic plowing lithography," Nanotechnology **24**, 015303 (2013).

[69]A. C. Ferrari et al., Nanoscale **7**, 4598–4810 (2014).

[70]F. Bonaccorso, L. Colombo, G. Yu, M. Stoller, V. Tozzini, A. C. Ferrari, R. S. Ruoff, and V. Pellegrini, Science **347**, 1246501 (2015).

[71]J. Coraux, A. T. N'Diaye, C. Busse, and T. Michely, Nano Lett. **8**, 565–570 (2008).

[72]A. Reina, X. Jia, J. Ho, D. Nezich, H. Son, V. Bulovic, M. S. Dresselhaus, and J. Kong, Nano Lett. **9**, 30–35 (2008).

[73]X. Li et al., Science **324**, 1312–1314 (2009).

[74]A. V. Zaretski and D. J. Lipomi, Nanoscale **7**, 9963–9969 (2015).

[75]M. Kratzer *et al.*, Appl. Phys. Lett. **106**, 103101 (2015).

[76]P. Blake *et al.*, Nano Lett. **8**, 1704–1708 (2008).

[77]S. Stankovich, D. A. Dikin, G. H. Dommett, K. M. Kohlhaas, E. J. Zimney, E. A. Stach, R. D. Piner, S. T. Nguyen, and R. S. Ruoff, Nature **442**, 282–286 (2006).

[78]S. Stankovich, D. A. Dikin, R. D. Piner, K. A. Kohlhaas, A. Kleinhammes, Y. Jia, Y. Wu, S. T. Nguyen, and R. S. Ruoff, Carbon **45**, 1558–1565 (2007).

[79]G. Eda, G. Fanchini, and M. Chhowalla, Nat. Nanotechnol. **3**, 270–274 (2008).

[80]M. Cai, D. Thorpe, D. H. Adamson, and H. C. Schniepp, J. Mater. Chem. **22**, 24992–25002 (2012).

[81]M. Segal, Nat. Nanotechnol. **4**, 612–614 (2009).

[82]A. Eckmann, A. Felten, A. Mishchenko, L. Britnell, R. Krupke, K. S. Novoselov, C. Casiraghi, "Probing the nature of defects in graphene by Raman spectroscopy," Nano Lett. **12**, 3925–3930 (2012).

[83]A. C. Ferrari and D. M. Basko, Nature Nanotech. **8**, 235 (2013).

[84]T. Mohiuddin, A. Lombardo, R. R. Nair *et al.*, Phys. Rev. B **79**, 205433 (2009).

[85]F. Ding, H. Ji, Y. Chen, A. Herklotz, K. Dorr, Y. Mei, A. Rastelli, and O. G. Schmidt, Nano Lett. **10**, 3453–3458 (2010).

[86]Y. Zang, F. Zhang, C.-a. Di, and D. Zhu, Mater. Horiz. **2**, 140–156 (2015).

[87]M. Huang, T. A. Pascal, H. Kim, W. A. Goddard, and J. R. Greer, Nano Lett. **11**, 1241–1246 (2011).

[88]M. L. Teague, A. P. Lai, J. Velasco, C. R. Hughes, A. D. Beyer, M. W. Bockrath, C. N. Lau, and N. C. Yeh, Nano Lett. **9**, 2542–2546 (2009).

Surface optical phonon – Plasmon interaction in nanodimensional CdTe thin films

J. Mitric[a,*], N. Paunovic[a], M. Mitric[b], B. Vasic[a], U. Ralevic[a], J. Trajic[a], M. Romcevic[a],
W.D. Dobrowolski[c], I.S. Yahia[d,e], N. Romcevic[a]

[a] Institute of Physics, University of Belgrade, Pregrevica 118, 11080 Belgrade, Serbia
[b] Institute Vinca, University of Belgrade, P.O. Box 522, 11001 Belgrade, Serbia
[c] Institute of Physics, Polish Academy of Science, al. Lotnikov 32/46, 02-668 Warsaw, Poland
[d] Department of Physics, Faculty of Science, King Khalid University, P.O. Box 9004, Abha, Saudi Arabia
[e] Nano-Science & Semiconductor Labs, Department of Physics, Faculty of Education, Ain Shams University, Roxy, Cairo, Egypt

ABSTRACT

Structural and optical properties of CdTe thin films were investigated applying atomic force microscopy (AFM), XRD powder technique, Raman spectroscopy and far–infrared spectroscopy. CdTe thin films were prepared by using thermal evaporation technique. In the analysis of the far – infrared reflection spectra, numerical model for calculating the reflectivity coefficient for system which includes films and substrate has been applied. Effective permittivity of film mixture (CdTe and air) was modeled by Maxwell – Garnet approximation. We reveal the existence of surface optical phonon (SOP) mode and coupled plasmon-SOP modes (CPSOPM).

1. Introduction

II – VI semiconductor compounds, especially thin films, have become very popular because of their applications in numerous electronic and optoelectronic devices. Due to low production cost, thin films nowadays enjoy great attention in basic research and solid state technology.

The interest in various properties of photonic CdTe is well justified, as this material plays an important role in expanding variety of applications as in: integrated optics, optoelectronics, or solar energy conversion [1].

Two main properties of CdTe thin film are its high optical absorption coefficient (a thin film of CdTe with thickness of approximately 2 μm will absorb nearly 100% of the incident solar radiation) and its near ideal band gap for photovoltaic conversion efficiency of 1.45 eV [2]. Also, its ease of film fabrication and low cost make it a representative material among II – VI semiconductors.

For fabrication of the CdTe films, various techniques have been applied: RF magnetron sputtering [3], molecular beam epitaxy (MBE) [4], pulsed laser deposition (PLD) [5], successive ionic layer adsorption and reaction method (SILAR) [6], metal organic chemical vapor deposition [7], screen printing [8], thermal evaporation method [9] etc. Thermal evaporation method shows some advantages such as: minimalization of impurities proportional to the growing layer, reduced

chances of oxidation and direction of propagation (occurs from the source to the substrate) [9,10]. This makes thermal evaporation technique the most suitable method, thanks to very high deposition rate, low material consumption and low cost of fabrication [11].

In the case of crystal with relatively small dimension, in the frequency range between bulk longitudinal optical phonon frequency (ω_{LO}) and transversal optical phonon frequency (ω_{TO}), a new mode known as a surface phonon mode appears [12,13]. It is known for the case of real crystal, that when its dimension is relatively small, surface modes and effects of dimension will be manifested in addition to the normal modes of infinite lattice. But, when crystal is reduced to extremely small dimensions, only the surface mode will persevere [12–14].

On the other side, electron – phonon interaction takes an important place in semiconducting materials [15]. In our earlier work we have registered plasmon (collective electron excitation) and LO phonons interaction in different systems [16–19]. Besides that, we have studied the impact of damping on interaction appearance [20], interaction between plasmon and different phonons [21,22], as well as interaction between plasmon and impurity local phonons [23–25].

In this work we report experimental studies of CdTe thin films prepared by thermal evaporation technique. Existence of nanodimensional structures in these thin films enabled us to observe effects associated with interactions between surface optical phonon (SOP) and

---

* Corresponding author.
E-mail address: jmitric@ipb.ac.rs (J. Mitric).

plasmon for the first time.

Samples characterization was performed using atomic force microscopy (AFM). Structural properties were analyzed using XRD powder technique, and optical properties were characterized using Raman and far–infrared spectroscopy.

2. Sample preparation and characterization methods

CdTe single crystal was grown by the Bridgman technique. Different thickness of CdTe thin films were deposited by thermal evaporation from a resistance heating quartz glass crucible onto glass substrates using high vacuum coating unit type Edward 306 A. Films were grown at a pressure of 106 Pa. The mechanical rotation of the substrate holder during deposition produced homogeneous film. The distance between the source heater and substrates holder is 21 cm, in order to avoid any heat flow from the source to the substrates.

The morphology of the four CdTe thin films of different thicknesses was investigated by Atomic force microscopy (AFM). Atomic force microscopy measurements were performed using NT-MDT system NTEGRA Prima. Imaging was done in tapping mode using NSG01 probes. All AFM measurements were done at ambient conditions. For the sake of statistical analysis of sample surface, we calculated histograms and bearing ratios for each topographic image. The histogram represents a height distribution density of all points in a two-dimensional topographic image, or in other words, it is a number of points with height given on x-axis. On the other hand, the bearing ratio curve gives a percent of points in a corresponding two-dimensional topographic image with a height less than the number given on x-axis.

The structural characteristics were obtained by the XRD powder technique. All samples were examined under the same conditions, using a Philips PW 1050 diffractometer equipped with a PW 1730 generator, $40 \, kV \times 20 \, mA$, using Ni filtered Co Kα radiation of 0.1778897 nm at room temperature. Measurements were carried out in the 2 h range of 10–100° with a scanning step of 0.05° and 10 s scanning time per step. Crystallite size was determined by using XFIT computing program which is based on Fundamental Parameter convolution approach [26].

Raman measurements were performed using commercial NTegra Spectra system from NT-MDT. A linearly polarized semiconductor laser operating at a wavelength of 532 nm was used. All the spectra were obtained by setting the laser power to 2 mW within the $\sim 0.5 \times 0.5 \, \mu m$ sized focus with exposure time of 600 s.

The far-infrared (FIR) reflectivity measurements were performed at room temperature with a BOMEM DA-8 Fourier-transform infrared spectrometer. A Hyper beamsplitter and deuterated triglycine sulfate (DTGS) pyroelectric detector were used to cover the wave number region from 80 to 650 cm^{-1}.

3. Results and discussion

3.1. Atomic force microscopy

Three dimensional topographic images of all four samples are shown in the left side of Fig. 1. As can be seen, sample surfaces are rather flat, but still they are characterized with bright protrusions and dark holes (which represent air) resulting in a small surface roughness of several nanometers.

In order to characterize fraction of both observed topographic features, the statistical analysis have been performed by calculating histograms and bearing ratios from two dimensional topographic images. The results for all four samples are given in the right side of Fig. 1. They show that the peaks in the histograms are positioned in the middle of bearing ratio curves. Therefore, from these curves we can conclude that the fraction of holes and protrusions are rather similar, around 50%.

In order to estimate thicknesses of studied films, their step edges were measured by AFM. 3D AFM topographic images of the step edges are depicted in Fig. 2(a1-d1). The films are brighter and the substrates

are dark in the images, while the step edges are clearly resolved. Based on the AFM images, height distributions were calculated and presented in Fig. 2 (a2-d2). In all histograms, there are two characteristic peaks: a lower one corresponds to the substrate, while a higher one corresponds to the film. Therefore, the film height can be then approximately calculated as a difference between these two peaks. Estimated film thicknesses are given in Fig. 2 (a2-d2). The best resolved height peaks were found on CdTe 1 in Fig. 2 (a2) due to a smooth sample surface as can be seen in Fig. 2 (a1).

3.2. XRD

Structures of four synthesized CdTe thin films with different thicknesses were identified by XRD pattern as shown in Fig. 3. The diffractograms confirm that all samples are monophased, and that they crystallized in sphalerite type structure in 216. space group, $F\bar{4}3m$. All of the observed diffraction peaks are indexed according to this space group. Therefore, in our thin film samples there is no other structures other than CdTe. In this structural type, Cd ions occupy $4a$ Wyckoff positions, [[0, 0, 0]] with local symmetry $\bar{4}3m$, while Te ions occupy $4c$ Wyckoff positions [[1/4, 1/4, 1/4]] with the same local symmetry. Cd ions are in tetrahedral surrounding of Te ions (and vice versa). The tetrahedrons are regular and share common vertices. Crystallite size (R) is determined and presented in Fig. 2 and Table 1.

3.3. Raman spectroscopy

The cubic face-centered structure of bulk crystal CdTe is characterized by the 216. space group $F\bar{4}3m$ and contains four formula units, while the primitive cell is one fourth as many. Optical modes consist of one three fold –degenerated mode F_2 which is active in IR and Raman spectra. The dipole mode F_2 is split into the transverse (TO) and longitudinal (LO) modes in the vibrational spectra. It is very well known that reduction of the particle dimensions to nanoscale results in a breakdown of phonon selection rules and allows phonons with $l \neq 0$ to contribute to Raman scattering [27–31]. Consequently, some new forbidden vibration modes (low frequency region, acoustic modes, and high frequency region, surface optical modes) occur due to imperfections, impurity, valence band mixing and/or nonspherical geometry of the nanostructures [14].

TO (142 cm^{-1}) and LO (170.5 cm^{-1}) modes for the CdTe bulk crystal are both active in the Raman spectra. Also, the modes in band near 120 cm^{-1} correspond to phonons of Te on the CdTe surface and can be seen in the Raman spectra [32].

Raman spectra of CdTe thin films of different thickness at room temperature are presented in Fig. 4.

For analyzing obtained spectra Lorentz profiles were used. Solid lines are their sums. In the top right corner Raman spectra of bulk CdTe crystal for ambient conditions is presented [32]. The observed Raman spectra for all samples among characteristic CdTe TO mode at 142 cm^{-1} and phonon of Te of the CdTe surface (127 cm^{-1}), show the LO phonon like frequency shift from 170.5 cm^{-1} to 164 cm^{-1}. That can be attributed to the surface optical phonon (SOP) mode effect [33–38]. It is clear that SOP phonon is wider compared to LO phonon of bulk crystal, as well as when it's compared to phonon of nanodimensional film. This effect is associated with interaction between SOP and plasmon, which will be mentioned later on.

In order to analyze the surface optical phonon we have to take into account that a part of crystallites are surrounded by air. We will analyze the dependence of the SOP mode position on filling factor (*f*) of the mixed material.

Surface phonon modes can be detected in systems where particle size is much smaller when compared to wavelength of exciting light source [39]. These modes can be obtained for in the case of polar crystals [40], so we consider expression for dielectric function which describes optical properties of polar semi – insulating semiconductor in
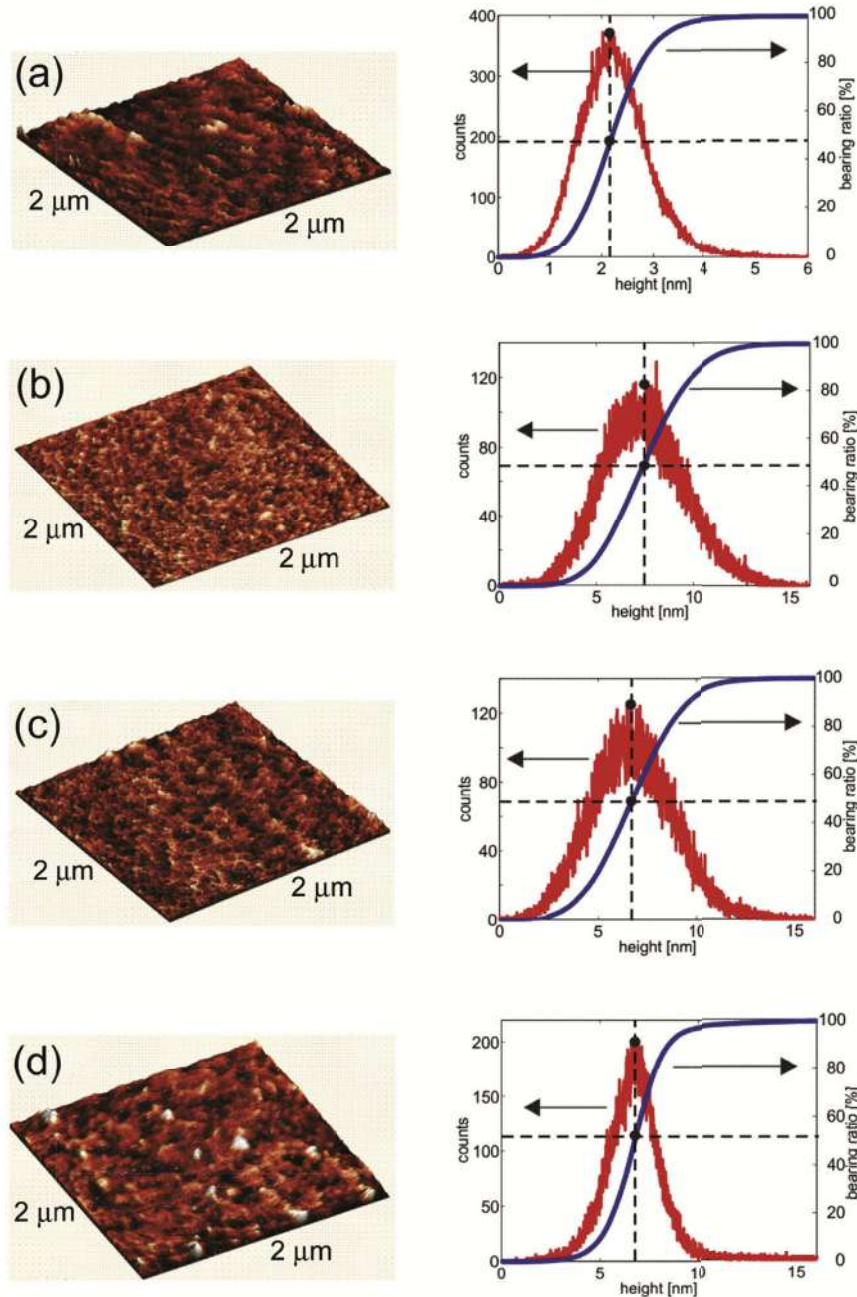
Fig. 1. Three-dimensional topographic image (left) and corresponding histogram and bearing ratio (right) for (a) CdTe 1, (b) CdTe 2, (c) CdTe 3, and (d) CdTe 4. Scan size is 2 μm.

IR region [24]:

$$\varepsilon_2(\omega) = \varepsilon_\infty \left(1 + \sum_{k=1}^{n} \frac{\omega_{LOk}^2 - \omega_{TOk}^2}{\omega_{TOk}^2 - \omega^2 - i\gamma_{TOk}\omega} - \frac{\omega_P^2}{\omega(\omega + i\Gamma)} \right) \tag{1}$$

ωTO and ωLO represent transverse and longitudinal optical bulk phonons, respectively; $\varepsilon\infty$ is the dielectric constant at high frequencies, ωP is plasma frequency and γ and Γ are the damping constants. Surface phonons can be considered similarly to phonons in infinite crystals, but with adapted wave functions to the geometry of the small particle.

Here, we will apply effective medium theory: Because the size of semiconducting nanoparticles, L, (with dielectric function ε_2, and are distributed in a medium with dielectric constant ε_1) is considerably

smaller than the interacting wavelength of visible light, λ ($\lambda \gg L$), we treat the heterogeneous composite as a homogeneous medium.

Even though there are numerous models for the effective dielectric permittivity for these kinds of mixtures [41], we decided to use Maxwell – Garnet model, because all our samples are thin films with well defined and separated nanosized grains. According to the Maxwell – Garnet mixing rule [42,43], effective permittivity of mixture, including spherical geometry of particles is given with:

$$\varepsilon_{eff} = \varepsilon_1 + 3f\varepsilon_1 \frac{\varepsilon_2 - \varepsilon_1}{\varepsilon_2 + 2\varepsilon_1 - f(\varepsilon_1 - \varepsilon_2)} \tag{2}$$

In this case, nanoparticles are spheres with permittivity ε_2 and are randomly distributed in homogeneous environment, with permittivity
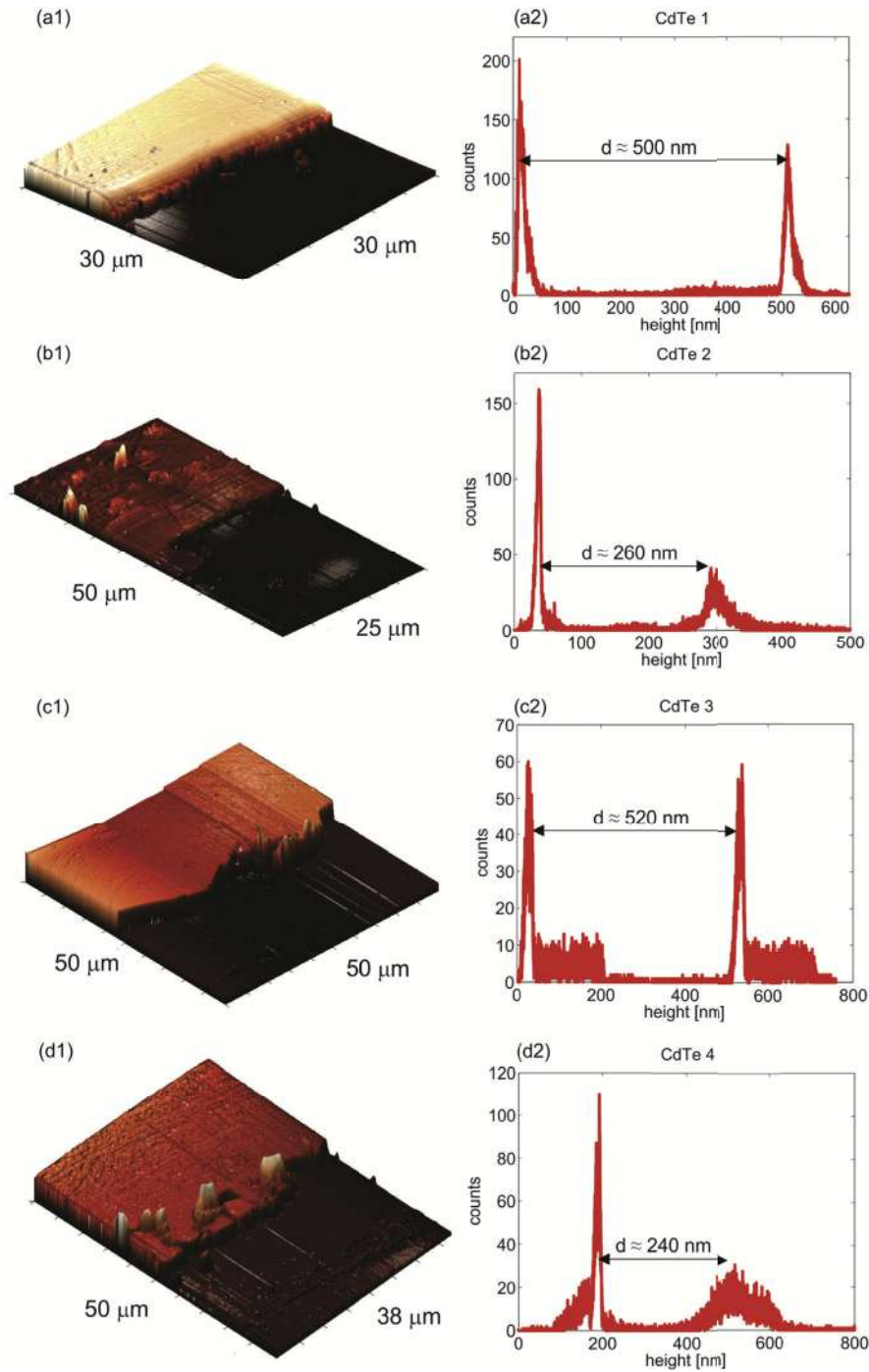
Fig. 2. (a1-d1) 3D AFM topographic images of step edges of studied films, and (a2-d2) corresponding height histograms. Average films thicknesses are denoted in the histograms.

ε_1 and occupy a volume fraction f.

Position surface optical phonon (SOP) mode frequencies are obtained from Ref. [44]:

$$\omega_{SOP} = max\left(I_m\left(-\frac{1}{\varepsilon_{eff}}\right)\right) \tag{3}$$

The result is shown in Fig. 5. The practical liner dependence of the position of the SOP mode on the filing factor f has been obtained. For the frequency of the SOP mode determined in Fig. 4 we have $f = 0.53$. This result is in accordance with the one obtained from the AFM measurements.

3.4. Far-infrared spectroscopy

Thicknesses of our films, as we will see, are in a range from $\sim 0.39\,\mu m$ to $\sim 0.72\,\mu m$, so reflectivity spectra contain information about CdTe films together with information about substrate. Representative scheme of our layered structure can be presented in Fig. 6 [45]. Medium 1 is air, medium 2 is thin bulk CdTe crystal layer and medium 3 is substrate glass, with dielectric functions ε_1 ($\varepsilon_1 = 1$), ε_2 and ε_3, respectively. We can now write [46]:

$$R_A = \frac{A_r}{A_i} = \frac{r_{12}e^{-i\alpha} + r_{23}e^{i\alpha}}{e^{-i\alpha} + r_{12}r_{23}e^{i\alpha}} \tag{4}$$
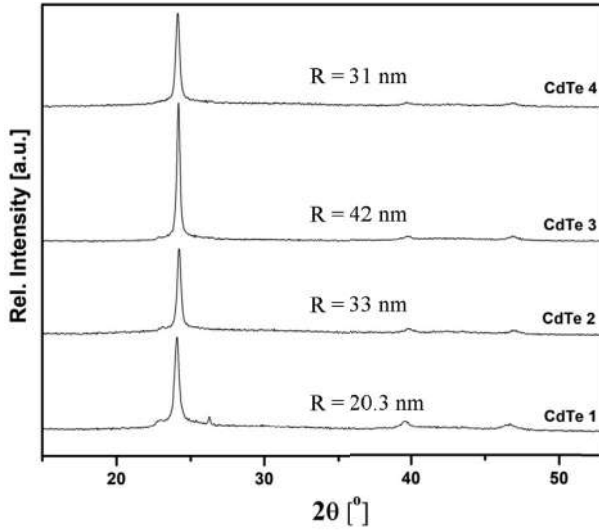
Fig. 3. XRD analysis of CdTe thin films of different thickness. Obtained crystallite sizes (R) are presented too.

Table 1
Parameters obtained from XRD measurements and FIR reflection spectroscopy. Thin films thickness - d, Crystallite size – R.

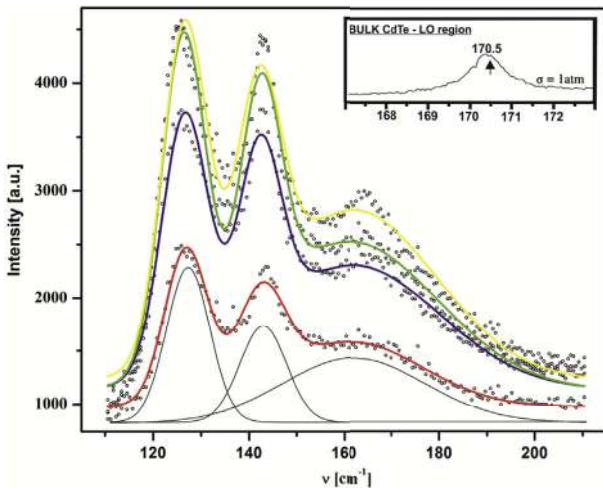| Name	d [μm]	R [nm]	ω_{l1} (ω_+) [cm^{-1}]	ω_{l2} (ω_-) [cm^{-1}]	ω_P [cm^{-1}]	ω_t [cm^{-1}]	f
CdTe 4	0.39	31.0	187	103	137.5	140.0	0.53
CdTe 2	0.43	33.0	174	78	96.6	140.5	0.53
CdTe 3	0.71	42.0	170	65	79.5	139	0.53
CdTe 1	0.72	20.3	165	30	35.2	140.5	0.53

Fig. 4. Raman spectra of CdTe thin films of different thickness. Experimental spectra are shown by open dots. Solid lines are sums of three Lorentz profiles as it shown for spectrum of CdTe 1. In the top right corner LO region of bulk CdTe is presented, taken from the literature [32].

$r_{ij} = (n_i - n_j)/(n_i + n_j) = (\sqrt{\varepsilon_i} - \sqrt{\varepsilon_j})(\sqrt{\varepsilon_i} + \sqrt{\varepsilon_j})$ describe Fresnel coefficients, A_i and A_r represent amplitudes of incident and reflection beams, n is complex index of refraction, ε is the dielectric constant and $\alpha = 2\pi\omega d(\varepsilon_2)^{1/2}$ is the complex phase change related to the absorption in the crystal layer with the thickness d.

Reflectance, R, is given with:

$$R = |R_A|^2 \tag{5}$$

In this case we decided to use dielectric function which takes into

consideration the existence of plasmon – phonon interaction in advance.

The dielectric function of the CdTe crystal layer is:

$$\varepsilon_2(\omega) = \varepsilon_{\infty CdTe} \prod_{j=1}^{2} \frac{\omega^2 + i\gamma_{lj}\omega - \omega_{lj}^2}{\omega(\omega + i\Gamma_p)(\omega^2 + i\gamma_t\omega - \omega_t^2)} \tag{6}$$

The ω_{lj} and γ_{lj} ($j = 1, 2$), parameters of the first numerator are the eigenfrequencies and damping coefficients of the longitudinal plasmon-phonon (LP + LO) waves, that arise as a result of the interaction of the initial phonon ($\omega_{LO,CdTe} = 170.5$ cm^{-1}) and plasmons (ω_P) modes. The parameters of the denominator correspond to the similar characteristics of the transverse vibrations (ω_t, γ_t) and plasmon damping Γ_P. As a result of the best fit, we obtain coupled mode frequencies (ω_{l1} and ω_{l2}).

The dielectric function of the glass substrate is:

$$\varepsilon_s(\omega) = \varepsilon_{\infty sup} \prod_{k=1}^{n} \frac{\omega_{LOk}^2 - \omega^2 + i\gamma_{LOk}\omega}{\omega_{TOk}^2 - \omega^2 + i\gamma_{TOk}\omega} \tag{7}$$

where ω_{TO} and ω_{LO} are the transversal and longitudinal optical vibrations, and γ_{TO} and γ_{LO} are damping parameters, respectively.

In our case, layer 2 consists of a CdTe crystals and air (see Fig. 6). The size of the crystallites (R) is given in Fig. 2 and Table 1. These crystallites are described by a dielectric function given in Eq. (1) or Eq. (6) and located randomly in homogeneous environment ε_1 (air) and occupy a volume fraction f, so we can use effective medium theory and Maxwell - Garnet mixing rule, given with Eq. (2).

The far – infrared reflectivity spectrum of the glass substrate is shown in Fig. 7(e). The calculated spectrum, presented by solid line, was obtained using the dielectric function given by equation (7). As a result of the best fit we obtained three modes, whose characteristic frequency are $\omega_{TO1} = 60$ cm^{-1}, $\omega_{LO1} = 140$ cm^{-1}, $\omega_{TO2} = 441$ cm^{-1}, $\omega_{LO1} = 443$ cm^{-1} and $\omega_{TO3} = 471$ cm^{-1}, $\omega_{LO3} = 522$ cm^{-1}. Frequency values of these modes have remained the same during the fitting procedure for all CdTe thin film samples.

The parameters obtained by the best fit between the experimental results and the models for CdTe film described earlier are also given in Table 1. The far-infrared spectra of CdTe thin films, in the spectral range of 80–600 cm^{-1}, at room temperature, are presented in Fig. 7. Experimental data are presented by circles, while the solid lines are calculated spectra obtained by a fitting procedure based on the previously presented model. Experimental and theoretical spectra show an excellent match.

The thicknesses of our films obtained by Far – infrared spectroscopy are 20% greater, which is within the limits of error for both techniques. When using Far – infrared spectroscopy for calculating thickness of layered structured, we bring errors in absolute measurements, because we calculate effective thickness. The important thing is, the trend is the same, the films does not differ in the relative thickness, i.e. thickness ratios between films are the same.

We note that the thickness (d) of the film changes in the range of ~ 0.39–~ 0.7 μm. While the thickness of the film is in the 0.40 μm region, the crystallite size is about 32 nm, and for a film thickness of about 0.72 μm, we have two sizes of crystallites different for a factor of 2. In addition, from Table 1, we have for thicker films CdTe 1 and CdTe 3, that the position of the coupled plasmon-phonon mode ω_{l1} is below the values of $\omega_{LO,CdTe} = 170.5$ cm^{-1}. On the other hand, these values are above $\omega_{LO,CdTe}$ for thin films CdTe 2 and CdTe 4. In both cases plasmon damping (Γ_p) is relatively low. The obtained eigenfrequencies of the plasmon – phonon coupled modes for CdTe thin films are presented in Fig. 8. As a result of the best fit from Fig. 7, we obtained the frequencies of coupled modes (ω_{l1} and ω_{l2}) marked by open circles and transverse mode frequencies which are denoted by - x. Value of ω_P are calculated by Refs. [16–18]:

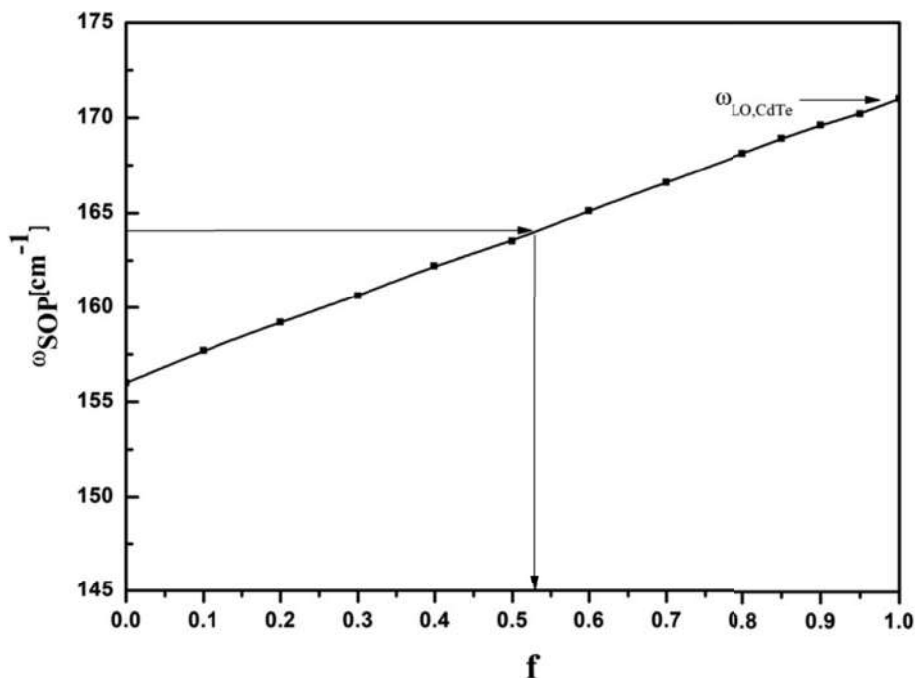$$\omega_P = \frac{\omega_{l1}\omega_{l2}}{\omega_t} \tag{8}$$

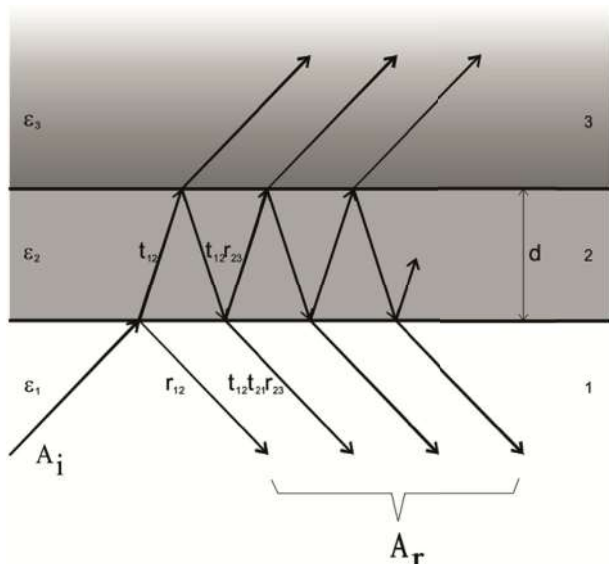**Fig. 5.** Surface optical phonon (SOP) mode position vs. filing factor.

Fig. 6. Schematic presentation of a three layer structure [46].

The calculated lines at Fig. 7 are solution of a real part of uncoupled dielectric function (Eq. (1)). However, for plasma-phonon modes positions are obtained:

$$\omega_{\pm} = \frac{\omega_P^2 + \omega_{LO}^2}{2} \pm \sqrt{\frac{(\omega_P^2 + \omega_{LO}^2)^2 - \omega_P \omega_{TO}}{4}} \qquad (9)$$

The full lines in Fig. 7 were obtained for the case $\omega_{LO,\text{CdTe}} = 170.5 \, \text{cm}^{-1}$. It is clear that all values of ω_{l1} and ω_{l2} are out of this theoretical model. Best fit, dashed lines in Fig. 7, was obtained for $\omega_{SOP} = 164 \, \text{cm}^{-1}$ which in Eq. (9) plays a role ω_{LO}. Shift of about $7 \, \text{cm}^{-1}$ is registered in relation to $\omega_{LO,\text{CdTe}}$, just like in the case of Raman spectra. As we said earlier, the LO phonon shift of CdTe crystal is attributed to the surface optical phonon (SOP) mode effect.

Based on these results, it is clear that in the case of CdTe thin films, prepared by using thermal evaporation technique, the filing factor is constant and does not depend on film thickness, crystallite size and
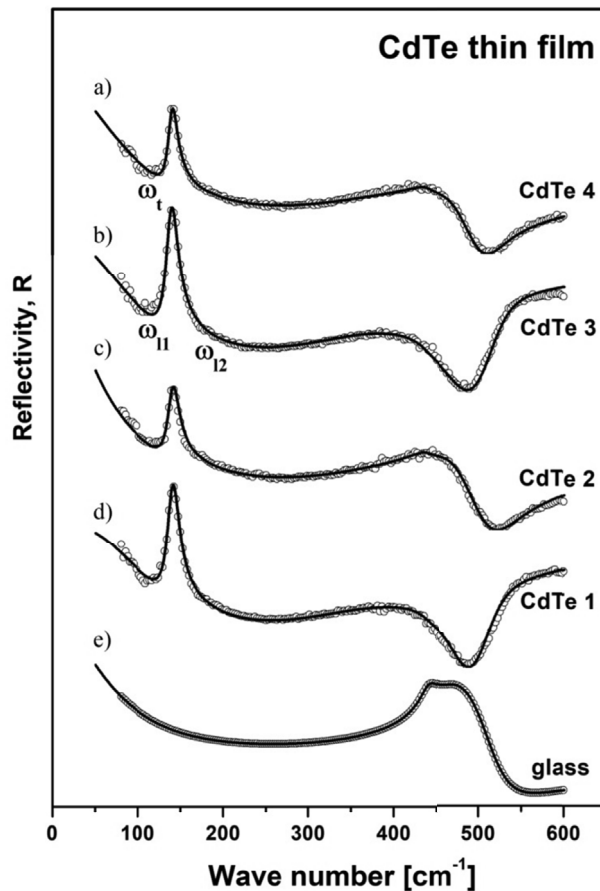

Fig. 7. Far – infrared reflection spectra of: CdTe thin films with thickness of (a) 0.39 μm, (b) 0.71 μm, (c) 0.43 μm, (d) 0.72 μm, and glass substrate (e). Experimental spectra are presented by circles while solid lines are calculated spectra obtained by a fitting procedure based on the model given by Eqs. (2) and (4)–(7).
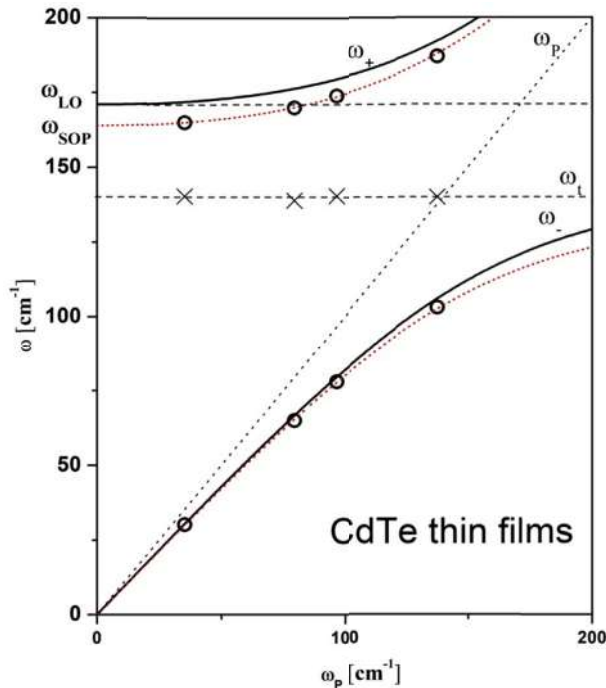
Fig. 8. The eigenfrequencies of the plasmon–phonon modes for CdTe thin films. The lines are calculated spectra [Re$\{\varepsilon_2\}$ = 0; ε_2 is given by Eq. (1)]: solid line with $\omega_{LO,CdTe}$ = 170.5 cm^{-1}; dashed line with ω_{SOP} = 164 cm^{-1}; ○ - ω_{l1}, ω_{l2}; x – ω_t.

concentration of free carriers. On the other hand, the reflection spectra depend on the thickness of the film and the concentration of free carriers in the film, which is expected. In general, thin films have a higher concentration of free carriers ($\sim\omega_p$) (see Table 1). The linear dependence of the position of the SOP mode on the filing factor causes the existence of a modified plasmon – phonon interaction, where the SOP has the role of the LO phonon.

Of course, there are many models that can describe the registered frequency shift of the LO phonon in CdTe e.g. a continuum model of the optical phonon confinement [47,48] would also give a shift of 7 cm^{-1}, but for spherical nanoparticles of about 5 nm, which is far from our case.

4. Conclusion

In this paper, we present results of investigation of CdTe thin films prepared with thermal evaporation technique, with different thicknesses. Sample's surfaces are rather flat, but still they are characterized with bright protrusions and dark holes (air) resulting in a small surface roughness of several nanometers. We showed that, when using thermal evaporation technique we get high quality thin films, especially for thicker films with greater crystallite size. We conclude that the filling factor of our thin films is constant and does not depend on film thickness, crystallite size or concentration of free carriers, but yet has linear dependence on SOP position. This kind of morphology, with filling factor of ~50% causes existence of surface optical phonon and its interaction with plasmon, because of the free surface around nanoparticles. A numerical model for calculating the reflectivity coefficient for complex system, which includes films and substrate, has been applied, and CdTe thin film were treated as a mixture of homogenous spherical inclusion in air modeled by Maxwell – Garnet formula.

Acknowledgements

References

[1] S. Chandra Ray, K. Mallick, Int. J. Chem. Eng. Appl. 4 (2013) 183–186.
[2] C.S. Ferekides, U. Balasubramanian, R. Mamazza, V. Viswanathan, H. Zhao, D.L. Morel, Sol. Energy 77 (2004) 823–830.
[3] R. Kulkarni, et al., Energy Procedia 110 (2017) 188–195.
[4] A. Arnoult, J. Cibert, Appl. Phys. Lett. 66 (1995) 2397–2399.
[5] P. Bhattacharya, D.N. Bose, Semicond. Sci. Technol. 6 (1991) 384–387.
[6] A.U. Ubale, D.K. Kulkarni, Indian J. Pure Appl. Phys. 44 (2006) 254–259.
[7] T.L. Chu, S.S. Chu, C. Ferekides, J. Britt, C.Q. Wu, J. Appl. Phys. 71 (1992) 3870.
[8] A. Nakano, et al., Sol. Cell. 17 (1986) 233.
[9] K.S. Rahman, F. Haque, 3rd International Conference on the Developments in Renewable Energy Technology (ICDRET), 2014, pp. 29–31.
[10] S. Lalitha, S. Zh Karazhanov, P. Ravindran, S. Senthilarasu, R. Sathyamoorthy, J. Janabergenov, Physica B 387 (2007) 227–238.
[11] S. Singh, et al., Thin Solid Films 519 (2010) 1078–1081.
[12] D.S. Chuu, C.M. Dai, W.F. Hsieh, C.T. Tsai, J. Appl. Phys. 69 (1991) 12.
[13] A. Singha, B. Satpati, P.V. Satyam, A. Roy, J. Phys. Condens. Mater. 17 (2005) 5708–5967.
[14] M. Gilić, J. Trajić, N. Romčević, M. Romčević, D.V. Timotijević, G. Stanišić, I.S. Yahia, Opt. Mater. 35 (2013) 1112–1117.
[15] M. Cardona (Ed.), Top. Appl. Phys, vol. 8, Springer, Berlin, 1975.
[16] N. Romčević, M. Romčević, A. Golubović, Le Van Khoi, A. Mycielski, Đ. Jovanović, D. Stojanović, S. Nikolić, S. Đurić, J. Alloy. Compd. 397 (2005) 52–57.
[17] M. Romčević, N. Romčević, V.N. Nikiforov, Infrared Phys. Technol. 42 (2001) 541–545.
[18] N. Romčević, M. Romčević, A. Milutinović, S. Kostić, J. Alloy. Compd. 478 (2009) 41–44.
[19] J. Trajić, M. Romčević, N. Romčević, B. Babić, B. Matović, P. Balaž, Opt. Mater. 57 (2016) 225–230.
[20] N. Romčević, M. Romčević, W.D. Dobrowolski, L. Kilanski, M. Petrović, J. Trajić, B. Hadžić, Z. Lazarević, M. Gilić, J.L. Ristic-Djurović, N. Paunović, A. Reszka, B.J. Kowalski, I.V. Fedorchenko, S.F. Marenkin, J. Alloy. Compd. 649 (2015) 375–379.
[21] J. Trajić, N. Romčević, M. Romčević, V.N. Nikiforov, Mater. Res. Bull. 42 (2007) 2192–2201.
[22] M. Romčević, N. Romčević, W. Dobrowolski, L. Kalinski, J. Trajić, D.V. Timotijević, E. Dynowska, I.V. Fedorchenko, S.F. Marenkin, J. Alloy. Compd. 548 (2013) 33–37.
[23] N. Romčević, J. Trajić, T.A. Kuznetsova, M. Romčević, B. Hadžić, D.R. Khokhlov, J. Alloy. Compd. 442 (2007) 324–327.
[24] J. Trajić, N. Romčević, M. Romčević, D. Stojanović, R. Rudolf, T.A. Kuznetsova, D.R. Khokhlov, J. Alloy. Compd. 493 (2010) 41–46.
[25] J. Trajić, N. Romčević, M. Romčević, D. Stojanović, L.I. Ryabova, D.R. Khokhlov, J. Alloy. Compd. 602 (2014) 300–305.
[26] R.W. Cheary, A. Coelho, J. Appl. Crystallogr. 25 (1992) 109–121.
[27] R. Triboulet & P. Siffert, first ed., Elsevier, 2010.
[28] H. Zeng, W. Cai, B. Cao, J. Hu, Y. Li, P.S. Liu, Appl. Phys. Lett. 88 (2006) 181905.
[29] A. Ghosh, R.N.P. Chodhary, J. Phys. D Appl. Phys. 42 (2009) 075416.
[30] F. Friedrich, N.H. Nickel, Appl. Phys. Lett. 91 (2007) 111903.
[31] J. Xu, W. Ji, X.B. Wang, H. Shu, Z.X. Shen, S.H. Tang, J. Raman Spectrosc. 29 (1998) 613.
[32] V.C. Stergiou, Y.S. Raptis, E. Anastassakis, N. Pelekaneos, A. Nahmani, J. Cibert, Phys. Status Solidi 223 (2001) 237.
[33] J.F. Scott, T.C. Damem, Optic Commun. 5 (1972) 410.
[34] R. Rossetti, S. Nakahara, L.E. Bru, J. Chem. Phys. 79 (1983) 1086.
[35] B.F. Variano, N.E. Schlotter, D.M. Hwangand, C.J. Sandroff, J. Chem. Phys. 88 (1988) 2848.
[36] A.V. Baranov, Y.S. Bobovich, N.I. Grebenshchikova, V.I. Petrov, M.Y. Tsenter, Optic Spectrosc. 60 (1986) 685.
[37] H. Jerominek, M. Pigeon, S. Patela, Z. Jakubczk, C. Delisle, R.J. Tremblay, Appl. Phys. 63 (1986) 957.
[38] E.F. Hilinski, P.A. Lucas, J. Chem. Phys. 89 (1988) 3435.
[39] J. Trajić, M. Gilić, N. Romčević, M. Romčević, G. Stanišić, B. Hadžić, M. Petrović, Y.S. Yahia, Sci. Sinter. 47 (2015) 145–152.
[40] G. Irmer, J. Raman Spectrosc. 38 (2007) 634.
[41] K. Karkkainen, A. Saviola, K. Nikoskinen, IEEE Trans. Geosci. Rem. Sens. 39 (5) (2001) 1013.
[42] J.C.M. Garnett, Trans. Roy. Soc. Can. CIII (1904) 385420.
[43] A. Saviola, I. Lindell, A. Priou (Ed.), Dielectric Properties of Heterogeneous Materials PIER 6 Progres in Electromagnetic Research, Elsevier, Amsterdam, 1992, pp. 101–115 1.
[44] B. Hadžić, N. Romcević, M. Romcević, I. Kuryliszyn-Kudelska, W. Dobrowolski, J. Trajić, D.V. Timotijević, U. Narkiewicz, D. Sibera, J. Alloy. Compd. 540 (2012) 49–56.
[45] M. Gilić, et al., Infrared Phys. Technol. 76 (2016) 276–284.
[46] J. Trajić, M. Gilić, N. Romčević, M. Romčević, G. Stanišić, Z. Lazarević, D. Joksimović, I.S. Yahia, Phys. Scr., T 162 (2014) 014031.
[47] R. Roca, C. Trallero-Giner, M. Cardona, Phys. Rev. B 49 (1994) 13704.
[48] M.P. Chamberlain, C. Trallero-Giner, M. Cardona, Phys. Rev. B 51 (1995) 1680.

Far-infrared spectroscopy of laser power modified MnO nanoparticles

B. BABIC[a], B. HADZIC[a], I. KURYLISZYN-KUDELSKA[b], N. PAUNOVIC[a], B. VASIC[a], W. D. DOBROWOLSKI[b], M. ROMCEVIC[a], J. TRAJIC[a,*], N. ROMCEVIC[a]

[a]Institute of Physics, University of Belgrade, Pregrevica 118, 11080 Belgrade, Serbia
[b]Institute of Physics, Polish Academy of Science, al. Lotnikow 32/46, 02-668 Warszawa, Poland

The influence of the locally induced laser heating on MnO nanoparticles were investigated by atomic force microscopy (AFM) and far-infrared spectroscopy (FIR) at room temperature, in the spectral region between 80 and 600 cm^{-1}. The FIR spectra were analyzed by using Maxwell-Garnet formula, where MnO nanoparticles are modeled as a mixture of homogeneous spherical inclusions in air. Laser induced heating leads to the conversion of the part MnO nanoparticles into the MnO_2, Mn_3O_4 and $MnOOH$, along with possible formation of elemental Mn on the sample surface.

1. Introduction

MnO is transitional metal oxide which crystallizes in the simple rock salt structure. It is well known that this structure has a certain number of defects, usually in the cationic sublattice, what leads to the formation of structure which can be described as an ordered Mn vacancy cubic structure with the formula $Mn_{1-\delta}O$, where $0 \leq \delta \leq 0.15$ [1-3].

Due to this non-stoichiometry, MnO has unique electrical, magnetic, optical and mechanical properties, characteristic for the rock salt structure [1, 2]. Recently, Hiramoto and co-workers proposed a new synthetic route which enables the control of the non-stoichiometric defects in the structure [4]. Bulk MnO acts as a p-type semiconductor and has anti-ferromagnetic properties [5]. But, the presence of impurities can significantly change the magnetic properties of the MnO [6 - 9].

The size of the particles has considerable influence on the properties of MnO. For instance, literature data shows that nanometric MnO has ferromagnetic characteristics [5]. New characteristics on nanometric scale can be explained with significant changes into the surface to volume ratio. The decreasing of the particle size increases the amount of edge atoms and, consequently, the number of unsaturated chemical bonds which, further, changes the physical and chemical properties of the material. Manganese can exists in the several oxidation states among which Mn(II) is the lowest. By different oxidation treatment, manganese can be transverse in to the different, higher, oxidation states.

Recently, we have investigated the influence of the lacer induced heating of ZnO(Co) [10], $Bi_{12}GeO_{20}$ [11] and MnO [12] nanoparticles, with different laser powers. It has been shown that laser induced heating leads to creation of new phases, depending on laser power.

In order to further investigate the influence of the locally induced laser heating on MnO nanoparticles, non-irradiated, as well as irradiated MnO sample, were investigated by using far-infrared spectroscopy (FIR) and atomic force microscopy (AFM).

2. Sample characterization

Commercially available polycrystalline MnO powder of the analytical grade (Sigma-Aldrich Co) was pressed into a pellet. Verdi G optically pumped semiconductor laser with wavelenght of 532 nm was used as excitation source. In this paper we analyzed one sample, at first before laser treatment and afterwards after treatment with a laser with a power of 24 mW.

AFM measurements of non-irradiated and irradiated sample with the highest energy were done using NT-MDT system NTEGRA Prima at ambient conditions. AFM images were recorded in tapping mode, using NSG01 probes from NT-MDT.

The far-infrared measurements on non-irradiated and irradiated sample with laser power (24mV) were carried out with a BOMEM DA-8 FIR spectrometer. A DTGS pyroelectric detector was used to cover the wave number range from 80 to 600 cm^{-1}.

3. Results and analysis

3.1. AFM measurements

AFM topographies of non-irradiated (a) and irradiated (b) MnO samples are presented on Fig. 1. Fig. 1 shows a clear difference between the surfaces of the sample before and after irradiation. Prior to irradiation, a granulated structure, with well recognized grain boundaries, is visible.

Grains size is about few tens of nanometers. In our previous investigations X-ray analysis showed that mean crystallite size is about 44 nm [12] which is in good agreement with results obtained with AFM.

After irradiation, the topography of the surface was significantly changed. The grain boundaries are not visible and surface is smooth. Due to the laser induced heating and increasing of the energy, MnO particles on the surface of the samples interact with the elements and compounds from the vicinity (mostly oxygen and water) and create compounds in which manganese is in the higher oxidation state. Process is spontaneous and these different species are inhomogeneously arranged on the surface of the sample and, consequently, clear boundaries between grains are lost.
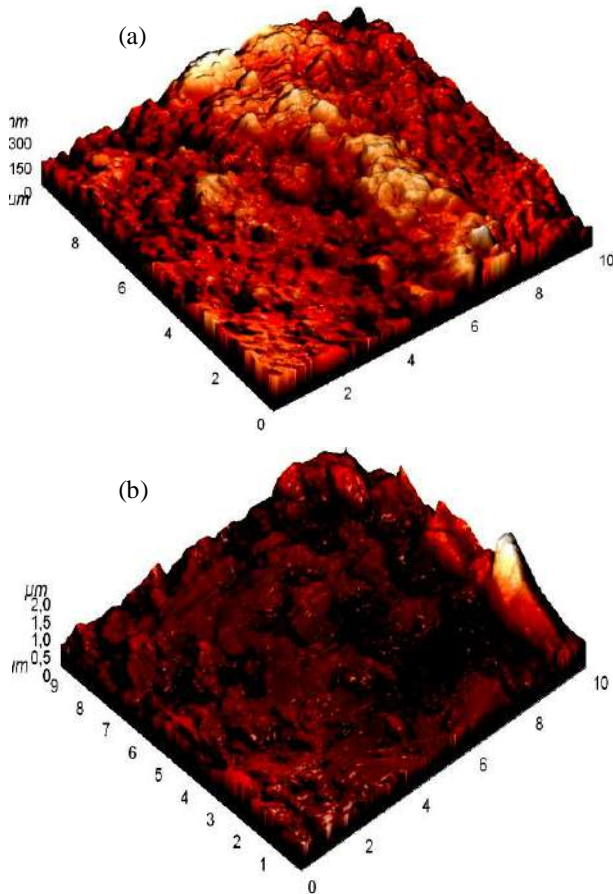

Fig. 1. AFM 3D topography of (a) non-irradiated and (b) irradiated sample of MnO nanoparticles

After irradiation, the topography of the surface was significantly changed. The grain boundaries are not visible and surface is smooth. Due to the laser induced heating and increasing of the energy, MnO particles on the surface of the samples interact with the elements and compounds from the vicinity (mostly oxygen and water) and create compounds in which manganese is in the higher oxidation state. Process is spontaneous and these different species are inhomogeneously arranged on the

surface of the sample and, consequently, clear boundaries between grains are lost.

3.2. Far-infrared spectroscopy

When visible light, of wavelength λ interacts with semiconducting nanoparticles (characteristic size, d, dielectric function ε_2) which are distributed in a medium with the dielectric constant ε_1 in the limit λ >> d, the heterogeneous composite can be treated as a homogeneous medium and effective medium theory is applied. There are many mixing models for the effective dielectric permittivity of such a mixture [13]. Since our samples are well defined and separated nanosized grains, we used Maxwell-Garnet model for present case. For the spherical inclusions case, the prediction of the effective permittivity of mixture ε_{eff} according to the Maxwell-Garnet mixing rule is [14]:

$$\varepsilon_{eff} = \varepsilon_1 + 3f\varepsilon_1 \frac{\varepsilon_2 - \varepsilon_1}{\varepsilon_2 + 2\varepsilon_1 - f(\varepsilon_1 - \varepsilon_2)} \qquad (1)$$

Here, spheres of permittivity ε_2 are located randomly in homogeneous environment ε_1 and occupy a volume fraction f. The observed nanoparticles are situated in air, therefore the ε_1 is 1. For dielectric function of observing nanoparticles (ε_2) we are using the standard model [15]:

$$\varepsilon_2(\omega) = \varepsilon_\infty + \sum_{k=1}^{l} \frac{\varepsilon_\infty\left(\omega_{LOk}^2 - \omega_{TOk}^2\right)}{\omega_{TOk}^2 - \omega^2 - i\gamma_{TOk}\omega} - \frac{\varepsilon_\infty\omega_P^2}{\omega\left(\omega + i\tau^{-1}\right)} \qquad (2)$$

where ε_∞ is dielectric constant at high frequencies, ω_{TOk} and ω_{LOk} are transverse and longitudinal frequencies, γ_{TOk} is the phonon damping, ω_P is the plasma frequency and τ is the free carrier relaxation time. The first term in (2) is the lattice contribution whereas the second term is the Drude expression for the free carrier contribution to the dielectric constant. In this case, ω_{TOk} is considered as characteristic frequency of the material and ω_{LOk} is connected with the oscillator strength ($S_k \sim \omega_{LOk}^2 - \omega_{TOk}^2$).

The far-infrared spectra of non-irradiated and irradiated MnO nanopowders, in the spectral range of 80 to 600 cm^{-1}, at room temperature are presented in Fig. 2. The experimental data are presented by circles, while the solid lines are calculated spectra obtained by a fitting procedure based on the previously presented model. Obviously, a very good correlation between experimental data and calculated spectra is achieved. Parameters, such as: filling factors, *f*, plasma frequencies, ω_P, effective permittivity of mixtures, ε_{eff}, and transversal and longitudinal frequencies ω_{TO}/ω_{LO}, for the non-irradiated and irradiated sample, estimated from the reflection spectra, are presented in Table 1. Induced laser heating leads to the increasing of the filling factor. Result is expected and in agreement with result obtained by AFM. Namely, phase transformation and loss of the grain boundaries leads to the decreasing of the space between particles. In accordance with that, the dielectric constant at high frequencies and plasma frequency decrease. Also, we should keep in mind that surface affected by the laser beam

is significantly smaller (radius 1 mm) in comparison with the overall surface of the pallet (radius 6 mm) which means that, in the case of the irradiation of the whole sample the differences would be more significant.
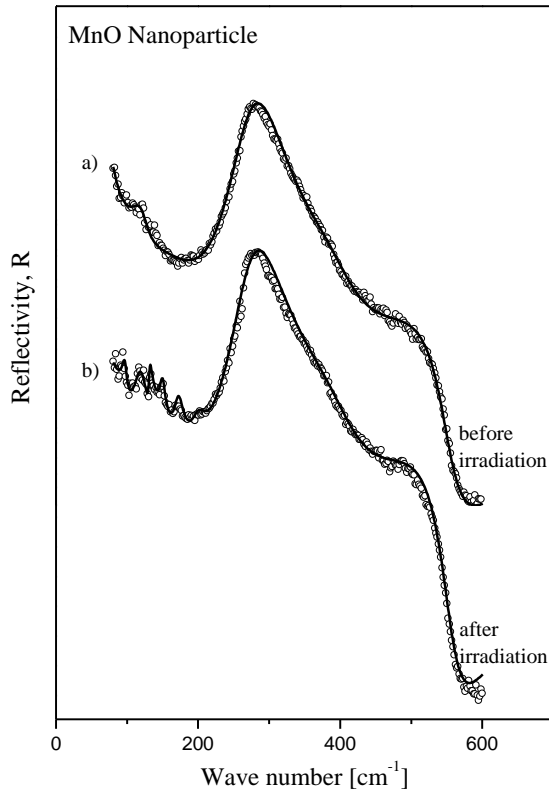

MnO Nanoparticle

Fig. 2. Far – infrared reflection spectra of (a) non-irradiated and (b) irradiated MnO nanoparticles. The experimental data are represented by circles. The solid lines are the calculated spectra obtained by fitting procedure based on the model given by Eqs. (1,2)

Five vibration modes were determined for both non-irradiated and irradiated sample and their values are presented in Table 1. To our knowledge, there are no literature data for the FIR characterization of the MnO and we compared these results with data collected by Raman spectroscopy. By summarizing different literature data [12, 16-24], three characteristics peaks for MnO are obtained in the range 520-545, 559-595 and 645-660 cm^{-1}. First two peaks we registered by using FIR spectroscopy, also. In both cases, non-irradiated and irradiated sample, additional two peaks, in the range of 310-410 cm^{-1} are recorded. According to literature data, these peaks can be attributed to the β-MnO$_2$ (TO/LO pair at 324/330cm^{-1}) [18, 22, 23] and α-MnO$_2$ (395/405cm^{-1}) [20, 21]. Additionally, according to Kim at al. [24] peak at 324 cm^{-1} can be attributed to Mn$_3$O$_4$.

Additional vibration peaks that appear in FIR spectra of irradiated samples can be identified in the following way: peaks at 131, 140, 171 and 199.5 cm^{-1} could be attributed to a α–MnOOH [20, 21] and peak at 171.5 cm^{-1} could be attributed to α–MnO$_2$ [20, 21].

Some authors peak at 171 cm^{-1} attributed to Mn$_5$O$_8$ phase (binary Mn$_2^{2+}$Mn$_3^{4+}$O$_8$ oxide with layer structure) [25]. These peaks are also registered at Raman spectra of the irradiated samples.

Table 1. Calculated fit parameters obtained from the far-infrared spectra of non-irradiated and irradiated MnO nanoparticles

	Before irradiation [cm^{-1}]	After irradiation [cm^{-1}]
f	0.81	0.89
ω_P	301	291
ε_∞	2.8	2.5
ω_{TO}/ω_{LO}	120/123	116.8/117
ω_{TO}/ω_{LO}	140/148	140/140
ω_{TO}/ω_{LO}	324/330	320/330
ω_{TO}/ω_{LO}	395/405	398/407
ω_{TO}/ω_{LO}	520/526	515/558
ω_{TO}/ω_{LO}	575/590	579/584
ω_{TO}/ω_{LO}	-	96.8/97.4
ω_{TO}/ω_{LO}	-	131/131.3
ω_{TO}/ω_{LO}	-	140/141
ω_{TO}/ω_{LO}	-	171.5/172
ω_{TO}/ω_{LO}	-	199.5/200

Mode at about 100 cm^{-1} (TO/LO pair is 116.8/117 cm^{-1} in our case) was registered before for this group of materials [26] as a "defect mode". Mod at 96.8/97.4 cm^{-1}, in the some region, can be describe us „defect mode", also. However, since it occurs only in an irradiated sample, we can assume that we have a case of disorder-enabled phonon (DAP) mode [27]. This is the case registered in a large number of A^{2}B^6 semiconductors [28].

Finally, it was shown that FIR spectroscopy is a useful technique for the characterization of laser power induced phase changes in MnO nanoparticles.

4. Conclusion

MnO nanoparticles modified by laser heating are investigated by using far-infrared spectroscopy. Effective permitivity of MnO nanoparticles (mixture of homogeneous spherical inclusions in air) are modeling by Maxwell-Garnet formula. In consequence of laser irradiation, volume fraction of nanoparticles increase while dielectric constant and plasma frequencies decrease, due to the formation of the different species on the surface of the MnO sample.

Additional vibration modes characteristic for the irradiated samples, were confirmed by using FIR method.

References

[1] M. Jimenez-Melendo, A. Dominguez-Rodriguez, J. Castaing, Acta Metallurgica et Materialia **43**, 3589 (1995).

[2] R. Aragon, Physical Review B **46,** 5328 (1992).

[3] M. J. Radler, J. B. Cohen, G. P. Sykora, T. Mason, D. E. Ellis, J. Faber Jr., Journal of Physics and Chemistry of Solids **53**, 141 (1992).

[4] M. Hiramoto, N. Okinaka, T. Akyimam, Materials Chemistry and Physics **134**, 98 (2012).

[5] I. Djerdj, D. Arcon, Z. Jaglicic, M. Niederberger, Journal of Physical Chemistry C **111**, 3614 (2007).

[6] N. Mironova-Ulmane, A. Kuzmin, M. Grube, Journal of Alloys and Compounds **480**, 97 (2009).

[7] J. Park, E. Kang, C. J. Bae, J. G. Park, H. J. Noh, J. Y. Kim, J. H. Park, H. M. Park, T. Hyeon, Journal of Physical Chemistry B **108**, 13594 (2004).

[8] A. E. Berkowitz, G. F. Rodriguez, J. I. Hong, K. An, T. Hyeon, A. Agarwal, D. J. Smith, E. E. Fullerton, Physical Review B **77**, 024403 (2008).

[9] J. J. Hauser, J. V. Waszczak, Physical Review B **30**, 5167 (1984).

[10] B. Hadžić, N. Romčević, D. Sibera, U. Narkiewicz, I. Kurylisyn-Kudelska, W. Dobrowolski, M. Romčević, Journal of Physics and Chemistry of Solids **91**, 80 (2016).

[11] A. Kovačević, J. Ristić-Djurović, M. Lekić, B. Hadžić, G. Saleh Isa Abudagel, S. Petričević, P. Mihailović, B. Matović, D. Dramlić, Lj. Brajović, N. Romčević, Materials Research Bulletin **83**, 284 (2016).

[12] B. Hadzic, B. Vasic, B. Matovic, I. Kuryliszyn-Kudelska, W. Dobrowolski, M. Romcevic, N. Romcevic, Journal of Raman Spectroscopy (2018) in press.

[13] K. Karkkainen, A. Sihvola, K. Nikoskinen, IEEE Transactions on Geoscience and Remote Sensing **39**, 1013 (2001).

[14] J. C. M. Garnett, Philosophical Transactions of the Royal Society of London, Series A **203** 385 (1904).

[15] J. Trajic, N. Romcevic, M. Romcevic, V. N. Nikiforov, Materials Research Bulletin **42**, 2192 (2007).

[16] F. Buciuman, F. Patcas, R. Cracium, D. R. T. Zahn, Physical Chemistry Chemical Physics **1**, 185 (1999).

[17] C. Julien, M. Massot, R. Baddour-Hadjean, S. Franger, S. Bach, J. P. Pereira-Ramos, Solid State Ionics **159**, 345346 (2003).

[18] C. M. Julien, M. Massot, C. Poinsignon, Spectrochimica Acta Part A **60**, 689 (2004).

[19] B. K. Pandey, A. K. Shahi, R. Gopal, Materials Focus **2**, 221 (2013).

[20] T. Gao, H. Fjellvag, P. Norby, Analytica Chimica Acta **648**, 235 (2009).

[21] S. Cheng, L. Yang, D. Chen, X. Ji, Z.-J. Jiang, D. Ding, M. Liu, Nano Energy **9** 161 (2014).

[22] C. M. Julien, M. Massot, Proceedings of the International Workshop Advanced Techniques for Energy Sources Investigation and Testing, Sofia, Bulgaria, September 2004, pp. 1–17.

[23] S. Kumar, A. K. Ojha, R. K. Singh, Journal of Raman Spectroscopy **45**, 717 (2014).

[24] M. Kim, X. M. Chen, X. Wang, C. S. Nelson, R. Budakian, P. Abbamonte, S. L. Cooper, Physical Review B **84**, 174424 (2011).

[25] J. Gao, M. A. Lowe, H.D. Abruna, Chemistry of Materials **23**, 3223 (2011).

[26] H. Kepa, T. Giebultowicz, B. Buras, B. Lebech, K. Clausen, Physica Scripta **25**(6A), 807 (1982).

[27] V. Dzagan, I. Lokteva, C. Himcinschi, X. Jin, J. Kolny-Olesik, D. R. T. Zahn, Nanoscale Research Letters **6**, 79 (2011).

[28] A. Ingale, K. C. Rustagi, Physical Review B **58**, 7197 (1998).

*Corresponding author: jelena@ipb.ac.rs